[redacted]

COPY 903

NATIONAL ADVISORY COMMITTEE FOR AERONAUTICS

NACA CONFERENCE ON AERODYNAMICS OF HIGH-SPEED AIRCRAFT

A COMPILATION OF THE PAPERS PRESENTED

Langley Aeronautical Laboratory
Langley Field, Virginia

NOVEMBER 1, 2, and 3, 1955

(NASA-TM-X-70033) NACA CONFERENCE ON AERODYNAMICS OF HIGH SPEED AIRCRAFT (NASA)

N74-73260
THRU
N74-73304
Unclas
00/99 36700

607

Z

NACA CONFERENCE ON

AERODYNAMICS OF HIGH-SPEED AIRCRAFT

A Compilation of the Papers Presented

Langley Aeronautical Laboratory
Langley Field, Va.

Nov. 1, 2, and 3, 1955

[redacted]

TABLE OF CONTENTS

Preceding page blank

Page

Page

INTRODUCTION

This document contains reproductions of technical papers presented by staff members of the NACA Laboratories at the NACA Conference on Aerodynamics of High-Speed Aircraft held at the Langley Aeronautical Laboratory November 1, 2, and 3, 1955. The primary purpose of the conference was to convey to contractors of the military services and others concerned with the design of aircraft the results of recent research and to provide those attending with an opportunity to discuss these results.

The papers in this document are in the same form in which they were orally presented at the conference to facilitate their prompt distribution. The original presentation and this record are considered as complementary to, rather than as substitutes for, the Committee's more complete and formal reports.

A list of the conferees is included.

Z

[redacted]

LIST OF CONFEREES

The following were registered at the NACA Conference on Aerodynamics of High-Speed Aircraft, Langley Aeronautical Laboratory, Langley Field, Va., November 1, 2, and 3, 1955:

ABBOTT, Ira H.	NACA Headquarters
ADAMSON, David	NACA - Langley Laboratory
ALEXANDER, John D.	Boeing Airplane Company
ALFORD, Joseph S.	Subcommittee on Internal Flow
ALFORD, William J., Jr.	NACA - Langley Laboratory
ALLEN, H. Julian	NACA - Ames Laboratory
AMES, Milton B.	NACA Headquarters
ANDERSON, Harvey L	Wright Air Development Center
ANDERSON, J. Edward	Minneapolis-Honeywell Regulator Co.
ANDERSON, Maj. Philip B., Jr.	Wright Air Development Center
ANTONATOS, Philip P.	Wright Air Development Center
ARCIDIACONO, Thomas	Fairchild Engine and Airplane Corp.
ARMSTRONG, Neil A.	NACA High-Speed Flight Station
ARMSTRONG, Lt. William O.	Wright Air Development Center
ARNDT, Comdr. Ralph W.	U. S. Naval Postgraduate School
ARONSON, Moses	Office of Naval Research, Sands Point
ATRAN, Leonard	Westinghouse Electric Corporation
AYDELOTTE, John H.	Boeing Airplane Company
BAKER, Paul	Republic Aviation Corporation
BAKER, Thomas F.	NACA High-Speed Flight Station
BARNES, Maj. Levi A.	Armed Forces Special Weapons Project, Albuquerque
BARON, Judson R.	Naval Supersonic Laboratory - M.I.T.
BASHARK, Nicholas	Air Research and Development Command, Wright-Patterson AFB
BEACH, William C.	North American Aviation, Inc.
BECK, Lt. Comdr. P. E.	Bureau of Aeronautics
BECKER, John V.	NACA - Langley Laboratory
BECKETT, Lt. Col. Walter R.	Air Research and Development Command, Baltimore
BEELER, De Elroy	NACA High-Speed Flight Station
BELCHER, Paul J.	Wright Air Development Center
BELL, Harold W.	North American Aviation, Inc.
BELLMAN, Donald R.	NACA High-Speed Flight Station
BENNETT, Dwight H.	Convair
BENSON, Willard R.	Picatinny Arsenal
BERINATI, V.	Bureau of Aeronautics
BERKOW, Lt. Col. Joseph J.	Wright Air Development Center
BERLER, Irving	Sperry Gyroscope Co.
BIELKOWICZ, Peter	USAF Institute of Technology, Wright-Patterson AFB

Preceding page blank

BIRD, John D.	NACA - Langley Laboratory
BITONDO, Domenic	Aerophysics Development Corporation
BITTERMAN, Norman G.	Wright Air Development Center
BLAIR, Morgan M.	North American Aviation, Inc.
BLEAKNEY, William M.	Hughes Aircraft Company
BLEICH, Lewis A.	Lear, Inc.
BLOM, Trygve	Wright Air Development Center
BLOOM, Harold L.	General Electric Company
BOATRIGHT, William B.	NACA - Langley Laboratory
BOBBITT, Percy J.	NACA - Langley Laboratory
BOCCIUS, Walter G. C.	Wright Air Development Center
BOGDONOFF, Seymour M.	Princeton University
BONNEY, E. Arthur	Applied Physics Laboratory - J.H.U.
BOTH, Capt. Harold, Jr.	Air University, Maxwell AFB
BRADSHAW, H. R.	Bureau of Aeronautics
BRAME, Charles B.	United Aircraft Corporation
BRAUN, Gerhard W.	Holloman Air Development Center
BRENHOLTZ, Maj. George	Air Research and Development Command, Baltimore
BRESSETTE, Walter E.	NACA - Langley Laboratory
BRITT, Maj. Daniel T., Jr.	Air Research and Development Command, Wright-Patterson AFB
BROBERG, R. F.	Bureau of Aeronautics
BRODSKY, Robert F.	Sandia Corporation
BROWN, Charles G.	Douglas Aircraft Company, Inc.
BROWN, Harvey H.	NACA Headquarters
BRUNO, Joseph F.	Bureau of Aeronautics
BRUNOW, Charles L.	Temco Aircraft Corporation
BRYAN, Brig. Gen. Thomas L., Jr.	Wright Air Development Center
BUCKLEY, Edmond C.	NACA - Langley Laboratory
BUFORD, William E.	Ballistic Research Laboratories, Aberdeen Proving Ground
BURSTEIN, Adolph	Convair
BUSEMANN, Dr. Adolph	NACA - Langley Laboratory
BUTMAN, Col. Paul M.	Air Research and Development Command, Kirtland AFB
BUTTERWORTH, Wesley T.	North American Aviation, Inc.
CAHILL, Jones F.	Lockheed Aircraft Corporation
CALHOUN, John T.	Beech Aircraft Corporation
CAMPBELL, John P.	NACA - Langley Laboratory
CARLSON, Harry W.	NACA - Langley Laboratory
CARLSON, John W.	Wright Air Development Center
CASH, George M.	Cornell Aeronautical Laboratory
CELNIKER, Leo	Lockheed Aircraft Corporation
CHAMBERLIN, Robert B.	General Electric Company
CHAPMAN, Charles E.	Convair
CHAPMAN, Dean R.	NACA - Ames Laboratory

CHAPMAN, G. E.	General Motors Corporation
CHARYK, Joseph V.	Lockheed Aircraft Corporation
CHAUVIN, Leo T.	NACA - Langley Laboratory
CHEILEK, Harold A.	Cornell Aeronautical Laboratory
CHUBB, Robert S.	Lockheed Aircraft Corporation
CHURCH, Arthur S.	Douglas Aircraft Company, Inc.
CLARK, John R.	Subcommittee on High-Speed Aerodynamics
CLARKE, Joseph H.	Brooklyn Polytechnic Institute
CLARKSON, Mark H.	Chance Vought Aircraft, Inc.
CLOUKEY, Capt. M. M.	Bureau of Aeronautics
COAD, Col. Hunter S.	Tactical Air Command, Langley AFB
COATES, Wendell M.	U. S. Naval Postgraduate School
COCHRAN, D.	Committee on Power Plants
COHEN, Charles J.	U. S. Naval Proving Ground, Dahlgren
COLBY, Starr J.	Douglas Aircraft Company, Inc.
COLE, Julian D.	The Rand Corporation
COLLINS, Comdr. Thomas W., Jr.	Office of Assistant Secretary of Defense for Research and Development
CONCHA, Joseph I.	Air Technical Intelligence Center, Wright-Patterson AFB
CONNORS, James F.	NACA - Lewis Laboratory
COOPER, Morton	NACA - Langley Laboratory
COWAN, Wesley	Naval Ordnance Test Station, Inyokern
CRONVICH, Lester L.	Applied Physics Laboratory, J.H.U.
CROTSLEY, Harmon H.	North American Aviation, Inc.
CROWLEY, John W.	NACA Headquarters
DAILEY, Vance	Naval Air Development Center, Johnsville
DALLOW, Thomas P.	Wright Air Development Center
DAROS, Charles	Douglas Aircraft Company, Inc.
DAY, Leroy E.	Naval Air Missile Test Center, Point Mugu
DAY, Richard E.	NACA High-Speed Flight Station
DECKER, James L.	Glenn L. Martin Company
DELL, Vernon C.	Naval Ordnance Laboratory, Corona
DELLMEIER, Guenther	Arnold Engineering Development Center, Tullahoma
DE LOS SANTOS, Socrates T.	David Taylor Model Basin
DESMOND, G. L.	Bureau of Aeronautics
DEVAULT, Robert	Marquardt Aircraft Company
DIEHL, Capt. Walter S.,	Subcommittee on Stability and Control
DISHER, John H.	NACA - Lewis Laboratory
DOMAN, James P.	Naval Air Material Center, Philadelphia
DONELY, Philip	Subcommittee on Aircraft Loads
DONLAN, Charles J.	NACA - Langley Laboratory
DOW, Norris F.	NACA - Langley Laboratory

DOWNS, William D.	Directorate of Research and Development Office, USAF
DRAKE, Douglas	Douglas Aircraft Company, Inc.
DRAKE, Hubert M.	NACA High-Speed Flight Station
DRALEY, Eugene C.	NACA - Langley Laboratory
DRELL, Harry	Lockheed Aircraft Corporation
DUBERG, John E.	NACA - Langley Laboratory
DuBOIS, Maj. Joseph M.	AF Development Field Office, NACA, Lewis Flight Propulsion Lab.
DUCOFFE, Arnold L.	Sandia Corporation
DUNCAN, Comdr. Richard L.	Naval Air Test Center, Patuxent River
DUNNING, Robert W.	NACA - Langley Laboratory
DURRENBERGER, John A.	Air Proving Ground Command, Eglin AFB
EARLY, Maj. James W.	Wright Air Development Center
EATON, Bruce G.	Westinghouse Electric Corporation
EBER, Gerhard R.	Air Development Center, Holloman AFB
EDKINS, D. P.	General Electric Company
EDWARDS, Richard H.	Hughes Aircraft Company
EINBINDER, Seymour K.	Picatinny Arsenal
ELLIS, Frampton E., Jr.	Bureau of Aeronautics
EMMONS, Paul C.	Bell Aircraft Corporation
ENGLERT, Gerald W.	NACA - Lewis Laboratory
EPSTEIN, Albert	Republic Aviation Corporation
EVANS, Albert J.	NACA Headquarters
EVANS, George	Sperry Gyroscope Company
EVANS, Melville B.	Convair
EVVARD, John C.	NACA - Lewis Laboratory
FAGET, Maxime A.	NACA - Langley Laboratory
FAGIN, Sydney	Naval Ordnance Laboratory, White Oak
FARBER, Joseph	General Electric Company
FAULDERS, Charles R.	North American Aviation, Inc.
FEDZIUK, Henry A.	NACA - Langley Laboratory
FINCH, Thomas W.	NACA High-Speed Flight Station
FISCHEL, Jack	NACA High-Speed Flight Station
FISHER, Robert	Marquardt Aircraft Company
FLATT, Joseph	Subcommittee on High-Speed Aerodynamics
FLEDDERMANN, Dr. Richard G.	Arnold Engineering Development Center, Tullahoma
FOLAND, Douglas H.	NACA - Langley Laboratory
FRANCIS, R. R.	Bureau of Aeronautics
FRICK, Charles W.	NACA - Ames Laboratory
FRICK, James P.	Convair
FRIEND, Carl F.	Lockheed Aircraft Corporation
FROEHLICH, Jack E.	Jet Propulsion Laboratory, C.I.T.
FUHRMAN, Robert A.	Ryan Aeronautical Company

GALOW, Gordon	Fairchild Engine and Airplane Corp.
GARDENIER, Hugh E.	Arnold Engineering Development Center, Tullahoma
GARRICK, I. E.	NACA -- Langley Laboratory
GAVIN, Joseph	Grumman Aircraft Engineering Corp.
GAYNOR, Frank A.	Subcommittee on Stability and Control
GEHRKENS, George R.	North American Aviation, Inc.
GENIESSEE, Major Eugene W., Jr.	Subcommittee on High-Speed Aerodynamics
GIBBONS, Henry B.	Chance Vought Aircraft, Inc.
GILRUTH, Robert R.	NACA - Langley Laboratory
GILSTAD, D. A.	Subcommittee on Aircraft Loads
GLUYAS, G. L.	Northrop Aircraft, Inc.
GODDARD, Frank	Jet Propulsion Laboratory, C.I.T.
GOETT, Harry J.	NACA - Ames Laboratory
GOODMAN, Theodore R.	Cornell Aeronautical Laboratory
GOODMANSON, Lloyd T.	Boeing Airplane Company
GOODWIN, Glen	NACA - Ames Laboratory
GOPPERT, Maj. Jean G.	AF Development Field Office, NACA, Langley Field, Va.
GORMAN, Comdr. Frank B.	Technical Office of BuAer, Wright-Patterson AFB
GOUGH, Melvin N.	NACA - Langley Laboratory
GRAHAM, Ernest W.	Douglas Aircraft Company, Inc.
GROGAN, G. C., Jr.	Convair
GUMBEL, Harold	Naval Air Missile Test Center, Point Mugu
GUSTAFSON, Robert	Subcommittee on High-Speed Aerodynamics
HALL, Russell S.	General Motors Corporation
HALLETT, Raymond	Douglas Aircraft Company, Inc.
HALLICK, Peter	Bureau of Aeronautics
HALLISSY, Joseph M., Jr.	NACA - Langley Laboratory
HAMILTON, William T.	Boeing Airplane Company
HARGIS, Calvin B.	Wright Air Development Center
HARKINS, Wallace H.	Marquardt Aircraft Company
HARKNESS, John L.	Defense Research Laboratory, University of Texas
HARRIS, T. Aubrey	NACA - Langley Laboratory
HARSHMAN, Jack D.	Boeing Airplane Company
HARTLEY, Richard M.	David Taylor Model Basin
HARVIE, Stuart	Grumman Aircraft Engineering Corp.
HASERT, Chester N.	AF Scientific Advisory Board
HAUSMANN, George F.	United Aircraft Corporation
HAYES, Dr. Wallace D.	Subcommittee on Fluid Mechanics
HAYNES, E.	Subcommittee on Fluid Mechanics
HEDRICK, Ira Grant	Grumman Aircraft Engineering Corp.
HEDRICK, William S.	FluiDyne Engineering Corporation
HELDENFELS, Richard R.	NACA - Langley Laboratory

HELFMAN, Sidney	Republic Aviation Corporation
HELMICK, Col. Paul F.	Air University, Maxwell AFB
HENDERSON, Arthur, Jr.	NACA - Langley Laboratory
HENRY, B. Z., Jr.	NACA - Langley Laboratory
HENRY, John R.	NACA - Langley Laboratory
HENSLEY, Reece V.	Fairchild Engine and Airplane Corp.
HEPPE, Ralph R.	Lockheed Aircraft Corporation
HEYDON, Douglas	Sperry Gyroscope Company
HIGGINS, Harry C.	Boeing Airplane Company
HILL, Paul R.	NACA - Langley Laboratory
HIPPLER, Jack B.	David Taylor Model Basin
HOADLEY, Henry H.	United Aircraft Corporation
HOFFMAN, Sherwood	NACA - Langley Laboratory
HOLDHUSEN, James S.	FluiDyne Engineering Corporation
HOLLENBERG, H. O.	Bureau of Aeronautics
HOLTBY, Kenneth F.	Boeing Airplane Company
HONG, James	Lockheed Aircraft Corporation
HORNER, Richard E.	AF Directorate of Requirements Office
HOYT, Herbert W.	Air Proving Ground Command, Eglin AFB
HUBBARD, Elbert C.	Naval Proving Ground, Dahlgren
HUBERT, Joseph	Grumman Aircraft Engineering Corp.
HUDSON, Verne L.	Boeing Airplane Company
HUFTON, P. A.	Royal Aircraft Establishment
HUTTON, Richard	Grumman Aircraft Engineering Corp.
HYATT, A.	Bureau of Aeronautics
INGHAM, Maj. John S.	Arnold Engineering Development Center, Tullahoma
ISENBERG, Joel S.	Bell Aircraft Corporation
IVEY, H. Reese	Tactical Air Command, Langley AFB
JACKOVICH, James C.	Air Technical Intelligence Center, Wright-Patterson AFB
JACKSON, David	Wright Air Development Center
JAGIELLO, Leonard	Naval Ordnance Test Station, Inyokern
JARMOLOW, Kenneth	Glenn L. Martin Company
JEWELL, Lt. Lawrence	Air Force Special Weapons Center, Kirtland AFB
JOHNSON, Roger P.	The Rand Corporation
JOHNSTON, Robert B.	The Rand Corporation
JOLINE, Everett	Sperry Gyroscope Company
JONES, Jim J.	NACA - Langley Laboratory
JONES, Maj. Kenneth L.	Wright Air Development Center
JONES, Robert T.	NACA - Ames Laboratory
KAPLAN, Carl	NACA - Langley Laboratory
KAPPUS, Peter	General Electric Company
KATKOV, R. B.	Northrop Aircraft, Inc.

KATZEN, Elliott D.	NACA - Ames Laboratory
KAUFMAN, Harold	Naval Air Development Center, Johnsville
KAVANAU, Lawrence L.	Lockheed Aircraft Corporation
KELLY, Howard	Naval Ordnance Test Station, Inyokern
KELLY, Mark W.	NACA - Ames Laboratory
KELSO, William R.	AF Directorate of Requirements Office
KINTAS, John	Beech Aircraft Corporation
KISTLER, Alan L.	Ballistic Research Laboratories, Aberdeen Proving Ground
KLAMPE, Dean G.	Ryan Aeronautical Company
KLECKNER, Harold F.	Douglas Aircraft Company, Inc.
KLEPINGER, Richard H.	Wright Air Development Center
KLINAR, Walter J.	NACA - Langley Laboratory
KNEMEYER, Franklin	Naval Ordnance Test Station, Inyokern
KNIGHT, Richard	Goodyear Aircraft Corporation
KOSSON, Robert L.	Curtiss-Wright Corporation
KUNEN, Alfred	Republic Aviation Corporation
KURZWEG, Dr. H. H.	Subcommittee on High-Speed Aerodynamics
LAMAR, William E.	Air Research and Development Command, Wright-Patterson AFB
LAMBERT, Lt. Col. Blake W.	Wright Air Development Center
LAPIN, Ellis E.	Douglas Aircraft Company, Inc.
LARSEN, Harold C.	USAF Institute of Technology, Wright-Patterson AFB
LAU, Conrad A.	Subcommittee on Stability and Control
LAVENDER, Robert	Redstone Arsenal
LEBOVITS, Morris	Radioplane Corporation
LEE, James M.	Bureau of Aeronautics
LEE, John G.	Subcommittee on High-Speed Aerodynamics
LEKUS, Louis J.	Chrysler Corporation
LEVY, Lionel L.	NACA - Ames Laboratory
LIGON, W. M.	Bureau of Aeronautics
LIN, Shao-Chi	AVCO Manufacturing Corporation
LINDEN, J. E.	Bureau of Aeronautics
LOBB, Rodmond K.	Naval Ordnance Laboratory, White Oak
LOBRECHT, Dorr, Jr.	Convair
LOCKE, F. W. S.	Bureau of Aeronautics
LOMAX, Harvard	NACA - Ames Laboratory
LONG, Col. Paul J.	Armed Forces Special Weapons Project, Albuquerque
LONGFELDER, Harlowe J.	Boeing Airplane Company
LOUDEN, F. A.	Committee on Aerodynamics
LOVE, Eugene S.	NACA - Langley Laboratory
LOWRIE, Walter O.	Glenn L. Martin Company
LOWRY, John G.	NACA - Langley Laboratory
LU, Hoshen	Republic Aviation Corporation

LUECHT, John W.	Chrysler Corporation
LUECK, David W.	Air Research and Development Command, Baltimore
MACALLISTER, Leonard C.	Ballistic Research Laboratories, Aberdeen Proving Ground
MAGNUS, Richard	Aerophysics Development Corporation
MALTHAN, Leonard V., Jr.	Douglas Aircraft Company, Inc.
MALVESTUTO, Frank S.	NACA - Langley Laboratory
MARGOLIS, Kenneth	NACA - Langley Laboratory
MARKS, Thomas R.	Westinghouse Electric Corporation
MARX, Michael F.	General Electric Company
MATTESON, R. C.	Subcommittee on Compressors and Turbines
MATTSON, Axel T.	NACA - Langley Laboratory
MAY, Ralph W.	NACA Headquarters
MAYDEW, Randall C.	Sandia Corporation
McCARTHY, John F.	Strategic Air Command, Offutt AFB
McCARTHY, Robert V.	Radio Corporation of America
McDOWALL, C. J.	Subcommittee on Engine Performance and Operation
McKAY, John B.	NACA High-Speed Flight Station
McLEISH, Flight Lt. I. S.	RCAF Headquarters
McLELLAN, Charles H.	NACA - Langley Laboratory
MELROSE, George B.	Bell Aircraft Corporation
MENDOZA, Alfred A.	Raytheon Manufacturing Company
MILLER, Chester W.	McDonnell Aircraft Corporation
MILLER, Paul Rex	Naval Air Test Center, Patuxent River
MILLER, Percy H.	Convair
MILLER, R. T.	Subcommittee on Internal Flow
MILLER, Robert	Grumman Aircraft Engineering Corp.
MILLIKAN, Dr. Clark B.	Committee on Aerodynamics
MITCHELL, James E.	Naval Proving Ground, Dahlgren
MITCHELL, Willis B.	Convair
MONGOLD, Clarence H.	McDonnell Aircraft Corporation
MONROE, Gerald M.	Chance Vought Aircraft, Inc.
MONTANY, Eugene R.	United Aircraft Corporation
MORRIS, Dean	Douglas Aircraft Company, Inc.
MORRIS, Lt. Comdr. Robert L.	Bureau of Aeronautics
MORROW, John D.	Redstone Arsenal
MORTON, Earl E.	Fairchild Engine and Airplane Corp.
MOSSMAN, Emmet A.	NACA - Ames Laboratory
MULHOLLAND, Frank J.	Subcommittee on Stability and Control
MULTHOPP, Hans	Glenn L. Martin Co.
MURTAUGH, Clyde R.	Temco Aircraft Corporation
MUSE, Thomas C.	Office of the Assistant Secretary of Defense for Research and Development

NELSON, William J.	NACA - Langley Laboratory
NESTINGEN, I. M.	Naval Ordnance Laboratory, White Oak
NEWBERRY, Clifford	Marquardt Aircraft Company
NEWBY, C. T.	Bureau of Aeronautics
NICOLAIDES, John D.	Subcommittee on Fluid Mechanics
NIELSEN, Jack N.	NACA - Ames Laboratory
NITIKMAN, A.	Northrop Aircraft, Inc.
NOVOTNY, Maj. Edmund E.	Air Research and Development Command, Kirtland AFB
NUCCI, Louis	Republic Aviation Corporation
OBERY, Leonard J.	NACA - Lewis Laboratory
O'DONNELL, Dr. William J.	Subcommittee on Internal Flow
O'KEEFE, Charles	Republic Aviation Corporation
O'MALLEY, James A.	Bell Aircraft Company
OSBORNE, Robert S.	NACA - Langley Laboratory
OSWALD, Telford W.	Hughes Aircraft Company
OUTMAN, H. V.	McDonnell Aircraft Corporation
PALMER, Carl B.	NACA Headquarters
PARAGHAMIAN, Berg	Glenn L. Martin Company
PARKINSON, John B.	NACA - Langley Laboratory
PARSONS, Thomas Richard	Massachusetts Institute of Technology
PASSMAN, Richard	Bell Aircraft Corporation
PATTERSON, A. Graham	Aircraft Armaments, Inc.
PAXHIA, Vincent B.	Bell Aircraft Corporation
PEARSALL, Maj. David W.	Armed Forces Special Weapons Project
PEARSON, E. O.	NACA Headquarters
PENDLEY, Robert E.	Douglas Aircraft Company, Inc.
PENN, Maj. William W., Jr.	AF Development Field Representative, NACA, Ames Laboratory
PERKINS, Courtland D.	Princeton University
PFENNINGER, W.	Northrop Aircraft, Inc.
PHILLIPS, Franklyn W.	NACA Headquarters
PHILLIPS, William H.	NACA - Langley Laboratory
PIERCE, Harold B.	NACA - Langley Laboratory
PIERCY, Thomas G.	NACA - Lewis Laboratory
PIETRANGELI, Gene	Applied Physics Laboratory, J.H.U.
PILLSBURY, Elmore	Fairchild Engine and Airplane Corp.
PITTS, William C.	NACA - Ames Laboratory
PLATOU, Anders S.	Ballistic Research Laboratories, Aberdeen Proving Ground
POLHAMUS, Edward C.	NACA - Langley Laboratory
POWELL, Harry K.	Wright Air Development Center
PRATT, Perry W.	Subcommittee on Engine Performance
PUCKETT, Dr. Allen E.	Subcommittee on High-Speed Aerodynamics
PURSER, Paul E.	NACA - Langley Laboratory

QUINLAN, Clarence N.	Air Proving Ground Command, Eglin AFB
QUISENBERRY, Maj. George B.	AF Directorate of Research and Development Office
RABB, Leonard	NACA - Lewis Laboratory
RABER, Christopher L.	Naval Air Development Center, Johnsville
RAINEY, Robert W.	NACA - Langley Laboratory
RALL, Lt. Frederick T.	Subcommittee on Internal Flow
RAMOS, Lamar A.	McDonnell Aircraft Corporation
RAYMOND, Joseph L.	The Rand Corporation
REAGAN, Roscoe R.	Douglas Aircraft Company, Inc.
REID, Dr. H. J. E.	NACA - Langley Laboratory
REINHARDT, William J.	Reaction Motors, Inc.
REISERER, Comdr. R. L.	Bureau of Aeronautics
RIDLEY, Lt. Col. Jack L.	Air Force Flight Test Center, Edwards AFB
RIDYARD, Herbert W.	NACA - Langley Laboratory
RINGLEB, Frederich O.	Naval Air Material Center, Philadelphia
ROBINS, A. Warner	NACA - Langley Laboratory
ROBINSON, Robert F.	Air Research and Development Command, Baltimore
ROBINSON, Russell G.	NACA - Ames Laboratory
ROCHÉ, Jean A.	AF Development Field Office, NACA, Langley Laboratory
ROGALSKI, Stanislaw W.	Stroukoff Aircraft Corporation
ROGERS, Arthur W.	Hughes Tool Company
ROOT, L. E.	Lockheed Aircraft Corporation
ROPER, Capt. Kenneth H.	USAF Institute of Technology, Wright-Patterson AFB
ROSE, Peter H.	AVCO Manufacturing Corporation
ROSSOW, Vernon J.	NACA - Ames Laboratory
ROSTKOWSKI, Capt. Frank J.	AF Development Field Office, NACA, Lewis Flight Propulsion Laboratory
RUBESIN, Morris W.	NACA - Ames Laboratory
RUBIN, Eugene S.	Naval Supersonic Laboratory, M.I.T.
RUTOWSKI, Edward S.	Douglas Aircraft Company, Inc.
SATIN, Alexander	Subcommittee on Internal Flow
SCARBOROUGH, Robert W.	Glenn L. Martin Co.
SCHAIRER, George	Boeing Airplane Company
SCHERBERG, Max G.	Wright Air Development Center
SCHMIDT, Ross Dean	Minneapolis-Honeywell Regulator Co.
SCHMIT, Lucien A.	Massachusetts Institute of Technology
SCHUBAUER, Dr. G. B.	National Bureau of Standards
SCHWEIGER, Marvin	United Aircraft Corporation
SCHWOERER, Frank, Jr.	Westinghouse Electric Corporation
SCOLATTI, Capt. Charles A.	Wright Air Development Center

SEABERG, Ernest C.	Radio Corporation of America
SEARS, Richard I.	Raytheon Manufacturing Co.
SEIDMAN, Oscar	Bureau of Aeronautics
SEIFF, Alvin	NACA - Ames Laboratory
SELLARS, John R.	Ramo-Wooldridge Corporation
SENS, William	United Aircraft Corporation
SHAPIRO, Norman M.	Redstone Arsenal
SHATUNOFF, Stanley	Fairchild Engine and Airplane Corp.
SHAW, James R.	Air Technical Intelligence Center, Wright-Patterson AFB
SHORTAL, Joseph A.	NACA - Langley Laboratory
SISK, Thomas R.	NACA High-Speed Flight Station
SLAVIN, Leon	Naval Air Development Center, Johnsville
SLAWSKY, Zaka I.	Naval Ordnance Laboratory, White Oak
SMELT, Ronald	Arnold Engineering Development Center, Tullahoma
SMETANA, Frederick O.	University of Southern California
SMITH, C. Branson	United Aircraft Corporation
SMULL, T. L. K.	NACA Headquarters
SOLOMON, George E.	Ramo-Wooldridge Corporation
SOULE, Hartley A.	NACA - Langley Laboratory
SPANGENBERG, G. A.	Bureau of Aeronautics
SPEAKER, R. F.	Bureau of Aeronautics
SPEARMAN, M. Leroy	NACA - Langley Laboratory
STACK, John	NACA - Langley Laboratory
STARK, James	Sandia Corporation
STEELE, Paul E.	North American Aviation, Inc.
STEIGER, Capt. Arthur R.	Development Director, Kirtland AFB
STEINMETZ, H. F.	McDonnell Aircraft Corporation
STEVER, Horton G.	Office of Deputy Chief of Staff, AF Development Department
STEWART, Homer J.	Jet Propulsion Laboratory, C.I.T.
STEWART, John D.	Convair
STEWART, William	British Joint Services Mission
STOOIMAN, Leo	Hughes Aircraft Company
STOUT, Maj. Byford H.	Air Research and Development Command, Wright-Patterson AFB
STROHMEYER, William E.	North American Aviation, Inc.
STROUKOFF, Michael	Stroukoff Aircraft Corporation
SWANSON, Robert S.	Lockheed Aircraft Corporation
SWEET, Lt. Col. Floyd J.	AF Scientific Advisory Board
TAVERNETTI, Lt. Comdr. Thomas F.	Bureau of Aeronautics
TAYLOR, Harlan D.	United Aircraft Corporation
TEIG, Comdr. V. E.	Committee on Aircraft Construction
TEMPLIN, R. J.	National Research Council, Ottawa
TEPLITZ, Jerome	Bureau of Aeronautics

THERIAULT, Paul W.	Lockheed Aircraft Corporation
THOMAS, Capt. J. A.	Bureau of Aeronautics
THOMPSON, Floyd L.	NACA - Langley Laboratory
THOMPSON, M. J.	University of Texas
TILGNER, Charles, Jr.	Committee on Aerodynamics
TIMMES, Comdr. F. X.	Bureau of Aeronautics
TINNAN, Lt. Leonard M.	Air Research and Development Command, Wright-Patterson AFB
TRENHOLM, John B.	Air Research and Development Command, Wright-Patterson AFB
TRUEBLOOD, Joseph R.	Air Research and Development Command, Baltimore
TURNER, Capt. Marion R.	Air Technical Intelligence Center, Wright-Patterson AFB
ULMANN, Edward F.	NACA - Langley Laboratory
UNDERWOOD, William J.	NACA Liaison Officer, Wright-Patterson AFB
VANDREY, Julius	Glenn L. Martin Company
VANIK, Milford F.	Boeing Airplane Company
VAN VOORHIS, Stanley N.	Massachusetts Institute of Technology
VINSON, Willis D.	North American Aviation, Inc.
WADE, Merwin G.	Convair
WAINWRIGHT, John Bennett	University of Southern California
WAITE, Frederick C., Jr.	Office of Naval Research, Sands Point
WALKER, Curtis L.	NACA Headquarters
WALKER, William E.	Ryan Aeronautical Company
WALTERS, Richard L.	Applied Physics Laboratory, J.H.U.
WAUGH, Merle G.	U. S. Naval Air Missile Test Center, Point Mugu
WEBB, Henry G.	North American Aviation, Inc.
WEEKS, Lawrence M.	McDonnell Aircraft Corporation
WEIL, Joseph	NACA High-Speed Flight Station
WEILER, Robert E.	Westinghouse Electric Corporation
WEITZEN, William	AF Directorate of Research and Development
WHITCOMB, Richard T.	NACA - Langley Laboratory
WIDMER, Robert H.	Committee on Aerodynamics
WILCOX, Fred A.	NACA - Lewis Laboratory
WILD, John M.	Arnold Engineering Development Center, Tullahoma
WILLIAMS, Walter C.	NACA High-Speed Flight Station
WILSON, Herbert A., Jr.	NACA - Langley Laboratory
WILSON, Robert E.	Naval Ordnance Laboratory, White Oak
WILSON, Robert G.	North American Aviation, Inc.
WINGO, Carl H., Jr.	Naval Proving Ground, Dahlgren

WITHINGTON, Holden W.	Boeing Airplane Company
WOLCOTT, Fred W.	Douglas Aircraft Company, Inc.
WOOD, Charles C.	NACA - Langley Laboratory
WOOD, Clotaire	NACA Headquarters
WOODCOCK, Robert J.	Wright Air Development Center
WOODS, Robert J.	Committee on Aerodynamics
WRIGHT, Dr. Theodore P.	Committee on Aerodynamics
WYSZPOLSKI, Eugene F.	Bureau of Aeronautics
YOSHIHARA, Hideo	Wright Air Development Center
ZAHRINGER, J. F.	Bureau of Aeronautics

WAVE
DRAG

APPLICATION AND LIMITATIONS OF THE AREA RULE

By Axel T. Mattson and Robert S. Osborne

Langley Aeronautical Laboratory

INTRODUCTION

Understanding of the application and limitations of the area-rule concept in the transonic and supersonic speed range has been improved during the past two years. Numerous wind-tunnel, rocket-model, and flight investigations have indicated the effectiveness of the area rule when applied to specific airplanes. The fuselage contours of a number of military airplanes have been designed or redesigned on the basis of this rule. However, perhaps the most important development during the past two years has been the extension of the area rule to the supersonic range. (See refs. 1 and 2, for example.) The purpose of this paper is to illustrate the effectiveness of the area rule when applied to specific airplanes, to discuss the effect of design Mach numbers and the effect of fuselage contouring on the flow fields, to compare experimental and calculated results, and to discuss the effectiveness of the area rule at lifting conditions.

DISCUSSION

Specific airplanes.- Data obtained from tests of scale models of various specific airplane configurations conducted at the Langley 8-foot transonic tunnels and the Langley 16-foot transonic tunnel are presented in figures 1 and 2. The wave-drag coefficients presented in these and other figures in this paper were obtained by subtracting the drag at a Mach number of 0.8 from the drag at higher Mach numbers for zero-lift coefficient. The sketches show the average area distribution of the configurations.

Figure 1 presents two examples of aircraft modified for a design Mach number of 1.0. The upper area diagram is for a model of a 45° swept mid-wing fighter. The dip in the rearward portion of the area distribution corresponds to the region between the wing and the tail. The configuration was modified by adding volume to smooth out the area distribution, and the peak wave drag was reduced 25 percent. It is notable that this sizable drag reduction was achieved without major redesign of the fuselage or increase in fineness ratio and required only the addition of volume in the proper location as indicated by the area diagram. The lower area diagram is for a 60° delta-wing multi-engine bomber configuration. The high area peak is due to the piling up of fuselage, wing, and nacelle volumes. This peak was reduced by indenting the fuselage and rearranging the nacelles fore and aft. The fuselage was also lengthened, and there resulted a 30-percent decrease in peak wave drag.

Figure 2 presents data for two configurations which were modified by using the supersonic area rule for a design Mach number of 1.2. The upper area diagram represents a 60° delta-wing single-engine fighter airplane having a relatively low equivalent-body fineness ratio. The bumps and steep gradients are obvious. In order to reduce the wave drag, the fuselage length was increased approximately 13 percent, and the fuselage was redesigned rearward of the canopy by indenting for the wing and tail. By thus reducing the irregularities and increasing the equivalent-body fineness ratio, the peak wave drag was reduced about 25 percent. The example in the lower part of figure 2 represents a high-wing fighter airplane using a 42° sweptback wing. In order to reduce the steep slopes of the area diagram and give a smooth distribution, several fuselage modifications were applied. These included extending the nose slightly, submerging the canopy, extending the rearward portion of the fuselage, and adding volume to the fuselage ahead of and behind the wing. Again, the peak wave drag was reduced about 25 percent.

The area rule has also been applied to seaplanes. Both wind-tunnel tests and towing-tank tests have demonstrated that a supersonic seaplane can successfully incorporate the hydrodynamic characteristics necessary for operation in open water without aerodynamic compromise. As a matter of interest, the results of recent transonic wing-tunnel studies (ref. 3 and unpublished data) of an "area rule" designed seaplane indicated that the subsonic drag level was only slightly higher than the basic friction drag, the Mach number for drag rise was 0.925, and the supersonic drag was sufficiently low to indicate possible flight at a Mach number of 1.4.

<u>Design Mach number</u>.- The supersonic area rule states that the drag of an airplane configuration at a given supersonic speed is related to longitudinal developments of cross-sectional areas as intercepted by planes tangent to the Mach cone. As a result, a design that is optimum for one Mach number will not be optimum for another Mach number. Presented in figure 3 are some data showing how the choice of the design Mach number affects the drag at other Mach numbers. These results (ref. 4) are for a swept wing in combination with bodies contoured for area-rule design Mach numbers of 1.0, 1.2, and 1.4. The experimental zero-lift wave-drag coefficients show that the lowest wave drag was obtained at or near the design Mach number. For the configurations presented, the lowest drag at each Mach number was obtained with the fuselage designed for that Mach number.

Presented in figure 4 is a comparison of the variation of wave-drag coefficient with Mach number for three straight-wing models. One of these is unindented and the other two are indented for $M = 1.10$ and

$M = 1.41$ (ref. 5). Both the indentation for a Mach number of 1.10 and the indentation for a Mach number of 1.41 reduced the wave drag of the basic configuration at low supersonic speeds with the greater reduction being obtained from the Mach number 1.10 indentation. The beneficial effects from the indentations decreased with increasing Mach number up to 1.3, above which no benefits were obtained from either indentation. Both indented configurations had approximately the same wave drag above a Mach number of 1.15.

It is of interest to note that for the swept-wing models, where all indented configurations exhibited substantial drag savings over the Mach number range tested with respect to the basic body configuration (see ref. 4), the wing leading edge was swept behind the Mach line at all supersonic Mach numbers considered. For the straight-wing case, however, the wing leading edge was ahead of the Mach line at Mach numbers of 1.10 and above, and it is apparent that it is in this Mach number range that the benefits of body contouring decrease.

Induced local flow fields.- It has been shown that the wave drag of a wing-body configuration can be reduced by indenting or contouring the body. The mechanism by which this drag reduction is achieved can be somewhat better understood if the local flow field in the vicinity of the wing and body is examined. Figure 5 gives a little insight into the mechanism by which body indentation manages to reduce the drag. Plotted in this figure are contours obtained from pressure-distribution measurements made in the Langley 8-foot transonic tunnel of the increment in local pressure coefficient due to indenting the fuselage. The incremental pressure coefficients shown were obtained by subtracting the pressure coefficients of the wing in the presence of the basic body from those of the wing in the presence of a body indented for a design Mach number of 1.2. The data are for an angle of attack of 0° and a Mach number of 1.13. The wing geometry is described in reference 4.

It can be seen that indenting the fuselage caused a reduction in pressure over the forward half of the wing and an increase in pressure over the rearward half of the wing which obviously reduces the pressure drag of the wing. The reduction in pressure forward is the result of expansion waves from the beginning of the indentation where the fuselage narrows down; the increase in pressure at the rear is due to compression waves from the portion of the indentation where the diameter increases. The expansion field dissipates rapidly as it travels across the span. The compression field, however, maintains its strength for a considerable distance across the span. Although the wing was cambered, the pressure contours over the lower surface of the wing were similar to those over the upper surface. It appears that the pressure fields cross the wing at approximately the Mach angle of the free-stream flow. Also, since the zero-pressure line and the line of maximum thickness of the wing should coincide for minimum drag, the design Mach number should influence the position of the maximum thickness line.

Presented in figure 6 is the spanwise distribution of pressure drag of the wing-body combination just discussed at an angle of attack of 0° and a Mach number of 1.13. It can be seen that reductions in drag are realized up to approximately 60 percent of the semispan of the wing with smaller reductions extending out to the wing tips. The reduction in wing pressure drag due to body indentation (represented by the region between the two curves) is approximately 80 percent of the total reduction obtained for the wing-body configuration. The remaining 20 percent is due to the favorable effect of the distribution of pressures over the indented fuselage.

Configuration geometry.- With regard to minimizing wave drag in general, it may be worthwhile to mention some observations based on the experimental and analytical experience of the National Advisory Committee for Aeronautics with the area rule. It is obvious that, when the necessary different series of area cuts are made down the vertical plane, down the horizontal plane, and down the planes in between, it is desirable for the area distributions to be smooth for all of these area cuts. There is a fair chance of achieving this, by appropriate body contouring, when the leading edge is swept behind the Mach lines. With insufficient sweep, it becomes impossible to get smooth area distributions in all the planes; and the possible improvements that can be attained by body contouring are limited.

Another way of approaching smooth area distributions in all the area cuts is to have most of the airplane volume close to the fuselage, as is fairly obvious geometrically. Experimental results do, in fact, show that the effectiveness of body contouring is increased when the centroid of the wing volume is inboard. This is a rather fortunate conclusion from the point of view of the structures man, who would prefer to taper the wing in thickness, with the thickest part near the root.

Inlet mass flow.- With regard to applying the area-rule concept to a configuration with inlet flow, the simplified procedure of removing a constant equivalent stream tube area from the inlet to the exit corresponding to the inlet mass flow is used. This procedure has been experimentally verified for bodies of revolution having inlet flow. It is obvious, however, that this procedure has practical limitations for inlets other than nose inlets (such as side inlets) when the inlet mass-flow ratios are less than 1. For example, removing 70 percent of the inlet area will leave sizable steps in the area curves. However, in lieu of this, one method now being used is to assume an inlet mass-flow ratio of one, subtract the equivalent stream tube area from the inlet to the exit in the area curves, and estimate the slight variations in external drag with mass-flow ratio from experimental results. Since the mass-flow ratios for most supersonic configurations are close to one, this method is within the accuracy of the analytical computation of wave drag for the configuration.

Experimental and calculated wave drag.- A basic question in a discussion of the application and limitation of the area rule is how well does the calculated wave drag agree with the measured wave drag. Comparisons have been made between experimental and calculated drag obtained in the Ames 6- by 6-foot supersonic tunnel and the Langley 8-foot transonic pressure tunnel and Pilotless Aircraft Research Division for 18 configurations ranging from isolated bodies to complicated four-engine bomber-type configurations. (See table I.) The comparisons are shown in figure 7, where the experimental wave-drag coefficients are plotted vertically and the calculated wave-drag coefficients plotted horizontally for Mach numbers of 1.3 and 1.9. (The flagged symbols are for Mach number of 1.9, the plain symbols for 1.3.) The calculations are satisfactory near a Mach number of 1.0 but improve rapidly as a Mach number of 1.3 is approached. The 45° line represents perfect agreement. The agreement in many cases is good; however, the worst disagreement is of the order of 20 percent. This should be expected since the area rule is a first-order effect and does not include such effects as flow separation and local flow fields produced by individual components.

With regard to the computing method, the first and most time-consuming step is obtaining the area distributions for the various area cuts. With regard to the next step, the actual calculation, some recent work by Holdaway and Mersman (ref. 6) results in a considerable improvement over the earlier Holdaway procedure by reducing the computing-machine time and improving the method of checking the computations.

Drag at lift.- Since the area rule is basically a zero-lift concept, it is of practical importance to know if the reductions in drag at zero lift are realized at lifting conditions. Presented in figure 8 is the drag increment due to area-rule application as a function of lift coefficient. The drag increment is the difference in drag between the basic configuration and the area-rule-modified configuration. The data are for the 60° delta-wing fighter airplane, the 45° swept mid-wing fighter airplane (fig. 1), and the 42° swept high-wing fighter airplane (fig. 2). In general, the reduction in drag is retained at the higher lifts. It appears that the relative effectiveness of the area rule at lifting conditions is a function of Mach number, configuration, and lift coefficient.

Recent application of the area rule.- Recently an investigation was conducted in the Langley 4 by 4-foot supersonic pressure tunnel and the Langley 8-foot transonic pressure tunnel to exploit the gains possible at higher Mach numbers and at lifting conditions by use of the area-rule concept. A basic wing-body combination was designed to provide high lift-drag ratios at subsonic speeds, relatively low wave drag at supersonic speeds, and satisfactory longitudinal pitching-moment characteristics. This wing-body combination was then contoured by use of the area-rule concept.

The wing selected (fig. 9) had an aspect ratio of 4 with the quarter-chord line swept 45° and a taper ratio of 0.15. The wing-section thickness ratio varied from 5 percent at the root juncture to 3 percent at the semispan and remained constant at 3 percent to the tip. The wing was cambered for a lift coefficient of 0.2. The basic body selected had a Sears-Haack shape and a fineness ratio of 12; the maximum cross-sectional area of the body was 4 percent of the wing area. This wing-body combination was then contoured according to the area-rule concept for a design Mach number of 1.4. The fuselage cross-sectional area for the contoured body was the same as the basic body near the probable center-of-gravity location, and the volume of the contoured wing-body combination was 3 percent greater than that of the basic body. The fuselage was contoured asymmetrically. The details and advantages of this asymmetrical contouring will be discussed in a later paper by Richard T. Whitcomb.

The results indicate that at the design Mach number of 1.4, the drag has been reduced by approximately 12 percent at a C_L of 0.15. The modification of the fuselage has reduced the wave drag throughout the Mach number range from 0.8 to 2. These results also indicate that for configurations with significant amounts of leading-edge sweep, body contours based on the area rule with the more recent extensions of body shaping have provided significant reductions in drag for a wide range of supersonic speeds. Since the effectiveness of body contouring is dependent on the relationship of the Mach angle to the wing geometry, it is probable that reductions in drag similar to those obtained at 1.4 for this configuration could be obtained at higher Mach numbers by using a larger amount of sweep for the wing.

Effect of nacelle arrangement.- The application of the area rule to the arrangement of components such as nacelles has been successful. The unsuccessful arrangements have been limited to configurations such as tip tanks or floats mounted on the tip of a wing with a relatively high aspect ratio, particularly if the body was to be contoured to conceal the effect of the tank. Again the limitation seems to be that of the ineffectiveness of body contouring when the centroids of the areas are too far from the body.

By use of the low-drag wing-body configuration just discussed, two four-nacelle-type configurations were investigated in the presence of the wing-body in the Langley 8-foot transonic pressure tunnel. The bodies representing the nacelles had a fineness ratio of 10. The total drag at a Mach number of 1.43 for the wing body for two four-nacelle arrangements is presented in figure 10. The nacelles were sting mounted from the rear, and, therefore, the data presented do not include the effect of pylons. However, preliminary results from recent tests including pylons indicate that the effect of adding pylons is to raise each drag curve presented by an equal amount. The lack of pylons, therefore, does not modify the interference effects shown in the figure.

Comparing the worst nacelle arrangement with the best arrangement indicates a drag decrease of approximately 14 percent at low lift coefficients. The best arrangement shown is effectively interference free. This is shown by comparing the sum of the drags of the four stores and wing-body measured separately with the combination value.

CONCLUSIONS

With respect to the application and limitations of the area-rule concept, the following conclusions can be made:

1. Recent research indicates that area-rule considerations can be effective in obtaining low wave drag up to Mach numbers of the order of 2.0.

2. Nacelle configurations in combination with a fuselage-contoured wing-body combination when arranged according to the area rule can have small interference drag.

3. At the present time, the limitations to the application of the area rule can be summarized as follows:

(a) The maximum area-rule design Mach number is limited to the case where the leading edge is swept behind the Mach lines.

(b) Effective contouring of the body according to the area rule at supersonic speeds is limited to the case where the wing centroids of cross-sectional area are relatively close to the body.

(c) The relative effectiveness of the area rule at lifting conditions is a function of Mach number, configuration, and lift coefficient.

(d) In most cases the theoretical computations based on the area-rule method are good; however, in some cases the error can be as much as 20 percent.

REFERENCES

1. Whitcomb, Richard T., and Fischetti, Thomas L.: Development of a Supersonic Area Rule and an Application to the Design of a Wing-Body Combination Having High Lift-to-Drag Ratios. NACA RM L53H31a, 1953.

2. Jones, Robert T.: Theory of Wind-Body Drag at Supersonic Speeds. NACA RM A53H18a, 1953.

3. Olson, Roland E., and Bielat, Ralph P.: An Aerodynamic and Hydrodynamic Investigation of Two Multijet Water-Based Aircraft Having Low Transonic Drag Rise. NACA RM L55A11a, 1955.

4. Loving, Donald L.: A Transonic Investigation of Changing Indentation Design Mach Number on the Aerodynamic Characteristics of a 45° Sweptback-Wing—Body Combination Designed for High Performance. NACA RM L55J07, 1955.

5. Hoffman, Sherwood, Wolff, Austin L., and Faget, Maxime A.: Flight Investigation of the Supersonic Area Rule for a Straight Wing-Body Configuration at Mach Numbers Between 0.8 and 1.5. NACA RM L55C09, 1955.

6. Holdaway, George H., and Mersman, William A.: Application of Tchebichef Form of Harmonic Analysis to the Calculation of Zero-Lift Wave Drag of Wing-Body-Tail Combinations. NACA RM A55J28, 1955.

TABLE I

CONFIGURATIONS REPRESENTED IN FIGURE 7

Configuration number	Configuration	Symbol
1	Body of revolution; F.R. = 9.8	○
2	Asymmetric body; F.R. = 10.2	□
3	53° delta wing-body	◇
4	Body of revolution (configuration 3 less wing); F.R. = 9.9	△
5	Straight-wing fighter airplane	▷
6	Configuration 5 less horizontal and vertical tails	⬦
7	Configuration 5 less wing, tail, and ducts	◊
8	60° delta wing multi-engine bomber airplane	▽
9	Configuration 8 less tail	⌂
10	53° modified delta-wing fighter airplane	◁
11	60° delta-wing fighter airplane	◸
12	Wing with basic body; $\Lambda_{c/4} = 45^{\circ}$; $A = 4$; $\lambda = 0.15$	⏢
13	Wing of configuration with body indented for $M = 1.2$	◡
14	60° delta wing-body	◇
15	Wing-body with $\Lambda_{c/4} = 45^{\circ}$; $A = 4$; $\lambda = 0.6$	◇
16	Wing-body with $\Lambda_{c/4} = 45^{\circ}$; $A = 3$; $\lambda = 0.2$	◠
17	Straight wing-body	▽
18	Body of revolution; F.R. = 10	◹

~~CONFIDENTIAL~~

AREA-RULE APPLICATION FOR M = 1.0

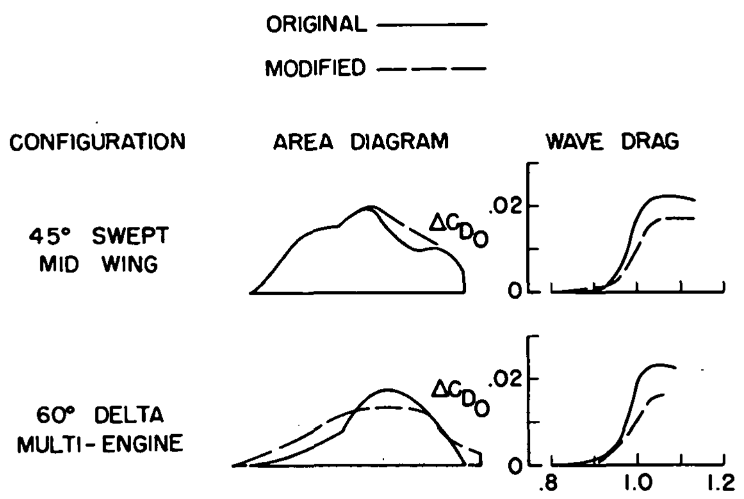

Figure 1

AREA-RULE APPLICATION FOR M=1.2

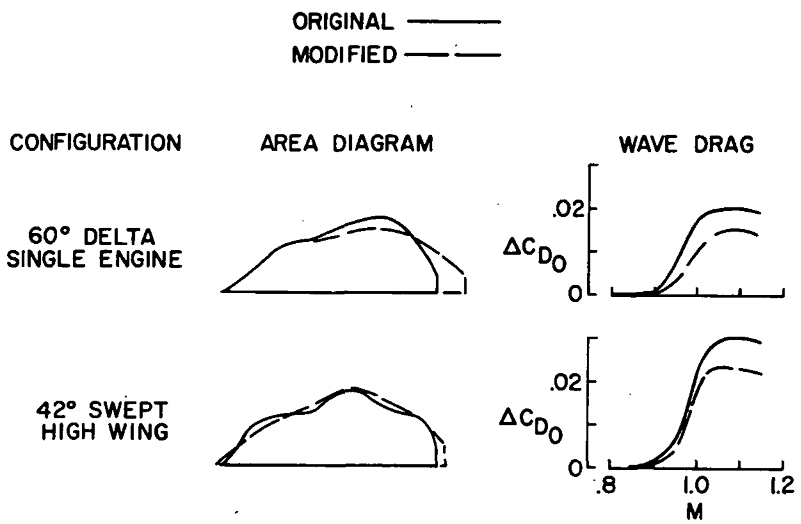

Figure 2

~~CONFIDENTIAL~~

EFFECTS OF DESIGN MACH NUMBER
SWEPT — WING CONFIGURATION

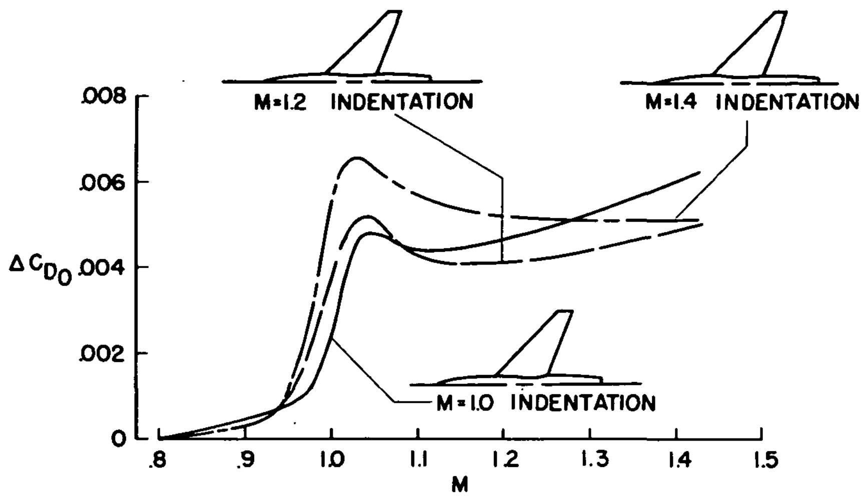

Figure 3

EFFECTS OF DESIGN MACH NUMBER
STRAIGHT — WING CONFIGURATION

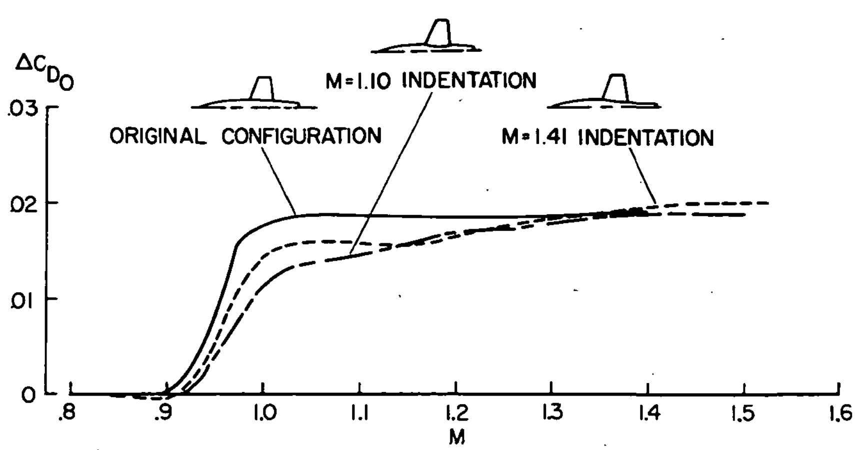

Figure 4

~~CONFIDENTIAL~~

PRESSURE-COEFFICIENT DIFFERENTIAL DUE TO INDENTATION
M=1.13; UPPER SURFACE

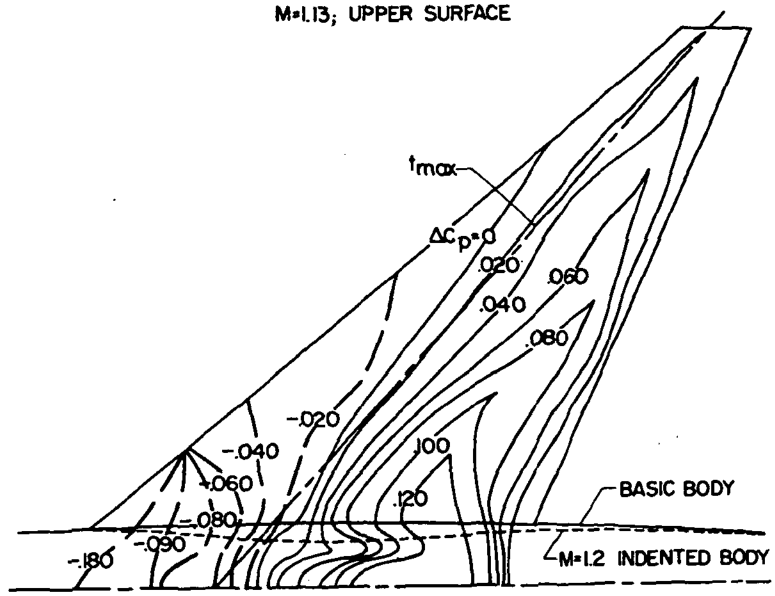

Figure 5

EFFECTS OF INDENTATION ON SPANWISE DRAG DISTRIBUTION
M=1.13

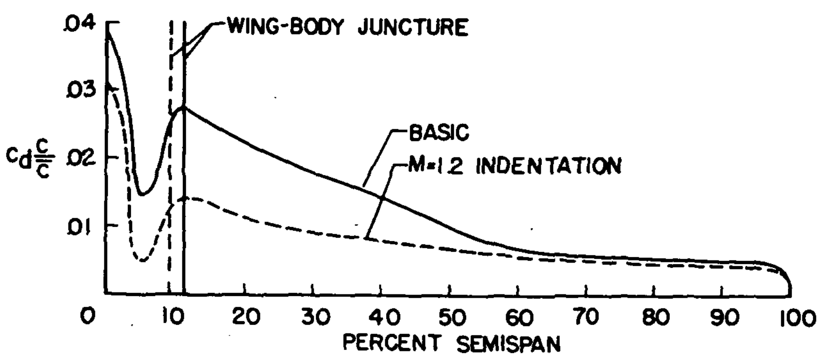

Figure 6

~~CONFIDENTIAL~~

CORRELATION OF EXPERIMENTAL AND CALCULATED WAVE DRAG

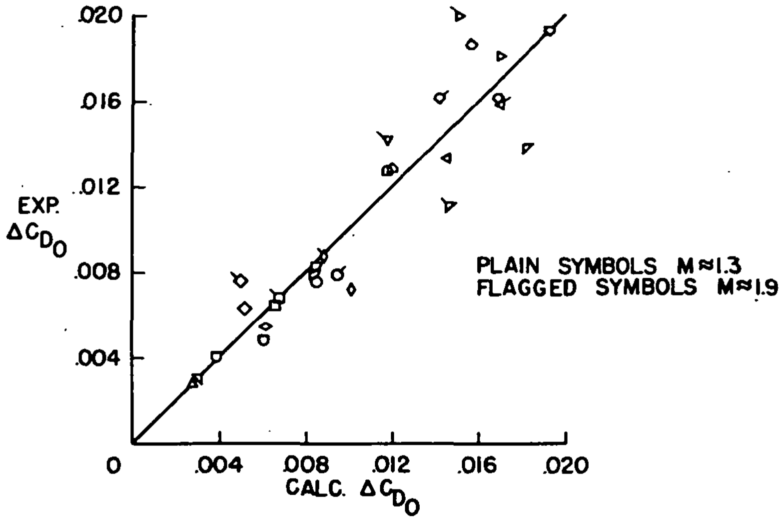

Figure 7

EFFECT OF LIFT COEFFICIENT ON DRAG REDUCTION DUE TO AREA-RULE MODIFICATION

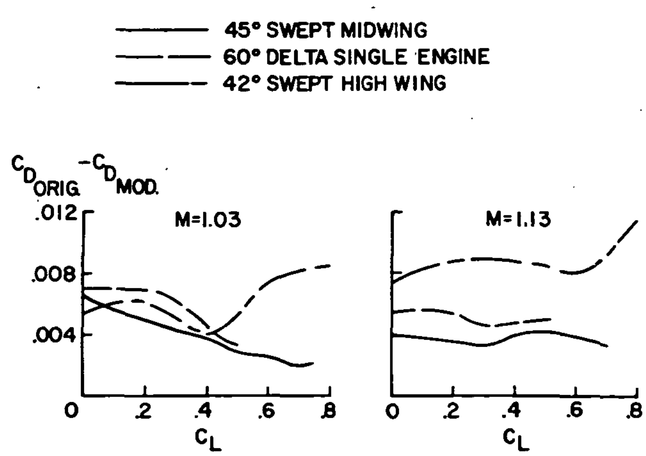

Figure 8

ASYMMETRICAL AREA-RULE APPLICATION FOR HIGHER MACH NUMBERS

$C_L = 0.15$

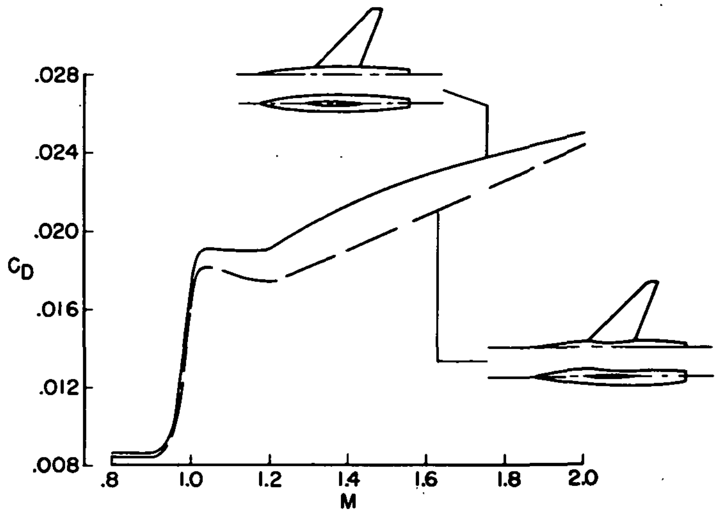

Figure 9

EFFECT OF NACELLE POSITION ON TOTAL CONFIGURATION DRAG

M = 1.43

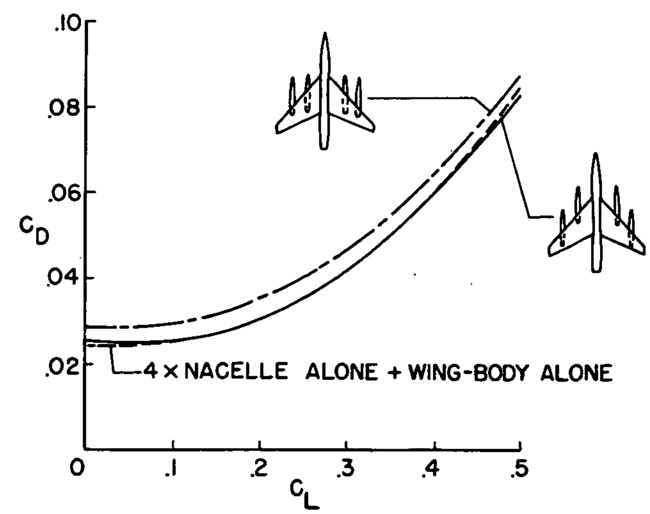

Figure 10

SEVERAL EXTENSIONS OF THE AREA RULE

By Richard T. Whitcomb

Langley Aeronautical Laboratory

This paper presents several extensions of the area rule which provide the basis for the design of fuselage contours resulting in improved drag characteristics for practical aircraft at moderate supersonic speeds. Considered are the selection of the envelope or total area development, and a method for accounting for the reflections of disturbances by the wing for asymmetrical configurations. In each case the considerations are approximations based on analyses of the physical flow rather than on analytical theory.

In order to obtain the fuselage cross-sectional area development which provides the approximate minimum wave drag for an airplane near the speed of sound, the single wing and tail areas are subtracted from the total or envelope area development which is indicated to have minimum drag characteristics for the fixed conditions for the configuration. However, at a given supersonic speed, the wing or tail has a number of area developments which may differ considerably. Consequently, a given fuselage area development cannot provide ideal total developments for each of the wing developments. A compromise fuselage area development must be utilized. Lomax and Heaslet have determined analytically (ref. 1) that, for the ideal conditions of fixed total volume and length, the compromise development which provides the minimum wave drag is obtained by subtracting the average of the area developments for the wing and tail from the total or envelope area development calculated to have minimum wave drag for such conditions. Experimental results for several configurations have indicated a similar conclusion (refs. 2 and 3, for example). It may be assumed that for the fixed conditions of practical airplanes, the minimum wave drag is obtained in a similar manner.

For most practical aircraft configurations, the cross-sectional areas are generally fixed near the nose, in the midregion, and near the tail as shown in figure 1. Obviously, in the midregion, the fixed area includes the average wing areas superimposed on fixed fuselage areas; whereas near the aft end of the airplane, the average tail areas are added to the fuselage area. At supersonic Mach numbers for the fineness ratios utilized for practical aircraft, the slender-body theory does not provide a reliable indication of the area development for minimum wave drag for such fixed conditions; the more explicit nonslender linear theory should be utilized. However, because of the extreme complexity of this more explicit theory, its use for the computation of the exact minimum-drag developments for these fixed conditions is impractical at present.

Recently, in unpublished work, Herman M. Parker, of the Langley Gas Dynamics Branch, has used this nonlinear theory to compute the minimum-drag developments for the similar but simpler conditions of fixed lengths and fixed maximum areas. Approximations of the developments for the fixed conditions of practical airplanes may be obtained through a consideration of the developments for these simpler conditions. Although such developments depend on fineness ratio and Mach number, for the values of fineness ratio of practical interest and for Mach numbers from 1.2 to 2 (the probable range in which fuselage contours will be designed on the basis of the area rule) the shapes are approximately the same. The shape for a mean condition of these ranges is shown in figure 1. It may be noted that this development consists of approximately straight lines over most of the length. This suggests that the minimum-wave-drag envelope for the fixed conditions shown at the top of the figure might be approximated by fairing straight lines tangent to the fixed area developments as shown.

The effects of fuselage modifications based on several envelope area developments have been determined during the tests of the airplane with 42° swept wings shown in figure 2. One envelope utilizes the straight-line fairings based on nonslender theory as just discussed; the other approximates that which would have minimum wave drag based on slender-body theory. The design Mach number was 1.2. The drag results obtained up to 1.2 indicate that the fuselage contours based on the straight-line fairing envelope produce significantly lower wave drag than did the contours based on the approximation of the slender-body theory. Before the nonslender theory became available, the use of the straight-line envelope rather than the slender-body-theory minimum-drag envelope was proposed as a means for improving the drag at off-design conditions. Experimental results for several configurations indicate that the use of such an envelope in preference to one based on slender-body theory reduces the wave drag at off-design conditions considerably more than at the design conditions.

The problem of reflections of disturbances by the wing or horizontal tail for asymmetrical configurations is illustrated by the sketch at the top of figure 3. Shown is the side view of a symmetric wing in combination with a fuselage indented only above the wing. Most of the disturbances of the indentation above the wing which are directed downward are reflected upward by the wing as shown; thus, the body shaping above the wing should have little effect on the flow below the wing and an exaggerated effect above the wing. (For symmetrical configurations, the reflection of disturbances produced by changes in the fuselage shape below the wing replace the disturbances produced by the upper part which could not pass through the wing. For such configurations, the reflection effects can be ignored.) The adverse effects that may be associated with such reflection of disturbances for asymmetrical configurations are illustrated by the drag results presented in figure 3. A symmetrical delta wing was investigated in combination with two indented fuselages. In one case the cross-sectional areas of the wing for a Mach number of 1 were removed symmetrically. In the other case, the total wing area was removed only above the wing. With the asymmetrical indentation, the drag was considerably higher than that for the symmetrical indentation throughout the Mach number range of the test. Further, the asymmetrical indentation produced adverse effects on the drag compared to that obtained with no indentation at Mach numbers above 1.1.

For the usual design conditions, the problem of determining these reflected effects exactly is extremely complex since the reflection is only partial. However, a reasonable approximation of the effect is obtained by assuming that the reflection is complete for disturbances originating in the region of the wing and not present for disturbances produced by the fuselage ahead of and behind the wing root. With such an assumption, the areas of the fuselage above and below the plane of the wing are considered separately; while fore and aft of the wing, the complete fuselage areas are utilized. (Such a procedure is strictly applicable only at Mach numbers where the Mach angle approaches or exceeds the wing leading-edge angle. However, experimental results for several asymmetric configurations, including those presented in figure 4, have indicated that fuselage contours based on these separate area developments provide improved reductions in drag even at lower Mach numbers.) Complete area developments necessary for the computations of drag or determination of fuselage contours are made up of the complete cross-sectional areas for the fuselage ahead of the leading edge of the wing followed by twice the variations of area with length for above or below the wing in the region of the wing as shown at the bottom of figure 3. Behind the trailing edge of the wing root, the area developments consist of the variation of area with length for the complete fuselage. In the region of the tail the variations of area above or below the tail are utilized.

The cross-sectional areas for cambered wings are divided in a similar manner, with the areas of the wing above the chord plane considered separately from those for below this plane. The wing areas for above or below the chord plane are considered with the corresponding fuselage areas. The favorable effects on drag that may be obtained through the use of fuselage contours designed on the basis of such divided areas for a cambered wing are illustrated in figure 5. The cambered 45° sweptback wing shown was tested in combination with two contoured bodies. One was shaped symmetrically using fuselage areas obtained by subtracting the average total wing areas from a favorable envelope area development; the other was shaped asymmetrically with the fuselage areas above and below the wing being obtained by subtracting twice the wing areas above and below the chord plane from favorable envelopes. Since the area for the cambered wing above the chord plane is greater than that below, the indentation of the fuselage above the wing is deeper than that below. The design Mach number was 1.4. This asymmetric configuration is the same as that described in figure 9 of the preceding paper by Axel T. Mattson and Robert S. Osborne. The drag results for a Mach number of 1.43, shown on the left, indicate that the asymmetrical indentation resulted in improvements in the drag throughout the lift-coefficient range. The reductions in drag at lift coefficients are larger than that obtained near zero lift. Such modifications also generally provide changes in the lift—pitching-moment characteristics in the positive direction which should have a favorable effect on the trim drag for most configurations at supersonic speeds. Such changes in moments obtained with asymmetric fuselages will be shown in a later paper by M. Leroy Spearman and Arthur Henderson, Jr.

In conclusion, it has been shown that, to obtain the fuselage area development which provides the approximate minimum wave drag for a usual airplane configuration at moderate supersonic speeds, the average wing and tail areas are subtracted from an envelope or total area development constructed by fairing approximately straight lines to the usual regions of fixed areas. Also, to obtain the most satisfactory reductions in drag and calculated wave drags utilizing the area rule, the area developments for the wing and fuselage above and below the wing or tail chord planes should be considered separately.

REFERENCES

1. Lomax, Harvard, and Heaslet, Max. A.: A Special Method for Finding Body Distortions That Reduce the Wave Drag of Wing and Body Combinations at Supersonic Speeds. NACA RM A55B16, 1955.

2. Loving, Donald L.: A Transonic Investigation of Changing Indentation Design Mach Number on the Aerodynamic Characteristics of a 45° Sweptback-Wing—Body Combination Designed for High Performance. NACA RM L55J07, 1955. (Prospective NACA paper.)

3. Holdaway, George H.: An Experimental Investigation of Reduction in Transonic Drag Rise at Zero Lift by the Addition of Volume to the Fuselage of a Wing-Body-Tail Configuration and a Comparison With Theory. NACA RM A54F22, 1954.

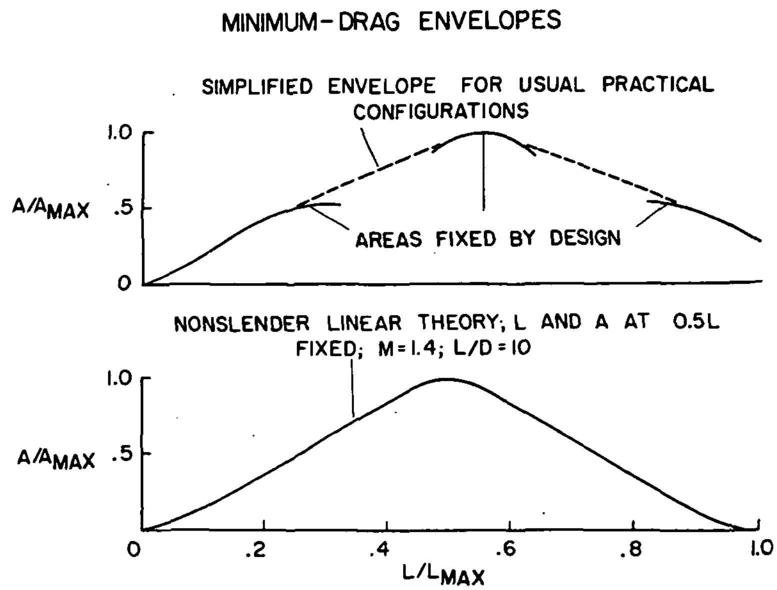

Figure 1

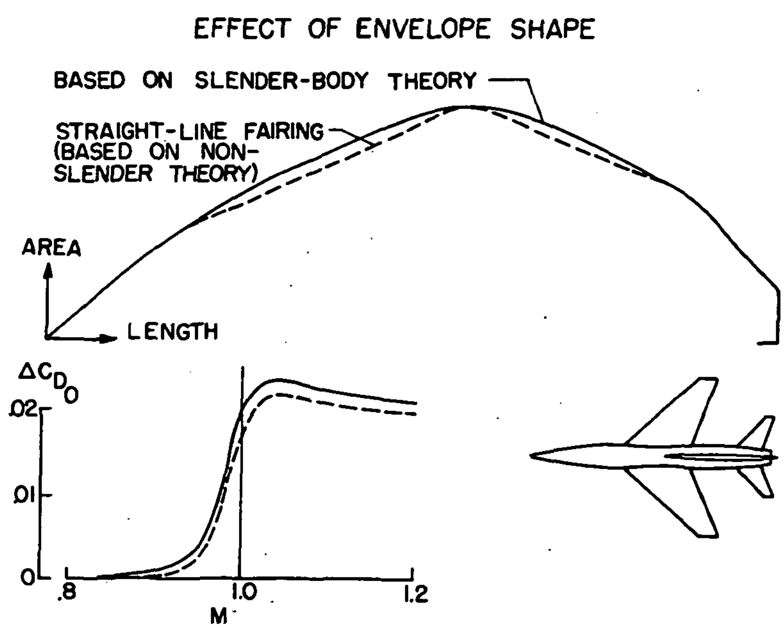

Figure 2

REFLECTION OF DISTURBANCES BY WING
FOR ASYMMETRIC CONFIGURATION

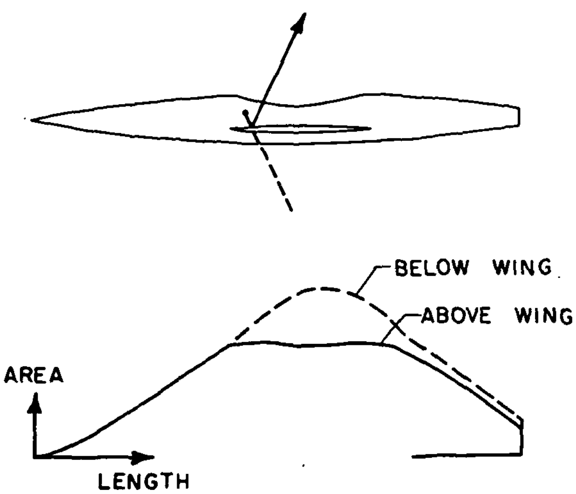

Figure 3

EFFECT OF ASYMMETRIC FUSELAGE INDENTATION

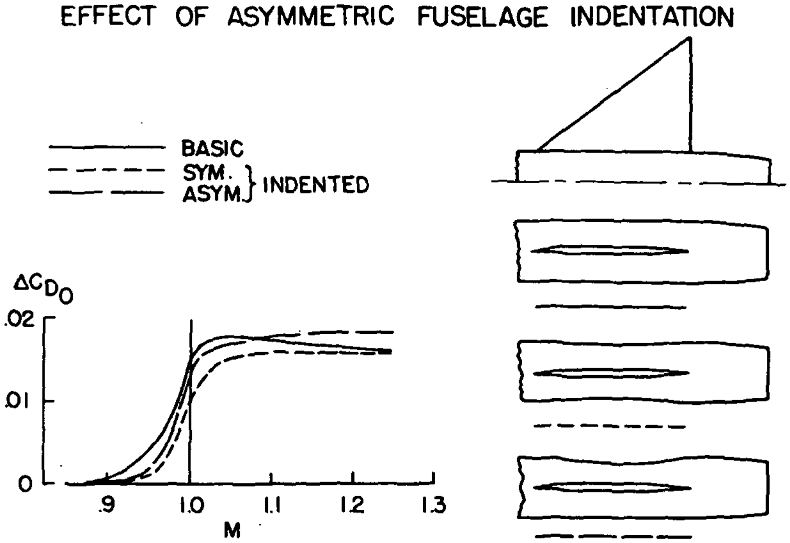

Figure 4

ASYMMETRIC FUSELAGE WITH CAMBERED WING

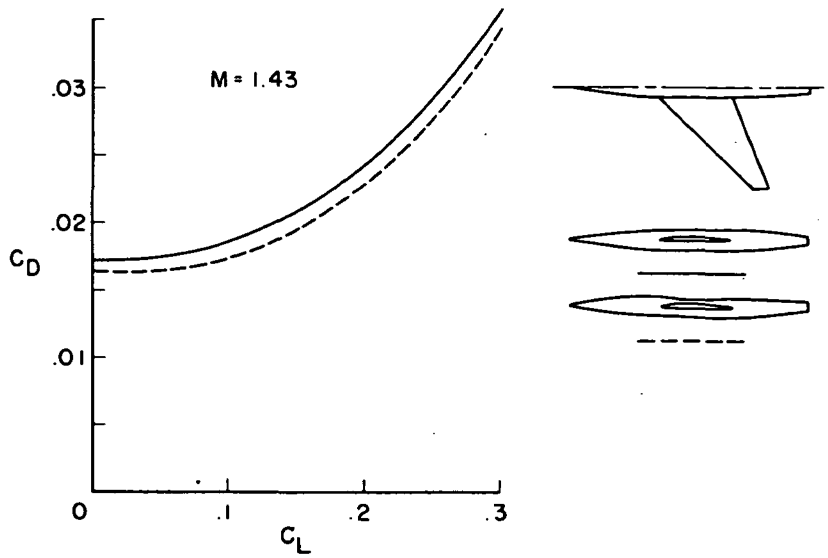

Figure 5

3

REDUCTION OF WAVE DRAG OF WING-BODY COMBINATIONS AT

SUPERSONIC SPEEDS THROUGH BODY DISTORTIONS

By William C. Pitts

Ames Aeronautical Laboratory

The word "interference" is usually associated with adverse effects. However, interference between the components of an airplane or missile can also be beneficial. The methods of drag reduction by body distortion are examples. Figure 1 shows a simplified picture of the mechanics of this beneficial interference. A wing with a biconvex section is mounted on a cylindrical body. The dashed curve represents a body distortion which produces a drag-reducing interference. This distortion creates a negative pressure region to relieve the compression of the air on the forward part of the wing, and it creates a positive pressure region to compensate for the expansion of the air flowing over the after part of the wing. The problem to be solved by all the drag-minimization theories is to determine the magnitude and shape of this distortion that will reduce the wave drag on the wing as much as possible without unduly increasing the body drag.

There are several methods for doing this. The original method is the transonic area rule, which is limited to Mach numbers near unity. The so-called supersonic area rule is limited to slender configurations. Separate linear-theory investigations have been made by Lomax and Heaslet (ref. 1) and by Nielsen (ref. 2) to study the problem of drag minimization outside the region of applicability of these rules. This paper will discuss the theoretical bases of the theories of references 1 and 2 and present experimental results. A method recently investigated at the Langley Aeronautical Laboratory will also be discussed.

In reference 1 the problem of drag minimization is solved without recourse to body boundary conditions. Rather than treating actual shapes, the theory deals with multipole distributions along the body axis to find the minimum condition. Then the body shape is found from the resulting multipole distribution as the last step. The resulting body contains two types of distortion. One type is the axisymmetric distortion due to the sources. The other type is the nonaxisymmetric distortion due to higher order multipoles. Figure 2 shows the experimental verification of the ability of these distortions to produce drag reductions. The theory was applied to a wing of elliptic plan form for a design Mach number of $\sqrt{2}$. The body contained both axisymmetric and nonaxisymmetric distortions. Transition was fixed to minimize change in viscous effects. The quantity ΔC_D is the drag with the distorted body minus the drag with the undistorted body, so that negative values represent drag reductions. The theoretical drag reduction at the design Mach number is shown. A significant portion of this reduction is also realized experimentally over the Mach number range of 1.1 to 1.4.

In reference 2 a different approach to the problem of determining the body distortions is used. The basic difference is that in reference 1 multipoles are distributed along the body axis, whereas in reference 2 the boundary conditions on the wing and body surfaces are satisfied by using the quasi-cylindrical theory of reference 3. The body shape is obtained by minimizing the expression for the drag of the entire combination by the standard method of the calculus of variation. The shape of the body distortions is the minimizing variable. Both axisymmetric and nonaxisymmetric distortions are obtained. The quasi-cylindrical restriction in this theory adds flexibility in that it makes possible direct computation of the drag reduction to be expected from the optimized configuration if it is operated at off-design conditions.

In figure 3, the model to which this theory was applied is shown. The design Mach number is $\sqrt{2}$. The wing leading edge is sonic. This model and models with wings of two other aspect ratios were tested to determine the sensitivity of the theory to aspect ratio. Several bodies were tested to determine the effect of the two types of distortion. Body B_1 is an undistorted cylindrical body with a conical nose, and B_2 contains the axisymmetric distortion. It is this distortion that removes volume from the body. The other distortions rearrange the volume without removing any. Bodies B_3 and B_4 contain both the distortion of B_2 and nonaxisymmetric distortions. Body B_4 is a modification of the optimized body B_3. The dashed curves in the upper sketch show the plan-form section of B_4.

The ability of each of these body distortions to produce a drag reduction at the design Mach number is shown in figure 4. Transition was fixed on all models to minimize change in viscous effects. The drag reduction due to the axisymmetric distortion is shown in the upper left of the figure. This is obtained by subtracting the drag of the model with the undistorted body B_1 from the drag with the body B_2. Similarly, the drag reductions due to the nonaxisymmetric distortions are obtained by subtracting the drag with the distorted body B_2 from the drags with bodies B_3 and B_4. These results are shown in the upper right and lower left parts of figure 4. The fourth part of the figure shows the total effect of both types of distortion by comparing bodies B_4 and B_1. As before, negative values of ΔC_D indicate drag reduction. The axisymmetric distortion provides a significant drag reduction for all aspect ratios although not to the extent predicted by theory.

This difference between theory and experiment is due to the fact that linear theory predicts too large a value for the wave drag of a wing with sonic leading edge. This means that the body shapes obtained are not the best possible for reducing the drag. If a better wing-alone theory were available for wings with sonic leading edge, a body shape that would give greater experimental drag reduction could be obtained. In the upper right of figure 4, theory predicts a large drag reduction for the nonaxisymmetric distortion of B_3. Actually the drag is increased. Liquid-film pictures showed that this increase is not due to flow separation. Instead it is a result of the large indentation in body B_3 which violates the quasi-cylindrical restriction of the theory. If this body is made more quasi-cylindrical by arbitrarily reducing the nonaxisymmetric distortion by one-half to obtain B_4, drag reduction in addition to that due to the axisymmetric distortion is obtained - as shown in the lower left part of the figure. The last part of figure 4 shows that the total effect of both types of distortion ($B_4 - B_1$) is to provide about 35 counts of drag reduction for all aspect ratios.

Figure 5 shows the effect of Mach number on drag reduction. As in figure 4, the quantity ΔC_D is compared for each of the distortions. The upper left part of the figure shows the effect of the axisymmetric distortion of B_2. The upper right part is for the nonaxisymmetric distortion of B_4. The lower part is for the combined effect of these two distortions. This figure supports the statement made for figure 4 that the difference between theory and experiment is due to the sonic leading edge of the wing. As the Mach number is increased from the value at which the leading edge is sonic ($M = \sqrt{2}$), theory and experiment come into good agreement. Figure 5 also shows that the nonaxisymmetric distortion is the most effective for maintaining drag reduction at other than the design Mach number. The axisymmetric distortion slightly increases the drag at $M = 1.75$. At this same Mach number the nonaxisymmetric distortion still provides about 10 counts of drag reduction. The loss of drag reduction as the Mach number is changed from its design value is primarily due to the movement of the Mach wave across the wing surface. The importance of this effect increases as the aspect ratio increases. This means that the Mach number range over which drag reduction is maintained will increase as the aspect ratio is decreased. For example, theory shows that the wing with aspect ratio of 1.33 maintains a drag reduction up to $M = 1.95$, compared with $M = 1.8$ for the wing with aspect ratio of 2.66.

The question arises as to how the supersonic area rule compares with these linear theories when applied to nonslender configurations. In order to compare the body shapes, the area rule and the quasi-cylindrical theory were applied to a wing with sonic leading edge and an aspect ratio of 1.33. The results are shown in figure 6. As might be expected, the body shapes differ considerably.

Another method of altering the body cross-sectional shape of swept-wing—body combinations to obtain further reductions in wave drag has been investigated recently at the Langley Aeronautical Laboratory. This method involves contouring the fuselage side to conform approximately to the streamline paths that would exist over the swept wing if it were of infinite span while preserving a satisfactory area development for the entire configuration.

The configuration investigated is shown in figure 7. The wing had an aspect ratio of 4.0, a taper ratio of 0.6, and a quarter-chord-line sweep of 45°. The solid lines indicate the body contour obtained through an axisymmetrical application of the transonic-area-rule principle. The dashed lines indicate the wing-body juncture of the second configuration, which was made to conform to the calculated streamline shape. This streamline shape was calculated with the use of experimental two-dimensional velocity distributions. These data were measured at a Mach number corresponding to the velocity component normal to the swept-wing leading edge. The body cross section was then adjusted at the top and bottom so that the longitudinal area development was identical with that of the axisymmetric area-rule configuration. The fairing behind the wing trailing edge was arbitrary.

Tests of the two configurations were made in the Langley transonic blowdown tunnel at a Reynolds number of about 2.5×10^{6} based on the wing mean aerodynamic chord and at angles of attack up to about 10°. Transition was fixed to minimize change in viscous effects.

Some of the results of the investigation are presented in figure 8. Plotted are drag coefficients based on total wing area as a function of Mach number for two lift coefficients, 0 and 0.4. The solid lines refer to the axisymmetric area-rule indentation, and the dashed lines refer to the distorted indentation. As indicated, significant reductions in drag were obtained by contouring the wing-fuselage juncture to conform approximately to the calculated streamline shape. These gains were maintained through a large range of lift coefficient as indicated by the data at a lift coefficient of 0.4.

In summary, the methods discussed provide sizable reductions in drag for aspect ratios of current interest. These drag savings are maintained over a wide Mach number range, particularly for low-aspect-ratio wings. At the design Mach number, a significant part of the drag reduction is due to the nonaxisymmetric distortion. At other than the design Mach number, most or all of the drag reduction is due to the nonaxisymmetric distortion.

REFERENCES

1. Lomax, Harvard, and Heaslet, Max. A.: A Special Method for Finding Body Distortions That Reduce the Wave Drag of Wing and Body Combinations at Supersonic Speeds. NACA RM A55B16, 1955.

2. Nielsen, Jack N.: General Theory of Wave-Drag Reduction for Combinations Employing Quasi-Cylindrical Bodies With an Application to Swept-Wing and Body Combinations. NACA RM A55B07, 1955.

3. Nielsen, Jack N., and Pitts, William C.: Wing-Body Interference at Supersonic Speeds With an Application to Combinations With Rectangular Wings. NACA TN 2677, 1952.

LINEAR-THEORY CONCEPTS OF DRAG MINIMIZATION

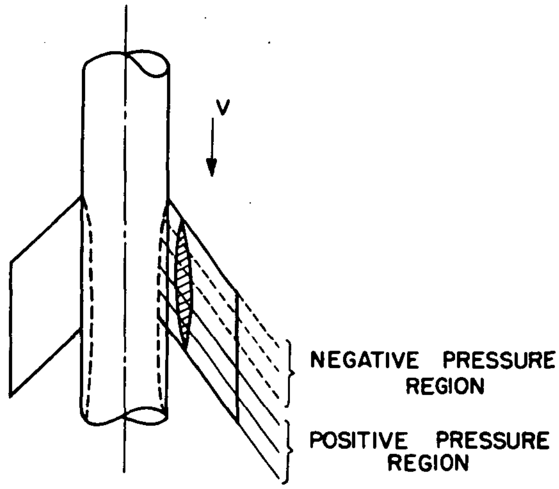

Figure 1

DRAG SAVING BY LOMAX METHOD

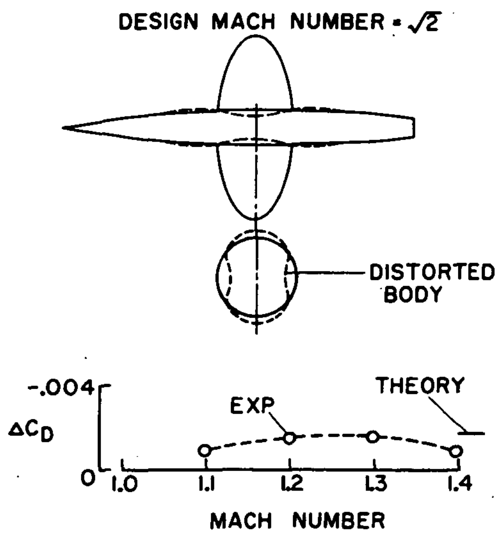

Figure 2

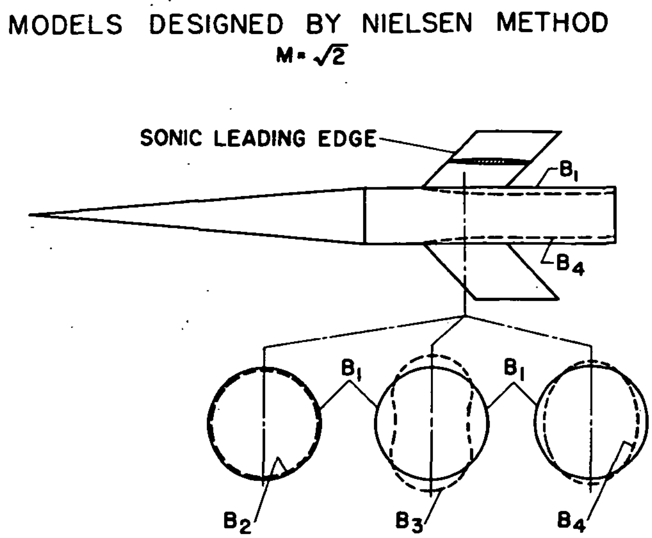

Figure 3

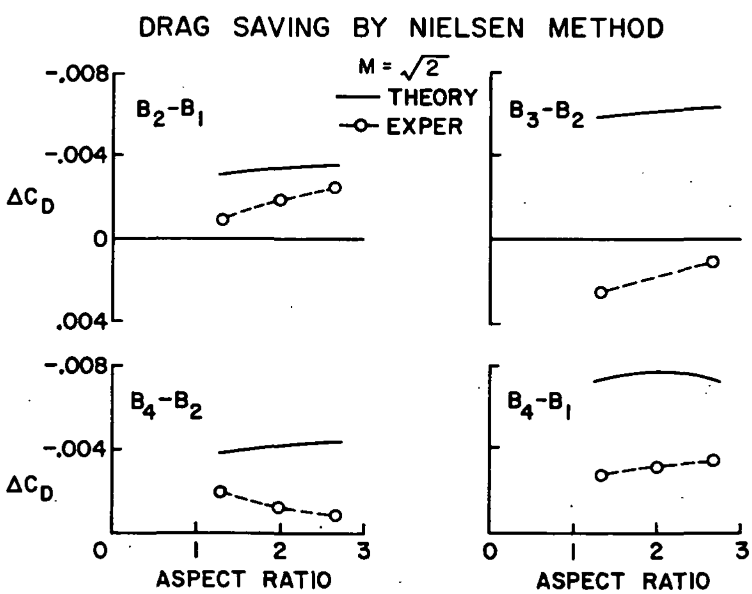

Figure 4

~~CONFIDENTIAL~~

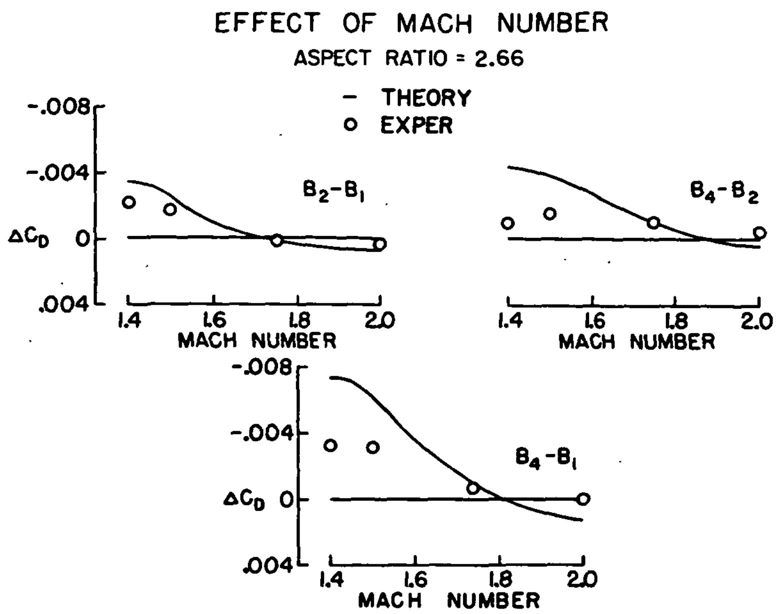

Figure 5

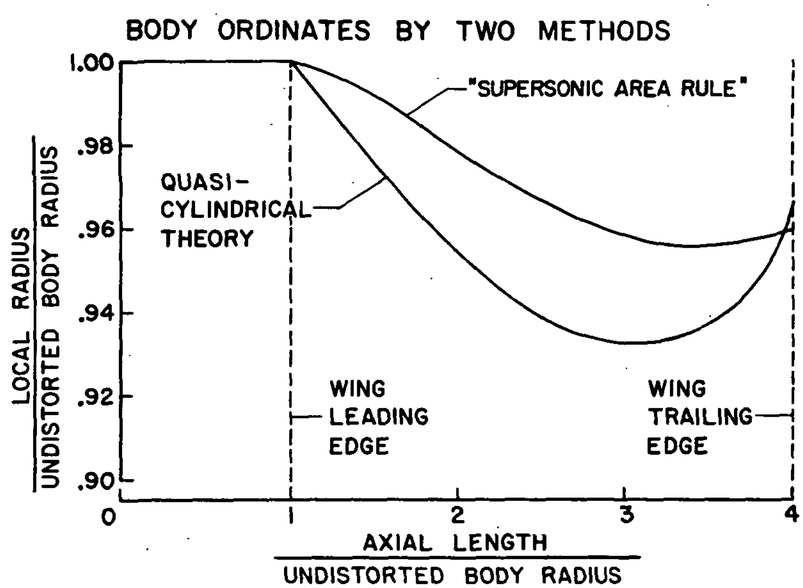

Figure 6

~~CONFIDENTIAL~~

MODEL DESIGNED ACCORDING TO STREAM LINE CONTOUR
DESIGN MACH NUMBER = 1.02

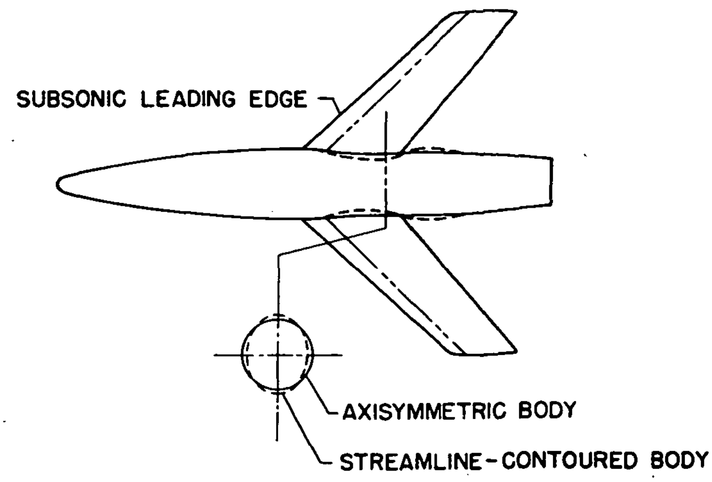

Figure 7

DRAG SAVING BY STREAMLINE CONTOURING
DESIGN MACH NUMBER = 1.02

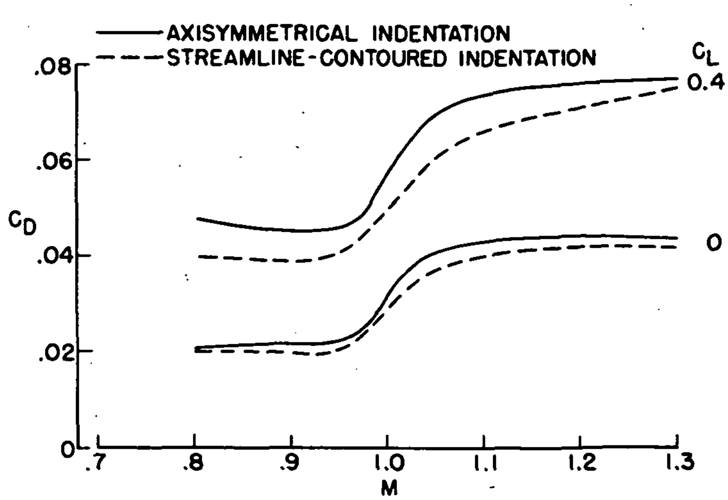

Figure 8

EXAMPLES OF FAVORABLE INTERFERENCE EFFECTS ON THE LIFT-DRAG CHARACTERISTICS OF AERODYNAMIC SHAPES AT SUPERSONIC SPEEDS

By Vernon J. Rossow

Ames Aeronautical Laboratory

This paper is concerned with possible increases in the lifting efficiency of supersonic aircraft. It will be assumed that there is available a fuselage as well as vertical and horizontal surfaces that can be modified or deflected. In general, these surfaces produce wave systems that contribute to the supersonic drag. Representative cases will be studied herein in an attempt to seek favorable interference effects by judicious arrangements of the surfaces available. The details of the analysis and additional examples will be found in reference 1.

A flow model which consists essentially of a horizontal surface with a supersonic stream flowing over it at a Mach number M_o is shown in figure 1. Placed on this surface is a vertical surface inclined at an angle δ to the supersonic stream. The shaded areas indicate the intersection of the horizontal surface with the pressure fields induced by the deflected vertical surface. These positive and negative pressure regions may be thought of as "pressure shadows" of the vertical surface. It is observed that the interference of the vertical surface on the horizontal surface induces positive lift in the region of the negative pressure shadow. Similarly, a negative lift is induced in the region of the positive pressure shadow.

By use of this basic concept, a number of lifting systems consisting of a wing and vertical surfaces can be constructed. One such airfoil system which is simple in form and which can be readily analyzed is shown in figure 2. The model consists essentially of a sweptforward wing with upper and lower end plates at each tip. The leading edges of the upper fins or end plates are deflected inward at an angle δ so that negative pressure shadows are cast across the upper surface of the wing; similarly, the leading edges of the lower fins are deflected outward to generate positive pressure shadows on the lower surface of the wing. It is seen from figure 1 that, within the linearized approximation, the only part of the horizontal surface which is actually needed to capture the indirect lift of the vertical surface is that portion lying within the pressure shadow as indicated by the shaded area. For this reason, the wing of the airfoil system shown in figure 2 is taken as a constant-chord wing with its leading and trailing edges swept along the Mach line. The wing is then completely covered by the pressure shadows of the fins. The trailing edge of the triangular end plates is also swept at the free-stream Mach angle. The wing may also be deflected to contribute to the lift.

The lifting efficiency of this airfoil system is calculated by superimposing linearized conical-flow solutions. In this way the tip effect of the end plates, the lift, and the pressure drag of the whole system can be found. The lifting efficiency calculated in this manner is judged by the drag factor $C_{D_i}/\beta C_L^2$ which enters into the equation for $(L/D)_{max}$ shown in the upper right-hand corner of figure 3. In this equation, C_{D_i} is the drag coefficient arising from the pressure drag due to lift; C_L is the lift coefficient; and C_{D_o} is the drag coefficient of the whole system when none of the surfaces are deflected, that is, the drag of the complete airplane at zero lift. All of the coefficients are based on the plan-form area of the wing. A point of reference for this figure is the two-dimensional wing or the delta wing with supersonic leading edges. These wings have a lift-curve slope of $4/\beta$ and, therefore, a drag factor of 0.25. This value is shown as the short-dashed curve on the right-hand side of figure 3.

The relative efficiency of each of the airfoil systems is indicated in figure 3. It is seen that, of the combinations shown, the most efficient method of obtaining lift is to deflect both the wing and the fins in the optimum ratio so that both the direct and indirect lifting ability of the system are utilized to the full extent. This result is not surprising since the lift is obtained from two sources, the deflections of the fins and the wing, which permit a reduction of approximately one-half of the angle of attack of the wing. Since the lift and drag are respectively proportional to the first and second power of the angle of attack, the lift is held constant and the drag due to lift is reduced. It is assumed that the vertical surfaces already exist on the aircraft and can simply be moved to the wing tips without adding to the wetted area of the airplane. Should it be necessary to add the fins as new surfaces, the increased friction drag would probably more than offset the gain realized from the reduction in drag due to lift.

The pressure fields generated by the fins may also be used to induce lateral forces on other vertical surfaces. Consider, for instance, the streamline paths over the wing as shown in plan view in figure 4. The upper fins of the airfoil system bend the streamlines on top of the wing outward so that the streamlines which pass along the center plane tend to be divided in half. A thin body which follows these streamlines may be introduced into the center plane on top of the wing. Similarly, a thin body could also be terminated below the wing as shown by the dashed lines. A perspective view of the airfoil system with the perturbation fuselage is shown in figure 5. The thin bodies may be thought of as perturbations on a conventional fuselage as illustrated in an approximate fashion in figure 6. The deflected end plates induce lateral velocities over the wing and it is assumed that the fuselage sides are contoured to follow these streamline paths. If the model is designed in this way, a thrust force is induced by the fins on the sides of the perturbation fuselage. When the wing is at an angle of attack, the negative pressure field on top of the wing and the positive pressure field on the bottom of the wing induce additional thrust forces on these fuselage perturbations.

The thrust on the fuselage, the lift, and the pressure drag are calculated by using the superposition of conical-flow solutions used for the simple airfoil system. The drag factor for the airfoil system with the perturbation fuselage is shown in figure 7 as a function of reduced aspect ratio. Also shown is the drag factor for the arrowhead wing. The efficiency of the arrowhead wing approaches the theoretical limit for slender planar wings, and, as such, represents a target which must be exceeded to be assured of a gain from indirect lift. In figure 7 it is seen that an improvement over the simple airfoil system is achieved by addition of the properly contoured fuselage. However, these new models are more efficient than the arrowhead wing only for the low value of reduced aspect ratio; that is, $\beta A < 2.2$.

Indirect lift on the two models described so far was induced by wing-tip end plates. Another method of producing indirect lift is to contour the fuselage so that lifting-pressure shadows fall on the wing. Such a perturbation fuselage with an accompanying wing is shown in figure 8. The deflected flat rectangular surfaces on the sides of the perturbation fuselage are treated as if a positive and a negative wedge were added to a fuselage. The leading and trailing edges of the wing are swept back along the Mach line. The wing-tip end plates are used to provide a means for controlling the airplane in addition to improving the lifting characteristics of the wing. The end plates may be used for lateral control, and, by using their ability to produce indirect lift, they can be used to roll and pitch the airplane or missile.

The drag factor for the airfoil system shown in figure 8 is calculated by linearized conical-flow theory and is shown in figure 7. An improvement in the lifting efficiency is achieved over the other models for wings of higher aspect ratio; however, the arrowhead wing is still superior for all but the lower values of βA. It is observed that the drag factor for the perturbation-wedge body crosses that for the airfoil system with and without a perturbation fuselage. This change in the relative efficiency of these models is a result of the wedge having a higher drag than the triangular end plates but still a stronger lifting-pressure shadow at the higher aspect ratios.

The models described previously received indirect lift by deflecting flat surfaces to produce pressure shadows on the wing. The shape which may be used is not restricted to flat surfaces, but a surface or obstruction of almost any shape may be used to induce the interference field. A body of revolution placed under a swept wing as shown in figure 9 is a choice which is relatively easy to analyze. The wing is assumed to be placed on a plane of symmetry of the cone and to be a perfect barrier, so that the flow field is the same as the axially symmetric case. By use of linear theory, the indirect pressures induced by the cone on the wing are easily calculated along with the lift and the drag of the whole system. The relative inefficiency of the half-cone model as shown in figure 7 is the result of several factors. First, the pressure field induced by a body of revolution is not as intense as that induced by a flat surface. Second, the wings of the other models receive indirect lift on both the top and the bottom surfaces, whereas the half-cone model receives indirect lifting pressures only on the bottom surface. Third, the wing plan form used is not so efficient as that of the other systems discussed.

The study of the models shown in figure 7 indicates that the lifting efficiency of an airplane or missile can, in certain cases, be improved by using vertical surfaces on the aircraft. It is also found that the models that had wings of higher aspect ratio are less efficient than the arrowhead wing. This observation leads to the conclusion that another wing plan form should be chosen for the indirect lifting system. The models described have a fairly poor wing, and the attempt was made to increase its lifting efficiency over a wing which is already quite good. The next step would be to take a good wing approaching the efficiency of the arrowhead wing and attempt to improve its lifting characteristics by use of interference fields. A step in this direction was made in the Ames 10- by 14-inch tunnel. The wing of the model tested was similar to an arrowhead wing and had a half-cone mounted on its bottom side. The drag factor for this combination was slightly better than for the swept wing (no fins) and is a definite improvement over the half-cone model shown in figures 7 and 9. These test results bear out the somewhat obvious contention that the wing plan form used in the airfoil system should be an efficient unit in itself. This model will be discussed in more detail in a later paper by H. Julian Allen and Stanford E. Neice.

In studying models of the half-body type at the Ames 6- by 6-foot supersonic tunnel, it was found that the indirect lift was dependent only on the base area of the body. Consequently, it was concluded that the body having the minimum drag for a given base area should be the body used to induce the indirect lift on the wing.

An investigation of interference effects of the type discussed in this paper is reported in reference 2. This study included a number of lifting systems consisting of wing-body combinations. The models differed somewhat from those considered herein, but the overall results indicate the same general conclusions.

The several models described are only a small fraction of the number of possible configurations, since the shape of any of the component parts may be varied throughout wide limits. However, it is hoped that this study will furnish the designer with some interesting and instructive examples of the use which can be made of interference fields for indirect lift and control purposes.

REFERENCES

1. Rossow, Vernon J.: A Theoretical Study of the Lifting Efficiency at Supersonic Speeds of Several Airfoil and Fuselage Combinations Which Utilize Indirect Lift. (Prospective NACA paper.)

2. Ferri, Antonio, Clarke, Joseph H., and Casaccio, Anthony: Drag Reduction in Lifting Systems by Advantageous Use of Interference. PIBAL Rep. No. 272, May 1955.

~~CONFIDENTIAL~~

PRESSURE SHADOWS INDUCED BY DEFLECTED SURFACE

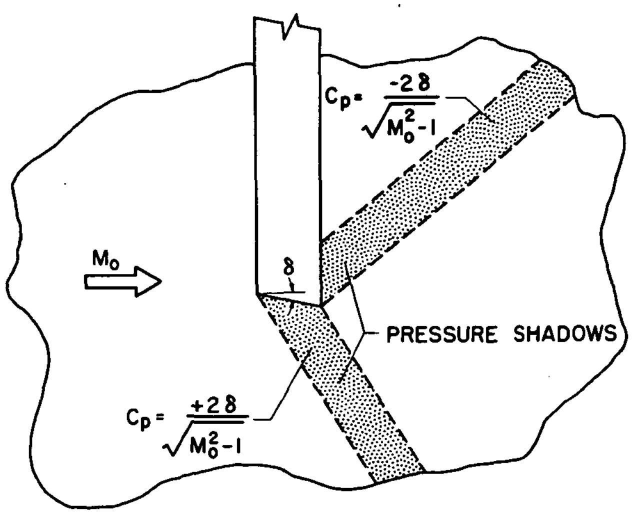

Figure 1

AIRFOIL SYSTEM

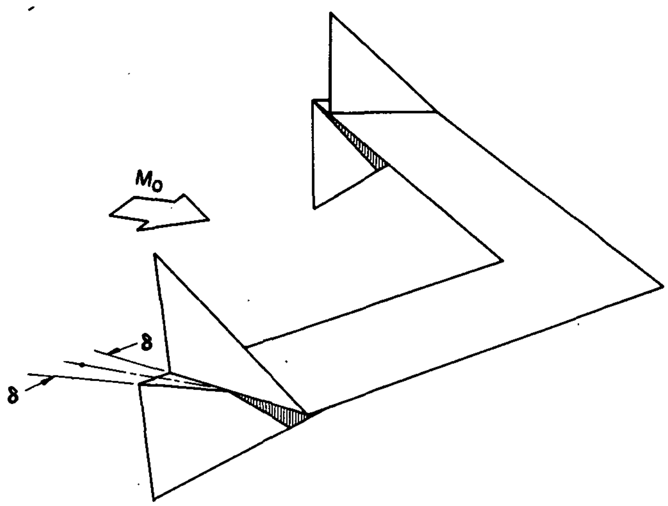

Figure 2

~~CONFIDENTIAL~~

DRAG DUE TO LIFT

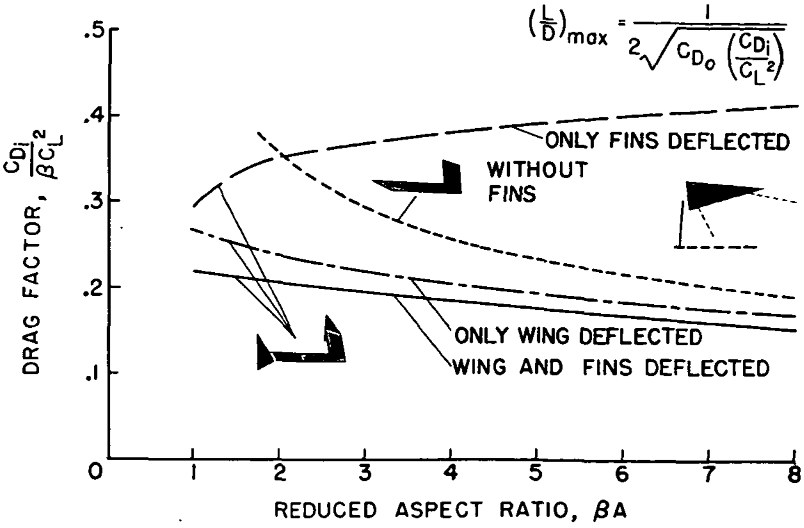

Figure 3

PLAN VIEW OF AIRFOIL SYSTEM

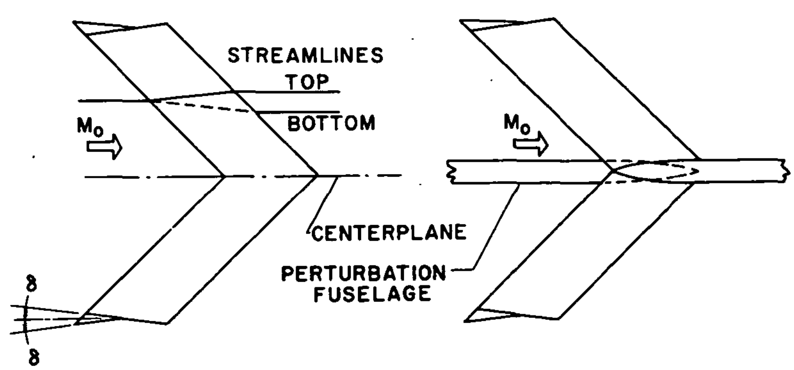

Figure 4

AIRFOIL SYSTEM WITH FUSELAGE PERTURBATION

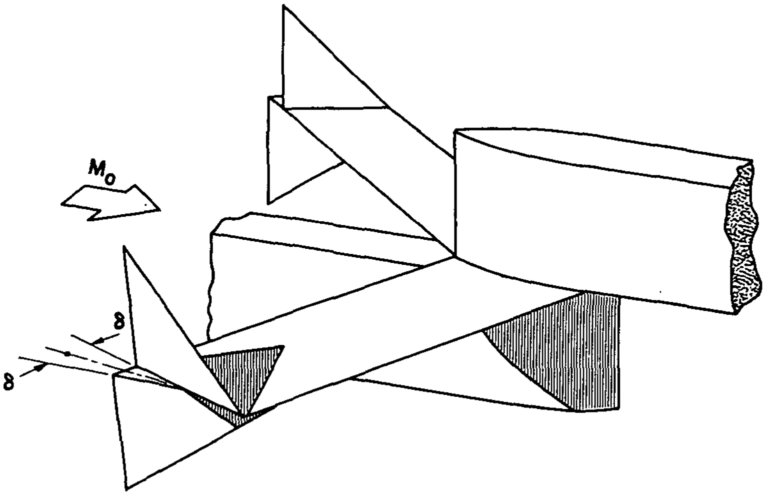

Figure 5

ADDITION OF PERTURBATION BODY TO A FUSELAGE

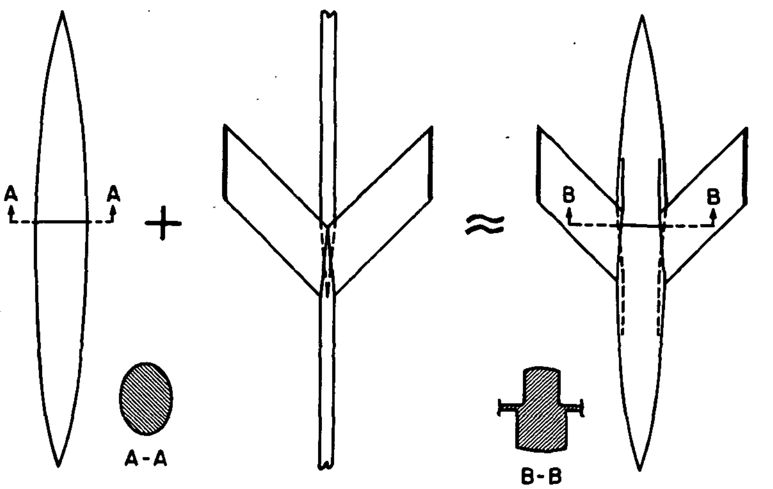

Figure 6

DRAG DUE TO LIFT

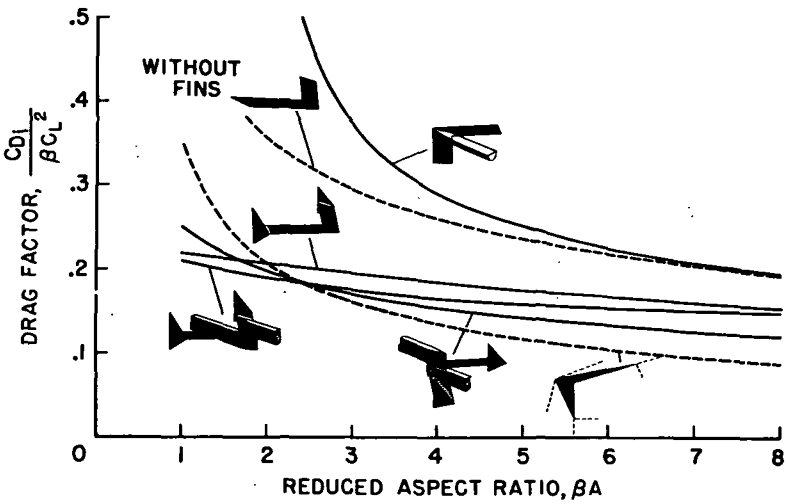

Figure 7

POSITIVE AND NEGATIVE WEDGE ADDED TO FUSELAGE

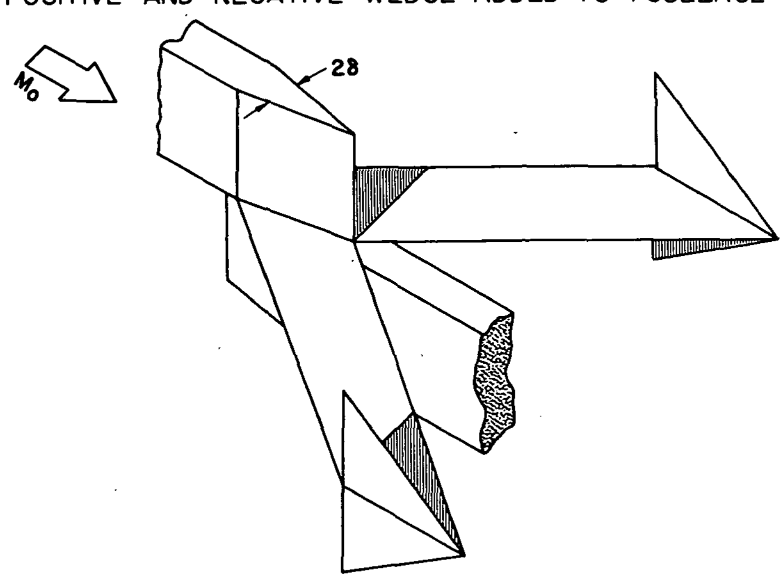

Figure 8

HALF-CONE MOUNTED UNDER A SWEPT WING

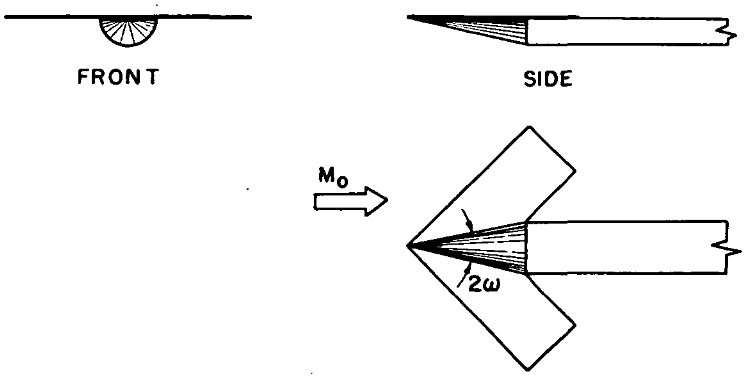

Figure 9

WAVE DRAG OF ARBITRARY CONFIGURATIONS IN TERMS OF AREAS AND FORCES IN OBLIQUE PLANES

By Harvard Lomax

Ames Aeronautical Laboratory

One approach to the study of interfering wings and bodies in a supersonic flow field is through the application of linearized theory as it is expressed by the wave equation. Among the merits of such an approach is the use that can be made of the vast amount of analysis developed in studying boundary-value problems associated with the wave equation. In particular two theorems regarding the wave equation, one derived by Green and the other derived by Hayes (ref. 1), can be combined with the result that the wave drag of an arbitrary system of objects can be expressed in terms of certain section areas and the resultant forces on these sections.

5

Hayes' theorem states that the momentum at a point on a large enclosing cylinder is invariant to the translation of sources along the oblique plane

$$x_1 = x + \beta y_1 \cos\theta + \beta z_1 \sin\theta$$

shown cutting the high-wing monoplane in figure 1. Green's theorem relates the source strengths to the geometry of, and pressures on, the airplane. By the combination of these theorems, the following drag formula is obtained:

$$\frac{D_w}{q} = \frac{-1}{4\pi^2}\int_0^{2\pi} d\theta \int_0^L dx_1 \int_0^L dx_2 \left[S''(x_1,\theta) - \frac{\beta l'(x_1,\theta)}{2q}\right]\left[S''(x_2,\theta) - \frac{\beta l'(x_2,\theta)}{2q}\right]\log_e |x_1 - x_2| \qquad (1)$$

The term $S(x,\theta)$ represents the normal projection of the area intersected by a particular oblique plane, and the term $l(x,\theta)$ represents the component of the resultant force on this section in the θ-direction. The primes indicate partial derivatives of these expressions with respect to x and the symbol β equals $\sqrt{M^2 - 1}$. The rest of this paper will be devoted to certain examples illustrating how this equation can be useful in the study of supersonic wave drag.

First, consider cases in which the wave drag can be expressed in terms of the oblique areas alone; that is, cases in which the drag equation reduces to the supersonic area rule formulated by Jones (ref. 2) and Whitcomb and Fischetti (ref. 3). According to equation (1), this occurs when the quantity $\beta l/2q$ can be neglected. Two important cases for which this is possible are well known. First, if the free-stream Mach number is almost 1, then β is approximately equal to 0 and the term is negligible. Second, if a swept uncambered wing is centrally mounted on a slender body, the loading on the wing is everywhere zero and the only contribution to the force term comes from the section obliquely cut from the fuselage. But if the fuselage is slender and the streamwise pressure gradients on it are small, l/q is negligible and the drag is again a function only of the oblique areas.

Other special cases exist for which the drag of a wing-body combination can be expressed in terms of simple geometry. One case is shown in figure 2. This case is represented by a supersonic-edge wing mounted asymmetrically on a body. The combination can be at an angle of attack and the wing can be supporting a load. Since the edges are supersonic, the upper and lower surfaces are noninteracting. Hence two symmetrical bodies can be constructed, one formed by reflecting the upper half about a reference plane and the other by reflecting the lower half about the same plane. The drag of the original combination is then half the sum of the two symmetrical bodies; but each of these are types that can be studied by the supersonic area rule.

These have been cases for which use of the force term in the drag equation could be neglected or avoided. Consider next an example (shown in fig. 3) in which the force term is as important as the area term. Suppose, as is shown in the figure, a thin, axially symmetrical cylindrical shell is cambered to support a certain outward force. Its oblique area distribution would then be negligible but $\beta l/2q$ would vary as indicated. If a slender body of revolution having a rate of change of area equal to the quantity $\beta l/2q$ were placed along the center line of the cylinder and the shell continued to support the same loading, the drag of the combination would, clearly, be zero - the two terms just canceling one another. The existence of such a zero-wave-drag body and shroud was first pointed out by Ferrari some years ago.

The previous examples illustrated two extremes: one in which the force term in the drag equation was negligible and the other in which the force term was all-important. The question naturally arises as to what are the effects of combining bodies with loaded surfaces having shapes more nearly like those in ordinary use. A qualitative answer to such a question for a conventional configuration is presented in figure 4. A slender body is presented having an $M = 1$ modification for a centrally mounted sweptback wing. The streamwise distribution of normal cross-sectional area is shown at the bottom of the figure and is equivalent to a low-drag body of revolution. Hence, at transonic speeds the drag is minimized. However, as the speed advances into the supersonic range, certain of the oblique area distributions obtained from such a configuration are equivalent to bodies of revolution having high wave drags. For instance, consider the free-stream Mach number to be 1.4. The oblique areas for $\theta = 90^{\circ}$ are still essentially the same as those found for all values of θ at $M = 1$, but the distribution for $\theta = 0^{\circ}$ is not the same and is shown at the upper part of the figure. Notice that, while the area of one wing panel is still spread smoothly over a large distance, the other accumulates in an undesirable narrow bump.

Suppose now that vertical plates are placed at the wing tips and made to carry an outward load. For $\theta = 90^{\circ}$ (see fig. 4), it can be seen that the added plates do not change the equivalent body of revolution for this case since the forces on the plates have no vertical components. For $\theta = 0^{\circ}$, on the other hand, the plates are as effective as the area distribution and can be used to smooth out the equivalent body of revolution in a manner such as is indicated in the figure.

The advisability of using such devices as shown in figure 4 depends entirely, of course, on a quantitative evaluation of the entire drag. In the arrangement shown, the end plates produce a vortex drag which could be prohibitively high. However, if the plate and fuselage were mounted beneath the wing, and the lift of the airplane were also taken into account, the plates would not only reduce the wave drag but would also reduce the overall vortex drag. Furthermore, a certain amount of their friction drag could be written off on their stabilizing properties.

Purely qualitative results such as the aforementioned merely bring out the necessity for carrying out detailed calculations that show numerically the effects of combining volumes with loaded surfaces in order to minimize their wave drag. Some examples showing the optimum lift and area distributions for bodies in the presence of given lifting wings are presented in the following paragraphs. In each case the term "optimum" is based on considerations of the wave and vortex drags only.

In the first place, if the body is slender and long enough for its fore and after Mach cones to enclose the wing, a comparatively simple equation can be written as follows giving the optimum magnitude of the body's volume:

$$\frac{4V_{OPT}}{\beta^2} = \iint\limits_{Wing} z \frac{\Delta p}{q} \, dx \, dy + \iint\limits_{Wing} y \frac{\Delta p}{q} \, dx \, dz \qquad (2)$$

The volume of the interfering body depends on the direction and magnitude of the wing loading and the position of the wing relative to the body axis. Notice also that the volume can be either negative or positive depending on its position. For example, if the wing is carrying lift and the added body is to have a positive volume, when it must be located beneath the wing. Two simple applications of the equation are shown in figure 5. Notice that, for the same total lift, a uniformly loaded semi-circular shell carries a body with $\pi/2$ times as much volume as a flat wing located an equal distance above the body.

Figure 6 shows the actual area distribution which the optimum body must have if it is to be located beneath a uniformly loaded elliptic wing. The axis of the body coincides with the x-axis and the location of the wing with reference to the body is shown in the upper left-hand corner. The variation of body area is shown directly underneath. The total volume represented by this area distribution was given by equation (2).

One can readily see that the idea of finding the optimum area distribution of a body under a lifting wing can be extended. For example, the optimum distribution of lift can be found to be carried by the body. Similarly, the optimum area and lift variations for bodies under a wing with thickness can be calculated. The results of such investigations are also presented in figure 6.

The next question is: What are the magnitudes of the gains in wave drag brought about by placing bodies with these area and lift variations under their respective wings? This question is answered in figure 7. The drag of the wing alone is used as a reference. For example, if a body with the proper area distribution were placed beneath the uniformly loaded elliptic wing (shown in fig. 6), the total wave drag of the combination could be made equal to the curve labeled WING + S_e in figure 7. As far as wave drag is concerned, not only is the body carried free, but drag reduction below that of the wing alone is obtained. Similarly, if the body can also be made to carry the lift shown in figure 6, the drag of the wing-body combination would be reduced to the curve labeled WING + S_e + l_e in figure 7. Analogous reductions for the nonlifting wing are also shown in the figure.

In the case of the nonlifting wing, no net lift is added to the body, but for the lifting wing the body must carry a downward force equal in magnitude to the full lift of the wing. Such a combination is of little interest since the wing and body together would have no total lift and, furthermore, the vortex drag would be very high. The dashed line in figure 7 represents the level to which the wave drag would be reduced by adding a body with an optimum area variation and a lift distribution that is optimum under the condition that no net lift be added to the body. It should be mentioned at this point that the gains shown for adding lift to the body may be difficult to achieve since a slender fuselage is not an efficient lifting device.

A final example is presented in figure 8. An infinitely long semicircular tube with a loading which is constant with respect to θ and the streamwise loading shown was analyzed. Although the total drag was retained in the results, only 80 percent of the lift was used and the chord of the wing was taken to be that which carried this 80 percent. The abscissa shown in the figure is the reduced aspect ratio based on the wing plan-form area. For the range of reduced aspect ratio given, almost the entire wing wave drag can be destroyed by a body with the proper area and lift distributions. Hence, again if no net lift is assumed to be carried on the body, the drag parameter $\dfrac{C_{D_W}}{\beta C_L{}^2}$ of a combination can be reduced to the level shown by the dashed line in the figure. It should be pointed out that for a given Mach number and lift this level is essentially the absolute minimum wave drag that can be achieved by any arrangement of volume and lift within the space contained within the fore and after Mach cones enclosing the configuration shown.

In figure 9 the sum of the wave and vortex drags of the half enshrouded body are presented for a range of reduced aspect ratio and the results compared with triangular and rectangular flat plates. Actually, in order to achieve the results shown for the semicircular wing and body, the wing should be cambered to provide minimum vortex drag and to provide an equivalent lift distribution that is as close to the optimum as possible so that the variation of lift required on the body would be small. This accomplished, the comparisons are fair since all coefficients are based on the wing wetted areas. The half enshrouded wing-body combination has the lowest value of $\dfrac{C_D}{\beta C_L{}^2}$ even though it is carrying a considerable volume. For example, a 40,000-pound airplane flying at a Mach number of 2 at 50,000 feet and having a wing chord equal to 10 feet and a plan-form span equal to 20 feet would carry an optimum volume equal to about 700 cubic feet. This volume is sufficient to fill a Sears-Haack body 45 feet long having a maximum diameter equal to 6 feet.

REFERENCES

1. Hayes, Wallace D.: Linearized Supersonic Flow. Rep. No. AL-222, North American Aviation, Inc., June 18, 1947.

2. Jones, Robert T.: Theory of Wing-Body Drag at Supersonic Speeds. NACA RM A53H18a, 1953.

3. Whitcomb, Richard T., and Fischetti, Thomas L.: Development of a Supersonic Area Rule and an Application to the Design of a Wing-Body Combination Having High Lift-to-Drag Ratios. NACA RM L53H31a, 1953.

OBLIQUE PLANE AND DRAG FORMULA

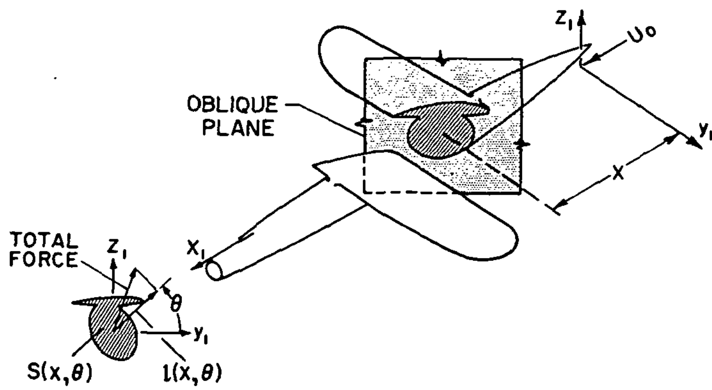

Figure 1

CASE FOR WHICH $\frac{l(x,\theta)}{q}$ IS EFFECTIVELY ZERO

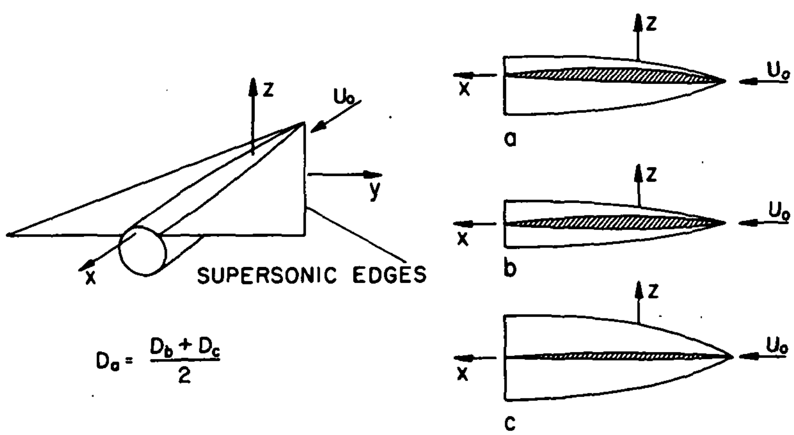

FOR BODIES b AND c, $\frac{l(x,\theta)}{q} \approx 0$

Figure 2

~~CONFIDENTIAL~~

COMBINATIONS WITH COMPLETELY CANCELLING MOMENTUM RADIATION

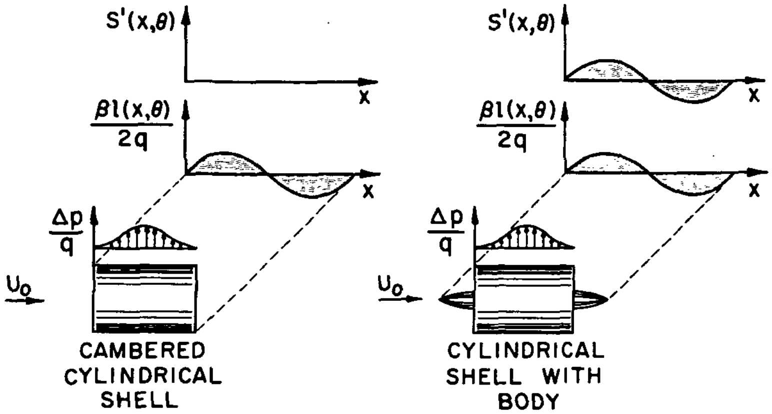

Figure 3

WING AND BODY WITH M = 1 MODIFICATION PLUS VERTICAL PLATES

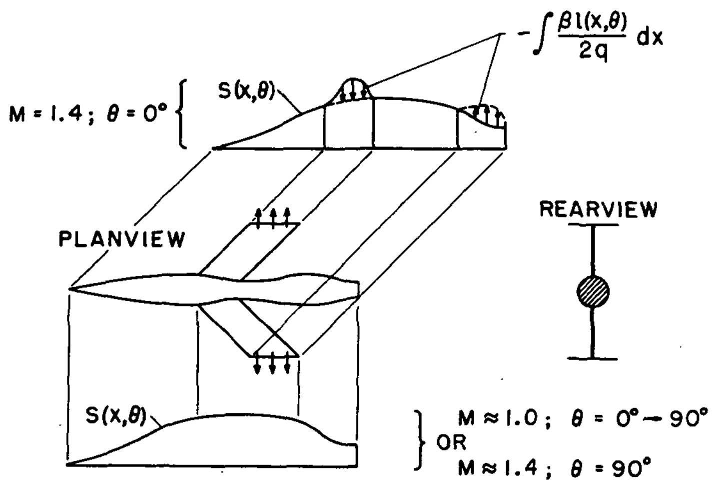

Figure 4

~~CONFIDENTIAL~~

OPTIMUM VOLUMES IN COMBINATION WITH LOADED PLATES

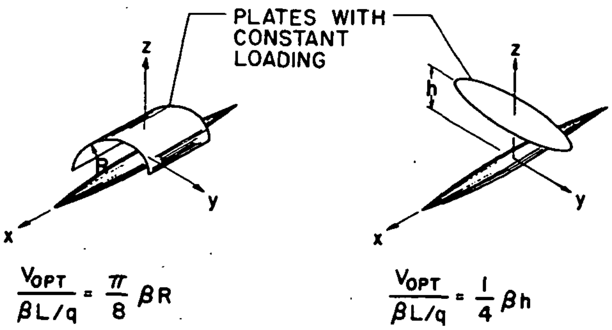

Figure 5

EQUIVALENT AREA AND LIFT OF WING RAISED ABOVE X-AXIS

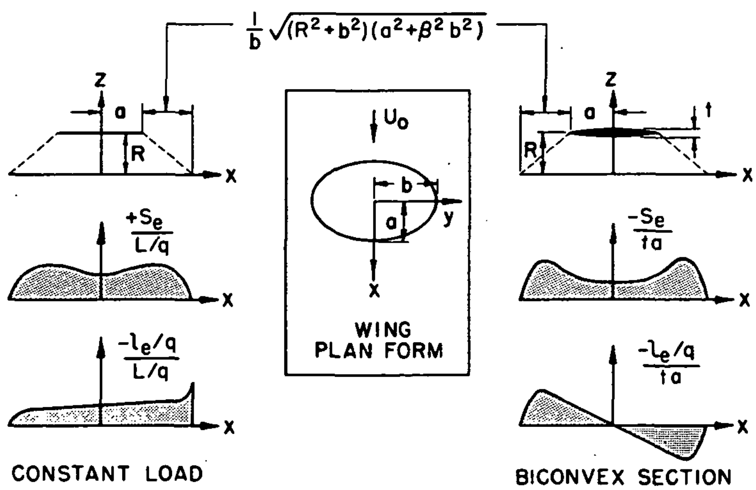

Figure 6

EFFECT ON WAVE DRAG OF RAISING WING
ABOVE BODY AXIS

$\beta A = 2$

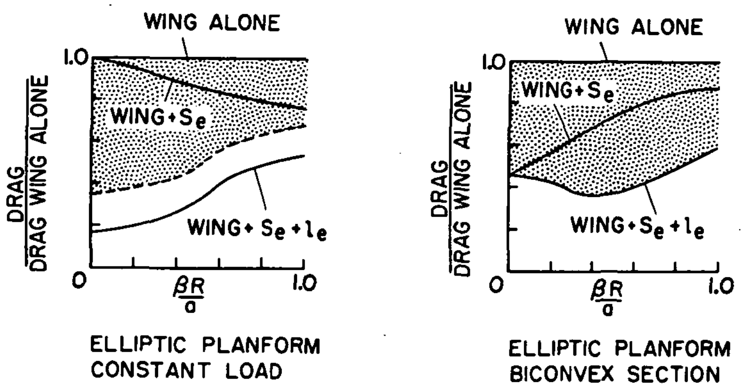

Figure 7

WAVE DRAG DUE TO LIFT OF SEMICIRCULAR
WING AND BODY

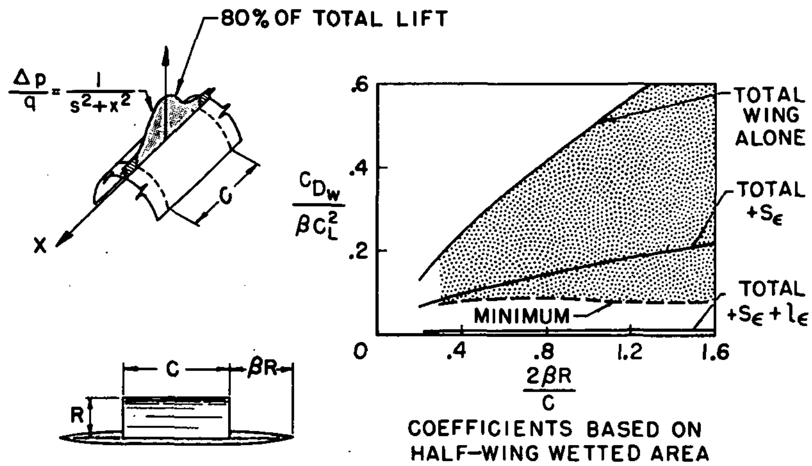

Figure 8

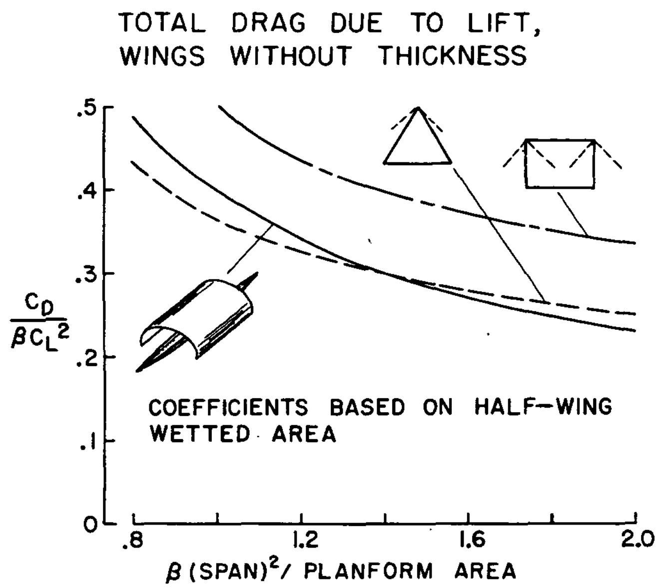
TOTAL DRAG DUE TO LIFT,
WINGS WITHOUT THICKNESS
$\frac{C_D}{\beta C_L^2}$
.5
.4
.3
.2
.1
0
.8
1.2
1.6
2.0
β (SPAN)^2/ PLANFORM AREA
COEFFICIENTS BASED ON HALF-WING
WETTED AREA

Figure 9

MINIMUM WAVE DRAG FOR ARBITRARY ARRANGEMENTS OF WINGS AND BODIES

By Robert T. Jones

Ames Aeronautical Laboratory

One of the present tasks of theoretical aerodynamics is to discover and to analyze airplane shapes that have a small wave resistance at supersonic speeds. The previous papers certainly furnish a convincing demonstration of the variety of the forms that present themselves when such a task is started.

In 1935 Busemann (ref. 1) showed that the wave drag of two airfoils could be canceled by reflection. Later Ferrari (ref. 2) showed that the drag of a body of revolution could be canceled by the addition of a ring airfoil to catch the wave from the nose and reflect it back to the tail. Even if the investigation is limited to such completely self-contained wave systems, these examples are only two of an infinite number of possibilities.

The examples in which the wave cancellation is complete are, however, limited to systems in which the net lift and lateral force are zero. Nevertheless, examples cited by Graham et al. (refs. 3 and 4) and in the preceding papers by Vernon J. Rossow and Harvard Lomax show that the wave drag associated with the lift can be diminished by various three-dimensional arrangements of wings and bodies. These examples lead to a search for some general statements or criteria regarding the wave drag of such three-dimensional arrangements. 6

In order to put the question in a definite form it will be assumed that the airfoils and bodies are contained in the interior of a definite three-dimensional region R. The total lift L and the volume v are assumed to be given. It is supposed that the wave drag D depends somehow on the distribution of the lift and the volume throughout R and that with distributions of a certain family (called "optimum" ones) the drag will have a minimum value. It is desired to find the optimum distributions, or the conditions determining them, and the value of the minimum drag. Problems of this type have been considered by E. W. Graham and his colleagues who give, for example, the optimum distribution of lift within a spherical region.

If the region R is restricted to the plan form S of a planar wing, then problems of a type previously discussed by the present writer are obtained (refs. 5 and 6). In the latter problems it was found that all distributions of lift or volume satisfying the given conditions could be characterized by relatively simple conditions. The present paper describes briefly the extension, and the additional conditions required, for three-dimensional regions.

As is usual in linearized-flow problems it will be assumed that the disturbance field of the airfoils and bodies can be produced by the action of a distribution of sources and "lifting elements" or horseshoe vortices. One of the difficulties associated with these problems is the determination of the actual geometric shapes produced by the distribution of singularities. In the present analysis the relation between the body shapes and the singularities is not known nor determined in detail. For slender bodies or thin airfoils closed within the region R it can be assumed that the total volume is proportional to the first moment of the source distribution with respect to a plane perpendicular to the flight direction, whereas the total lift is proportional to the total strength of the lifting elements.

Suppose a region R together with a distribution of singularities such as sources or lifting vortices is given. (See fig. 1.) Then by Hayes' theorem (ref. 7), the drag will be unchanged by a reversal of the whole system. (The geometry of the flow, including that of the airfoils and bodies, will be changed by the reversal but the total lift and the total volume will not.) Then the drag may be computed by means of a fictitious "combined disturbance field" obtained by superimposing the disturbances in the forward and the reversed motion. The perturbation velocities in this combined field may be denoted by

$$\bar{u} = \frac{u_f + u_r}{2}$$

$$\bar{v} = \frac{v_f + v_r}{2}$$

$$\bar{w} = \frac{w_f + w_r}{2}$$

An arrangement of sources or lifting elements or their combination which yields the minimum drag is then characterized by the conditions

$$\left.\begin{aligned} \bar{w} &= \text{Constant} \\ \bar{v} &= 0 \\ \frac{\partial \bar{u}}{\partial x} &= \text{Constant} \end{aligned}\right\} \qquad (1)$$

throughout R.

If conditions (1) are satisfied, then the integrated drag of the whole system will be given simply by

$$D_{MIN} = L \frac{\bar{w}}{V} + \nu \rho V \frac{\partial \bar{u}}{\partial x}$$

The first term on the right-hand side of this expression will be recognized as the drag arising from a rearward inclination of the lift vector, whereas the second term is simply the product of the volume and the constant gradient of pressure in the combined flow field.

These conditions may be verified by making use of a "mutual drag relation," essentially similar to the well-known Ursell-Ward reciprocal relation, which connects the drag of any two interfering distributions of singularities in the combined flow field. According to this relation the drag of distribution A caused by the interference of a second distribution B is equal to the drag added to B by the interference of A. Now let A be a distribution within R_A satisfying conditions (1). For B select a distribution having zero total lift and zero total volume. If R_B is contained within R_A, then the addition of B will amount simply to a redistribution without changing the total lift L or the volume ν of A. The drag of A + B may then be written in shorthand notation

$$D(A + B) = D_{AA} + D_{AB} + D_{BA} + D_{BB}$$

Then, since by the mutual drag relation $D_{AB} = D_{BA}$ may be written as

$$D(A + B) = D_{AA} + 2D_{BA} + D_{BB}$$

Here D_{BA} is the drag of B in the combined disturbance field of A. Since $\bar{w}$ = Constant, $\bar{v} = 0$, and $\frac{\partial \bar{u}}{\partial x}$ = Constant in R_A, this interference drag may be written as

$$D_{BA} = L_B \frac{\bar{w}_A}{V} + \nu_B \rho V \left(\frac{\partial \bar{u}}{\partial x}\right)_A$$

However, since L_B and ν_B are zero, D_{BA} vanishes and the added drag is that of distribution B alone or D_{BB}. Now the drag of a system alone, that is, without interference, cannot be negative; hence, $D(A + B)$ cannot be less than $D(A)$ under conditions (1).

On the other hand, suppose, for example, that the sidewash $\bar{V}_A$ was not zero. A distribution of lateral forces could then be found which would result in a negative interference drag, dominating the quadratic term D_{BB}, so that the total drag could be reduced. Hence, if the drag of distribution A actually is a minimum value, conditions (1) must be complied with.

Since $w = \frac{\partial \phi}{\partial z}$, $v = \frac{\partial \phi}{\partial y}$, and $\frac{\partial u}{\partial x} = \frac{\partial^2 \phi}{\partial x^2}$, it can be seen that conditions (1) do not agree, in general, with the linearized-flow equation

$$\left(1 - M^2\right)\phi_{xx} + \phi_{yy} + \phi_{zz} = 0$$

but only if $\frac{\partial \bar{u}}{\partial x} = 0$ (or, unless the distribution of singularities is continuous throughout R). Since $\frac{\partial \bar{u}}{\partial x}$ is proportional to the drag per unit volume, one concludes that the drag cannot be minimized in an absolute sense unless the drag associated with the volume of the system is zero. Examples such as the Busemann biplane satisfy the latter condition, namely, $\frac{\partial \bar{u}}{\partial x} = 0$.

As Graham, et al., has pointed out, distributions of the sort being considered here are not unique, since other solutions such as those shown in figure 2 may be added to them without changing the lift or the drag.

It is interesting to note that conditions analogous to the conditions $\bar{w}$ = Constant and $\bar{v} = 0$ were found by Munk in connection with the vortex drag of lifting systems at subsonic speeds. In that problem the conditions apply to the two-dimensional motion associated with the trace of the wing system in the Trefftz plane. If the idea of superimposed flow fields is utilized in the subsonic problem, one finds that the cylindrical flow associated with the Trefftz plane extends along the whole flight path and hence includes the region R. Conditions (1) thus apply at both subsonic and supersonic speeds but are unnecessarily restrictive at subsonic speeds.

Munk's conditions of constant downwash and zero sidewash were used by Hemke (ref. 8) to determine the effectiveness of end plates in reducing the vortex drag of a wing at low speeds. The previous paper by Vernon J. Rossow and the work of Ferri et al. (ref. 9) call attention to the possibility of obtaining favorable wave interference from such vertical surfaces at supersonic speed. It will be interesting to see how the condition $\bar{v} = 0$ might be used to determine an optimum setting and camber for such a surface. This application is illustrated in figure 3 for an end plate on the tip of a wing.

With the wing in forward motion, the lateral velocity v_f at the surface of the end plate is simply the lateral slope of the fin surface times the stream velocity. The condition $\bar{v} = 0$ implies that $v_r = -v_f$, and this condition is obviously satisfied by keeping the geometry of the fin fixed when the flow is reversed. At the same time, however, recall that the distribution of lift and lateral force must be kept the same in forward and reversed flow. Hence, in order to achieve the minimum drag one must find the particular camber and setting of the fin that will yield the same distribution of lateral force for either direction of motion. At first it seems impossible to satisfy such a requirement since, for example, the direction of lift of an inclined surface is usually reversed by reversing the direction of flow. However, the form of the adjacent wing surface must, in general, change with reversal, since $\bar{w} \neq 0$ and since the lift distribution on the wing must remain unchanged. Then it is evident that the conditions may be satisfied if the pressures on the fin surface are dominated by the wing pressures through interference.

It must be admitted that the considerations have thus far been rather abstract. A more concrete result would yield the actual magnitudes of the minimum drag associated with various regions. Such results for distributions of lift in spherical and ellipsoidal regions have been given in reference 4. A somewhat more general result, applicable to arbitrary regions R, can be obtained if merely a lower bound for the wave drag is sought rather than the actual minimum value. Since this lower bound coincides with the minimum value in the examples found thus far, it may be taken as an approximation to the actual drag in many cases.

To obtain such a lower bound, use is made of Lomax's formula expressing the drag in terms of areas and pressures intercepted by oblique planes. By utilizing Hayes' method of equivalent positions (ref. 7) or the present writer's method of superimposing plane waves (ref. 6), one can construct, at each angle θ, three equivalent linear distributions, namely, a volume distribution, a lift distribution, and a side-force distribution. By a harmonic analysis (ref. 10) it is possible to show that the drag associated with the leading term in the expansion of the lift distribution $l(x)$, proportional to the total lift L, cannot be diminished by interference. The possibility, already known, that the drag associated with the volume can be eliminated appears in this analysis. Hence, for the lower bound the value given by the first term in the expansion of the lift distribution is used. This step amounts to the assumption that each "lifting line" obtained by integrating the spatial lift distribution over the intersecting Mach planes is elliptically loaded. For a single elliptically loaded lifting line parallel to the flight direction, the wave drag is:

$$D_{WAVE} = \frac{M^2 - 1}{2} \frac{L^2}{\pi q l^2} \tag{2}$$

where l is the length of the line. For the whole region R the following is obtained

$$D_{WAVE} \geqq \frac{M^2 - 1}{2} \frac{L^2}{\pi q \bar{l}^2} \tag{3}$$

where

$$\frac{1}{\bar{l}^2} = \frac{1}{\pi} \int_0^{2\pi} \frac{\sin^2\theta \, d\theta}{\left[l(\theta)\right]^2} \tag{4}$$

and $l(\theta)$ is the projected length of R as defined in figure 4.

It will be evident from equation (3) that the wave drag depends inversely on the square of an average projected length of the airfoil system - just as the vortex drag depends inversely on the square of the span. However, because of the weighting factor $\sin^2\theta$ the lateral dimensions of R are relatively unimportant compared to the dimension, or length, along the flight direction. Figure 5 shows the magnitude of the error made by using the actual length l and equation (2) for the wave drag of several lifting surfaces.

Generally speaking, the losses associated with the production of a given force in a frictionless fluid are diminished by increasing the area involved in the production of the force and diminishing the pressure. Thus the wave drag is diminished by making the "area" $\bar{l}^2$ as large as possible. The vortex drag is diminished by making the square of the span as large as possible. On the other hand, to diminish the friction drag the actual area S of the wing system must be made as small as possible.

At subsonic speeds the conditions are satisfied by making b^2 large compared with S or using a wing of high aspect ratio. It is a matter of ordinary observation to see that this condition determines the rather special form of subsonic aircraft. In addition, at supersonic speeds a large value of $\frac{\bar{l}^2}{S}$ is needed.

At subsonic speeds, the elliptically loaded lifting line achieves the minimum value of the pressure drag for the whole area covered by the wake of the lifting line. At supersonic speeds such a lifting line develops, according to linear theory, an infinite drag. However, if the line is yawed behind the Mach angle the drag is finite and is actually the smallest value obtainable by any distribution within the region of the parallelogram ABCD shown in figure 6. Such an oblique lifting line maximizes both $\frac{b^2}{S}$ and $\frac{\bar{l}^2}{S}$ simultaneously. At moderate supersonic Mach numbers, the results obtained with a V-shaped lifting line - approximating a swept wing - are nearly as good.

When a wing is made narrower so as to approach a "lifting line" while maintaining a fixed total lift, the lifting pressure must increase. Eventually the pressure, or the lift coefficient, will exceed the limitation imposed by the small disturbance theory or flow separation will occur. Beyond this point increases of aspect ratio either laterally or longitudinally will not necessarily increase the lift-drag ratio.

REFERENCES

1. Busemann, A.: Aerodynamischer Auftrieb bei Überschallgeschwindigkeit (Supplement). Fifth Volta Congress, Reale Academia D'Italia, 1935.

2. Ferrari, C.: Campi di corrente impersonora attorno a solidi di rivoluzione. L'Aerotecnica, vol. XVII, fasc. 6, June 1937, pp. 507-518. (Also available as Brown Univ. Graduate Div. of Applied Math. Trans. 3965a.)

3. Graham, E. W., Beane, B. J., and Licher, R. M.: The Drag of Non-Planar Thickness Distributions in Supersonic Flow. The Aero. Quarterly, vol. VI, pt. 2, May 1955, pp. 99-113.

4. Graham, E. W., Lagerstrom, P. A., Licher, R. M., and Beane, B. J.: A Theoretical Investigation of the Drag of Generalized Aircraft Configurations in Supersonic Flow. Rep. No. SM-19181, Douglas Aircraft, Co., Inc., July 1955.

5. Jones, Robert T.: The Minimum Drag of Thin Wings in Frictionless Flow. Jour. Aero. Sci., vol. 18, no. 2, Feb. 1951, pp. 75-81.

6. Jones, Robert T.: Theoretical Determination of the Minimum Drag of Airfoils at Supersonic Speeds. Jour. Aero. Sci., vol. 19, no. 12, Dec. 1952, pp. 813-822.

7. Hayes, Wallace D.: Linearized Supersonic Flow. Rep. AL-222, North American Aviation, Inc., June 18, 1947.

8. Hemke, Paul E.: Drag of Wings With End Plates. NACA Rep. 267, 1927.

9. Ferri, Antonio, Clarke, Joseph H., and Casaccio, Anthony: Drag Reduction in Lifting Systems by Advantageous Use of Interference. PIBAL Rep. No. 272 (Contract AF 18(600)-694), May 1955.

10. Jones, R. T., and Cohen, D.: Aerodynamics of Wings at High Speeds. Section A of Vol. VII, High-Speed Aerodynamics and Jet Propulsion. (To be published by Princeton Univ. Press.)

CONDITIONS FOR MINIMUM DRAG
DISTRIBUTIONS OF LIFT AND VOLUME IN REGION R

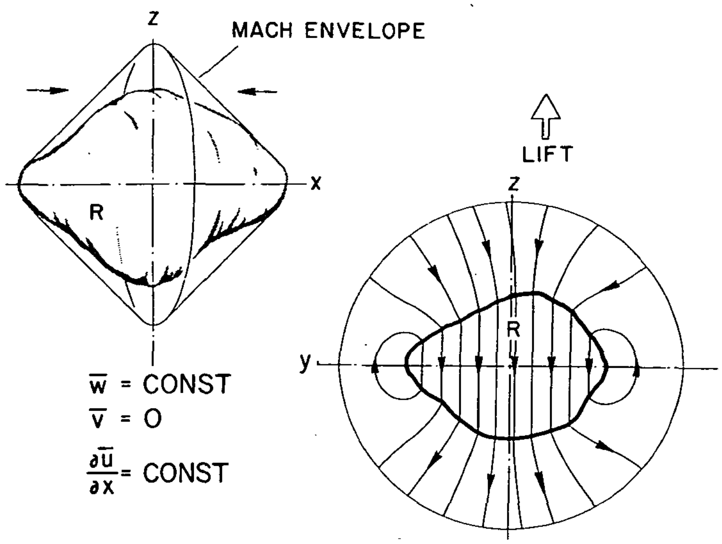

Figure 1

DISTRIBUTIONS OF LIFT AND VOLUME WITH
SELF-CONTAINED WAVE SYSTEMS

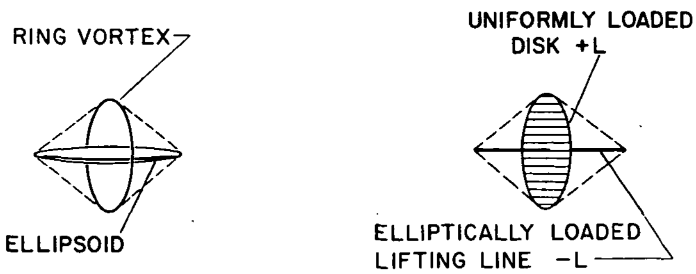

Figure 2

[redacted]

USE OF CONDITION $\bar{v} = 0$ TO DETERMINE OPTIMUM SETTING OF VERTICAL FIN ON WING TIP

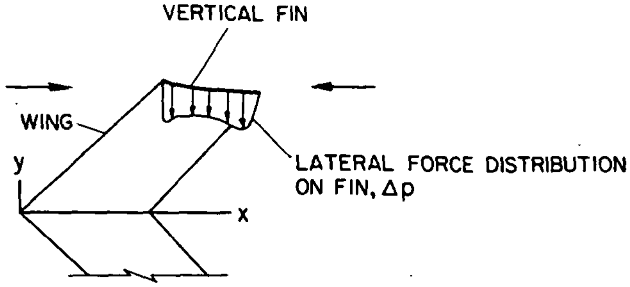

$\Delta p_f = \Delta p_r$; LATERAL FORCE DISTRIBUTION UNCHANGED

$v_f = -v_r$; FIN GEOMETRY UNCHANGED

Figure 3

LOWER BOUND FOR WAVE DRAG ASSOCIATED WITH THE REGION R AND THE LIFT L

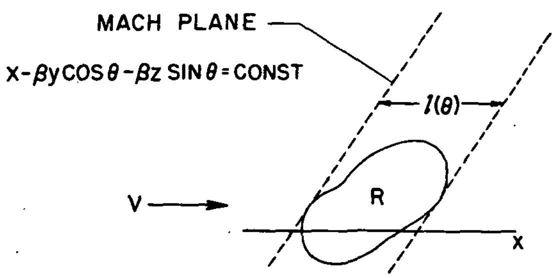

Figure 4

[redacted]

APPROXIMATE EXPRESSION FOR WAVE DRAG OF LIFTING SURFACE

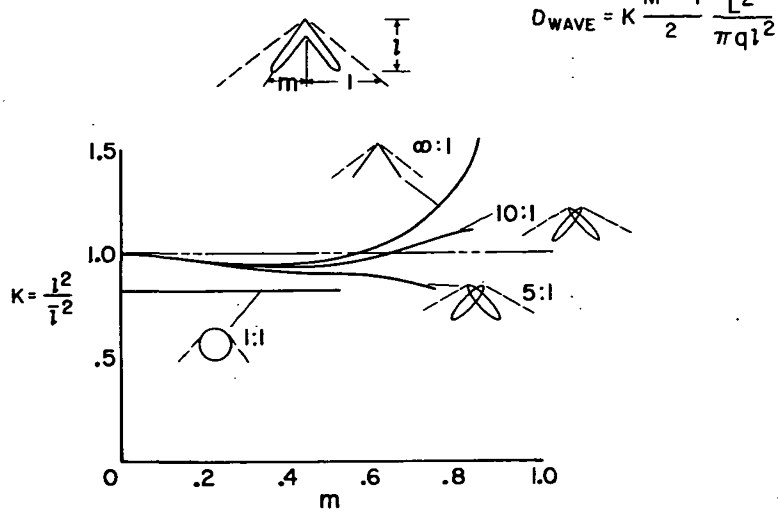

Figure 5

IDEAL DISTRIBUTION OF LIFT FOR PARALLELOGRAM ABCD

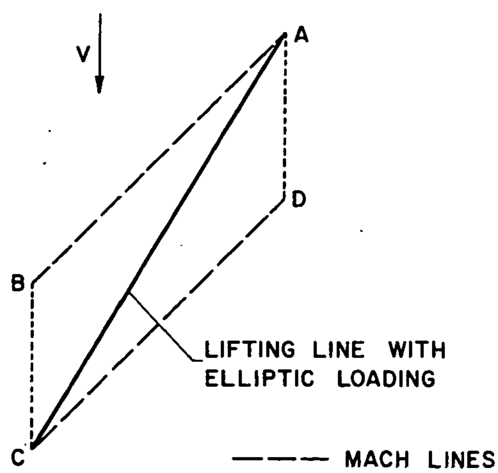

Figure 6

SUPERSONIC DRAG DUE TO LIFT

By Charles W. Frick, Gaynor Adams, and Eugene Migotsky

Ames Aeronautical Laboratory

This paper reports the progress of research on drag due to lift of wings at supersonic speed. Aircraft of more conventional form than those discussed in previous papers by R. T. Jones and Harvard Lomax, that is, arrangements that have a horizontal plane of symmetry, are considered. The methods of the previous papers, however, are again used to extend current knowledge and to outline new areas of analytical and experimental research.

It is of interest to discuss the drag due to lift of wings at supersonic speed in a historical sense. Early analytical studies, particularly those of Jones, showed that low values of drag could be achieved by sweeping the wing behind the Mach lines so that the drag due to lift approximates values for subsonic speed. Low drag at subsonic speed is achieved because the streamwise component of the force normal to the flat wing surface is opposed by a suction force on the leading edge that results from the peak pressure at that point. These two forces balance one another for the case of infinite aspect ratio.

Analytical studies for supersonic flow showed that, for wings with leading edges swept well behind the Mach lines, these two forces still tend to balance one another to give low drag. This point is illustrated in figure 1 where for triangular airfoils at near sonic speed the net suction force is equal to one-half the streamwise component of the force normal to the flat-wing surface. The drag due to lift then is given by

the usual formula $\dfrac{C_D}{{C_L}^2} = \dfrac{1}{\pi A}$.

Experimental measurements for swept wings, however, give a drag due to lift about twice the theoretical value, that is, $2/\pi A$. A study of the flow about the wing showed that, whereas in the theory the streamlines of the flow bend sharply about the leading edge to give the high pressure peak which contributes the leading-edge suction force, in the real flow the streamlines leave the wing tangentially on both the upper and lower surface and the suction force is not realized. A study of this type of flow has been made by Brown and Michaels of the Langley Aeronautical Laboratory (ref. 1). It is interesting to note that, in the real flow, a vortex sheet discharges from the edge rolling up in a region lying above the wing surface and trailing back into the wing wake. Since at very low supersonic speeds there is little wave drag due to lift, obviously the increase in drag due to the loss of the leading-edge suction force must appear as vortex drag and this vortex filament represents in part the increased vortex drag.

During the investigation of triangular wings, it became apparent that the low theoretical drag due to lift of the flat-plate wing could be obtained by cambering the airfoils so as to approximate the same span-load distribution as the flat plate (elliptical) while reducing the local pressure in the vicinity of the wing leading edge so as not to produce the flow separation that occurs on flat wings (ref. 2). The results of an experimental investigation of wings incorporating such conical camber are shown in figure 2. These results show that, at cruising lift coefficients not less than 0.2 or greater than 0.4, there is a reduction in the drag for the cambered wing below the value for the flat wing. This gain, however, is accompanied by a penalty in minimum drag at zero lift, which may be important insofar as the maximum flight speed is concerned. A comparison between the measured drag values for the aspect-ratio-2 triangular wing with conical camber and the ideal flat-wing polar is also presented in figure 2. The comparison shows that the cambered wing achieves the same drag values as the ideal flat wing in the range of lift coefficients near the design value of 0.25. These data illustrate the fact that the increase in minimum drag is not significant in cruising flight.

Figure 3 shows a comparison between the experimental values for the flat plate and cambered triangular wings and the theoretically predicted drag due to lift parameter plotted as a function of the reduced aspect ratio. The upper branch of this curve shown by the solid line gives the results for flat wings with no leading-edge suction force. The dashed line shows the branch of the curve with full leading-edge suction. These results demonstrate that the use of conical camber in the low supersonic Mach number range permits the achievement of low drag due to lift.

The previous discussion has been concerned with drag at lift for transonic and low supersonic Mach numbers. There is, however, increasing interest in cruising flight at supersonic speed. Analysis shows that the effect of flight velocity on engine efficiency is so favorable that even with the relatively inefficient airframes that can now be devised for supersonic cruising, it is most desirable to fly at the highest permissible Mach number subject to temperature limitations, for example, Mach numbers not less than 2 or greater than 3. Values of βA of about 4 or perhaps greater are considered since the true wing aspect ratio cannot be permitted to fall below about 2.0 without incurring low-speed problems.

For values of reduced aspect ratio of 4 or greater, the data of figure 3 show that the leading-edge suction force is theoretically nonexistent and that the drag resulting therefrom appears as wave drag. The question arises whether it is possible through the use of wing camber to reduce the wave drag due to lift. This question, of course, has been answered by the work of Jones on optimum airfoils (ref. 3). However, in the analysis of this reference, the methods of deriving wing contours are not set forth explicitly. In fact, no direct method is presently available for deriving the surface shape and ordinates for optimum lift distribution. The subsequent portion of this paper is concerned with conveying some physical feeling for what is required to achieve near-optimum wings to fill this need. The reader is also referred to a report (ref. 4) by the Douglas research group of Graham, Lagerstrom, and others for other views on this subject.

It is expedient first to try to determine what gains are possible through the use of wing camber and for this purpose the concept of the lower bound drag proposed by Jones is again utilized. Figure 4 shows the equation which was proposed modified somewhat for the current analysis. The length $l(\theta)$, which is the distance along the wing axis intercepted by the first and last Mach planes at angle θ which touch the airfoil, was nondimensionalized by dividing by the streamwise length of the airfoil c_o. As the Mach planes are rotated through the angle θ, the ratio $l(\theta)/c_o$ varies from a maximum at $\theta = 0$ to a value of unity at $\theta = \pi/2$ and $3\pi/2$. The reciprocal of this quantity appears in the integrand and is plotted separately in figure 4. There also appears in the integrand a factor $\sin^2 \theta$ which weights the values of the reciprocal of the length in such a way as to give greatest influence to values near $\pi/2$ and $3\pi/2$.

The major parameter in determining the lower bound wave drag due to lift is the ratio of the square of the overall length to the wing area, that is, the aspect ratio of the airfoil when viewed in the cross-stream direction, designated in this paper as the length aspect ratio. The influence of this parameter on wave drag due to lift may be compared with the influence of span aspect ratio on the vortex drag. The influence of the integral itself on wave drag may be considered as comparable to the effect of taper ratio on vortex drag.

Utilizing this equation, the lower bound of the wave drag due to lift can be calculated as shown in figure 5. Further, the minimum vortex drag can be calculated from the formula

$$\frac{C_D}{{C_L}^2} = \frac{1}{\pi A}$$

The sum of these two contributions is then the lower bound of drag due to lift assuming, of course, that the skin-friction drag does not vary with lift coefficient. It should be noted that the lower bound curve only admits no lower drag. It is possible that the minimum drag lies above these values. However, a comparison between this lower bound and the values of drag for flat wings gives an indication of the possible benefit of camber.

As noted previously, the theory of airfoils of minimum drag due to lift, reference 3, has been concerned with the definition of conditions necessary to achieve this end and not with the derivation of the shapes that correspond thereto. For this reason, figure 6 has been prepared to give some physical feeling for the problem. Figure 6 shows the wing lying in the xy plane with the traces of the Mach planes for various angles θ. The inclination of the trace relative to the streamwise axis is given by the formula

$$\varphi = \tan^{-1}\left(\frac{1}{\cos\theta}\right)$$

A sufficient condition for the achievement of the lower bound drag is that the integrated load for all traces (at any one value of θ) lying between the foremost and rearmost planes which intersect the airfoil when projected on a streamwise axis describe an elliptic load distribution. The span loading also, of course, is elliptic. In the two plots in figure 6, the loading over flat-plate wings is compared with elliptic loading for two values of βA for two Mach plane angles θ. A feeling for the influence on drag of these departures from elliptic loading can be obtained from the knowledge that the formula that applies is exactly that for the calculation of vortex drag. It is evident from these charts that the load distribution for $\beta A = 2$ does not depart greatly from the ellipse at $\theta = 45^{\circ}$ and that the lower bound can be approached by adjusting the chordwise loading distribution to be elliptic instead of triangular. This, of course, is the finding of Jones for the case of slender triangular airfoils.

For the case of the flat wing with sonic edges, $\beta A = 4$, the loading for all Mach plane cuts becomes important even though the drag is averaged according to the weighting factor $\sin^2\theta$. The load distribution departs so radically from the optimum that the average drag becomes very large.

At the present time, calculations necessary to derive near-optimum wings are being made consisting of the superposition of a number of loadings chosen to contribute to the required loading. Some of the results of the first calculations are shown in figure 7. Two simple cases were chosen for wings with sonic edges with a view toward improving the distribution of loading in the Mach plane cuts for $\theta < 45^{\circ}$ and for $\theta > 45^{\circ}$. Both show a reduction in drag. The wing with conical camber has a value of the drag parameter very nearly equal to the minimum drag attainable with the flat wing. These wings in no sense approach the optimum. Calculations are proceeding to derive wings falling nearer the lower bound.

It should be mentioned that for the optimum wings there is a by-product advantage of no little consequence in that the wings are self-trimming. If elliptic loading is obtained for a Mach plane orientation of $\theta = 90^{\circ}$, the center of pressure of the design lift occurs at 25 percent of the mean aerodynamic chord, and no trim drag is incurred at the design lift. This point has been noted previously by staff members of the Langley Aeronautical Laboratory.

It is apparent from the foregoing discussion that the plan form of the wing will have an important effect on the difference between flat-wing drag values and those of the lower bound. This point is illustrated by the results of figure 8 where the comparison is made for wings of diamond plan form. For these wings, the lower bound indicates that a maximum reduction of drag due to lift of 20 percent may be possible compared with a reduction of 33 percent for triangular wings. On this figure, the result has been plotted for an optimum wing of this plan form derived by the Douglas wing-research group (ref. 4) shown by the diamond point which falls on the lower bound. For comparison, the best triangular wing of figure 7 is plotted to show the effects of plan form. This comparison demonstrates that it is more profitable to study triangular airfoils for low drag than those of diamond plan form.

Figure 9 shows the comparison of the lower bound with flat-wing drag for rectangular wings. The data here also show that there is less to be gained by camber than for triangular plan forms, the best of which is shown by the circle point which strikes the lower bound for the rectangular wing. Also shown by the cross points are calculated drags for rectangular wings taken from reference 3. These particular wings are not optimum, however.

Figure 10 shows the drag due to lift for a sweptback wing. The values for flat wings are much lower than for the other wings investigated for two reasons: first, for values of βA less than 8, the leading edge is swept behind the Mach lines so that the leading-edge suction force is obtained and second, the geometry of the plan form is such as to give load distributions for $\theta \approx \pi/2$ and $3\pi/2$ that approach the idealized loading. These effects are so important that the flat wing for values of βA less than 6 is almost the equivalent of the optimum wing. Experience has shown, however, that the sweepback angles of 60° to 70° required to achieve these values at Mach numbers from 2 to 3 are very undesirable because of the attendant stability and control problems. It is questionable whether the indicated drag reductions are large enough to influence the design compromise.

Only the branch of the drag curve for flat wings which corresponds to full leading-edge suction has been plotted since it has been previously shown that camber readily permits the attainment of this contribution to low drag.

The salient points of the foregoing discussion can best be brought out by the comparison of figure 11 where the lower bound and flat-plate wing values are given for four wings of reduced aspect ratio 4. For the optimum wings to which the lower bound values apply, the vortex drag is the same and has a value of 0.08. Examination of the lower bound values for the rectangular airfoil shows that the wave drag even for this optimum case is almost twice the vortex drag. The reason for this is clearly illustrated in the equation of figure 4, which shows that the length aspect ratio is an important parameter. For this wing, this geometric parameter is small.

This large wave drag could be reduced by increasing the root chord length by tapering the wing to a point, as shown by the diamond plan form. The increase in the aspect ratio viewed from the side should reduce the wave drag by 75 percent. The calculated reduction, however, is 20 percent since the influence of the plan-form change on the value of the integral term has been large enough to offset the improvement in the length aspect ratio.

If the elements of the diamond plan form are sheared rearward, the triangular wing is obtained. The length aspect ratio for this wing is the same as for the diamond plan form. The reduction in drag is, therefore, attributable to the influence of the integral term in the equation for wave drag. Further shearing of the wing reduces the wave drag further as shown by the swept wing. This process can be extended until the total drag approaches the vortex drag.

From a comparison of the flat-wing values with the lower bound, it is evident that the greatest percentage improvement in the drag due to lift may occur for the triangular wing if the minimum lies near the lower bound. It would appear that only for this plan form are the gains due to camber indicated to be of sufficient magnitude to offset the penalty in minimum drag that will be incurred.

3Z

REFERENCES

1. Brown, C. E., and Michael, W. H., Jr.: Effect of Leading-Edge Separation on the Lift of a Delta Wing. Jour. Aero. Sci., vol. 21, no. 10, Oct. 1954, pp. 690-694, 706.

2. Boyd, John W., Migotsky, Eugene, and Wetzel, Benton E.: A Study of Conical Camber for Triangular and Sweptback Wings. NACA RM A55G19, 1955.

3. Jones, R. T.: Theoretical Determination of the Minimum Drag of Airfoils at Supersonic Speeds. Jour. Aero. Sci., vol. 19, no. 12, Dec. 1952, pp. 813-822.

4. Graham, E. W., Lagerstrom, P. A., Beane, B. J., Licher, R. M., and Rodriguez, A. M.: Reduction of Drag Due to Lift at Supersonic Speeds, Part 2. USAF Tech. Rep. No. 54-524, Wright Air Dev. Center, U. S. Air Force, Aug. 1954.

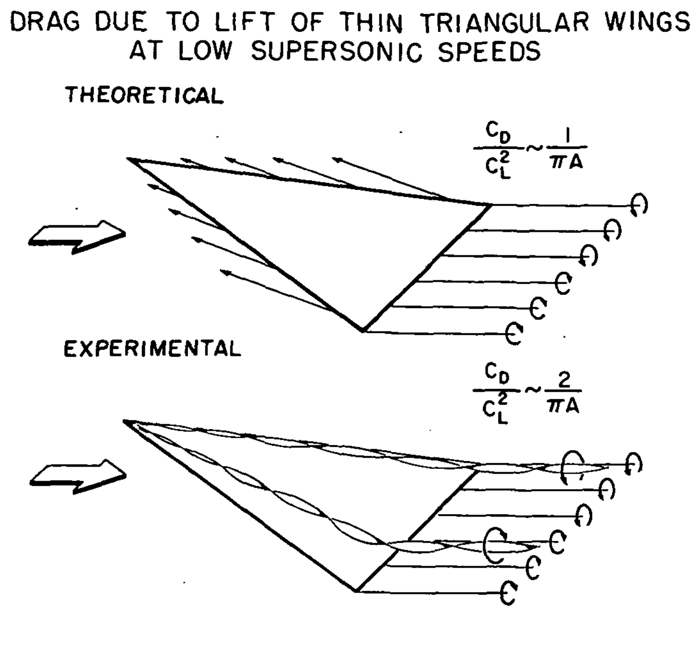

Figure 1

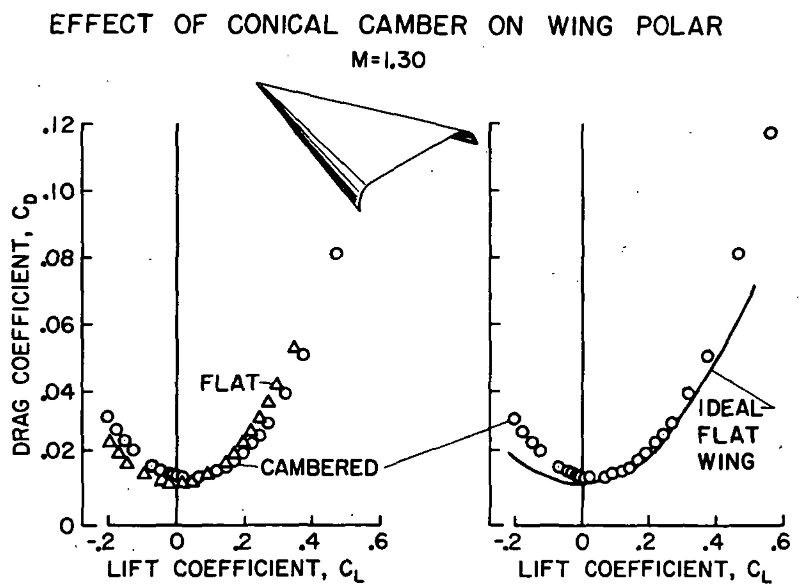

Figure 2

DRAG DUE TO LIFT FOR TRIANGULAR WINGS

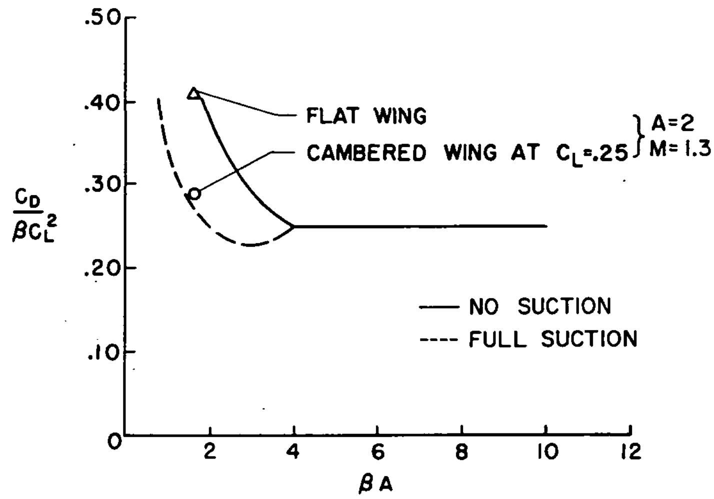

Figure 3

LOWER BOUND WAVE DRAG DUE TO LIFT

$$\left(\frac{C_D}{\beta C_L^2}\right)_W = \frac{\beta}{2\pi^2}\left(\frac{S}{c_o^2}\right)\int_0^{2\pi}\frac{\sin^2\theta}{\left[\frac{l(\theta)}{c_o}\right]^2}\,d\theta$$

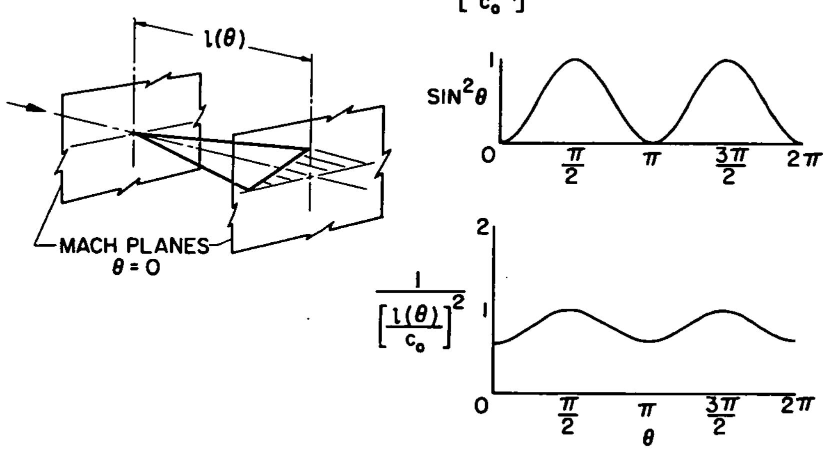

Figure 4

LOWER BOUND OF DRAG DUE TO LIFT

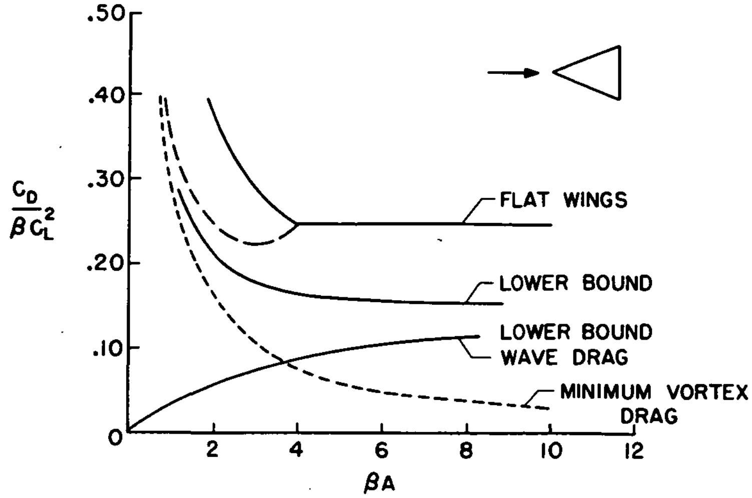

Figure 5

FLAT TRIANGULAR WING LOADINGS FOR MACH PLANE CUTS

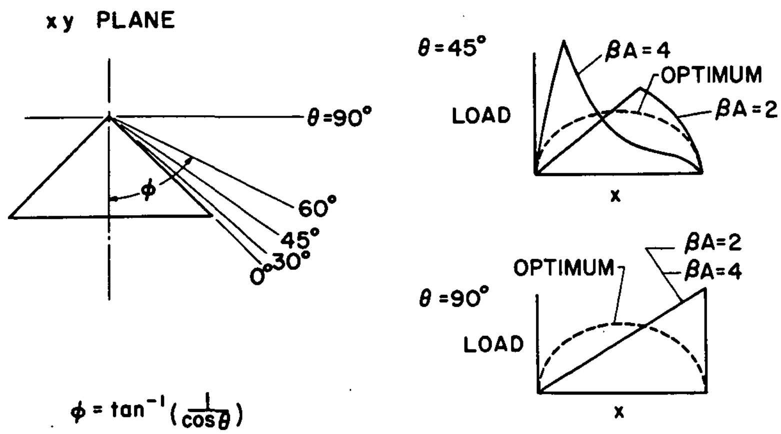

Figure 6

DRAG DUE TO LIFT OF TRIANGULAR WINGS

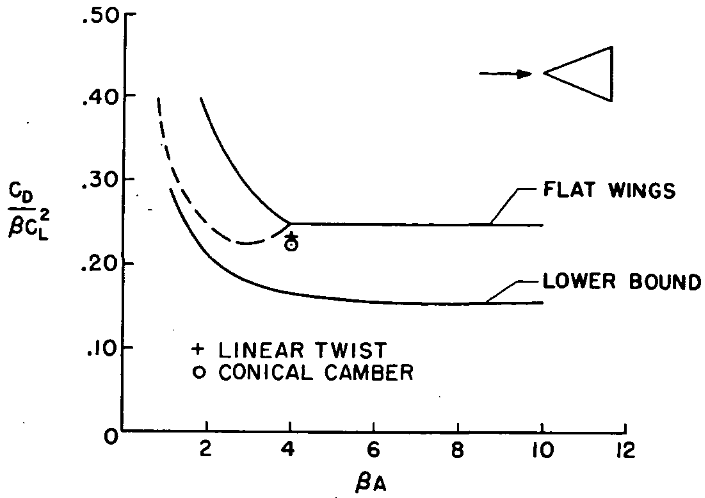

Figure 7

DRAG DUE TO LIFT FOR DIAMOND PLAN FORMS

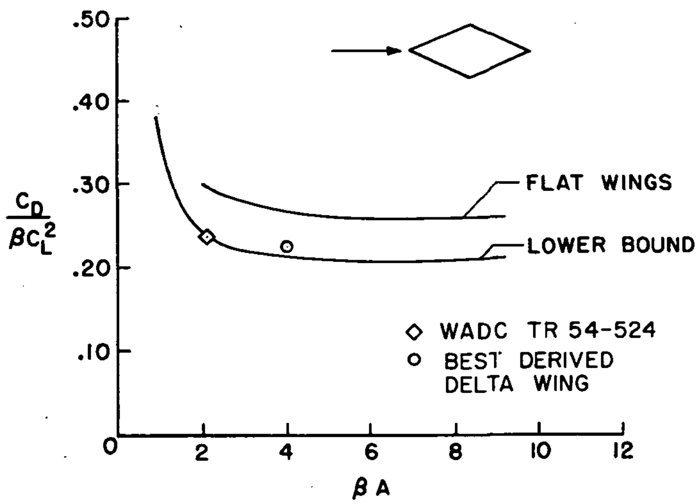

Figure 8

DRAG DUE TO LIFT OF RECTANGULAR WINGS

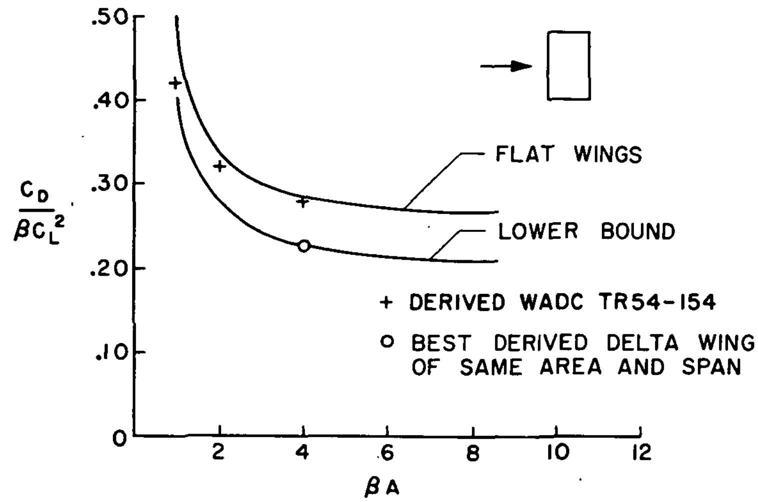

Figure 9

DRAG DUE TO LIFT OF SWEPT BACK WINGS

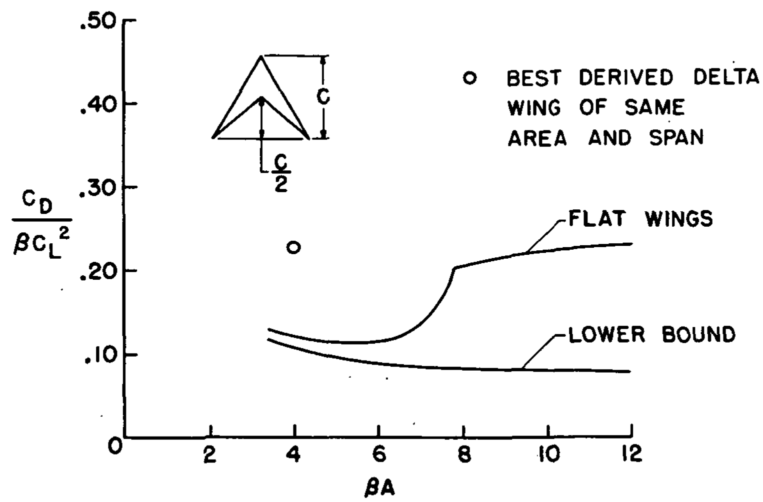

Figure 10

COMPARISON OF DRAG DUE TO LIFT OF WINGS OF VARIOUS PLANFORMS OF SAME AREA AND SPAN

PLAN $\beta A = 4$	LOWER BOUND $\frac{C_D}{\beta C_L^2}$	FLAT PLATE WING $\frac{C_D}{\beta C_L^2}$
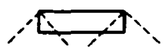	.229	.285
	.210	.265
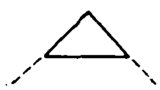	.165	.250
	.108	.125

Figure 11

DRAG OF CANOPIES AT TRANSONIC

AND SUPERSONIC SPEEDS

By Sherwood Hoffman and A. Warner Robins

Langley Aeronautical Laboratory

SUMMARY

Area-rule analysis provides a good basis for the design of efficient canopies at transonic and supersonic speeds. However, detailed canopy design is important for minimizing the subsonic drag increment. Body indentation may be expected to reduce the canopy drag from 25 to 50 percent at low supersonic speeds. In general, the inclined flat windshield is as good as the vee windshield from a drag standpoint. The pressure drag of canopies can be adequately predicted with area-rule theory above Mach number 1.1.

INTRODUCTION

The design of pilot canopies for minimum drag is important for optimum performance of airplanes at high speeds. Recent tests indicate that the drag of conventional type canopies varies from 10 to 20 percent of the airplane drag above Mach number 1.0. In order to aid the designer in minimizing this drag penalty, the National Advisory Committee for Aeronautics has conducted several investigations to determine some of the basic drag properties of canopies, such as the effect of windshield shape, size, and location on drag, as well as the usefulness of the area rule for reducing and predicting the drag due to canopies. The purpose of this paper is to give a short account of these investigations with the view of providing a basis for the design of efficient canopies at transonic and supersonic speeds.

8

SYMBOLS

A cross-sectional area

A_c canopy frontal area

A_f fuselage frontal area

A_{max}	maximum cross-sectional area
C_{D_O}	zero-lift drag coefficient
ΔC_{D_O}	zero-lift drag-rise (or pressure drag) coefficient
F	fineness ratio
l	total length of configuration
l_A	forebody length
M	Mach number
x	longitudinal distance

RESULTS AND DISCUSSION

Canopy-Fuselage Total Drag

Windshield shape.- An example of the effect of windshield shape on drag is given in figure 1. The three configurations near the top of the figure were identical except for the shape of the windshield. The vee and flat windshields were derived from the round windshield. All three canopies had a frontal area equal to 0.165 the fuselage frontal area and an equivalent body fineness ratio of 7. The body is a drooped-nose forebody of fineness ratio 5.6. Both the canopies and body had elliptical cross sections. The total drag coefficients are for zero angle of attack and are based on the body frontal area. The tests were made in the Langley 8-foot transonic tunnel (ref. 1) and in the Langley 4- by 4-foot supersonic pressure tunnel (ref. 2) for the ranges of Mach number shown.

The comparison shows that windshield shape may have an important effect on drag at all Mach numbers. The vee windshield has about twice the subsonic drag increment of the flat windshield at high subsonic speeds, approximately 30 percent more drag than the flat windshield at transonic speeds, and slightly more drag than the flat and round windshields near Mach number 2.0. Calculations from pressure surveys (ref. 2) on the flat and vee windshields show that the lower drag for the flat windshield is associated with the flow expansions around the edges of the windshield so as to produce lower pressure over the canopy frontal projection.

The apparent superiority of the flat over the vee in this case is not necessarily representative of flat and vee windshields in general. In a second case, the incremental differences were smaller, and, in a third case, there was no measurable difference due to windshield shape. It is significant, however, that a flat windshield may be used without any drag penalty relative to a vee windshield.

Canopy size.- The effect of canopy size on drag is shown also in figure 1 (refs. 1 and 2). The frontal area of the large flat-face canopy was reduced about 40 percent, the fineness ratio was increased from 7 to 10, and the windshield sweepback was increased from 55° to 65°. These changes gave a large reduction in the canopy drag, reducing the drag increment by about 60 percent at supersonic speeds. It is evident from this comparison and others that minimum frontal area, high fineness ratio, and low windshield slope (ref. 3) for canopies on pointed bodies are necessary for low drag above Mach number 1.0.

Canopy-Fuselage Pressure Drag

The effect that canopy variables have on the pressure drag or drag rise can be predicted in a qualitative way with the transonic area rule (ref. 4) and in a quantitative way with the supersonic area-rule theory (refs. 5 and 6). The test drag-rise coefficients used for the comparisons were obtained by subtracting the drag coefficient at a Mach number of 0.8 from the corresponding drag coefficients at higher Mach numbers.

Windshield shape and canopy size.- A comparison of the normal cross-sectional area distributions of the flat and vee windshields with the measured drag rises near M = 1.0 (fig. 2) shows that the results are in agreement with the concept of the transonic area rule. The vee windshield has a somewhat more rapid rate of development of cross-sectional area than the flat windshield, and, hence, a slightly greater drag rise at transonic and supersonic speeds. As the Mach number increases, the effect of windshield shape on the pressure drag decreases.

When the fineness ratio of the large flat-face canopy was increased from 7 to 10 by reducing its frontal area, the rate of development of its cross-sectional area was improved markedly (fig. 2), giving a smoother overall slope distribution on its area diagram and considerably less pressure drag throughout the Mach number range (fig. 2).

The theoretical variations (fig. 2) were computed for a range of Mach numbers from 1.0 to 1.41. The theory predicts the relative effects of changing windshield shape and canopy size, as well as the order of magnitude of the pressure drag above M = 1.1. The theoretical values are high for the canopy-body combinations; however, the agreement is within 15 percent above M = 1.1. This agreement is good in view of the fact that the theory gives only a first-order approximation of the total pressure drag. It should be remembered, however, that there may be significant differences in the subsonic drag level which would affect the total drag at supersonic speeds.

Canopy location.- The results in figure 3 were obtained from zero-lift rocket-model tests of canopy-fuselage combinations by the Langley Pilotless Aircraft Research Division. A flat-face canopy of fineness ratio 7, windshield sweepback of 63°, and circular cross section was tested in three longitudinal positions between the nose and maximum-diameter station of a parabolic fuselage, as is shown in the figure. The comparisons show that moving the canopy rearward to the maximum-diameter station gives increasing values of pressure drag. For the present case, the incremental drag increased about 20 percent by moving the canopy from the forward to the rearward position at supersonic speeds. The rearward displacement of the canopy increases the rate of development of normal cross-sectional area and gives more frontal area, which, according to the transonic area rule, corresponds to increasing unfavorable interference and higher drag. The supersonic area rule theory predicts the effect of rearward displacement, and, as in the case of the earlier comparisons, gives fairly good predictions of the total pressure drag above $M = 1.1$.

Body indentation.- The aforementioned tests show that the canopy drags may be high. For canopies having about one-sixth the body frontal area, the canopy pressure drag may be as high as the fuselage pressure drag. A possible solution to this problem, recently investigated by the Langley Pilotless Aircraft Research Division, is body indentation according to the transonic area rule to reduce the pressure drag. Figure 4 shows the results of such a symmetrical body modification on the pressure drag of canopies having flat and vee windshields. The symmetrical indentations used were designed to cancel the exposed canopy cross-sectional areas normal to the body axis. The indentations reduced the fuselage volume by approximately 3 percent.

The normal area indentation produced substantial reductions in the total pressure drag of both the flat and vee windshields (fig. 4) at transonic and supersonic speeds. The test results for the flat windshield are compared with the theoretical pressure drags for both the indented and original configurations in this figure. The theory indicates a large reduction in pressure drag due to indentation and shows that the effectiveness of the transonic indentation diminishes with increasing Mach number. The actual reduction in drag is slightly less than one-half of that predicted; nevertheless, the actual reduction is an appreciable part of the canopy drag.

These tests and others show that $M = 1.0$ indentations may be expected to give from 25 percent to 50 percent reduction in canopy drag at low supersonic speeds. Greater reductions may be possible from supersonic indentations or unsymmetrical indentations.

Canopy-Airplane Drag

The results just described are applicable, more or less, to airplanes having a smooth total normal area distribution for the body, wings, and other components. For a more practical case, where the airplane area diagram has a bump due to the wing, the optimum canopy size and location may depend, to a large extent, on designing the canopy to make the total normal area distribution smooth, as is shown in figure 5. The configuration is a fighter airplane, with a canopy modification that was recently tested in the Langley 8-foot transonic tunnel. The original model had a small canopy and a poor area distribution in the region of the wing and small canopy. The canopy volume was almost doubled and its fineness ratio was increased to make the total airplane area distribution smooth. As a result, the total drag coefficient (based on wing plan-form area) was reduced about 4 percent and the pressure drag by approximately 7 percent at $M = 1.13$. The reductions at transonic speeds were less, with no reduction being noted below a Mach number of 0.9.

CONCLUSIONS

Area-rule analysis provides a good basis for the design of efficient canopies at transonic and supersonic speeds. However, detailed canopy design is important for minimizing the subsonic drag increment. The canopy should be so designed as to provide, together with the airplane, a smooth overall area distribution, it being kept in mind that minimum frontal area, low windshield slope, and high fineness ratio for canopies are compatible with low drag. Body indentation for canopies according to the transonic area rule may be expected to reduce the canopy drag from 25 to 50 percent at low supersonic speeds. In general, the inclined flat windshield is as good as the vee windshield from a drag standpoint. The order of magnitude of the pressure drag of canopies on pointed-nose fuselages can be adequately predicted with area-rule theory above Mach number 1.1.

REFERENCES

1. Cornette, Elden S., and Robinson, Harold L.: Transonic Wind-Tunnel Investigation of Effects of Windshield Shape and Canopy Location on the Aerodynamic Characteristics of Canopy-Body Combinations. NACA RM L55G08, 1955.

2. Robins, A. Warner.: Force and Pressure Measurements on Several Canopy-Fuselage Configurations at Mach Numbers 1.41 and 2.01. NACA RM L55H23, 1955.

3. Kell, C.: Measurements of the Effects of Windscreen Shapes on the Drag of Cockpit Canopies at Transonic and Low Supersonic Speeds Using the Free Flight Model Technique. Rep. No. Aero 2529, British R. A. E., Nov. 1954.

4. Whitcomb, Richard T.: A Study of the Zero-Lift Drag-Rise Characteristics of Wing-Body Combinations Near the Speed of Sound. NACA RM L52H08, 1952.

5. Jones, Robert T.: Theory of Wing-Body Drag at Supersonic Speeds. NACA RM A53H18a, 1953.

6. Holdaway, George H.: Comparison of the Theoretical and Experimental Zero-Lift Drag-Rise Characteristics of Wing-Body-Tail Combinations Near the Speed of Sound. NACA RM A53H17, 1953.

EFFECT OF WINDSHIELD SHAPE AND CANOPY SIZE ON TOTAL DRAG

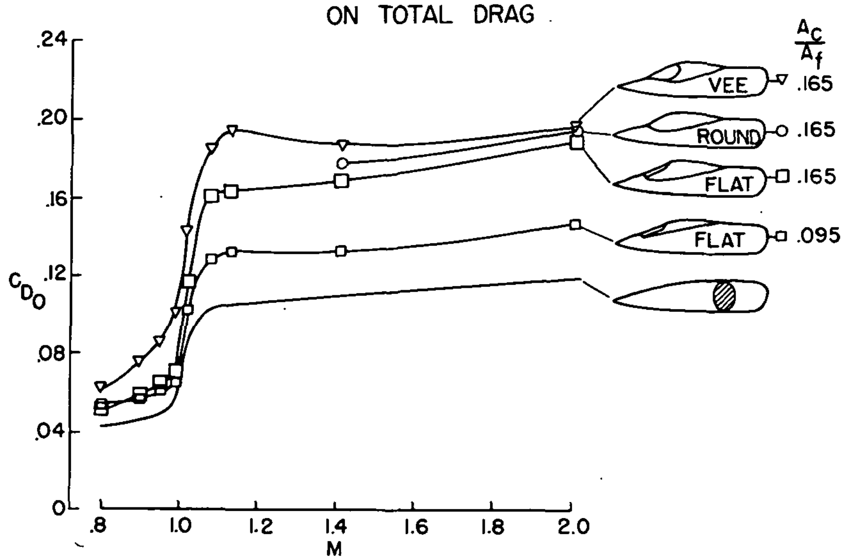

Figure 1

EFFECT OF WINDSHIELD SHAPE AND CANOPY SIZE ON PRESSURE DRAG

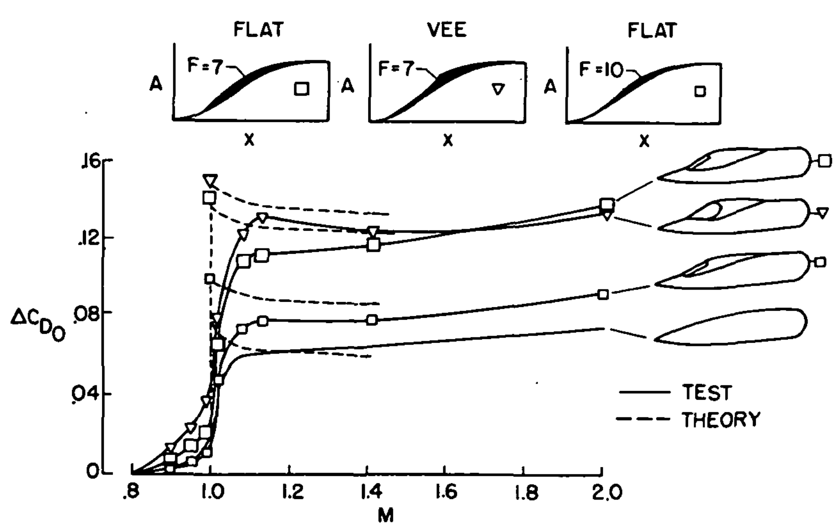

Figure 2

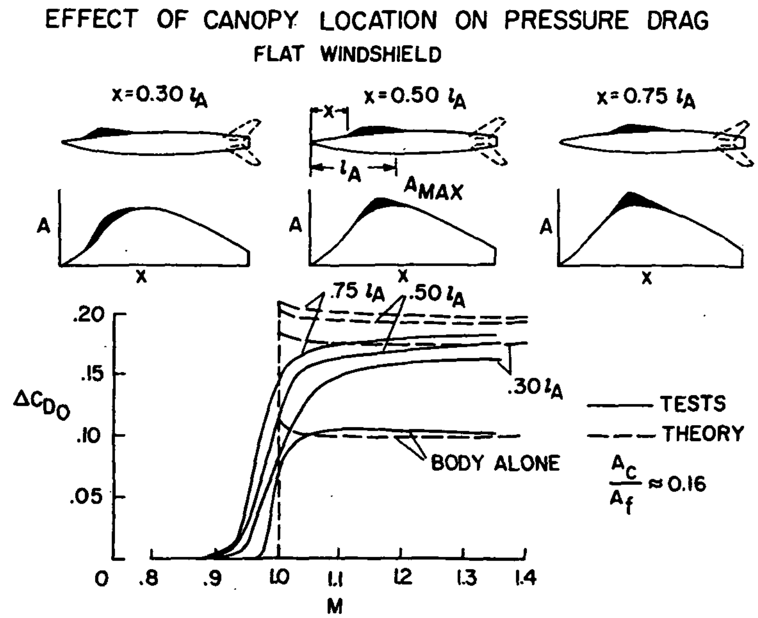

Figure 3

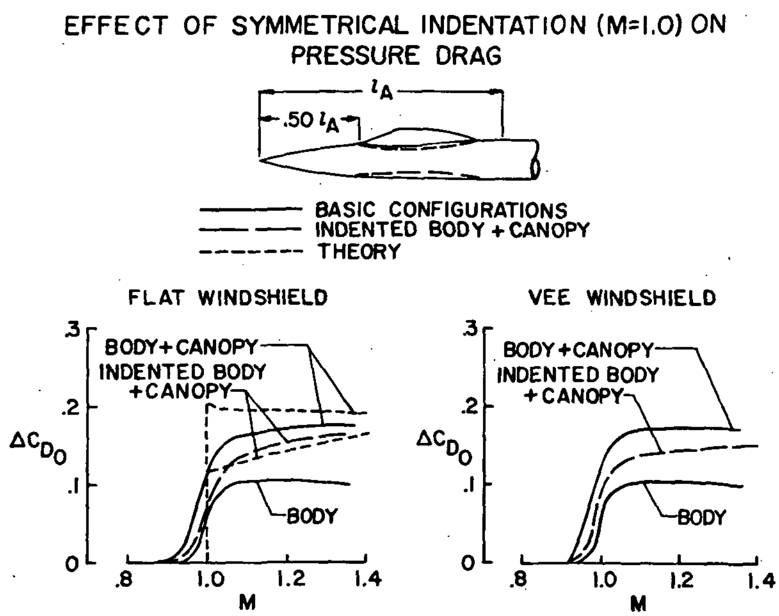

Figure 4

CANOPY MODIFICATION TO CONFORM WITH COMPLETE CONFIGURATION

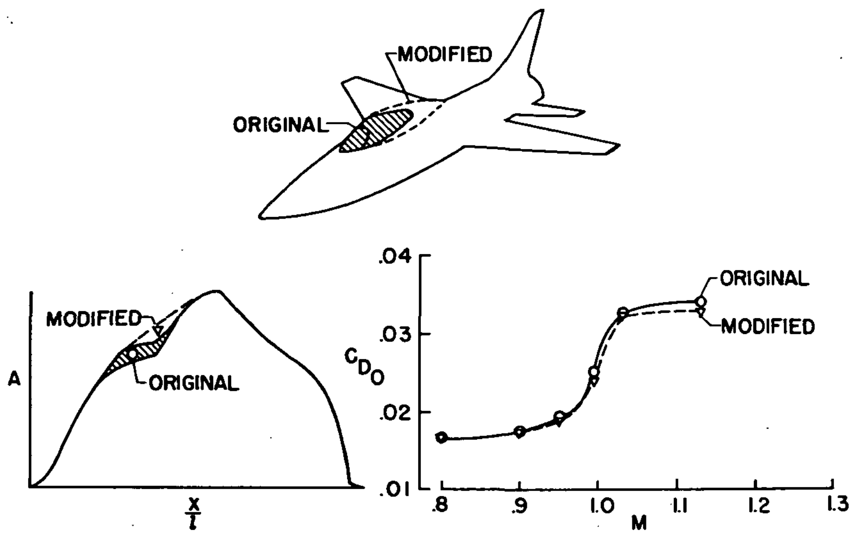

Figure 5

EXTERNAL-STORE DRAG REDUCTION AT TRANSONIC AND LOW SUPERSONIC MACH NUMBERS BY APPLICATION OF BALDWIN'S "MOMENT-OF-AREA RULE"

By Lionel L. Levy and Robert R. Dickey

Ames Aeronautical Laboratory

INTRODUCTION

Several theories have been developed in recent years which indicate methods for modifying wing-body combinations in order to obtain low wave drag at transonic and supersonic speeds. As outlined in reference 1, the modifications according to Baldwin's "moment-of-area rule" consist, in part, of the addition of auxiliary wing-mounted bodies of revolution. It is this feature which makes the method particularly appealing as a means of reducing the drag of aircraft fitted with external stores. This paper is concerned with the application of the moment-of-area rule to the drag reduction of external-store installations. First, however, a brief description of the moment-of-area rule is presented.

MOMENT-OF-AREA RULE

Baldwin has expressed the wave-drag equation for the supersonic area rule in powers of the speed parameter β, as shown at the top of figure 1. The constant coefficients are independent of Mach number and depend only upon the configuration geometry, that is, upon distributions of area and moments of area about the longitudinal axis. In general, a_0 depends only upon the area distribution, a_2 depends upon the second-moment-of-area distribution as well as the area distribution, a_4 depends upon the fourth- and second-moment-of-area distributions and the area distribution, and so on. For a Mach number of 1 the drag equation becomes a function of the area distribution only, and thus reduces to that of the transonic area rule. As the Mach number is increased above 1 the drag becomes dependent upon the distributions of the second and higher order moments of area. The theory thus offers, in principle at least, a means of optimizing the geometry of a configuration at a Mach number of 1 in order to obtain a low wave drag at that Mach number and to obtain a low rate of increase in drag as the Mach number is increased above 1. In the applications of the moment-of-area rule made thus far, however, low drag has been obtained

9

for only sonic and low supersonic speeds, as only the distributions of area and second moment of area have been optimized.

As an illustration of the application of the optimization procedure, consider the wing-body combination shown on the left in figure 1. Also shown directly below, in solid lines, are the distributions of area and second moment of area for this basic configuration. The second-moment-of-area distribution of the body is small compared with that of the wing and is therefore neglected. The shapes of these distribution curves are not conducive to low drag in that the area distribution has a bump at the location of the wing and the second-moment-of-area distribution is short and has steep slopes. For a given volume and length the optimum shapes of the distribution curves are shown by the dashed lines. The optimum second-moment distribution is obtained by utilizing auxiliary bodies of revolution, or pods, mounted on the wing as shown on the right in figure 1. The optimum area distribution is obtained by reshaping the body after the pods have been added.

Experimental values of the zero-lift wave-drag coefficients for both the basic and the modified configurations are shown in figure 2. Also shown for comparison are experimental values of the wave drag of a similar configuration modified according to the transonic area rule. Note that the moment-of-area-rule modification resulted in lowest wave drag at all Mach numbers. The higher drag for the transonic-area-rule modification at a Mach number of 1 is believed to result from effects associated with the greater slopes of the body indentation on that configuration.

APPLICATION TO EXTERNAL-STORE INSTALLATIONS

The applications of the moment-of-area rule to external-store installations which have been made to date have been concerned with the installation of four air-to-air missiles on several wing-body combinations representative of current airplane designs. It was evident that the auxiliary wing-mounted pods used in the moment-of-area method would provide excellent positions for mounting the missiles. With missiles installed, an optimum or near-optimum second-moment-of-area distribution and area distribution for a complete configuration would be maintained by altering the wing pods to compensate for both these distributions for the missiles. With complete success in maintaining optimum distributions, a modified configuration with missiles would be expected to have not only lower wave drag than the basic configuration with missiles, at transonic and low supersonic speeds, but also lower drag than the basic configuration without missiles. This would be the result of eliminating or reducing the interference drag between various components of the modified configuration itself as well as eliminating the interference drag due to the addition of the missiles.

In experimentally evaluating these possible benefits of the moment-of-area rule, three configurations consisting of a high-fineness-ratio Sears-Haack body and a thin wing of either unswept, sweptback, or triangular plan form were selected. These configurations, complete with modifications and four typical air-to-air missiles, are shown in figure 3. Note that the modified body of each configuration was obtained by making additions to the body, as probably would be done in modifying the fuselage of an existing airplane, rather than by making an indentation. These additions or gloves were made along the sides of the bodies rather than around the bodies (in a circular fashion) in order to simplify their fabrication. The distributions of area and second moment of area for the modified and the basic configurations are shown in figure 4. In the case of the unswept-wing configuration it was possible to obtain the desired shape of the distribution curves without increasing their peak values. For the other two configurations the desired shapes were obtained at a slight cost of increases in the peak values, as shown in the lower part of figure 4.

For purposes of evaluating the results for the modified configurations, data were also obtained for the basic configurations without missiles, and with missiles mounted in a more conventional manner. Several of the basic configurations with conventional missile installations are shown in figure 5. In one case the missiles were mounted so that they were unstaggered in the streamwise direction. In the other cases the missiles were staggered streamwise so that the addition of the missiles would provide at least a limited improvement in the distributions of area and second moment of area. This is demonstrated at the top of figure 6 for the unswept-wing configuration.

Tests of the basic and modified configurations with and without missiles were conducted in the Ames 2- by 2-foot transonic tunnel at Mach numbers from 0.6 to 1.4 and at a Reynolds number of 1.5×10^6 based on the mean aerodynamic chords of the models. A turbulent boundary layer was artificially produced on each configuration with the aid of boundary-layer transition strips in order to permit, with a minimum degree of uncertainty, evaluation of the wave drag of each configuration from its total-drag measurements.

The results of the total-drag measurements for the unswept-wing configuration are presented in figure 7. Note the reductions in drag obtained by merely staggering the conventionally mounted missiles in the streamwise direction. Of all the configurations with missiles, the modified configuration had the lowest total drag at all Mach numbers above 0.94. At subsonic speeds the higher drag of the modified configuration is directly attributable to the skin-friction drag of the increased surface area associated with the added volume of the wing pods and the body glove. For this configuration these additions increased the volume by about 15 percent. The total-drag results for the sweptback- and the triangular-wing configurations are shown in figure 8. It is seen that each of the modified configurations with missiles had lower total drag at transonic speeds than did each of the corresponding basic configurations with the staggered conventional missile installation. Unlike the unswept-wing configurations, however, at subsonic Mach numbers below 0.9 and at supersonic Mach numbers above 1.2 there was little difference in the drag. For these configurations the volume was increased by about 11 percent for the swept-wing and 10 percent for the triangular-wing configuration.

In considering these total-drag results in terms of full-scale airplanes, it is, of course, important to take into account the effect of Reynolds number on the skin-friction drag components. In view of the fixed transition of the boundary layer at the low Reynolds number of this investigation, and the probable natural transition at flight Reynolds numbers, the skin-friction drag penalty for a modified configuration at flight Reynolds numbers would be expected to be less than that observed here.

The wave-drag components of these total-drag measurements, however, would be expected to be directly applicable at flight Reynolds numbers. In evaluating the wave-drag components, the usual procedure was followed of assuming that the subsonic level of the drag at a Mach number of 0.6 is a good measure of the skin-friction drag throughout the speed range of this investigation. This is believed to be a good assumption in the present case because of the fixed transition provided. The resulting wave-drag values for the unswept-wing configuration are presented in figure 9.

As was pointed out previously, complete success in the application of the moment-of-area rule would be expected to result in a modified configuration with missiles having less wave drag than the basic configuration without missiles. This expectation was achieved in the case of the unswept wing only near sonic speed. The wave-drag results for the swept- and triangular-wing configurations are shown in figure 10. Note that the modified configurations with missiles had essentially the same or higher wave drag than the corresponding basic configurations without missiles. This result is believed to be partially due to the increased peak values of the distributions of area and second moment of area shown in figure 4 for these modified configurations.

The effectiveness of the moment-of-area rule in reducing the drag of external-store installations has been demonstrated thus far by comparing the results for the modified configurations with missiles and those for the corresponding basic configurations without missiles. An equally important comparison is that between the modified and basic configurations with missiles installed in both cases. It is evident from the results for all three wing plan forms that the missile installation on the modified configuration is a decided improvement over the conventional installation on the basic configuration. For example, at sonic speed, the wave drag of each modified configuration with missiles was about one-half that of the corresponding basic configuration with the staggered conventional missile installation.

A major source of this improvement of the modified configurations with missiles over the basic configurations with missiles was the reduction of the interference drag due to the addition of the missiles. This is clearly demonstrated in figure 11. Shown for each of the three wing plan forms is the wave drag due only to the addition of four missiles to both the basic and the modified configurations. Also shown, in dashed lines, to provide a measure of the interference drag is 4 times the wave drag of one isolated missile. As seen here, addition of the missiles to each of the modified configurations resulted in an installation wave drag of about the same order of magnitude as the wave drag of the missiles alone, whereas the wave drag of the conventional installations was approximately 3 and 6 times greater, respectively, for the conventional staggered and unstaggered missile installations.

CONCLUDING REMARKS

The results presented here indicate that the drag of a wing-body combination fitted with external stores can be substantially reduced at transonic and low supersonic speeds by modifying the complete configuration according to Baldwin's moment-of-area rule. Furthermore, in cases where the indicated modifications are not feasible, drag reductions can also be realized by relocating the stores in positions which more nearly satisfy the moment-of-area rule.

REFERENCE

1. Baldwin, Barrett, S., Jr., and Dickey, Robert R.: Application of Wing-Body Theory to Drag Reduction at Low Supersonic Speeds. NACA RM A54J19, 1955.

~~CONFIDENTIAL~~

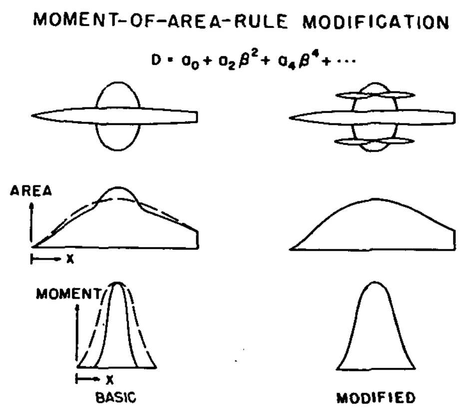

Figure 1

EFFECT OF MODIFICATIONS ON EXPERIMENTAL WAVE DRAG; $C_L = 0$

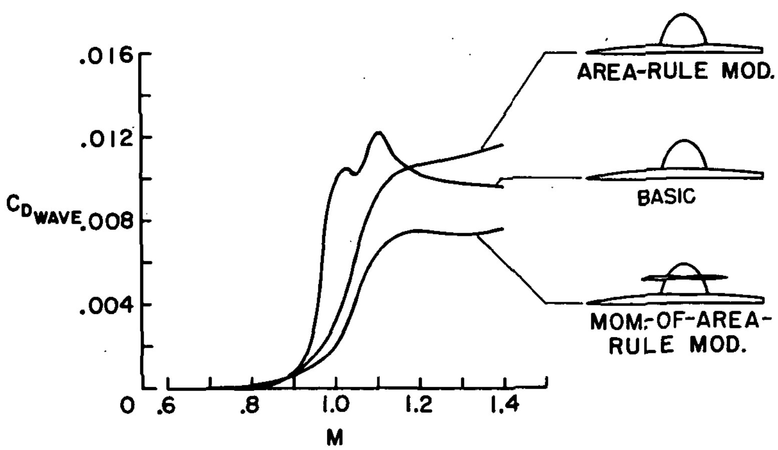

Figure 2

~~CONFIDENTIAL~~

MODIFIED CONFIGURATIONS WITH MISSILES

Figure 3

AREA AND MOMENT DIAGRAMS FOR MODIFIED CONFIGURATIONS WITH MISSILES

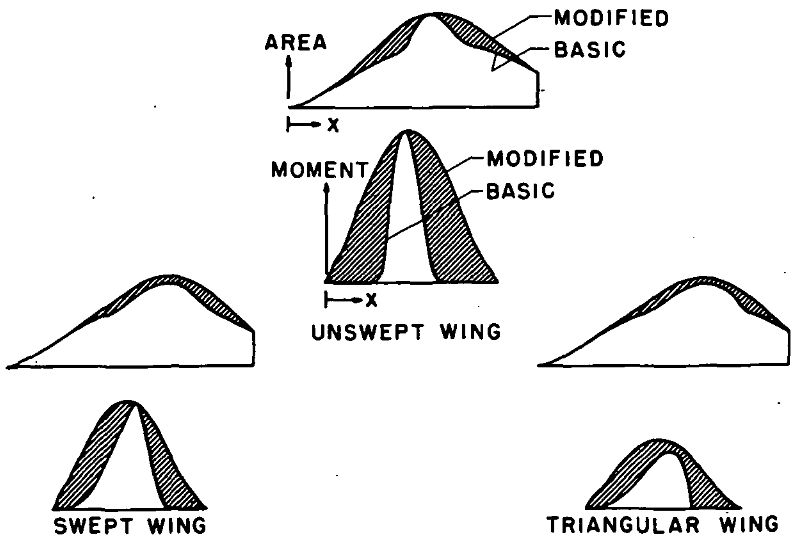

Figure 4

BASIC CONFIGURATIONS WITH CONVENTIONAL MISSILE INSTALLATIONS

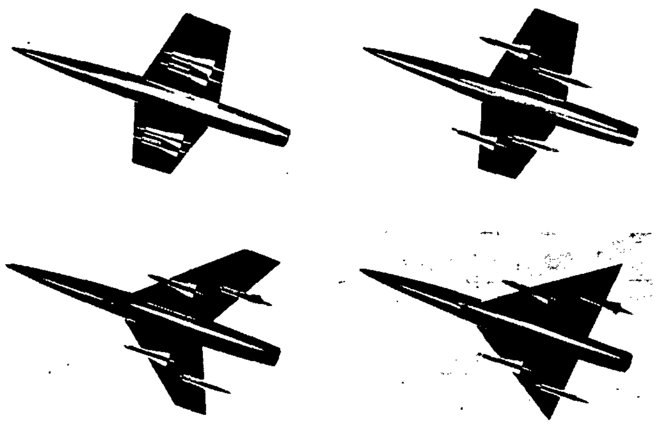

Figure 5

AREA AND MOMENT DIAGRAMS FOR BASIC CONFIGURATIONS WITH CONVENTIONAL MISSILE INSTALLATIONS

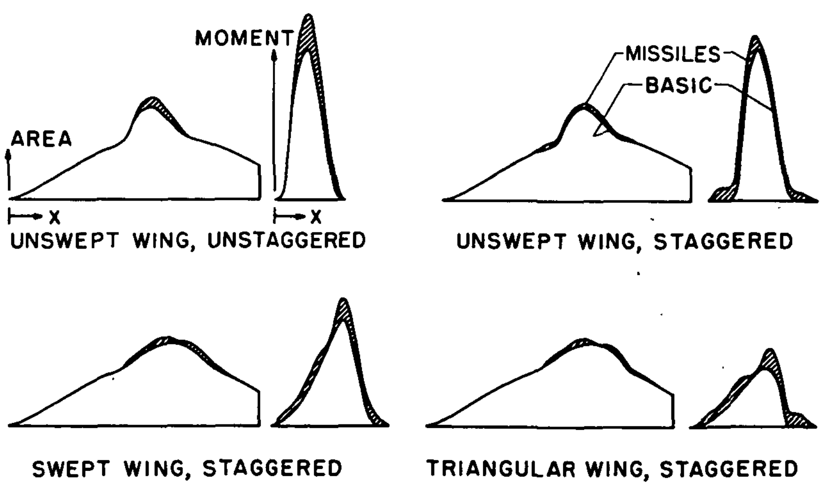

Figure 6

TOTAL DRAG OF UNSWEPT-WING CONFIGURATIONS; $C_L = 0$

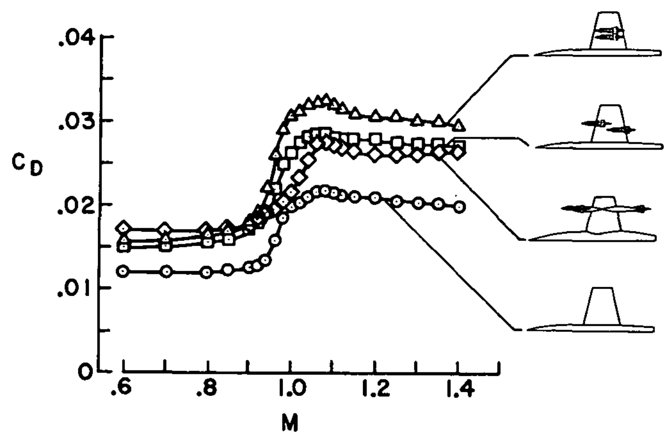

Figure 7

TOTAL DRAG OF SWEPT- AND TRIANGULAR-WING CONFIGURATIONS; $C_L = 0$

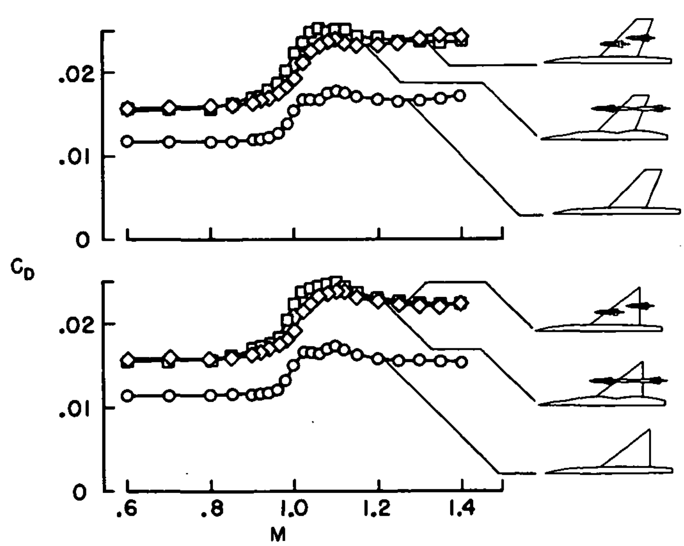

Figure 8

WAVE DRAG OF UNSWEPT-WING CONFIGURATIONS; $C_L = 0$

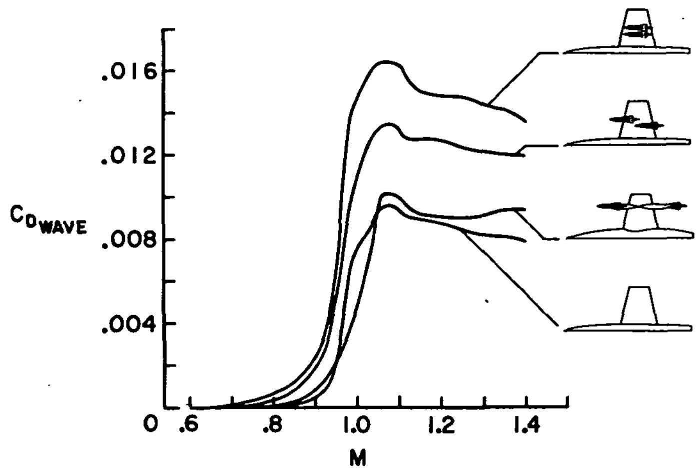

Figure 9

WAVE DRAG OF SWEPT-AND TRIANGULAR-WING CONFIGURATIONS; $C_L = 0$

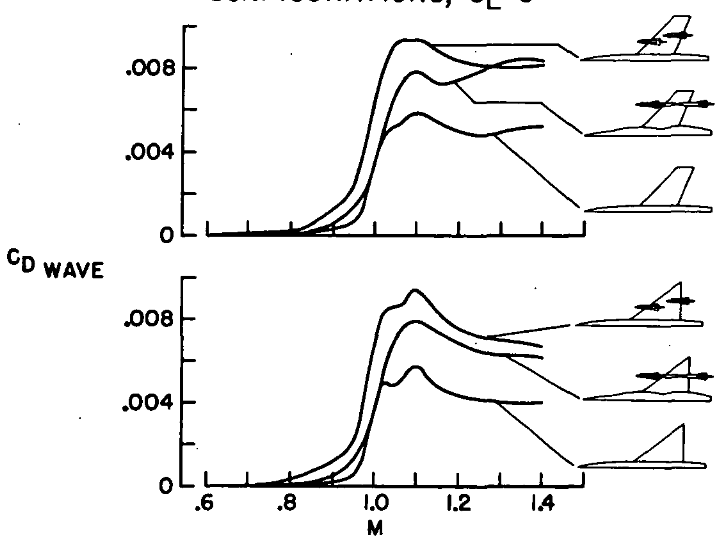

Figure 10

WAVE DRAG DUE TO ADDITION OF MISSILES; $C_L = 0$

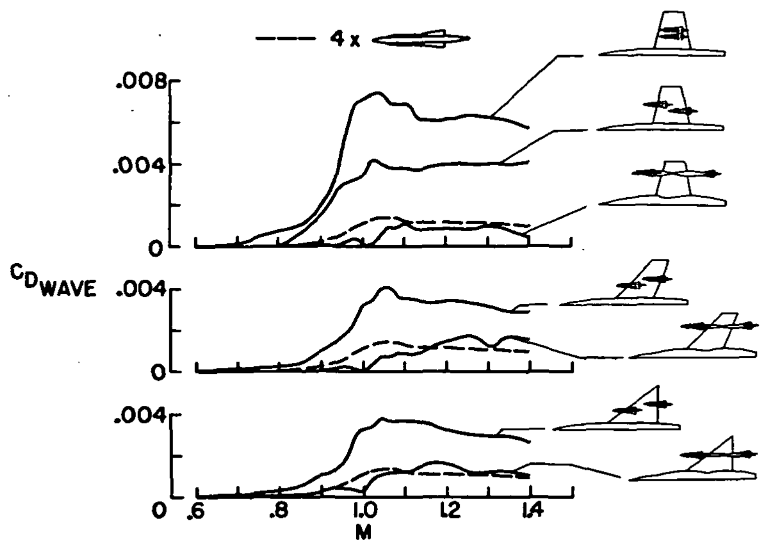

Figure 11

THEORETICAL PREDICTION OF THE SIDE FORCE ON STORES ATTACHED TO CONFIGURATIONS TRAVELING AT SUPERSONIC SPEEDS

By Percy J. Bobbitt, Frank S. Malvestuto, Jr.,
and Kenneth Margolis

Langley Aeronautical Laboratory

SUMMARY

Linear-theory evaluations of the important flow-field and interference effects necessary to the calculation of the store side forces have been illustrated and discussed. By taking into account these effects good agreement has been obtained between the theoretical predictions of the side force on the store and experimental values for the configurations examined. An appendix has been included which discusses the calculations and presents some of the equations necessary to obtain the flow-field and interference quantities.

INTRODUCTION

The aerodynamic forces and moments on stores and store-pylon arrangements situated below wings have in recent years been the subject of an intensive experimental effort. The effect on the store loads of store position, store size, pylon, wing plan form, and Mach number have all been investigated to varying degrees of thoroughness. Obviously, the general store problem has many variables. Although the complexity of the problem dictated that the initial approach be experimental, it also requires that an analytical or semiempirical method be developed to indicate trends, if not magnitudes, of the forces acting on the store when the many variables involved are changed. Subsonically, a good start toward this goal has been made by the National Advisory Committee for Aeronautics and the results were presented in reference 1.

The object of the present paper is to present some preliminary results of a study made to examine how well the aerodynamic forces acting on stores attached to configurations traveling at supersonic speeds may be predicted theoretically. The methods used to attack the problem are in general based on linearized theory and would naturally be expected to give the best results when the aircraft configurations are at small angles of attack and are composed of slender bodies and thin wings.

In the present paper the discussion is restricted to the lateral force component; however, the determination of the lift and drag forces on the store is amenable to the same type of theoretical treatment used to determine the side force.

SYMBOLS

C_Y	lateral-force coefficient, $\dfrac{\text{Side force on store}}{q \times \text{Frontal area of store}}$
α	angle of attack of wing
A	aspect ratio
M	Mach number
V	stream velocity
b	span
σ	sidewash angle in radians, approximately equal to $-\frac{v}{V}$
l	fuselage length
x	longitudinal distance
α_s	angle of attack of store
Y	lateral force on store in presence of reflection plane
Y_i	lateral force on isolated store
r	maximum store radius
s	distance from reflection plane to center of base
x_s	longitudinal distance from nose of store
l_s	length of store
v	sidewash or lateral velocity
q	free-stream dynamic pressure

$\beta = \sqrt{M^2 - 1}$

m tangent of wing semiapex angle

ϕ perturbation velocity potential

DISCUSSION

The presentation of data in the following section falls into three main categories: First, some of the basic flow fields necessary to the prediction of the store side forces are discussed; second, the interference effects between the wing or wing pylon and the store are analyzed; and lastly, the lateral forces acting on a store, calculated analytically, are compared with experimental values.

Figure 1 shows the wing-body-store arrangement used to illustrate some of the component flow fields. The triangular wing has a sweep of 60° and an aspect ratio of 2.31. The fuselage has a fineness ratio of 10, a near-parabolic nose shape, and a cylindrical afterbody. Subsequent flow-field variations are given at three spanwise stations of the wing shown in figure 1. These stations are at 0.25b/2, 0.50b/2, and 0.75b/2. The vertical distance below the wing at which the flow-field calculations were made is 0.10b/2.

Force calculations, which will be discussed later, have been made for the modified Douglas Aircraft Company (DAC) store shown in figure 1 attached to the triangular wing at the 0.50b/2 station. Exact dimensions of the DAC store and fuselage are given in reference 2.

Flow Fields

One of the more important flow-field effects is the sidewash produced by the wing at an angle of attack. A recent theoretical investigation of the angle-of-attack flow field has been made (see appendix) and a sampling of the results is shown in figure 2. This figure shows the chordwise variation of sidewash angularity below the wing at an angle of attack for two Mach numbers ($M = 1.6$ and $M = 2.1$). At a Mach number of 1.6, the leading edge of the wing is subsonic, that is, the Mach cone emanating from the wing-fuselage juncture is ahead of the leading edge; at a Mach number of 2.1, the wing leading edge is supersonic. It might be pointed out that the $-\sigma$ on the vertical scale indicates that the direction of the sidewash below the wing is from the wing root toward the wing tip.

The sidewash angularity due to the wing being at an angle of attack has a value of zero at the Mach cone emanating from the wing-root—fuselage juncture, rises rapidly to its maximum value at a longitudinal station just to the rear of the wing leading edge, and then decreases at a less rapid rate. Note that in going from the inboard to the outboard station there is a large increase in the magnitude of the induced angle of sidewash.

The main difference to be noted between the lateral angularity for the supersonic-edge Mach number shown on the right of figure 2 and that of the subsonic-edge condition is that, for the supersonic-edge case, the sidewash angularity has a constant value at all span stations in the region ahead of the Mach cone from the wing root that is followed by a rapid dropoff, whereas the maximum values increase spanwise for the subsonic-edge case. In the rearward portions of the wing there does not appear to be a significant difference between the sidewash-angularity magnitudes for the two Mach numbers shown. Lateral-angularity curves for Mach numbers other than those in figure 2 indicate appreciable differences in the magnitude of the sidewash in the rearward portion of the wing.

In addition to the angle-of-attack sidewash, other flow-field effects of importance are those due to fuselage thickness, wing thickness, and fuselage angle of attack. The fuselage angle-of-attack sidewash was found to be negligible at the points located 0.10b/2 below the wing. For other positions relative to the wing-fuselage, the fuselage angle-of-attack sidewash could have a large effect so that each individual configuration must be considered separately.

Some illustrative chordwise variations of the sidewash angularity due to body thickness and wing thickness are shown in figure 3. The Mach number for these calculations is 1.6. It should be pointed out that the analyses from which the variations shown in figure 3 were taken (see appendix) apply for all supersonic Mach numbers and the Mach number of 1.6 was chosen because experimental force data were available at this Mach number.

The sidewash angularity due to body thickness has a value of zero at the Mach cone originating at the fuselage nose and rises rapidly to its maximum value. Behind a Mach line stemming from the end of the fuselage nose, the body-thickness sidewash angularity is negligible. Maximum values of the body-thickness angularities decrease as the distance from the body increases.

Sidewash angularity due to wing thickness (fig. 3) has been plotted for wing thicknesses of 3 percent and 5 percent. The variations depicted are along the 0.50b/2 station. It can be seen that regions of both positive and negative angularity occur and that, if a store were immersed in this sidewash field at various longitudinal positions, it would be subjected to both positive and negative resultant loads. Note that the magnitudes of the sidewash angularity due to body thickness and that due to wing thickness are comparable (fig. 3).

Interference Effects

Several theoretical studies have been made to evaluate the induced effects of the wing and wing pylon on the store. (See appendix.) The theoretical wing-pylon-store model used in the interference calculations is shown in figure 4. What is referred to herein as the wing is actually an infinite wing or reflection plane at an angle of attack of 0°. The store in one analysis has been connected to the wing with a pylon and in another it has not. The analyses allow the store to be placed at small angles of incidence to the free stream. A positive store incidence angle is the case where the store nose has been moved toward the wing. In the analyses the store or store pylon has been placed in a uniform sidewash field as indicated by the arrows. This sidewash field causes a side force on the store and it is the effect of the wing and pylon on this side force that is of interest.

The left-hand part of figure 5 has been presented to illustrate the effect of the wing interference on the side force on the store where the store is not connected with a pylon. The plot on the right-hand side shows the pylon effect. It can be seen in the left-hand plot that both a decrease in the distance of the store from the wing and a positive increase in the store angle of attack cause an increase in the side force on the store. When a pylon is added to the system (right-hand plot of fig. 5), there is a large change in the induced load on the store in the direction to increase the side force on the store.

Side-Force Distribution on Store

The discussion until now has been related to the more important flow-field and interference effects. In order to depict how the side force will distribute itself along a store when it is immersed in the various sidewash fields and subject to the wing interference, figure 6 has been prepared. Figure 6 shows the side-force distribution on the DAC store located at the 0.50b/2 station under the 60° swept delta wing. The wing-body-store configuration is at an angle of attack of 6°. It can be noted that the resultant side force on the store is directed from the wing root toward the wing tip and also that, if moments were taken about the store midpoint, they would be in the direction tending to push the nose of the store out toward the wing tip.

Store Side-Force Correlations

With the theoretical raw materials discussed in the previous sections, side-force-coefficient calculations have been made for the DAC store located in various positions beneath swept, unswept, and delta wings. Figures 7 and 8 show correlations for the store located below the delta wing and figures 9 and 10, correlations for the unswept and swept wings. The experimental values shown on these figures have been obtained from references 3 and 4. All correlations are at a Mach number of approximately 1.6.

In figure 7 the effect of store lateral location and angle of attack on the store side-force coefficient for the 60° delta-wing configuration is shown. The store beneath the wing in this figure is not connected with a pylon. Two spanwise locations (0.50b/2 and 0.85b/2) have been considered. Note that there is a large increase in the side-force coefficient when the store is moved from the midspan to the tip location. This increase is primarily due to the larger magnitude of the angle-of-attack sidewash in the tip region which is illustrated in figure 2. The agreement between the theoretical predictions and experiment is good for both lateral locations.

The effect of longitudinal store position on the side force on the store located beneath the same 60° delta wing as that of figure 7 has been depicted in figure 8. When the store is moved from its location beneath the rear portion of the wing toward the leading edge, figure 8 shows that the store experiences a large increase in side force. Agreement between the theoretical predictions and experiment is good for both locations of the store considered.

It might be mentioned in connection with figure 8 that the upsweep of the experimental side-force-coefficient curve with increasing α is characteristic of the experimental side-force variations with α for stores situated beneath wings of most all plan forms. Static-force tests on the isolated store show a similar upsweep as the store angle of attack is increased. This fact would seem to indicate that, if in the theoretical calculations the crossflow viscous effects of Allen were taken into account, better agreement between the theory and experiment would be obtained at the moderate angles of attack.

Figure 9 shows the effect of spanwise store location on the side force on the store located under an unswept wing of aspect ratio 4. An extremely short pylon connects the store to the wing (see ref. 3) in both locations treated (0.47b/2 and 0.80b/2). It can be seen that the increase in the side-force coefficient experienced when the store is moved toward the wing tip is acceptably predicted by the theory.

The effect of a pylon on the side force on a store under a 45° swept wing of aspect ratio 4 is shown in figure 10. The lower two curves are for the pylon-off configuration and the upper two curves, for the pylon-on case. The agreement between theory and experiment for both conditions is good.

A note of caution is in order. The agreement obtained between the theoretical predictions of the side force on the DAC store and experiment shown in figures 7 to 10 may be fortuitous to some extent. The fact that the store has a finite base could have benefited the agreement since, as is well known, linearized theory predicts an unrealistic zero lift force on closed bodies of revolution at an angle of attack in a uniform stream. It is possible that experimental force data on the isolated store could be used together with the theoretical flow fields and interference effects to give reliable estimates of the side force on stores of almost all shapes. The limitations of the pure theoretical approach can not be defined until more correlations between theory and experiment such as those presented herein have been made.

CONCLUSIONS

In conclusion, it may be said that the important flow-field and interference effects can be calculated by theory and that, by taking into account these flow-field and interference effects, good agreement has been obtained between the theoretical predictions of the side force on the store and experimental values for the configurations examined. Although the application of theory in this paper has been specialized primarily to side force on the store, indications are that the other aerodynamic forces are also amenable to this same type of theoretical treatment.

An appendix has been included which discusses the calculations and presents some of the equations necessary to obtain the flow-field and interference quantities.

APPENDIX

REMARKS AND EQUATIONS PERTAINING TO THE CALCULATION OF FLOW FIELDS, INTERFERENCE EFFECTS, AND STORE SIDE FORCES

In the text some illustrative flow-field variations, interference effects, and store side forces have been discussed with no indication given as to how they were obtained. The methods used in the evaluation of several of these effects are well known and only a few remarks are needed to make clear the procedure, whereas for others useful equations are presented and discussed. More extensive treatments of some of the effects have been made at the Langley Aeronautical Laboratory than indicated in the following sections; however, the objectives of the present paper obviate the need for more detailed descriptions.

Angle-of-Attack Sidewash

From a procedure paralleling that used by Nielsen and Perkins in reference 5 to determine the downwash in the flow field exterior to flat lifting triangles of infinite chord, the sidewash or lateral flow below this same lifting wing has been obtained. The analyses apply for all leading-edge sweeps and supersonic Mach numbers, both the subsonic-wing leading-edge and supersonic-wing leading-edge conditions being considered. The equation for the sidewash below the wing at a point (x,y,z) for the subsonic-edge case is given by

$$v = \frac{V\alpha}{\left(1 - s_o^2\right)E\left(\sqrt{1 - \beta^2 m^2}\right)}\left\{-E\left(\sqrt{\sigma_1}, s_o^2\right) + \frac{\left[1 - \left(1 - s_o^4\right)\lambda_1\right]\sqrt{\sigma_1}\sqrt{1 - \sigma_1}\sqrt{1 - s_o^4\sigma_1}}{1 - \left[1 - \left(1 - s_o^4\right)\lambda_1\right]\sigma_1} + E\left(\sqrt{\sigma_2}, s_o^2\right) - \frac{\left[1 - \left(1 - s_o^4\right)\lambda_2\right]\sqrt{\sigma_2}\sqrt{1 - \sigma_2}\sqrt{1 - s_o^4\sigma_2}}{1 - \left[1 - \left(1 - s_o^4\right)\lambda_2\right]\sigma_2}\right\} \qquad \text{(A1)}$$

where

$$s_o = \frac{1 - \sqrt{1 - \beta^2 m^2}}{\beta m}$$

The procedure for calculating the λ and σ functions is straightforward and requires just a few steps although the calculations themselves are a little lengthy. First calculate p and q:

$$p = \frac{\beta \frac{z}{x}}{1 + \sqrt{1 - \left(\beta \frac{y}{x}\right)^2 - \left(\beta \frac{z}{x}\right)^2}} \tag{A2}$$

$$q = \frac{\beta \frac{y}{x}}{1 + \sqrt{1 - \left(\beta \frac{y}{x}\right)^2 - \left(\beta \frac{z}{x}\right)^2}} \tag{A3}$$

and then τ_1, δ_1, τ_2, and δ_2:

$$\tau_1 = \left[p\sqrt{\sqrt{\left(p^2 - q^2 + s_o^2\right)^2 + 4p^2q^2} + p^2 - q^2 + s_o^2} + q\sqrt{\sqrt{\left(p^2 - q^2 + s_o^2\right)^2 + 4p^2q^2} - \left(p^2 - q^2 + s_o^2\right)}\right] \frac{1}{\sqrt{2}\sqrt{\left(p^2 - q^2 + s_o^2\right)^2 + 4p^2q^2}} \tag{A4}$$

$$\delta_1 = \left[-p\sqrt{\sqrt{\left(p^2 - q^2 + s_o^2\right)^2 + 4p^2q^2} - \left(p^2 - q^2 + s_o^2\right)} + q\sqrt{\sqrt{\left(p^2 - q^2 + s_o^2\right)^2 + 4p^2q^2} + p^2 - q^2 + s_o^2}\right] \frac{1}{\sqrt{2}\sqrt{\left(p^2 - q^2 + s_o^2\right)^2 + 4p^2q^2}} \tag{A5}$$

$$\tau_2 = \frac{\sqrt{\sqrt{\left[1 + s_o^2(p^2 - q^2)\right]^2 + 4s_o^4p^2q^2} + 1 + s_o^2(p^2 - q^2)}}{\sqrt{2}\sqrt{\left[1 + s_o^2(p^2 - q^2)\right]^2 + 4s_o^4p^2q^2}} \tag{A6}$$

$$\delta_2 = \frac{\sqrt{\sqrt{\left[1 + s_o^2(p^2 - q^2)\right]^2 + 4s_o^4p^2q^2} - \left[1 + s_o^2(p^2 - q^2)\right]}}{\sqrt{2}\sqrt{\left[1 + s_o^2(p^2 - q^2)\right]^2 + 4s_o^4p^2q^2}} \tag{A7}$$

Substitute τ_1 and δ_1 in the following two equations to determine λ_1 and σ_1 and substitute τ_2 and δ_2, to obtain λ_2 and σ_2.

$$\lambda = \frac{\left[(1 + \tau^2 + \delta^2) - \sqrt{(1 + \tau^2 + \delta^2)^2 - 4\tau^2}\right]\left\{1 + (1 - s_o^4)(\tau^2 + \delta^2) - \sqrt{\left[1 + (1 - s_o^4)(\tau^2 + \delta^2)\right]^2 - 4(1 - s_o^4)\tau^2}\right\}}{4(1 - s_o^4)\tau^2} \tag{A8}$$

$$\sigma = \frac{\tau^2 + \delta^2 - \lambda}{(\tau^2 + \delta^2 - \lambda) - \left[\lambda(1 - s_o^4)(\tau^2 + \delta^2) - 1\right]} \tag{A9}$$

The elliptic functions $E\left(\sqrt{\sigma}, s_o^2\right)$ and $E\left(\sqrt{1 - \beta^2m^2}\right)$ in the expression for v (eq. (A1)) may be obtained from tables (refs. 6 and 7) or by series expansion.

The equation for the sidewash in the region below the wing and behind the Mach cone emanating from the wing apex when the wing leading edge is supersonic is

$$v = \frac{V\alpha}{\pi\sqrt{\beta^2m^2 - 1}}\left[\tan^{-1}\frac{1 + \beta^2m\,\frac{y}{x}}{\sqrt{\beta^2m^2 - 1}\sqrt{1 - \left(\beta\,\frac{y}{x}\right)^2 - \left(\beta\,\frac{z}{x}\right)^2}} - \tan^{-1}\frac{1 - \beta^2m\,\frac{y}{x}}{\sqrt{\beta^2m^2 - 1}\sqrt{1 - \left(\beta\,\frac{y}{x}\right)^2 - \left(\beta\,\frac{z}{x}\right)^2}}\right] \tag{A10}$$

Sidewash in the region behind the plane Mach wave off the wing leading edge and ahead of the Mach cone from the wing apex is

$$v = \frac{V\alpha}{\sqrt{\beta^2m^2 - 1}} \tag{A11}$$

For the sonic-edge wing the sidewash expressions simplify to

$$v_{\beta m=1} = \frac{2V\alpha\beta\,\frac{y}{x}\sqrt{1 - \left(\beta\,\frac{y}{x}\right)^2 - \left(\beta\,\frac{z}{x}\right)^2}}{\pi\left[1 - \left(\beta\,\frac{y}{x}\right)^2\right]} \tag{A12}$$

It should be pointed out that, although the expressions given herein apply directly to determining the angle-of-attack sidewash below the infinite-chord triangular wing, they may also be used directly in sidewash determinations for some regions below wings having finite taper and chord.

Consider an infinite-chord triangular wing and a conventional wing (see sketch), both having the same leading-edge sweep and both traveling at the same velocity.

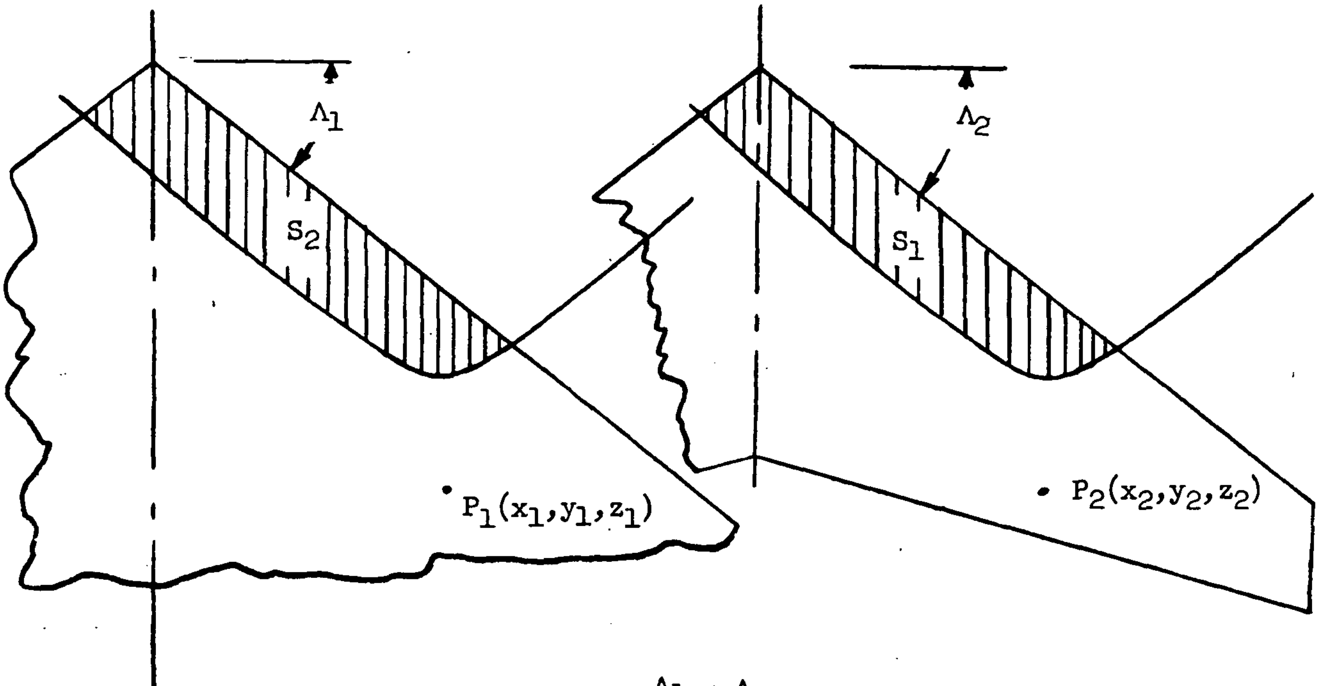

$$\Lambda_1 = \Lambda_2$$

$$S_1 = S_2$$

Points P_1 and P_2 below these wings are in the same position with respect to the wing leading edges and root chords so that forecones from these points cut off equal areas, S_1 and S_2, of the wing. Since the loadings in the two areas are the same, the flow fields at the points P_1 and P_2 are the same. For points the forecones of which intersect the tip of a wing or the wake behind a wing, additional considerations are, of course, necessary and the expressions for the sidewash velocity given here do not apply.

Sidewash Field Due to Body Thickness

The potential in space at a point (x,y) due to an axial distribution of sources is (ref. 8)

$$\phi = -\frac{V}{2\pi}\int_0^{x-\beta r} \frac{f_0(\xi)\,d\xi}{\sqrt{(x - \xi)^2 - \beta^2 r^2}} \tag{A13}$$

where $f_0(\xi)$ represents the source strength function, r is the radial distance from the x-axis to the field point at which the potential is desired, ξ is the longitudinal distance to each individual source, and x is the longitudinal distance to the field point at which the potential is desired. This equation is not often used in the form shown because of the difficulty involved in obtaining the $f_0(\xi)$ function and because interest is generally limited to the potential (or one of its derivatives) on the body surface where the expression for ϕ may be simplified and the distribution function can be approximated with a fair degree of accuracy. The problem at hand, however, does not allow the conveniences available when only the region in the vicinity of the body boundary is considered and some attempt must be made to approximate the $f_0(\xi)$ function for use in equation (A13).

The procedure used to obtain the distribution function for the fuselage shown in figure 1 (see ref. 2 for dimensional detail) for a free-stream Mach number of 1.6 utilized the small r or slender-body distribution function as a starting point. First, an expression for $\partial\phi/\partial r$, as given by

$$\frac{\partial\phi}{\partial r} = \frac{V}{2\pi r}\int_0^{x-\beta r} \frac{f_0'(\xi)(x - \xi)\,d\xi}{\sqrt{(x - \xi)^2 - \beta^2 r^2}} \tag{A14}$$

was determined analytically by assuming the fuselage nose shape to be parabolic (a very close approximation to the actual nose shape) and by using the small r distribution function associated with this shape. Calculations were then made to obtain $\partial\phi/\partial r$ at points on the surface of the actual fuselage including the cylindrical part so that it could be determined how much the calculated flow differed from the required tangential flow, that is, a comparison of $\left(\frac{\partial\phi}{\partial\frac{r}{V}}\right)_{surface}$ and $\left(\frac{dr}{dx}\right)_{surface}$ was made. Differences between $\left(\frac{\partial\phi}{\partial\frac{r}{V}}\right)_{surface}$ and $\left(\frac{dr}{dx}\right)_{surface}$ indicated that certain changes were necessary in the distribution function. Four distribution functions were tried before an acceptable one was found.

The sidewash at a point in the field is, of course, the radial velocity $\partial\phi/\partial r$ at that point multiplied by the cosine of the angle it makes with the horizontal.

Calculations of Sidewash Due to Wing Thickness

The calculation of the lateral-flow component requires the determination of the perturbation velocity $\partial\phi/\partial y$. The general expression for the linearized perturbation velocity potential in space due to wing thickness is

$$\phi(x,y,z) = -\frac{V}{\pi}\iint_R \frac{\lambda(\xi,\eta)d\xi\, d\eta}{\sqrt{(x - \xi)^2 - \beta^2(y - \eta)^2 - \beta^2 z^2}} \tag{A15}$$

where x, y, and z are the rectangular coordinates of the field point (that is, the point at which the potential is desired) and ξ and η are the rectangular coordinates (analogous to x and y) for the sources and sinks which are distributed in the $z = 0$ plane. The source-distribution function $\lambda(\xi,\eta)$ is related to the particular thickness distribution involved and is given as

$$\lambda(\xi,\eta) = \left[\frac{\partial}{\partial\xi} z(\xi,\eta)\right]_{z=0}$$

The integration is performed over the region R that is enclosed by the traces in the $z = 0$ plane of the Mach forecone emanating from the point (x,y,z) and by the wing plan-form boundaries. Differentiation of equation (A15) with respect to y will then yield the required lateral component $\partial\phi/\partial y$. The differentiation may, of course, be done after obtaining the potential or by suitable differentiation under the integral sign in either the initial or intermediate stages of integration.

With regard to carrying out the details of the calculation, some remarks are in order. If the distribution function $\lambda(\zeta,\eta)$ is continuous, the double integration may be analytically performed directly or if the resulting integrals are difficult to handle, a straightforward numerical procedure can be employed. On the other hand, if the distribution function $\lambda(\xi,\eta)$ is discontinuous, as is the situation for a multiwedge-type surface, the numerical procedures probably constitute the most efficient methods of solution. In this connection, however, it should be pointed out that superposition of simple wedge-type distributions to build up the desired distribution simplifies the calculations considerably in many cases and even enables analytical solutions to be obtained more readily.

Side Force Acting on a Slender Store in the Presence of an Infinite Wing at Zero Angle of Attack

The following expression for the side force r acting on a store situated below an infinite wing (fig. 4) was evolved from a slender-body-theory analysis. The side-force expression is independent of Mach number and therefore is only a rough estimate of the side force at Mach numbers where strong shock interactions occur between the store and the reflection plane.

In coefficient form, the side-force expression is

$$C_Y = \frac{Y}{qS} = \frac{2\beta}{S}\int_0^l H(x)S'(x)dx + \frac{2\alpha_s\beta}{S}\int_0^l \pi r(x)\,\frac{dH(x)}{dx}\,\frac{dx}{d\xi}\,dx \qquad \text{(A16)}$$

where

x axial coordinate of store

$r(x)$ local radius of store

$S(x) = \pi r^2(x)$

$S'(x) = \dfrac{dS(x)}{dx}$

S base area

l length of store

s distance of store axis from infinite wing at base

$\xi = \dfrac{s + \alpha_s(l - x)}{r(x)}$

$$\frac{dx}{d\xi} = -\frac{r^2(x)}{\left[s + \alpha_s(l - x)\right]\frac{dr(x)}{dx} - \alpha_s r(x)} = -\frac{r(x)}{\xi\frac{dr(x)}{dx} + \alpha_s}$$

The $H(x)$ function and its derivative $\frac{dH(x)}{dx}$ are defined compactly in terms of the elliptic nome q

$$H(q) = 1 + 2\sum_{m=1}^{m=\infty}\frac{(1 - q)^2 q^m}{\left(1 - q^{m+1}\right)^2} \tag{A17}$$

$$\frac{dH(x)}{dx} = \frac{dH(q)}{dq}\frac{dq}{d\xi}\frac{d\xi}{dx}$$

$$= -8\sum_{m=1}^{m=\infty}\frac{q^{m+\frac{1}{2}}}{\left(1 - q^{m+1}\right)^3}\left[m - (m + 2)q + (m + 2)q^{m+1} - mq^{m+2}\right]\frac{d\xi}{dx} \tag{A18}$$

where

$$q = \frac{1}{\left(\xi + \sqrt{\xi^2 - 1}\right)^2}$$

$$\frac{dq}{d\xi} = -\frac{2}{\left(\xi + \sqrt{\xi^2 - 1}\right)^2\sqrt{\xi^2 - 1}}$$

For small values of q (order of 0.1) only three or four terms of the expansion are necessary whereas for larger values of q (order of 0.5 or 0.6) as many as 13 or 14 terms may be required.

The Interference Effect of a Pylon and Infinite Wing on the Side Force on a Store

The problem of determining the side force of stores connected to wings with pylons is similar in some respects to the problem of determining the lift force on wing-tip tanks. Recognizing this, the transformation procedures of reference 9, which treat wing-tip tanks, have been incorporated in an analysis paralleling that of the previous section to compute side forces on stores attached to an infinite wing with a pylon. Compact expressions for the store side force, like those of the previous section, are not possible for the pylon case. The involved nature of the calculative procedure for obtaining the store side force prevents a more detailed description in this paper.

It should be pointed out here as in the previous section that, when strong shock interactions between the store and wing are present, the applicability of a subsonic crossflow analysis is questionable.

Store Side Force

The determination of the side force and moments acting on the store situated under the right wing panel and immersed in the various sidewash fields requires a knowledge of the pressure difference across the store which, in turn, requires a knowledge of the perturbation velocities on the store surface. The equation for the perturbation velocity potential from which the perturbation velocities have been derived (ref. 8) is

$$\phi = \frac{V \cos \theta}{2\pi r} \int_0^{x-\beta r} \frac{f_1'(\xi)(x - \xi)d\xi}{\sqrt{(x - \xi)^2 - \beta^2 r^2}} \qquad \text{(A19)}$$

where the distribution function $f_1'(\xi)$ for a slender body of revolution immersed in a uniform lateral field is

$$f_1'(\xi) = -2\sigma S(x)$$

The angle θ in equation (A19) is measured clockwise from the horizontal. The symbols x, ξ, and r are defined in the section entitled "Calculation of Sidewash Due to Wing Thickness." Since the store lies in a nonuniform sidewash field, the change in the induced lateral angle of incidence along the store should be accounted for to obtain the best results. In the calculations made for the Douglas store, it has been assumed that the effect of the change in incidence along the store could be accounted for by allowing σ in the distribution function to vary with ξ

$$f_1(\xi) = -2\sigma(\xi)S(\xi)$$

The integrations necessary to obtain ϕ or one of its derivatives must be solved numerically. It is expedient in most cases to perform a parts integration prior to doing the numerical integrations to eliminate the square root in the denominator.

.9Z

REFERENCES

1. Alford, William J., Jr.: Effects of Wing-Fuselage Flow Fields on Missile Loads at Subsonic Speeds. NACA RM L55E10a, 1955.

2. Jacobsen, Carl R.: Effects of the Spanwise, Chordwise, and Vertical Location of an External Store on the Aerodynamic Characteristics of a 60° Delta Wing at Mach Numbers of 1.41, 1.62, and 1.96. NACA RM L52H29, 1952.

3. Guy, Lawrence D.: Loads on External Stores at Transonic and Supersonic Speeds. NACA RM L55E13b, 1955.

4. Smith, Norman F., and Carlson, Harry W.: Some Effects of Configuration Variables on Store Loads at Supersonic Speeds. NACA RM L55E05, 1955.

5. Nielsen, Jack N., and Perkins, Edward W.: Charts for the Conical Part of the Downwash Field of Swept Wings at Supersonic Speeds. NACA TN 1780, 1948.

6. Jahnke, Eugene, and Emde, Fritz: Tables of Functions. Fourth ed., Dover Publications, 1945.

7. Byrd, Paul F., and Friedman, Morris D.: Handbook of Elliptic Integrals for Engineers and Physicists. Lange, Maxwell & Springer, Ltd. (New York), 1954.

8. Ferri, Antonio: Elements of Aerodynamics of Supersonic Flows. The Macmillan Co., 1949.

9. Hartley, D. E.: Theoretical Load Distributions on Wings With Tip-Tanks. Rep. No. Aero. 2469, British R.A.E., June 1952.

[redacted]

WING - BODY - STORE ARRANGEMENT

WING SWEEP 60°; BODY FINENESS RATIO 10

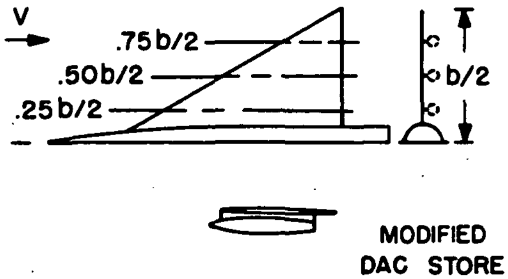

Figure 1

CHORDWISE VARIATION OF SIDEWASH ANGULARITY

AT AN ANGLE OF ATTACK

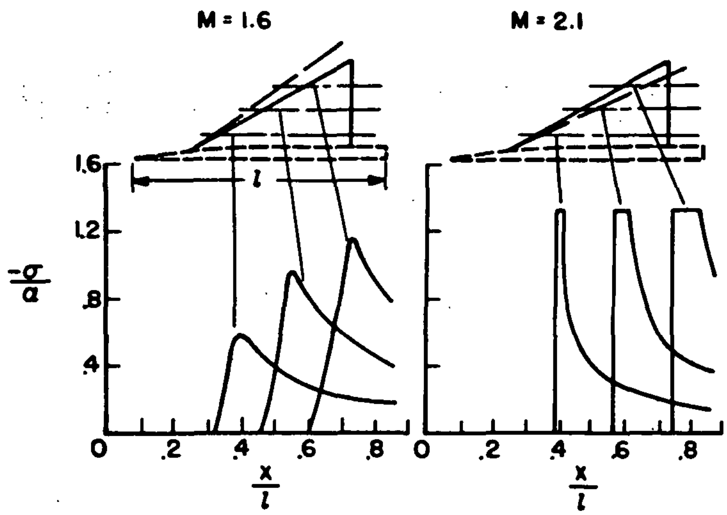

Figure 2

[redacted]

CHORDWISE VARIATIONS OF SIDEWASH ANGULARITY
DUE TO BODY AND WING THICKNESS

M=1.6

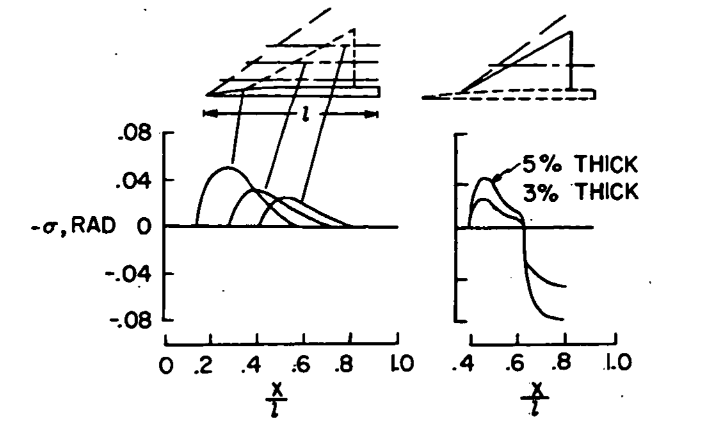

Figure 3

INFINITE WING-PYLON-STORE CONFIGURATION USED
TO ILLUSTRATE INTERFERENCE CALCULATIONS

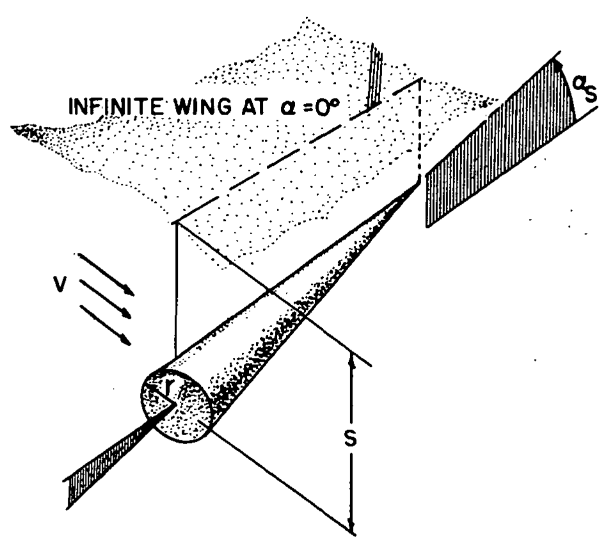

Figure 4

WING AND PYLON INTERFERENCE EFFECTS ON THE STORE SIDE FORCE

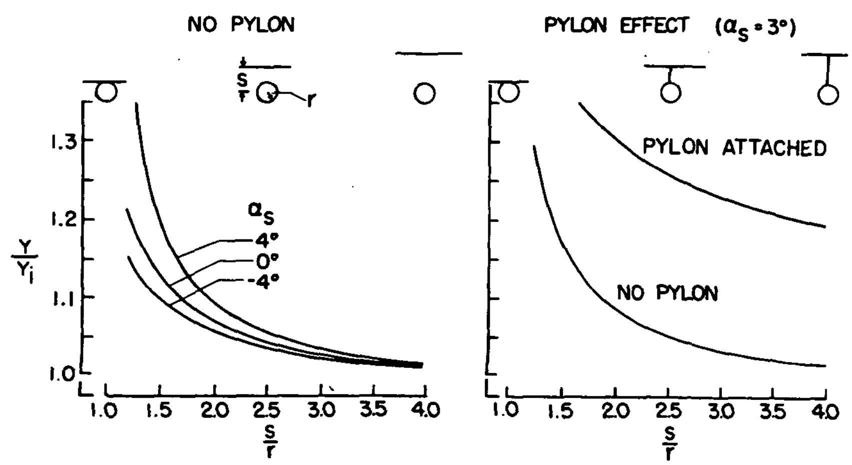

Figure 5

SIDE-FORCE DISTRIBUTION ON STORE

M = 1.6 ; α = 6°

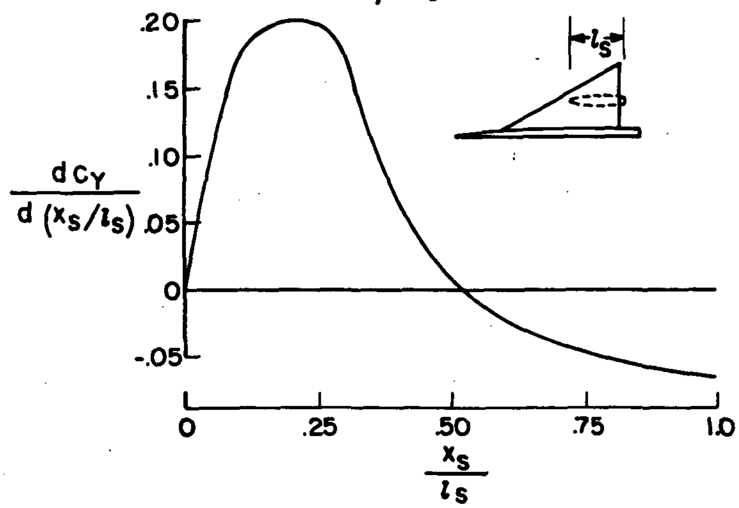

Figure 6

[redacted]

EFFECT OF STORE LATERAL LOCATION AND ANGLE OF ATTACK ON C_Y (NO PYLON)

$M \approx 1.6$

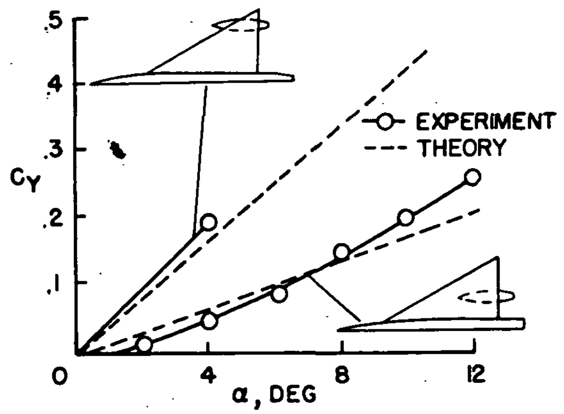

Figure 7

EFFECT OF LONGITUDINAL STORE POSITION ON THE SIDEFORCE ON STORE UNDER 60° DELTA WING (PYLON ATTACHED)

$M \approx 1.6$

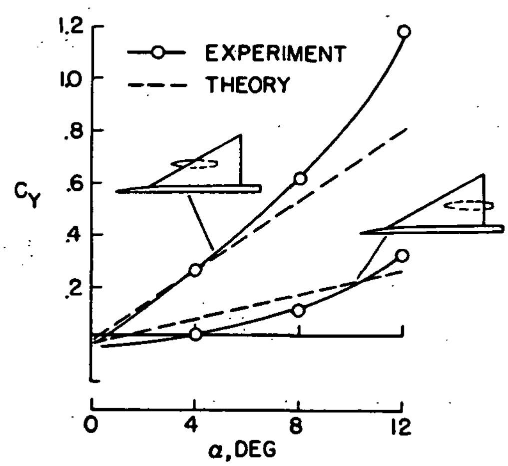

Figure 8

[redacted]

SIDE FORCE ON STORE UNDER UNSWEPT WING

A=4; M≈1.6

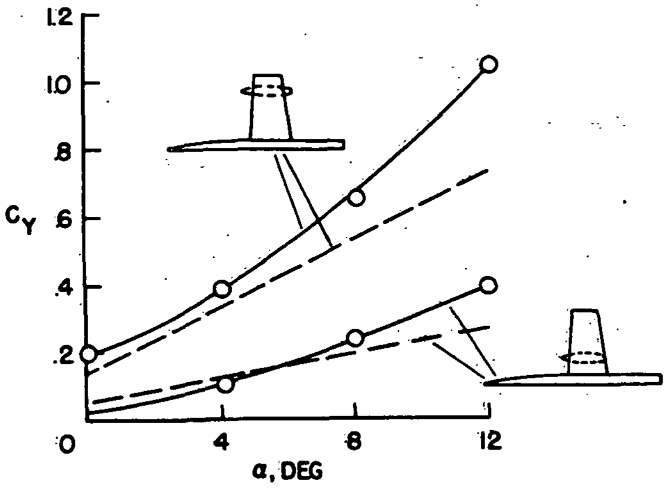

Figure 9

EFFECT OF PYLONS ON SIDE FORCE ON STORE
UNDER 45° SWEPT WING
A=4; M≈1.6

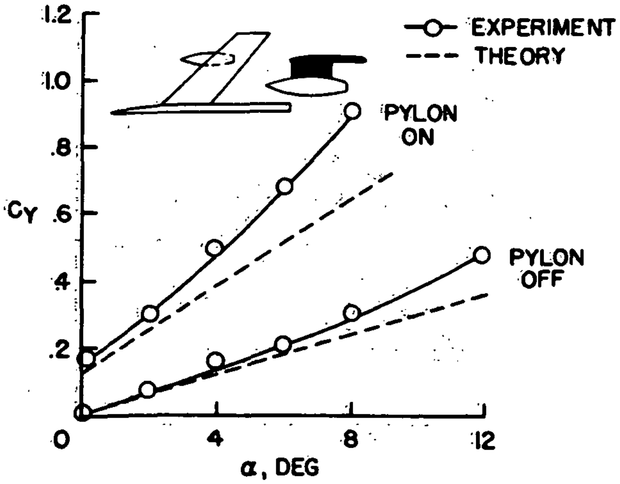

Figure 10

PROPULSION AERODYNAMICS

EFFECTS OF INTERNAL BOUNDARY-LAYER CONTROL

ON THE PERFORMANCE OF SUPERSONIC AFT INLETS

By Leonard J. Obery and Carl F. Schueller

Lewis Flight Propulsion Laboratory

SUMMARY

Removal of compression-surface boundary layer from the throat of a supersonic aft inlet is shown to increase the critical total pressure recovery to values comparable to the better axisymmetric nose inlets. Throat bleed on two-dimensional- and three-dimensional-type inlets by discrete slots or by porous plates has provided gains in critical recovery of as much as 7 percent at Mach number 2.0. A proper combination of bleed ahead of the inlet and at the inlet throat to control both fuselage and compression-surface boundary layer is shown to produce maximum values of propulsive thrust.

INTRODUCTION

For some time it has been realized that the fuselage boundary-layer air must be removed ahead of a side inlet to obtain acceptable inlet performance. However, a new boundary layer is formed on the compression surface and its interaction with the inlet terminal shock may also adversely affect the inlet performance. A typical example of the flow into a supersonic inlet is shown in figure 1. The oblique shock generated by the two-dimensional ramp falls just ahead of the inlet lip and the terminal shock is located just outside the cowl. If the static pressure gradient across the terminal shock is high enough, the boundary layer formed along the compression surface will separate ahead of the shock and will form effectively another wedge, throwing up an additional oblique shock. Therefore in a real or viscous flow there will be some area across the the inlet face for which three-shock compression exists. The extent of the second oblique shock will be controlled by the amount of boundary-layer separation which, in turn, depends on the strength of the inlet normal shock. The boundary layer considered here is only that formed on the compression surface; however, a somewhat similar condition would also result if the fuselage boundary layer were allowed to flow into the inlet.

The added compression wave generated by the separated region increases the recovery across the supersonic portion of the inlet to a value higher than it would have been for the original two-shock geometry.

However, the separated region may continue downstream, becoming larger as it progresses as shown by the velocity profile and, finally, adversely affecting the subsonic diffuser pressure recovery. Even if the separated flow should reattach along the diffuser wall, it would still be a region of low-recovery air which would have to mix with the higher energy air of the main stream and again result in low subsonic diffuser recovery. Usually this poorer subsonic recovery will more than offset any gains made in the supersonic compression region of the diffuser.

From this concept a solution to the problem is evident. If this low-energy air can be eliminated before it can adversely affect the subsonic diffuser recovery, the overall performance of the inlet should be improved. There are at least three ways to eliminate the low-energy air. In the first case, as shown by figure 2(a), if all the boundary-layer air on the compression surface were removed ahead of the inlet terminal shock, there would be no shock-boundary-layer interaction and, thus, no separated air to reduce the subsonic diffuser pressure recovery. In this case, additional oblique shock compression could not be expected since its source, the separated region, has been removed. However, efficient supersonic compression can be built into the inlet simply through the geometry of the compression surface. This method of removal should require the least mass flow to be bled from the main stream. Secondly, the compression-surface boundary layer could be allowed to separate and form an additional wedge. The low-energy separated region could then be removed from the inlet either by a flush slot or by a ram scoop as shown in figures 2(b) and 2(c). In either of the latter two cases, it should be possible to retain the advantage of the improved supersonic recovery available from the separation wedge without incurring the subsonic diffuser penalties attendant upon the simultaneous diffusion of low-energy and high-energy air streams. Although the two latter schemes probably require a greater amount of air to be bled from the inlet, they also offer compression by an aerodynamic surface and thereby may permit a larger throat area for subsonic or transonic speeds.

EXPERIMENTAL DISCUSSION

These three methods of boundary-layer control were investigated at $M_o = 2.0$ on a proposed inlet of a present-day supersonic airplane and are reported in reference 1. The results are shown in figure 3. Twin inlets were mounted on the sides of the fuselage and all the fuselage boundary layer was removed ahead of the inlets. Compression-surface boundary-layer control was effected in three ways: by a perforated second ramp to reduce or eliminate the boundary-layer separation or by an internal flush slot or ram scoop to remove it after separation. For this and the rest of the tests described herein, the bleed exit was vented to free-stream static pressure; thus, the boundary-layer air was pumped from the inlet only by the pressure differential existing between inlet and free stream. No external source of power was needed for any of the removal systems.

For the no-bleed inlet, that is, an inlet which effectively had the flush slot completely faired over, the critical total pressure recovery was about 86 percent. Bleeding the boundary layer after it had separated by either a ram scoop or a flush slot increased the critical recovery to about 89 percent. Here about 3 percent of the mass flow was bled from the inlet as shown by the difference in supercritical mass flow ratios. Although both methods of removal were equally effective at critical mass flow ratio, the subcritical performance of the flush slot bleed was superior to that of the ram scoop bleed. Thus far for inlets tested at the Lewis Flight Propulsion Laboratory using comparable ram scoop and flush slot bleeds, the flush slot configurations have been as good or better aerodynamically.

When the compression-surface boundary layer was removed through perforations on the second ramp, no increase in critical total pressure recovery was obtained. In this case, about 1 percent of the mass flow was bled from the inlet. Here, apparently, the improved subsonic diffusion which would be expected from removal of the low-energy air was offset by a lower supersonic recovery, since with bleed on the ramp no added oblique compression shocks would be formed. However, even though the critical recovery was not increased, the stable subcritical range was extended. The lack of pressure recovery improvement at critical mass-flow ratio probably resulted both from too little bleed and from loss of extra supersonic compression rather than from any inherent disadvantage of bleed through a perforated surface.

Of course, if the bled air is discharged to the free stream without being used for any other purpose, such as cabin ventilation, the inlet must be charged with an additional drag term. Calculations were made for these inlets using reasonable values of bypass drag and, as shown in reference 1, boundary-layer throat bleed in this case paid for itself by increasing the propulsive thrust level by almost 4 percent.

Another two-dimensional type of inlet which used throat bleed was investigated both at the Langley Aeronautical Laboratory as reported in reference 2, and at the Lewis Flight Propulsion Laboratory by John L. Allen and Thomas G. Piercy. This inlet (fig. 4) also had double-ramp compression surfaces but was mounted as a ventral normal wedge inlet. Compression-surface boundary-layer air was bled from the inlet through porous plates extending from about midway along the second ramp to well inside the cowl lip. Removal of the boundary layer through the porous plates increased the diffuser critical total pressure recovery by about 7 percent at Mach number 2.0. In this case, throat bleed increased the critical total pressure recovery at Mach number 2.0 from a relatively poor value of 81 percent to a value comparable to the better nose inlets of 88 percent. As the free stream Mach number decreased, the improvement in critical total pressure recovery also decreased. This general trend for the greatest gains in pressure recovery to occur at the higher Mach numbers has been true for all the inlets tested to date. Recent preliminary tests at Mach 3.1 have also been in agreement with this trend. Inlet critical recoveries in these tests have been increased by 10 percent to 15 percent through the use of throat bleed.

Area suction through a slotted plate has also been investigated by Ernest A. Mackley and Clyde Hayes of the Langley Aeronautical Laboratory on a scoop inlet of the type shown in figure 5. Boundary-layer removal was used on the wall opposite the compression surface in this case. The slotted wall was flat and the compressed flow ahead of the bleed plate was two-dimensional even though the outer cowl lip was elliptical in plan form as shown by section A-A. Again with this inlet the critical total pressure recovery was increased by about 5 percent at Mach number 2.0 by bleeding in the order of 6 percent of the main mass flow.

So far all the inlets discussed have had various types of two-dimensional supersonic compression. For these, boundary-layer bleed at the inlet throat has provided gains in total pressure recovery of from 3 percent to 7 percent even on inlets which previously were considered good; for example, 86 percent for free-stream Mach number $M_o = 2.0$ at critical mass flow ratio for the first inlet. The same concepts of throat bleed can also be applied to three-dimensional inlets. The results from such an investigation (ref. 3) are shown in figure 6. This test was conducted on a twin side-inlet configuration which had half-cone supersonic compression surfaces mounted directly on the fuselage. Most of the fuselage boundary layer was diverted around the inlet by the cone and flowed under the floor of the inlet. The boundary layer developed on the cone was bled from the inlet throat either by a porous surface which extended from the cowl lip aft for about one-half of the inlet diameter inside the inlet or by a flush slot located just aft of the inlet throat. The same amount of mass flow could be removed by either bleed system. For this inlet, bleeding the optimum amount of low energy air from the inlet by a flush slot increased the diffuser total pressure recovery by almost 6 percent. Incidentally, this inlet operated in a nonuniform flow field which had an average Mach number of about 2.1 at an airplane Mach number of 2.0. Thus the 87-percent total pressure recovery obtained with the inlet operating slightly subcritical shows the merit of throat bleed. Removal of the boundary-layer air by the porous surface increased the peak total pressure recovery to almost the same value as the flush slot inlet but this peak was reached with slightly more boundary-layer removal and with somewhat more subcritical spillage.

The mass-flow ratios shown represent the total amount of air entering the inlet. In this case, it was possible to capture a slightly larger stream tube by bleeding the compression surface boundary layer. Values of mass-flow ratio greater than unity resulted from the choice of reference area in the reference mass flow.

The amount of throat boundary-layer air removed was also varied during this test. Calculations were made to indicate what increases in effective thrust minus drag could be realized by using throat bleed. It was calculated that the propulsive thrust of the flush slot configuration was about 5 percent greater than the no-bleed inlet. A mass flow bleed of about 3 percent was required to obtain maximum thrust minus drag and additional bleed only served to lower the inlet overall thrust minus drag. Generally, the trend for the greatest gains from throat bleed to be made with about 3 to 5 percent mass flow removal has been observed in the inlet tests so far. Too much bleed has, in all cases to date, reduced the diffuser total pressure recovery at critical mass flow ratio.

As might have been anticipated from the internal performance curves, the increase in propulsive thrust was less for the porous surface configuration than for the flush slot inlet. Somewhat more bleed mass flow was also required to reach peak thrust minus drag.

As discussed previously for the two-dimensional-type inlets, the performance gains were smaller at the lower Mach numbers. At Mach number 1.5, although the diffuser pressure recovery was increased by bleeding the boundary layer through the flush slot, the drag added by the bleed system almost counterbalanced the pressure-recovery gain and only a slight increase in propulsive thrust could be calculated. However, the fact that only a small gain in thrust minus drag was realized is not entirely an unfavorable result for it does indicate that the benefits of throat bleed which were obtained at the higher Mach numbers are not necessarily accompanied by performance penalties at the lower Mach numbers, at least to 1.5.

All the inlet installations discussed so far have had full fuselage boundary-layer removal or, expressed in the usual terms, were at h/δ of at least 1.0. Therefore two boundary-layer removal systems are provided in the immediate vicinity of the inlet and some combination of bleed ahead of the inlet and at the inlet throat should provide an optimum overall system. This hypothesis was investigated recently with the model of reference 4. As shown in figure 7, this was a bottom-inlet model with a single-ramp compression surface. The fuselage boundary-layer thickness is represented by δ. The inlet was mounted to the body in such a manner that the distance h from the ramp leading edge to the fuselage could be varied from the value of δ, that is, a full boundary-layer thickness to 0 or flat against the fuselage. The internal boundary-layer air was removed through a flush slot opening at the inlet throat. The amount of air bled from the inlet was controlled by varying the size of the bleed exit. Thus, at any selected value of h various amounts of mass flow could be bled from the inlet throat through the internal boundary-layer removal system. The performance of this configuration is shown in figure 8. The experimentally determined pressure-recovery—mass-flow curves are shown for h/δ values of 1, 2/3, 1/3, and 0. For the no-bleed inlet the expected trend occurred; as the inlet was moved into the fuselage boundary layer the critical pressure recoveries steadily decreased until at $h/\delta = 0$ a recovery of only about 72 percent was obtained. However, by using various amounts of throat bleed the critical total pressure recovery could be kept at 88 percent as h/δ was reduced and, although the complete data were not obtained, results from a similar model in this series of tests indicated that with more throat bleed it would be possible to maintain an 88 percent recovery even at $h/\delta = 0$. The critical pressure recovery of the internal bleed inlet at $h/\delta = 0$ was about as high as the no-bleed inlet at $h/\delta = 1.0$.

As seen from the mass flow increments, greater amounts of flow were removed through the internal bleed as the inlet was moved closer to the body. This flow was spilled out through openings in either side of the body and the spillage drag, as well as the drag of the rest of the model, was measured by an internal balance. As such, the drags which were obtained from this investigation are valid only for this configuration; however, the trends of the inlet propulsive thrust parameter obtained with this configuration should at least be representative of most cases. Calculations of the inlet propulsive thrust were made for the various values of h/δ (fig. 9) and it was found that the thrust minus drag for the no-bleed inlet steadily decreased as the inlet was moved into the fuselage boundary layer. Now, however, when the optimum amount of throat bleed was used, the inlet propulsive thrust was at all times greater than the no-bleed case and would have reached a maximum somewhere between $h/\delta = 1/3$ and 0. For this case, an increase of about 9 percent in propulsive thrust could be added to the aircraft through the use of throat bleed. In addition to increasing the aircraft performance potential, this investigation indicates by the flatness of the performance curve that the designer may have some choice in the amount of boundary-layer removal he must provide ahead of the inlet and at the inlet throat.

CONCLUDING REMARKS

From the tests performed so far at the various laboratories, removal of the compression-surface boundary layer has emerged as a powerful method of increasing the diffuser total pressure recovery. The critical total pressure recovery of side inlets has been increased to about the same value as the best axially symmetric nose inlets. Throat bleed has increased the recovery on various types of side inlets: two-dimensional ramp type inlets, scoop inlets which turn the supersonic air stream in toward the body, and three-dimensional half-cone compression inlets, and increases have been made even when the no-bleed performance was considered quite acceptable. These increases have been obtained with various kinds of boundary-layer removal including concentrated removal by flush slots or ram scoops and area removal by porous plates. Throat bleed has proved most effective at the higher Mach numbers. Specifically, diffuser recoveries have been increased as much as 7 percent at Mach number 2.0 but only about 3 percent at Mach number 1.5. Preliminary results indicate that larger gains may be made at the higher Mach numbers. Too much bleed at any free-stream Mach number has generally reduced the total pressure recovery at critical mass-flow ratio. From 3 percent to 5 percent of the main stream mass flow appears to be about the optimum amount, although this may well depend on such factors as amount of boundary-layer separation and scale size or Reynolds number. It also appears that consideration should be given again to the fuselage boundary-layer removal ahead of the inlet. A proper combination of removal systems ahead of the inlet and at the inlet throat is required to obtain optimum values of propulsive thrust.

REFERENCES

1. Obery, Leonard J., and Cubbison, Robert W.: Effectiveness of Boundary-Layer Removal Near Throat of Ramp-Type Side Inlet at Free-Stream Mach Number of 2.0. NACA RM E54I14, 1954.

2. Hasel, Lowell E.: Investigation at Mach Numbers of 1.41, 1.61, and 1.82 of Two Variable-Geometry Inlets Having Two-Dimensional Compression Surfaces. NACA RM L54K04, 1954.

3. Stitt, Leonard E., McKevitt, Frank X., and Smith, Albert B.: Effect of Throat Bleed on the Supersonic Performance of a Half Conical Side Inlet System. (Prospective NACA paper.)

4. Campbell, Robert C.: Performance of a Supersonic Ramp-Type Side Inlet With Combinations of External and Internal Boundary-Layer Removal. (Prospective NACA paper.)

SUPERSONIC INLET FLOW PATTERN

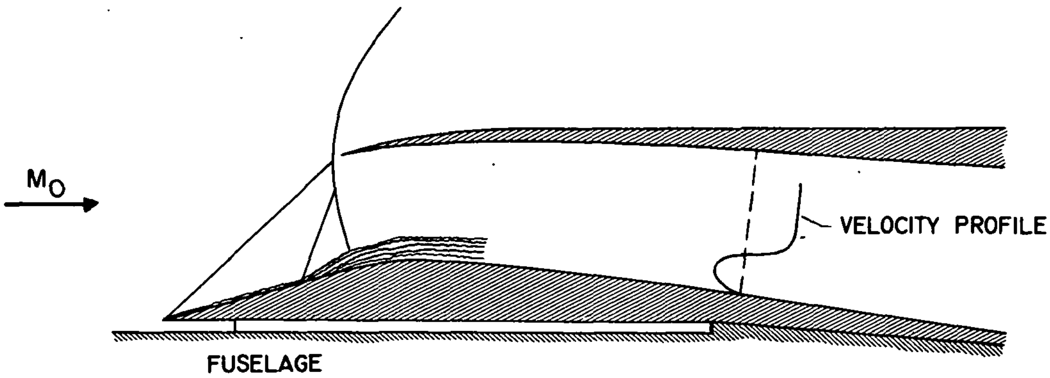

Figure 1

METHODS OF COMPRESSION SURFACE BOUNDARY LAYER CONTROL

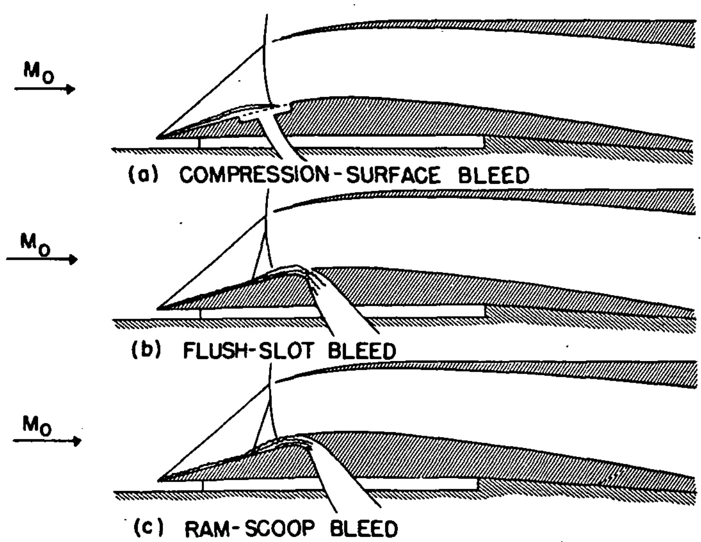

Figure 2

EFFECT OF THROAT BLEED, DOUBLE RAMP INLET

M_0, 2.0 α, 0°

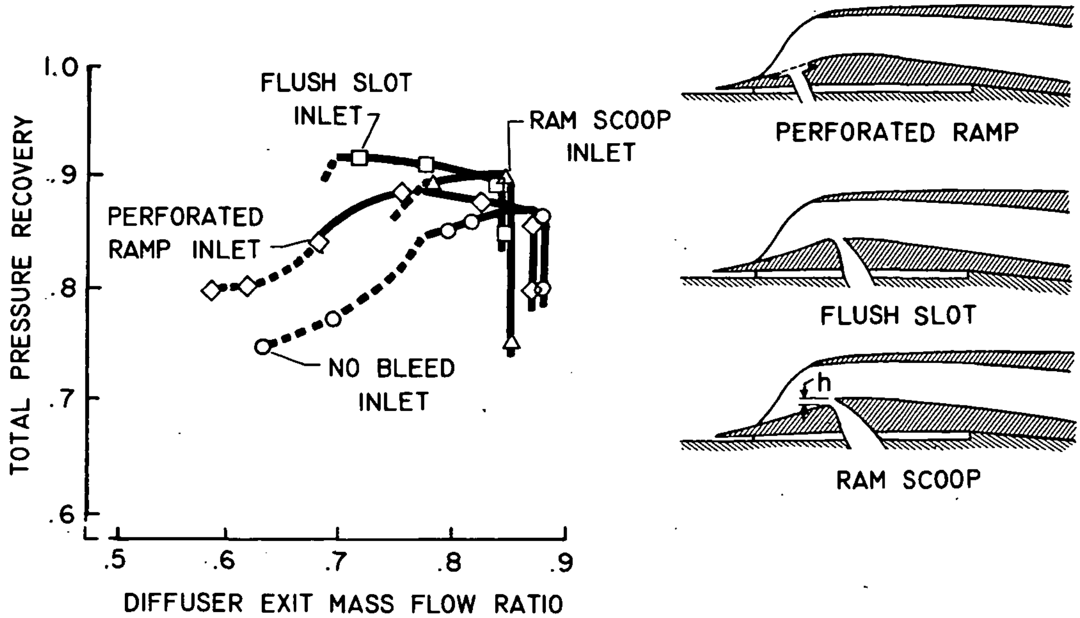

Figure 3

EFFECTIVENESS OF THROAT BLEED WITH MACH NUMBER

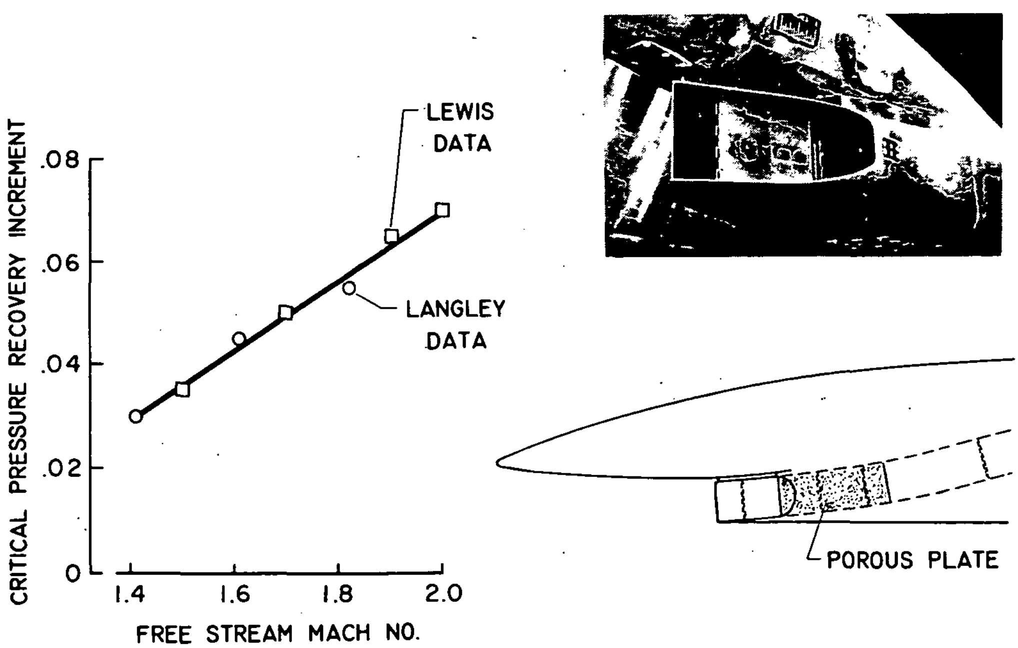

Figure 4

~~CONFIDENTIAL~~

THROAT BLEED SYSTEM FOR SCOOP INLET

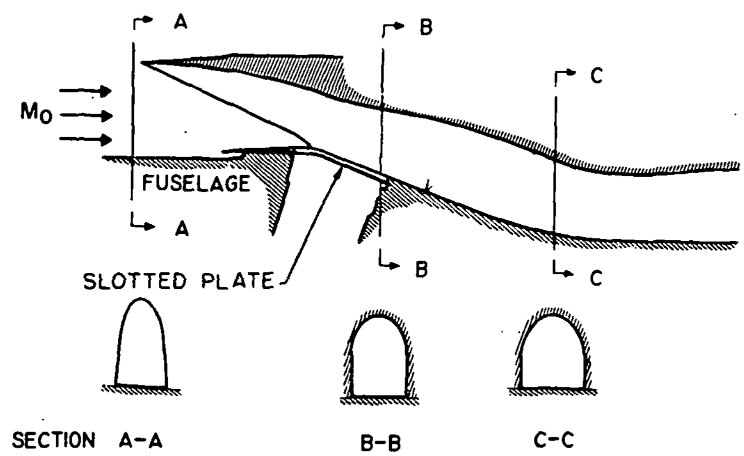

Figure 5

EFFECT OF THROAT BLEED, HALF-CONE INLET

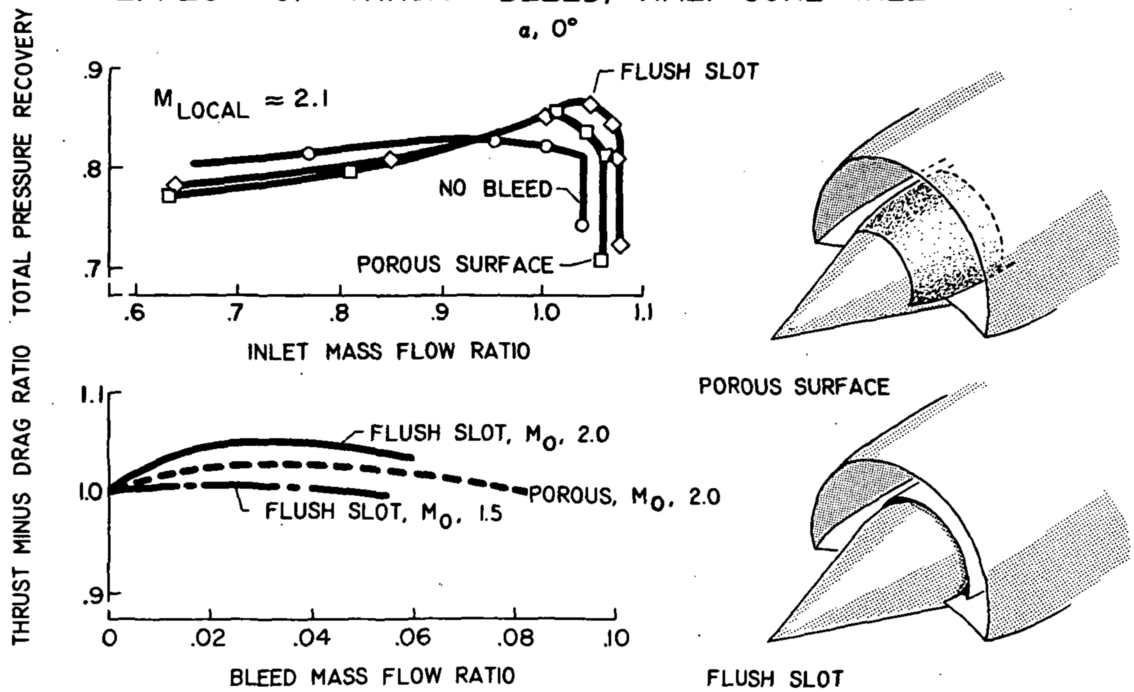

Figure 6

~~CONFIDENTIAL~~

VARIABLE EXTERNAL AND INTERNAL BOUNDARY LAYER REMOVAL MODEL

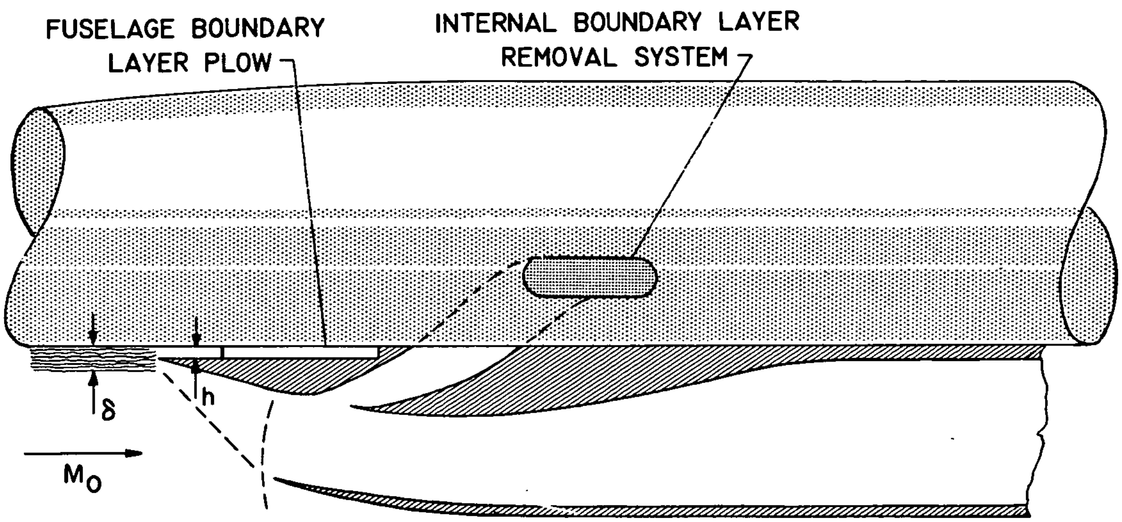

Figure 7

PERFORMANCE WITH VARIABLE BLEED SYSTEMS

M_0, 2.0 α, 0°

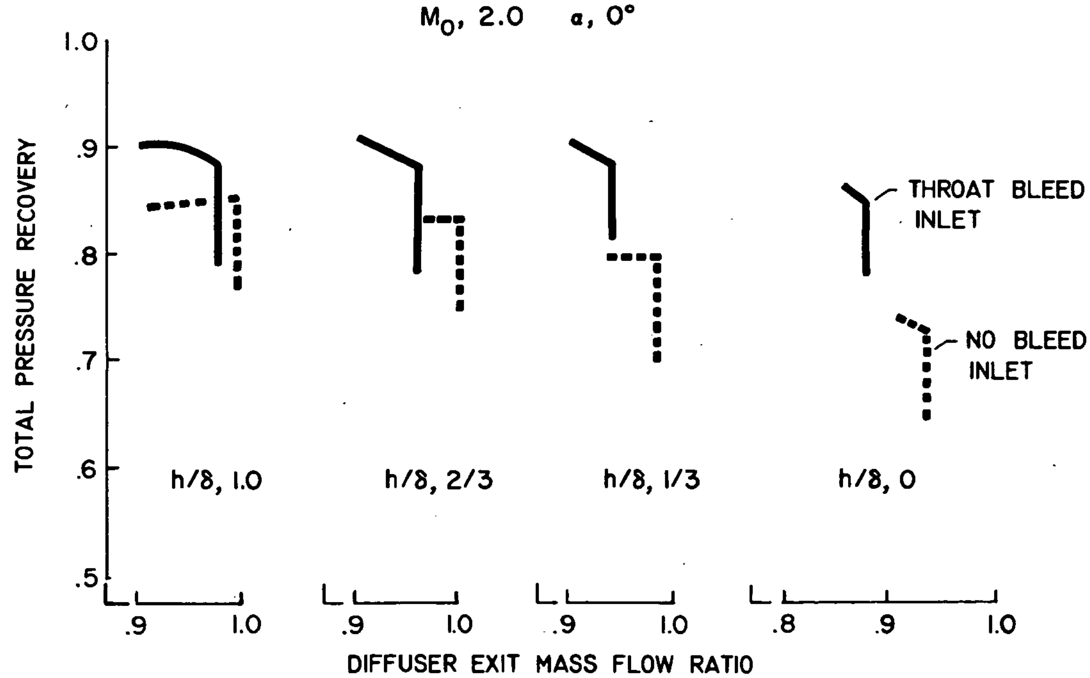

Figure 8

EFFECT OF VARIABLE BLEED SYSTEMS
ON PROPULSIVE THRUST

M_0, 2.0

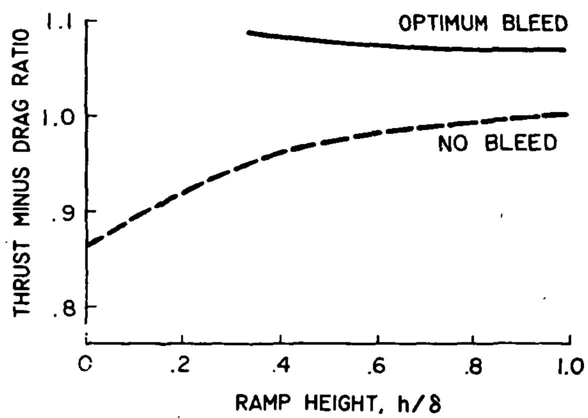

Figure 9

FACTORS AFFECTING THE FLOW DISTORTIONS

PRODUCED BY SUPERSONIC INLETS

By Thomas G. Piercy

Lewis Flight Propulsion Laboratory

SUMMARY

Typical effects of distortions on turbojet-engine performance are reviewed. Sources of distortion in the supersonic inlet are enumerated and steps are suggested which might be taken to reduce their effects. Also, parameters affecting the mixing of these flow distortions in the subsonic diffuser are discussed.

No simple solution to the distortion problem is currently evident. Satisfactory duct-engine combinations will require careful attention to detail and perhaps compromises in both the airframe and the engine designs.

INTRODUCTION

The performance of many current subsonic and transonic airplanes has been reduced to some extent by the presence of nonuniform flow at the compressor of the turbojet engine. These flow distortions are characterized by variations in the velocity or total pressure of the air entering the compressor and are usually expressed either as the maximum variation in velocity ΔV or total pressure ΔP divided by a reference velocity or pressure.

In this paper typical effects of distortion on turbojet-engine performance are reviewed. Sources of distortion in the supersonic inlet are then enumerated and are suggested which might be taken to reduce their effects. Also parameters affecting the damping out of these flow distortions in the subsonic diffuser are discussed.

SYMBOLS

D	diameter of constant-area straight section
D_h	hydraulic diameter of inlet throat

H_i inlet-throat height

h/δ parameter defining amount of external boundary layer removed

l length of constant-area straight section

L length of subsonic diffuser

m mass flow

M Mach number

P total pressure

ΔP difference between maximum and minimum values of total pressure as measured by rake

Δp static-pressure increment

q dynamic pressure

ΔV difference between maximum and minimum velocities

V^* stagnation speed of sound

δ boundary-layer thickness

θ_c cone half-angle

Subscripts:

0 in free stream

b in annulus

av average

EFFECT OF DISTORTIONS ON ENGINE PERFORMANCE

The penalty of flow distortion on engine performance is dependent upon the particular engine under consideration and upon the type of flow distortion (that is, whether the flow varies radially between the compressor hub and blade tip, or varies circumferentially around the compressor annulus, or, as is the usual case, whether the flow has components of both radial and circumferential distortion). Also the magnitude and extent of the flow distortion affects engine performance. The effects of distortion in reducing cyclic efficiencies and in increasing stress and vibrations are reported in references 1 to 3.

A typical effect of circumferential distortion is shown in figure 1. When circumferential distortion enters the compressor, the distortion, although reduced in magnitude, persists through the last compressor stage. Temperature gradients then exist at the turbine as the result of circumferential variation in the fuel-air ratio caused by the distorted air flow. Although the turbine rotor feels only the average temperature, the turbine stator at some point is subjected to higher than the average temperatures. In order to prevent failure of the stator due to overheating, the average turbine temperature must be reduced (refs. 1 to 3.)

The amount of necessary turbine-temperature reduction for several engines is shown in figure 1 as a function of the entering total-pressure distortion. Reducing the turbine temperature as required results in the indicated net thrust losses. These reductions in engine thrust can amount to as much as 1 percent for each 2 percent of total-pressure distortion.

Another effect of flow distortion is that of reducing the stall margin of the compressor. This effect is illustrated in figure 2 for two typical engines. Compressor pressure ratio is plotted as a function of the corrected engine speed. In the left-hand plot, the presence of radial distortion lowered the compressor surge limit line in comparison with the steady-state operating line and caused the rotating stall region to move to higher corrected engine speeds. (See, for example, refs. 1 and 3.) Lowering of the surge limit line reduces the acceleration margin of the compressor. Movement of the rotating stall region to higher corrected engine speeds indicates that the maximum flight speed at altitude may be reduced by the occurrence of rotating stall.

In the right-hand plot, the presence of circumferential distortion for another typical engine again lowered the compressor surge limit line. The acceleration margin of the compressor is again reduced. For distortions of the order 32 percent the maximum possible corrected engine speed is about 108 percent. Hence, the cruising speed of the airplane can be affected by the occurrence of compressor surge.

Another typical effect of flow distortion is the reduction of maximum altitude due to compressor surge (for example, ref. 1). An example of this effect is presented in figure 3. Altitude is plotted as a function of the compressor speed. With uniform flow at the compressor, a maximum altitude of about 62,000 feet was achieved. This limit is primarily a result of Reynolds number effect. At the higher compressor speeds, the altitude was limited by the maximum turbine-outlet temperature.

When circumferential distortion was introduced into the compressor, the maximum altitude was reduced to as low as 47,000 feet. Although the distortion level was about 20 percent for both cases presented, quite different effects on the altitude limits were observed. The greatest reduction in altitude occurred with the extended circumferential distortion rather than the localized distortion. In order to get the compressor out of surge for these cases, it was necessary to drop to an altitude of 35,000 feet.

DISTORTION PRODUCED IN SUPERSONIC INLETS

Intuitively, it might be said that the distortion existing at the exit of the subsonic diffuser depends upon the amount of distortion entering the inlet throat, upon the existence of additional sources of distortion within the inlet, and upon the amount of mixing, or damping, of these distortions in the subsonic diffuser.

Mixing in the Subsonic Diffuser

The amount of mixing that takes place in the subsonic diffuser is known to be a function of the length of the diffuser. For example, the total-pressure distortions at the diffuser exit of a variety of side-inlet types and for Mach numbers ranging from 1.5 to 3.0 are presented in figure 4 as a function of the ratio of diffuser length L to throat hydraulic diameter D_h. The data points represent the distortion for either critical or engine-inlet matching conditions. These distortions were obtained from the data of references 4 to 10 and from various unpublished data.

Although there is considerable scatter of the data, there is a definite trend of lower distortions with increased diffuser length. This scatter is due, in part, to the difference of distortion existing at the inlet throat, a factor which is considered later. Also, part of the scatter is due to the difference in average Mach number of the ducts. For example, when mixing takes place in a straight duct of constant area at a constant Mach number (ref. 11), as shown in the right-hand side of the figure, a smooth curve, similar to that sketched in through the data points at the left, results.

The effect of average Mach number on mixing is considered in figure 5. At the left the theoretical variation of the velocity distortion is plotted as a function of the average flow Mach number for three values of total-pressure distortion. In this example, velocity distortion is arbitrarily defined as the difference between the maximum and minimum velocity ΔV divided by a constant velocity, in this case the stagnation speed of sound V^*. At the lower Mach numbers the velocity distortion increases for a given level of total-pressure distortion. Thus, increased mixing may be expected to occur in a duct at the lower flow Mach numbers.

Note, also, that, for a given average Mach number, the velocity distortion decreases as the total-pressure distortion decreases. Thus, the decrease of distortion by mixing is proportional to the distortion. For example, the mixing that occurs in a straight duct of constant area at a given flow Mach number would tend to decrease the distortion asymptotically toward some minimum value. There are some indications that this minimum value is probably that determined by the flow profile for fully developed pipe flow and would increase as the Mach number increases.

To illustrate some of these effects, total-pressure distortions measured in a constant-area duct at flow Mach numbers of 0.20 and 0.37 are presented at the right-hand side of the figure. At the lower Mach number, distortion decreases fairly rapidly through mixing. However, the distortion decreases less rapidly at the higher Mach number due both to the decreased rate of mixing and the decreased residence time in any given length of duct. The lowest value of distortion that could be expected with longer mixing lengths would be about 2 percent at the flow Mach number 0.2 and about 7.5 percent at Mach number 0.37 based on a fully developed turbulent profile. All distortions for the remainder of this paper are presented in terms of total pressure rather than velocity.

The amount of mixing that occurs in the inlet subsonic diffuser will depend upon the average Mach number of the duct, inasmuch as the flow is diffused from a relatively high Mach number at the inlet throat to a lower Mach number at the diffuser exit. An example of the importance of low average Mach numbers in the diffuser duct is presented in figure 6. The distortion at the diffuser exit for critical inlet operation is plotted against free-stream Mach number for two nose-inlet models which were identical with the exception that the cowl and centerbody surfaces were altered to give different rates of initial area expansion at the inlet lip. These data, although not reported, were obtained from the investigations of references 12 and 13.

Although the distortion at the inlet throat was identical for both models, the model with 12 percent initial area expansion per inlet-throat hydraulic diameter had lower distortion at the diffuser exit than the model with the smaller area expansion. The two models discharged at the same Mach number and, of course, had the same Mach number at the inlet lip. The variation of Mach number through the ducts, however, was different because of the change in initial area expansion. The model with the larger area expansion diffused more rapidly, giving a lower average duct Mach number. The lower distortion is thus believed to be the result of more efficient mixing in the subsonic diffuser.

There is evidence from these same data that constant-area throat inlets, which have proven desirable in some cases from stability considerations, and internal contraction inlets, which promote low cowl drags, will have higher distortions as the result of reduced mixing. Judging from figure 6, mixing is promoted by rapidly expanding the diffuser duct. Carrying this concept a little further, it would appear that lower distortions could be produced by overexpanding the diffuser duct area to provide low Mach numbers to increase the mixing. The flow could then be rapidly accelerated at the diffuser exit to the desired Mach number. This concept is feasible inasmuch as the use of rapid acceleration will, of itself, reduce distortion. Flow acceleration has been known for some time to achieve more nearly uniform flow at the throats of subsonic wind tunnels. An example of rapid flow acceleration at the diffuser exit is given in figure 7. Total-pressure distortions were measured in a constant-area straight duct with and without the benefit of rapid acceleration. Acceleration from Mach number 0.37 to 0.50 in the annulus was provided by a hub simulating the accessory housing of the turbojet engine. Insertion of the hub decreased the total-pressure distortion from about 16 percent to about 12 percent at the end of the straight section with essentially no loss in total-pressure recovery.

Forced Mixing Devices

The use of freely rotating blade rows to reduce flow distortion at low flow velocities was reported in reference 14. The use of such blade rows has since been investigated theoretically and the results have appeared promising in that distortion reduction can be achieved with little or no total-pressure loss. Such a blade is free wheeling at a speed determined by the blade angle and average axial Mach number and reduces distortion by acting as a turbine in the higher than average velocity flow and as a compressor in the low velocity flow. The blade row then transfers energy to the low velocity region with no net work with the exception of that required to overcome bearing friction. A model of the freely rotating blade-row apparatus has been built and tested, and the results are presented in figure 8. These data were obtained from an investigation made by William T. Beale of the Lewis laboratory. A blade row and a row of straightener vanes were mounted on a hub in a straight duct. Distortion was introduced by throttling the duct flow across screens placed in a portion of the forward duct. The distortion in the annulus at B was then measured and plotted as a function of the distortion at A ahead of the hub. The variation of the Mach number in the annulus due to the throttling is also plotted on the abscissa.

The distortion in the annulus is lower than that ahead of the hub for any point below the slanted line through the origin of coordinates. When circumferential distortion was introduced, some distortion reduction was achieved without the benefit of the blade row. This reduction was the result of the flow acceleration provided by the hub and was not affected by the row of flow straighteners. When the blade row was added, the distortion in the annulus was further reduced. When radial rather than circumferential distortion was introduced, about the same distortion reduction was achieved across the blade row. At an annulus Mach number of 0.5, the total-pressure distortion was reduced from 25.5 to 15 percent across the blade row. For this reduction in distortion the total-pressure loss was about 2.5 percent.

Screens have also been used as forced mixing devices (for example, refs. 15 to 17). An example of their use is shown in figure 9. The total-pressure distortion was measured behind screens of varying solidity, that is, the blockage area of the screen expressed as a percentage of the duct cross-sectional area. Two typical applications are considered: the curve for the lower Mach number 0.20 is representative of a ram-jet application, whereas that for the higher Mach number 0.50 is more typical of the diffuser discharge Mach number of a present-day turbojet engine; the Mach number ahead of the screens was about 0.20 and 0.37, respectively. For both cases increasing the screen blockage reduced the distortion. However, there is a limit to the amount of screen blockage that may be added without causing choking at the screens. With choking, of course, inlet mass flow would be reduced.

The total-pressure loss across the screens is plotted at the right, again as a function of the screen solidity. At a solidity of 30 percent, the total-pressure loss was 2 percent at the low average Mach number and about 8 percent at the higher Mach number.

In order to propel future aircraft to higher supersonic speeds, higher weight-flow turbojet engines will be required. For such engines the diffuser discharge Mach numbers will be of the order 0.6 or even higher over portions of the flight range. Hence, mixing in the subsonic diffuser will probably be reduced. Forced mixing devices will be used with caution inasmuch as figure 9 indicates higher total-pressure losses will be incurred at higher duct Mach numbers. For such configurations the distortion entering the inlet throat must be kept to a minimum.

Distortion at the Inlet Throat

Distortion at the inlet throat is caused primarily by nonuniform compression. In the next few figures origins of these distortions are examined and the resulting distortions at the diffuser exit are presented.

In figure 10 the total-pressure variation across the inlet throat was determined for the full-scale J-34 nose inlet at Mach number 1.8. These data were obtained from related tests of reference 18. Total-pressure profiles at the inlet throat are presented as a function of inlet mass-flow ratio. For the indicated configuration a vortex sheet, originating at the intersection of the oblique and normal shocks, enters the inlet throat for values of mass flow less than the critical value. Theoretically, the air entering the inlet next to the cowl will be at a pressure recovery of about 81 percent, whereas the air below the vortex sheet is at a pressure recovery of about 96 percent. As indicated, the measured total pressures across the vortex sheet agreed quite well with the theoretical values. As the mass flow was reduced, the vortex sheet progressed further toward the cone surface.

The distortion at the inlet throat was determined from these profiles between the indicated limits to eliminate the effects on the boundary layer, and the results are presented in figure 11. As the mass flow was reduced, inlet distortion increased due to further entry of the vortex sheet. Presented for comparison is the distortion measured at the diffuser exit. As the inlet mass flow was reduced, the exit distortion increased, corresponding to the increase of distortion at the inlet throat. However, as the mass flow was reduced, the average Mach number of the flow through the diffuser decreased. Hence, at the lower mass-flow ratios the distortion at the diffuser exit decreased, because of increased mixing, although the inlet distortion remained high.

The entrance of the vortex sheet is seen, then, to increase the distortion level of the diffuser. By delaying entry of the vortex sheet lower distortions can be achieved. This may be done, for example, by positioning the oblique shock ahead of the inlet lip so that the vortex sheet will pass around the inlet for subcritical inlet operation rather than into the inlet. With variable-geometry inlets having internal contraction sufficient to choke the inlet, the entry of a vortex sheet is unavoidable and, as a result, the distortion entering the inlet is apt to be large. Moreover, mixing in the subsonic diffuser of inlets having internal contraction will probably be reduced because of the higher inlet-throat Mach numbers.

Another example of nonuniform compression is that occurring at angle of attack (fig. 12). The distortion was measured at the inlet throat, at two intermediate positions, and at the diffuser exit for the full scale J-24 conical-nose inlet at Mach number 2.0 for critical inlet operation. These data have been recently obtained and have not been previously published.

Theoretically, at zero angle of attack, 3 to 4 percent distortion would be expected at the inlet throat because of the nature of the conical flow field. Seven percent distortion, however, was measured. The higher distortion is due to boundary-layer effects which were not considered. Similarly, at an angle of attack of 10°, nonuniform compression would be expected to yield inlet-throat distortions of the order 14 to 15 percent around the inlet-throat circumference. The actual distortion measured, even at an angle of attack of 3°, was over twice this theoretical shock value, again because of shock—boundary-layer interaction. Along the upper surface of the cone, the Mach number behind the oblique shock was quite high because of the reduced compression. The terminal shock was then strong enough to separate the compression surface boundary layer and to increase the distortion.

As the flow traversed the diffuser, distortion decreased because of mixing. However, the mixing was not sufficient to overcome the large initial distortion, and the distortion increased at the diffuser exit as angle of attack was increased.

At zero angle of attack, the distortion measured at the second measuring station was larger than at the inlet throat. This increase was due to separation of the boundary layer from the centerbody surface between the two measuring stations. Thus, sources of distortion exist within the inlet. Separation, rapid duct turns, struts, and so forth are all possible sources of distortion within the inlet.

In order to reduce the characteristic increase of distortion of conical-nose inlets at angle of attack, such inlets must be shielded from angle-of-attack effects. For example, the inlets could be located beneath and behind the wings and close to the fuselage. Preliminary test results indicate also that alinement of the spike centerbody with the free-stream direction reduced the nonuniform compression and hence reduces distortion.

Other inlet types may be required to reduce distortion at angle of attack. For example, horizontal ramp inlets are less sensitive to angle of attack, inasmuch as changes in angle of attack merely change the effective angle of compression.

The occurrence of shock—boundary-layer interaction was seen to have an important effect on distortion in figure 12. This factor is examined more closely in figure 13. The flow in the throat of a conical-nose inlet for critical inlet operation at a Mach number of 1.8 was determined for a range of values of the conical compression angle θ_c (ref. 18). By varying the compression angle, the Mach number ahead of the terminal shock was changed.

The thickness of the compression surface boundary layer δ expressed as a percentage of the inlet height H_i is presented at the left of the figure. Between cone angles of 30° and 25°, the boundary-layer thickness changed only from 3 to 4 percent of the inlet-duct height. For the 20° cone half-angle, however, the boundary-layer thickness doubled due to separation at the terminal shock. The occurrence of this separation had been predicted theoretically on the basis of the static-pressure rise across the terminal shock.

The distortion at the inlet throat is plotted at the right, again as a function of the cone half-angle. Although the distortion did not change for the higher cone angles, the distortion increased considerably for the separated flow case at a cone half-angle of 20°.

The distortion measured at the diffuser exit is again plotted for comparison. As the cone half-angle was decreased from 30° to 25°, the average-flow Mach number of the duct decreased as a result of the reduced throat Mach numbers, and the exit distortion decreased although the distortion at the throat remained about the same. At θ_c of 20° the increased mixing could not overcome the high initial distortion, and the distortion at the exit increased somewhat.

Suitable control of the compression-surface boundary layer would be expected to reduce these separation effects. For example, in figure 14 a typical ramp side inlet had provisions for both external and internal boundary-layer removal. With no external removal, the distortion at the diffuser exit varied between 40 and about 63 percent for critical inlet operation. By moving the inlet out of the boundary layer, the distortion was progressively decreased until for complete external removal, the distortion was in the 15 to 19 percent level. The lowest distortion was measured with internal boundary-layer removal was used in conjunction with external removal. For these cases the distortion was reduced to a more acceptable level of 7 to 10 percent. Thus, suitable removal of the boundary layer with side inlets is essential not only from the standpoint of increasing the pressure recovery but also of decreasing the distortion.

CONCLUDING REMARKS

Distortion at the compressor can be reduced by reducing the distortion entering the inlet throat, by elimination of internal sources of distortion, and by improving the mixing in the subsonic diffuser.

The distortion which exists at the inlet throat is primarily a result of nonuniform compression and may result from the entrance of the vortex sheet, operation at angle of attack, shock-boundary-layer interaction, or combinations of these effects. A few steps can obviously be taken to reduce these sources of distortions. For example, entrance of the vortex sheet can be delayed by positioning oblique shocks ahead of the inlet lip. Shock-boundary-layer interaction can be controlled to some extent by the use of boundary-layer control such as compression surface bleed.

With conical-nose inlets, large distortions at angle of attack are indicated. Low distortions can be achieved only by shielding such inlets from angle of attack. Other than conical compression inlets may be required to reduce angle-of-attack effects. For example, horizontal ramp inlets are less sensitive to angle of attack.

The mixing of distorted flows in the subsonic diffuser is primarily a function of the length and the average Mach number of the duct. Additional mixing can be obtained with forced mixing devices but generally at the expense of pressure recovery and weight. This brief review of the problem would indicate that severe distortion problems can be expected in the future with high compression inlets and high weight-flow engines required for flight at the higher supersonic speeds. With such configurations the average duct Mach number will be high and little mixing will occur in the subsonic diffuser. The flow distortion entering the inlets must thus be kept to a minimum, and sources of distortion within the inlet must be eliminated. No simple solution to the distortion problem is currently evident. Satisfactory duct-engine combinations will require careful attention to detail and perhaps compromises in both the airframe and the engine designs.

REFERENCES

1. Wallner, Lewis E., Conrad, E. William, and Prince, William R.: Effect of Uneven Air-Flow Distribution to the Twin Inlets of an Axial-Flow Turbojet Engine. NACA RM E52K06, 1953.

2. Huntley, Sidney C., Sivo, Joseph N., and Walker, Curtis L.: Effect of Circumferential Total-Pressure Gradients Typical of Single-Inlet Duct Installations on Performance of an Axial-Flow Turbojet Engine. NACA RM E54K26a, 1955.

3. Walker, Curtis L., Sivo, Joseph N., and Jansen, Emmert T.: Effect of Unequal Air-Flow Distribution From Twin Inlet Ducts on Performance of an Axial-Flow Turbojet Engine. NACA RM E54E13, 1954.

4. Obery, Leonard J., Stitt, Leonard E., and Wise, George A.: Evaluations at Supersonic Speeds of Twin-Duct Side-Intake System with Two-Dimensional Double-Shock Inlets. NACA RM E54C08, 1954.

5. Valerino, Alfred S.: Effects of Internal Corner Fillets on Pressure Recovery - Mass Flow Characteristics of Scoop-Type Conical Supersonic Inlets. NACA RM E52J10, 1952.

6. Goelzer, H. Fred, and Cortright, Edgar M., Jr.: Investigation at Mach Number 1.88 of Half of a Conical-Spike Diffuser Mounted as a Side Inlet with Boundary Layer Control. NACA RM E51G06, 1951.

7. Valerino, Alfred S.: Performance Characteristics at Mach Numbers to 2.0 of Various Types of Side Inlets Mounted on Fuselage of Proposed Supersonic Airplane. I - Two-Dimensional Compression-Ramp Inlets With Semi-Circular Cowls. NACA RM E52E02, 1952.

8. Esenwein, Fred T.: Performance Characteristics at Mach Numbers to 2.0 of Various Types of Side Inlets Mounted on Fuselage of Proposed Supersonic Airplane. III - Normal-Wedge Inlets With Semicircular Cowl. NACA RM E52H20, 1952.

9. Stitt, Leonard E., McKevitt, Francis X., and Smith, Albert B.: Effect of Throat Bleed on Supersonic Performance of a Half-Conical Side Inlet System. NACA RM E55J07, 1955. (Prospective NACA paper.)

10. Piercy, Thomas G., and Johnson, Harry W.: Investigation at Mach Number 2.93 of Half of a Conical-Spike Diffuser Mounted as a Side Inlet with Boundary-Layer Control. NACA RM E52G23, 1952.

11. Piercy, Thomas G., and Klann, John L.: Experimental Investigation of of Methods of Improving Diffuser-Exit Total-Pressure Profiles for a Side-Inlet Model at Mach Number 3.05. NACA RM E55F24, 1955. .

12. Nettles, J. C.: The Effect of Initial Rate of Subsonic Diffusion on the Stable Subcritical Mass-Flow Range of a Conical Shock Diffuser. NACA RM E53E26, 1953.

13. Beke, Andrew, and Allen, J. L.: Force and Pressure-Recovery Characteristics of a Conical-Type Nose Inlet Operating at Mach Numbers of 1.6 to 2.0 and at Angles of Attack to 9°. NACA RM E52I30, 1952.

14. Johnston, I. H.: The Use of Freely Rotating Blade Rows To Improve Velocity Distributions in an Annulus. Memo. No. M. 109, National Gas Turbine Establishment, British Ministry of Supply, Feb. 1951.

15. Collar, H. R.: Effect of Gauze on the Velocity Distribution in a Uniform Duct. R. & M. No. 1807, British A.R.C., 1939.

16. Farley, John M., and Seashore, Ferris L.: Full-Scale, Free-Jet Investigation of Methods of Improving Outlet Flow Distribution in a Side-Inlet Supersonic Diffuser. NACA RM E54L31a, 1955.

17. Piercy, Thomas G., and Weinstein, Maynard I.: Preliminary Investigation at Mach Number 1.9 of Simulated Wing-Root Inlets. NACA RM E54I24, 1955.

18. Kremzier, Emil J., and Wise, George A.: Effect of Centerbody Boundary-Layer Removal Near the Throat of Three Conical Nose Inlets at Mach 1.6 to 2.0. NACA RM E55H16a, 1955.

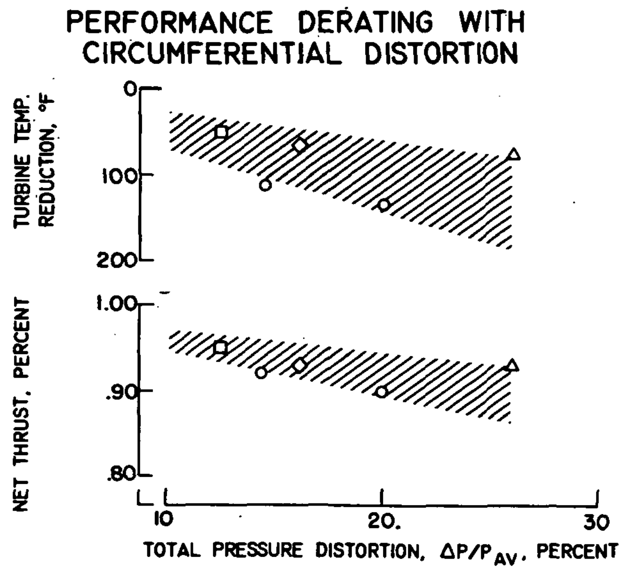

Figure 1

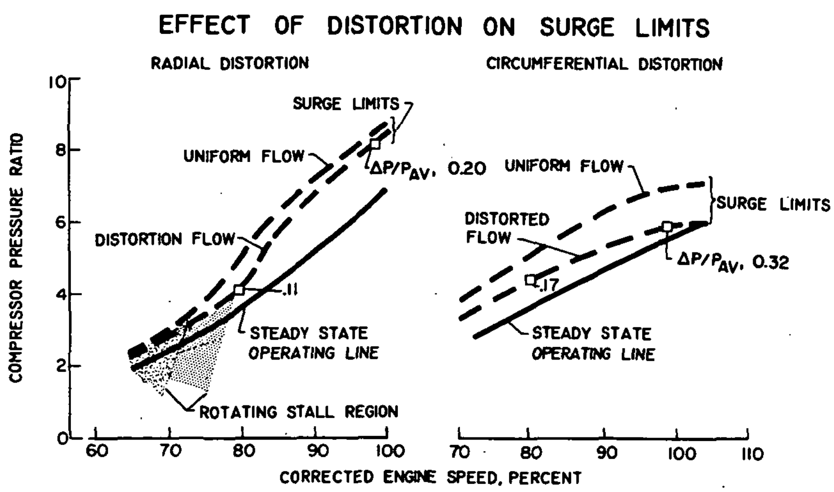

Figure 2

EFFECT OF DISTORTION ON SURGE AT ALTITUDE

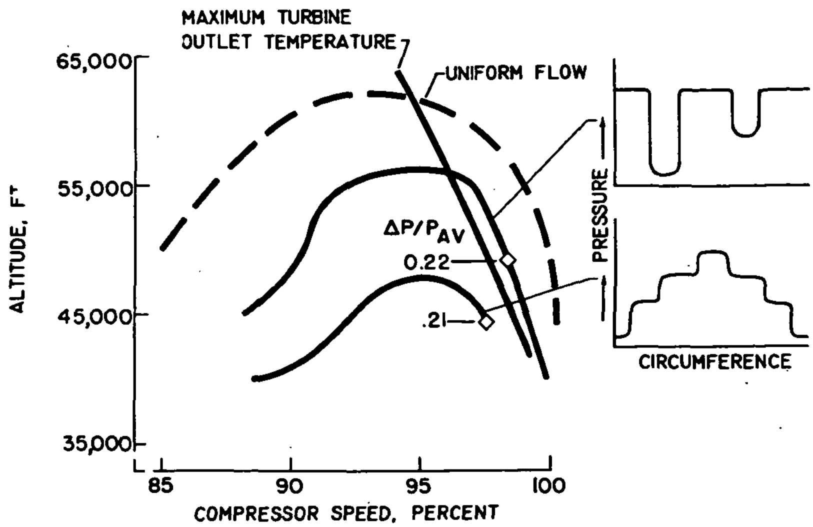

Figure 3

EFFECT OF MIXING LENGTH ON DISTORTION

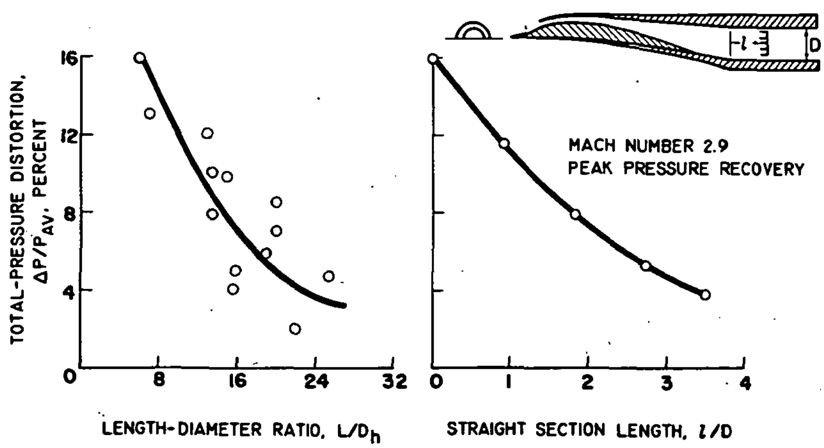

Figure 4

EFFECT OF AVERAGE FLOW MACH NUMBER ON MIXING

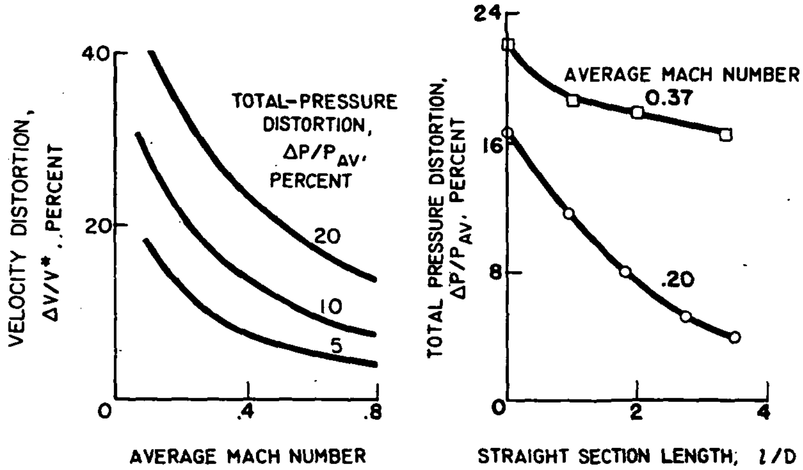

Figure 5

EFFECT OF COWL AREA DISTRIBUTION ON DISTORTION
CRITICAL INLET OPERATION

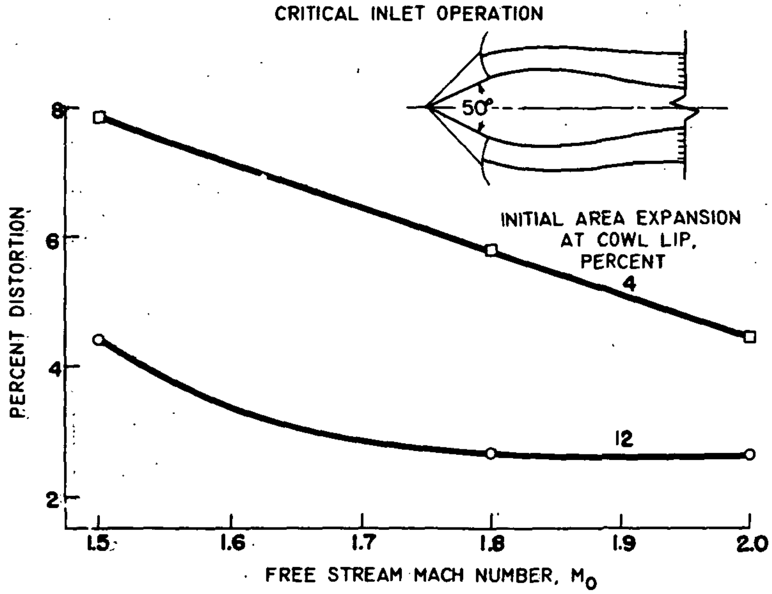

Figure 6

EFFECT OF FLOW ACCELERATION ON DISTORTION

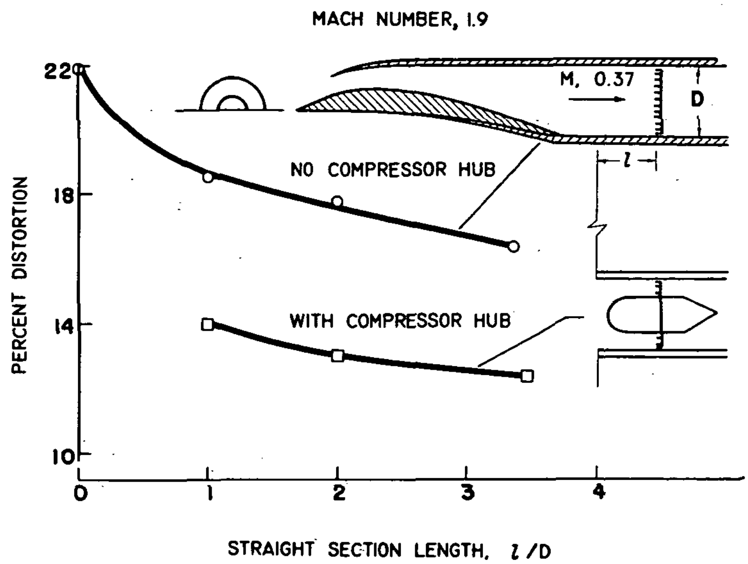

Figure 7

EFFECT OF FREELY ROTATING BLADE ROWS ON DISTORTION

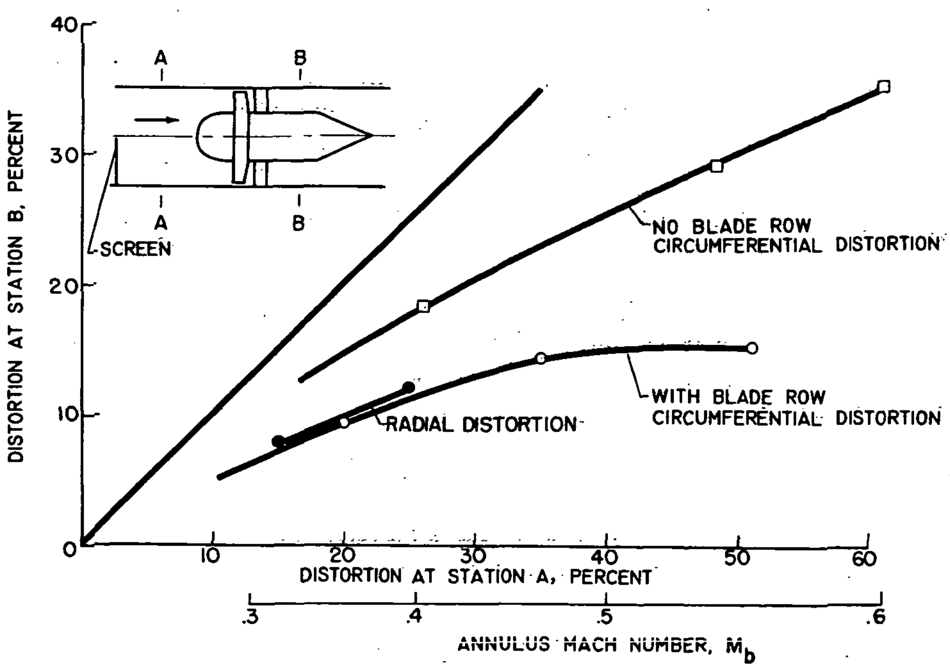

Figure 8

EFFECT OF SCREENS ON DISTORTION

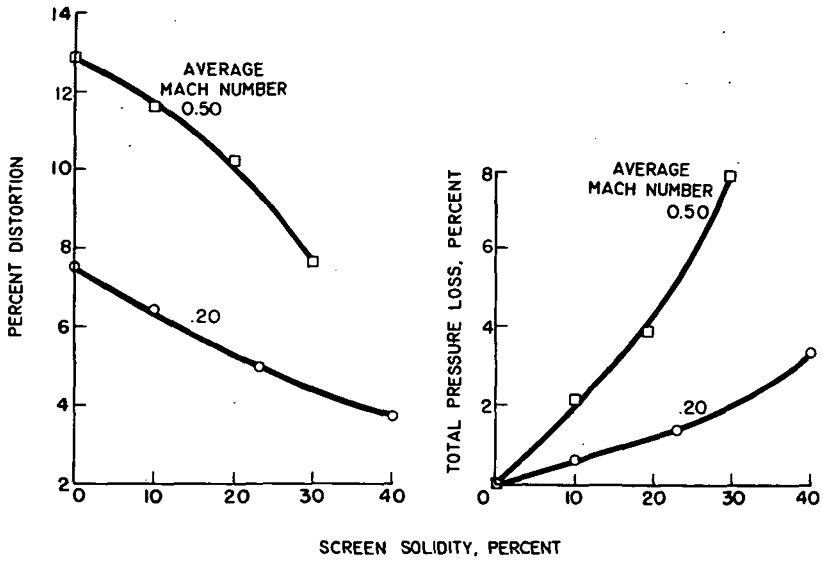

Figure 9

EFFECT OF VORTEX SHEET ON DISTORTION

MACH NUMBER, 1.8

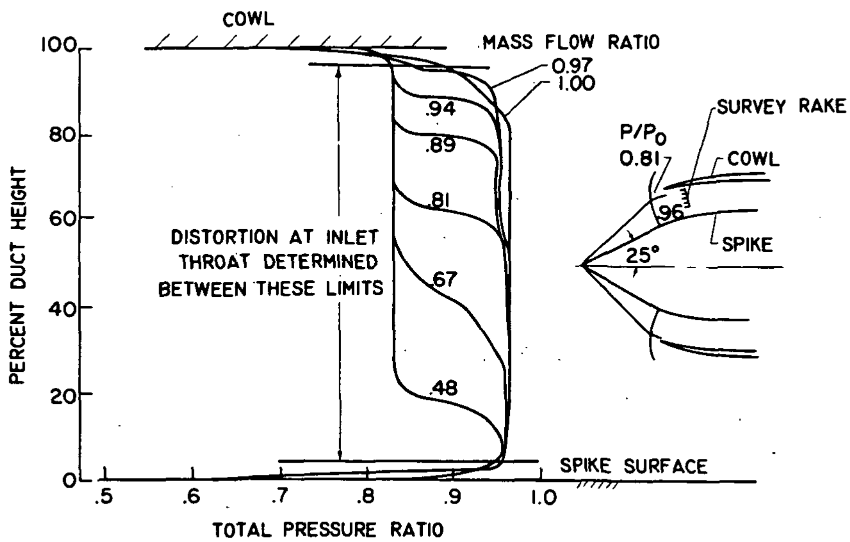

Figure 10

[redacted]

EFFECT OF VORTEX SHEET ON DISTORTION

MACH NUMBER, 1.8

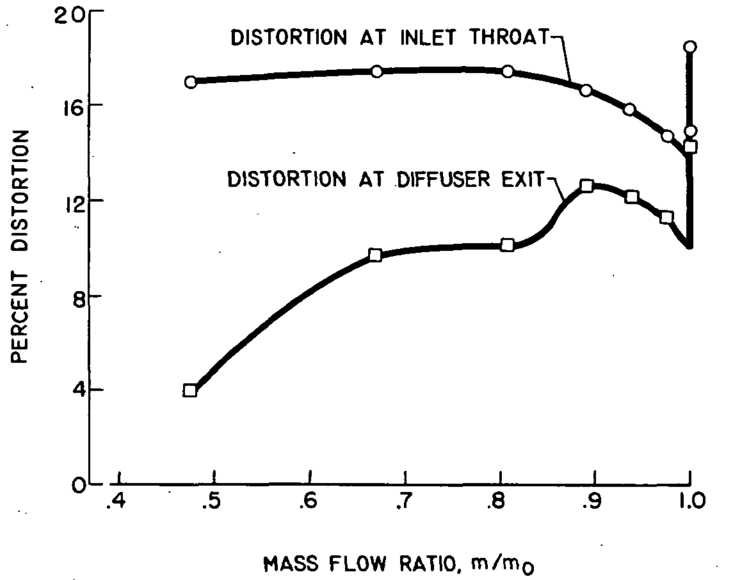

Figure 11

EFFECT OF ANGLE OF ATTACK ON DISTORTION

MACH NUMBER, 2.0

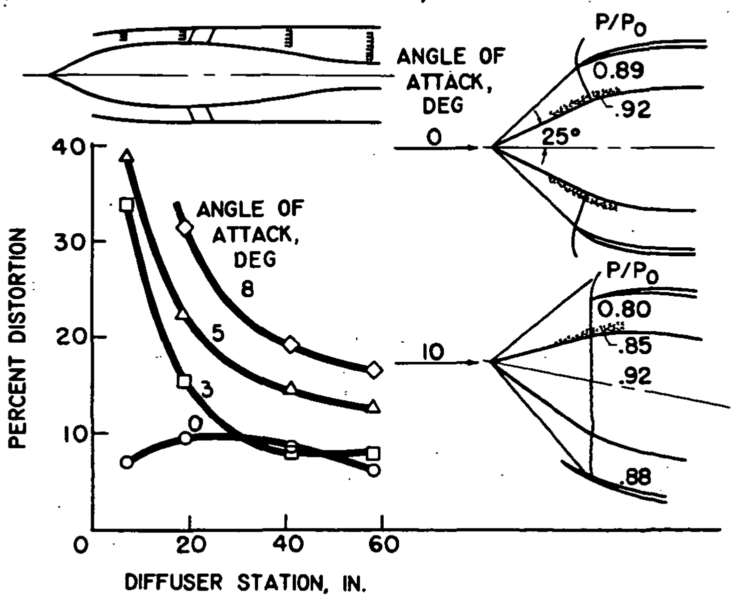

Figure 12

[redacted]

~~CONFIDENTIAL~~

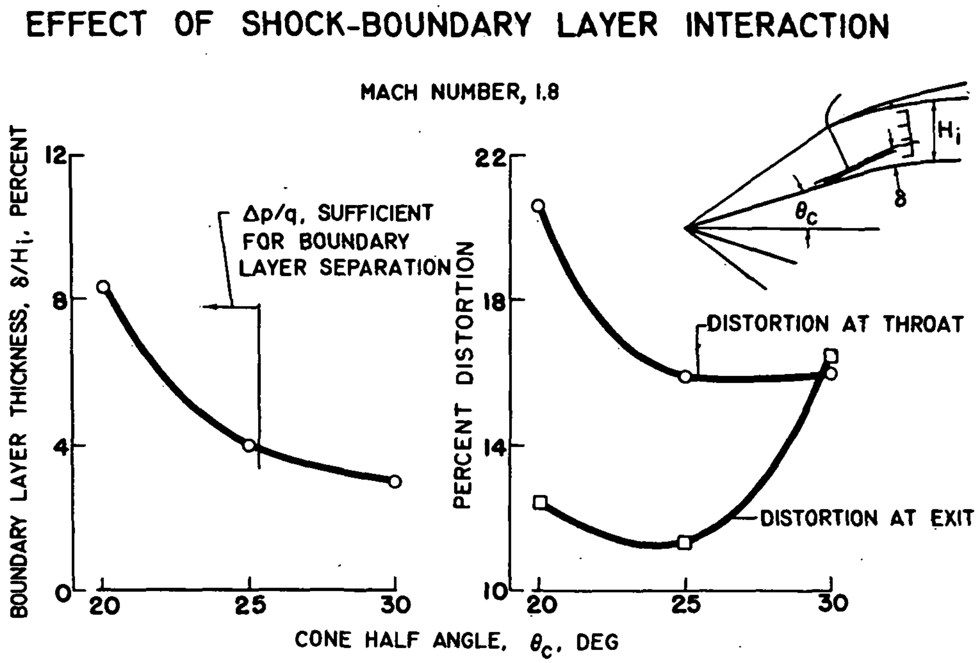

Figure 13

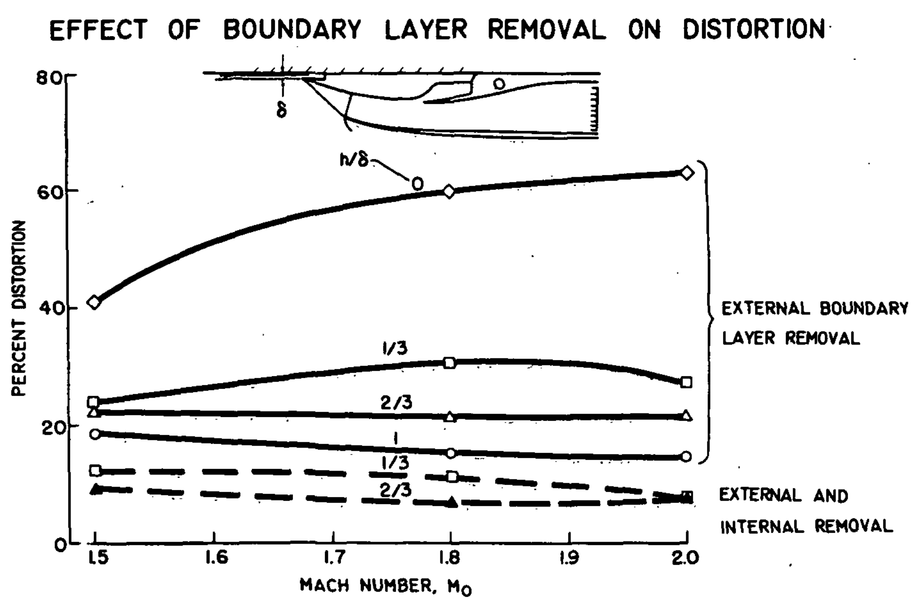

Figure 14

~~CONFIDENTIAL~~

13

SOME ASPECTS OF SUPERSONIC INLET STABILITY

By James F. Connors

Lewis Flight Propulsion Laboratory

SUMMARY

Supersonic inlet stabilization can be generally achieved for Mach numbers up to approximately 2.0 by careful consideration of the possible buzz-triggering conditions. Boundary-layer control and constant-area sections can be effectively utilized on inlets designed to provide stable flow regulation over the entire engine operating range. For Mach numbers above 2.0, the attainment of stability becomes increasingly more difficult as local Mach numbers (and thus normal-shock strengths) increase to aggravate further the shock-boundary-layer interaction problems.

A different approach to the problem of stable flow regulation can be made by assuming that inlets will be generally stable only for limited ranges before becoming inherently unstable. In these cases, variable-geometry techniques seem to provide an adequate solution.

It has also been demonstrated that the engine itself can, in some instances, exert a stabilizing influence on the inlet. Further definition of this effect is needed with full-scale inlets and more advanced engines.

INTRODUCTION

At supersonic speeds, the inlet-buzz condition is characterized by large pressure and mass-flow oscillations which must be avoided or attenuated for satisfactory engine operation. Otherwise, the attendant flow pulsations could result in flameout in the combustor or even structural damage to the engine. In most instances, the origin of inlet buzz can be traced back to either of two triggering mechanisms: (1) the vortex sheet or slipline intercepting the cowl lip or (2) compression-surface flow separation. Both of these are quite similar in principle and have been recognized for some time. In each case, the initiation of buzz is distinguished by a sudden change or discontinuity in the total-pressure profile at the diffuser entrance with a subsequent tendency towards separation of the internal flow.

SYMBOLS

M_o	free-stream Mach number
M	Mach number
δ	boundary-layer thickness
h	height of boundary-layer diverter
m_{crit}	critical mass flow entering inlet
m_i	injection mass flow
m_o	maximum mass flow that can enter inlet
θ_l	cowl-position parameter
θ_s	conical shock angle
α	angle of attack

DISCUSSION

Inlet Flow-Stabilization Techniques

In the past, sporadic success in attenuating buzz has been achieved through the use of constant-effective-area or zero-diffusion throat sections. (See ref. 1.) This scheme allows the entrance flow with its discontinuous profile to mix before undergoing subsonic diffusion. With nose inlets, buzz can also be generally avoided for Mach numbers up to 2.0 first by observing the slipline criterion of reference 2 (usually by positioning the oblique shock slightly inside or well ahead of the cowl) and secondly by using compression-surface angles which are large enough to keep the local Mach number below the normal-shock value of approximately 1.3 which is required for separation of a turbulent boundary layer (ref. 3). Near Mach 2.0, however, the design of high-compression multiple-shock inlets dictates the use of initially smaller compression-surface angles and correspondingly higher surface Mach numbers. In these cases, boundary-layer-control techniques, such as illustrated in figure 1, can be utilized.

The data in figure 1 were obtained at a free-stream Mach number of 1.9 with the double-cone axisymmetric nose inlet of reference 4. This configuration employed two conical compression surfaces with half-angles of 20° and 28° and with corresponding supercritical surface Mach numbers of 1.49 and 1.2, respectively. Supercritically, the oblique shocks were located just inside the cowl. As the normal shock moved subcritically upstream of the cowl, the slipline (indicated by the dashed line) did not move across the cowl lip, and there were no adverse effects due to interaction of the bow shock with the second-cone boundary layer. With no boundary-layer control, stable subcritical operation was obtained down to a mass-flow ratio of approximately 0.7. At this minimum stable condition, the normal shock was located at the break between the two conical surfaces. Simultaneously, with the onset of buzz and as the bow shock moved out on the first cone, the boundary layer was observed to lift off the surface and separate. This separation was, of course, due to the increased surface Mach number on the first cone.

In this case, where to apply boundary-layer control was clearly defined. The center body was vented to ambient pressure and two double rows of holes were installed on the first cone. With boundary-layer suction thus applied, stable subcritical operation was obtained down to a mass-flow ratio of approximately 0.1. At the minimum stable condition, the bow shock stood upstream of the bleed holes. With suction, however, the critical pressure recovery was reduced from 0.92 to about 0.9; apparently, the bleed holes created some additional supersonic losses. In both cases, the supercritical mass-flow ratio was unity. The maximum bleed flow was estimated at approximately 1.5 percent of critical mass flow.

The effect of angle of attack on both pressure recovery and mass flow is illustrated by the data in figure 2. Angle of attack generally caused reduction in both pressure recovery and stable mass-flow range. The stable operating range of the inlet is indicated by the cross-hatched areas for the no-suction and suction cases. As the inlet goes to angle of attack, the compression-surface Mach numbers decrease on the windward side and increase on the lee side. At the higher angles, the second-cone Mach number was thus sufficiently increased on the lee side so that the interaction between the bow shock and the boundary layer was no longer satisfactory and the accompanying separation was enough to trigger buzz prematurely. In this particular case, stability might have been improved still further at the higher angles of attack if additional suction had been applied on the lee side of the second cone. Thus, in this Mach number range, it is evident that boundary-layer suction can be effectively utilized in the attainment of stable flow regulation.

For free-stream Mach numbers considerably above 2.0, the local-surface Mach numbers correspondingly increase, and it is no longer clearly defined as to where to apply the control most effectively from a stability viewpoint. At these high Mach numbers, the point of incipient separation will, of course, vary with diffuser-normal-shock position since the up-stream surface Mach numbers are now everywhere greater than a critical normal-shock separation value (which is again approximately 1.3). Very little data are available on inlet stability near Mach 3.0. In one case, at least, some degree of success has been achieved with mass-flow injection (or boundary-layer energizing) on a half 2-cone side inlet at a free-stream Mach number of 2.96. (See ref. 5.)

The results of this study are summarized in figure 3. The inlet utilized two semi-cones with angles of 20° and 34° with corresponding supercritical surface Mach numbers of 2.25 and 1.71, respectively. A gap was provided between the first and second cones for injection of high pressure air parallel to the second compression surface. In a flight application this injection air could be supplied, for example, by compressor bleed. At the top of the figure are shown sketches of typical minimum-stable-mass-flow patterns with and without injection. Performance results are summarized in the table below. With the inlet out of the boundary layer ($h/\delta > 1.0$) there was no stable subcritical range without flow injection. However, with an injection mass-flow ratio of 0.02, the subcritical stability range was equal to 24 percent of critical mass flow. A total-pressure-recovery decrement of 0.04 was encountered just due to the change in geometry (that is, the provision of the injection gap). Actually, the critical pressure recovery falls off quite markedly as the inlet is submerged in the boundary layer. For an $h/\delta \approx 0.26$, an injection mass-flow ratio of 0.04 increased the subcritical stability range from approximately 7 to 49 percent of critical mass flow.

Variable-Geometry Techniques for Stable Flow Regulation

The techniques discussed so far have been directed towards the development of inlets that would provide stable flow regulation over the entire operating range. Actually, in a typical supersonic flight application, the turbojet engine can have two distinct operating areas which require stable regulation. The first is for a limited range at high mass-flow ratios and occurs during transient operation, for example, during wind gusts or an overshoot of the controls system. Here, thrust must be maintained. Consequently, stable flow regulation must be accomplished without excessive loss in recovery or increase in drag. The second operating area occurs during throttle closure to engine-idle air-flow setting. For this condition, stability can be attained with little regard for loss in recovery or increase in drag, since the aircraft is to undergo rapid deceleration.

With two such modes of operation, another approach can be made to the problem of attaining stable flow regulation. This method assumes that inlets will generally be stable only for a limited mass-flow range before becoming inherently unstable. In this case, variable-geometry techniques as illustrated in figure 4 can provide an adequate solution.

Variable geometry, for example, in the form of a translating spike or a bypass arrangement, can be effectively used at the higher mass-flow ratios. Here, the normal shock is maintained at the throat, while the reduced air-flow requirements of the engine are met by supersonic spillage behind an oblique shock or by spillage through the bypass. Thus, buzz-triggering conditions at the cowl lip may be avoided altogether.

At the lower mass-flow ratios, or for flight conditions corresponding to throttle closure where pressure recovery is not too important, spoiler techniques may find some application. These techniques largely involve the use of variable-geometry devices to force a bow shock to stand well upstream of the cowl with attendant large mass-flow spillage rates. The actual form of such spoilers can be quite varied. In the axisymmetric case, variable flaps or projections moving out of the compression surfaces might conceivably be employed to detach the flow and force a bow wave ahead of the inlet. Two-dimensionally, such a technique has been effectively demonstrated by means of a variable-second-ramp side inlet for Mach numbers of 1.5 to 2.0. (See ref. 6.) The results for $h/\delta > 1.00$ are shown in figure 5. This particular inlet geometry permits an increase in the second-ramp angle to values in excess of the local shock-detachment values. Thus, for stable operation at low mass flows (for example, where engine-idle conditions correspond to mass-flow ratios of approximately 0.4) this scheme proved quite satisfactory. Data are shown for only two second-ramp positions - the 18° ramp representing the design operating position and the 30° ramp representing the detachment or low-mass-flow condition. At each Mach number, stable operation was obtained for mass-flow ratios in the vicinity of 0.4, the hypothetical engine-idle condition. At Mach 2.0, the data for the two second-ramp positions do not overlap with respect to stable mass-flow range; however, it might be anticipated that the intermediate ramp positions would provide a continuous transition of stable operation down to the engine-idle mass flow.

Another technique for attaining stability, but at the expense of recovery, consists of retracting the compression surface and positioning the oblique shock well inside the cowl lip. This method can be demonstrated with a translating-spike inlet configuration. As illustrated in figure 6, a cowl-position parameter θ_l will be used to define the range of spike translation. This parameter is the angle between the inlet axis and a line from the spike tip to the cowl lip. The design position is that point where θ_l equals the conical shock angle. As shown in figure 7 for a single-cone axisymmetric nose inlet at a Mach number of 2.0 (ref. 7), large stable mass-flow ranges were obtained with values of cowl-position parameter 2° to 3° greater than the design shock-on-lip value. In this case, the position of the oblique shock well inside the cowl prevents the slipline from intercepting the cowl lip. As the tip shock is moved inside (that is, increasing θ_l from the design value), the stable operating range increases quite markedly and, correspondingly, critical pressure recovery decreases. For 4° greater than the design value, stable operation can be obtained down to the hypothetical engine-idle condition (mass-flow ratio ≈ 0.4). As the tip shock is moved outside (that is, decreasing θ_l from the design value), no significant increase in the stable range occurs; however, the maximum or supercritical mass flow decreases along with recovery. In considering the two directions of translation, it should be pointed out that, for smaller movements of the spike, retraction of the compression surface permits stable regulation down to the engine-idle condition. Results for an angle of attack of 9° are also included in figure 7. These results are somewhat similar to those for the case of an angle of attack of 0°; however, stability ranges, in general, have been decreased and larger θ_l must be used to attain the large stable subcritical ranges.

Effect of Turbojet Engine on Inlet Stability

All the foregoing discussion has been concerned with results from cold-flow tests wherein a variable-area sonic exit was used to simulate the exit conditions anticipated in an actual engine application. Little information is currently available on the combined effects of an inlet operating in conjunction with a turbojet engine. Accordingly, at Mach numbers 1.8 and 2.0, a study was conducted on an annular nose inlet with a translating spike and a variable-bypass arrangement. (See refs. 8 and 9.) Performance was evaluated both with a cold-flow exit plug and with a J-34 turbojet engine. Results pertinent to the inlet stability ranges are shown in figure 8. Compared with the cold-flow plug, the engine had a definite stabilizing influence on subcritical operation of the inlet. The buzz regions are identified by the cross-hatched areas for the cold-flow plug and by the dotted portions of the figure for the engine. In all cases studied, the unstable regions were greater with the plug than with the engine. The actual damping mechanism, however, is not understood. Opening the bypass destabilized the inlet generally, but more so with the plug than with the engine. As buzz was initiated, the total-pressure amplitude at the compressor face was about the same in either case; however, the frequency of buzz with the engine was about twice that with the plug.

These data are, of course, for a conservative engine which was choked at the exhaust nozzle and which was not designed for supersonic application. As such, these results should not be construed as being general. More advanced engines employing higher compressor blade loadings, with choking occurring at a much earlier station in the engine, may well yield considerably different results.

CONCLUDING REMARKS

Supersonic inlet stabilization can be generally achieved for Mach numbers up to approximately 2.0 by careful consideration of the possible buzz-triggering conditions. Boundary-layer control and constant-area sections can be effectively utilized on inlets designed to provide stable flow regulation over the entire engine operating range. For Mach numbers above 2.0, the attainment of stability becomes increasingly more difficult as local Mach numbers (and thus normal-shock strengths) increase to aggravate further the shock-boundary-layer interaction problems.

A different approach to the problem of stable flow regulation can be made by assuming that inlets will be generally stable only for limited ranges before becoming inherently unstable. In these cases, variable-geometry techniques seem to provide an adequate solution.

It has also been demonstrated that the engine itself can, in some instances, exert a stabilizing influence on the inlet. Further definition of this effect is needed with full-scale inlets and more advanced engines.

REFERENCES

1. Nettles, J. C.: The Effect of Initial Rate of Subsonic Diffusion on the Stable Subcritical Mass-Flow Range of a Conical Shock Diffuser. NACA RM E53E26, 1953.

2. Ferri, Antonio, and Nucci, Louis M.: The Origin of Aerodynamic Instability of Supersonic Inlets at Subcritical Conditions. NACA RM L50K30, 1951.

3. Nussdorfer, T. J.: Some Observations of Shock-Induced Turbulent Separation on Supersonic Diffusers. NACA RM E51L26, 1954.

4. Connors, James F., and Meyer, Rudolph C.: Performance Characteristics of Axisymmetric Two-Cone and Isentropic Nose Inlets at Mach Number 1.90. NACA RM E55F29, 1955.

5. Piercy, Thomas G.: Preliminary Investigation of Some Internal Boundary-Layer-Control Systems on a Side Inlet at Mach Number 2.96. NACA RM E54K01, 1955.

6. Obery, L. J., Cubbison, R. W., and Mercer, T. G.: Stabilization Techniques for Ramp-Type Side Inlets at Supersonic Speeds. NACA RM E55A26, 1955.

7. Gorton, Gerald C.: Investigation at Supersonic Speeds of a Translating-Spike Inlet Employing a Steep-Lip Cowl. NACA RM E54G29, 1954.

8. Nettles, J. C., and Leissler, L. A.: Investigation of Adjustable Supersonic Inlet in Combination With J34 Engine up to Mach 2.0. NACA RM E54H11, 1954.

9. Beheim, Milton A. and Englert, Gerald W.: Effects of a J34 Turbojet Engine on Supersonic Diffuser Performance. NACA RM E55I21, 1955. (Prospective NACA paper.)

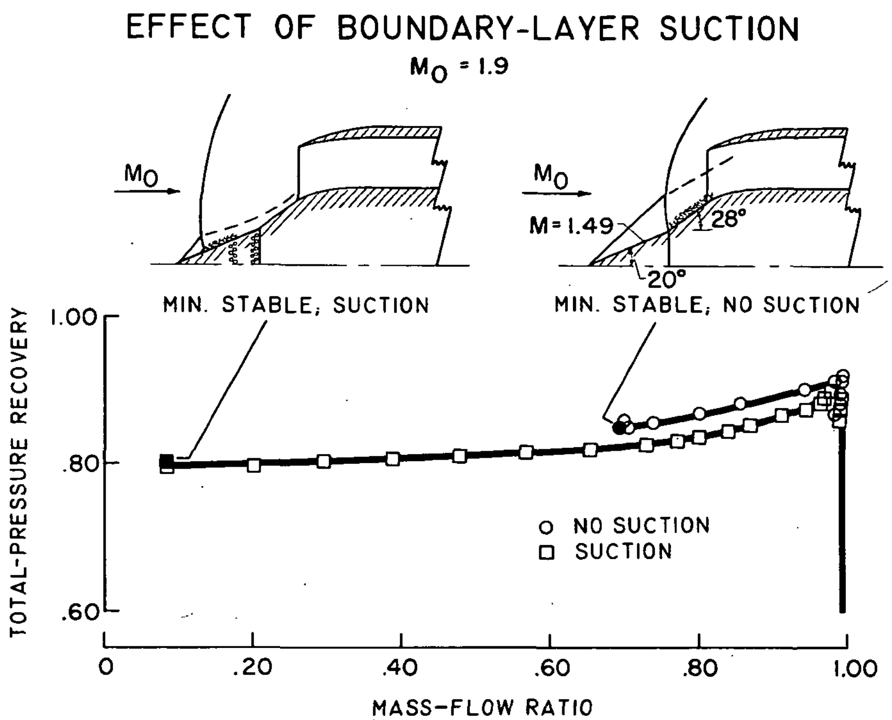

Figure 1

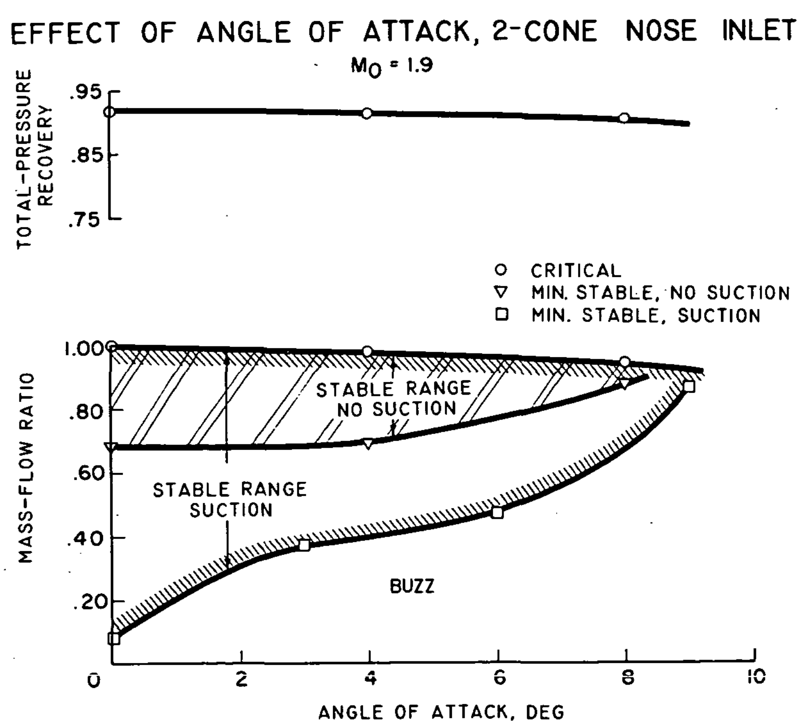

Figure 2

~~CONFIDENTIAL~~

EFFECT OF MASS-FLOW INJECTION

$M_0 = 2.96$

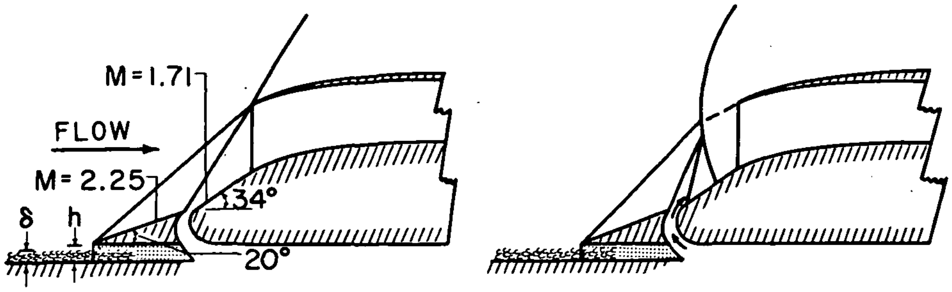

NO INJECTION | MASS-FLOW INJECTION

h/δ	STABLE RANGE, NO INJECTION	STABLE RANGE, INJECTION	INJECTION MASS-FLOW RATIO, m_i/m_0	TOTAL-PRESSURE-RECOVERY DECREMENT
1.05	0(m_{crit})	.24(m_{crit})	.02	.04
.79	.03	.175	.03	.01
0.26	0.07	0.49	0.04	0.002

Figure 3

VARIABLE-GEOMETRY TECHNIQUES FOR STABLE FLOW REGULATION

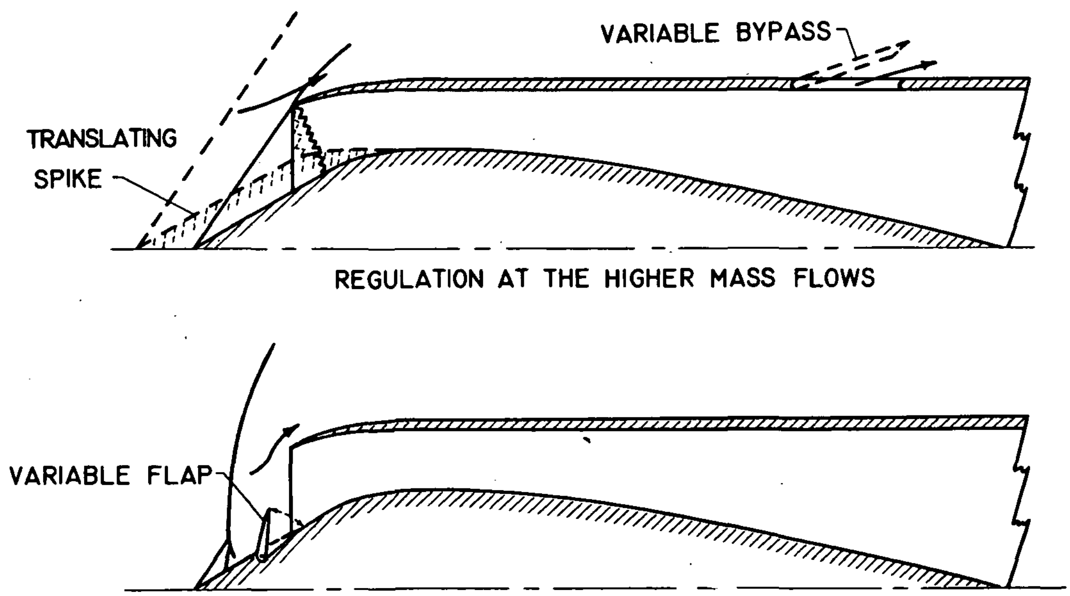

REGULATION FOR THROTTLE CLOSURE

Figure 4

~~CONFIDENTIAL~~

FLOW STABILIZATION AT LOW MASS-FLOW RATIOS

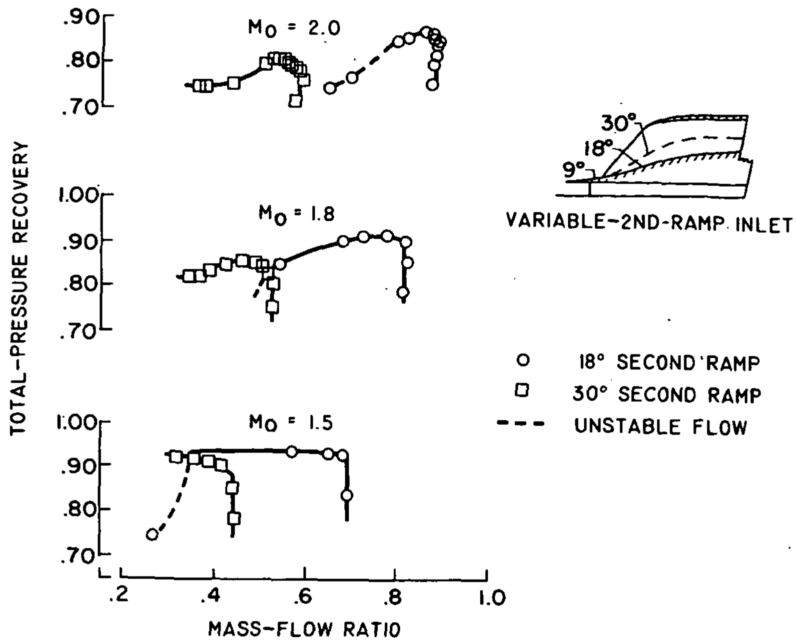

Figure 5

TRANSLATING SPIKE

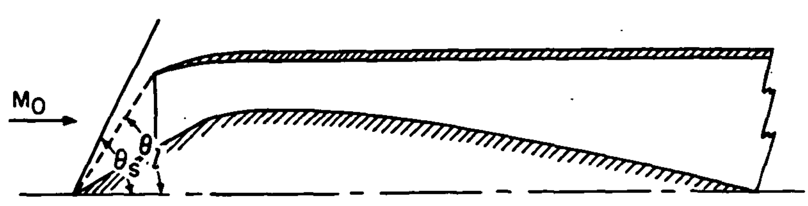

θ_l = COWL - POSITION PARAMETER

(DESIGN) $\theta_l = \theta_s$

Figure 6

~~CONFIDENTIAL~~

EFFECT OF SPIKE TRANSLATION

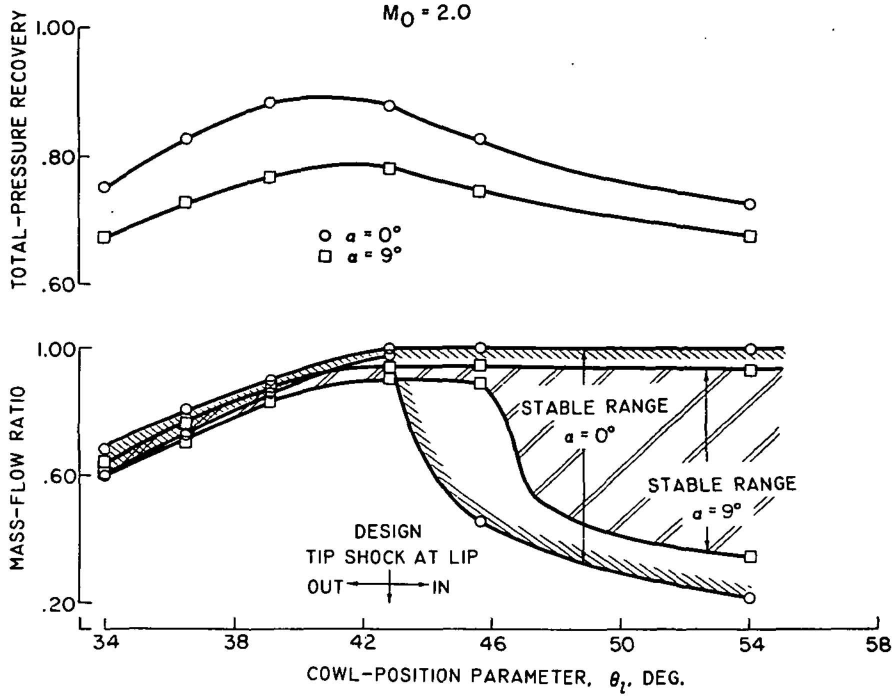

Figure 7

EFFECT OF THE J-34 ENGINE

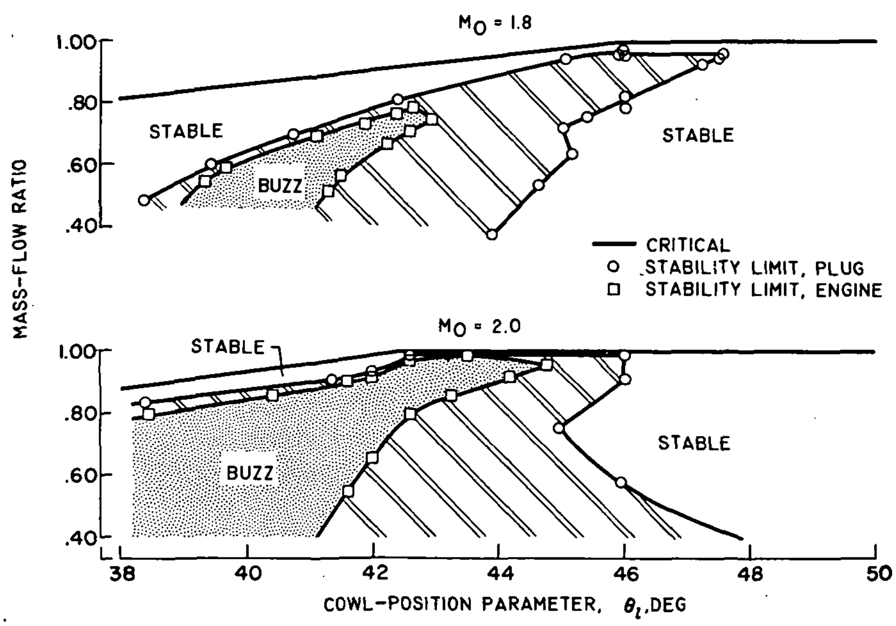

Figure 8

~~CONFIDENTIAL~~

BYPASS-DUCT DESIGN FOR USE WITH SUPERSONIC INLETS

By Charles C. Wood and John R. Henry

Langley Aeronautical Laboratory

SUMMARY

A successful method for designing bypass ducting for use with supersonic inlets has been developed experimentally. The design is shown to be satisfactory in all aspects of performance. Further refinement will be possible in detailed development for specific applications.

14

INTRODUCTION

Figure 1 is a sketch illustrating the use of an engine bypass ducting system in conjunction with a supersonic inlet. The inlet is followed by a subsonic diffuser. Near the exit of the subsonic diffuser, the flow is divided into two parallel streams – the bypassed air and the air consumed by the engine. The problems associated with matching inlet performance with engine requirements and the use of the bypass duct as a solution to these problems are referred to in references 1 and 2. In brief, with a bypass-ducting system, the inlet would be sized to pass a flow which always would be equal to or greater than that demanded by the engine. For conditions where the engine demands less flow, the excess air would be bypassed around the engine and discharged from the airplane at the most convenient location.

This paper is concerned with the detail design of the subsonic ducting in the region where the bypass air is removed from the total flow passed by the inlet. In particular, the effects of bypassing the air on the engine-face velocity distributions and on the total-pressure losses are to be evaluated in order that the designer may have more specific information on which to base his designs and analyses.

SYMBOLS

H_B mean total pressure at bypass

H_E mean total pressure at engine-face station

H_{MAX}	maximum total pressure
H_{MIN}	minimum total pressure
H_R	mean total pressure at reference station
M	Mach number
M_E	Mach number at engine-face station
U	maximum velocity

IDEAL BYPASS-DUCT DESIGN

The ideal bypass-duct design would consist of an arrangement which removes the bypass flow uniformly from the entire periphery of the duct. Such a ducting design would bleed off uniformly all the boundary layer or low energy air, which is generally the source of flow distribution distortions. However, wrapping annular ducting around the entire periphery of the main duct introduces so many design complications that in most cases it would be impractical. For this reason, the experimental investigations to be described were confined to designs where all the bypass air was removed from one wall or a limited sector of the duct. The subsonic diffuser was supplied with air flow by an inlet bell, and the various effects of the supersonic inlet operation were simulated by varying the supply pressure.

RESULTS

Model I

The first configurations investigated are shown in figure 2. In model Ia, a conventional 6° diffuser designed for the maximum engine air-flow condition was altered by cutting a hole in one side and adding a scoop to obtain high recovery in the bypass flow. Four scoop projections were tested ranging from the full scoop of model Ia to the flush scoop of model Ib. Only results for models Ia and Ib will be presented since the performance is bracketed by these two configurations. The inlet area of the extended scoop was designed to intercept about a third of the air flow at a scoop inlet velocity ratio of 1.0. For ease of fabrication and test measurement, rectangular ducting was used; however, the general principles indicated by the test data should be applicable to any cross-sectional shape.

Figure 3 summarizes the performance of models Ia and Ib for the case where the diffuser was operating at a point just below the choke condition. The diagrams are velocity distributions in which velocity is plotted horizontally against distance across the duct vertically. The center of the maximum velocity region is indicated by the arrow. The shaded areas, then, represent retarded velocity regions. The bottom line corresponds to the wall on the bypass side, and the top line to the wall opposite to the bypass. Stations R and E are the reference and engine-face stations, respectively. The two distributions on the left side of figure 3, which were measured with no scoop in place and with the opening sealed and faired, are normal for this type of diffuser. The performance for model Ia with the scoop in place is given at the top of figure 3, where the percent of bypass flow is given on the top line, the total-pressure-recovery ratio for the engine-face station on the second line, and the bypass duct recovery on the third line. Total-pressure recovery is given in terms of the mean total pressure at station R.

The large region of retarded velocity and the accompanying low pressure recovery obtained with no bypass flow resulted from the high angle of attack on the scoop for this condition and the high expansion angle on the downstream face of the scoop. With the design bypass flow of 32 percent, the angle of attack was eliminated and the boundary layer bypassed; thus, the bad flow on the bypass side was eliminated. However, a large retarded velocity region was obtained on the side opposite the scoop because of the alteration to the diffuser pressure gradients caused by bypassing about a third of the air. Bypassing this amount of air is equivalent to a sudden area increase in the diffuser of about 50 percent, which produces a rapid rate of boundary-layer growth. The engine-face total-pressure recovery with 32 percent bypass was fairly high, 98.6 percent, because of the reduced air flow (and thus dynamic pressure) in the engine duct and because the velocity distribution was somewhat better than with no bypass flow.

Eliminating the scoop extension by using a flush scoop, model Ib, considerably improved the velocity distribution and engine recovery with no bypass flow. With the design bypass flow of 32 percent, the distribution was again distorted as in model Ia because of the increased diffuser pressure gradient. Eliminating the scoop extension reduced the bypass recovery from 98 to 96.8 percent.

The performance of these two configurations and the other scoop designs not discussed here was not considered to be satisfactory from either the flow distribution or loss standpoint. The data showed that the design approach of cutting a hole in the wall of a diffuser and adding a scoop is oversimplified and that the basic diffuser lines ought to be laid out with specific consideration for the bypass operation.

Model II

Model II, shown sketched in figure 4, was designed using the information derived from the tests of model I; model Ib is also shown in this figure for comparison. In model II, the adverse effects of the extended scoop were eliminated by moving the bypass inlet back to the diffuser exit and by increasing the diffuser exit area by an amount sufficient to include the bypass inlet area. Thus, the bypass design became a splitter-type configuration, which, of course, retains the ability to recover ram pressure in the bypass duct. For the same diffuser angle, the model II type of design would be longer than model I. For model II, two diffuser area ratios were tested which, with no bypass flow, produced at the engine-face station Mach numbers of about 0.4 and 0.7. These two conditions were desired in order to bracket the current turbojet-compressor-inlet Mach number values of 0.5 to 0.6.

Figure 5 presents the performance of model II for the ducting for a Mach number of 0.4, and the corresponding performance of model Ib is included for comparison. With or without bypass flow, substantially more uniform velocity distributions were obtained at the engine face with model II than with model Ib. The improvement without bypass flow is directly due to the contraction which the flow experiences between the reference station and station E with no flow through the bypass. With the design bypass flow of 32 percent, the improved velocity distribution and engine total-pressure recovery of model II were due to the fact that the diffuser pressure gradients in the region of the bypass for model II correspond to those for a 6° diffuser; whereas, in model Ib, the bypass flow sets up gradients appreciably higher than those for the basic 6° diffuser.

The data for model II presented in figure 5 are for the condition where the diffuser was operating just below the choke point, and a Mach number of about 0.4 existed at station E with no bypass flow. As noted previously, data for the same condition were taken for a Mach number at station E of about 0.7. The performance at the higher Mach number level was nearly identical to the data for a Mach number of 0.4 and will not be presented here.

The velocity distribution for model II depreciated some on the opposite wall with increasing bypass flow. In laying out the duct design, this effect could be reduced by taking most of the area expansion on the diffuser wall containing the bypass, thus favoring the boundary layer development on the opposite wall. An alternative design would be to include an area contraction just upstream from the engine on the opposite wall.

[redacted]

Distorted Inlet Flow, Model II

In order to determine the effectiveness of the model II design for off-design inlet operating conditions, the diffuser was tested in the choked condition with a normal shock standing in the diffuser and in some cases with various types of spoilers mounted on the diffuser wall. Data for one of the most extreme conditions have been selected for presentation here. A diagram for the diffuser flow pattern is shown in figure 6. The normal shock occurred at a Mach number of 1.52. The diffuser area ratio for this case normally produced a Mach number of about 0.4 at station E with no bypass flow. For the flow conditions illustrated, however, the engine-face Mach number was about 0.6 due to the total-pressure losses incurred in the shock and in the subsequent separated flow region. As generally occurs in cases of this type, the flow always separated from the same wall – in this case, the bypass wall.

The amount of flow distortion produced by the shock—boundary-layer interaction is readily apparent from the reference station measurement. The installation of the bypass splitter and varying the amount of bypass flow did not alter the reference-station total-pressure distribution appreciably. The velocity distributions obtained at the engine face are not appreciably different from those obtained when the diffuser was operating just below the choke condition. The outstanding conclusion to be derived is that even with a flow distortion at the reference station of the magnitude indicated, the model II design produced fairly uniform distributions at the engine face. The total-pressure recovery in the engine duct was high because it received the high total-pressure portion of the entire flow. Conversely, the bypass recovery was low. Other tests with the higher Mach number ducting and with separated flow on the opposite wall produced essentially the same performance and, therefore, these results may be considered typical.

Total-Pressure Distortions

The total-pressure distortions obtained at the engine face are summarized for several models in figure 7. In obtaining the distortion factor, 5 percent of the cross-sectional area adjacent to each duct wall was ignored; in other words, this amount of area was assigned to the low energy part of the boundary layer. The distortion factor is defined as the difference between the maximum and minimum total pressure divided by the mean total pressure at the engine-face station. The abscissa is the percent of bypass flow. The plot on the left side of figure 7 is for the diffuser operating just below the choked condition. For this case, model Ia with the extended scoop produced distortions as high as 50 percent. The flush scoop of model Ib reduced the 50-percent value to about 11 percent with no bypass. At high bypass flows, both models Ia and Ib produced a distortion of about 9 percent. This relatively low value was

[redacted]

obtained in spite of bad velocity distributions because of the low engine-face Mach number level of the tests of about 0.2. At low Mach numbers, the dynamic pressure is very small relative to the total pressure and, therefore, large variations in velocity distribution do not affect the total-pressure distortion appreciably. For model II, the distortions for the bypass system for Mach numbers of 0.4 and 0.7 were on the order of 4 and 7 percent, respectively, the difference between the two values being due almost entirely to the change in Mach number rather than a change in velocity distribution. The model II results are considered to be within the range of values acceptable for engine operation.

The right-hand plot of figure 7 summarizes the data for the tests where the diffuser flow was distorted by shock—boundary-layer interaction. The lower Mach number ducting for model II, which produced a Mach number of about 0.6 at the engine with no bypass, had distortions on the order of 9 percent, which is probably on the borderline of being acceptable. Model Ib had prohibitive distortions. It is evident that model II resisted the effects of distorted flow upstream from the bypass much more successfully than model I.

CONCLUDING REMARKS

A successful method for designing bypass ducting for use with supersonic inlets has been developed in this preliminary investigation. The design has been shown to be satisfactory in all aspects of performance. Further refinement should be possible in detailed development for specific applications.

REFERENCES

1. Connors, James F.: Some Aspects of Supersonic Inlet Stability. (Prospective NACA paper.)

2. Wilcox, Fred A., and Perchonok, Eugene: Aerodynamic Control of Supersonic Inlets for Optimum Performance. (Prospective NACA paper.)

SUPERSONIC INLET WITH BYPASS

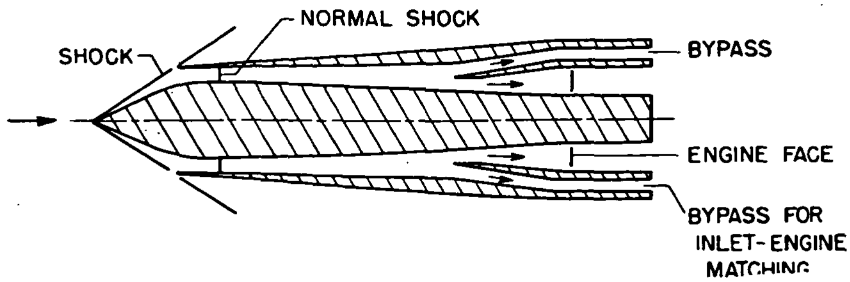

Figure 1

MODEL I DESIGN

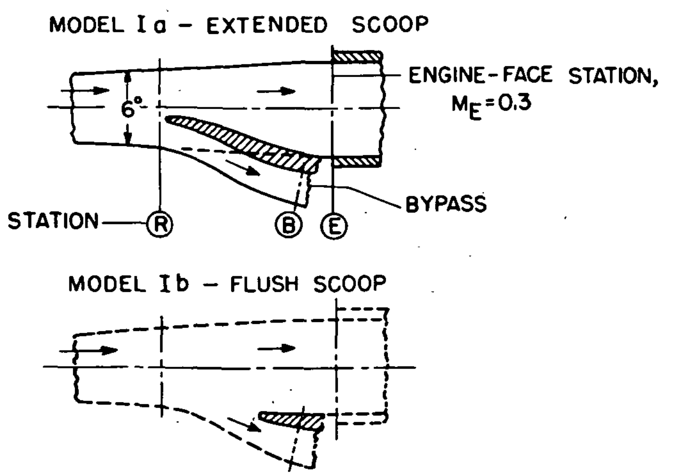

Figure 2

MODEL I VELOCITY PROFILES

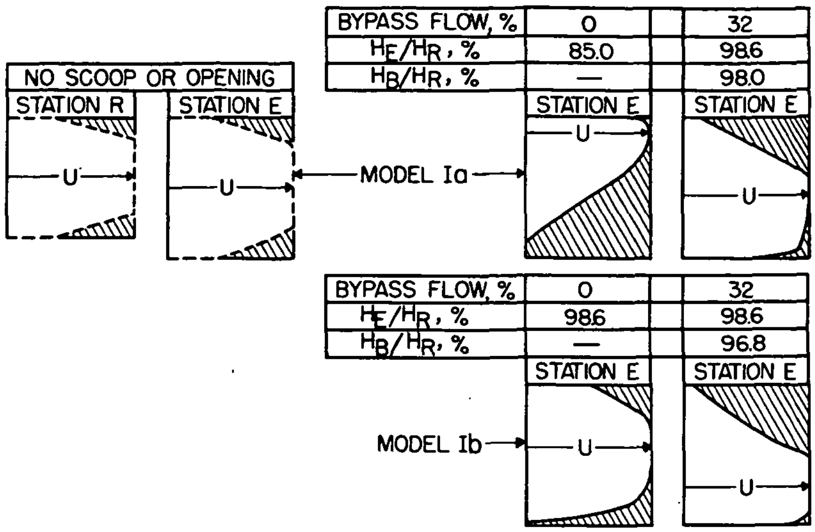

Figure 3

MODEL II DESIGN

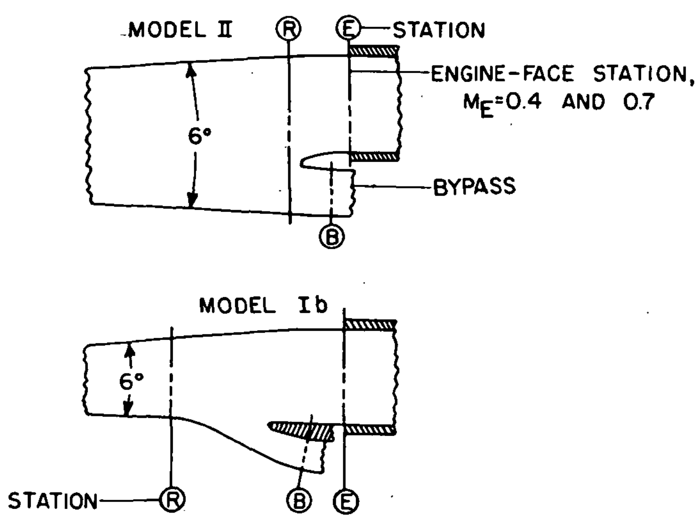

Figure 4

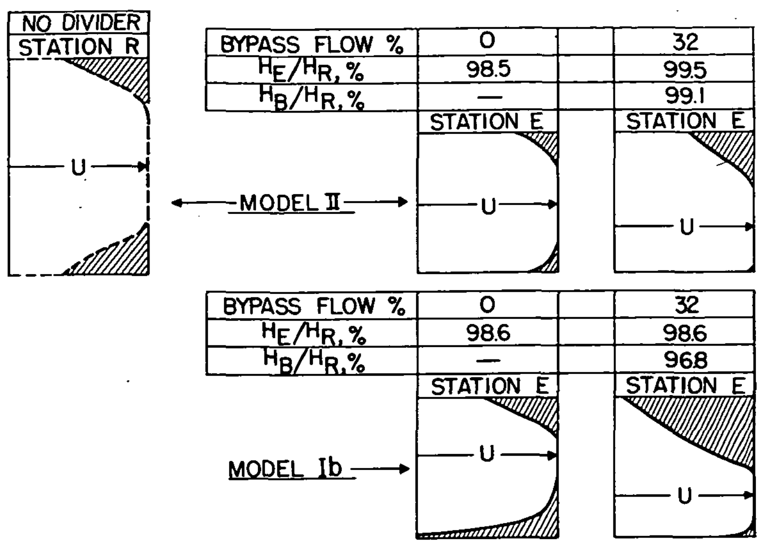

Figure 5

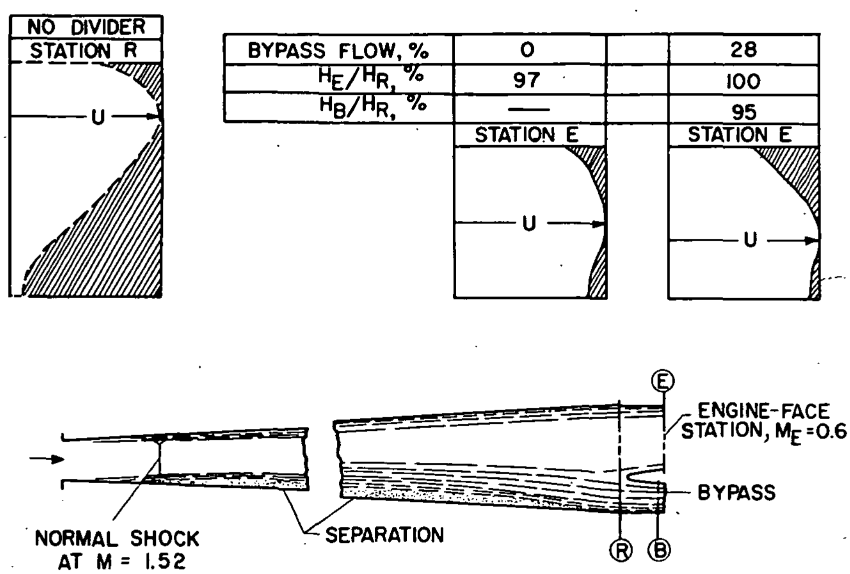

Figure 6

TOTAL-PRESSURE DISTORTIONS AT ENGINE FACE

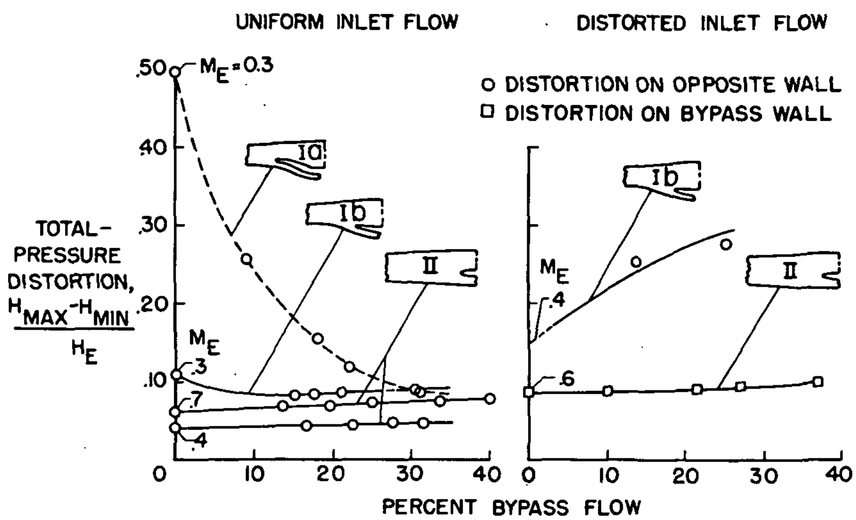

Figure 7

A STUDY OF A SYMMETRICAL, CIRCULAR, INTERNAL COMPRESSION INLET

By Emmet A. Mossman and Frank A. Pfyl

Ames Aeronautical Laboratory

SUMMARY

A preliminary experimental study of symmetrical, circular, internal compression inlets has shown that they attain pressure recovery equal to that measured by conical nose inlets at Mach numbers up to about 2.3. This pressure recovery was obtained with configurations having essentially zero pressure drag of the external surfaces.

15

INTRODUCTION

Recently, an experimental investigation has been made at Mach numbers up to 2.5 of an inlet which shows promise. The purpose of this paper is to present an interim report describing the development of the inlet and the progress that has been made to date.

SYMBOLS

M	Mach number
m	mass flow, lb-sec/ft
P_t	total pressure, lb/sq ft
A	area, sq ft
p	static pressure, lb/sq ft
X	longitudinal distance, ft
D	diameter, ft

Subscripts:

∞	free stream
1	inlet
max	maximum
min	minimum
c	compressor
t	total
0	entrance

DISCUSSION

Up to the present time, external compression inlets have produced relatively efficient supersonic compression of the induction air, but the wave drag of the external cowls has been high. On a typical airplane this inlet drag is from 10 percent to 20 percent of the total airplane drag at Mach numbers above 2.0. This cowl drag is mainly a function of the initial lip angle. It has been found experimentally that the best overall performance of conical inlets occurs when the lip internal surfaces are nearly alined with the flow direction immediately behind the conical shock wave (fig. 1). This figure shows also the flow angularity behind a 30° cone and the angle of shock detachment. If 3° is added for lip thickness, the external lip angle approaches even closer to the angle of shock detachment. These considerations indicate that the drag of external compression inlets will be large and will probably increase with Mach number because the lip angles must increase.

If the lip angles could be kept low, the pressure drag could be markedly reduced. The internal compression inlet shown in figure 2 is designed for use with a typical jet engine. The resulting external surfaces have very low angularity, approximately 1°; consequently, the wave drag would be negligible. The relative dimensions of the nacelle shown at the bottom of the figure are for a $M = 2.0$ design. As the design Mach number increases, both the inlet and exit diameters increase relative to the engine envelope diameter, and the nacelle will approach even closer to a straight tube. A symmetrical circular configuration was selected which allows the minimum area of the internal duct to be varied by translation of the center body. The photographs at the top of figure 2 show the cone extended for starting, an off-design or transitional position, and the design position with the cone fully retracted. The movement of the center body should be programmed with the flight Mach number. In addition, an automatic control is necessary which can sense the position of the terminal shock wave and actuate the center body to maintain the shock position near the minimum area. Control mechanisms for supersonic inlets which might be adapted to this internal compression inlet are described in reference 1. The angularities of the compression surfaces are low - 8° to 10° for the cone and 1.5° to 2.0° for the lip annulus. These angles are kept low to avoid shock-induced separation during the internal compression process by limiting the pressure rise in an incident wave to less than the value which has been found to cause separation. It would be desirable to reduce the length of the internal ducting. However, in the present design it has not been found necessary to include long stabilizing sections rearward of the minimum-area station. Consequently, the present internal compression inlet is slightly shorter than equivalent conical inlets. The internal compression inlet has been tested only at 0° angle of attack.

Use of the internal compression inlet will result in a net gain only if the pressure recovery is sufficiently high. The conical inlet will be used arbitrarily in the following discussion as a standard for comparison. The maximum pressure recovery of conical inlets is shown in figure 3 for the Mach number range from 1.8 to 2.5. A solid-line curve representing the present state of the art is shown in the figure and will be used for comparison purposes. The experimental pressure recovery of the internal compression inlet as a function of Mach number for four internal shapes is shown in figure 4. Comparison of the data with the best external conical-shock inlets shows that the pressure recovery is about the same over a range of Mach numbers to 2.3. For three of the inlets the compression surfaces were generated by straight lines, the ratio of the minimum area to the inlet area being varied. The fourth case, which gave the highest pressure recovery at Mach numbers greater than 2.1, has a curved center body and a curved lip annulus. It should be noted that the contraction ratio for this inlet corresponds to that for inlets with straight internal elements which gave low pressure recovery for the same Mach number range.

Some idea of why the inlet with the curved center body and curved lip annulus gave higher pressure recovery than the other internal compression inlets was gained by mapping the internal flow field by using the method of characteristics. Figure 5 shows the shock-wave pattern and the computed pressure distribution on the center body and lip annulus for one of the inlets with straight internal elements. The shock waves from the center body and annulus initially had about the same strength. However, the pressure rise at the first reflection of the shock wave from the annulus on the center body was much larger than it was for the first reflection of the center-body shock on the annulus. The pressure gradients behind the shock intersections also were dissimilar. In an effort to equalize both the pressure ratio across each shock-boundary intersection and the pressure gradients behind the intersections, curved compression elements were employed; and as noted previously, the modification was moderately successful. It is thought that further improvements are possible, especially at higher Mach numbers, by shaping the internal surfaces to follow contours derived by the characteristics method.

Of importance to the inlet designer is the off-design performance. On the left-hand side of figure 6 the take-off performance of the internal compression inlet is shown. The take-off characteristics are similar to those for the conventional conical inlet. The curves on the right-hand side of this figure illustrate the "matching" characteristics of the inlet and engine combination. The ordinate of this curve is the ratio of the capture (or entrance) area to the streamtube area supplied by the inlet or required by the engine. The air handling qualities of the inlet are shown by the solid-line curve. The internal compression inlet is assumed to operate as a normal-shock inlet at Mach numbers up to 1.6. Above a Mach number of about 1.8, the inlet operates with the streamtube area equal to the inlet area and has no spillage drag.

The engine air requirements (in terms of the streamtube-area ratio) are shown by the dashed-line curve in figure 6. For this particular engine at M above 1.2, a maximum of 3 percent of the inlet air would have to be bypassed for maximum efficiency. Below a Mach number of 1.2, either the rotational speed of the engine could be reduced slightly or some loss in pressure recovery would be incurred. Many other matching programs could be devised, but figure 6 indicates that the problems should be no more severe with the internal compression inlet than they are with other types of supersonic inlet-engine combinations.

CONCLUDING REMARKS

A preliminary experimental study of symmetrical, circular, internal compression inlets has shown that they attain pressure recovery equal to that measured by conical nose inlets at Mach numbers up to about 2.3. This pressure recovery was obtained with configurations having essentially zero pressure drag of the external surfaces.

REFERENCE

1. Wilcox, Fred, and Perchonok, Eugene: Aerodynamic Control of Supersonic Inlets for Optimum Performance. (Prospective NACA paper.)

LIP ANGLES OF CONICAL INLETS

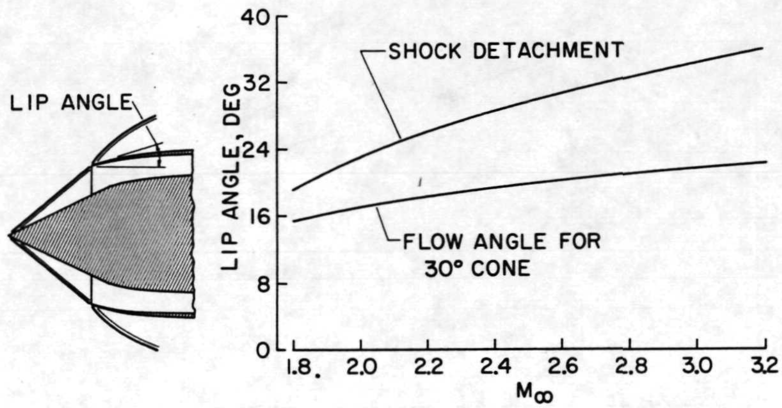

Figure 1

INTERNAL COMPRESSION INLET

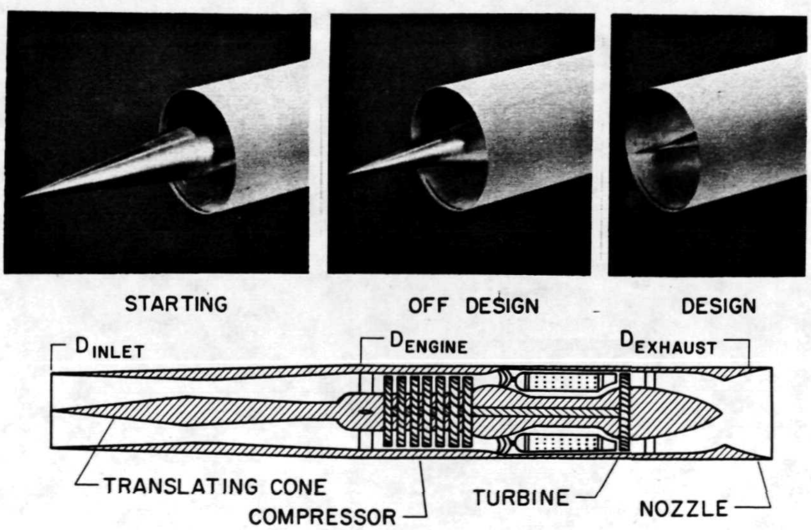

Figure 2

~~CONFIDENTIAL~~

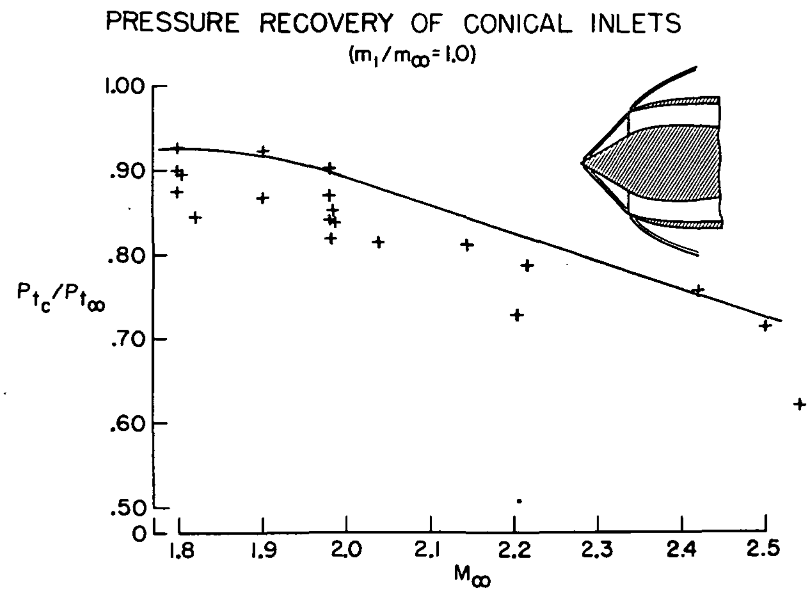

Figure 3

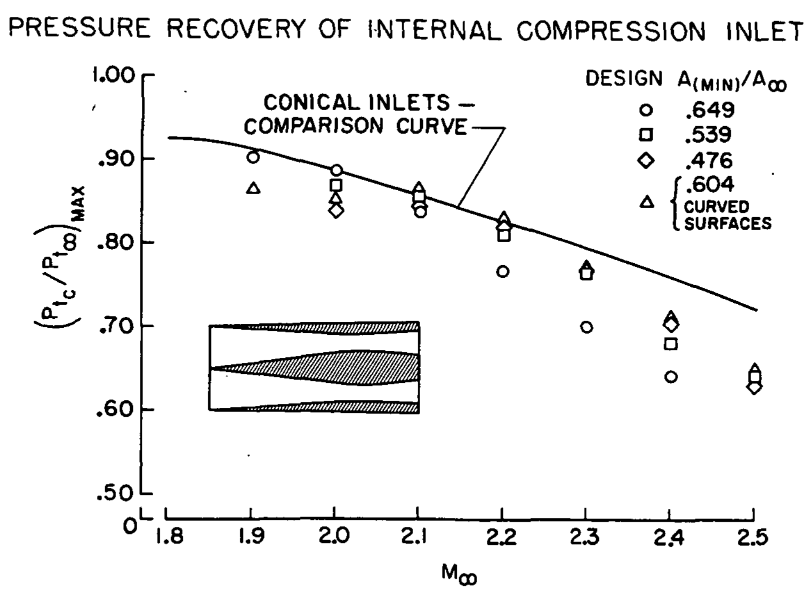

Figure 4

~~CONFIDENTIAL~~

THEORETICAL PRESSURE DISTRIBUTION ON COMPRESSION SURFACES

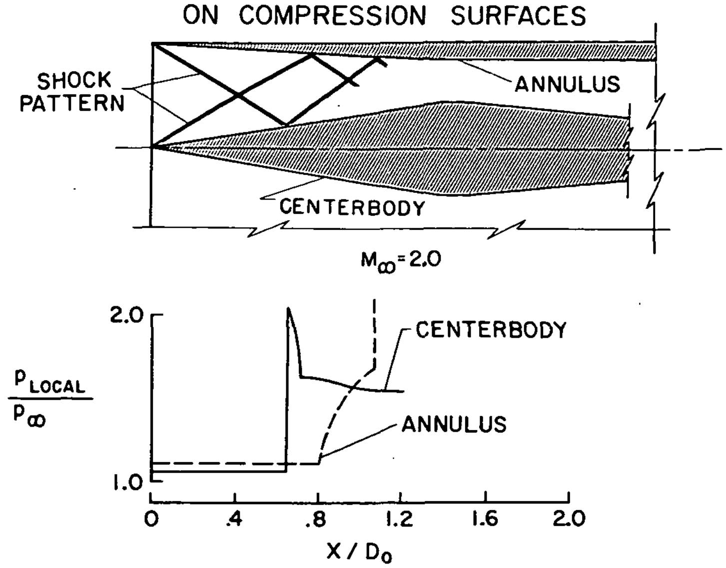

Figure 5

PERFORMANCE OF THE INTERNAL COMPRESSION INLET AT OFF-DESIGN CONDITIONS

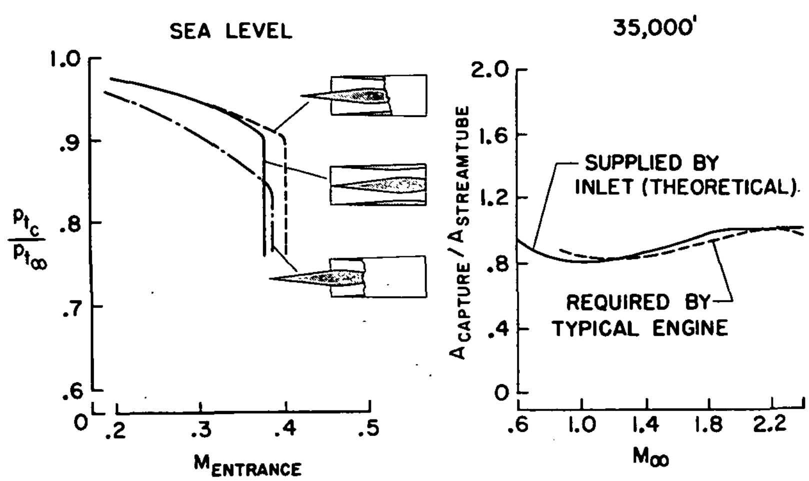

Figure 6

AERODYNAMIC CONTROL OF SUPERSONIC INLETS

FOR OPTIMUM PERFORMANCE

By Fred A. Wilcox and Eugene Perchonok

Lewis Flight Propulsion Laboratory

SUMMARY

Aerodynamic means of controlling a translating spike and bypass of supersonic inlets are discussed. These include determination and use of normal-shock position, oblique-shock position, and diffuser-exit Mach number as control parameters. Although the discussion is limited to axially symmetric inlets, these same control parameters can be used for a single side inlet feeding a turbojet engine, the translating spike being replaced by a variable-ramp compression surface.

INTRODUCTION

Variable-geometry inlets for turbojet engines at supersonic flight speeds offer improvement in overall performance over the fixed inlet. The translating spike and the variable bypass are two variable features commonly considered for the axially symmetric inlet. The spike is used to spill excess air behind the oblique shock when the engine requires less air flow than the inlet provides. Or, it may be employed to optimize inlet performance by maintaining the oblique shock near the cowl lip when a bypass is used for air spillage. Air spillage by either translating the spike or opening the bypass results in less drag than spillage behind the expelled normal shock of a fixed inlet.

16

In order to attain the best possible performance, these variable-geometry features must be properly positioned. Control systems to provide optimum settings must be supplied with input signals which are representative of the desired inlet performance and in addition lend themselves to control application.

The purpose of this paper is to discuss and evaluate some of the input signals or control parameters which have been experimentally employed to operate turbojet inlet-control systems. These include the normal-shock position, the oblique-shock position, and the diffuser-exit Mach number. The discussion is based on results obtained at the Lewis Laboratory during control investigations of ram-jet engines (refs. 1 to 5) as well as during a study on the control of a supersonic inlet for the J-34 turbojet engine (refs. 6 and 7).

SYMBOLS

A_2	flow area at diffuser exit, 1.54 sq ft
H	pitot pressure, lb/sq ft abs
M	Mach number
p	static pressure, lb/sq ft abs
T	total temperature, $^{\circ}R$
θ_l	angle between line connecting spike tip and cowl lip and inlet center line, deg
θ_s	angle formed by inlet oblique shock with inlet center line, deg

Subscripts:

r	reference
s	sensing
o	free stream
2	diffuser exit, station immediately ahead of bypass

DISCUSSION

A typical variable-geometry supersonic inlet for a turbojet engine is shown schematically in figure 1. The control parameters to be discussed are also listed in this figure. With any supersonic inlet, the position of the inlet normal shock is a reliable indication of inlet performance. Optimum performance for inlets of the type shown is generally obtained with the normal shock at or near the cowl lip. Determination of normal-shock position will thus provide a useful inlet control parameter.

A convenient way of determining normal-shock position is by measuring its static pressure rise. Three techniques for measuring the normal-shock pressure rise are shown in figure 2. The spike static wall orifice is located on the center body in the plane of the cowl lip. The probe static orifice is located on a small probe extending slightly ahead of the cowl lip. A backward-facing pitot tube is located somewhat inside the cowl. In each case a reference orifice is located forward on the spike surface out of the region of influence of the normal shock. Details of these orifices are given in figure 3. The differential pressure between the sensing and reference orifices is used as the control input signal. In figure 2, this differential pressure has been nondimensionalized by dividing by the free-stream static pressure to generalize the parameter and thus make it independent of altitude.

Values of this parameter are plotted for normal-shock positions ahead of and behind the plane of each sensing orifice in terms of percent change in diffuser-exit corrected air flow. With the use of the spike static wall orifice as sensor (ref. 2), the parameter is essentially zero when the shock is downstream of the orifice. As the shock moves forward and crosses the sensing orifice, the static pressure at the sensing orifice rises and causes the value of the parameter to rise. A desired value for the parameter is selected along this rise and a control system is designed to maintain this value. If the measured differential pressure is greater than the setting, air spillage is increased and thus moves the normal shock downstream. If the measured differential is less, spillage is decreased and the normal shock is moved upstream. If the control setting is made at a value of the parameter other than zero, compensation for altitude changes must be provided.

Owing to both normal-shock curvature and boundary-layer growth along the spike, the spike static orifice signaled a normal-shock position at which some normal-shock air spillage existed. This means that to obtain critical inlet operation, the orifice would have to be moved somewhat downstream of the lip plane. This difficulty was not experienced with the probe static sensor, and, in addition, movement of the orifice with spike translation is avoided. The data for the probe static sensor (ref. 7) indicate a sharp rise in the parameter at the control point. Such an input signal provides close control of normal-shock position. However, if the slope of the parameter becomes too steep, control-system oscillation may result.

An even greater rise in differential pressure is obtained with the backward-facing total probe. For downstream shock locations, the value of the parameter falls well below zero. If the control setting is made at zero, the necessity of measuring p_0 and providing altitude compensation is avoided. The backward-facing total probe thus provides a signal having the desirable features of both a steep slope near the control setting and no need for altitude compensation.

At low supersonic flight Mach numbers, difficulties are sometimes experienced with normal-shock sensing systems. For some diffuser designs, the normal shock will not enter the cowl because of excessive internal contraction. In other cases, the normal shock will enter the cowl but a shock detaches from the external cowl surface. As illustrated in figure 4 this detached wave interferes with the static probe, resulting in little change in the value of the control parameter as the normal-shock position varies. For such an inlet, the backward-facing total probe provides a more usable signal, primarily because of its location away from the influence of the detached wave. Again no altitude compensation is required since the control setting may be made at a parameter value of zero.

If a translating spike is used for flow spillage, the inlet oblique shock may at times fall either inside or outside the cowl lip. The variation in normal-shock position parameter for the probe static orifice and the backward-facing total probe for these extreme positions of the oblique shock is shown in figure 5. The backward-facing total probe provides a parameter passing well below zero for both cases. The value of the parameter for the probe static orifice shifts upward when the oblique shock falls ahead of the cowl. This is believed caused by the combined effects of the static pressure rise across the oblique shock and by misalinement of the probe with the local flow.

The results of applying normal-shock position sensing to control of a translating spike are given in figure 6. The data were obtained at $M_0 = 2.0$ with a J-34 engine installed in an axially symmetric pod-mounted nacelle. An electric actuator was used to position the spike. The current to the actuator was controlled by the voltage output of a pressure transducer connected between a static probe and its reference orifice. In order to achieve a variation in spillage air flow, the engine speed was varied from 9,210 to 11,630 rpm. The solid line represents the spike position angle required for critical inlet operation. The data points represent the spike position set by control. The data show that the control set the spike position within 1° of that required for critical inlet operation.

Besides being used to spill air, the spike can be used to optimize inlet performance by keeping the inlet oblique shock near the cowl lip over a range of flight Mach number when a bypass is employed to spill the excess air. A way in which the oblique-shock position can be determined and set at the cowl lip is shown in figure 7. Two pitot tubes are used, one a sensing tube at the cowl lip and the other a reference tube at the spike tip. The difference between the pressure measured by each tube provides the control signal. This difference in pressure is again divided by free-stream static pressure to nondimensionalize the parameter and make it independent of altitude. The oblique-shock position error plotted in figure 7 is defined as the difference between spike position angle and conical shock angle. If the oblique shock falls within the cowl, the oblique-shock parameter is essentially zero because both tubes read total pressure behind a free-stream normal shock. As the oblique shock passes in front of the cowl lip, there is a rise in the oblique-shock parameter because the loss in total pressure across the oblique and normal shocks ahead of the cowl-lip pitot tube is less than the total-pressure loss across the single normal shock of the spike pitot tube. The analytically computed rise is in agreement with the measured value. Details of the sensing pitot tube used are given in figure 8.

A value of the oblique-shock position parameter is selected to be maintained by the control system. The data indicate that a control system based on this parameter can hold the oblique-shock position angle to within a fraction of a degree by retracting the spike when the oblique shock falls outside the cowl and extending the spike when the shock falls inside the cowl.

Consideration has been given the problem of obtaining effective control input signals for shock positioning systems when the inlet is operated at angle of attack. By locating the sensing and reference orifices on the horizontal center line of the inlet, satisfactory control has been obtained for both oblique- and normal-shock sensing systems up to 10° angle of attack, the maximum investigated (refs. 2 and 5).

The techniques described for positioning the normal shock by translating the spike can also be applied to the control of the bypass discharge area. Experimental results for such a system are shown in figure 9. The bypass was actuated with a hydraulic servo system, and the control input signal was provided by a static orifice probe located at the cowl lip. The solid lines in the lower half of the figure represent diffuser performance at $M_0 = 1.8$ and 2.0 with the spike positioned at the θ_l values indicated. Values for the normal-shock position parameter provided by the probe static orifice are given in the upper part of the figure. Although the slope of the normal-shock position parameter is very steep at the control setting selected, satisfactory action was obtained without hunting of the control system. (See ref. 7.) The steady-state points set by the control are indicated by the data points which fall within 1.5 percent of the desired corrected air flow. This scatter is the approximate accuracy of air-flow measurement.

The response of this control system to manual displacement of the bypass away from the control setting was also satisfactory. When the bypass was closed from an initial control position of one-half open by manually overriding the control, the inlet operating point was taken into a region of heavy pulsing. When the control was turned on, it restored the desired operating condition in 0.22 second and permitted only 3 cycles or pulsing. It did this in spite of the fact that during the pulsing cycle the normal shock was intermittently passing the sensing orifice. Satisfactory action was also obtained when the bypass was manually opened, placing the operating point in the supercritical region to the right of the control point.

The third control parameter to be considered is the diffuser-exit Mach number M_2 which has application primarily in the control of the bypass. In the lower part of figure 10, the diffuser pressure recovery is shown as a function of diffuser-exit Mach number, defined as immediately ahead of the bypass. The diffuser discharges through parallel outlets, the engine, and the bypass. At a given stream Mach number, peak diffuser performance occurs at only one value of exit Mach number. Since the exit Mach number is a function of diffuser-exit corrected air flow, M_2 can be held at the desired value as the engine air flow varies by changing the amount of air spilled through the bypass. The ratio of static pressure to total pressure at station 2 is representative of the value of exit Mach number and is the control parameter selected. The variation of this ratio with diffuser-exit Mach number, plotted in the upper part of figure 10, is continuous and is readily adapted to control design.

By comparing the measured pressure ratio to a desired ratio (control setting, which must be scheduled with flight Mach number), the exit Mach number can be set and maintained at a desired value. If the measured ratio is greater than the control setting, the bypass is opened to increase the diffuser air flow and the exit Mach number. If the measured ratio is less, the bypass is closed and therefore the exit Mach number is reduced. With turbojet engines, the diffuser-exit Mach number is sufficiently great to give reasonable accuracy in determining the pressure ratio.

The data points in figure 10 were set with a control system in which the pressure ratio was measured electrically with pressure transducers and the bypass actuated by a hydraulic servo system. The scatter in the data points corresponds to ±5.3 percent of diffuser corrected air flow and was the result of using a single tube to measure diffuser-exit total pressure. Shifts in total-pressure profile with engine operating condition caused this single measurement to deviate from the average. It thus appears necessary to use some means of total pressure averaging for this control signal.

CONCLUDING REMARKS

Although the discussion is limited to axially symmetric inlets, these same control parameters can be used for a single side inlet feeding a turbojet engine, the translating spike being replaced by a variable-ramp compression surface. The twin-duct arrangement presents new problems.

There is a need in this relatively new and rapidly expanding field of inlet control to find new inlet-control parameters as well as to improve the techniques of using the existing ones. Much of this can be done with properly instrumented scale tests of the inlet alone. Work is continuing at the Lewis Laboratory on such inlet models as well as on the full-scale inlet-engine combination.

REFERENCES

1. Vasu, G., Wilcox, F. A., and Himmel, S. C.: Preliminary Report of Experimental Investigation of Ram-Jet Controls and Engine Dynamics. NACA RM E54H10, 1954.

2. Wilcox, Fred A., Perchonok, Eugene, and Hearth, Donald P.: Investigation of an On-Off Inlet Shock-Position Control on a 16-Inch Ram-Jet Engine. NACA RM E54I21, 1954.

3. Dunbar, William R., Vasu, George, and Hurrell, Herbert G.: Experimental Investigation of Direct Control of Diffuser Pressure on 16-Inch Ram-Jet Engine. NACA RM E55D15, 1955.

4. Hurrell, Herbert G., Vasu, George, and Dunbar, William R.: Experimental Study of Shock-Positioning Method of Ram-Jet-Engine Control. NACA RM E55F21, 1955.

5. Wilcox, Fred A., and Hearth, Donald P.: Application of Oblique-Shock Sensing System to Ram-Jet-Engine Flight Mach Number Control. NACA RM E54L22a, 1955.

6. Leissler, L. Abbott, and Nettles, J. Cary: Investigation to Mach Number 2.0 of Shock-Positioning Control Systems for a Variable-Geometry Inlet in Combination With a J34 Turbojet Engine. NACA RM E54I27, 1954.

7. Wilcox, Fred A.: Investigation of a Continuous Normal-Shock Positioning Control on the Bypass of a Supersonic Inlet in Combination With the J34 Turbojet Engine. (Prospective NACA paper.)

[redacted]

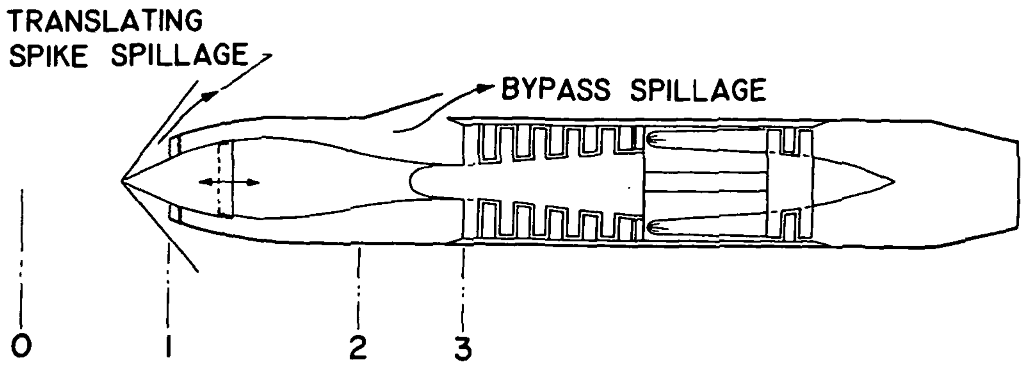

VARIABLE GEOMETRY	CONTROL PARAMETER
TRANSLATING SPIKE	NORMAL–SHOCK POSITION
	OBLIQUE-SHOCK POSITION
BYPASS	
	DIFFUSER-EXIT MACH NUMBER

Figure 1

NORMAL–SHOCK POSITION SENSING

$M_o = 2.0$

OBLIQUE SHOCK AT COWL LIP

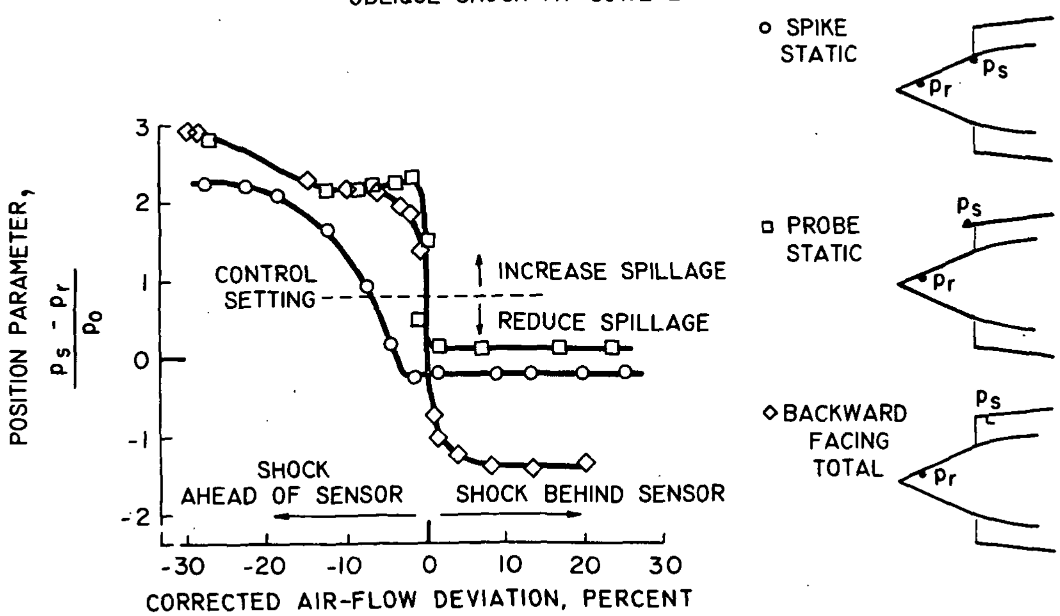

Figure 2

[redacted]

INSTALLATION DETAILS OF PROBE STATIC AND BACKWARD-FACING TOTAL PROBE

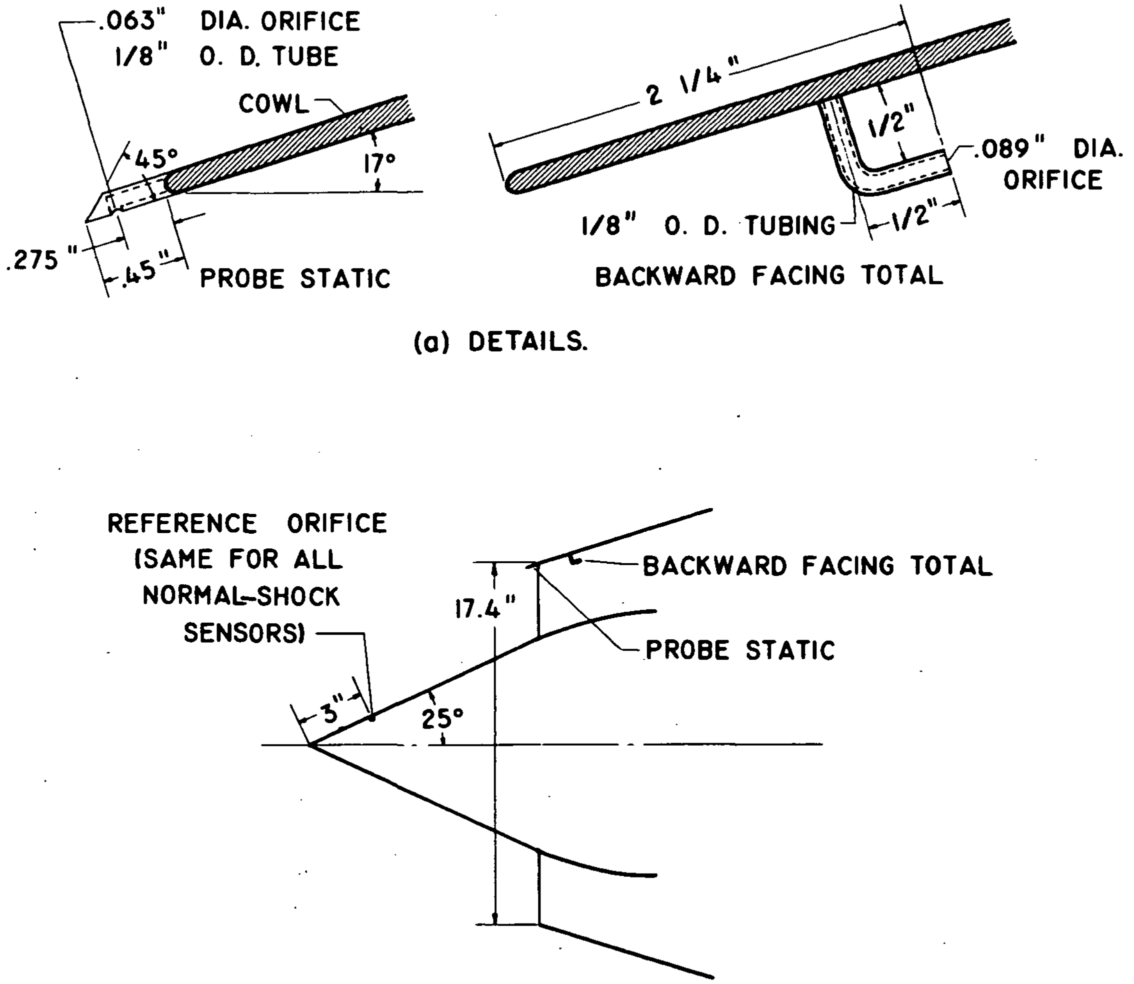

(a) DETAILS.

(b) INSTALLATION ON COWL.

Figure 3

~~CONFIDENTIAL~~

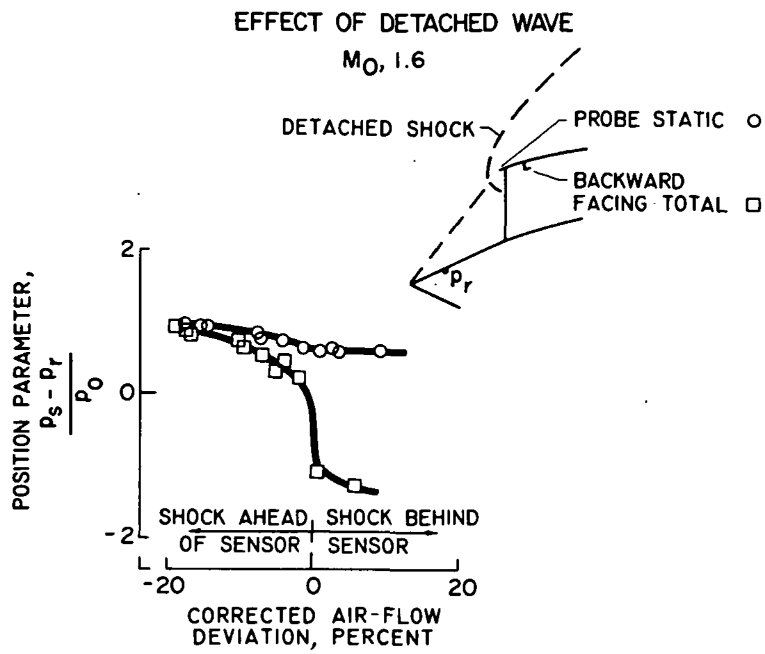

Figure 4

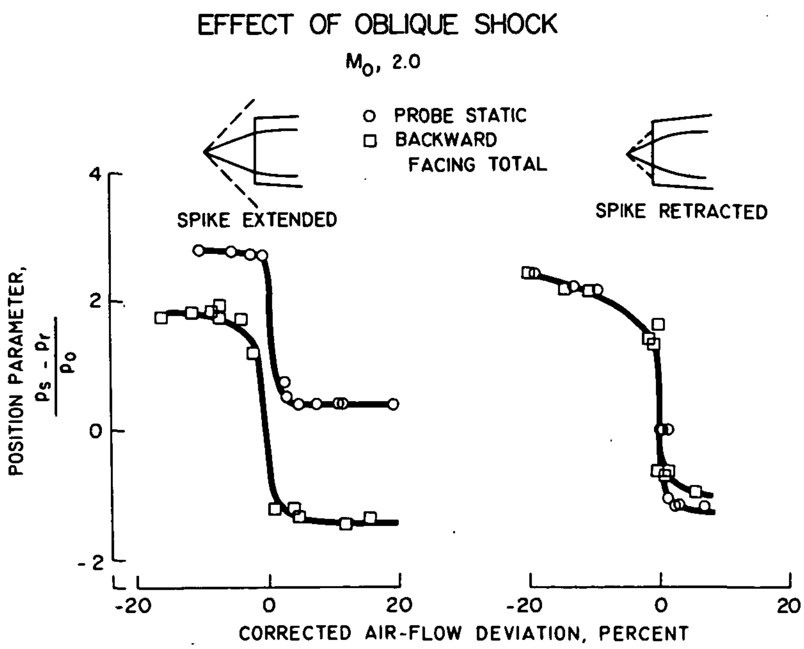

Figure 5

~~CONFIDENTIAL~~

CONTROL OF SPIKE BY NORMAL SHOCK

PROBE STATIC SENSOR M_O, 2.0

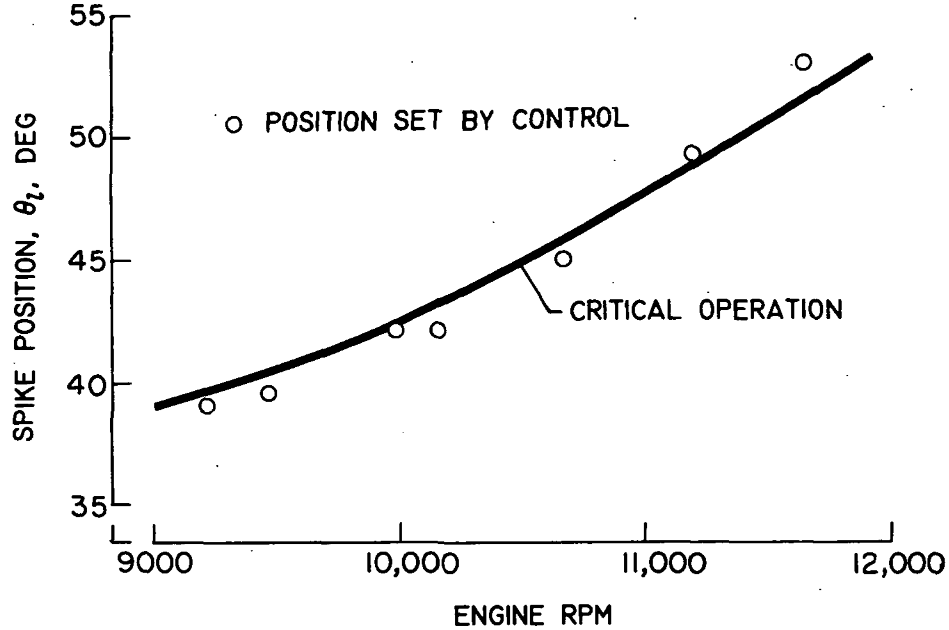

Figure 6

OBLIQUE-SHOCK POSITION SENSING

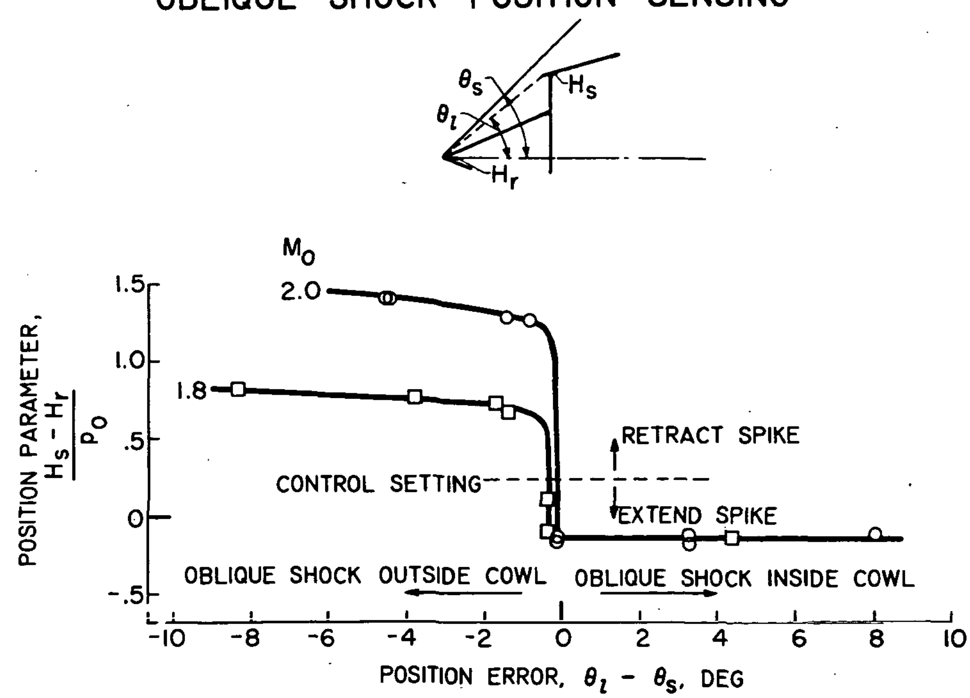

Figure 7

[redacted]

~~CONFIDENTIAL~~

OBLIQUE - SHOCK POSITION SENSOR

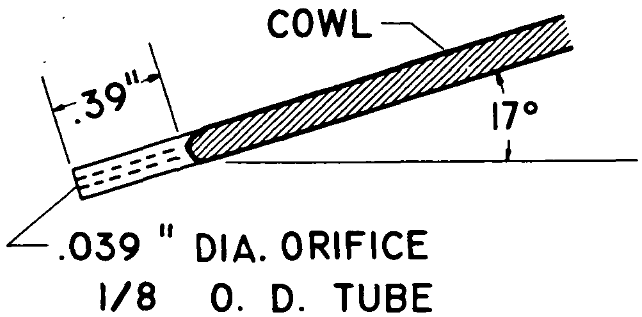

(a) DETAIL.

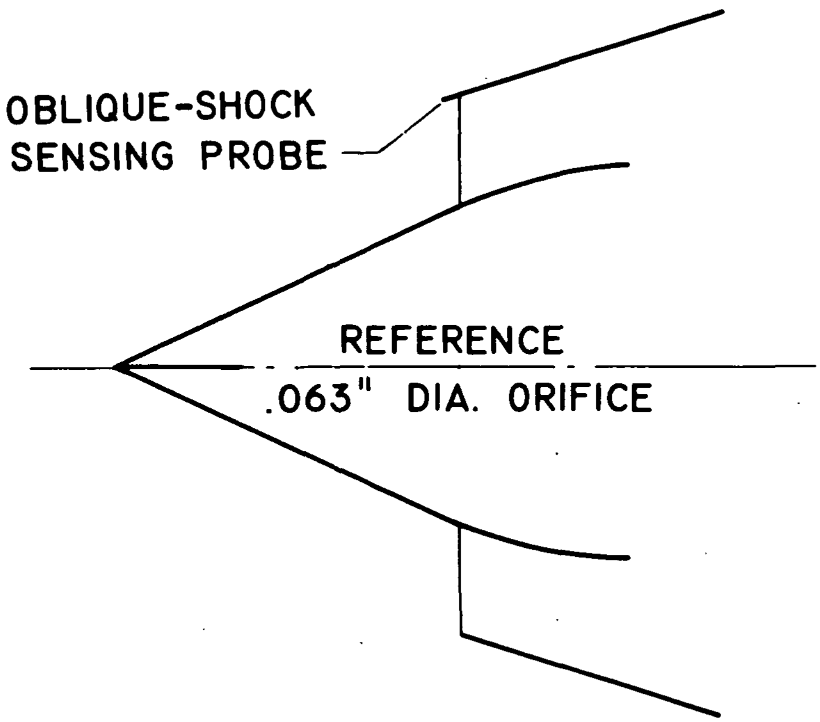

(b) INSTALLATION ON COWL.

Figure 8

~~CONFIDENTIAL~~

CONTROL OF BYPASS BY NORMAL SHOCK

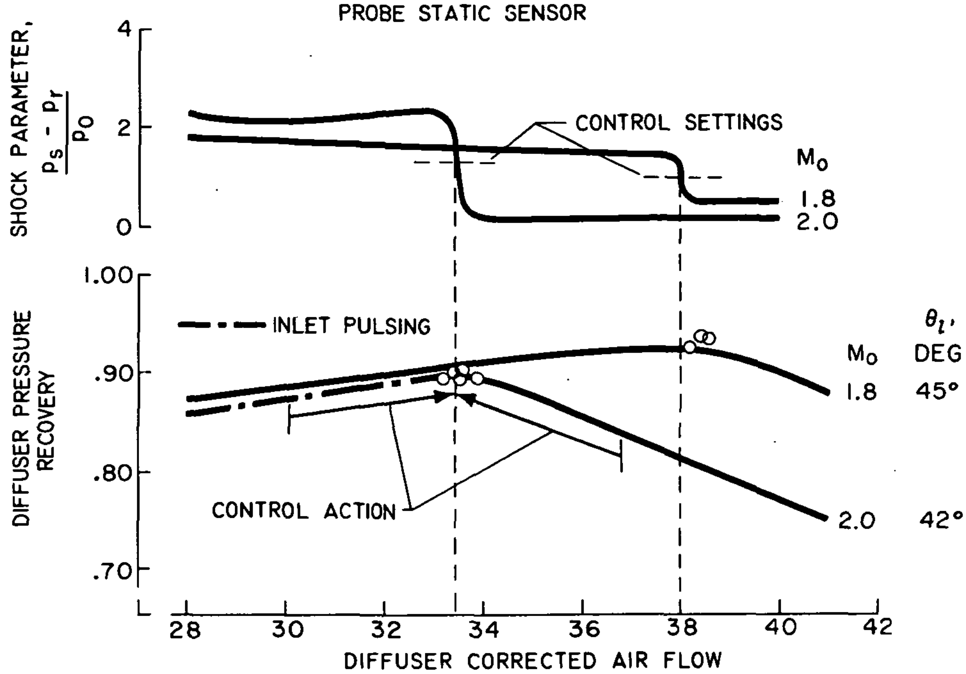

Figure 9

CONTROL OF BYPASS BY DIFFUSER-EXIT MACH NUMBER

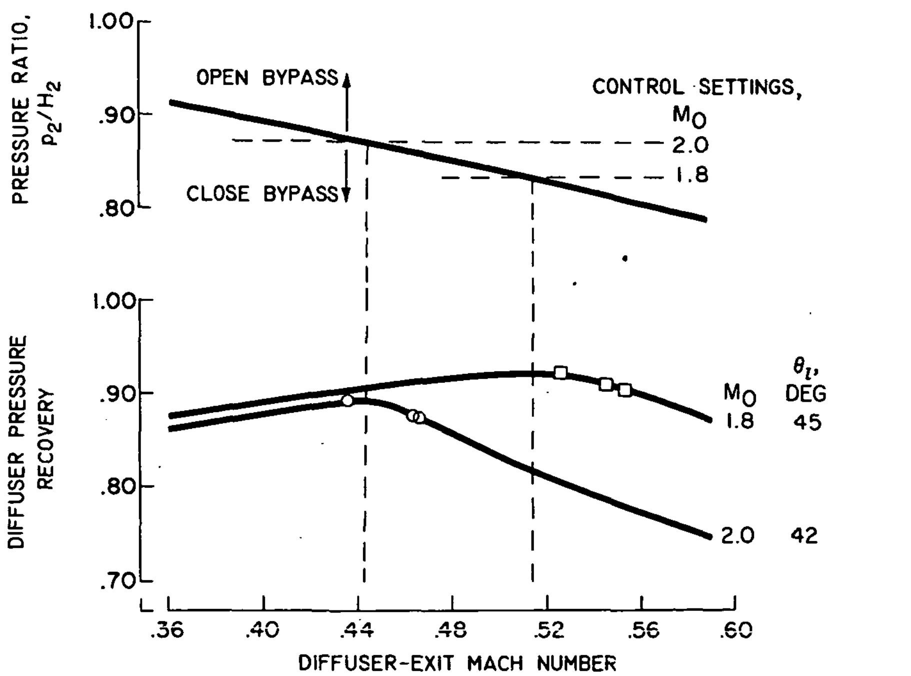

Figure 10

JET EFFECTS ON BASE AND AFTERBODY DRAG

By William J. Nelson and Beverly Z. Henry, Jr.

Langley Aeronautical Laboratory

INTRODUCTION

The widespread use of afterburners has led to the introduction of exit nozzles whose area is variable. In a typical installation (fig. 1) the afterbody of the fuselage or nacelle housing the jet engine is designed to fit the tailpipe closely for the high-speed condition when the exit nozzle is full-open. The reduction in area in going to the cruise condition is accompanied by a large increase in the area of the base annulus, or by a reduction of the base diameter through contraction of the afterbody. In either case, the drag penalties may be large. For installations of the type indicated at the lower left of the figure, the increased drag is that associated with reduced pressures over the enlarged base annulus. For those of the type indicated at the lower right, increases in drag result from flow changes over the afterbody as well as changes in base pressure.

It is the purpose of this paper to review briefly those parameters which influence base and afterbody drag at transonic speeds and to indicate the magnitude of the jet effects in this speed range. Since this is the cruise range, the discussion will be restricted to systems using sonic nozzles.

17

SYMBOLS

C_D	drag coefficient
C_p	pressure coefficient, $\dfrac{p - p_\infty}{q_\infty}$
H	total pressure
M	Mach number
d	diameter
p	static pressure

q dynamic pressure

t total temperature

x distance from model base

β boattail angle

Subscripts:

∞ free stream

b base

j jet

MAX model maximum

APPARATUS

Two experimental setups, shown in figure 2, were used in obtaining the greater part of the data to be presented herein. The strut-supported fuselage model shown on the left was used in the Langley 8-foot transonic tunnel tests. This model was equipped with a combustion chamber which permitted simulation of hot jets as well as cold. Fuel and combustion air were introduced through the support struts. This equipment, along with data from tests of many models, is described in reference 1. The small-scale apparatus shown in the right half of the figure was used in tests conducted in the Langley internal aerodynamics laboratory. The afterbody models were attached to the downstream end of a support tube which extended into the entrance bell ahead of the tunnel. The jet was simulated with cold air introduced through the support tube.

All models were fitted with static-pressure orifices. The drag was obtained by integration of pressures along the afterbody and across the base annulus.

RESULTS AND DISCUSSION

Effect of Jet Temperature

In order to facilitate isolation of the many parameters involved in this problem, the greater part of the data to be presented were taken with a cold jet. Before these results are examined, however, the magnitude of the temperature effects will be established. This is done in figure 3 where the drag increment between hot- and cold-jet tests is plotted as a function of the jet temperature.

For low-drag bodies - those with low boattail angles and small base annuli - the effect of jet temperature on afterbody drag was negligible, as indicated by the circles. The maximum effect of jet temperature was found to occur with the blunt cylindrical afterbody, where at $M \doteq 0.9$ the drag coefficient was reduced by 0.02 as the jet temperature increased from 0 to 1,200° F; this increment was more than doubled as the stream Mach number was increased to 1.1. Between these two extremes lie many models of moderate boattail angle and varying base area; these are indicated by the square symbols. Although jet temperature influences the absolute value of these drag coefficients, the validity of comparisons based upon cold jet tests is probably not impaired.

Effect of Stream Mach Number

In figure 4, the pressure at the base of cylindrical afterbodies is presented as a function of stream Mach number. Negative values of the coefficient indicate base pressures below the static pressure of the stream; hence, the greater the negative value of the coefficient the higher the drag. With no flow from the jet, the base pressure coefficient varies with Mach number as indicated by the middle curve. This coefficient may be increased or decreased by the presence of the jet. The effect of the jet, as indicated in the figure, depends upon the pressure ratio.

At supersonic speeds, a considerable volume of data has been available for some time (for example, refs. 2 to 4). However, in the transonic range, where changes in magnitude of the jet effects occur rapidly, only a relatively small amount of data has been available (for example, refs. 1 and 5). This is the range of greatest current interest for cruise and it is in this range that all of the data presented in the subsequent figures were obtained.

Effect of Jet Diameter

In figure 5, the effect of the jet is shown as a function of the jet diameter. Again, the afterbody was cylindrical and the jet was cold. At small ratios of the jet diameter to base diameter, the jet lies well within the wake boundary. In this region, increasing the jet pressure ratio increases its effectiveness as a pump and leads to progressively higher values of the base pressure coefficient. The no-flow point from the preceding figure is indicated by the circular symbol. For the larger jets, increased pressure leads to increased interference with the external flow and reduces the expansion in the vicinity of the base. For these cases, increasing the jet pressure ratio reduces the base pressure coefficient. Along a given curve, the jet pressure ratio is constant. Increasing the jet diameter increases the base pressure coefficient until the point is reached where the favorable interference effects compensate the improved pumping effectiveness of the larger jet. Beyond this point, increasing jet diameter reduces the base pressure coefficient.

Afterbody Pressure Distribution

The effect of the jet is not restricted to changes in the base pressure coefficient. In figure 6, the static pressure along cylindrical and bottailed afterbodies is presented as a function of the distance ahead of the base. The solid line represents data taken with no flow through the jet and the dashed curves represent data taken at a jet pressure ratio of 5. The base pressure coefficient is indicated by the symbols.

Along the cylindrical body, the static pressure at $M_\infty = 0.9$ remained nearly constant to within 1 model diameter of the base. Downstream of this point, the static-pressure coefficient became increasingly negative, approaching the base pressure at $x/d_{MAX} = 0$. At a jet pressure ratio of 5, the higher value of $C_{p,b}$ resulted in an increased gradient along this afterbody. Along the conical body, the static pressure well ahead of the cone-cylinder juncture was constant, but rapid expansion around this corner resulted in very high negative pressure coefficients locally. These were followed by decreasing values of C_p toward the base. With a gradual increase in wall curvature, the peak negative pressure was much smaller. For this model, the pressure at the base and that along the afterbody in the vicinity of the base was positive. The jet effect on both boattailed bodies was favorable.

Since the walls of the cylindrical afterbody are parallel to the model axis, only the base pressure contributes directly to its drag. For the boattailed models, however, pressures along the afterbody are of primary importance in determining the drag. High negative pressure coefficients in this region lead to high drag.

Effect of Boattail Angle

In figure 7, the drag of boattailed afterbodies is presented in coefficient form as a function of the boattail angle. The upper pair of curves was obtained in tests of conical afterbodies whose general proportions were those of a nacelle installation. For these, the ratio of jet diameter to model diameter was 0.49. The lower set of curves was obtained in tests of contoured bodies whose proportions were more representative of fuselage installations; for this case, the jet diameter was equal to 25 percent of the model diameter.

For conical afterbodies, the drag coefficient decreased rapidly as the boattail angle was increased from 0, reaching a minimum at about 7°; beyond this point, the drag increased sharply and it became approximately constant for the jet-off case at boattail angles greater than 30°. The effect of the jet was favorable between 4° and 17° but unfavorable outside this range.

For the contoured bodies, the effect of the jet was favorable over a much wider range of boattail angles, but the point of minimum drag remained at an angle less than 10°. In the region of lowest drag, the flow over both models was attached along the entire afterbody; whereas, at 16° on the cones and 24° on the contoured bodies, the flow was clearly separated over much of the body.

Effect of Base Annulus Size

In figure 8, the drag characteristics of a series of contoured afterbodies are presented. These models had a common boattail angle but differed in base diameter. The drag coefficient was obtained from hot-jet tests. At values of d_b/d_{MAX} approaching 0.25 the base annulus approached 0, as the afterbody was faired directly to the edge of the jet. Since the jet diameter was constant, increasing the base diameter increased the area of the base annulus. At both Mach numbers for which data are presented, the effect of the jet was unfavorable when the base annulus was large. When the base was small, increasing the jet pressure ratio reduced the drag. At small diameter ratios, substantial increases in area of the base annulus may be effected without increasing the drag. At the larger diameters, however, small changes in base diameter lead to marked changes in drag; in this range, a variable afterbody may be desirable.

CONCLUDING REMARKS

Figure 9 summarizes the effects of several geometric parameters on the drag of boattailed afterbodies at $M_\infty = 0.9$. The no-flow drag coefficient of the cylindrical body, represented by the open bar, was less than 1/2 that obtained at a jet pressure ratio of 5. With a small amount of boattailing, the no-flow value of C_D was substantially smaller and the jet effect was favorable. These results illustrate the advantage of boattailing the afterbody, for by simply chamfering the cylinder along an 8° line, reducing its base diameter 15 percent, the drag at $H_j/p_\infty = 5$ has been reduced to about 1/6 of its original value.

In the center of this figure, the drag of two conical afterbodies is compared with that of curved profiles of equal boattail angle. Differences in model proportions are indicated but these differences are small and their influence is probably negligible. With a boattail angle of 8°, the flow over both the conical and the curved profile was unseparated and the drag was low, but that of the curved profile was smaller. When the boattail angle was increased to 45°, the drag of both bodies was substantially higher, but again lower drag was associated with the curved profile.

At the bottom of the figure, two contoured bodies of equal boattail angle but different base diameter are compared. The jet-off drag of the more highly boattailed bodies was less than 1/2 that of the model with the large base. The jet effect was unfavorable for the latter but favorable for the small base annulus and thus magnified the gains obtained by reducing the area of the base annulus.

The preceding comparisons were based upon the results of cold-jet tests. For several of these models, however, hot-jet data are also available. For these, shaded triangles indicate drag coefficients obtained with a 1,200° jet. As previously noted, the effect of heat was beneficial.

Thus, it has been shown that the transonic drag of a blunt afterbody may be substantially reduced by even a small amount of boattailing just ahead of the base, that a gradual increase in angle along the afterbody is to be preferred over an abrupt change in slope, that minimum drag occurs at a boattail angle of less than 10°, and that the area of the base annulus should be kept small. For the blunt, high-drag bodies, the effects of the jet were generally large and unfavorable; whereas, for low drag bodies, the jet effect was smaller and in many cases favorable.

REFERENCES

1. Henry, Beverly Z., Jr., and Cahn, Maurice S.: Preliminary Results of an Investigation at Transonic Speeds To Determine the Effects of a Heated Propulsive Jet on the Drag Characteristics of a Related Series of Afterbodies. NACA RM L55A24a, 1955.

2. Bromm, August F., Jr., and O'Donnell, Robert M.: Investigation at Supersonic Speeds of the Effect of Jet Mach Number and Divergence Angle of the Nozzle Upon the Pressure of the Base Annulus of a Body of Revolution. NACA RM L54I16, 1954.

3. Cortright, Edgar M., Jr., and Kochendorfer, Fred D.: Jet Effects on Flow Over Afterbodies in Supersonic Stream. NACA RM E53H25, 1953.

4. Chapman, Dean R.: An Analysis of Base Pressure at Supersonic Velocities and Comparison With Experiment. NACA Rep. 1051, 1951. (Supersedes NACA TN 2137.)

5. Salmi, Reino J.: Experimental Investigation of Drag of Afterbodies With Exiting Jet at High Subsonic Mach Numbers. NACA RM E54I13, 1954.

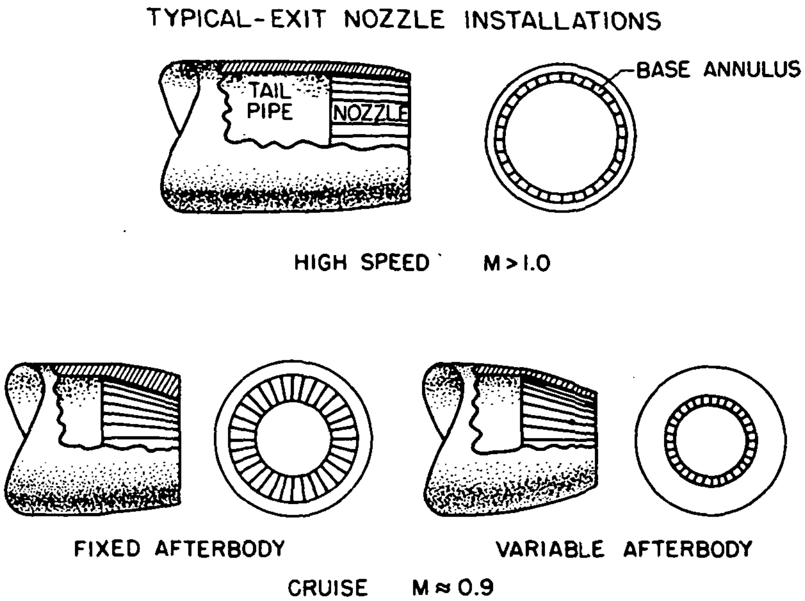

Figure 1

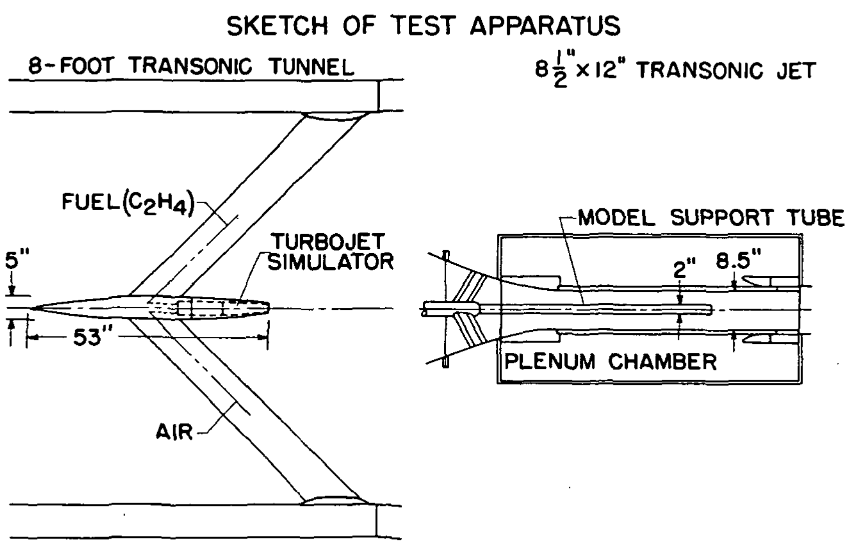

Figure 2

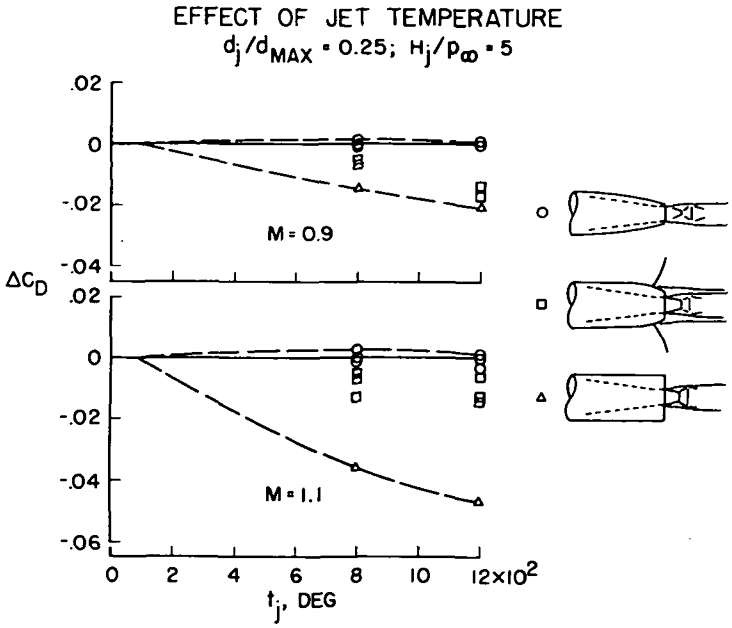

Figure 3

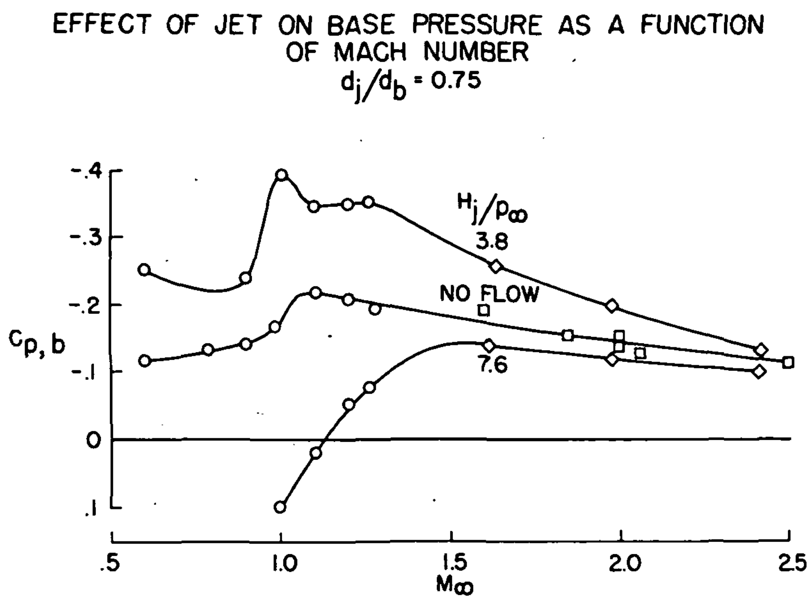

Figure 4

EFFECT OF JET ON BASE PRESSURE AS A FUNCTION OF JET SIZE

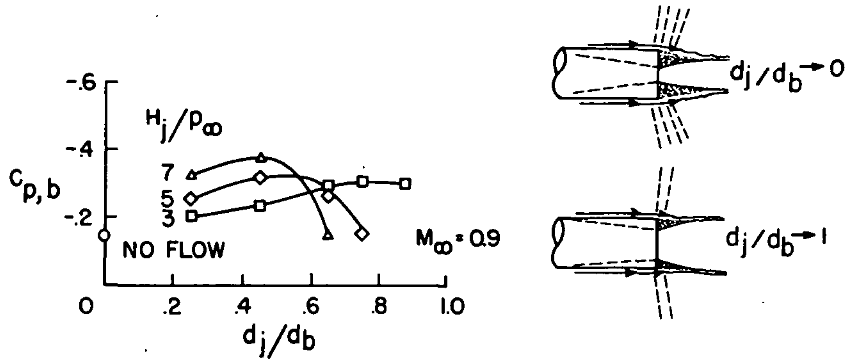

Figure 5

EFFECT OF JET ON TYPICAL PRESSURE DISTRIBUTIONS
$H_j/p_\infty = 5$; $M_\infty = 0.9$

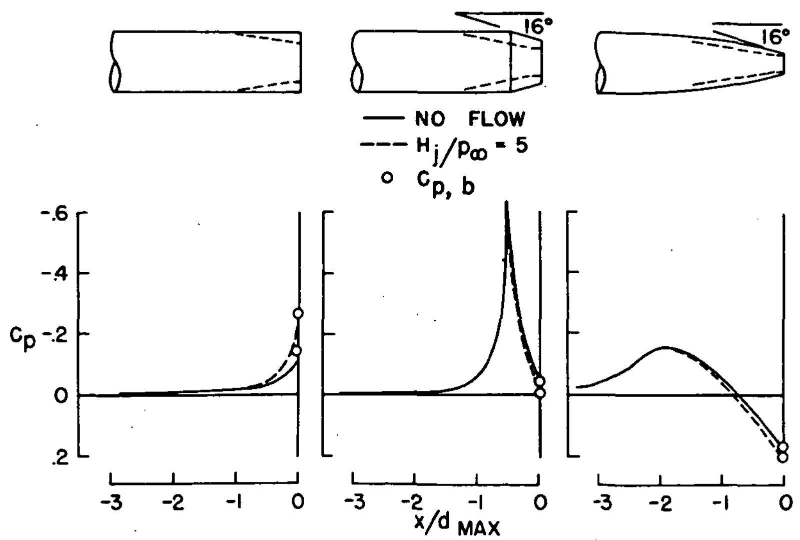

Figure 6

[redacted]

EFFECT OF JET ON DRAG AS A FUNCTION OF BOATTAIL ANGLE

$M_{\infty} = 0.90$

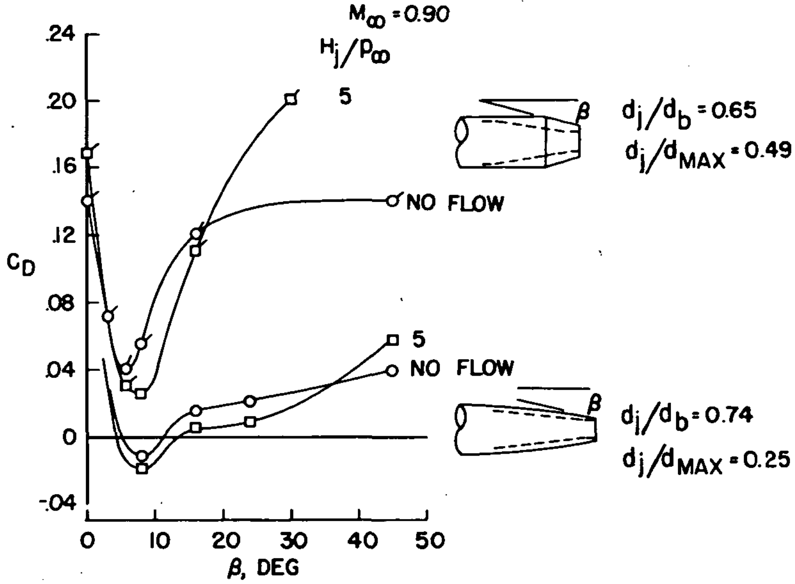

Figure 7

EFFECT OF JET ON DRAG AS A FUNCTION OF BASE SIZE

$d_j/d_{MAX} = 0.25$; $\beta = 16°$; $t_j = 1200°F$

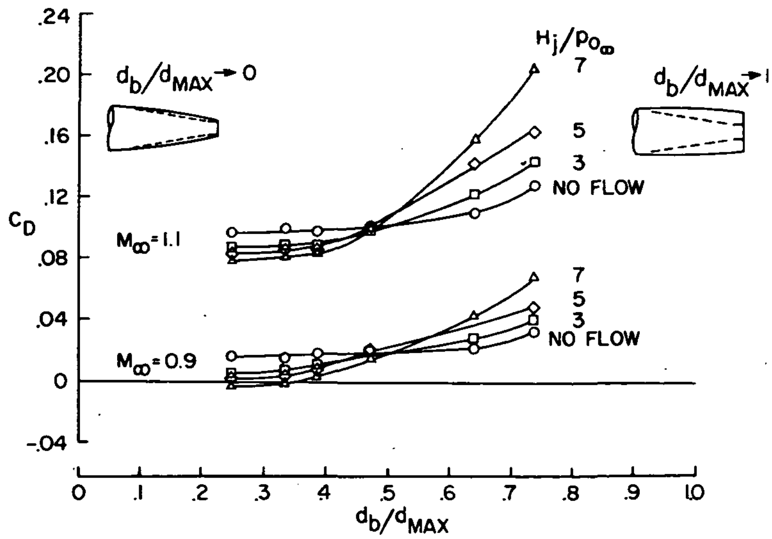

Figure 8

[redacted]

~~CONFIDENTIAL~~

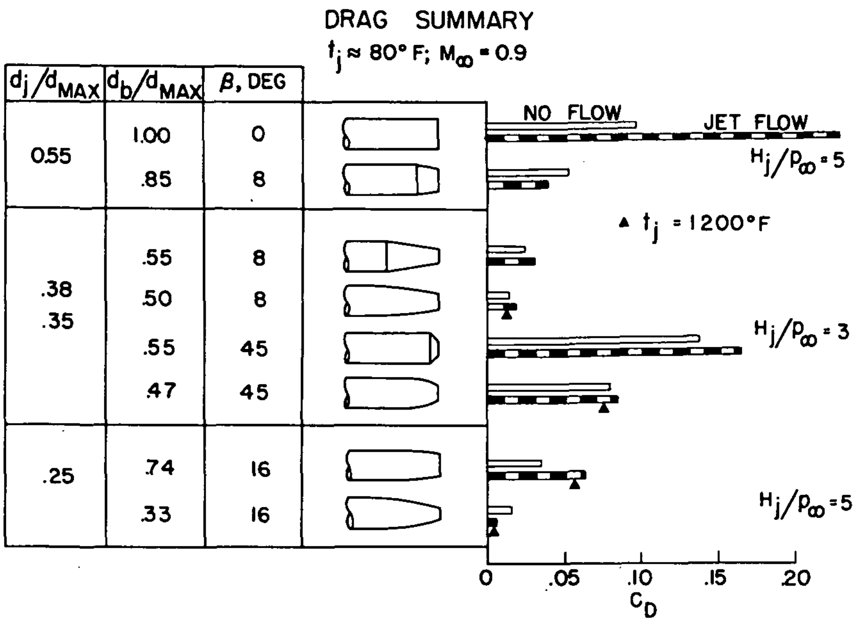

Figure 9

~~CONFIDENTIAL~~

INTERFERENCE EFFECTS UPON FUSELAGE DRAG OF A JET EXHAUSTING FROM A WING-MOUNTED NACELLE

By Robert W. Rainey

Langley Aeronautical Laboratory

INTRODUCTION

Numerous investigations have been made at supersonic speeds to determine the effects of the addition of wing-mounted nacelles upon the aerodynamic characteristics of individual components or entire configurations. In the majority of these tests, the effects of a jet exhausting from these nacelles have not been investigated. It is the purpose of this paper to show some variations in fuselage drag due to the interference of a jet exhausting from a wing-mounted nacelle and to analyze the jet-interference flow fields that caused these drag variations. All results presented are for a Mach number of 1.94.

SYMBOLS

C_D fuselage drag coefficient, $\frac{\text{Fuselage drag}}{q_\infty S}$

d diameter

M Mach number

p static pressure

q dynamic pressure

S fuselage frontal area

x distance from fuselage base to nacelle base

y minimum gap between nacelle and fuselage surfaces in a plane passing through the nacelle and fuselage axes

z distance from wing chord to nacelle center line

18

Subscripts:

j	jet exit
∞	free stream

APPARATUS AND TESTS

The investigation was conducted in the Langley 9-inch supersonic tunnel at Mach numbers of 1.94 and 2.41. As shown in figure 1, a semispan model installation was utilized in conjunction with a boundary-layer bypass plate; therefore, the supports beneath the plate are of no consequence to the configuration tested. The fuselage had a fineness ratio of 10 and consisted of forebodies and afterbodies which were parabolic arcs of revolution and a cylindrical midsection. The fuselage terminated with a recessed, bluff base. Boundary-layer transition was induced artificially ahead of the wing-fuselage juncture. The wing was untapered, swept $26\frac{1}{2}^{\circ}$, and extended from behind the boundary-layer bypass plate through an access within the fuselage and through another wing support in the top nozzle block of the tunnel. The spanwise location of the nacelle was varied by sliding the wing-nacelle assembly within the wing supports. The total and base drags of the fuselage alone, the fuselage in the presence of the wing, and the fuselage in the presence of the wing-nacelle assembly for various nacelle locations and jet-pressure ratios were measured.

For the configuration tested, the orientation of the nacelle with respect to the wing in a plane through the nacelle center line is indicated in figure 2. The nacelle fineness ratio was 5, and it consisted of forebodies and afterbodies which were parabolic arcs of revolution and a cylindrical midsection. The wing section can be seen here and was necessarily thick to accommodate the air-supply tubes to the nacelle. The pylon section was similar to the wing section.

RESULTS AND DISCUSSION

Because of the large amount of data obtained, no presentation of the overall results is made; rather, three examples of fuselage drag variations at a Mach number of 1.94 are presented and analyzed with the use of schlieren photographs. The three configurations utilized in this analysis are shaded in figure 2.

In figure 3 are presented the variations of fuselage drags with jet-static-pressure ratio for one nacelle location. The drags of the fuselage in the presence of the wing are indicated as the "no nacelle" values. The lowest value of p_j/p_∞ is for jet-off conditions. Some related schlieren photographs showing the jet-interference flow field for this nacelle location are presented in figure 4.

In figure 4 some of the multiple reflections of disturbances between the fuselage and nacelle are visible. With jet off, the increased pressure on the afterbody as a result of these reflections reduced the fore drag coefficient from 0.212, with no nacelle, to 0.190 with a small reduction in base drag. Therefore, there was a reduction in total drag also.

At this nacelle location, with the jet on, the exit shock intersected the fuselage near the cylindrical midsection and undoubtedly had little effect upon the local pressure drag. The distribution of interference pressures on the fuselage surface in the expansion region between the exit shock and the shock from within the jet canceled the effects of the pressure rises across the shocks. The overall result was no change in fore drag. However, at the higher jet-pressure ratios, the shock from within the jet moved downstream of the base of the fuselage. The increased Mach number and reduced pressure at the lip of the fuselage base was more than sufficient to offset the effects of the pressure rise across the shock wave and established a reduced base pressure (or an increased base drag). This increase in drag is reflected as a 21-percent increase in total drag as compared with the jet-off total drag value.

In figures 5 and 6 are presented the second example of fuselage-drag variations due to jet interference and the related schlieren photographs. In this instance the nacelle was far enough outboard so that no multiple reflections occurred between body and nacelle. With jet off, the nacelle trailing shock passed downstream of the body trailing shock. The base of the body and a portion of the afterbody were located within the expansion flow regions propagated from the nacelle and pylon after-portions. Therefore, the fore and base drags were higher than their values with no nacelle. Consequently, the total drag was higher also.

Starting the jet eliminated the trailing shock and created the exit shock which passed within the wake of the fuselage. The pressure rise across this shock was transmitted through the wake to the base and thereby reduced the base drag with no effect on fore drag. At a jet-pressure ratio above about 20, the exit shock progressed forward to the base of the fuselage and reduced the fore drag also. The sum of these drag changes is indicated in the total-drag curve. The reduction in total drag due to jet interference was about 15 percent of the jet-off total drag.

The last examples of the effects of jet interference upon fuselage drags (and related schlieren photographs) are presented in figures 7 and 8. Similar to the last example, the jet-off body drags were higher than the no-nacelle values because the base and afterportions of the fuselage were subjected to the low-pressure field propagated from the base and afterbody of the nacelle. These effects more than canceled the combined effects of the pressure rise due to the disturbances between the nacelle and fuselage and the trailing shock behind the nacelle that intersected the fuselage wake.

With the jet started, the pressure rise across the exit shock was sufficient to reduce the fore drag. The expansion region between the exit shock and shock within the jet reduced the base pressure slightly and thereby increased the base drag. At a pressure ratio above about 20, however, the pressure rise through the exit shock had increased to the extent that it compensated for the effects of the low-pressure flow region, and the base drag no longer increased but decreased slightly at the higher jet pressures. The reduction in total drag due to jet interference was about 19 percent of the jet-off total drag.

CONCLUDING REMARKS

In conclusion, it has been shown that at a Mach number of 1.94 the jet-interference effects from a wing-mounted nacelle may increase or decrease the fuselage base or fore drags, or combinations thereof, dependent upon the combinations of nacelle location and jet-pressure ratio. These results indicated that the total-drag changes may be about 20 percent of the total drag of the fuselage with jet off. The fuselage-drag variations due to jet interference may also be of the same order of magnitude as the fuselage-drag changes due to the addition of the nacelle or due to varying the nacelle location with the jet off. These results also indicate that it is not sufficient to consider only the location of the exit shock and shock from within the jet in the analyses of fuselage drag; rather, the entire jet-interference flow field must be considered.

Other results obtained in this investigation indicated that with the nacelle located outboard of the fuselage about 4 jet-exit diameters at a Mach number of 1.94 and about 3 jet-exit diameters at a Mach number of 2.41 and with jet off, the nacelle increased the fuselage drag to the highest value obtained; operating the jet decreased the drag. Conversely, with the nacelle at the most inboard position ($y/d_j \approx 1$) and with jet off, the nacelle interference reduced the fuselage drags; however, operating the jet increased the fuselage drag.

Examination of the data also showed that at a given longitudinal nacelle position, lowering the nacelle as it is brought inboard so as to maintain a constant radial distance from the fuselage axis resulted in changes in drag with changes in jet pressure that were dependent upon the vertical position of the nacelle.

MODEL INSTALLATION IN LANGLEY 9-INCH SUPERSONIC TUNNEL

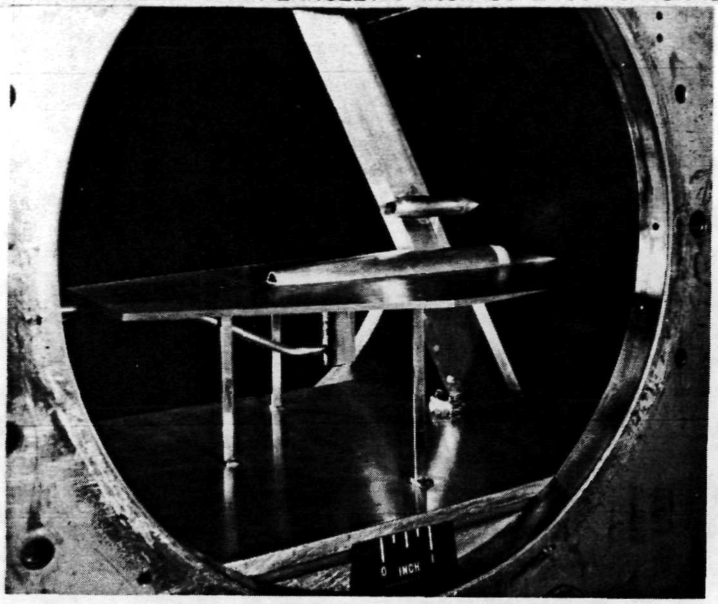

Figure 1

WING-NACELLE ASSEMBLIES
SONIC JET; NO BASE ANNULUS

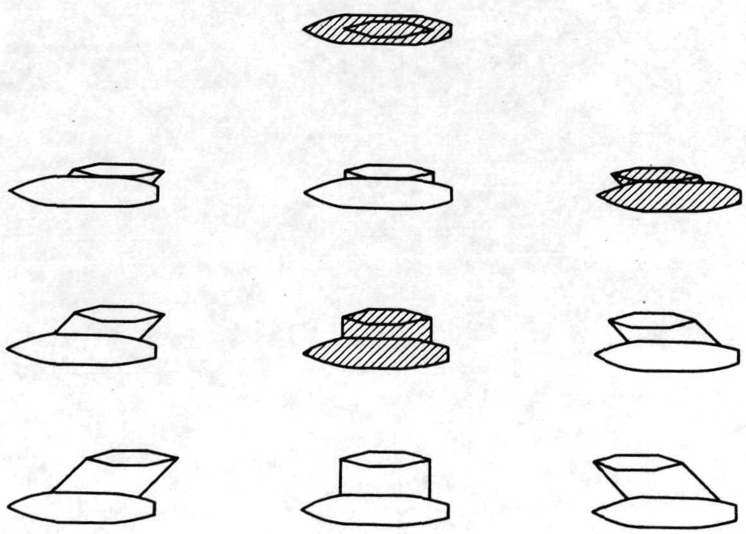

Figure 2

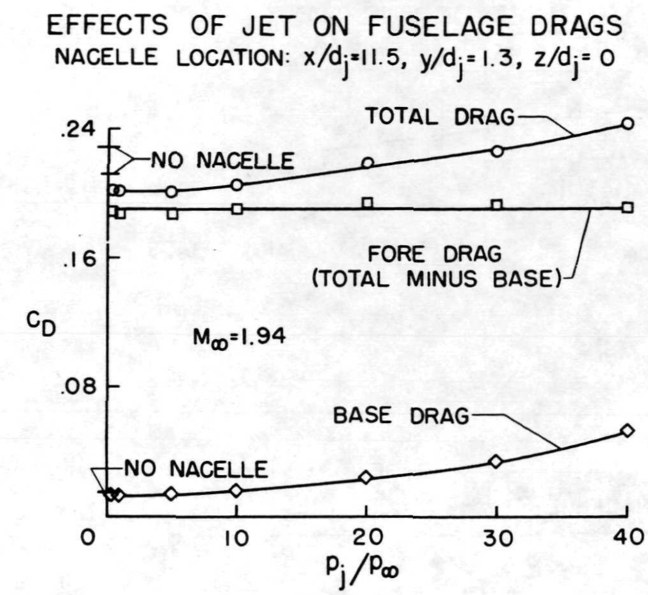

Figure 3

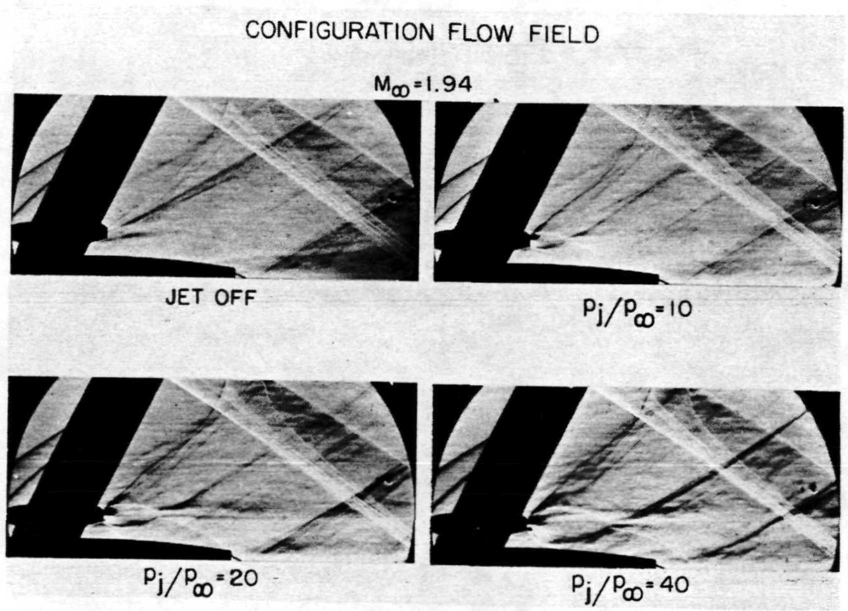

Figure 4

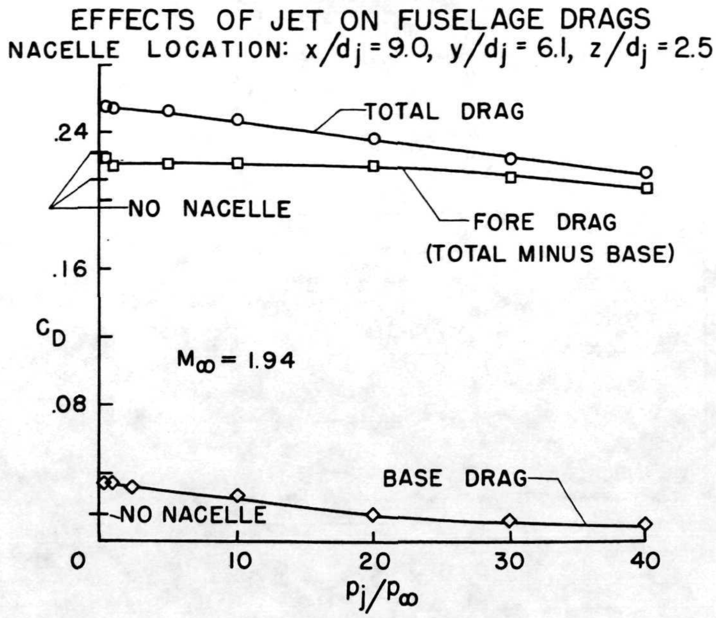

Figure 5

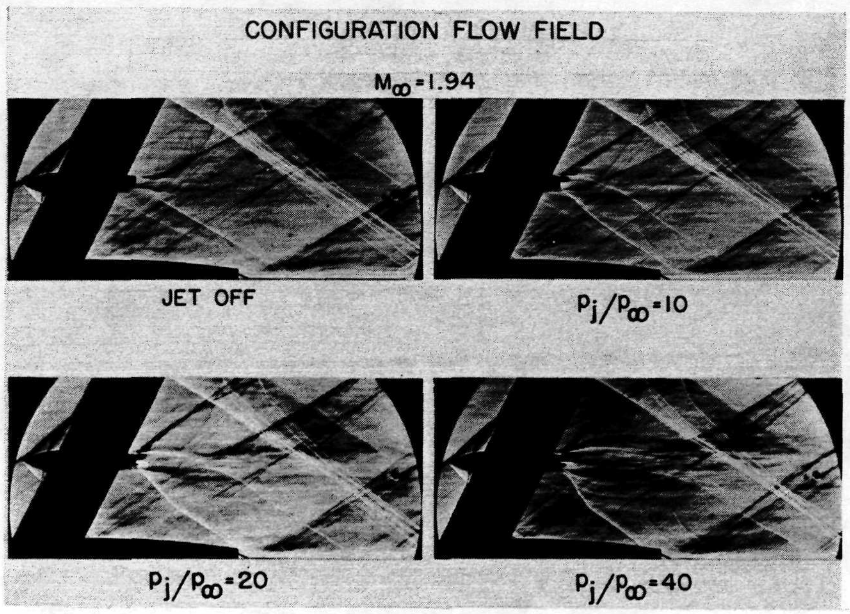

Figure 6

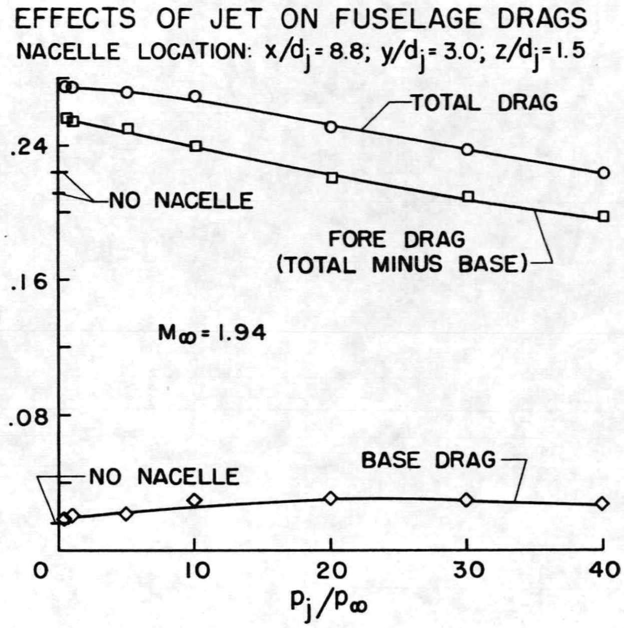

Figure 7

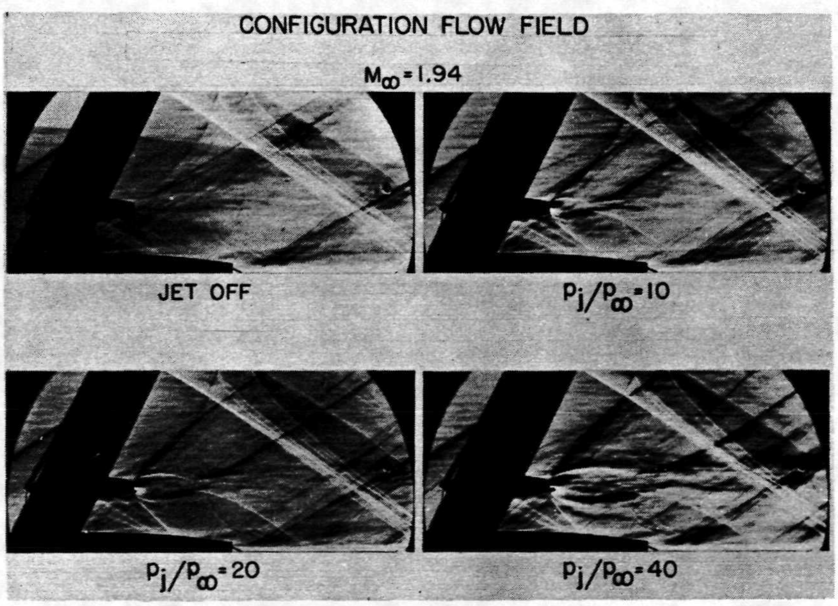

Figure 8

INTERACTION BETWEEN JETS AND VARIOUS AERODYNAMIC SURFACES

By Gerald W. Englert

Lewis Flight Propulsion Laboratory

INTRODUCTION

Advantages may at times be gained by positioning the jet exhaust nozzles at some location other than the rearmost extremity of the airplane. Inspection of a number of airplanes shows that the various surfaces in the near proximity of the exhaust jet may range over a wide variety of shapes and forms. For instance the engine fairing and jet from a wing-mounted nacelle (fig. 1) may interact with the flat surface of the wing and the curved surface of the fuselage. Jets exhausting from fuselage stations and from underneath tail booms may interact with surfaces which are concave and wrap around the jet, such as "sugar scoop" type exits, or with surfaces which are convex and bend away from the jet. Flat contours and wedge-shaped geometries may also be found in these locations.

The engine and exhaust system may be faired quite integral with the other nearby components such as jet exhaust from a fuselage station, or they may be somewhat separated from the airplane by means of slender struts, such as on some nacelle installations.

A preliminary systematic experimental study was made of the interaction between an exhaust jet and boattail (ref. 1) with various nearby surfaces and with various fairings between these surfaces and the boattail. The surfaces and fairings were all of simple contour for ease of interpretation of results. The trends obtained in this study may, however, aid in the understanding of configurations on actual aircraft.

SYMBOLS

A nozzle cross-sectional area at exit station, sq ft

A_m cross-sectional area based on maximum boattail diameter, sq ft

D drag, lb

N force normal to nozzle center line and in the plane of symmetry

19

M_0	free-stream Mach number
P	total pressure, lb/sq ft
p	static pressure, lb/sq ft
p_0	free-stream static pressure, lb/sq ft
q_0	free-stream dynamic pressure, lb/sq ft
R	nozzle exit radius, 0.167 ft
Y	distance from nozzle center line to line of intersection of surface middle chord with plane of symmetry
δ	jet deflection (fig. 5), deg

APPARATUS

A sketch of the main apparatus used to conduct this study in the Lewis 8- by 6-foot supersonic tunnel is shown in figure 2. The basic exit model was attached to the tunnel walls by means of hollow support struts which served to duct high-pressure air to a convergent nozzle. The external aerodynamic surfaces were mounted in view of schlieren apparatus. Both the nozzle center line and the aerodynamic surface were at zero angle of attack with respect to the free stream.

The surfaces studied were a flat plate, 60° and 120° wedges; 180° arc convex surfaces having radii of curvature equal to 1, 2, and 3 nozzle exit radii; and 60° and 180° arc concave surfaces having radii of curvature equal to 1.4 nozzle exit radii. Representative types of these various contours are shown in figure 3. All surfaces extended a distance of 9 nozzle exit radii downstream of the nozzle exit stations. The flat plate was 6 nozzle exit radii in width. The wetted surface area of the wedges was equal to that of the flat plate.

The maximum width of the fairings was equal to the maximum diameter of the boattail, which was equal to 2 nozzle diameters. These fairings had a length to width ratio of 3 up to the start of the base region and positioned the surfaces a distance of 2 nozzle exit radii away from the nozzle center line. The fairings were terminated as a sharp trailing edge, a blunt base, or a curved base.

DISCUSSION

Figure 4 shows a typical pressure distribution on a flat external aerodynamic surface with no fairings present. The distributions are similar to those in reference 2. The contour lines are lines of constant pressure coefficient. Differences in pressure coefficient between adjacent lines were generally kept at values of 0.025 so that the spacing of the lines is an indication of the pressure gradients. These data are for a total to static pressure ratio of 5 across the nozzle and a free-stream Mach number of 1.6.

A schematic model of the flow pattern in the interaction region obtained by use of schlieren apparatus is shown in figure 5. The ordinate of the pressure contour plot corresponds to the point on the external surface at the nozzle exit station.

Boattail shocks (fig. 5) are formed by the abrupt change of direction of the supersonic external flow as it intersects the jet stream (ref. 3). The intersections of the boattail shocks with the enternal surface are shown by the dashed lines in the contour plot.

Jet shocks may also impinge upon the surface. Jet shocks may be formed whenever a nozzle is operated at pressure ratios greater than design (ref. 4). When the external stream is supersonic these shocks are found to pass through the mixing zone and to extend well out into the free stream. The intersection of a jet shock with the surface is also shown by the dashed lines on figure 4.

Upstream of the location where the jet shock strikes the surface is another low-pressure zone which is formed by the aspirating effect of the jet, especially when the ratio of jet to free-stream velocity is greater than 1. Here are shown pressure coefficients near free-stream values. The pressures then abruptly rise to values of 0.25 in the jet shock region. Downstream of the shock intersection the pressure gradually decreases.

Figure 6 shows the effect of placing a blunt base fairing between the external surface and boattail. The fairing blocked the external flow somewhat from the interaction region; thus, it formed a much more pronounced low-pressure region near the nozzle exit station. This low pressure in conjunction with the high-pressure-shock interaction zone was influential in causing a pitching moment on the surface. The low-pressure zone also tended to attract the jet toward the surfaces. For convenience δ (fig. 5) will be defined as the angle of deflection of that portion of the jet up to the jet-shock intersection.

Figure 7 presents the influence of the various type fairings on jet deflection. As the base is blocked off by curved or blunt base fairings the effect of the low-pressure zones becomes apparent inasmuch as the initial part of the jet is well deflected toward the external surfaces. This trend was found to be true even at subsonic free-stream Mach numbers. It should be pointed out that as the jet progresses downstream and passes over the higher pressure interaction regions, the jet is deflected away from the surface and thus satisfies momentum-normal-force relations.

The low-pressure regions near the nozzle exit are also present on the trailing edge of the afterbody. These pressures (fig. 8) as expected are quite dependent on the type of fairing. Base drag then increased with increase of blockage of the external flow. The pressure distributions as shown on figures 4 and 6 were integrated to find the resultant normal force on the surface. When the external flow was supersonic (fig. 9) the resultant normal force was one of repulsion of the surface; that is, it was directed away from the nozzle axis of symmetry. The sum of the repulsion forces due to the high-pressure-shock interaction zones was thus greater than that of the low aspirated and base-pressure regions. Addition of blunt or curved base fairings appreciably lowered this net repulsion force because of the base-pressure effect on the upstream portion of the plate. This trend was generally true over the range of pressure ratios studied. These data were for a free-stream Mach number of 1.6.

When the free-stream Mach number was lowered from a supersonic to a subsonic value (fig. 10), the resultant normal force changed from one of repulsion to one of attraction of the external surface. This is due to the absence of strong shock interaction in the subsonic case and the well recognized differences of pressure area relationships between subsonic and supersonic flow. That is, the external air contracts as it flows between the diverging jet and the external surface. This contraction is accompanied by a reduction in pressure when the flow is subsonic and an increase is pressure when the flow is supersonic.

The results of changing surface contour to wedge-, concave-, and convex-shaped surfaces at a free-stream Mach number of 1.6 are shown in figure 11. All of these surfaces had equal projected areas in a direction normal to the nozzle axis. The wedge-shaped surfaces had a weaker shock interaction than the convex surface at all pressure ratios studied since its surface was bent away more from the jet. Neither surface experienced any appreciable aspiration effects or low-pressure zones as they were too well exposed to the external stream. The concave surfaces, however, enclosed the jet enough to sustain an appreciable region of low pressures which tended to offset the shock interaction and thus lower the repelling normal force below that of the convex surface at pressure ratios greater than 2.

Similar to the flat plate, no appreciable jet deflection was observed for any of these surfaces in the absence of blockage of fairings (fig. 12). This was found true over the whole range of pressure ratios measured (jet off to about 10).

The surfaces without fairings had their leading-edge stations in a plane with the nozzle exit. These surfaces could therefore have no effect on the boattail drag when the flow between them and the boattail was supersonic. As the surfaces were moved toward the nozzle axis of symmetry, however, the leading edges penetrated the subsonic boundary layer and wake region generated by the exit model and boattail. The surfaces at this point tended to increase the local boattail pressure and thus decrease drag (fig. 13). A strong hysteresis effect was observed as the surface was then gradually moved away from the boattail. The arrowheads on the curves denote the direction of travel of the surfaces.

CONCLUDING REMARKS

Appreciable differences in force coefficient resulted from changes in surface contour and type of fairing. Sizable jet deflection was observed when the external flow was somewhat blocked from the interaction region by fairings which caused low-pressure zones near their base. Problems arising from overheating of nearby surfaces due to hot exit gases may therefore become more serious if blunt or curved base fairings are used. The low base pressures tended to offset the repelling forces due to the shock intersection of the surfaces with the boattail and jet shocks at supersonic speeds. In passing from supersonic to subsonic flight speeds the shock interaction with the external aerodynamic surfaces may be decreased to such an extent that the resultant normal force may change from one of repulsion to one of attraction. This normal-force reversal may add to airplane control difficulties.

REFERENCES

1. Englert, Gerald W., Wasserbauer, Joseph F., and Whalen, Paul: Interaction of a Jet and Flat Plate Located in an Airstream. NACA RM E55G19, 1955.

2. Bressette, Walter E., and Faget, Maxime A.: An Investigation of Jet Effects on Adjacent Surfaces. NACA RM L55E06, 1955.

3. Cortright, Edgar M., Jr., and Schroeder, Albert H.: Investigation at Mach Number 1.91 of Side and Base Pressure Distributions Over Conical Boattail Without and With Flow Issuing From Base. NACA RM E51F26, 1951.

4. Love, Eugene S., and Grigsby, Carl E.: Some Studies of Axisymmetric Free Jets Exhausting From Sonic and Supersonic Nozzles Into Still Air and Into Supersonic Streams. NACA RM L54L31, 1955.

VARIOUS GEOMETRIES IN JET INTERACTION ZONES

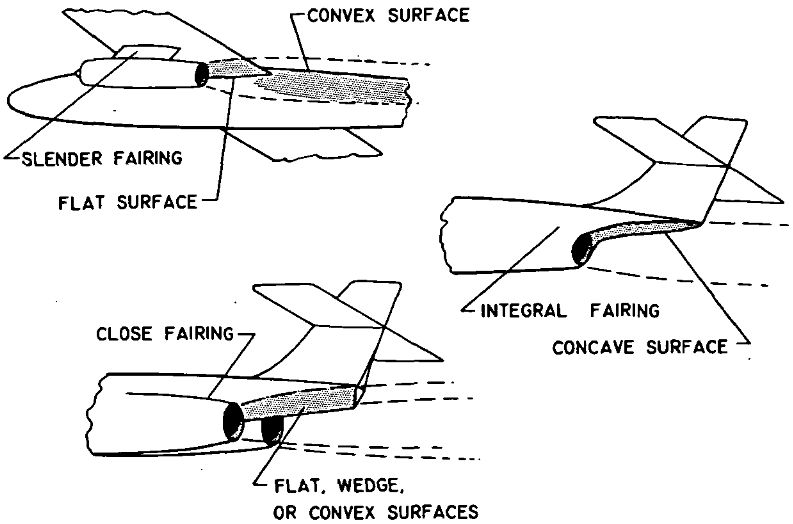

Figure 1

EXPERIMENTAL APPARATUS

8X6 FOOT TUNNEL TEST SECTION

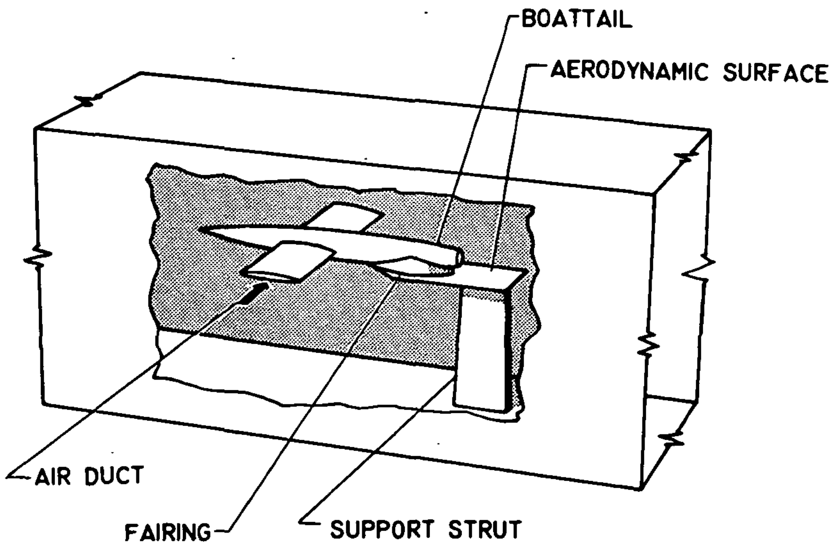

Figure 2

EXPERIMENTAL INTERACTION MODELS

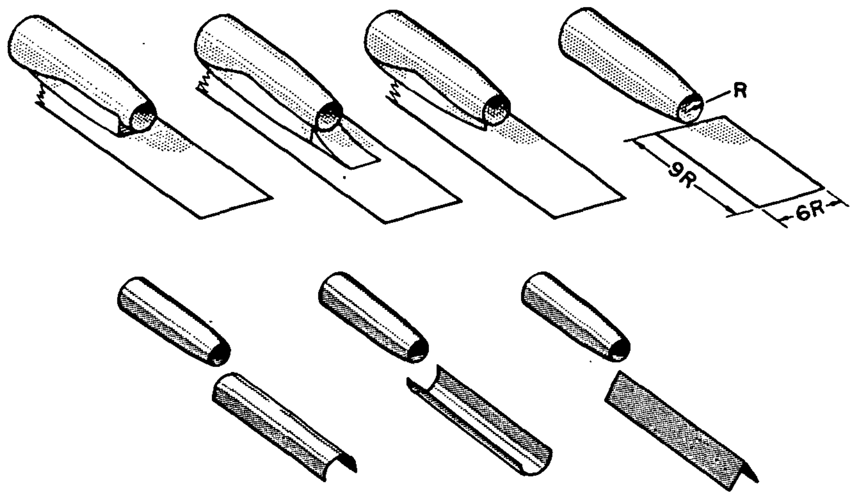

Figure 3

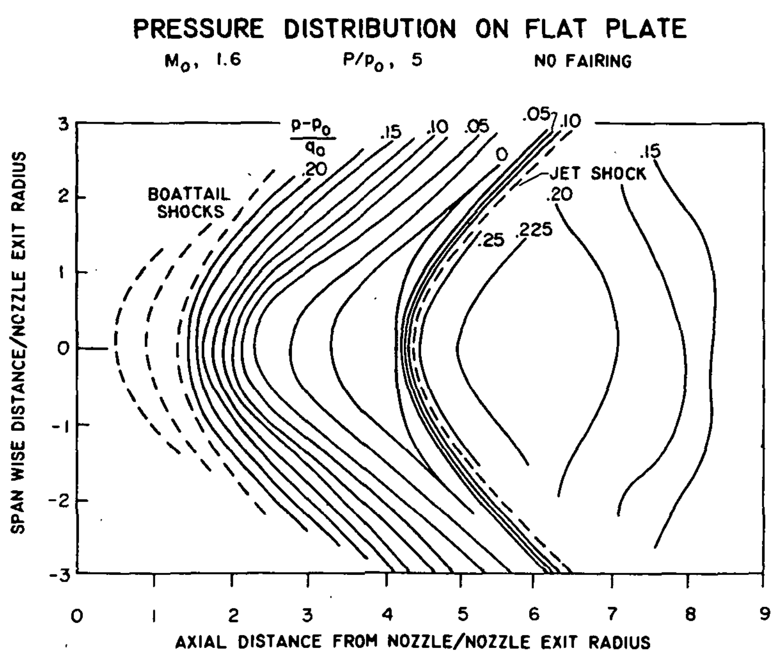

Figure 4

[redacted]

FLOW PATTERN IN INTERACTION REGION

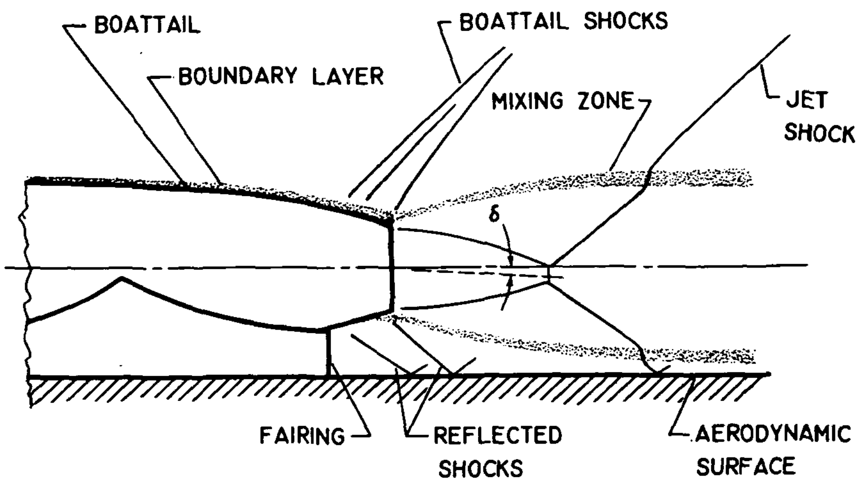

Figure 5

PRESSURE DISTRIBUTION ON FLAT PLATE

M_0, 1.6 P/p_0, 5 BLUNT BASE FAIRING

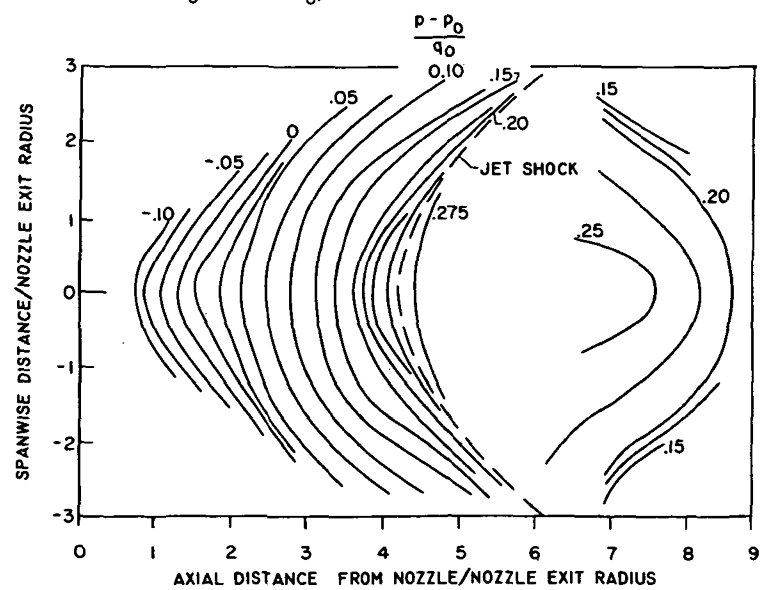

Figure 6

INFLUENCE OF FAIRINGS ON JET DEFLECTION

P/p_0, 5

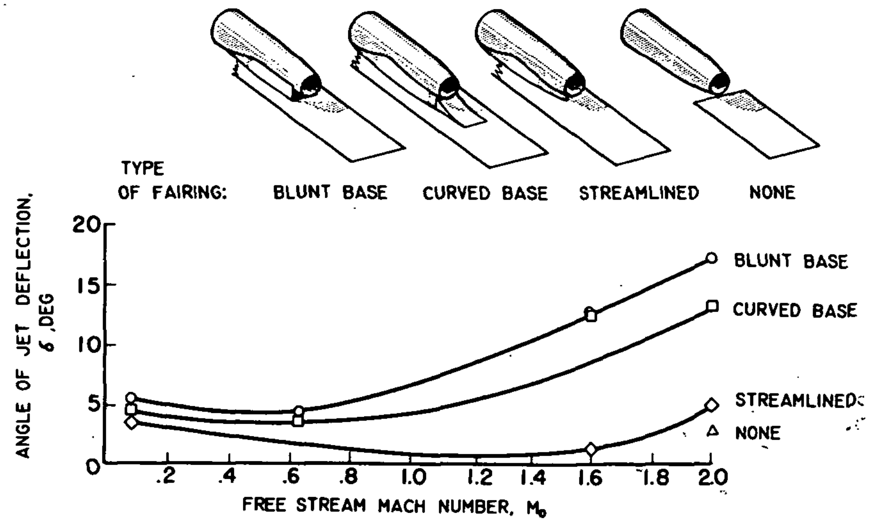

Figure 7

EFFECT OF CONFIGURATIONS ON BASE PRESSURE

M_0, 1.6

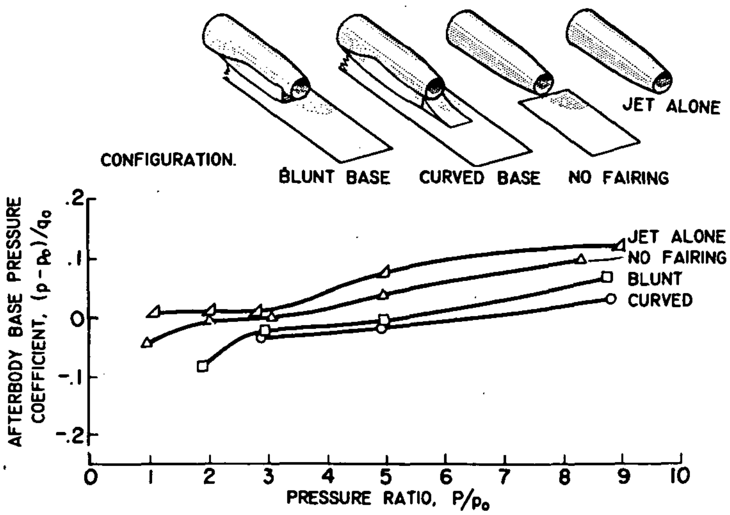

Figure 8

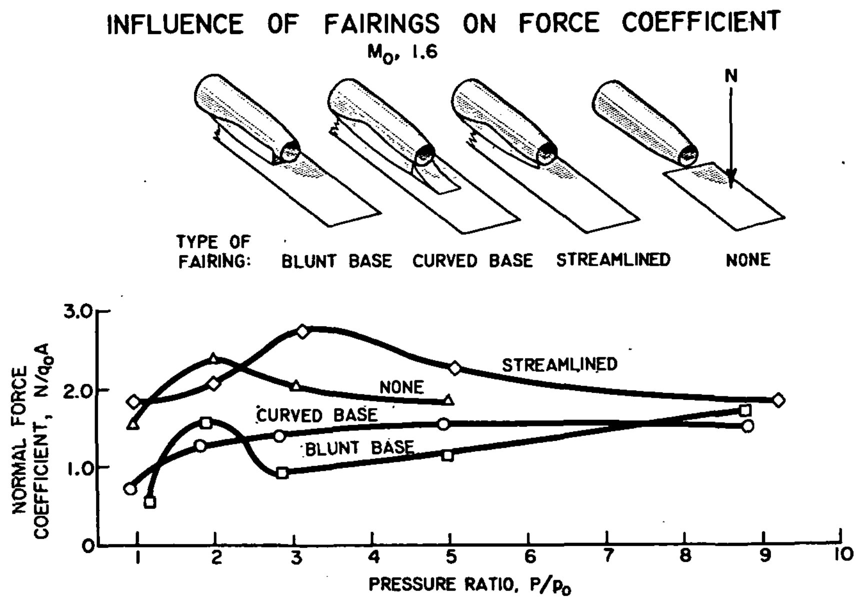

Figure 9

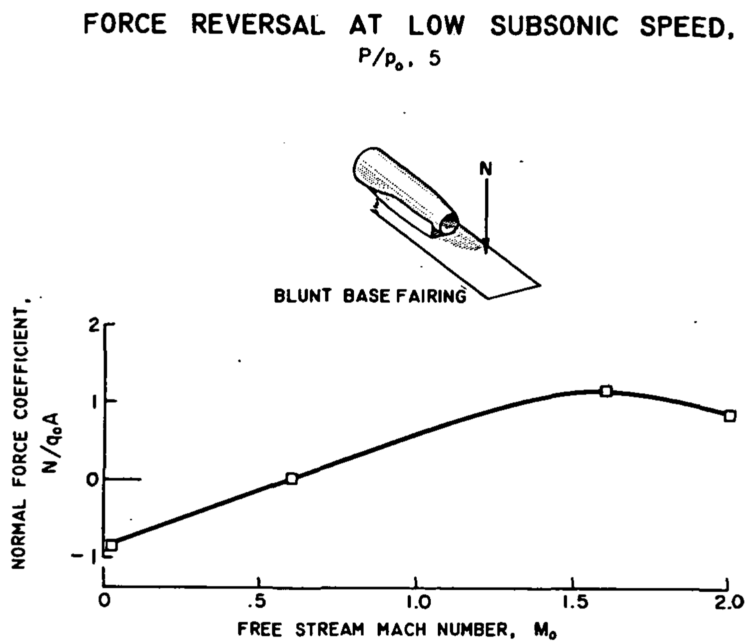

Figure 10

[redacted]

EFFECT OF SURFACE CONTOUR ON FORCE COEFFICIENT

M_0, 1.6

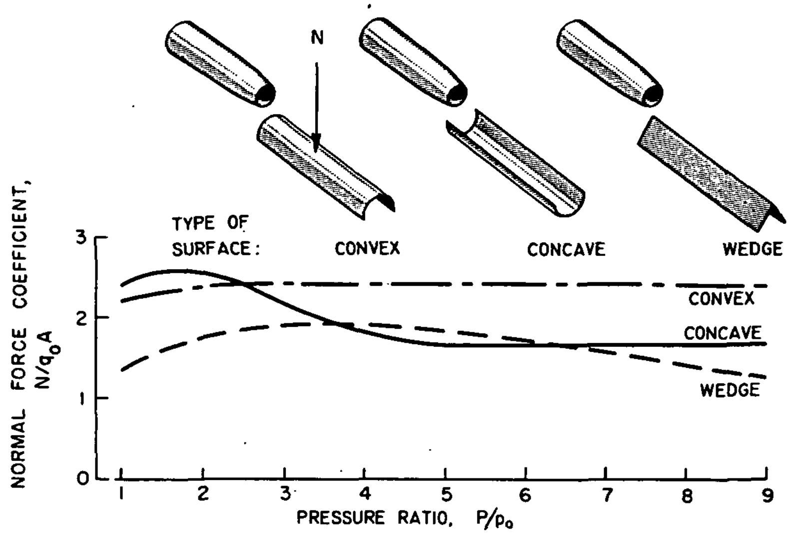

Figure 11

INFLUENCE OF SURFACE CONTOUR ON JET DEFLECTION

M_0, 1.6

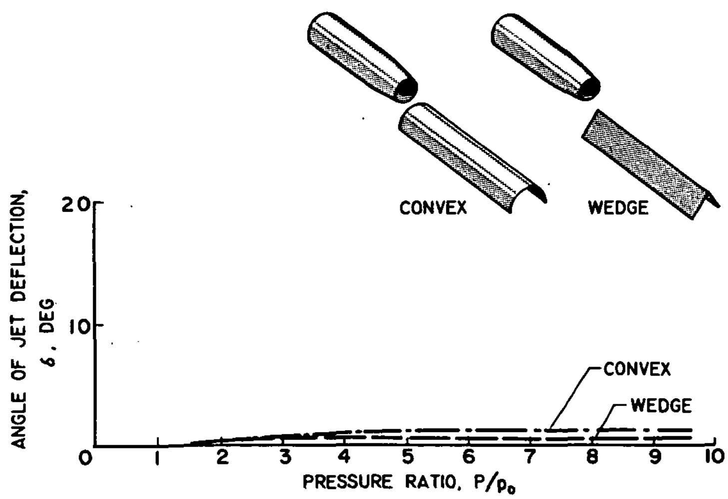

Figure 12

[redacted]

EFFECT OF SURFACE CONTOUR ON BOATTAIL DRAG

P/p_0, 2 M_0, 1.6

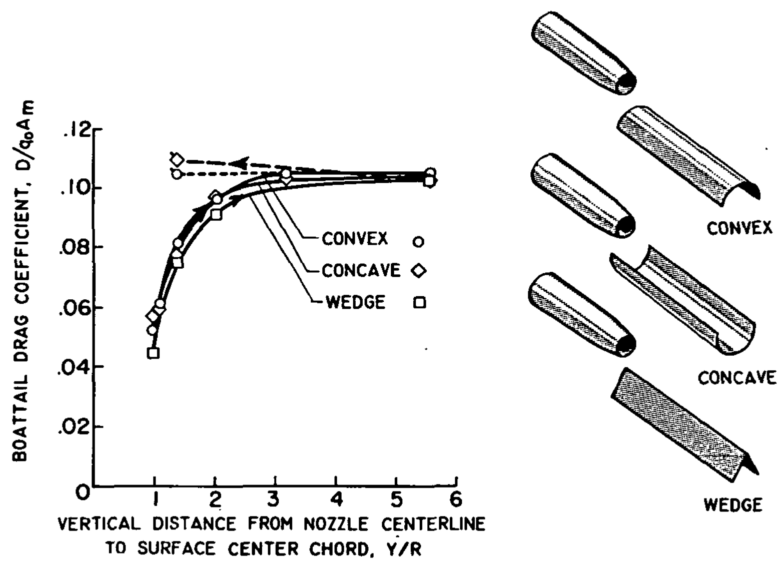

Figure 13

AIRPLANE AND MISSILE DYNAMICS

EFFECTS OF WING-BODY GEOMETRY ON THE LATERAL-FLOW ANGULARITIES AT SUBSONIC SPEEDS

By Frank S. Malvestuto, Jr., and William J. Alford, Jr.

Langley Aeronautical Laboratory

SUMMARY

The lateral flow characteristics in the region of a vertical tail have been investigated experimentally and theoretically at low subsonic speeds. The effects of changes in wing-body geometry such as nose position and shape, fuselage cross-sectional shape, and wing vertical position are described. The theoretical model which approximates the separated flow phenomena by a simple cylinder-vortex flow is described in an appendix.

The results indicated that a simultaneous change in nose fineness ratio and length caused an unfavorable change in the sidewash angles along the tail station. The addition of the wing to the bodies has a predominant effect on the lateral angularities, particularly at very high angles of attack. The fuselage cross-sectional shape has a marked effect on the lateral angularity produced by the wing-body combinations at low and moderate angles of attack. At high angles of attack where the effect of the wing is important, the change in lateral angularity associated with body cross-sectional shape still may be of the same order of magnitude as the sideslip angle of the airplane. The effect of raising the wing vertically on the circular cross-sectional body was to cause the sidewash angles along the tail station to become more negative.

INTRODUCTION

The estimation of the aerodynamic coefficients of an airframe, in particular the coefficients important in stability, require a knowledge of the flow fields associated with the airframe for a variety of flight conditions.

The modern airframe, characterized by a thin wing and a long body and in flight at high angles of attack, produces in many cases local fields of separated flow. These separated flows are regions of strong vortical motion or swirl and can impose irregular aerodynamic loadings on parts of the airframe that come under their influence.

The purpose of the present paper is to present some results of a low-speed experimental investigation, involving separated flow phenomena. The object of the experiment was to determine the effects of body and wing-body geometry on the lateral or sidewash angles along a line representing a possible vertical-tail station. In addition, the results of a theoretical investigation which considers the effects of separated flow are presented and are compared with experiment.

SYMBOLS

α angle of attack, deg

β angle of sideslip, deg

σ angle of sidewash, deg (see fig. 1)

β_T total angle of sidewash, deg $\left(\beta_T = \beta + \sigma\text{; see fig. 2}\right)$

v sidewash velocity, positive to the right when viewed from the rear, see figure 1, ft/sec

V_∞ free-stream velocity, ft/sec

V_c crossflow velocity in plane normal to fuselage center line, ft/sec $\quad V_c = V_\infty \cos \beta\sqrt{\tan^2\beta + \sin^2\alpha}$

M Mach number

z vertical distance from fuselage surface, positive up, ft

b_V span of vertical tail, ft

TEST CONFIGURATIONS

Presented in figure 1 are configurations used in investigations made at a velocity of 120 miles per hour (which corresponded to a Reynolds number of 7.6×10^6 based on the original body length) in the Langley 300 MPH 7- by 10-foot tunnel, in which flow-field surveys were made by utilizing a rake of six hemispherically headed pressure probes. Each probe was instrumented to measure local pitch and sideslip angularities and dynamic pressure. The location of the survey probes for the present investigation are shown by the dashed lines labeled b_V, which are indicative of a possible vertical tail location.

Presented in figure 1 are the plan and side views of the body and wing. The wing had 45° sweepback of the quarter-chord line, an aspect ratio of 4, a taper ratio of 0.3, and NACA 65A006 airfoil sections parallel to the fuselage center line. Also shown in figure 1 are the three different fuselage cross-sectional shapes investigated. These shapes included a circular cross section, a rectangular cross section with major length horizontal, and a rectangular cross section with the major length vertical. For the two rectangular cross sections, the major length was 50 percent greater than the minor length and all corners were rounded. For all three fuselages the axial distribution of cross-sectional area was identical.

For the fuselage of circular cross section, tests were also made to determine the effects of changes in nose length and nose shape. The original ogival nose was moved forward by 50 percent of its length by the insertion of a cylindrical section at its base. The second nose modification was to replace the original nose plus the cylindrical insert with an elongated ogive.

RESULTS AND DISCUSSION

Effect of Isolated Body Geometry

The effects of isolated body geometry, for the circular cross section, on the sidewash angularity along a vertical line representative of a possible vertical-tail location are presented in figure 2 for an angle of attack of 24° and a sideslip angle of 5°. Shown on the right are the calculated total angularity contours in a crossflow plane, that is, in a plane that cuts the body normal to its longitudinal axis.

The symbol V_c represents the component of the free-stream velocity in this plane, that is, the crossflow velocity. This velocity makes an angle with the vertical because the body is at an angle of sideslip. The contours are for the case where the flow has separated and can be approximately represented by a vortex pair symmetrically placed with respect to the direction of the crossflow velocity.

The locations and strengths of the vortices were estimated by a simple theoretical procedure that is described in the appendix. This procedure allows the estimation of the vortex paths and strengths from the nose to the rear of the body and is dependent upon a knowledge of the viscous force acting on the nose or expanding section of the body and of the viscous-force distribution along the cylindrical afterbody.

The effect of flow separation approximated in terms of the vortex pair is seen to be important. For example, along the dashed vertical line above the body where a vertical tail is generally located, the angularity is positive and increases in magnitude as the vortices are approached. It should be noted that these positive angularities are in a direction to decrease the angle of sideslip β of the airplane and are therefore generally considered favorable from stability considerations. Below the vortex pair the angles are seen to be negative and quite large in magnitude. In contrast to the positive angles, these negative angles tend to increase the angle of sideslip and are therefore considered unfavorable.

In order to show more clearly the magnitudes and directions of the sidewash angularities a cross plot of the theoretical values along the vertical line are presented on the left part of figure 2, along with the experimentally determined angles. The change in the sign of the lateral angularities mentioned earlier is now evident. The qualitative agreement between the experiment and predicted angularities implies that the separated flow is indeed vortical and that the assumed vortex model is useful in qualitative studies of the lateral flow.

Effect of Nose Length and Nose Shape

The effects of nose length and nose shape on the induced sidewash angle σ for the body of circular cross section are presented in figure 3. The conditions depicted are for an angle of attack of 16° and an angle of sideslip of 5°.

Consider first the effect of change in nose location. The nose was moved forward by 50 percent of its length by the insertion of a cylindrical segment at its base. The corresponding angularity variations with vertical distance are seen to show little effect of moving the original nose forward (fig. 3). The original nose plus the inserted cylindrical section were then replaced by a new nose of ogival shape and having the same length as the original nose plus the cylindrical section. This change in nose geometry has an effect on the induced sidewash angularity variation and moves the crossover point from positive to negative sidewash to a higher location relative to the crossover point for the original configuration and for the forward-nose configuration.

Preliminary theoretical studies indicate that the larger viscous force associated with this last mentioned modification of the nose section results in stronger vortices located higher in the nose-base plane relative to the other arrangements and hence results in the vortex pair remaining higher above the afterbody as they travel downstream, whereby the crossover point from positive to negative angles was higher, as shown in figure 3.

Effect of Body Cross-Sectional Shape

The effects of body cross-sectional shape on the induced sidewash angles along the vertical tail station for a moderate attitude ($\alpha = 8^{\circ}$, $\beta = 5^{\circ}$) are presented in figure 4. Shown on the left are the wing-off results and on the right are results with a 45° swept wing attached to the bodies to provide a midwing configuration. The wing-off results (fig. 4) indicate that for all cross sections, both circular and rectangular, the variation of the angularity with vertical distance is generally the same and the crossover from positive to negative angularities occurs at approximately the same vertical distance above the body. It should be noted, however, that the rectangular cross section with major length vertical gives results that are somewhat more favorable than the others.

From examination of the angularity variations for the midwing-body combination (fig. 4), the effect of wing-body interference for the different body cross sections is evident, especially on the lateral flow along the part of the tail near the body, where the tail loading is generally predominant. It is observed that the effect of this interference is to cause the induced angularity above the circular fuselage to become unfavorable (more negative) and to cause the induced angularity above the rectangular shapes to become more favorable (more positive.) Similar effects of wing-body interference for the different cross-section shapes have also been observed at an angle of attack of 16° and an angle of sideslip of 5°.

In order to give some indication of the angularity variation along the vertical-tail station at a rather high attitude, the results for both the wing-off and the midwing configurations at an angle of attack of 24° and an angle of sideslip of 5° are presented in figure 5. It is to be noted that for this high-attitude condition the body-alone results show a marked effect of body cross section on the flow separations and hence on the flow-angularity variations. Examination of the wing-body results for this high attitude (fig. 5) indicates that the wing vortex streams predominate. This result might be explained by noting that the wing downwash field accompanying the strong vortex flow of the wing will tend to deflect the body vortices and thereby minimize the effect of body vortex flow and, hence, of cross section on the lateral angularity along the vertical tail station. Unpublished wing-alone results follow very closely the angularity variations shown for the wing-body combinations and support the statements that for this high attitude the wing-flow effects are predominant.

A word of caution is necessary regarding the order of differences between the angularity characteristics for the different wing-body combinations, which appear small when compared with the corresponding wing-off angularity characteristics. It should be noted that these apparently small differences for the wing-body combination are, in some cases, of the order of 5°, which is the angle of sideslip of the configuration. These differences therefore can contribute to significant changes in the force and moment contribution of a vertical tail immersed in the flows of the different wing-body combinations.

Effect of Wing Height

The effect of vertical position of the wing on the sidewash angularities along the vertical tail station are presented in figure 6 for the circular-cross-section wing-body combinations. Shown on the left of the figure are the characteristics for the moderate attitude of $\alpha = 8^{\circ}$, $\beta = 5^{\circ}$ and on the right, the characteristics for the high attitude of $\alpha = 24^{\circ}$, $\beta = 5^{\circ}$. Presented for comparison are the body-alone characteristics for the same attitudes.

At the moderate attitude the high-wing position is seen to be the least favorable. The wing in this position tends to deflect somewhat the body vortices. At the high attitude the predominant effect of the wing is again evident. It should be observed that the higher the wing is placed on the body, the higher are the wing vortices relative to the vertical-tail station; and hence the crossover from positive to negative angularity occurs at a higher location along the vertical-tail station. This higher location of the crossover point results in a greater portion of the angularity distribution being negative along the tail station and, therefore, an increased unfavorable effect on stability. It should also be noted that, at the high attitude, the effect of wing vertical position (fig. 6) is stronger than the effect of body cross-sectional shape (fig. 5).

CONCLUDING REMARKS

An experimental and theoretical investigation of the lateral flow characteristics in the region of a vertical tail has been discussed. The following results are indicated:

1. The concept of a simple vortex model is useful in the qualitative analysis of the separated-flow phenomena associated with wing-body configurations.

2. The effect of increasing the length and fineness ratio of the body nose is to cause an unfavorable contribution to the lateral angularities along the vertical-tail station.

3. The addition of a wing to the body has a predominant effect on the lateral angularities but the effect of fuselage cross-sectional shape produces changes in the sidewash angles that may be of the same order of magnitude as the sideslip angle of the airplane.

4. The effect of raising the wing vertically, on the circular-cross-section body, is to cause the sidewash angles along the vertical tail to become more unfavorable.

APPENDIX

ESTIMATION OF VORTEX STRENGTH AND POSITION IN BASE PLANE OF EXPANDING NOSE SECTION

The object of this appendix is to discuss briefly an approximate method now under way at the Langley Laboratory for estimating the position and strength of a vortex pair that is assumed to represent the vortex wake pattern that exists on the lee side of a slender, pointed nose, lifting body of revolution. The wake pattern is by no means as simple, as is evident from visual studies of the flow made by water-tank and vapor-screen techniques (refs. 1 to 4). For slender, pointed-nose bodies, however, the development of the flow over the expanding nose section seems to consist of two well-defined spiral surfaces of separation that grow continuously as the expanding nose section is traversed from the front to the rear. The predominant effect of this type of separation seems to occur in planes normal to the longitudinal axis of the body, that is, in the so-called crossflow planes.

In a crossflow plane, fixed in space, that is traversed by the body, the type of flow separation under discussion appears similar to the separated flow about a two-dimensional circular contour that is impulsively set in motion. This association between the body crossflow and the two-dimensional cylinder flow was pointed out and discussed in references 1 and 2.

For the present purpose it is tacitly assumed that the flow separation behind a slowly expanding two-dimensional cylinder moving in a downward direction is a good approximation to the flow separation in the fixed crossflow plane traversed by the body. The implication here of course is that along the body the separation surfaces grow conically in the axial direction. In addition, the assumption is made that the spiral separation surfaces of vorticity can be approximated by a potential vortex pair that are symmetrically located with respect to the direction of the component of the resultant free-stream velocity in the crossflow plane. (See fig. 2.) With these assumptions in mind, it is clear that the simplified analytical model that will be used to approximate the actual flow is that of a two-dimensional, cylinder-vortex flow in which the cylinder expands and the flow changes homogeneously with time. It is to be emphasized that the use of a cylinder-vortex-flow model has been considered by other authors to depict the flow over lifting slender bodies. (See refs. 4 to 7.)

Consider now the local aerodynamic force acting on the cylindrical trace of the body in the fixed crossflow plane as the body passes through this plane. With respect to a system of axes fixed to the downward moving two-dimensional cylinder in this plane, the local vertical force dN for zero sideslip may be expressed as follows:

$$dN = dN_o + \frac{D}{Dt} I + \rho \frac{D}{Dt} \Sigma z_i \Gamma_i \tag{1}$$

where

N_o	slender-body potential-flow force derived by Munk
$-I$	momentum of fluid induced by vortices in the presence of the body
z_i	location of each vortex relative to the fluid
D/Dt	differential operator
t	time, sec
Γ_i	circulation of each vortex (Γ is absolute value)

The term $\frac{D}{Dt} I$ can be considered as the negative of the total rate of change of the fluid momentum induced by the vortices in the presence of the body (ref. 8). The last term may be considered as the concentrated force that would be required to move the vortices with a given velocity for unsteady motion (ref. 8).

For the cylinder-vortex flow under consideration, the momentum (I) is given by:

$$I = -2\rho_\infty \frac{a^2}{r} \sin \gamma \, \Gamma + 2\rho_\infty r \sin \gamma \, \Gamma \tag{2}$$

where

a	local radius of body in crossflow plane
r	distance from center of body to vortex element
γ	acute angle between r and crossflow direction

Now if, as stated previously, it is assumed that the flow separation is conical, the vortex pair remains stationary with respect to the expanding contour of the moving cylinder in the fixed crossflow plane and hence the concentrated force term of equation (1) is equal to zero.

There remain to be determined the relations between the vortex strength Γ and the position (r, γ) of the vortices. In the fixed crossflow plane the equilibrium position of the vortex pair can be obtained from the Foppl relations which relate the locus of positions of the symmetrical vortex pair to the strength of the vortices required for the vortex pair to remain stationary. The Foppl relations may be expressed as

$$2r \sin \gamma = r - \frac{a^2}{r} \tag{3}$$

which is the equation of the curve that the vortices must lie on for equilibrium. The relation

$$\begin{aligned} \Gamma &= 2\pi V_c r\left(1 - \frac{a^2}{r^2}\right)^2\left(1 + \frac{a^2}{r^2}\right) \\ &= 2\pi V_c r H(\lambda) \end{aligned} \tag{4}$$

gives the strength of the vortices in terms of their position and the crossflow velocity V_c.

The substitution of the necessary preceding relations into expression (1) for the local force and replacement of dN_o by $2\rho\pi V_\infty^2 \cos \alpha \sin \alpha \, a\left(\frac{da}{dx}\right)dx$ yields $\left(\text{with } x = tV_\infty \cos \alpha \text{ as the axial coordinate}\right)$:

$$\begin{aligned} dN = {} & 2\rho\pi V_\infty^2 \cos \alpha \sin \alpha \, a \, da \, + \\ & 4\rho\pi V_\infty^2 \cos \alpha \sin \alpha\left(\frac{1}{\lambda} - 1\right)(1 - \lambda^2)H(\lambda)a \, da \end{aligned} \tag{5}$$

By use of the relation $C_N = \dfrac{N}{\frac{1}{2}\rho V_\infty^2 \pi a_b^2}$, equation (5) can be nondimensionalized and yields, after integration from $a = 0$ to $a = a_b$ (the radius of the base of the nose section):

$$C_N = 2 \cos \alpha \sin \alpha + 4\left(\frac{1}{\lambda} - 1\right)\left(1 - \lambda^2\right)H(\lambda)\cos \alpha \sin \alpha \tag{6}$$

Equation (6) gives the total force acting on the nose section in terms of the position of the vortex pair, since γ, the angular coordinate of the position, is according to relation (3) a function of $\lambda = \frac{a}{r}$. From equation (6), it is then possible to determine the position of the vortex pair provided a knowledge of C_N or of $(C_N - 2 \cos \alpha \sin \alpha)$, the viscous force, is available. (See refs. 3 and 9.) Once r and γ are known the vortex strength Γ can be determined from equation (4) and the lateral velocities and angularities can then, of course, be calculated by classical methods.

If the body has a cylindrical aftersection, the strength and position of the vortices determined in the base of the expanding section will serve as initial conditions for estimating the vortex path along the afterbody, using the procedures set forth by Jorgensen and Perkins in reference 4. This method requires a knowledge of the viscous force distribution along the afterbody sections.

The reader should be cautioned that the preceding first-order results for the estimation of vortex position and strength are tentative. Detailed examination of the assumptions and approximations made are now underway, particularly in regard to the effect of (a) the replacement of the surfaces of separation by a symmetrical vortex pair which introduces a multi-valuedness in the pressure field that is not correct and (b) the stability of the vortex pair for conical type flows.

It should also be noted that the preceding analysis is for zero sideslip. The derived relations are, of course, valid for the sideslip condition provided that the crossflow velocity V_c for sideslip is used and the vortices located symmetrically with respect to this sideslip crossflow velocity direction. The force C_N is the force parallel to this direction.

REFERENCES

1. Allen, H. Julian: Pressure Distribution and Some Effects of Viscosity on Slender Inclined Bodies of Revolution. NACA TN 2044, 1950.

2. Gowen, Forrest E., and Perkins, Edward W.: A Study of the Effects of Body Shape on the Vortex Wakes of Inclined Bodies at a Mach Number of 2. NACA RM A53I17, 1953.

3. Allen, H. Julian, and Perkins, Edward W.: Characteristics of Flow Over Inclined Bodies of Revolution. NACA RM A50L07, 1951.

4. Jorgensen, Leland H., and Perkins, Edward W.: Investigation of Some Wake Vortex Characteristics of an Inclined Ogive-Cylinder Body at Mach Number 1.98. NACA RM A55E31, 1955.

5. Michelson, I.: On the Motion of Vortices Behind a Circular Cylinder. TM-377, U.S. Naval Ordnance Test Station.

6. Lagerstrom, P. A., and Graham, M. E.: Aerodynamic Interference in Supersonic Missiles. Rep. No. SM-13743, Douglas Aircraft Co., Inc., July 1950.

7. Kuchemann, D.: A Non-linear Lifting-Surface Theory for Wings of Small Aspect Ratio with Edge Separations. Rep. No. Aero. 2540, British R.A.E., Apr. 1955.

8. Sedov, L. I.: On the Theory of the Unsteady Motion of an Airfoil. NACA TM 1156, 1947.

9. Kelly, Howard R.: The Estimation of Normal-Force, Drag, and Pitching-Moment Coefficients for Blunt-Based Bodies of Revolution at Large Angles of Attack. Jour. Aero. Sci., vol. 21, no. 8, Aug. 1954, pp. 549-555, 565.

SKETCH OF WIND-TUNNEL MODEL USED FOR SIDEWASH-ANGULARITY MEASUREMENTS

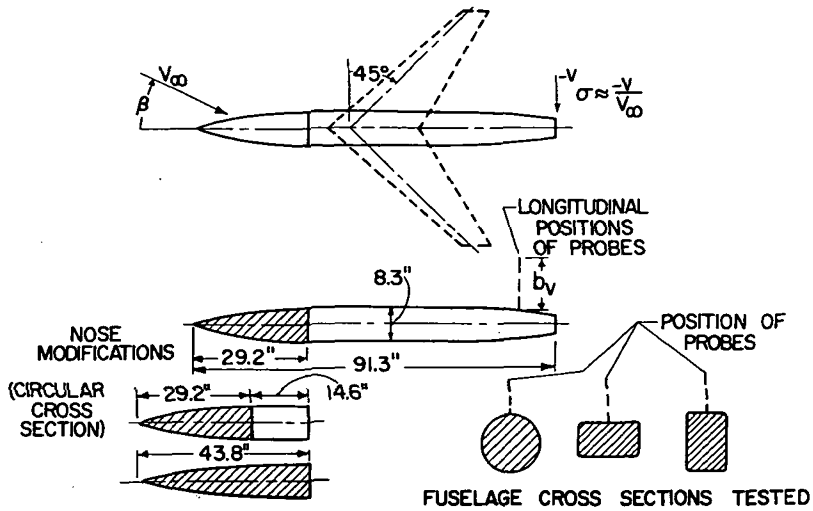

Figure 1

ILLUSTRATION OF CALCULATED TOTAL SIDEWASH ANGULARITIES IN BODY CROSS-FLOW PLANE

CIRCULAR CROSS-SECTION; $\alpha = 24°$, $\beta = 5°$

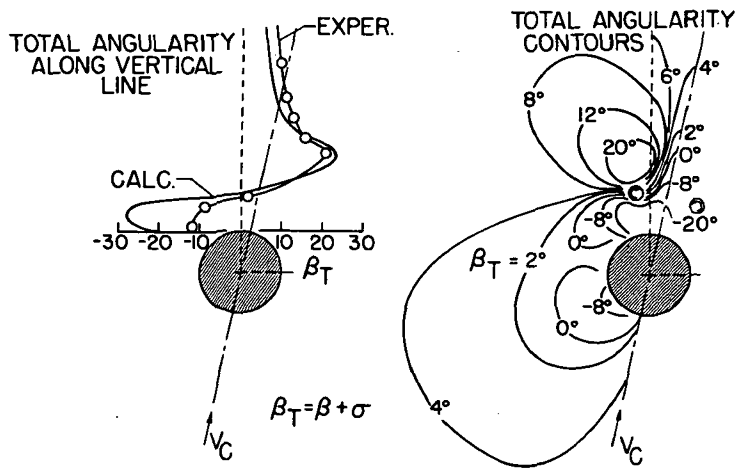

Figure 2

EFFECT OF BODY NOSE CHANGES ON SIDEWASH ANGULARITY
BODY OF CIRCULAR CROSS-SECTION

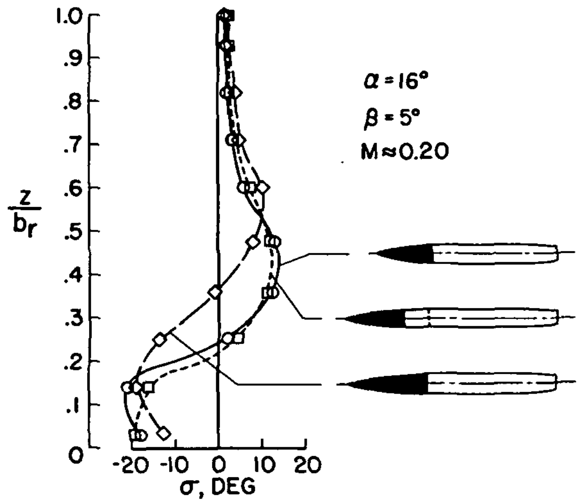

Figure 3

THE EFFECT OF BODY CROSS SECTION ON SIDEWASH ANGULARITY
M ≈ 0.20

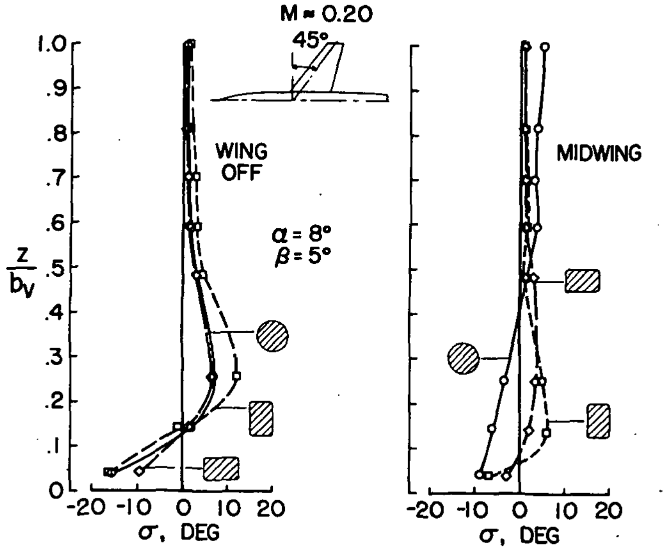

Figure 4

THE EFFECT OF A BODY CROSS SECTION ON THE SIDEWASH ANGULARITY

M≈0.20; $\alpha = 24°$; $\beta = 5°$

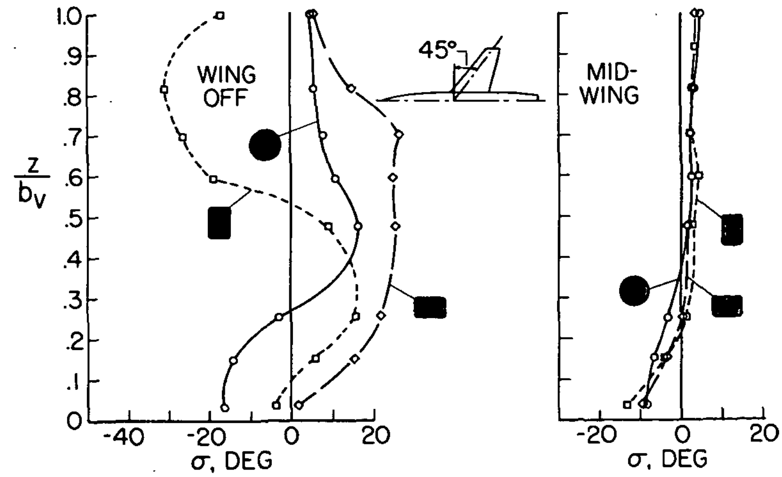

Figure 5

EFFECT OF WING HEIGHT ON SIDEWASH ANGULARITY

BODY OF CIRCULAR CROSS-SECTION; 45° SWEPT WING

M≈0.20

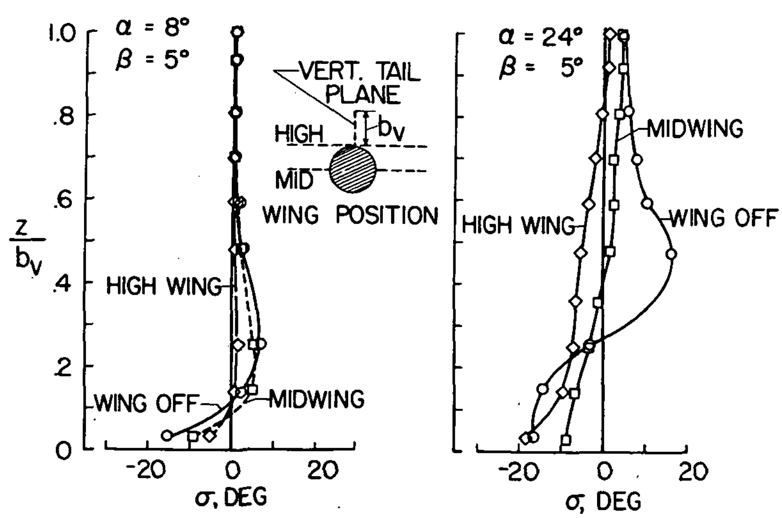

Figure 6

SUPERSONIC WAVE INTERFERENCE AFFECTING STABILITY

By Eugene S. Love

Langley Aeronautical Laboratory

SUMMARY

Some of the significant interference fields that may affect stability of aircraft at supersonic speeds are briefly summarized. Illustrations and calculations are presented to indicate the importance of interference fields created by wings, bodies, wing-body combinations, jets, and nacelles.

INTRODUCTION

In aircraft and missile configurations one aerodynamic surface more often than not lies within the region of influence of the flow field generated by another aerodynamic surface or by a jet. When this occurs, the flow field is regarded as an interference flow field. This paper will attempt to cover, in a general way, interference flow fields that may affect stability, not with the idea that these fields have not been known to exist, but rather with the intent of drawing increased attention to their relation to stability.

The interference from vortex flows is known to have important effects upon stability; however, because of time limitations, vortex flows and viscous effects will, with minor exceptions, be neglected.

SYMBOLS

A	aspect ratio
b	span
c	chord
C_{m_α}	slope of pitching-moment curve
C_{n_β}	rate of change of yawing-moment coefficient with sideslip
C_Y	side-force coefficient

D	body diameter
d_j	jet diameter at jet exit
M_∞	free-stream Mach number
M_j	jet Mach number at jet exit
p	local static pressure
p_j	static pressure at jet exit
p_∞	free-stream static pressure
q	local dynamic pressure
q_∞	free-stream dynamic pressure
S	surface area
x	longitudinal coordinate
y	spanwise coordinate
z	vertical coordinate
α	angle of attack
β	sideslip angle; also $\sqrt{M_\infty^2 - 1}$
γ_∞	specific-heat ratio of free stream
γ_j	specific-heat ratio of jet
δ	flow-deflection angle; also bluntness angle of airfoil
ϵ	upwash angle
θ_N	nozzle divergence angle
θ_s	shock angle

DISCUSSION

Wings

Consideration will be given first to the interference flow fields arising from the wings. Figure 1 presents the portion of a two-dimensional wing interference flow field bounded by the leading-edge and trailing-edge shocks, generally referred to as the direct field of the wing as contrasted with the indirect field, which is defined as the field downstream of the trailing-edge shock. Superposed on the direct field are a body and tail surfaces. Insofar as the tail surfaces only are concerned, the effects of the indirect wing interference field are, in general, not large until the direct field comes in close proximity of the tail surfaces. As illustrated by the direct field, the effect of increasing Mach number is to sweep the field back over the tail surfaces as shown. When this occurs, the properties of the flow field in which the vertical tail yaws and horizontal tail pitches may be significantly altered; as a result, large changes in the tail contribution to stability may be expected. The variation in dynamic pressure in the direct field is indicated at several positions by the ratio of local to free-stream dynamic pressure q/q_{∞} and is seen to be appreciable.

Figure 2 shows the direct flow field at $M_{\infty} = 3.0$ with the configuration at an angle of attack. A comparison of the field with that given in figure 1 for the same semiwedge angle of the leading edge δ and the same thickness ratio t/c shows that the effect of increasing α is to decrease the dynamic pressures in the upper-surface interference field, the converse being true for the lower-surface interference field. Also, increasing α tends to move the direct field off the tail surfaces. In contrast with the effect of angle of attack, when the wing is placed at incidence as might occur with missiles (illustrated in the sketch at the bottom of fig. 2), the direct field from the upper surface moves well onto the upper tail surfaces.

In order to emphasize the effects of angle of attack and to show in proper perspective the effects of bluntness and of thickness on the dynamic pressures in the direct field, figure 2 also shows the configuration with a flat-plate wing $\left(\delta = 0^{\circ},\ \frac{t}{c} = 0\right)$. Thickness distribution and thickness ratio alter, for the most part, the distribution of dynamic pressure, whereas the wing bluntness is the primary factor in determining the general magnitude of the dynamic pressures. This effect may be readily visualized at $\alpha = 0^{\circ}$ by considering the thickness ratio to be reduced by thinning the center portion of the wing while holding the bluntness, or semiwedge angle δ of the wing, constant. Obviously, the Mach number at which this type of interference is encountered is dependent upon overall geometry; for example, the low position of the horizontal tail indicated in figure 1 at $M_\infty = 3.0$ would be well removed from the trailing shock of the direct field. The present trend in the design of supersonic aircraft is toward much shorter tail lengths than pictured; for such configurations the direct fields would be encountered at lower Mach numbers than implied by these examples. This type of interference diagram can also be of assistance in estimating, for example, where a given amount of vertical tail area might be added to obtain the most favorable gain in yaw stabilization, or in assessing the downwash in the region of tail surfaces immersed in the direct field.

An experimental illustration of the effects of Mach number and angle of attack shown in figures 1 and 2 may be seen in figure 3 which presents schlieren photographs of a configuration of similar geometry in which the two-dimensional portions of the wing flow field are accentuated in the profile views.

In the lower-surface interference flow field for $M_\infty = 3.0$ and $\alpha = 20^\circ$ shown in figure 2, a significant loss in dynamic pressure remains near the downstream edge of the interference field, although the local Mach number is obviously still less than the free-stream value. This loss may be traced directly to the shock losses. Some discussion of the shock losses, or the "q-loss" effects thus seems in order. In figure 4 curves for constant local shock inclination θ_s are presented which show the dynamic-pressure ratio q_1/q_∞ as a function of the free-stream Mach number M_∞ for the particular case of the flow downstream of the shock having returned to a Mach number M_1 that is essentially equal to M_∞; that is, $M_1 = M_\infty$ without being affected by a change in shock inclination. Such conditions occur only in two-dimensional flows, but these flows serve to illustrate the point in simplified form. A two-dimensional surface satisfying these conditions is shown in the upper right of figure 4. In the region immediately downstream of the centered expansion, but upstream of the reflected influence from the shock, the only significant difference of the local flow from the free-stream flow is a loss in dynamic pressure. If a stabilizing surface (as illustrated by the flat plate) were yawed in this region, the side force acting on this surface would be reduced by the factor q_1/q_∞ as compared to that acting on the same surface yawing in the free stream. Therefore, the surface area must be increased by the ratio q_∞/q_1; that is, $S_1 = \frac{q_\infty}{q_1} S_\infty$, if the surface is to realize the same side force that is obtained by the original surface area S_∞ in free stream. For example, at $M_\infty = 3.5$ and $\theta_s = 48^\circ$ $(\delta \approx 30^\circ)$ the area of the surface would need to be doubled. Downstream of the initial reflection from the shock the required increase in area would be lessened according to the influence of the attenuation in shock strength.

With regard to shock strength, there is the inherent requirement that, for q-loss effects to be significant, the shock must be strong. Values of the shock-strength parameter $(M_\infty \sin \theta_s - 1)$ are superposed on the q-loss curves. Since normal shocks have zero strength at $M_\infty = 1$, it is clear that, in general, the q-loss effect becomes important only at the higher free-stream Mach numbers. The shock-strength parameter affords a simple and convenient means of judging the necessity for considering the possibility of significant q-loss effects.

This simplified illustration of the q-loss effect indicates that conditions will arise where it will be necessary to account for, or compensate for, this effect upon stabilizing surfaces by increasing stabilizing-surface area, improving the lift effectiveness of the surface, or by juggling the q-loss through changes in configuration design. For realistic configurations such as those shown in the lower right of figure 4, the determination of the q-loss and the necessary compensation requires more elaborate calculations. However, it may be reasoned that at the higher Mach numbers a blunt-nose configuration having a detached shock may produce a large q-loss and a large gradient in q-loss; canard surfaces placed well forward would be subjected to these losses. A typical supersonic aircraft configuration as illustrated might experience significant q-loss effects upon its tail surfaces as a result of the total loss through shocks from the nose, canopy, and wing leading and trailing edges, although the individual shocks might have relatively small q-loss effects. In recent tests of a configuration having a short fuselage, the vortex layer stemming from the intersection of the nose and canopy shocks was observed to pass across the vertical tail. Since this vortex layer divides regions of different q-loss, this phenomenon may prove to be another factor for consideration. For configurations at high angle of attack, the q-loss and also the q-gain (such as shown previously for the lower surface of wings at angle of attack) may be expected to have important effects.

Beyond Mach numbers of the order of about 1.3, the downwash that exists at the trailing edge of an airfoil at lower speeds reverts to upwash. This upwash is considered in figures 5 and 6 for two-dimensional airfoils and fields of flow. The magnitude of the initial upwash ϵ_i immediately downstream of the trailing edge of a symmetrical airfoil is shown in figure 5. The initial upwash increases with Mach number, angle of attack, and bluntness; at the higher Mach numbers and angles of attack, it is apparent that the initial upwash of even a flat plate cannot be considered negligible.

The upwash that is likely to occur in the vicinity of a downstream horizontal tail as a result of the presence of the wing is of particular importance. In this regard, the relative magnitude of the initial upwash for the flat plate and blunt airfoil may be misleading and must be moderated because of the manner in which the downstream interference from the wing flow fields reduces the upwash. At the top of figure 6 the downstream upwash for a flat plate is illustrated. As shown by the sketch, the initial upwash from the trailing edge of the flat plate does not decrease until some distance x_i is reached, at which point the wing interference field begins to reduce the upwash. An example of the variation of x_i/c with Mach number is shown to the right of the sketch. The effect that increasing Mach number has in increasing the initial upwash, as was shown in figure 5, is seen to be offset by the decrease in the downstream extent of the initial upwash. It is important to note, however, that at $M_\infty = 5$ the initial upwash angle, which is about 4° for this angle of attack, would remain for about a half chord length downstream before it would begin to decrease.

For the thick airfoil the initial upwash begins to decrease immediately behind the trailing edge since the wing interference field comes into play immediately, as shown by the sketch in the lower portion of figure 6. An example of the decay in upwash for a thick airfoil is shown to the right of the sketch. From this example, one may conclude that at large α and high Mach numbers, tail surfaces that are closely coupled to the wings will experience several degrees of upwash. Further, the large upwash near the trailing edge of the wing is important to wing-body interference.

Bodies

The interference flow fields created by bodies will be considered next. Figure 7 presents isobar-streamline fields for a slender and a bluff body. (The field for the slender body was obtained by extensions to the characteristic calculations of ref. 1.) For clarity only a few of the calculated isobars and streamlines are shown for the bodies. It is apparent that the aerodynamic characteristics of surfaces immersed in such fields will be altered considerably, as will be shown subsequently. The field for the bluff body is quite different from that for the slender body. In the bluff-body field the division line of pressure gradients that has its orgin at the point of tangency on the body surface is sharply defined. Ahead of this line the pressures in the field are falling; behind it they are rising.

Inasmuch as the nose shock establishes the forward limit of the body interference field, it is of interest to examine the forward limit of the field as given by the exact shock and by the commonly employed approximate limits given by the shock based on the nose angle only and by the free-stream Mach line. Figure 8 presents a comparison of the exact and the approximate limits at several Mach numbers for the bluff body of the preceding figure. One readily observes that large errors may be introduced by either of the approximate limits. An example of the reliability of the exact shock calculations may be seen by comparing the calculated exact shock for $M_\infty = 1.94$ with the upper left-hand schlieren photograph of figure 3. The wing and forebody are the same for both the calculation and the photograph; the experimental nose shock is seen to touch the forward wing tip as predicted by the exact calculation. Figure 8 also shows that the division line of pressure gradients experiences significant changes in inclination with Mach number.

As an aid in illustrating the effect of flow inclinations produced by the body, the flow inclination has been calculated at several Mach numbers for the point in the field designated in figure 8 by the circled cross $\left(\frac{x}{D} = 4.18, \ \frac{y}{D} = 2.50\right)$. In the upper left of figure 9 the calculated inclination at this point is presented as a function of Mach number. In general, the flow inclination increases with free-stream Mach number until the exact shock passes behind the point at $M_\infty \approx 2.63$. This change of flow inclination with Mach number explains for the most part some results of a skewed-store investigation conducted at the Langley Laboratory (ref. 2). These results at Mach numbers of 1.41 and 1.96 are shown in the lower half of figure 9. The side-force coefficient of the store in the presence of the wing-body combination is shown for the skewed and unskewed condition. The order of magnitude of the skew necessary to produce zero side force at $\alpha = 0^\circ$ is in general agreement with that indicated to be necessary from a consideration of the flow inclination created by the body alone (upper left). Some differences are to be expected because of the omission of the effects of the presence of the wing and because of differences in body geometry. The experimental store investigation of reference 2 also showed that increasing the forebody length (no change in forebody shape) reduced the amount of skew necessary for $C_Y = 0$ at $\alpha = 0^\circ$. This variation is also to be expected as indicated by the calculated change in flow inclination with forebody length shown in the upper right of figure 9.

Wing-Body Interference

The interference between bodies and wings is considered in this section. Wing-body interference has been and remains the subject of extensive theoretical and experimental studies and is perhaps the most familiar type of interference problem. Therefore, only a few aspects of the problem are considered herein. It is instructive to examine first a general representation of wing-body interference. Figure 10 presents some examples of experimental results in the low angle-of-attack range from tests at the Langley Laboratory (refs. 3, 4, and 5) of wing-body combinations which show, in additive form, the ratio of the slope of the pitching-moment curve of the components and of the interference quantities to the slope of the pitching-moment curve of the wing-body combination where:

W_e exposed wing alone

$W(B)$ wing in presence of body

$w(b)$ interference on wing due to body

B body alone

$b(w)$ interference on body due to wing

WB wing-body combination

C_{m_α} slope of pitching-moment curve

For emphasis, the regions corresponding to interference quantities have been cross-hatched, single cross-hatching denoting a positive moment contribution and double cross-hatching meaning a negative moment contribution.

For most aircraft configurations that are subjected to significant interference at low angle of attack, the interference on the body due to the wing $b(w)$ is more important than the interference on the wing due to the body $w(b)$, as indicated in these examples. Particular attention is drawn to the interference of the body due to the wing and to its variation with the ratio of wing span to maximum body diameter b/D. Since this interference is always stabilizing it is apparent that the wing-lift carryover effects upon the body are more important than the tip effects which are destabilizing. As b/D increases, both the wing-lift carryover effects and tip effects move rearward on the body, and eventually the tip effects move off the body. At a value of b/D corresponding to the condition for which tip effects would vanish (as illustrated by the sketches) the interference on the body due to the wing reaches a maximum; further increase in b/D reduces the interference as the result of loss of wing-lift carryover.

The relation of the wing interference field to this interference on the body due to the wing is illustrated in figure 11 for a series of rectangular wing and body combinations for which the chord of the wing was held constant. The upper portion of the figure presents only the interference on the body due to the wing (in the same form as shown in fig. 10) as a function of b/D for several Mach numbers, and as a function of Mach number for several values of aspect ratio A (and span-diameter ratio). The point to be noted is not so much the similar areas represented by the interference quantities, whether expressed as a function of b/D or of M_∞, which may result from no more than a fortuitous choice of scales of the abscissas, but rather the similar trends in the interference pitching moment with either b/D or M_∞. Because of these similar trends, it is suspected that the results may be correlated on the basis of equal areas of influence created on the body by the wing. On this basis a simple expression may be derived that will give equal areas of influence on the body from a strip on the wing for rectangular wing and cylindrical body combinations. This expression is $M_i \approx \left(\frac{A^2}{2\beta}\right)\left(\frac{D}{b}\right)c^3 p_i$ where M_i is the interference pitching moment, p_i is the average interference pressure, and β is the speed parameter $\sqrt{M_\infty^2 - 1}$. Inasmuch as the chord is constant for the wings of this series, the results may be correlated by the factor $\left(\frac{A^2}{2\beta}\right)\left(\frac{D}{b}\right)$ with the implication that differences observed in such a correlation are indicative of the changes in p_i due to Mach number. The correlation is shown at the bottom right and serves to substantiate the idea that the observed similarities in trends of the interference pitching moment are due primarily to simulation of equivalent areas of influence.

Figure 12 presents schlieren photographs illustrating a type of interference that stems from wing-body junctures and is apparently peculiar to lifting conditions. The top two photographs at $M_\infty = 2.62$ show that under lifting conditions a shock may originate near the trailing edge of the wing at the wing-body juncture as the result of wing-body interaction and viscous effects. Shocks of this type can interact with the horizontal tail and affect the longitudinal stability. With decreasing Mach numbers such shocks tend to become more diffuse, as shown at $M_\infty = 2.22$; at $M_\infty = 1.62$ separation occurs ahead of the wing-root juncture, and the shocks and downstream pressure gradients associated with this separation alter the loading on the wing.

Jets and Nacelles

The theoretical interference flow field produced by a supersonic jet exhausting into a supersonic stream is illustrated in figure 13 in isobar-streamline form. (The basic characteristic net for fig. 13 is given in ref. 1; the isobars were computed from this net.) The initial conditions are indicated in the figure. The static-pressure ratio of about 9 corresponds to the upper limit of operation of turbojet with afterburner or to the lower or moderate range of rocket operation. Attention is directed to the large gradients in pressure and to the flow inclinations that occur in the ambient field as a result of the jet presence. Of particular importance in evaluating the limits of the interference field is the large curvature of the exit shock. This curvature is accentuated for jet interference fields by the transition from a two-dimensional turning at the jet exit to a three-dimensional turning away from the jet exit.

Figure 14 gives some examples of the calculated pressures that the interference field of figure 13 would create on a flat plate immersed in the field at several radial positions. Only the pressure immediately downstream of the interaction of the exit shock with the plate are presented. It is at once apparent that the jet may create large loads on the plate and that the regions of influence may be extensive. The importance of the plate position in the field and its angle of attack are equally apparent. These theoretical indications are in qualitative agreement with experimental findings. (See ref. 6, for example.)

If the plate considered in figure 14 were a stabilizing surface, the jet would be expected to have a significant effect upon stability. At the top of figure 15 the calculated jet and interference field has been reproduced to scale in conjunction with a supersonic aircraft configuration. For an inboard nacelle location as shown, the jet interference field would interact with both the vertical and horizontal tail surfaces. For an outboard location there would be less need for considering the jet-interference field, but the nacelle-interference field would have a direct effect. An experimental example of nacelle interference obtained in tests at the Ames Laboratory is shown at the bottom of the figure. The lateral stability derivative C_{n_β} is presented as a function of Mach number for the configuration shown on the right with nacelles off and for the complete configuration. At low Mach numbers the nacelle interference produces a significant loss in C_{n_β}, whereas at the higher Mach numbers, where the nacelle nose shock interacts with the vertical tail, this loss is reduced.

CONCLUDING REMARKS

A summary has been presented of some of the more important interference fields that may affect stability at supersonic speeds. Illustrations and calculations are included to show the importance of interference fields created by wings, bodies, wing-body combinations, jets, and nacelles.

REFERENCES

1. Schäfer, M.: Steady Supersonic Flows. British M.A.P. Völkenrode. Reps. and Translations No. 995, Apr. 15, 1948. Reps. and Translations No. 996, May 1, 1948.

2. Guy, Lawrence D.: Loads and External Stores at Transonic and Supersonic Speeds. NACA RM L55E13b, 1955.

3. Coletti, Donald E.: Investigation of Interference Lift, Drag, and Pitching Moment of a Series of Triangular Wing and Body Combinations at a Mach Number of 1.94. NACA RM L55I14, 1955. (Prospective NACA paper.)

4. Coletti, Donald E.: Investigation of Interference Lift, Drag, and Pitching Moment of a Series of Triangular Wing and Body Combinations at a Mach Number of 1.62. NACA RM L55B25, 1955.

5. Coletti, Donald E.: Investigation of Interference Lift, Drag, and Pitching Moment of a Series of Rectangular Wing and Body Combinations at Mach Numbers of 1.62, 1.93, and 2.41. NACA RM L52E26, 1952.

6. Bressette, Walter E.: Investigation of the Jet Effects on a Flat Surface Downstream of the Exit of a Simulated Turbojet Nacelle at a Free-Stream Mach Number of 2.02. NACA RM L54E05a, 1954.

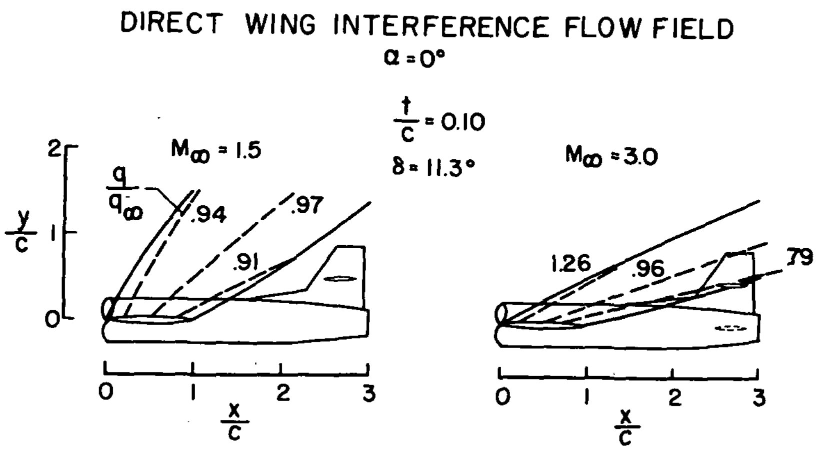

Figure 1

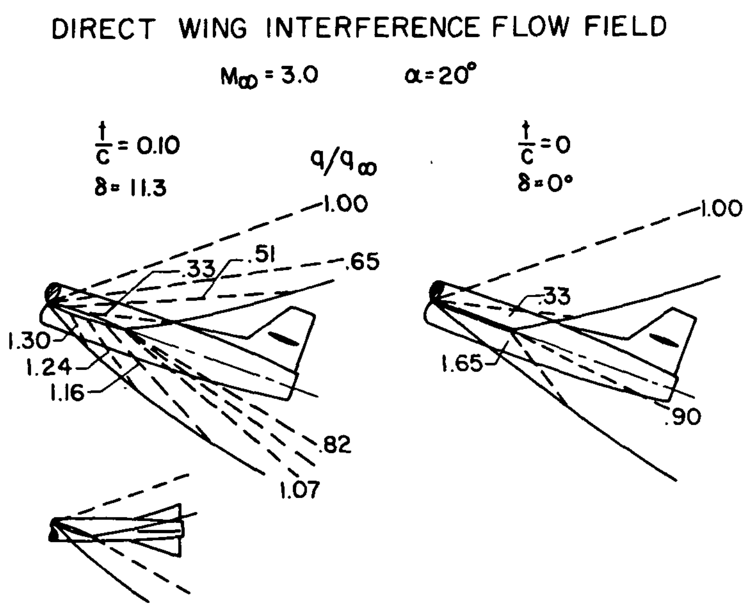

Figure 2

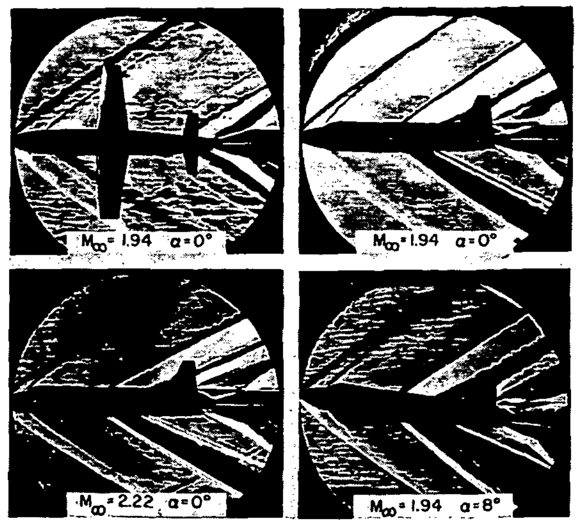

Figure 3

"q-LOSS" EFFECT

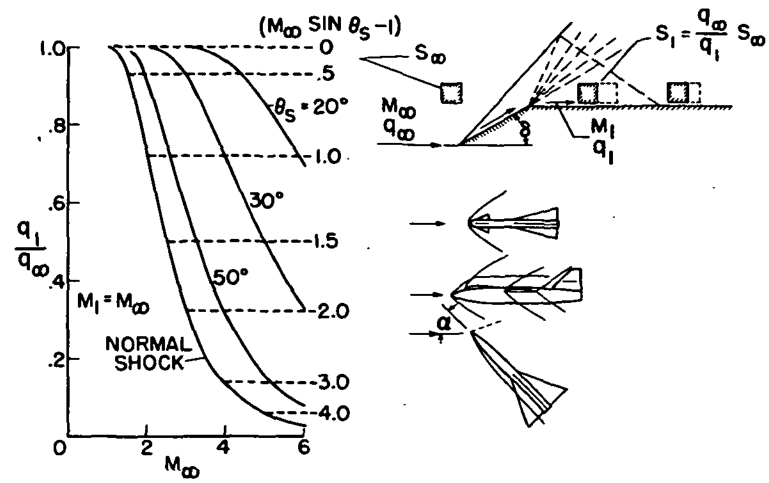

Figure 4

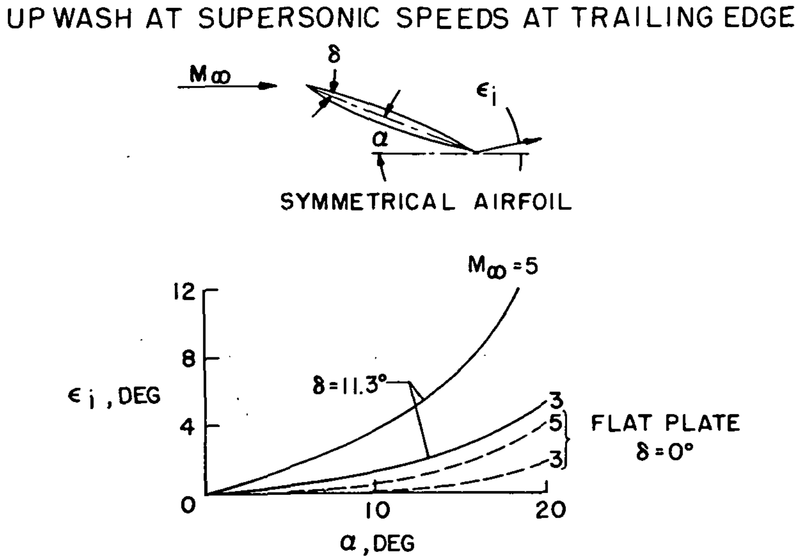

Figure 5

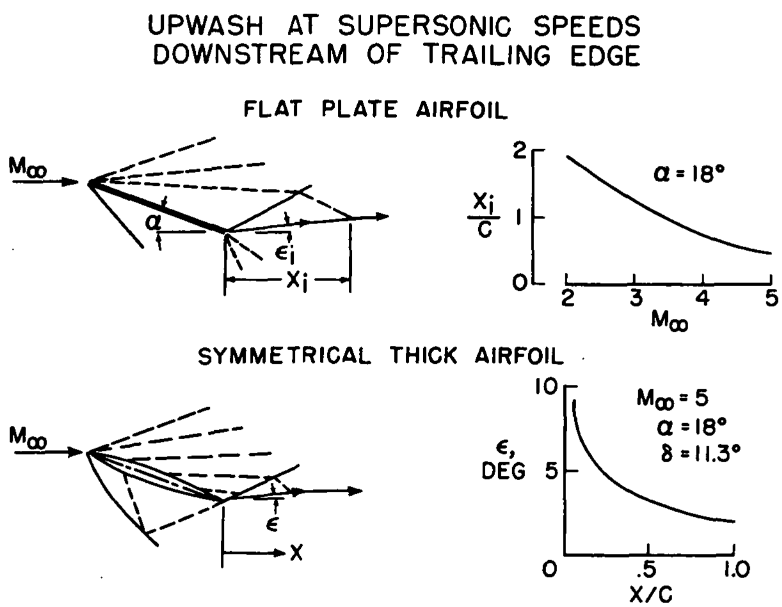

Figure 6

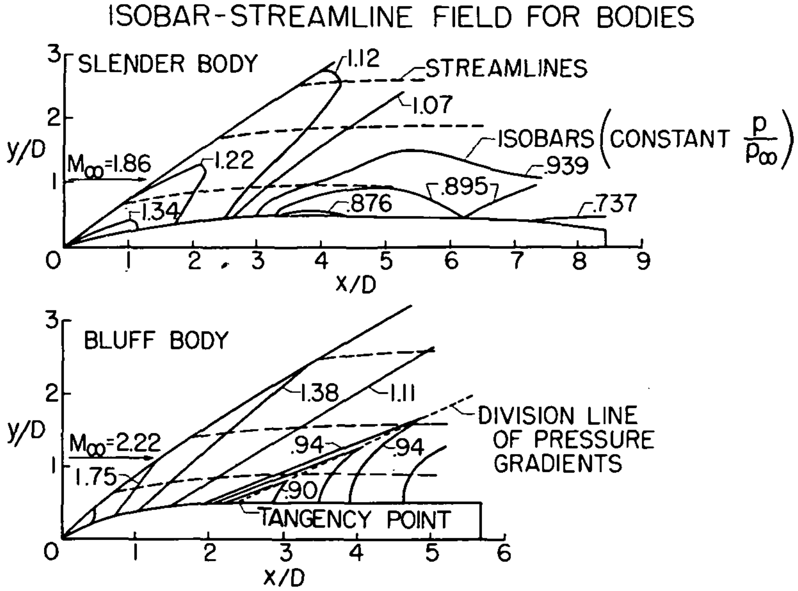

Figure 7

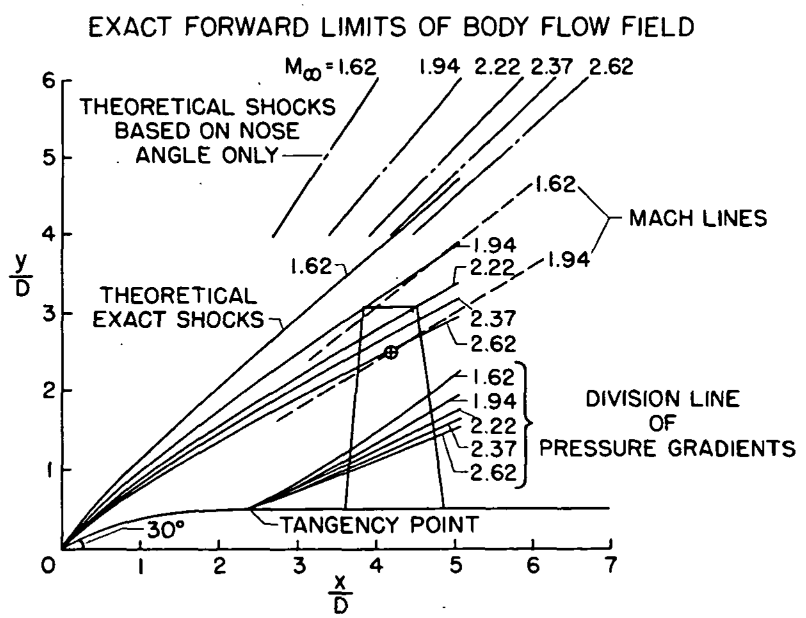

Figure 8

[redacted]

FLOW INCLINATION FROM BODY INTERFERENCE FIELD

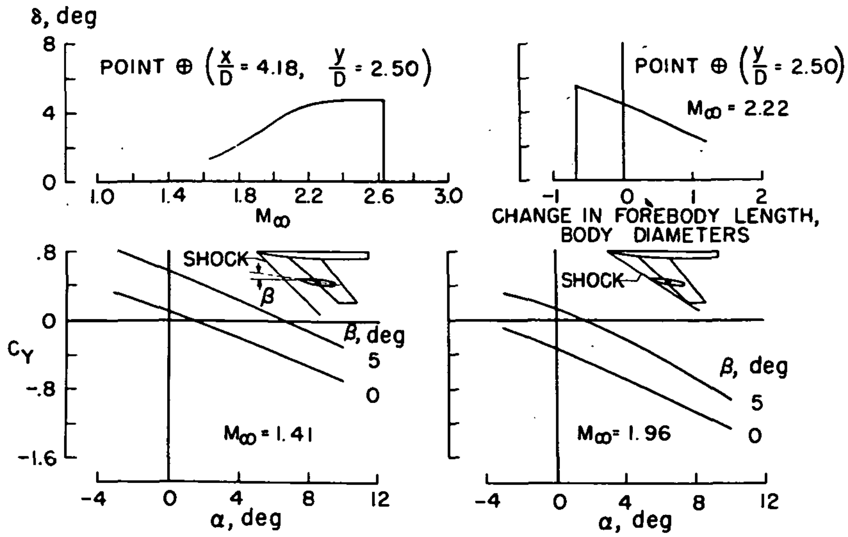

Figure 9

WING-BODY INTERFERENCE

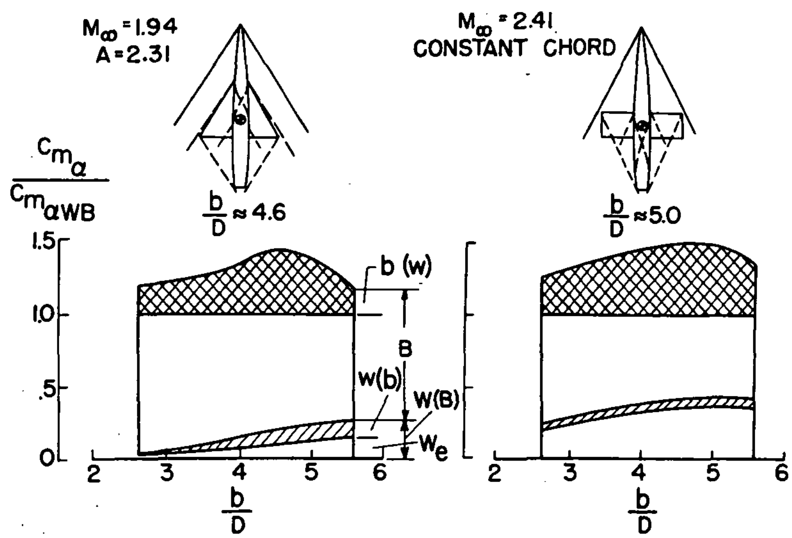

Figure 10

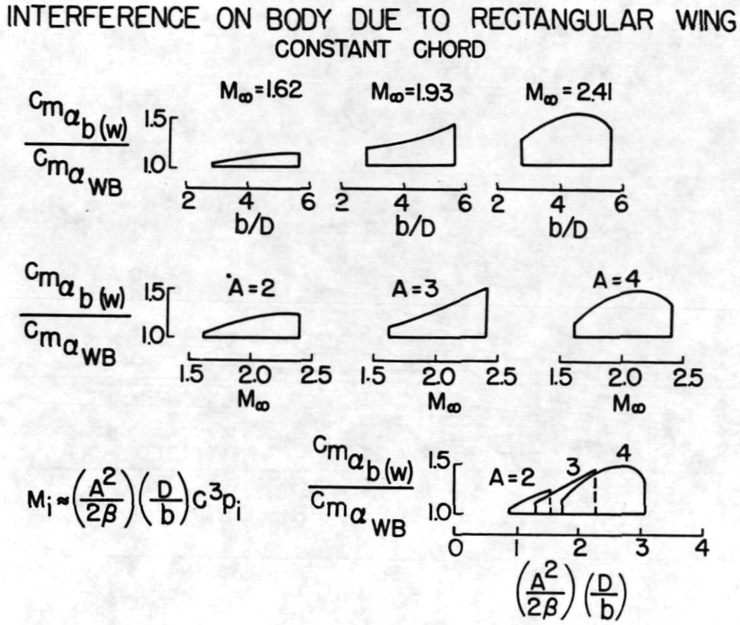

Figure 11

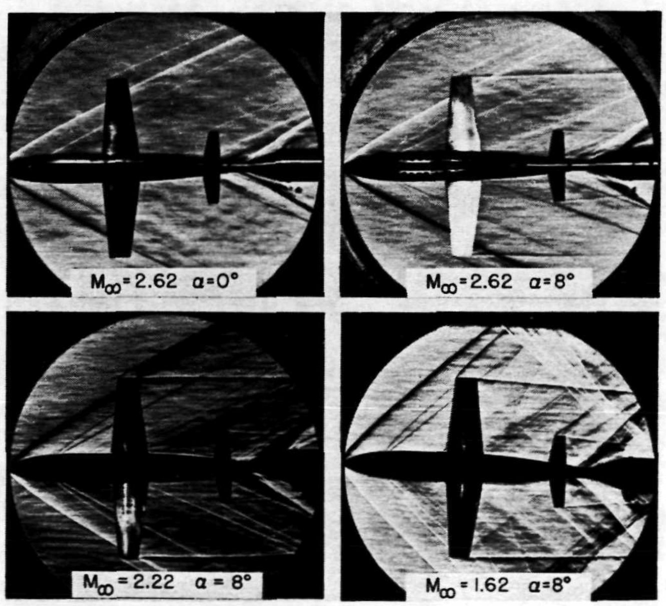

Figure 12

ISOBAR-STREAMLINE FIELD FOR SUPERSONIC JET IN SUPERSONIC STREAM

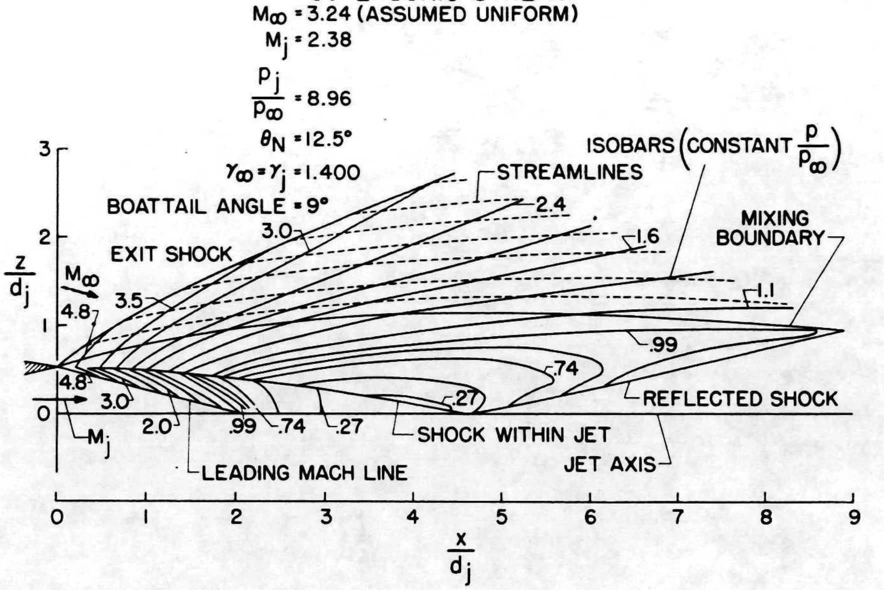

Figure 13

PRESSURES ON FLAT PLATE ASSOCIATED WITH AMBIENT JET INTERFERENCE FIELD

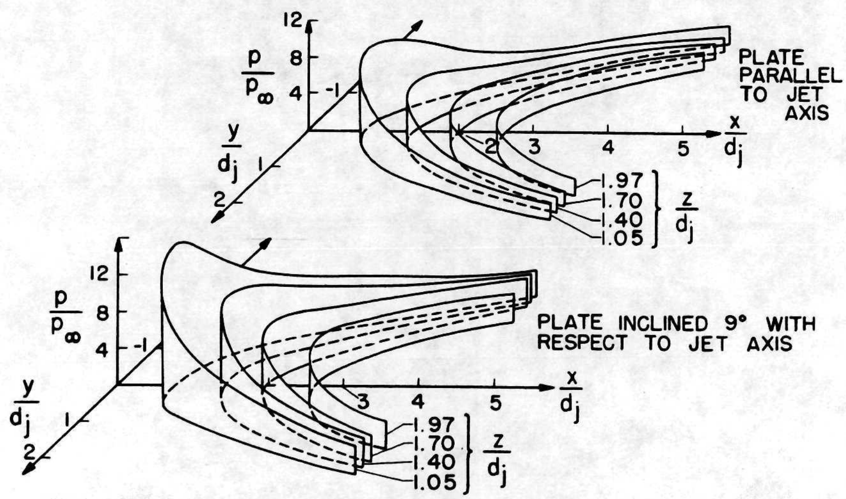

Figure 14

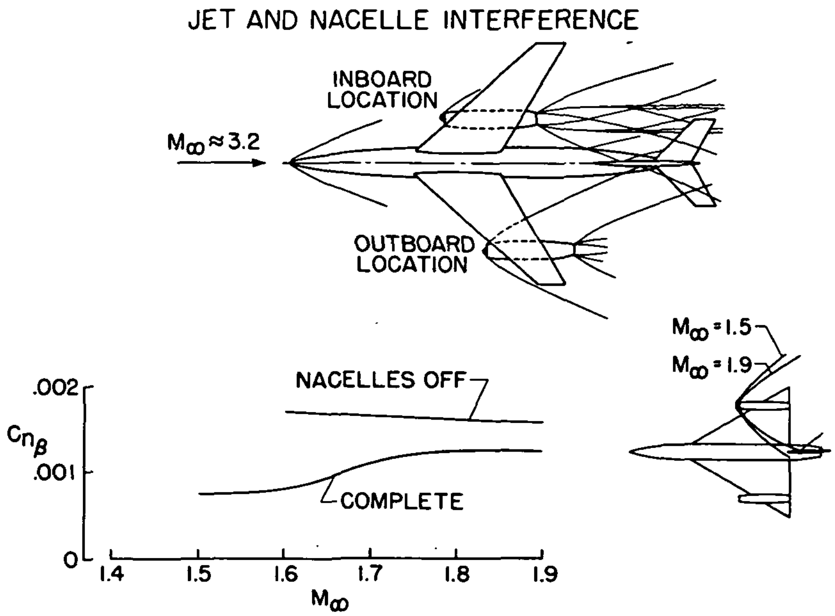
JET AND NACELLE INTERFERENCE
INBOARD LOCATION
$M_\infty \approx 3.2$
OUTBOARD LOCATION
$M_\infty = 1.5$
$M_\infty = 1.9$
.002
Cn_β
.001
0
NACELLES OFF
COMPLETE
1.4
1.5
1.6
1.7
1.8
1.9
M_∞

Figure 15

EFFECT OF AIRPLANE CONFIGURATION ON STATIC STABILITY AT SUBSONIC AND TRANSONIC SPEEDS

By Edward C. Polhamus and Joseph M. Hallissy, Jr.

Langley Aeronautical Laboratory

SUMMARY

Some recent wind-tunnel results are discussed relative to several static-stability problems which are currently of interest to the designer of fighter aircraft. Data are presented in both the subsonic and transonic speed ranges and for angles of attack to 25° in many cases.

The results indicate that rather large amounts of taper might provide the best opportunity of obtaining swept wings having high aspect ratios without encountering violent pitch-up and of eliminating the more moderate pitching-moment nonlinearities of moderate-aspect-ratio wings. With regard to the problem of maintaining directional stability throughout the angle-of-attack range, it has been shown that a large number of factors are involved and that, in general, configurations having long expanding fuselage noses, rectangular fuselages, or high wings should be avoided and that care must be exercised in the selection of the longitudinal location of T-tails. Since large variations of pitching moment with sideslip can occur, it may be necessary to consider this effect in the selection of a configuration.

INTRODUCTION

The high-speed capabilities of modern fighter aircraft have been obtained, to a large extent, through changes in geometric and mass characteristics which for many of these aircraft have produced serious stability problems. The purpose of this paper is to discuss recent wind-tunnel results related to some of these problems in the subsonic and transonic speed range. From the numerous problems, those selected for discussion herein are pitch-up and other pitching-moment nonlinearities, the variation of the directional stability parameter with angle of attack, and the effect of sideslip on the pitching moment. The data presented are referred to the body system of axes.

SYMBOLS

C_L	lift coefficient
$C_{L_{MAX}}$	maximum lift coefficient
n	nose length
C_m	pitching-moment coefficient
C_{n_β}	rate of change of yawing-moment coefficient with sideslip
$C_{n_{\beta,t}}$	tail contribution to C_{n_β}
α	angle of attack, deg
β	angle of sideslip, deg
$\Lambda_{c/4}$	sweep angle of wing quarter-chord line, deg
A	wing aspect ratio
c	local chord
λ	wing taper ratio, $\frac{\text{Tip chord}}{\text{Root chord}}$
M	Mach number

DISCUSSION

Longitudinal Stability

Pitch-up.- Considerable research has been conducted in the past with regard to the pitch-up problem (see refs. 1 to 6, for example) and the findings have, to some extent at least, been incorporated in the configurations of modern fighter aircraft. This is illustrated in figure 1 where the combination of wing aspect ratio and quarter-chord sweep angle is plotted for the current fighter configurations. Also presented is the Shortal-Maggin wing pitch-up boundary (derived from wings having moderate taper) with pitch-up occurring above the boundary (see ref. 1) and it will be noted that the wings of current fighters do not exceed this boundary to any great extent in the pitch-up direction. The vertical location of the horizontal tail of these current configurations is indicated by the type of symbol used, with the open symbols representing a high tail, the filled symbols, a low tail, and the half-filled, a tailless configuration. Low tails lie in a region where the rate of change of downwash with angle of attack is decreasing with angle of attack while high tails lie in a region where the opposite trend usually prevails. The 10° line (relative to the chord line) emanating from the trailing edge of the wing mean aerodynamic chord has been found (refs. 7 and 8) to separate these two regions. It will be noted that, in general, the aircraft whose wings lie above the pitch-up boundary have utilized this downwash characteristic of low tails to counteract the wing pitch-up. It should be pointed out that those configurations that are above the boundary but which utilize high tails have experienced pitch-up problems.

Inasmuch as it is desirable, from a drag-due-to-lift standpoint, to utilize wings having high aspect ratios, a transonic wind-tunnel investigation aimed toward developing a 45° sweptback wing with an aspect ratio of 4 (which is somewhat higher than the current fighter configurations, see fig. 1) having satisfactory pitching-moment characteristics has recently been conducted and some of the results are presented in figure 2 for a Mach number of 0.94. On the left side of this figure the pitching-moment coefficient is plotted as a function of lift coefficient for four wing-body combinations varying only in wing taper ratio. For a taper ratio of 0.6 the curve is very nonlinear and indicates an extremely rapid pitch-up. It has been shown in the past that the pitch-up condition for a wing similar to this one can be improved over a large portion of the speed range by means of wing fixes. These fixes, however, require careful tailoring and are usually ineffective at Mach numbers of the order illustrated here possibly because of shock-induced separation over the aft portion of the wing (ref. 6). It is therefore of considerable interest to note that as the wing becomes more tapered the abrupt pitch-up tendency gradually decreases. Instead of an abrupt pitch-up the pointed wing has a gradual decrease in stability starting at a relatively low lift coefficient. This characteristic of highly tapered wings has also been noted at low speeds (ref. 2) and is due, in part at least, to the fact that while tip stall occurs earlier, a smaller portion of the total load is involved and the moment arms are less than on the wings having large tip chords. In addition it should be pointed out that, as the sweepback of the trailing edge is reduced, less area probably lies behind the shocks. (See sketches on fig. 2.) In view of the rather noticeable improvement associated with the pointed wing, a tail-on investigation has been conducted and the results are presented on the right side of figure 2. In an attempt to counteract the gradual decrease in stability the tail was placed slightly (approximately 5 percent of the wing semispan) below the wing chord plane. With the tail on, the wing with a taper ratio of 0.6 still shows a rather severe pitch-up tendency. All of the more tapered wings provided considerable improvement with regard to pitch-up, but it will be noted that nonlinearities still exist at moderate lift coefficients. It should be pointed out, however, that a tail considerably lower than that used is feasible and with a lower tail the pointed wing might, in view of its superior tail-off characteristics, eliminate these nonlinearities.

Nonlinearities at moderate lifts.- Although fairly linear pitching-moment characteristics can quite often be obtained for complete configurations having nonlinear wing-body combinations, there are some undesirable effects of these tail-off nonlinearities. These nonlinearities, for example, can result in violent pitch-downs for swept wings at negative angles of attack, nonlinear stick travel in maneuvers, and, in some cases, the tail loads required for trim can reduce the tail loads available for maneuvers. It is therefore desirable to have wing-body configurations characterized by linear pitching moments. Figure 3 briefly summarizes the results of a systematic wind-tunnel study to develop a linear wing-body combination which in addition to the previously mentioned advantages might not be limited with regard to a satisfactory tail location. The left part of the figure illustrates the approach used in the investigation. For this particular case the basic wing was a 3-percent-thick 45° delta wing, shown on the left side of figure 3, which has a reduction in stability at moderate lift coefficients due to tip stalling of the highly loaded tip. Rather than attempting to eliminate the reduction in stability at moderate lifts, various amounts of the stalled tips were clipped in an attempt to extend the reduced stability to the low lift range and thereby to obtain a linear curve. The results of clipping the wing to an aspect ratio of 3 is shown by the dashed curve and it will be observed that the pitching moment is linear up to lift coefficients of the order of 0.7 followed by an increase in stability. With this approach, an extensive investigation was conducted (ref. 9) in which the wing sweep angle was varied and various amounts of tip were clipped. What appeared, from a study of these results, to be a very satisfactory plan form is shown on the right side of figure 3. The wing has an unswept 80-percent-chord line, an aspect ratio of 3.5, and a taper ratio of 0.07. In order to determine the characteristics of a complete model employing this wing, a fuselage and tail in several positions were added. The low tail resulted in a gradual increase in stability while the T-tail resulted in a gradual decrease in stability with pitch-up not occurring until the tail enters the wake of the stalled wing. A bitail configuration was also tested and it is interesting to note that the opposite trends of the T- and low tails can be combined to provide an intermediate curve. It should be pointed out that the center-of-gravity position has been adjusted to facilitate a comparison of the curve shapes and that the tail contribution, of course, is dependent upon tail position and area.

Directional Stability

The configuration trends associated with high-performance aircraft have created deficiencies in static directional stability that have been recognized for some time. Recent flight experiences (see ref. 10, for example) in which violent coupled motions were encountered during rolling maneuvers have placed even greater emphasis on the static directional stability problem, and the fact that modern aircraft encounter large angles of attack has made the variation of directional stability with angle of attack extremely important.

Wing-fuselage contribution.- Figure 4 illustrates the variation of directional stability with angle of attack for various wing-body configurations (refs. 11 to 13 and unpublished data) at a Mach number of 0.80. On the left part of the figure the variation for wings having relatively little sweepback is presented and on the right, that for wings having relatively high sweep angles. It will be noted that the unswept wing provides a desirable reduction in the wing-fuselage instability with increasing angle of attack. However, when either moderate or high sweep angles are employed (in the conventional manner) an undesirable increase in the instability occurs. It appears, however, that if sweep is incorporated by means of an M-type composite plan form, desirable characteristics similar to those of the unswept wing can be obtained.

Effect of fuselage shape on tail contribution.- The general trend of increasing wing-fuselage instability with angle of attack indicated in figure 4 points up the importance of minimizing or eliminating any decrease in the tail contribution with angle of attack in order to avoid static instability. With regard to the tail contribution it has been shown in reference 14 that fuselage nose length (the expanding portion of the nose) has an important effect on the location of the fuselage vortices and the resulting flow field in which the vertical tail must operate. In order to illustrate the effect of these flow fields, figure 5 presents the effect of nose length on the tail contribution to directional stability. (With the medium nose the configuration is identical to that of ref. 11.) Here the directional stability contributed by the tail has been normalized by dividing by the value at zero angle of attack and is presented as a function of angle of attack at a Mach number of 0.80 for three nose lengths. On the left side of figure 5 the wing-off results are presented and it will be noted that for the short and medium nose length only a mild reduction in stability occurs with angle of attack. However, when the nose length was increased by 50 percent of the medium nose, an extremely rapid reduction occurred with instability indicated above about 17°. This large loss of stability appears, from the flow-field studies, to result from the upward displacement (associated with the longer nose) of the fuselage vortices which leaves a large portion of the tail in the unfavorable sidewash field below the adjacent vortex. On the right side of figure 5, the wing-on results are presented and, while the wing reduces the variation with nose length somewhat, a rather rapid decrease with angle of attack still occurs for the long nose. The favorable effect of the wing associated with the long nose may be due to a tendency for the wing to pull the fuselage vortices down and thereby to leave less of the tail in the unfavorable sidewash field. The results indicate that, at least for fuselages of circular cross section, rapid decreases in the tail contribution can be avoided providing excessive nose lengths are not used.

The fuselages of modern aircraft, however, quite often depart considerably from a circular cross section and, as was shown in reference 14, departures from a circle can cause large changes in the flow angularity at the tail. The effect that this angularity can have on the tail contribution to directional stability is shown in figure 6 for four different fuselage cross sections. The data were obtained from reference 15 and it should be pointed out that the fuselages are not identical to those of reference 14. All four fuselages had the same longitudinal distribution of cross-sectional area and, of course, the same volume. As in figure 5, the tail contribution normalized by the value at zero angle of attack is plotted against angle of attack. On the left side of the figure the wing-off results are presented. The tail contribution in the presence of the circular fuselage is relatively independent of angle of attack; however, for the two rectangles and the square there is a large loss with increasing angle of attack. For the tall rectangle the departure from the results obtained for the circle begins at about 5° and reaches zero directional stability at about 17°. Above about 20° the stability is restored rather rapidly apparently because of the fact that as the angle of attack becomes large relative to the sideslip angle $\left(C_{n_\beta}\right.$ was obtained over a range of sideslip angle of $\left.\pm 5^{\circ}\right)$ the fuselage vortices tend to become symmetrically disposed relative to the tail and therefore to counteract each other. As the height of width ratio is reduced, the instability is extended to higher angles of attack. The wing-on results, presented on the right side of figure 6, indicate that, although the effect of fuselage cross section is somewhat reduced, the characteristics of the square and rectangular fuselages are still undesirable.

Effect of wing height on tail contribution.- Another parameter which was shown in reference 14 to have a large effect on the flow field in the vicinity of the tail is that of wing height. The effect of wing height (obtained from ref. 16 and an extension of the investigation of ref. 15) on the tail contribution to directional stability at low speeds, is presented in figure 7. As in the previous figures, the C_{n_β} contributed by the tail normalized by the value at zero angle of attack is presented as a function of angle of attack. Presented on the left are the results for the configuration having a circular fuselage and on the right, the results for the configuration having a square fuselage. The results for the circular fuselage indicate the usual large loss in tail contribution associated with a high wing. However for the square fuselage little effect of wing height is indicated and rather large losses with angle of attack occur for all three wing heights. By comparing these data with the wing-off results shown on the left side of figure 6, it will be seen that a favorable wing-fuselage interference occurs with the square fuselage, especially when the low wing position is used. This is in contrast to the results for the circular fuselage, which indicate the usual unfavorable interference.

In connection with the favorable wing-fuselage interference associated with the low wing and the square fuselage, figure 8 presents some interesting results of an investigation conducted at high subsonic speeds (ref. 17). Three different fuselage cross sections were investigated in conjunction with a low wing. The results are presented for a Mach number of 0.80 and show that the relationship between the circular and square fuselages is similar to that obtained at low speeds with somewhat similar configurations. However, when only the lower half of the fuselage was square the tail contribution was even greater than that obtained with the circular fuselage. It appears that the unfavorable effect of the square fuselage alone has been eliminated by sufficiently rounding the top corners, while the favorable wing-body interference has been maintained by the relatively square bottom corners.

Three-body configuration.- In addition to the fuselage-shape effects discussed in the preceding sections, the large fuselage volumes required by current fighter configurations contribute considerably to the magnitude of the flow angularity at the tail. In view of this, it was felt that if the required volume were divided between three bodies, large local flow angularities might be reduced somewhat. A preliminary wind-tunnel investigation to determine what type of static directional and longitudinal stability characteristics might be obtained with three-body configurations has been conducted at low speed and some of the results are presented in figure 9. The configuration consisted of one central and two outboard bodies with conventional tail assemblies attached to the two outboard bodies. On the left, the pitching-moment coefficient is presented as a function of lift coefficient, and fairly acceptable longitudinal characteristics are indicated. The rate of change of directional stability with angle of attack is presented on the right and a gradual reduction is indicated above about 8°. However, even at an angle of attack of about 26°, which corresponds to the maximum lift coefficient, only about 30 percent of the total stability is lost. In connection with directional stability, it should be pointed out that this type of configuration has inertia characteristics which under certain conditions, at least, may tend to reduce the inertia coupling problem encountered by many current fighter configurations.

Effect of horizontal tail on directional stability.- Inasmuch as horizontal-tail position is an important factor in connection with longitudinal stability, its effect on directional stability should be discussed. In general, low horizontal tails provide a slight increase in directional stability over that provided by a vertical tail alone. This increase is relatively independent of angle of attack and Mach number at subsonic speeds. T-tails generally provide a rather large increase at low speeds. However, at high subsonic Mach numbers the effect of a T-tail is dependent to a large extent on angle of attack and fore-and-aft position. This is illustrated in figure 10 where the total directional stability parameter C_{n_β} is presented as a function of angle of attack at a Mach number of 0.90. A comparison of the vertical tail alone and the vertical tail with the T-tail in the forward position indicates a large variation of the horizontal-tail effect with angle of attack. Below an angle of attack of about 3° the horizontal-tail effect is unfavorable and results in directional instability at negative angles of attack greater than about 9°. This, of course, could be important during coupled motions where large negative angles of attack can be encountered. When the horizontal tail was mounted in a rearward position the normal low-speed end-plating effect was restored and the variation with angle of attack somewhat reduced. It should be pointed out, however, that the effect of longitudinal position appears to be a function of plan form. For example, the results of reference 13 indicate that with a rectangular vertical and horizontal tail with coinciding leading edges an unfavorable end-plating effect was obtained at high subsonic speeds. It therefore appears that the extent of the vertical tail span over which the adverse gradients are additive may be more important than the local juncture effect. It appears, therefore, that if a T-tail is desired, extreme care should be exercised in the selection of the fore-and-aft location.

Pitching moment due to sideslip.- A parameter which has received little attention in the past but which is becoming important in connection with the coupled motions is the variation of pitching moment with sideslip. This variation is dependent on a large number of parameters and only a few will be illustrated here. Reference 18 contains a summary of the effects of the various aircraft components. To illustrate the effect that the overall configuration can have, figure 11 presents the variation of the pitching-moment coefficient with sideslip angle for several configurations at a Mach number of 0.80 and zero angle of attack. For the configuration having a sweptback wing and a low horizontal tail, positive increments of pitching moment are indicated with rather large increments occurring with the wing in the high position. For the moderately sweptback wing configuration having a T-tail, large negative increments are produced with increasing sideslip. The fact that large positive or negative increments can occur, depending upon the configuration, indicates that it may be necessary to consider the pitching moment due to sideslip in the selection of a configuration.

CONCLUDING REMARKS

A study of recent subsonic and transonic data indicates that rather large amounts of taper might provide the best opportunity of obtaining swept wings having high aspect ratios without encountering violent pitch-up and of eliminating the more moderate pitching-moment nonlinearities of moderate-aspect-ratio wings.

With regard to the problem of maintaining directional stability throughout the angle-of-attack range, it has been shown that a large number of factors are involved and that, in general, configurations having long expanding fuselage noses, rectangular fuselages, or high wings should be avoided and that care must be exercised in the selection of the longitudinal location of T-tails.

Since large variations of pitching moment with sideslip can occur, it may be necessary to consider this effect in the selection of a configuration.

REFERENCES

1. Shortal, Joseph A., and Maggin, Bernard: Effect of Sweepback and Aspect Ratio on Longitudinal Stability Characteristics of Wings at Low Speeds. NACA TN 1093, 1946.

2. Furlong, G. Chester, and McHugh, James G.: A Summary and Analysis of the Low-Speed Longitudinal Characteristics of Swept Wings at High Reynolds Number. NACA RM L52D16, 1952.

3. Donlan, Charles J., and Weil, Joseph: Characteristics of Swept Wings at High Speeds. NACA RM L52A15, 1952.

4. Weil, Joseph, and Gray, W. H.: Recent Design Studies Directed Toward Elimination of Pitch-Up. NACA RM L53I23c, 1953.

5. Toll, Thomas A.: Longitudinal Characteristics of Wings. NACA RM L53I21b, 1953.

6. West, F. E., Jr., and Henderson, James H.: Relationship of Flow Over a 45° Sweptback Wing With and Without Leading-Edge Chord-Extensions to Longitudinal Stability Characteristics at Mach Numbers From 0.60 to 1.03. NACA RM L53H18b, 1953.

7. Mitchell, Jesse L.: The Static and Dynamic Longitudinal Stability Characteristics of Some Supersonic Aircraft Configurations. NACA RM L52A10a, 1952.

8. Few, Albert G., Jr.: Some Effects of Sweep and Thickness on the Experimental Downwash Characteristics at Transonic Speeds of a Series of Highly Tapered Wings With an Aspect Ratio of 3 - Transonic-Bump Method. NACA RM L55J12, 1955.

9. Few, Albert G., Jr., and Fournier, Paul G.: Effects of Sweep and Thickness on the Static Longitudinal Aerodynamic Characteristics of a Series of Thin, Low-Aspect-Ratio, Highly Tapered Wings at Transonic Speeds - Transonic-Bump Method. NACA RM L54B25, 1954.

10. NACA High-Speed Flight Station: Flight Experience With Two High-Speed Airplanes Having Violent Lateral-Longitudinal Coupling in Aileron Rolls. NACA RM H55A13, 1955.

11. Goodson, Kenneth W., and Becht, Robert E.: Wind-Tunnel Investigation at High Subsonic Speeds of the Stability Characteristics of a Complete Model Having Sweptback-, M-, W-, and Cranked-Wing Plan Forms and Several Horizontal-Tail Locations. NACA RM L54C29, 1954.

12. Wiggins, James W.: Wind-Tunnel Investigation at High Subsonic Speeds of the Static Longitudinal and Static Lateral Stability Characteristics of a Wing-Fuselage Combination Having a Triangular Wing of Aspect Ratio 2.31 and an NACA 65A003 Airfoil. NACA RM L53G09a, 1953.

13. Sleeman, William C.: An Experimental Study at High Subsonic Speeds of Several Tail Configurations on a Model With a Straight Wing. (Prospective NACA paper.)

14. Malvestuto, Frank S., Jr., and Alford, William J., Jr.: Effects of Wing-Body Geometry on Lateral Flow at Subsonic Speeds. (Prospective NACA paper.)

15. Letko, William, and Williams, James L.: Experimental Investigation at Low Speed of Effects of Fuselage Cross Section on Static Longitudinal and Lateral Stability Characteristics of Models Having 0° and 45° Sweptback Surfaces. NACA TN 3551, 1955.

16. Goodman, Alex: Effects of Wing Position and Horizontal-Tail Position on the Static Stability Characteristics of Models With Unswept and 45° Sweptback Surfaces With Some Reference to Mutual Interference. NACA TN 2504, 1951.

17. King, Thomas J.: Wind-Tunnel Investigation at High Subsonic Speeds of Some Effects of Fuselage Cross-Section Shape and Wing Height on the Static Longitudinal and Lateral Stability Characteristics of a Model Having a 45° Swept Wing. NACA RM L55J25, 1955.

18. Polhamus, Edward C.: Some Factors Affecting the Variation of Pitching Moment With Sideslip of Aircraft Configurations. NACA RM L55E20b, 1955.

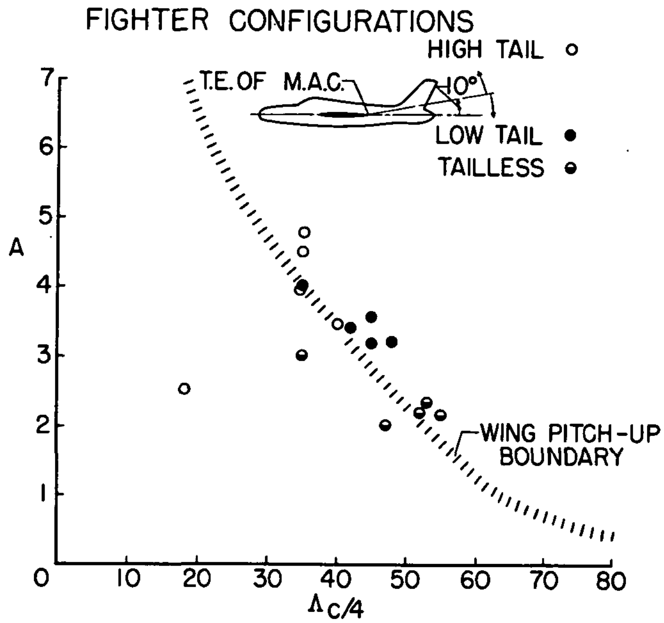

Figure 1

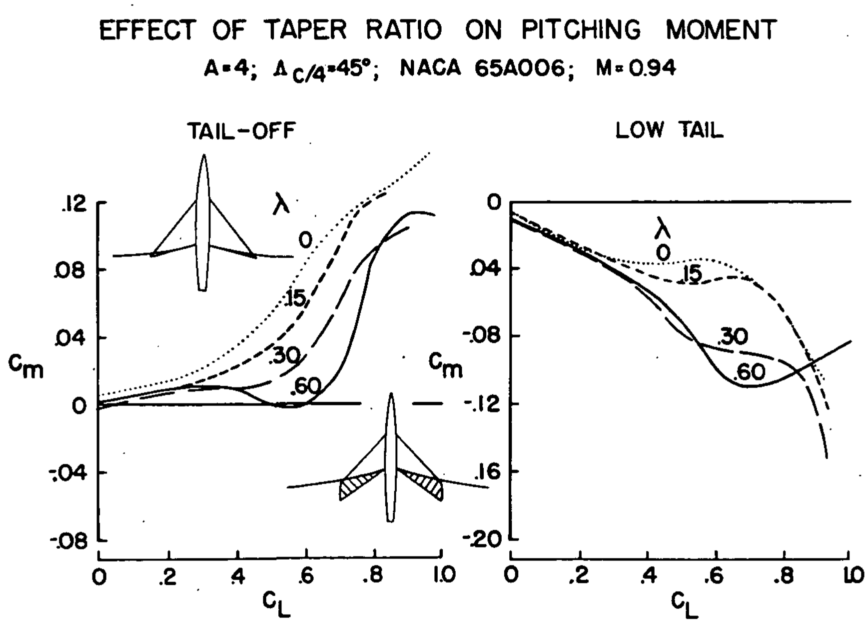

Figure 2

LONGITUDINAL STABILITY
M = 0.90

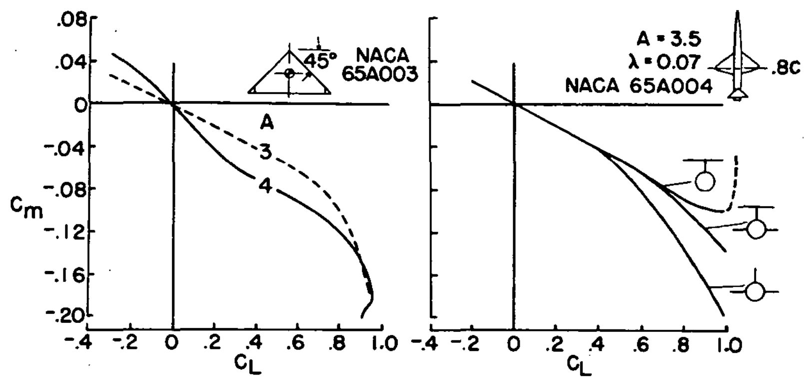

Figure 3

EFFECT OF WING PLAN FORM ON C_{n_β}, TAIL OFF
M = 0.80

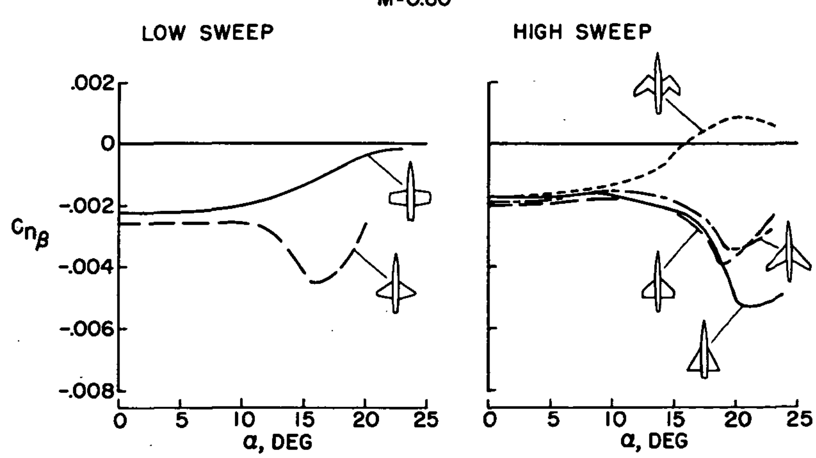

Figure 4

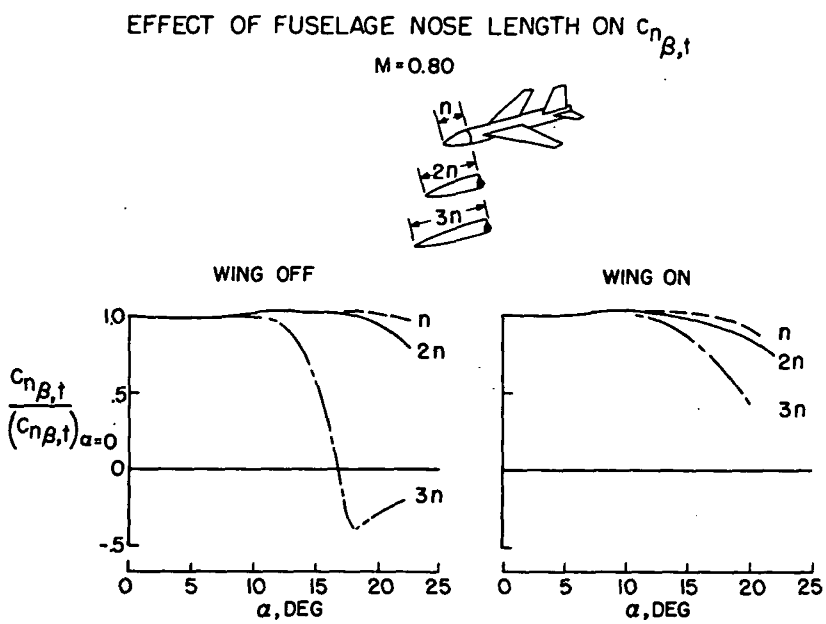

Figure 5

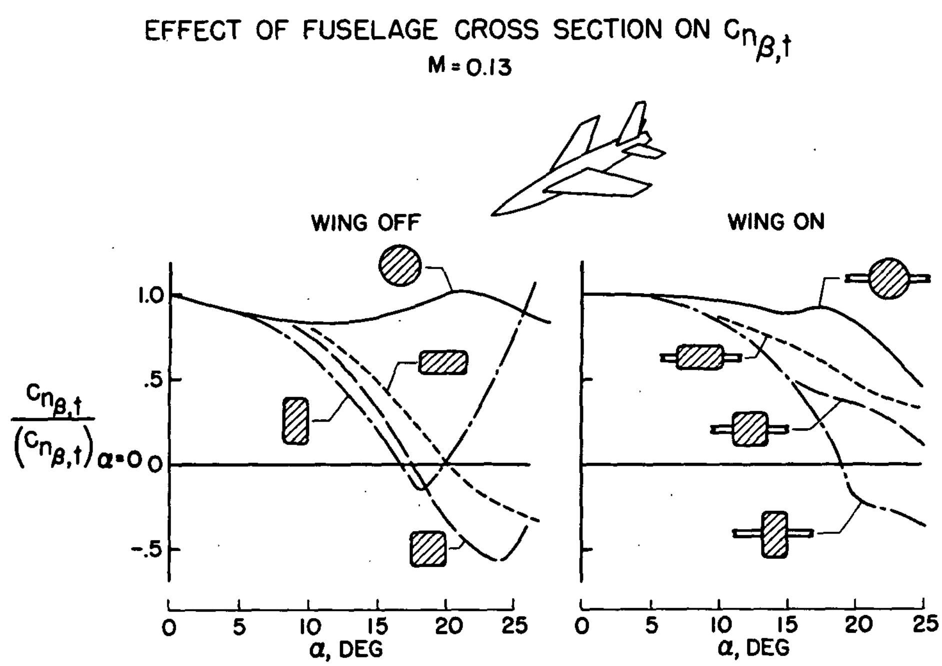

Figure 6

EFFECT OF WING HEIGHT ON $C_{n_{\beta,t}}$

M = 0.13

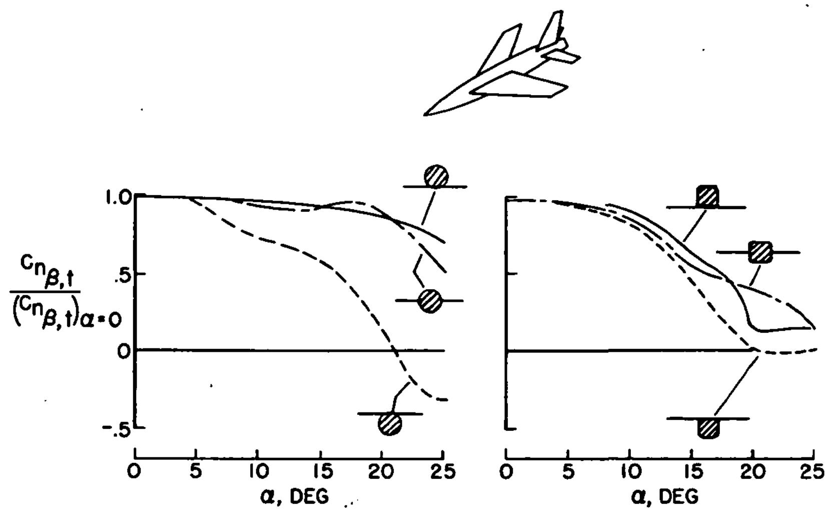

Figure 7

EFFECT OF FUSELAGE CROSS SECTION ON $C_{n_{\beta,t}}$

M = 0.80

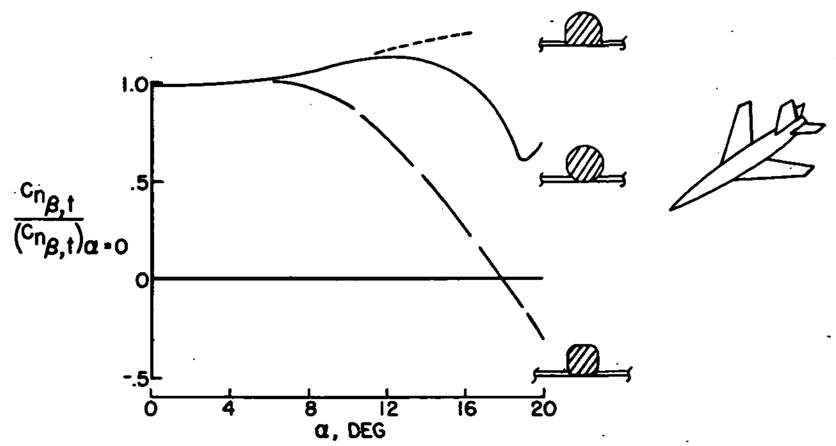

Figure 8

STABILITY OF 3-BODY CONFIGURATION
M=0.20

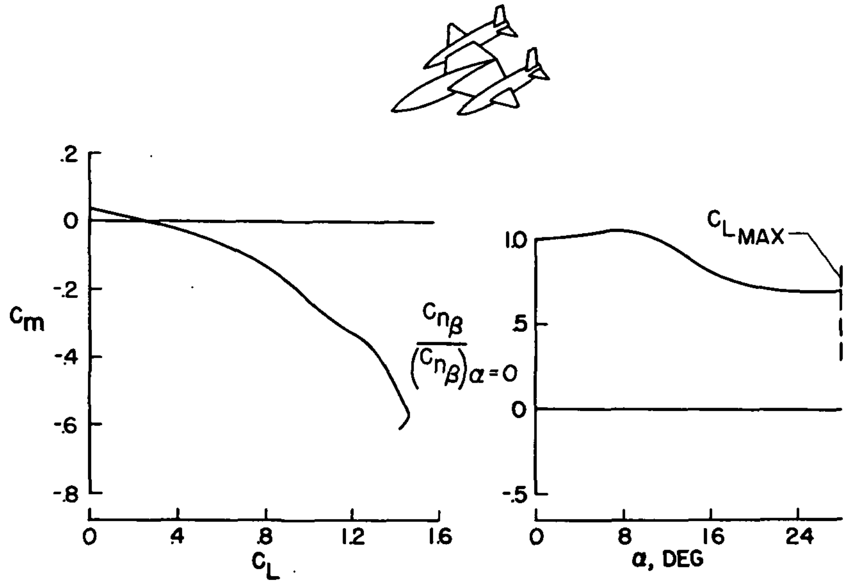

Figure 9

EFFECT OF HORIZONTAL-TAIL POSITION ON C_{n_β}
M = 0.90

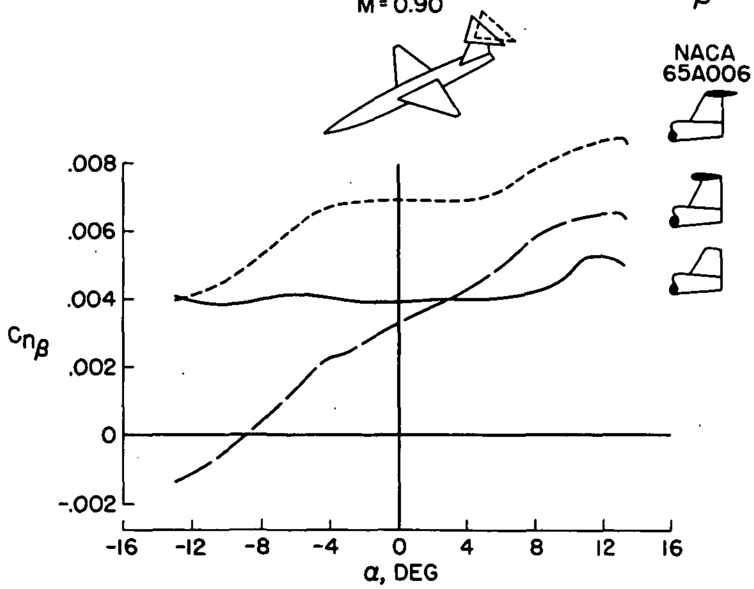

Figure 10

EFFECT OF CONFIGURATION ON VARIATION OF C_m WITH β

$M = 0.80$

$\alpha = 0°$

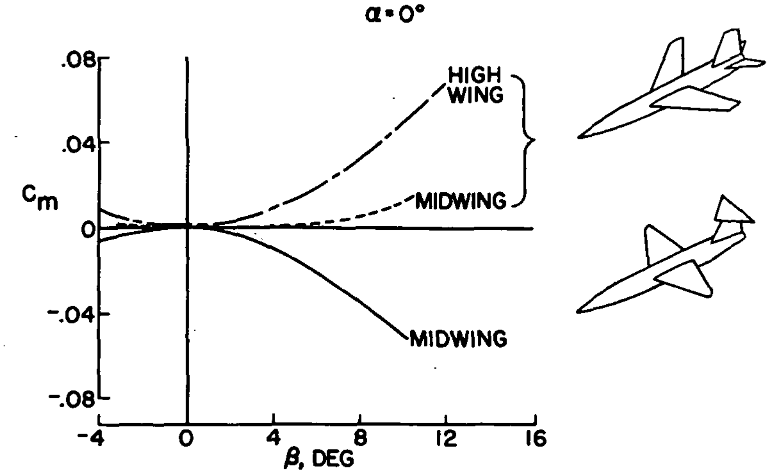

Figure 11

Page intentionally left blank

SOME EFFECTS OF AIRCRAFT CONFIGURATION ON STATIC LONGITUDINAL AND DIRECTIONAL STABILITY CHARACTERISTICS AT SUPERSONIC MACH NUMBERS BELOW 3

By M. Leroy Spearman and Arthur Henderson, Jr.

Langley Aeronautical Laboratory

SUMMARY

The longitudinal problem of airplane configurations at supersonic Mach numbers below 3 is generally one of excessive stability so that the large control deflections required for trim may result in undesirably low trimmed lift-drag ratios. These characteristics may be relieved to a certain extent by positive increases in the pitching moment at constant lift that may be effected through the use of such devices as body camber.

The directional stability is characterized by a rapid deterioration with increasing Mach number. This trend results primarily from the loss in vertical-tail lift-curve slope with increasing Mach number and is considerably aggravated for most configurations by the highly unstable wing-body combinations that occur from the use of large high-fineness-ratio bodies and from the far rearward center-of-gravity positions. Hence, a large percentage of the tail contribution is lost in overcoming the unstable moment of the wing-body combination and only a small percentage is available to provide a positive stability margin. Any decrease in tail contribution resulting from interference effects, aeroelasticity, control deflection, and so on, subtracts directly from the stability margin and may lead quickly to directional divergence. The concept of the wing-body induced sidewash field has been shown to be of some importance in qualitatively determining the effect of angle of attack on the directional characteristics of the wing-body combination and on the tail contribution.

INTRODUCTION

Some of the major problems discussed herein regarding the static stability and control of aircraft operating in the low supersonic speed range are as follows:

Longitudinal:
- Excessive static margin
- High trim drag, low trim L/D
- Decrease in stability with increasing Mach number

Directional:
- Magnitude of unstable yawing moment of wing-body combination
- Effect of Mach number on C_{n_β}
- Effect of angle of attack on C_{n_β}
- Nonlinear variation of C_n with β
- Effect of external stores

SYMBOLS

C_D	drag coefficient
C_L	lift coefficient
C_m	pitching-moment coefficient
C_n	yawing-moment coefficient
C_{n_β}	yawing moment due to sideslip
C_Y	lateral-force coefficient
C_{Y_β}	lateral force due to sideslip
ΔC_{Y_t}	increment in lateral-force coefficient contributed by vertical tail
D	drag
i_t	incidence of horizontal tail
L	lift
M	free-stream Mach number
V	free-stream velocity
v_σ	lateral velocity component due to sidewash

α angle of attack

β angle of sideslip

DISCUSSION

Longitudinal Stability

The longitudinal problem, which will be considered first, is primarily one of excessive stability. This excessive stability is a result of several generally well-known factors. These factors include the increase in stability of the wing-body combination that is caused by a rearward shift of the wing center of pressure and a stabilizing interference effect of the wing lift carried over to the afterbody. The stability is further increased because of the loss of the subsonic type of wing downwash at the tail since the major portion of this downwash is confined to the wing-tip Mach cones and at supersonic speeds begins to move off of the horizontal tail. In addition, in the case of most low-tail airplanes, stabilizing upwash from the body may be encountered. At the same time that the stability is increased, the effectiveness of the tail in producing pitching moment is reduced. As indicated by the example shown in figure 1, these effects combine to cause large untrimmed pitching moments that must be overcome through rather large control deflections, and the result is high trim drag and low trim lift-drag ratios. In addition, because of the large control deflections required for trimming, little excess control deflection may be available for maneuvering.

Some recent investigations have indicated that body camber, similar to that proposed from area-rule considerations (see ref. 1), may be useful in providing positive increments of pitching moment at constant lift in such a manner as to relieve the control-deflection requirements. The effects of body camber are shown in figure 2 for a 60° delta wing-body at $M = 1.6$. The reflexed or cambered body produces constant pitching-moment increments throughout the lift range with no change in drag and should be useful in shifting the pitching-moment level for a basic configuration so that the pitch-control requirements might be relieved and the drag due to trimming reduced.

Although the excessive longitudinal stability presents serious control problems in the Mach number range from 1 to about 2, there are indications that a reduction in longitudinal stability will occur as the Mach number increases toward 3 or above. Such an effect is indicated in figure 3 for three different aircraft configurations in the Mach number range from about 1.4 to 3.0. Here there is a general decrease in longitudinal stability for the complete configuration that is apparently dictated by a decrease in the stability of the tail-off configuration. This stability decrease occurs in part from a decrease in the stabilizing carryover lift effect of the wing on the afterbody as indicated in reference 2. At higher Mach numbers, the added effects of large changes in dynamic pressure in the wing flow field may cause additional changes in the longitudinal stability.

Directional Stability

The second phase of the supersonic stability problem which will now be discussed is that of static directional stability in the supersonic Mach number range below 3. The directional stability, in contrast to the longitudinal problem, is characterized by a rapid deterioration in the stability with increasing Mach number. A typical variation of the stability parameters C_{n_β} and C_{Y_β} with Mach number is shown in figure 4. It will be noted that there is a progressive decrease in the stability level of the complete configuration until a Mach number is reached where directional instability occurs. This loss in stability results from the characteristic decrease in lift-curve slope of the vertical tail with increasing Mach number, which is reflected, in turn, in a decreased tail contribution to the total stability.

The situation is considerably aggravated for most current designs by a large unstable wing-body yawing moment. This large unstable moment generally results from the use of large, high-fineness-ratio fuselages with far rearward center-of-gravity positions. The adverse effects of such center-of-gravity positions on directional stability are twofold in that the unstable yawing moment of the body is increased while the vertical-tail moment arm is reduced.

The results shown are for zero angle of attack and for a rigid model. It will be noted that a considerable portion of the tail contribution is required to overcome the large unstable wing-body yawing moment. It is obvious that any loss in vertical-tail contribution resulting from wing-body wakes, interference flow fields, or vorticity – as well as aeroelastic effects – could readily lead to directional instability. The problem is most acute at the higher Mach numbers where the stability level is already marginal.

A means by which the tail contribution to C_{n_β} can be increased by a relatively simple modification is illustrated in figure 5. These results are for zero angle of attack and a Mach number of 2.6. The results for the basic tail indicate a reversal in C_{n_β}. The modification, which consisted of the addition of wedges to both sides of the trailing-edge portion of the vertical tail, removed the reversal and resulted in a substantial increase in tail effectiveness. This improvement was obtained with only a slight increase in drag. As shown by the results on the right-hand side of figure 5, the effectiveness of the wedges, as predicted by two-dimensional shock-expansion theory, is in good agreement with the experimental results.

The results thus far have been confined to zero angle of attack. An example of the angle-of-attack effects that might occur are shown in figure 6 for a 35° swept-wing airplane at $M = 1.6$. The directional stability decreases quite rapidly with angle of attack and instability occurs above about 10°. The nonlinear variation of C_n with β that is apparently influenced by the wing-body characteristics may add considerably to the directional problems since regions of instability might be reached through rudder deflections, for example.

In such cases, the directional instability may be delayed to higher angles of attack or higher Mach numbers simply by increasing the size of the vertical tail. Indiscriminate use of this method, of course, may result in undesirably high lateral forces and rolling moments and may increase the structural and weight problems associated with the vertical tail.

The loss in directional stability indicated here with increasing angle of attack and for other configurations in this Mach number range appears to be due in part to an effect of the disturbance caused by the wing-body juncture acting on the vertical tail and afterbody. This wing-body disturbance is apparent in the schlieren photographs shown in figure 7 for a high-wing position and a low-wing position of a 45° swept wing on a body of revolution at angles of attack of 5° and 10° and at a Mach number of 2. The shock lines from the wing are visible in both cases. The disturbance induced by the wing-body juncture is clearly visible for the high-wing case and is alined in the free-stream direction so that it passes the region normally occupied by the vertical tail. For the low-wing arrangement, the disturbance is confined to the afterbody region and hence is not visible in the photographs.

This wing-body disturbance is the same as that which occurs at subsonic speeds, and at angles of sideslip provides the same type of sidewash distribution at the vertical tail as that discussed in reference 3. At Mach numbers somewhat greater than 2, however, where the Mach lines from the wing are directed more nearly over the vertical tail, additional changes in tail contribution, as pointed out in reference 2, might be experienced because of the large changes in dynamic pressure in the wing flow field.

Some effects of the wing-body induced sidewash field are shown in figure 8 for a wing-body-tail combination at a Mach number of 2. The nature of the induced sidewash for the high- and low-wing positions is shown in the upper-right diagram. This sidewash results from the differential wing pressures near the wing root that are created by the lateral component of velocity due to sideslip. For the high-wing case, this sidewash is adverse above the center of the wing wake and is favorable below it. The reverse is true for the low-wing case. At zero angle of attack, the afterbody lies in the same type of flow region for either wing position and the values of C_{n_β} are the same for the tail-off configurations. With increasing angle of attack, the low-wing arrangement becomes increasingly unstable since the afterbody moves down through a region of adverse sidewash. For the high-wing arrangement, there is little change in stability with increasing angle of attack since the afterbody moves into an undisturbed flow region.

With the addition of the vertical tail at $\alpha = 0^\circ$, both configurations become stable. However, the tail contribution is less with the high wing since this arrangement places the tail in a region of adverse sidewash. With increasing angle of attack, the tail contribution continues to decrease for the high-wing arrangement as the tail passes through the region of adverse sidewash. For the low-wing arrangement, the tail contribution increases with increasing angle of attack as the tail passes through a region of favorable sidewash.

The effect of the wing sidewash on the vertical-tail loading, as obtained from pressure measurements on the tail, is shown in the lower right-hand side of figure 8. At $\alpha = 0^\circ$, the overall loading is less for the high-wing position, and, at $\alpha = 15^\circ$, the loading actually changes sign near the root of the vertical tail for the high-wing position. Unfortunately, in either case, the directional stability for the complete configurations reduces with increasing angle of attack but for two different reasons – for the high wing, because of a decreasing tail contribution, and, for the low wing, because of an increase in the instability of the wing-body combination. These effects of wing-body induced sidewash are dependent on the wing position relative to the body crossflow. The body crossflow, in turn, is dependent on the body cross-sectional size and shape.

Some effects of various tail modifications on the directional stability of two different configurations at Mach numbers of 1.6 and 2 are shown in figure 9. Both configurations have body shapes and wing positions that might be expected to cause adverse sidewash in the wake above the wing-body juncture. As a result, the variation of C_{n_β} with angle of attack indicates a large loss in vertical-tail contribution for the basic tails whereas the tail-off configurations show some improvement. For the configuration shown on the left-hand side of figure 9, the addition of a dorsal fin had little effect on C_{n_β} since the fin was placed in a region of adverse sidewash. The addition of a small ventral fin having about two-thirds the area of the dorsal fin provided a stabilizing increment of C_{n_β} that increased slightly with angle of attack because of the more favorable flow beneath the body.

For the configuration shown on the right-hand side of figure 9, modifications to the basic tail consisting of an extended chord and of an extended tip were made. These modifications provided equal increments of C_{n_β} at zero angle of attack. With increasing angle of attack, however, the increment provided by the extended chord decreases since this area extension is adversely affected by the sidewash. The increment of C_{n_β} provided by the extended tip remains essentially constant with angle of attack up to 15° since this area extension remains above the flow-field disturbance from the wing-body juncture.

The configuration shown in figure 10 has a midwing with a large negative dihedral angle. This arrangement places the wing in a position relative to the body crossflow such that a favorable sidewash above the wing similar to that for a low-wing circular-body configuration might be expected. Accordingly, the variation of C_{n_β} with angle of attack indicates little change in the tail contribution, although the directional stability decreases as a result of the increasing instability of the tail-off configuration. The substitution of an enlarged tail in the region of favorable sidewash causes a large increase in C_{n_β} at $\alpha = 0^{\circ}$ and an increase in the tail contribution with increasing angle of attack. The addition of a ventral fin to the basic model is beneficial, but its effect is much less than that for the enlarged tail, although the area of the ventral fin is about twice that of the area increase for the enlarged tail. It might be expected that, for a configuration of this type, a chordwise extension to the vertical tail would be more effective than a spanwise extension in increasing C_{n_β}.

It should be pointed out that ventral fins or lower-surface vertical tails should always provide good directional characteristics at high angles of attack since these surfaces, regardless of the initial wing-body induced sidewash characteristics, move into a region of undisturbed flow. The directional characteristics of a lower-surface vertical-tail arrangement and an upper-surface vertical-tail arrangement at a Mach number of 2 are compared in figure 11. The directional stability decreases rapidly with angle of attack for the conventional tail arrangement, primarily because of a decrease in the tail contribution. For the lower-surface arrangement, however, a large increase in the directional stability with angle of attack for the complete model is indicated in spite of a decrease experienced by the tail-off configuration.

An additional example of the sensitivity of the directional stability to configuration changes is shown in figure 12. This figure shows some effects of two different external-store installations on a 45° swept-wing airplane at an angle of attack of 15° and M = 1.4. Both installations – one body-mounted store and two wing stores – caused an increase in the lateral force. The body-store configuration was directionally unstable whereas the two wing stores caused a fairly large increase in the directional stability. These changes in C_{n_β} were somewhat greater than would be expected from consideration of the isolated store forces and indicate rather large mutual interference effects between the various components that tend to complicate the quantitative prediction of the store effects.

CONCLUDING REMARKS

The longitudinal problem of airplane configurations at supersonic Mach numbers below 3 is generally one of excessive stability so that the large control deflections required for trim may result in undesirably low trimmed lift-drag ratios. These characteristics may be relieved to a certain extent by positive increases in the pitching moment at constant lift that may be effected through the use of such devices as body camber.

The directional stability is characterized by a rapid deterioration with increasing Mach number. This trend results primarily from the loss in vertical-tail lift-curve slope with increasing Mach number and is considerably aggravated for most configurations by the highly unstable wing-body combinations that occur from the use of large high-fineness-ratio bodies and from the far rearward center-of-gravity positions. Hence, a large percentage of the tail contribution is lost in overcoming the unstable moment of the wing-body combination and only a small percentage is available to provide a positive stability margin. Any decrease in tail contribution resulting from interference effects, aeroelasticity, control deflection, and so on, subtracts directly from the stability margin and may lead quickly to directional divergence. The concept of the wing-body induced sidewash field has been shown to be of some importance in qualitatively determining the effects of angle of attack on the directional characteristics of the wing-body combination and on the tail contribution.

REFERENCES

1. Whitcomb, Richard T.: Several Extensions of the Area Rule. (Prospective NACA paper.)

2. Love, Eugene S.: Supersonic Wave Interference Affecting Stability. (Prospective NACA paper.)

3. Malvestuto, Frank S., Jr., and Alford, William J., Jr.: Effects of Wing-Body Geometry on Lateral Flow at Subsonic Speeds. (Prospective NACA paper.)

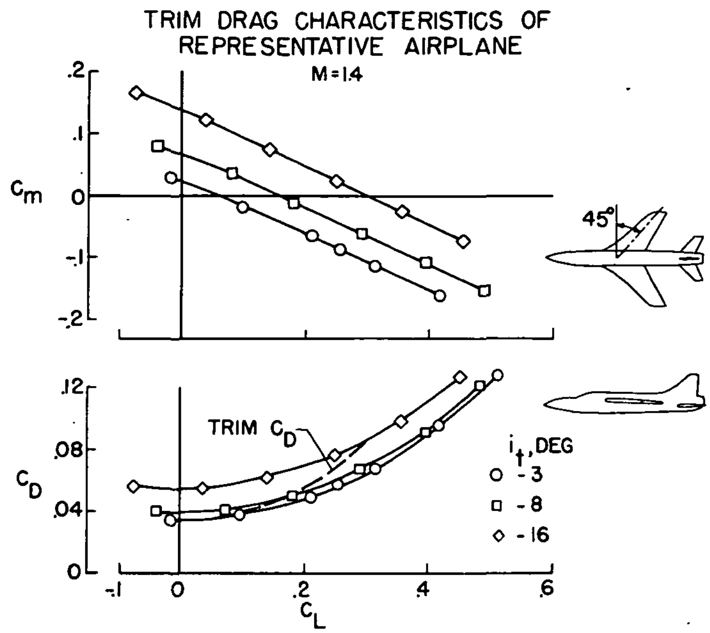

Figure 1

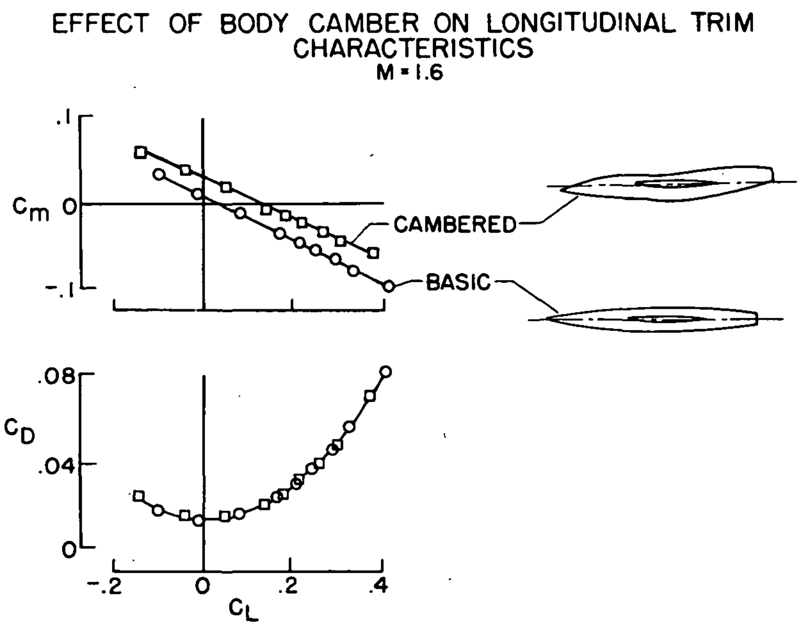

Figure 2

VARIATION OF $\partial C_m / \partial C_L$ WITH M

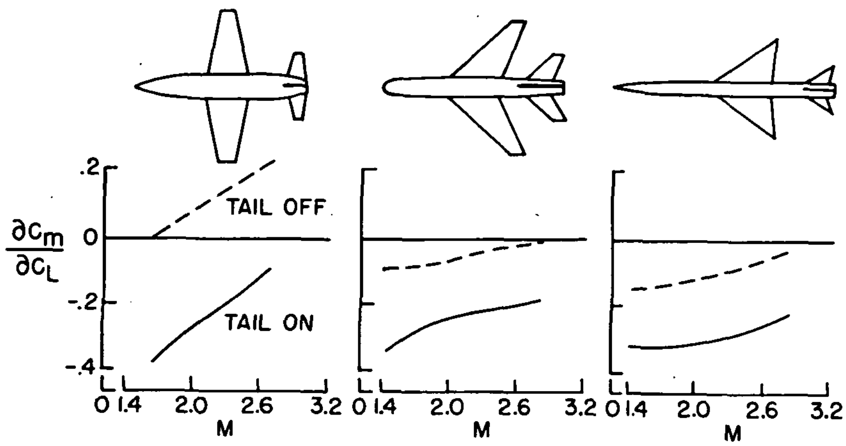

Figure 3

EFFECT OF MACH NUMBER ON
DIRECTIONAL STABILITY AT $\alpha = 0°$

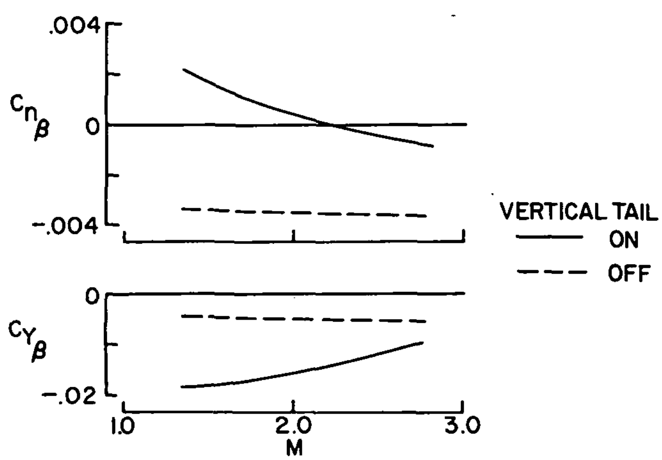

Figure 4

[redacted]

EFFECT OF TAIL SECTION MODIFICATION ON DIRECTIONAL STABILITY

$\alpha = 0°$; $M = 2.6$

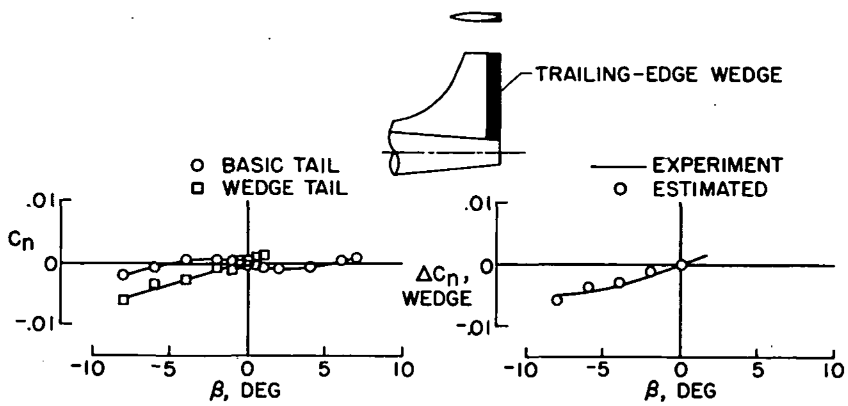

Figure 5

EFFECT OF ANGLE OF ATTACK ON DIRECTIONAL STABILITY

M=1.6

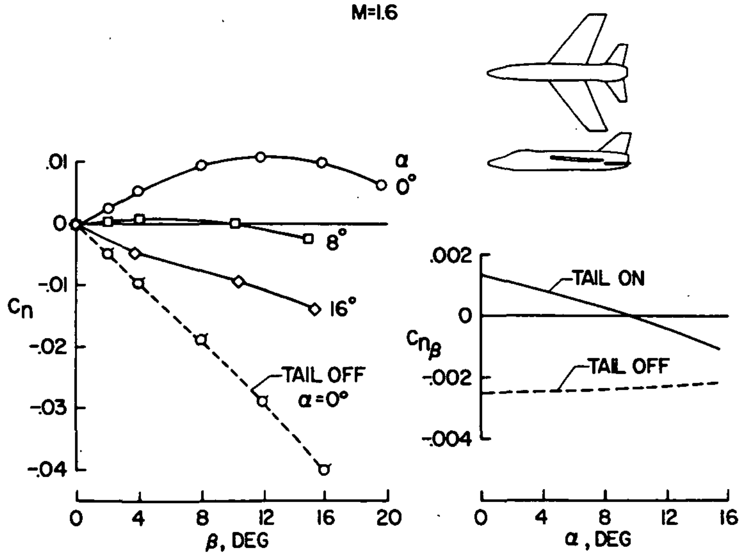

Figure 6

[redacted]

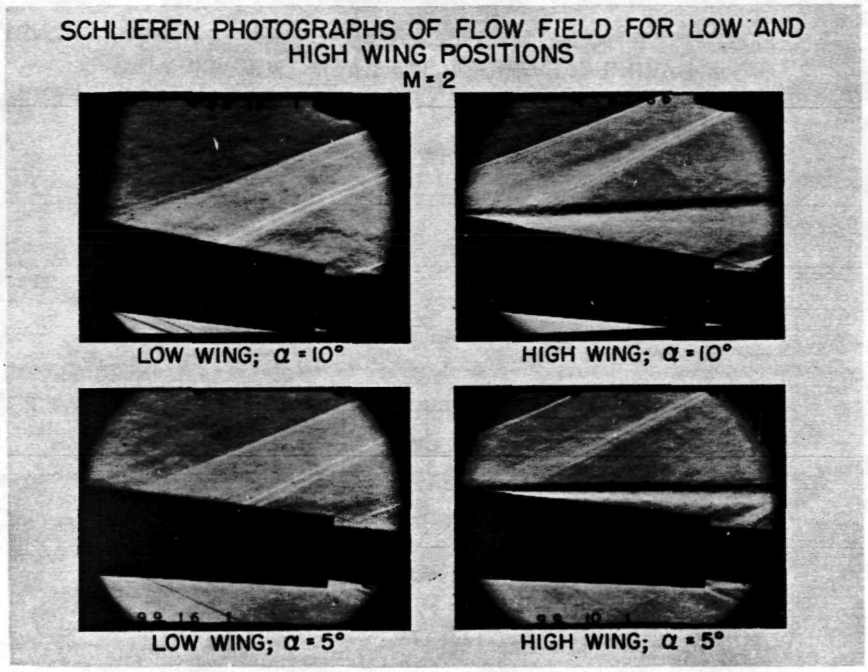

Figure 7

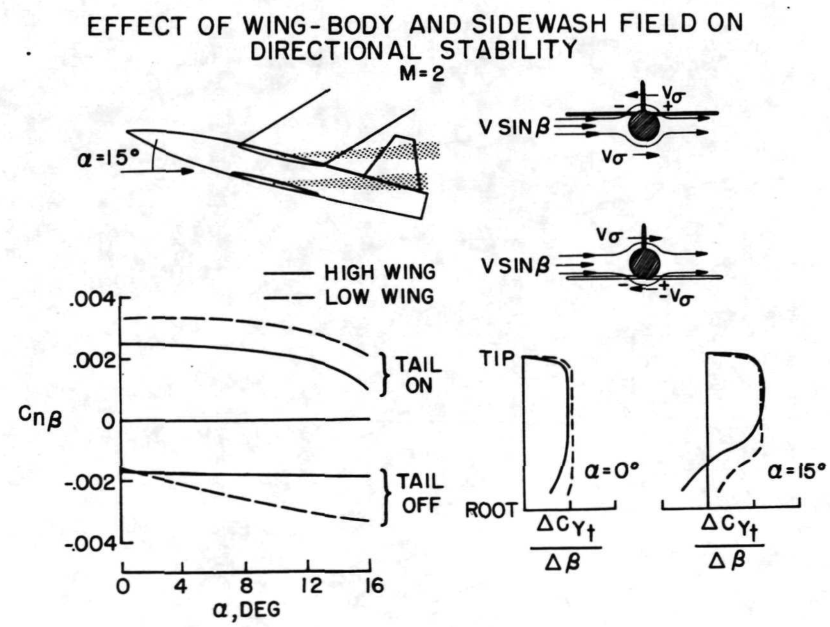

Figure 8

EFFECTS OF TAIL MODIFICATIONS FOR CONFIGURATIONS
HAVING ADVERSE SIDEWASH ABOVE WING

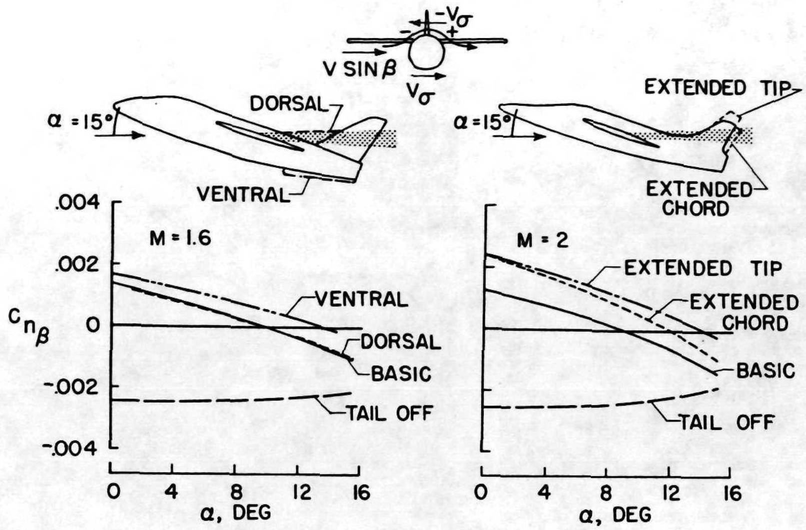

Figure 9

EFFECT OF TAIL MODIFICATIONS FOR CONFIGURATION
HAVING FAVORABLE SIDEWASH ABOVE WING
M = 2

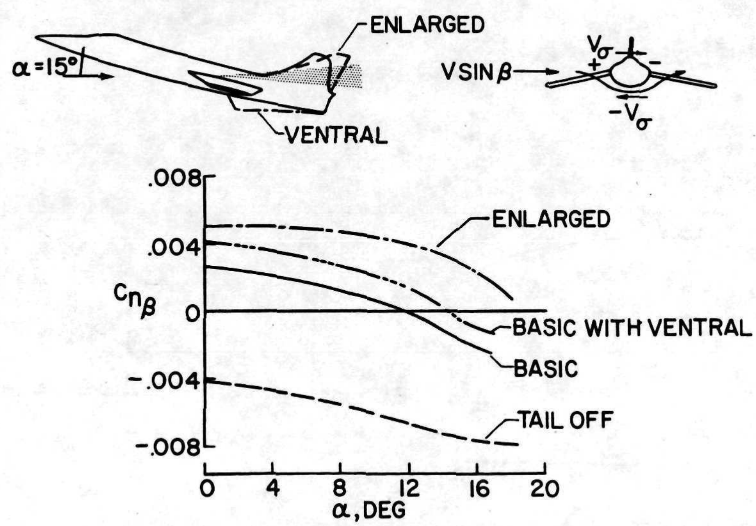

Figure 10

EFFECT OF TAIL LOCATION ON VARIATION OF Cn_β WITH α

M = 2

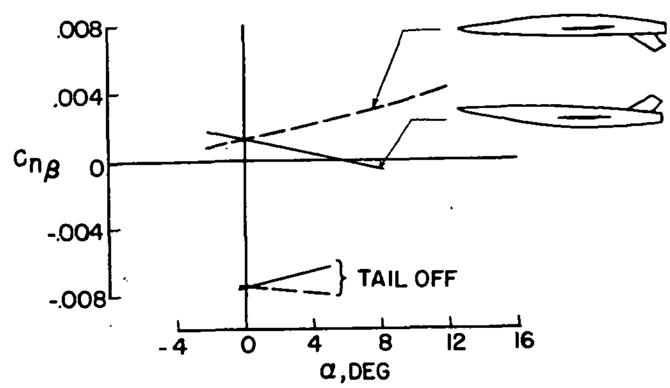

Figure 11

EFFECT OF STORES ON DIRECTIONAL STABILITY

$\alpha = 15°$; M = 1.4

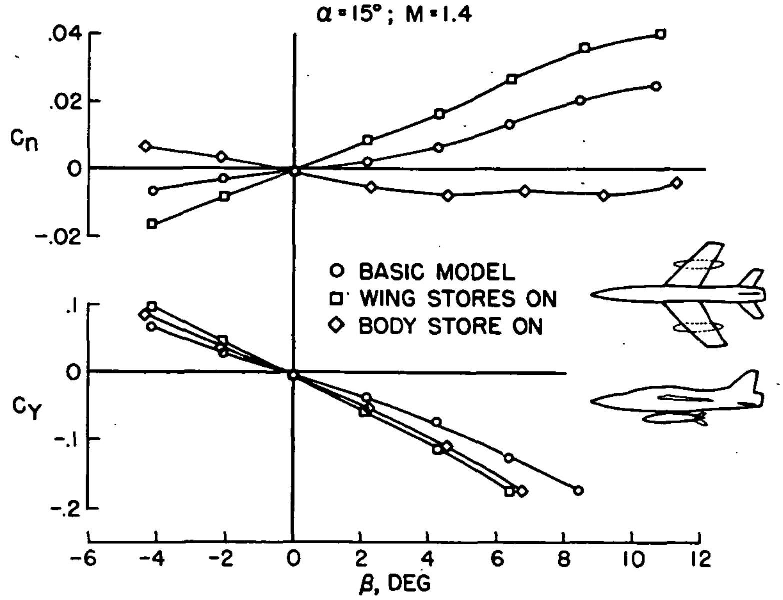

Figure 12

FLOW-FIELD EFFECTS ON STATIC STABILITY AND CONTROL AT HIGH SUPERSONIC MACH NUMBERS

By Edward F. Ulmann and Herbert W. Ridyard

Langley Aeronautical Laboratory

24

SUMMARY

Recent wind-tunnel investigations of aircraft-type configurations at Mach numbers 4.06 and 6.86 have provided data which show that flow-field interference is of primary importance in stability and control calculations at high supersonic Mach numbers and that the location of stabilizing and control surfaces that give highest effectiveness can be determined by theoretical studies of these flow fields. A method has been derived which predicts the trend of downwash around a circular body as the angle of attack is increased. A method has also been derived which gives good predictions of the tail contributions to lateral stability through a considerable angle-of-attack range.

INTRODUCTION

The importance of flow-field interference at supersonic Mach numbers below 3.0 has been discussed in reference 1. These effects become increasingly important as the Mach number is increased beyond 3.0. In this paper, some illustrations of the effects of these flow fields will be presented and it will be shown that, for close coupled configurations, it is possible to predict some effects of flow-field interference on longitudinal and lateral stability and control.

Figures 1 and 2 present schlieren photographs of the flow around a model that has been extensively tested at Mach numbers 4.06 and 6.86 in the Langley 11-inch hypersonic tunnel and the Langley 9- by 9-inch Mach number 4 blowdown jet (refs. 2 to 8). The model has a tapered wing and a cruciform tail arrangement. Several important features of the flow around this model can be seen in these photographs. The fuselage is fairly blunt and the resultant strong bow wave causes total-pressure losses that reduce the lift of the wing and the tail.

In the side view (fig. 2) the wing is obscured by the body but the shocks from the wing can be seen. These shocks enclose regions of greatly different dynamic pressure above and below the wing. The vertical tails are almost completely covered by these regions at both Mach numbers but, as will be shown, this is not necessarily a bad situation if the tail surfaces are arranged properly. It is obvious from the photographs and from considerations of shock-field strength that these flow fields are nonisentropic and that their effects on the tail surfaces cannot be accurately predicted by potential-theory or linear-theory methods.

It should be noted that this paper will not consider the vortex type of interference. At high supersonic Mach numbers, the wing trailing vortices would not be expected to have much effect on the tail surfaces for close coupled configurations such as that shown in figure 1, which have a wing span considerably larger than the tail span. This supposition is supported by experimental data which gave a tail efficiency (ratio of lift-curve slopes of tail in the presence of the body to the tail in the presence of the body-wing configuration) of 94 percent at zero angle of attack and Mach number 6.86 for the trapezoidal wing model shown in figure 1.

SYMBOLS

C_L — lift coefficient, $\frac{\text{Lift}}{q_\infty S}$

C_Y — lateral-force coefficient, $\frac{\text{Lateral force}}{q_\infty S}$

C_m — pitching-moment coefficient about center of gravity, $\frac{\text{Pitching moment}}{q_\infty S\bar{c}}$

C_n — yawing-moment coefficient about center of gravity, $\frac{\text{Yawing moment}}{q_\infty Sb}$

C_{Y_β} — rate of change of lateral-force coefficient with angle of sideslip

C_{n_β} — rate of change of yawing-moment coefficient with angle of sideslip

ΔC_{Y_β} — increment in C_{Y_β} due to the addition of one or more vertical tail surfaces to a configuration

ΔC_{n_β} — increment in C_{n_β} due to the addition of one or more vertical tail surfaces to a configuration

α	angle of attack, deg
β	angle of sideslip, deg
b	wing span
$\bar{c}$	wing mean geometric chord
ϵ	effective downwash angle of the horizontal tail, deg
i_t	horizontal-tail incidence angle, deg
M	Mach number
q	dynamic pressure
R	Reynolds number based on $\bar{c}$
S	total wing area

Subscripts:

∞	free-stream value
U	in shock field from upper surface of a wing
L	in shock field from lower surface of a wing

LONGITUDINAL STABILITY AND CONTROL

Some effects of these flow fields on the longitudinal stability and control of this model will be considered first. A very important consideration regarding longitudinal stability is, of course, the location of the horizontal tail surfaces. Any analysis to determine the optimum location of the horizontal tail must consider the local dynamic-pressure and Mach number variations in the region of the tail, the downwash velocities, and the effects of the viscous wake.

At high supersonic Mach numbers, the horizontal tail surfaces may be directly affected by the compression and expansion fields from the wing, since these fields are swept back sharply. Thus it is instructive to examine the possible variations of dynamic pressure in the shock fields from a wing through the Mach number range. In figure 3 the ratio of the dynamic pressure in the flow fields influenced by the constant-thickness portion of a 4-percent-thick wedge-slab airfoil at an angle of attack of 15° is presented. From the figure, it is seen that the dynamic pressure in the compression field from the lower surface increases greatly with Mach number, whereas the dynamic pressure in the expansion field from the upper surface becomes so low as to be negligible at Mach numbers around 8 and 10. The ratios of the lift coefficients of surfaces in these regions to the lift coefficients of the same surfaces in the free stream would be higher in the compression field and lower in the expansion field than the dynamic-pressure ratios in figure 3. The reason for this is that the lift-curve slopes increase in the compression field because of the lower local Mach number in this region and decrease in the expansion field because of the higher local Mach number. Flow separation from the upper surface of such a wing would become a consideration at some angle of attack depending on the flow conditions. It is of interest to note that separation and the condition of high Mach number and low dynamic pressure which exists above the wing without separation both act to decrease the effectiveness of any aerodynamic surfaces located in this region.

A theoretical example of the effects of these dynamic-pressure variations and the accompanying Mach number and downwash variations on the stability and control effectiveness of horizontal tail surfaces is presented in figure 4. For simplicity of presentation, the two-dimensional flow field around a flat-plate wing is shown at a Mach number of 4.0. A 10° single-wedge horizontal tail surface is placed in three locations: in the expansion field from the upper surface of the wing, in the plane of the wing, and in the compression field from the lower surface of the wing. A surface at location C (in the compression field) will be in the region of high dynamic pressure as was indicated in figure 3, but the downwash angle at location C is equal to the angle of attack of the wing, and $d\epsilon/d\alpha = 1$. Thus, the tail surface will be at zero angle of attack to the local flow and will produce no lift and therefore no stabilizing moment, as is indicated in the table in figure 4.

The same downwash situation will exist at tail location A, and the pitching-moment contribution of a tail surface there is also zero, as indicated in the table. A stabilizer located in the region between the shock and the expansion from the wing trailing edge (as at location B) will be in a region of very small upwash (about 0.4° at this angle of attack and Mach number). The dynamic pressure will be close to the free-stream value; $d\epsilon/d\alpha$ will be very close to zero; and the tail will produce a stabilizing moment. In reference 1, Love has shown that, as wing thickness and leading-edge bluntness are increased, there is a large increase in upwash velocity at wing trailing edges at high angles of attack. However, this upwash decreases rapidly with distance downstream from the trailing edge. The configurations which will be discussed in this paper have thin wings and small leading-edge bluntness and should, therefore, produce only small values of upwash at the tail.

If these surfaces are considered to be all-movable control surfaces, their effectiveness $\partial C_m/\partial i_t$ relative to the in-line tail at location B is indicated in the table as $\left(\frac{\partial C_m}{\partial i_t}\right)\bigg/\left(\frac{\partial C_m}{\partial i_t}\right)_B$. (See fig. 4.) The control at location A would be only 0.6 as effective as that at B; a control at location C would be three times as effective as one at B; but the zero stabilizing moment and the obvious difficulties with ground clearance might well preclude the use of the low tail position.

However, a tail location slightly below the wing chord plane should be used to keep the tail out of the wing wake at low angles of attack, since at high Mach numbers and low Reynolds numbers a thick boundary layer is formed on the wing resulting in a thick wake which causes serious losses in tail effectiveness.

Figure 5 presents data obtained on the trapezoidal wing model which show the same variations of stability with tail location indicated by the simplified analysis presented in figure 4. The variation of pitching-moment coefficient with angle of attack is presented at $M = 6.86$ for the trapezoidal wing model (fig. 1) with three tail arrangements: a "plus" tail and high and low tails with 17° dihedral. At the top of figure 5, the locations of these tail surfaces are shown relative to the wing flow field at an angle of attack of 2°. As discussed previously, a configuration having a tail surface located just below the wake should have the highest stability, and this is confirmed by the experimental data – the plus tail configuration being the most stable.

Thus, it has been shown that for this configuration the trends of stability changes with tail location can be predicted from considerations of the two-dimensional wing flow field. But when actual values of the stability and control parameters are required, the body flow field with its upwash, the total-pressure loss caused by the bow wave, and the local dynamic-pressure changes must be considered.

Figure 6 compares experimental effective downwash values for the complete-model and the body-tail configurations with a theoretical prediction of local downwash angle at the root chord of the horizontal stabilizer. It is seen that both the body-tail and the complete-model configurations produce values of upwash at low angles of attack. These upwash values decrease at moderate angles of attack and change to downwash at high angles of attack.

The theoretical method is based on body crossflow theory and takes into account the large decreases in the total pressure of the crossflow which occur when the crossflow velocity is supersonic. The result of this method is shown as the dashed-line curve and it is seen that it predicts the experimental trend for the body-tail configuration with good accuracy. The trend is obviously quite different from potential theory which predicts a constantly increasing upwash with angle of attack.

In order to investigate the magnitude of the interference effects for this configuration, the lift and pitching-moment curves for the body-wing, the body-tail, and the body-wing-tail combinations are compared in figures 7 and 8 with the curves obtained by taking the sum of the theoretical lifts and pitching moments of the appropriate components. For most cases the difference between the experimental and the summation theories indicates that there are fairly large interactions in certain angle-of-attack ranges for these configurations.

The effect of tail location on longitudinal control as obtained from tests of the model with high and low horizontal tail surfaces with positive and negative dihedral is shown in figure 9. The change in pitching moment for a tail deflection of -10° is presented, and the lower tail configuration shows much greater effectiveness as angle of attack is increased, since the tail surfaces move into the region of higher local dynamic pressure and lower Mach number produced by the wing as indicated by the simplified analysis (fig. 4).

LATERAL STABILITY

The next part of the paper will be devoted to a discussion of the effects of shock-field interaction on lateral stability derivatives and a method of predicting these effects.

The effect of adding the wing to the body on the variation of the directional stability parameter $C_{n_{\beta}}$ with angle of attack for the test airplane model at Mach number 6.86 is presented in figure 10. The data indicate that at angles of attack greater than 10° the wing produces a stable increment of yawing moment due to the effect of the compression field from the wing lower surface on the afterbody. Data have also been obtained on high and low wing configurations which show a greater increase in $C_{n_{\beta}}$ for the high wing location, as would be expected.

Figure 11 presents the effect of tail arrangement on the variation of the directional stability parameter through the angle-of-attack range. With no vertical tails present there is a considerable increase in stability as the angle of attack is increased.

The upper and lower vertical tails produce about the same increment in directional stability at an angle of attack of 0°, but the contribution of the upper tail decreases as the angle of attack increases, whereas that of the lower tail increases. At an angle of attack of 16°, the lower tail has the same value of C_{n_β} as the two-tail configuration, showing that an upper vertical stabilizer may become totally ineffective at high Mach numbers and high angles of attack. The same trends were also found at Mach number 4 in tests of the same model (ref. 7).

A method has been derived to predict these effects of angle of attack on the lateral stability parameters. In this method the sidewash field produced by yawing the body predicted by potential theory is superimposed on the shock-expansion fields from the wing, and the forces and moments on the vertical-tail surfaces are obtained by a strip-theory method. This method has been used to calculate the increments in C_{n_β} and C_{Y_β} due to the addition of the vertical tail surfaces to the airplane configuration, and a comparison with the theoretical values of these increments at Mach number 4.06 is presented in figure 12. The computed values of ΔC_{Y_β} through the angle-of-attack range are in excellent agreement with the experimental values for the three tail arrangements. The predictions of ΔC_{n_β} are also good for the configuration with upper and lower vertical tails, but the predictions for the upper tail alone and the lower tail alone are less accurate, although the trend with angle of attack is given correctly for the lower tail configuration. These increments have been obtained with and without horizontal tails on the model, and show very little effect of the horizontal tail surfaces as would be predicted by the theory.

Figure 13 presents the same comparison at Mach number 6.86. The trends are estimated very accurately, but the absolute values of the slope increments are usually too high. It was realized that the predictions were probably too high because the total-pressure losses through the body shock wave had not been considered. In order to check this, the flow field around the body at zero angles of attack and sideslip was calculated by the method of characteristics, and the increments in side force and yawing moment on the vertical stabilizers in this flow field were computed. The results for the configuration with both upper and lower tails are indicated by the short lines on the zero angle-of-attack ordinate and show better agreement with experiment than the results of the method which does not consider the losses through the body bow wave.

Theoretical calculations of C_{Y_β} and C_{n_β} and their variations with angle of attack have been made by this method for two other configurations at $M = 4.06$. These configurations (fig. 14) have wings and tails with sharp leading edges and wedge slab sections. A comparison of the theoretical and experimental results is presented in figure 15. The agreement was better than that obtained for the trapezoidal wing model, probably because of the sharp leading-edge wing and tail airfoil sections and the rectangular plan form of the wing. The agreement for the model with delta tail surfaces was about as good as that shown in this figure for the trapezoidal tail surfaces.

CONCLUDING REMARKS

The analysis of the data presented here has shown that flow-field interference is of primary importance in stability and control calculations at high supersonic Mach numbers and that the location of stabilizing and control surfaces that give highest effectiveness can be determined by theoretical studies of these flow fields. A method has been derived which predicts the trend of downwash around a circular body as the angle of attack is increased. A method has also been derived which gives good predictions of the tail contributions to lateral stability through a considerable angle-of-attack range. The method used in the lateral stability case considered the two-dimensional flow fields from the wings but not the vortex fields from the wing or the body. Further work remains to be done on longer, more slender configurations for which the vortex type of interference will probably be important.

REFERENCES

1. Love, Eugene S.: Supersonic Wave Interference Affecting Stability. (Prospective NACA paper.)

2. Penland, Jim A., Ridyard, Herbert W., and Fetterman, David E., Jr.: Lift, Drag, and Static Longitudinal Stability Data From an Exploratory Investigation at a Mach Number of 6.86 of an Airplane Configuration Having a Wing of Trapezoidal Plan Form. NACA RM L54L03b, 1955.

3. Ridyard, Herbert W., Fetterman, David E., Jr., and Penland, Jim A.: Static Lateral Stability Data From an Exploratory Investigation at a Mach Number of 6.86 of an Airplane Configuration Having a Wing of Trapezoidal Plan Form. NACA RM L55A21a, 1955.

4. Dunning, Robert W., and Ulmann, Edward F.: Static Longitudinal and Lateral Stability Data From an Exploratory Investigation at Mach Number 4.06 of an Airplane Configuration Having a Wing of Trapezoidal Plan Form. NACA RM L55A21, 1955.

5. Dunning, Robert W., and Ulmann, Edward F.: Exploratory Investigation at Mach Number 4.06 of an Airplane Configuration Having a Wing of Trapezoidal Plan Form – Longitudinal and Lateral Control Characteristics. NACA RM L55B28, 1955.

6. Fetterman, David E., Jr., Penland, Jim A., and Ridyard, Herbert W.: Static Longitudinal and Lateral Stability and Control Data From an Exploratory Investigation at a Mach Number of 6.86 of an Airplane Configuration Having a Wing of Trapezoidal Plan Form. NACA RM L55C04, 1955.

7. Dunning, Robert W., and Ulmann, Edward F.: Exploratory Investigation at Mach Number 4.06 of an Airplane Configuration Having a Wing of Trapezoidal Plan Form – Effects of Various Tail Arrangements on Wing-On and Wing-Off Static Longitudinal and Lateral Stability Characteristics. NACA RM L55D08, 1955.

8. Penland, Jim A., Fetterman, David E., Jr., and Ridyard, Herbert W.: Static Longitudinal and Lateral Stability and Control Characteristics of an Airplane Configuration Having a Wing of Trapezoidal Plan Form With Various Tail Airfoil Sections and Tail Arrangements at a Mach Number of 6.86. NACA RM L55F17, 1955.

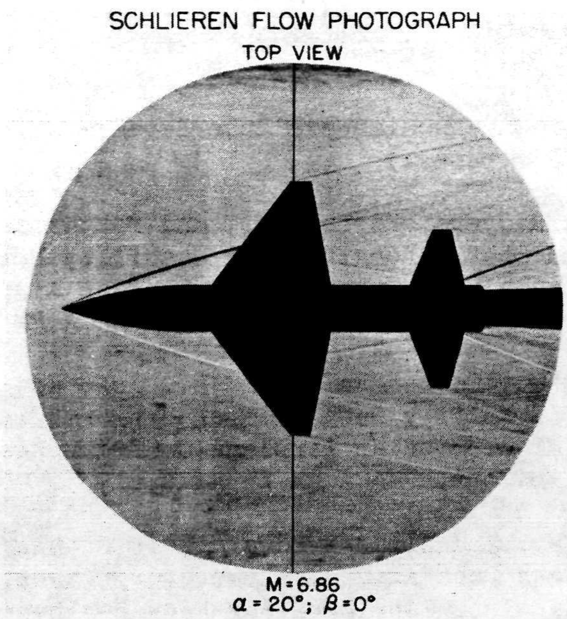

Figure 1

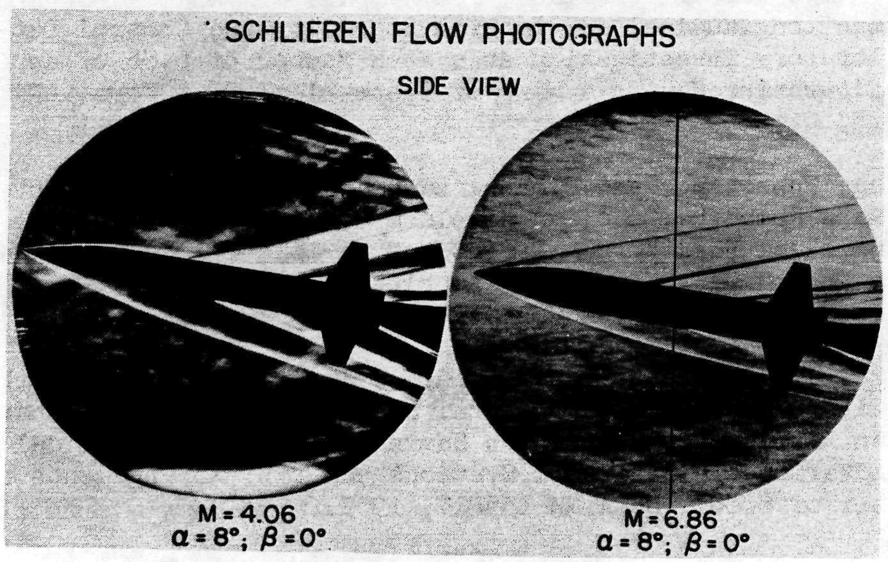

Figure 2

VARIATION OF DYNAMIC PRESSURE WITH MACH NUMBER

$\alpha = 15°$

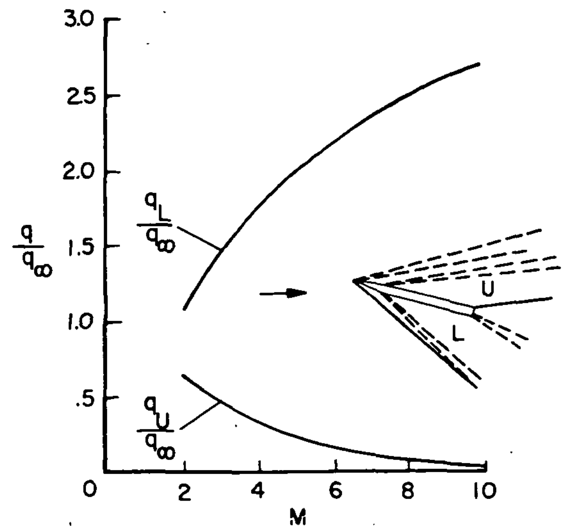

Figure 3

EFFECT OF TAIL LOCATION ON LONGITUDINAL STABILITY AND CONTROL

$M = 4; \quad \alpha = 10°$

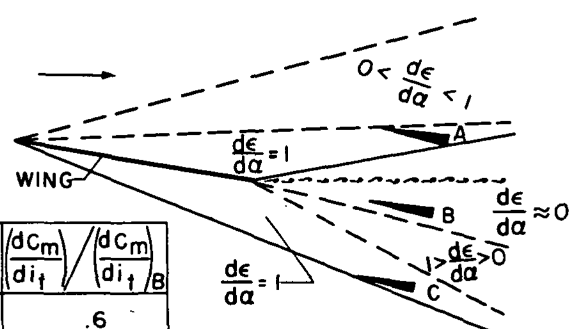

HORIZONTAL-TAIL LOCATION	$\frac{dC_m}{d\alpha}$	$\left(\frac{dC_m}{di_t}\right) \Big/ \left(\frac{dC_m}{di_t}\right)_B$
A	0	.6
B	STABILIZING	1.0
C	0	3.0

Figure 4

[redacted]

EFFECT OF TAIL LOCATION ON LONGITUDINAL STABILITY
M = 6.86

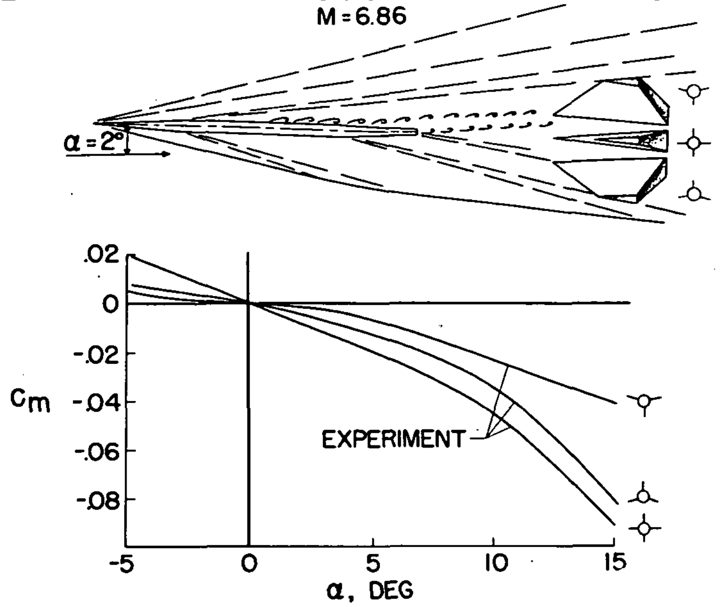

Figure 5

VARIATION OF EFFECTIVE DOWNWASH ANGLE WITH ANGLE OF ATTACK
M = 6.86

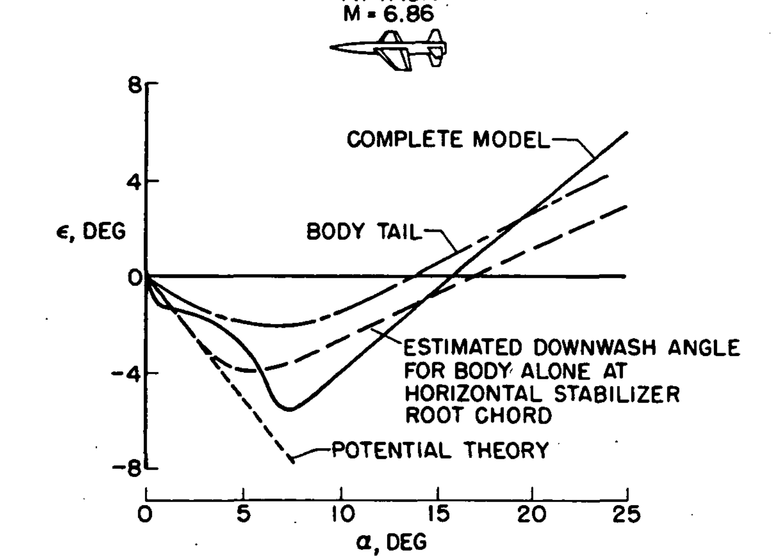

Figure 6

[redacted]

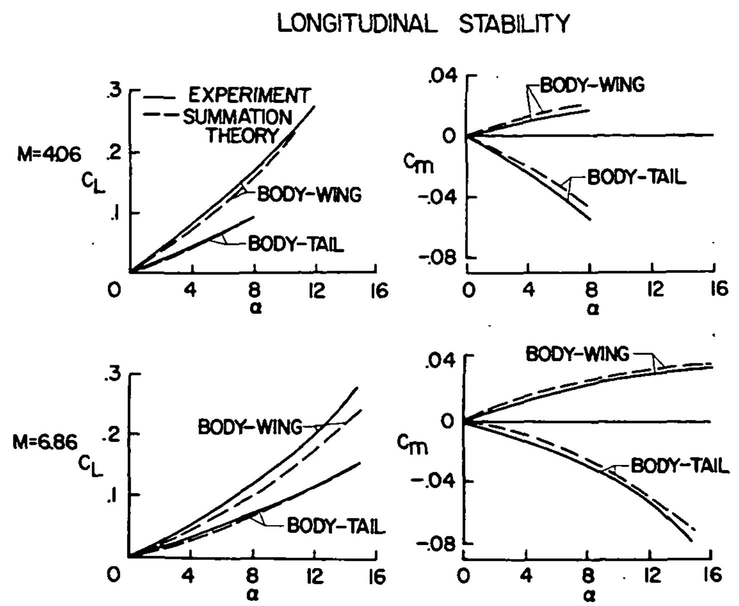

Figure 7

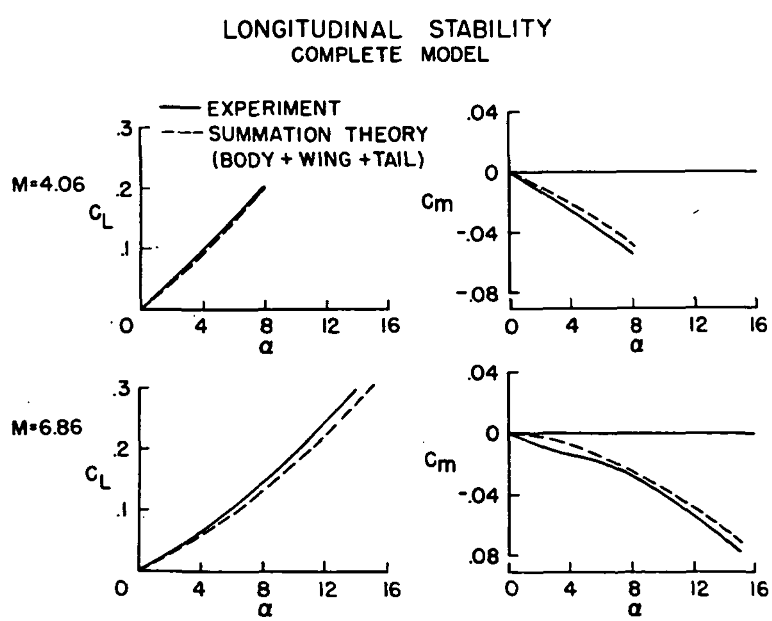

Figure 8

EFFECT OF TAIL LOCATION ON LONGITUDINAL CONTROL

M = 6.86

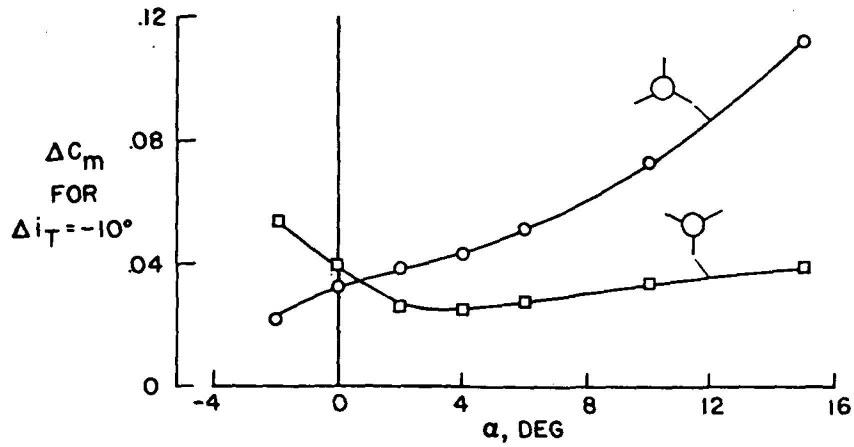

Figure 9

EFFECT OF WING ON DIRECTIONAL STABILITY

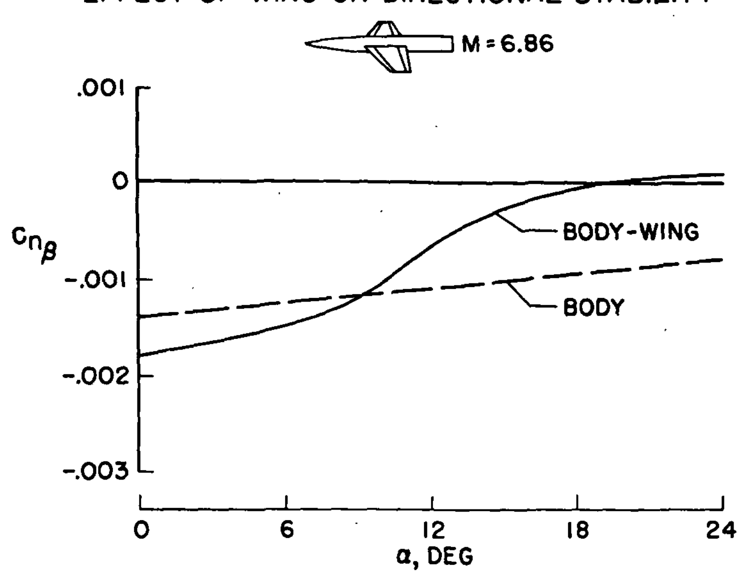

Figure 10

EFFECT OF TAIL ARRANGEMENT ON DIRECTIONAL STABILITY

M=6.86; R=343,000

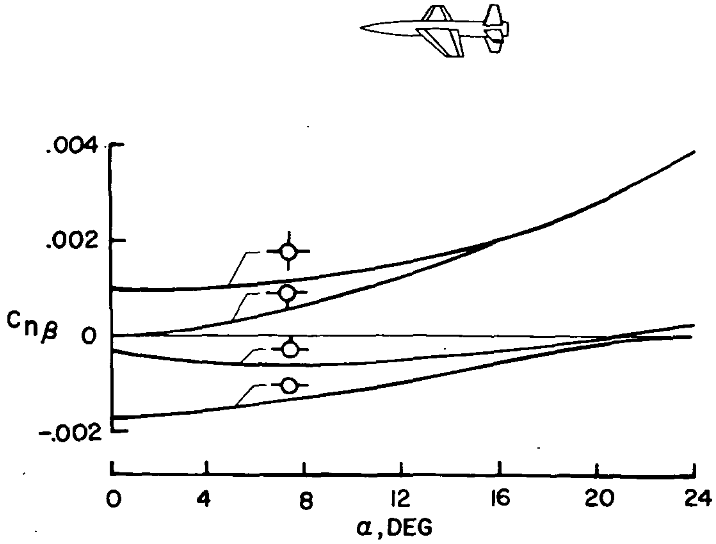

Figure 11

PREDICTION OF LATERAL STABILITY

M=4.06; R = 2.7×10[6]

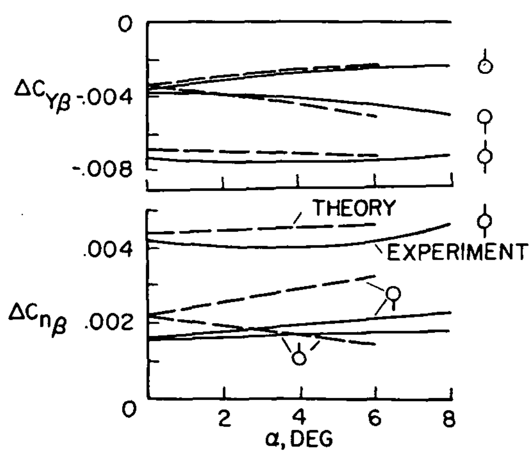

Figure 12

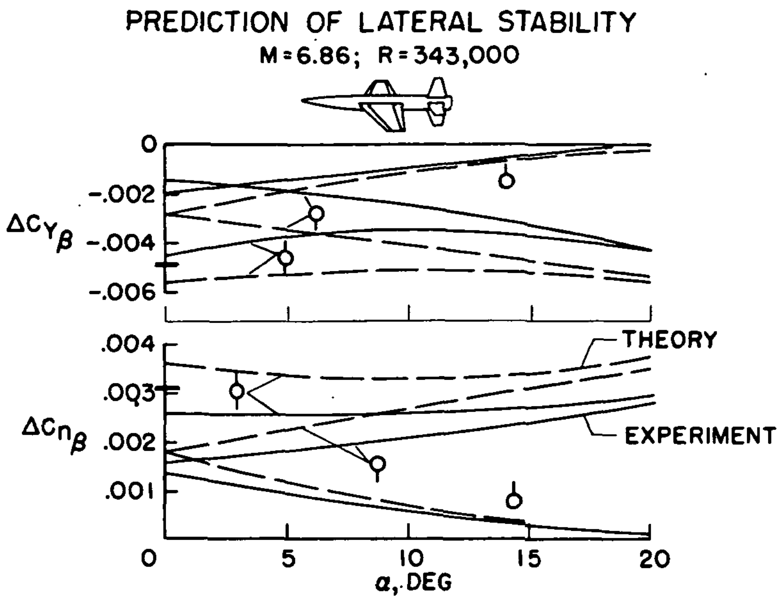

Figure 13

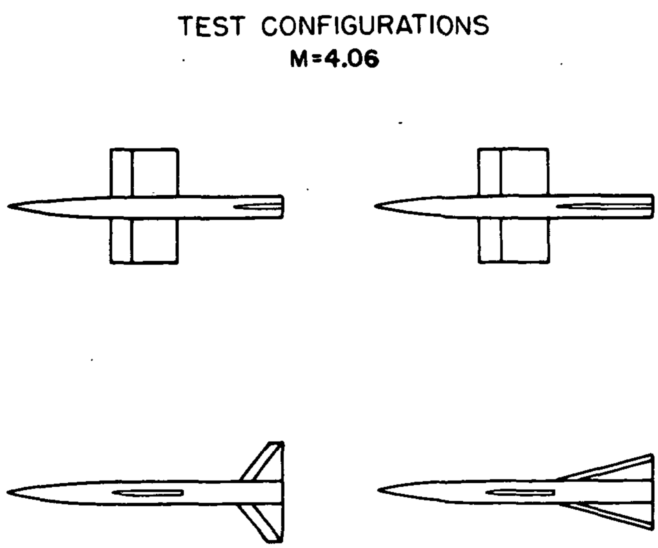

Figure 14

PREDICTION OF LATERAL STABILITY

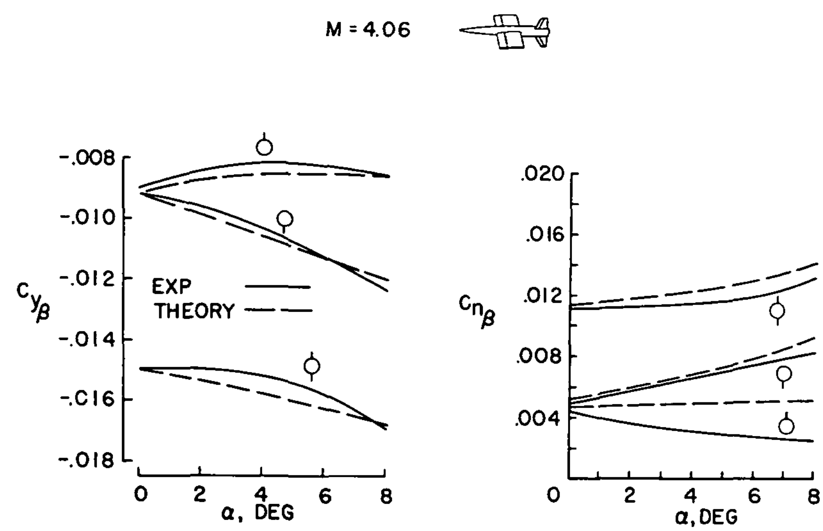

Figure 15

Preceding page blank

RECENT RESULTS OF STUDIES ON DYNAMIC STABILITY DERIVATIVES

By John D. Bird and William B. Boatright

Langley Aeronautical Laboratory

INTRODUCTION

The solution of the automatic-control and guidance problems of both airplanes and missiles requires extensive dynamic analyses. In many cases, these analyses are subject to large uncertainties because of inadequate knowledge of some of the dynamic stability derivatives. The purpose of this paper is to discuss some of the more interesting results from recent investigations of the lateral stability derivatives of high-speed airplane configurations and components, and in some instances to consider how well these quantities can be calculated by available procedures. The discussion is concerned with work in the low-subsonic, high-subsonic, and supersonic speed ranges in that order.

25

DISCUSSION

In the past, the various stability derivatives have been considered, for the purpose of stability analyses, to be independent of frequency of oscillation, and they have been determined in wind-tunnel tests by procedures involving steady sideslipping, rolling, and yawing motions. For unswept-wing airplanes, these procedures have given derivatives that show reasonably satisfactory agreement with flight experience. However, for swept- and delta-wing airplanes designed for high-speed flight, this circumstance is no longer the case for the high-angle-of-attack range where separation effects become important. Recent oscillation-in-yaw tests in the Langley free-flight and stability tunnels at low speed have shown that the lateral stability derivatives of these plan forms have large damping in yaw and appreciable directional stability at the higher angles of attack where the steady-state derivatives indicate much smaller values.

Figure 1 shows data on the damping in yaw and directional stability determined in the Langley stability tunnel by Lewis R. Fisher from oscillation tests of a thin 60° delta wing. The oscillation tests from which these data were obtained were the type that is most easily conducted in a wind tunnel and involved a rotational oscillation about the assumed center-of-gravity location. In the axis system normally employed in lateral-stability work, this motion consists of both yawing and sideslipping and results in the combination derivatives $C_{n_{r,\omega}} - C_{n_{\dot{\beta},\omega}}$ and $C_{n_{\beta}}$ plus the square of the reduced frequency multiplied by $C_{n_{\dot{r},\omega}}$ as factors indicative of damping in yaw and directional stability. The derivatives C_{n_r} and C_{n_β} obtained from steady-yawing and sideslipping tests are also shown for comparison. These steady-state derivatives are the quantities frequently employed in lateral-stability analyses. Throughout this paper the subscript "ω" is employed to designate results obtained in oscillation tests. The small lift curve in the lower left-hand side of figure 1 is shown to provide some orientation with regard to lift coefficient and angle of attack.

The large effect of frequency on the oscillatory yaw damping and directional stability and the significance of the $C_{n_{\dot{\beta},\omega}}$ derivative at the higher angles of attack are immediately apparent. In the angle-of-attack range where flow separation becomes a factor, but which is normally only approached at low speeds in landing, the damping in yaw and directional stability are appreciably more favorable than is indicated by the steady or zero frequency derivatives. Values of the damping in yaw near unity are obtained for the oscillatory contribution of the wing, whereas the steady-state contribution of the wing is about zero. The damping in yaw for a complete model, including the major factor of the tail contribution, is frequently no more than -0.25. Other data, not shown herein, indicate that amplitude of motion has a large influence on these high-angle-of-attack derivatives at low frequencies.

An analysis made in conjunction with a similar set of experiments made in the Langley free-flight tunnel assumes the damping to be caused by a lag in the buildup and decay of the separated flow that is characteristic of delta wings at the higher angles of attack. Calculations based on this assumption are in qualitative agreement with the experimental result for 30° angle of attack.

A recent investigation by Campbell and Woodling (ref. 1) indicates that the oscillatory derivatives shown herein may, at the higher angles of attack, make the damping rate of the lateral oscillation of a delta-wing airplane several times as great as the steady-state derivatives could accomplish alone.

In unpublished results obtained a few years ago, data from steady-roll tests were employed to show the existence, because of separation effects, of large losses in damping in roll at high subsonic speeds and moderate angles of attack for a range of wing plan forms, and to show the beneficial influence of a fence on this loss in roll damping. More recently, oscillation tests in the Ames 12-foot pressure tunnel, some of which are already in published form (for example, ref. 2 by Beam, Reed, and Lopez), have substantiated these losses in roll damping at high subsonic speeds and have shown that such separation effects may extend to other derivatives. Figure 2 shows data from oscillation tests of a delta-wing model at a Mach number of 0.6 which illustrate this result. These results indicate a large increase in the derivative $C_{l_{r,\omega}} - C_{l_{\dot{\beta},\omega}}$ at an angle of attack of about 12° which was not evident at a Mach number of 0.25. The improvement in the pitching-moment curve, presumably indicating a reduction in the separation on the tip which accompanied the addition of the fence and the corresponding reduction in the increase in the derivative $C_{l_{r,\omega}} - C_{l_{\dot{\beta},\omega}}$ near an angle of attack of 12°, is readily evident.

In recent years, semiempirical procedures have been developed and improved to the point where the steady-rolling derivatives of wings and relatively uncomplicated airplane configurations may be estimated reasonably well for the subsonic Mach number range. Figure 3 gives a comparison of the experimental and calculated steady-rolling derivatives for two airplane models for the purpose of illustrating how well these procedures apply to configurations having the irregularities of form of practical aircraft. These data are for unswept- and 45° swept-wing models and came from investigations made by Sleeman and Wiggins (ref. 3) in the Langley high-speed 7- by 10-foot tunnel. The calculations were made by using procedures given in papers by Goodman and Adair (ref. 4), Wiggins (ref. 5), and Michael (ref. 6), and involve the use of the experimental lift and drag characteristics.

The calculations are only in fair agreement with experiment in some of the cases shown. The most serious discrepancy arises because of the difficulty of estimating the sidewash effect of the rolling wing-fuselage combination on the vertical tail. This difficulty largely accounts for the difference shown between calculation and experiment for C_{n_p} and is felt to be associated with the relative flatness of the fuselages in the vicinity of the wing juncture. Calculations of the derivative C_{n_p} for the wing-fuselage combination are usually in much better agreement with experiment than is shown herein for the complete model.

Consider now some of the information available at supersonic speeds. Figure 4 shows results from an investigation of the damping in roll of aircraft configurations and components in combination made in the Langley 9-inch supersonic tunnel by McDearmon and Clark (ref. 7) by using the steady-roll technique. These results show the influence on C_{l_p} of what might normally be called a secondary interference effect.

Figure 4 presents the variation of C_{l_p} with Mach number for a model of the Bell X-1A airplane with and without certain component modifications at an angle of attack of 0°. For the complete configuration, an appreciable loss in damping in roll is shown near a Mach number of 2.2.

The body-wing tests and the tests of the complete model with a pointed canopy instead of the more blunt original canopy do not show this loss in C_{l_p} and agree reasonably well with the theoretical result for the wing alone. These results indicate that the loss in C_{l_p} experienced by the original model was associated with a separation phenomenon on the relatively blunt original canopy which influenced the wake and, therefore, the contribution of the tail to C_{l_p}. Additional tests with the horizontal tail removed indicate that the vertical tail is far more important than the horizontal tail in contributing to this loss. It is interesting to note that, at a free-stream Mach number of 2.2, the dorsal-nose shock becomes attached. The importance of this coincidence is not known. Theoretical calculations that were made of the body fin effects on the wing damping did not predict a loss in damping near a Mach number of 2.2.

It should be mentioned that damping-in-roll tests on two other airplanes have not shown the loss in damping in roll experienced by this model and have agreed well with theoretical values of C_{l_p}. Both of these models had more pointed canopies than the Bell X-1A.

Figure 5 shows results from a recent investigation made in the Langley 9-inch supersonic tunnel by Boatright (ref. 8) on a model of the Douglas D-558-II airplane. These tests were conducted at Mach numbers of 1.62, 1.91, and 2.41. The results at a Mach number of 1.62 are considered representative and are presented in figure 5. The sweptback wing of this airplane had 3° incidence and 3° negative dihedral. In order to simulate more closely the turbulent-boundary-layer conditions of the full-scale airplane, transition strips were fixed near the nose of the body and near the wing and tail leading edges for all tests.

In figure 5, $C_{l_{r,\omega}} - C_{l_{\dot{\beta},\omega}}$ is plotted against angle of attack. Results are shown for the complete configuration, the body-tail combination, and the body-wing combination. Tests were conducted at the two oscillation frequencies denoted by the circular and square symbols. Two surprising results are apparent from these tests. The first is the relative magnitude of the derivatives measured. Estimates of the value of this derivative, based on static-force measurements, give a value of $C_{l_{r,\omega}} - C_{l_{\dot{\beta},\omega}}$ of the order of 0.1. The values shown are much greater and are negative. Secondly, there is a large negative contribution to this derivative as a result of the body-wing combination. That is, the moment associated with this derivative would cause a roll to the left when the airplane is yawing to the right. This occurs in spite of the fact that the measured C_{l_β} values of the body-wing combination were slightly negative. That is, in a static condition, sideslip to the right produces rolling moment to the left. Whether the large negative values of $C_{l_{r,\omega}} - C_{l_{\dot{\beta},\omega}}$ of the wing are due principally to the sweepback, the negative dihedral or body interference effects on the wing is not understood. However, the large negative values of $C_{l_{r,\omega}} - C_{l_{\dot{\beta},\omega}}$ of the wing are predominant in determining the values of this derivative for the complete configuration. This also is contrary to the usual assumption that the major contributor to this cross derivative in the low-angle-of-attack range results from the vertical tail.

Although the values of $C_{l_{r,\omega}} - C_{l_{\dot{\beta},\omega}}$ are greatly different from the one estimated, calculations of the period and damping for this particular airplane showed little effect of the magnitude of this derivative on the stability of the airplane at low angles of attack. Other calculations made in a program currently under way to evaluate the importance of some of the effects shown in this paper indicate this derivative to be very important at higher angles of attack.

CONCLUDING REMARKS

It is evident from the material presented herein that the understanding of the behavior of the dynamic lateral stability derivatives is far from complete. The significance of the results presented in terms of airplane dynamic stability will have to be evaluated for each particular design under consideration.

REFERENCES

1. Campbell, John P., and Woodling, Carroll H.: Calculated Effects of the Lateral Acceleration Derivatives on the Dynamic Lateral Stability of a Delta-Wing Airplane. NACA RM L54K26, 1955.

2. Beam, Benjamin H., Reed, Verlin D., and Lopez, Armando E.: Wind-Tunnel Measurements at Subsonic Speeds of the Static and Dynamic-Rotary Stability Derivatives of a Triangular-Wing Airplane Model Having a Triangular Vertical Tail. NACA RM A55A28, 1955.

3. Sleeman, William C., Jr., and Wiggins, James W.: Experimental Investigation at High Subsonic Speeds of the Rolling Stability Derivatives of a Complete Model With an Aspect-Ratio-2.52 Wing Having an Unswept 72-Percent-Chord Line and a High Horizontal Tail. NACA RM L54I20, 1955.

4. Goodman, Alex, and Adair, Glenn H.: Estimation of the Damping in Roll of Wings Through the Normal Flight Range of Lift Coefficient. NACA TN 1924, 1949.

5. Wiggins, James W.: Wind-Tunnel Investigation at High Subsonic Speeds To Determine the Rolling Derivatives of Two Wing-Fuselage Combinations Having Triangular Wings, Including a Semiempirical Method of Estimating the Rolling Derivatives. NACA RM L53L18a, 1954.

6. Michael, William H., Jr.: Flow Studies in the Vicinity of a Modified Flat-Plate Rectangular Wing of Aspect Ratio 0.25. NACA TN 2790, 1952.

7. McDearmon, Russell W., and Clark, Frank L.: Wind-Tunnel Investigation of the Damping in Roll of the Bell X-1A Research Airplane and Its Components at Supersonic Speeds. NACA RM L55I19, 1955.

8. Boatright, William B.: Wind-Tunnel Measurements of the Dynamic Cross Derivative $C_{l_r} - C_{l_{\dot{\beta}}}$ (Rolling Moment Due to Yawing Velocity and to Acceleration in Sideslip) of the Douglas D-558-II Airplane and Its Components at Supersonic Speeds Including Description of the Technique. NACA RM L55H16, 1955.

EFFECT OF FREQUENCY OF OSCILLATION ON LOW-SPEED STABILITY DERIVATIVES OF A 60° DELTA WING

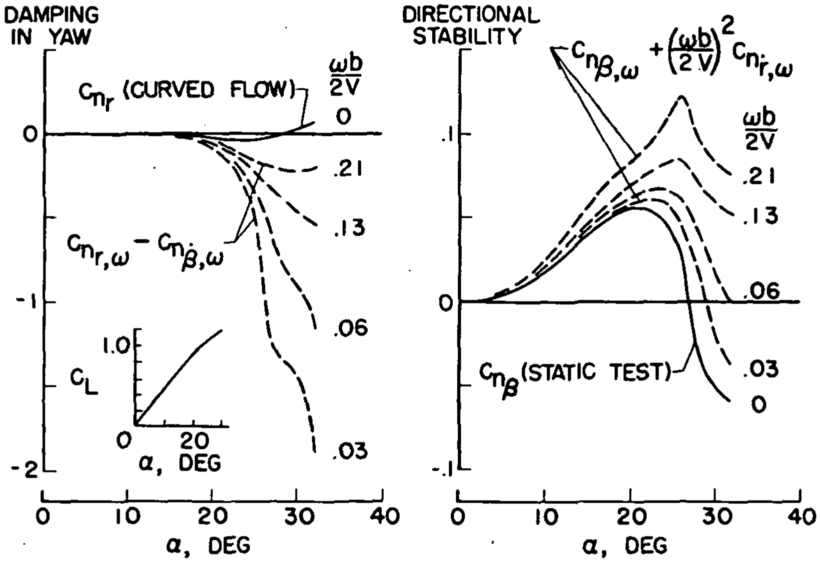

Figure 1

EFFECT OF FENCES ON STABILITY DERIVATIVES OF A DELTA-WING MODEL

M = 0.6

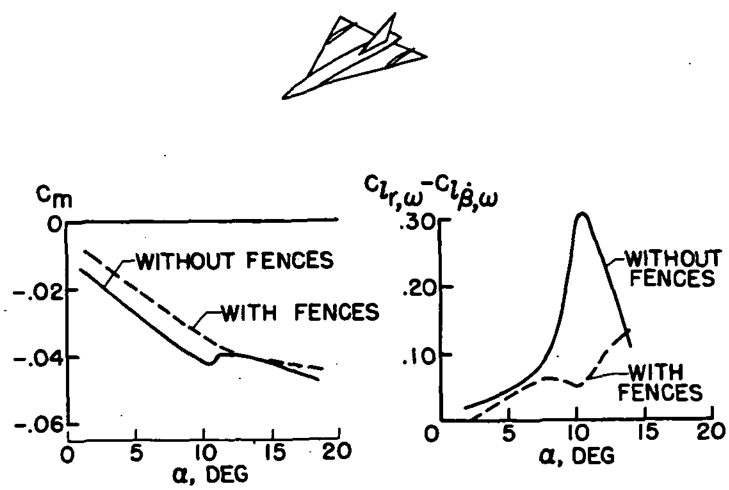

Figure 2

~~CONFIDENTIAL~~

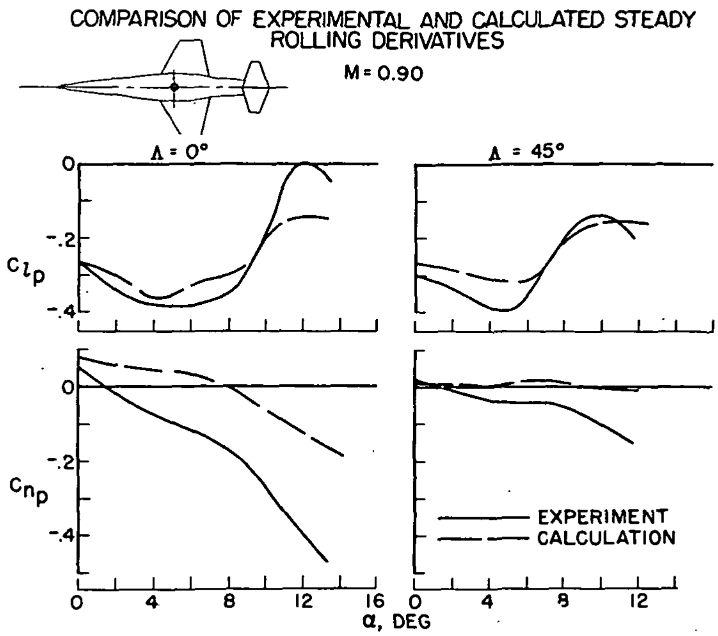

Figure 3

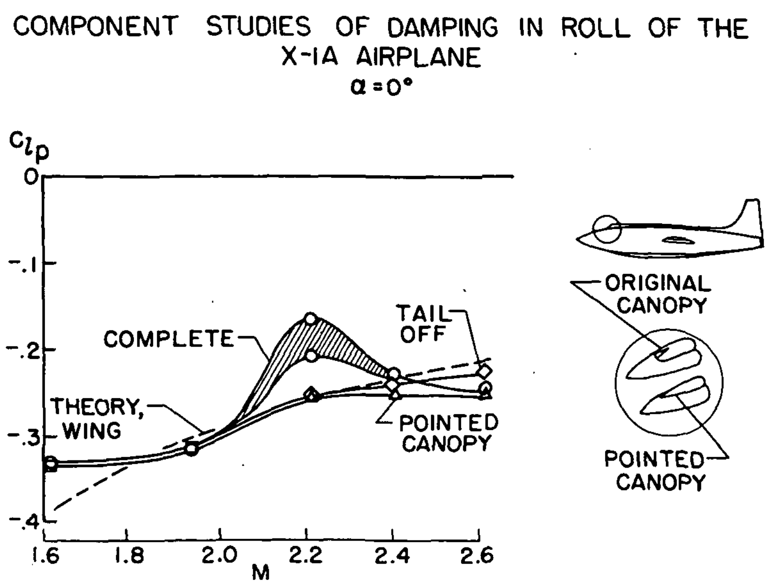

Figure 4

~~CONFIDENTIAL~~

VARIATION OF $C_{l_{r,\omega}} - C_{l_{\dot{\beta},\omega}}$ WITH α FOR THE D-558-II AIRPLANE

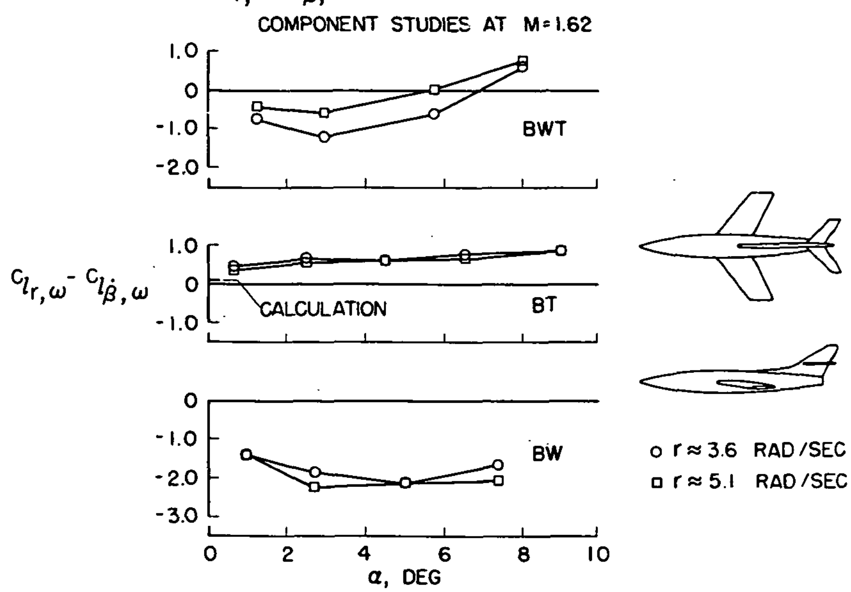

Figure 5

Preceding page blank

SOME RECENT RESEARCH ON THE HANDLING QUALITIES OF AIRPLANES

By Walter C. Williams
NACA High-Speed Flight Station

and William H. Phillips
Langley Aeronautical Laboratory

INTRODUCTION

The problem of interpreting the pilot's opinion of the handling of an airplane in engineering terms has been the subject of investigation for a number of years. Up to and through World War II there was little change in the requirements since, generally speaking, the airplanes were of the same type. In recent years, however, speed range of military airplanes has doubled and configurations have been drastically altered. It has been attempted, therefore, to continue research into the handling qualities of airplanes so that the requirements would meet the needs of the newer speed ranges and configurations.

Some of this work has been underway at the NACA High-Speed Flight Station using research airplanes as well as some of the more recent operational airplanes (three fighters and one medium bomber). The ranges of configurations covered included straight-wing airplanes, swept-wing airplanes having 35° to 60° of sweep, and delta-wing configurations which were tailless. In addition, both civilian and military test pilots as well as military operational pilots have been consulted. This paper does not attempt to specify directly new requirements since either the information does not cover a large enough number of airplanes or the investigations are not complete enough at this time to state requirements definitely. This paper is, therefore, an indication of the thinking of the National Advisory Committee for Aeronautics with regard to deficiencies or possible changes in the handling-qualities specifications. Since this paper, in outline, follows the handling-qualities specifications, the longitudinal case will be discussed first.

26

DISCUSSION

Longitudinal Stability and Control

Dynamic longitudinal stability.- In connection with dynamic longitudinal stability, periods and times to damp have been determined by using the usual pulsing techniques. These data are shown in figure 1. The speeds are from subsonic to moderately high supersonic with an altitude range from 10,000 to 50,000 feet. Also illustrated in this figure is the present military specification which requires damping to one-half amplitude in one cycle as well as the older requirement of damping to one-tenth amplitude in one cycle. The corresponding scales are also shown. The pilots in this case did not feel that the damping was sufficient for satisfactory handling qualities, but as the damping approached the old requirement of one-tenth amplitude in one cycle the airplanes became more satisfactory. There is evidence from studies of tracking runs that damping of the order shown in conjunction with the characteristics of the usual powered control system adversely affects the gunnery. Extension of these data will be accomplished in the near future with the installation of artificial damping in one of these airplanes because it appears that the pilot prefers the short-period oscillation well damped. This study of the pitch damping requirements is a subject of intense investigation at this time because it has been found, as is pointed out subsequently, that there are other characteristics of the airplane that are seriously affected by pitch damping.

Longitudinal trim changes with speed.- Figure 2 shows three different types of variation of elevator or stabilizer angle and force with Mach number. All these airplanes have irreversible control systems with artificial feel. In none of these cases did the pilot object strenuously to the trim changes in the transonic region for the case of accelerating through this speed range. It is noted that the trim force changes are quite moderate, under 10 pounds. There was, however, a gradation of pilot opinion between the various airplanes. The pilots objected most to airplane A where there was a reversal of the elevator force and position with speed. They objected somewhat less to airplane B where the reversal was of smaller magnitude, in this case only 3 pounds. They preferred the characteristics of airplane C where increasing speed always calls for increasing push force, even though, between Mach numbers of 0.95 and 1.1, there is a change in force of the order of 10 pounds, which, however, is always in the stable direction. It appears, therefore, that if the trim changes are light (of the order of 10 pounds) the pilot will not object too strenuously; it is further apparent that he still desires trim characteristics such that increasing speed calls for increasing push force. In the older airplanes having similar force variations with speed but with a much higher level of changes, in some cases as high as 50 to 60 pounds, the pilot found such trim curves extremely undesirable. For the problem of cruising within the regions of trim changes, either where the trim variation is very flat or reversed, the problem is a little more involved. It was found that the pilot encountered some difficulty in actually setting up the trim speed in this region. However, once the speed was established, with practice he could fly reasonably steadily in this speed range. It did, however, require continuous attention and a moderate amount of control manipulation. For a long-range cruise it would be rather tiring. For flight at high altitude (50,000 feet) it is possible that the entire flight speed range of the airplane is within the trim-change region. In discussions with military pilots it was found that they were working continuously to fly formation in this speed range.

Pitch-up with decreasing speed.- In the past there has been much discussion of longitudinal instabilities during constant-speed accelerated maneuvers which involved nonlinearities in the variation of pitching moment with lift coefficient. Since that time, however, much has been learned to eliminate this problem through actual design procedures.

Another subject of research has been that of instabilities or pitch-ups during maneuvers made at constant g with decreasing speed, particularly for the case of decreasing speed from supersonic to subsonic speeds. Many airplanes studied in the past had constant-speed pitch-ups at transonic speeds. For the present discussion, airplanes are considered which had linear stability with lift through the range covered.

In order to study the problems associated with slowing down while holding constant g, measurements have been made on three airplanes of the longitudinal control deflections and forces as a function of Mach number and normal acceleration. In addition tests were made in which the pilot attempted to hold the normal acceleration constant in turns while slowing down at various rates. The control deflections and forces to hold 1g are shown in figure 2. The corresponding curves in an accelerated turn may be visualized by adding the increments due to increasing C_N or g shown in figure 3, which gives the variation of force per g and elevator control per unit C_N as a function of Mach number. As shown in this figure, airplane A exhibited a large loss in control effectiveness in the transonic range. The instability shown in the curve of δ_e as a function of M for 1g would therefore be accentuated at higher values of g. On the other hand, the loss in control effectiveness for airplane C is very slight, and when combined with the stable curve for 1g would result in nearly constant control deflection to hold some value of normal acceleration in a turn. (The characteristics of airplane B are intermediate between those of A and C.)

The variation of force per g with Mach number for the three airplanes is also shown in figure 3. The curves differ considerably from the position curves because of the characteristics of the individual feel devices. The characteristics are such, however, that a marked decrease in pull force would be required in airplane A when slowing down through the transonic range in a turn, whereas the force for airplane C would be about constant.

Time histories of the maneuvers at constant g made with these airplanes are now presented. It should be noted that changing the rate of decrease of Mach number when decelerating from supersonic to subsonic speeds by making runs with afterburner on and off had little effect on the general conclusions to be drawn from these runs.

The maneuver made with airplane A (fig. 4) shows that the pilot had little difficulty in maintaining the average value of g throughout the maneuver. In entering the region of greatest trim change, however, the airplane was disturbed in pitch, and from then on, because of low damping in pitch, the pilot had difficulty in controlling the maneuver precisely.

Similar results are shown in the case of airplane B (fig. 5). This run was made at a somewhat higher value of g. A fairly abrupt stabilizer motion made on entering the unstable region may be seen. The resulting disturbance continued as the Mach number decreased further. In this case, precision of control was further adversely affected by large control friction and breakout forces.

The maneuver made with airplane C (fig. 6) shows, in contrast, a very steady and precise control of normal acceleration, with little change required in stabilizer position or force.

These data show that, for airplanes with adequate control power and positive stability with change in angle of attack, the pilot can control the average normal acceleration reasonably well in maneuvers in which the speed decreases from supersonic to subsonic. When there are large trim changes and low damping in pitch, however, precise control is difficult. Increases in pitch damping and improvements in the power control system are expected to alleviate these problems.

Most of the difficulties experienced in earlier airplanes with excessive pitch-up in reducing speed have occurred at low altitude, where the deceleration is greater and the normal acceleration due to a given change in angle of attack is increased. Also, these airplanes usually had conventional elevators which experience large increases in effectiveness as the speed is decreased from supersonic to subsonic. The provision of all-moving tails, which maintain more nearly constant effectiveness, has been found to alleviate these problems greatly. Nevertheless, the unsteadiness encountered in the present tests at high altitude would be expected to increase at lower altitude. The conclusion may be drawn, therefore, that efforts should be made to avoid as much as possible trim changes and variations in control effectiveness with Mach number in the transonic range.

Lateral Stability and Control

<u>Lateral-directional oscillations</u>.- The next subject to be discussed is lateral-directional stability and control, in particular, damping of

the lateral-directional oscillations. This particular requirement has probably been the source of more discussion and/or controversy than any of the other requirements. This is probably because it depends on many variables and leans extremely heavily on pilot opinion. The pilots, in this case, were required to fill out a form which covered maneuvers used in operations typical of cruise, instrument, and gunnery flying. As a basis for a start, figure 7 illustrates the present requirement that specifies the cycles to damp as a function of the parameter ϕ/v_e which is the ratio of bank angle to equivalent side velocity. The upper curve on this plot is the damping requirement as stated in the present Military Specifications. For most configurations with controls fixed and free the lower curve covers the case of artificial damping devices inoperative in the power-approach condition. As can be seen in this figure, there are airplanes that fall into the satisfactory zones but are considered unsatisfactory or marginal at best by the pilots. This is particularly true in the case of high values of ϕ/v_e. Actually, the curve reported in reference 1 calling for a very much higher degree of damping at the higher values of ϕ/v_e more nearly agrees with the pilot opinion. When these characteristics were looked at from many viewpoints with the use of other criteria, it was found that one of the primary sources of pilot satisfaction or dissatisfaction was the ratio of roll to yaw, as this curve indicates. It was found that the airplanes could acutally be separated into two general regions depending on the value of the ratio of rolling rate to yawing rate. Figure 8 goes back to the original requirement of time to damp to one-half amplitude as a function of period for airplanes having values of roll-to-yaw ratios less than 4. These data show that this requirement would be quite adequate. It is indicated that for general flying, not the close flying of gunnery or bombing, the pilot would tolerate less damping where the period was high. However, in considering the case of roll-to-yaw ratios greater than 4, as shown in figure 9, it can be seen that, regardless of the damping, the airplanes are generally unsatisfactory. In obtaining data on a subject like this, of course, there are many influences. However, on the basis of these data and what might be called general pilot opinion on the flying of any particular airplane, high ratios of roll to yaw are very objectionable to the pilot since any correction in yaw or a side gust results in excessive rolling which causes changes in heading.

Lateral control.- The lateral-control requirements and changes made thereto along with the increase in speeds of the airplanes have always, up to now, resulted in increasing roll velocities and increasing rolling accelerations. During the past year or two, however, the rates have become high enough to be in resonance with the pitch and/or yaw frequencies of the airplanes so that a serious roll-coupling problem on a number of airplanes has resulted. Calculations have shown that the value of the roll rate as well as the angle of bank reached has, of course, very serious effects upon the degree of roll coupling that exists, or at least on the motions resulting from roll coupling. It is indicated that a reduction in either roll rate or angle of bank reached during a roll, or both, will have very beneficial effects on the roll coupling to the point that it could be relegated to a very restricted portion of the flight envelope; it might be added that these calculations also showed that increasing the damping in pitch had a very beneficial effect on the roll coupling. In any event it appeared to be of urgent importance to reexamine carefully the roll requirements, both at high and low speeds. A number of flight and analog investigations bearing on this problem have been carried out at the NACA High-Speed Flight Station and at the Langley Aeronautical Laboratory. The findings from these investigations are summarized in figures 10 to 12. This, incidentally, is one of the problems discussed quite thoroughly with military pilots.

Figure 10 presents a summary of the aileron control characteristics for a typical airplane at a Mach number of 0.8 and altitude of 30,000 feet. Maximum rolling velocity and time to roll to 90° are plotted as a function of total aileron deflection.

The solid line indicates the minimum time required to pass through 90° bank angle. It is apparent that above an aileron deflection of 20° a region of diminishing returns is present. Note that this airplane would barely meet the present specifications of 100° change in bank angle in one second with maximum aileron deflection. This curve does show the difficulty of making a test to prove this requirement since the time measurement requires very high accuracy because of the small slope of t with δ_a. It also shows that the designer may have to double the aileron power to gain 1/10 second in time to reach a given bank angle.

Another manner in which the aileron capabilities have been evaluated is by not only including the time to accelerate and roll through a given bank angle but also to include the time required to become reasonably stabilized at the desired bank angle. This time designated t^* is of considerable significance when making offensive or tracking maneuvers. The dashed curve represents the average time required by pilots to complete rolls from a 45° bank turn to 45° in the opposite direction. It would appear that the time t^* decreases with aileron deflection until about 21° of total aileron is used; above this deflection the time required increases fairly rapidly. This was primarily attributable to overshoot. The aileron deflection for minimum t^* agreed very well with the pilots' opinions of the optimum aileron required for the 90° maneuver. The peak roll velocity attained for optimum conditions in this maneuver would be about 2 radians per second and it is evident that the ultimate roll rate is fairly well developed in 90°. It should also be mentioned that studies of this type covered a Mach number range of 0.7 to 1.2 for this airplane and the t^* curves and accompanying pilot impressions did not appreciably change over the entire speed range.

In figure 11 is shown one type of analysis of aileron requirements based on this investigation. Maximum ~~roll~~ velocity is plotted as ordinate and maximum roll acceleration as abscissa. These quantities were obtained from 90° maneuvers of the type summarized in figure 10. The approximate test envelope is shown by the dashed line. If in figure 10 the regions of t that are less and greater than 1.75 seconds are arbitrarily separated, the flight envelope of figure 11 is divided as shown into three regions: a region of perhaps too slow response for general use, a region in which combinations of roll acceleration and roll velocity produced satisfactory results, and a region of roll velocity and acceleration that was obviously too much for the average pilot to cope with. As a point of interest the center of the satisfactory range is defined fairly well by a value of $p_{max} = 2$ radians per second and a value of $p_{max} = 5$ radians per second squared.

A flight and analog investigation of the aileron power required for visual tracking in pursuit-type attack and evasive maneuvers has been completed at the Langley Aeronautical Laboratory. The flight investigation was necessarily restricted to subsonic speeds. A similar flight study is under way at the NACA High-Speed Flight Station and will include work at supersonic speeds.

The analog-computer investigation consisted of a determination of the theoretical values of rolling velocity and rolling acceleration required of an attacking airplane in order to follow a target airplane during various turn entry maneuvers. Some results of this investigation are plotted in figure 12. These results show that in the target maneuvers involving 90° bank, the rolling velocity and rolling acceleration required of the attacking airplane decrease rather rapidly as the range increases. When the target makes a 180° roll, however, the rolling velocity and rolling acceleration required of the tracking airplane are considerably greater and do not decrease rapidly with increasing range. The values of rolling velocity and rolling acceleration obtained from these analog-computer studies are in good agreement with those obtained from flight tests under similar conditions. It therefore appears that the rolling requirements of an attacking airplane can be determined on a rational basis by means of analog-computer studies of this type. Also, the analog computer allows studies of a much wider range of conditions with closer control of the variables than is possible in flight tests. Extension of these calculations to supersonic speeds and to cases in which the attacker is overtaking the target is now in progress. Results obtained so far for a Mach number of 1.4 show that values of rolling velocity about 50 percent greater than those plotted in figure 12 are required in order to follow similar target maneuvers.

Interviews with military pilots indicated that as far as high-speed control was concerned they felt the present airplanes had more aileron control than they would ever use. They found it hard to recall any case where they had hit the stops in using ailerons at high speeds. They generally felt that the deflection could be cut down without serious effect. They felt, further, generally speaking, that not over 180° of bank angle would be required in any tactical maneuver. There were a few holdouts but the general concensus was that if the airplane were satisfactory within this bank-angle range the tactical mission would not be restricted. Since it has been established that, for high-speed flight, aileron power was greater than required, the low-speed case should then be considered; that is, the take-off and landing as well as whatever low-speed maneuvering may be required in flight.

Rudder-fixed rolls were made at V_i = 160 knots with landing gear down with two airplanes. The roll specification for low-speed flight calls for an average $pb/2V$ of 0.05 for the first 30° of bank.

One of these airplanes had an average $pb/2V$ of 0.036 for the first 30° of bank and the pilots feel the lateral control to be entirely adequate for low-speed flight.

The other had an average $pb/2V$ for the first 30° of bank angle which was about 60 percent of the required minimum of 0.05 (about 0.03). This is brought about by a reduction in aileron effectiveness at the high angle of attack (11°) and adverse sideslip coupled with relatively high dihedral effect. Some pilots consider this airplane to have marginal lateral control power for landing.

Actually, it appears that, for the most part, present-day airplanes have sufficient lateral control power; however, consideration has to be given to cross-wind landings and take-offs and need for counteracting wakes of other airplanes during the close-pattern landings which appear to be a military requirement. It is felt that the present low-speed lateral-control requirement is perhaps unrealistic in that it could not be met on current airplanes which the pilots felt were satisfactory.

Rudder control.- Among other studies has been the use of rudder during high-speed maneuvers. It appears for the high-speed roll case that the pilot has a very difficult time coordinating any maneuver with the use of rudder because of the high roll rates. Also, because the airplane rolls about an axis inclined to the flight path with the cockpit usually well forward in the airplane, it is possible for the ball-bank indicator, which is one way of the pilot's knowing what sideslip is occurring, to give him fallacious indications with the result that perhaps the control introduced based on reading of the ball would be in the wrong direction. The pilot, of course, is undergoing the same acceleration forces. However, this does not mean that the rudder is not useful to the pilot in supersonic flight. It has been found that some pilots use the rudder quite a bit either to help damp high-speed lateral oscillations or to account for lateral trim changes that may occur in transonic or supersonic flight.

Control-System Characteristics

Research on power control systems has been continued using both theoretical methods and ground simulator studies in an attempt to formulate requirements for satisfactory characteristics. It is realized that because of the large number of variables affecting the characteristics of a power control system, a simple requirement for control friction or breakout force will not be adequate to rule out all unsatisfactory conditions.

A study is being conducted, using a ground simulator known as the pitch chair, to determine the boundaries between satisfactory and unsatisfactory regions in terms of such control-system parameters as valve friction, flexibility, backlash, and so forth.

Figure 13 illustrates some of the results obtained in this study. This figure shows a sketch of the control system which is being used. Provisions are made to add static friction to the control stick, static friction at the valve, and flexibility between the control stick and the valve. It should be noted that in this case the control feel device, which is a simple spring, is located at the control stick ahead of the region where flexibility is present. The curves in the lower left-hand part of the figure show the case for a rigid control system. At very low values of friction, less than 1/2 pound, conditions are considered to be tolerable though not entirely satisfactory because small movements of the airplane can cause the pilot to apply inadvertent control motions as a result of inertia of his hand and arm. Increasing values of valve friction in this case are acceptable provided the stick friction remains greater than the valve friction. This is true because the stick friction will then serve to center the valve and prevent the power control system from motoring in the absence of the pilot's inputs. However, when the combined values of stick friction and valve friction exceed approximately 3 pounds, the pilots considered the characteristics to be unsatisfactory because of the difficulty of making small control corrections when the breakout force exceeded 3 pounds.

The right-hand part of figure 13 shows similar results for the case in which flexibility is present between the control stick and the valve. In this case any amount of valve friction exceeding about 4 ounces at the control stick led to very unsatisfactory control characteristics. The introduction of flexibility ahead of the feel device, however, gave results more nearly similar to those in the left-hand part of the figure.

CONCLUSIONS

A few tentative conclusions can be drawn from the investigations which have been discussed. It appears that increased damping in pitch should be provided in modern airplanes. This damping could be artificial since airplanes meeting the present requirements without artificial damping, although unsatisfactory, are not considered dangerous. Increases in damping in pitch will not only improve dynamic longitudinal stability but will improve longitudinal characteristics in maneuvers made with large speed losses as well as alleviate the roll-coupling problem. The exact degree of longitudinal damping desired is the subject of study at present and it is not possible to state the exact requirement.

It appears that trim changes involved in force changes of less than 10 pounds will not be extremely undesirable to the pilot; however, the more nearly the case of true stability with speed, that is, increase in push force for increase in speed, the more desirable the airplane will be. In the case of speed losses during maneuvers from supersonic to subsonic speeds it appears that one of the primary factors involved is the trim changes with speed coupled with low damping, so if effort is made to satisfy this case there will be improvement in the maneuvering characteristics. It is difficult at this time to state any definite requirement.

For a case of dynamic lateral stability the pilots are not satisfied with airplanes having high roll-to-yaw ratios and the results indicate that any airplane having a roll-to-yaw ratio greater than 4 will be considered undesirable by the pilot.

For the high-speed case, the lateral-control requirements can probably be relaxed - in fact, appreciably reduced. Study should be made of the mission the airplane is expected to perform. For the present it appears that the low-speed requirements are very stringent and some relaxation could be tolerated.

For a rigid power boost system some valve friction can be tolerated if there is greater stick friction. The combination of the two should not exceed 3 pounds. For a system having flexibility, the requirements for valve friction are very stringent if the feel system is at the stick. Placing the feel system at the valve results in requirements similar to those for the rigid case.

REFERENCE

1. Liddell, Charles J., Jr., Creer, Brent Y., and Van Dyke, Rudolph D., Jr.: A Flight Study of Requirements for Satisfactory Lateral Oscillatory Characteristics of Fighter Aircraft. NACA RM A51E16, 1951.

PITCH DAMPING OF SEVERAL AIRPLANES
hp = 10,000 TO 50,000 FEET

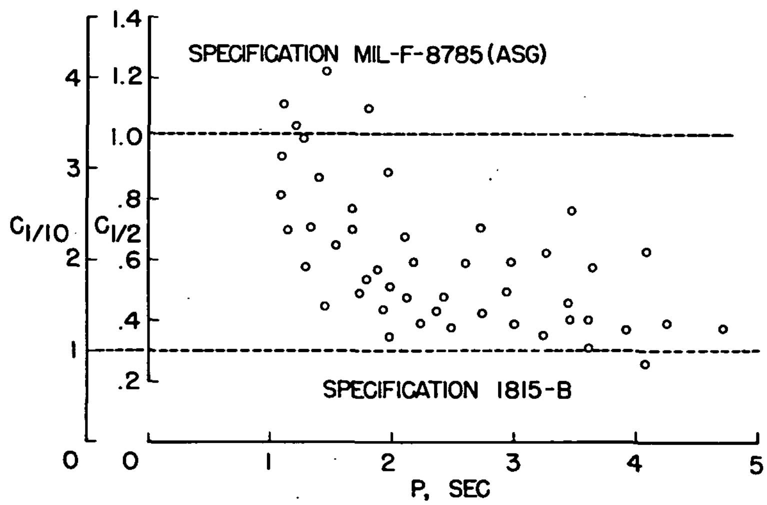

Figure 1

LONGITUDINAL TRIM CHARACTERISTICS OF SEVERAL AIRPLANES

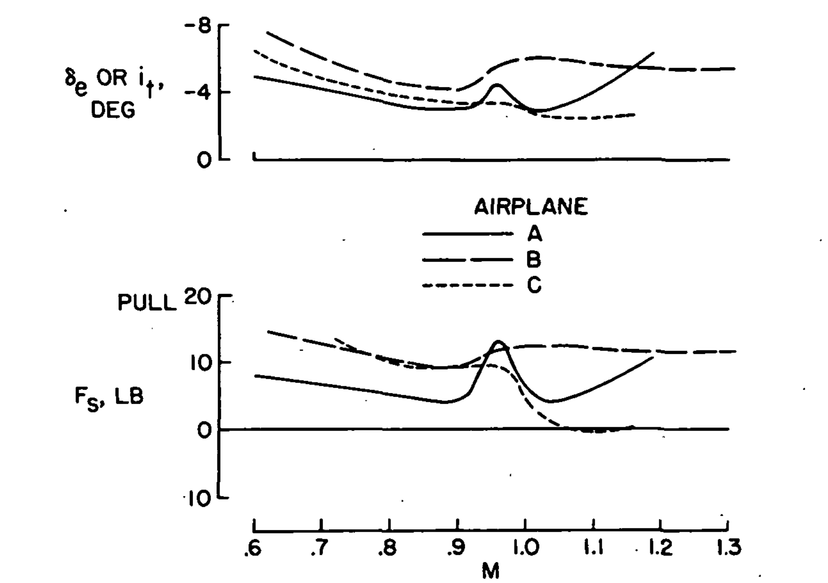

Figure 2

LONGITUDINAL CHARACTERISTICS IN ACCELERATED MANEUVERS

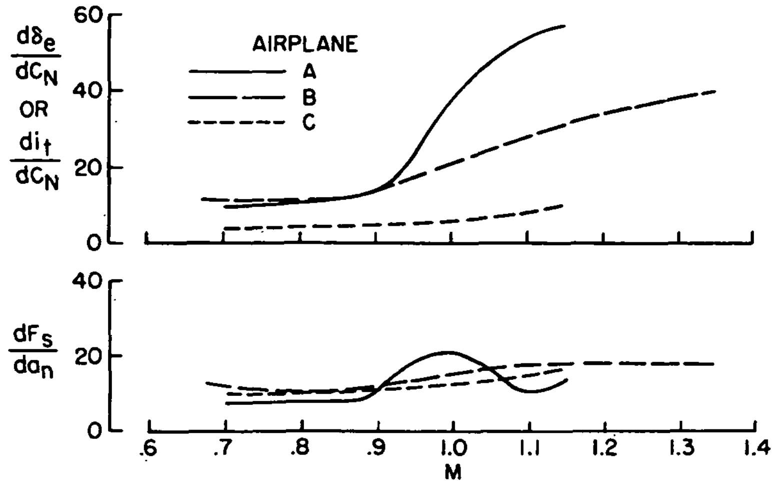

Figure 3

EFFECT OF CONSTANT g DECELERATION
AIRPLANE A

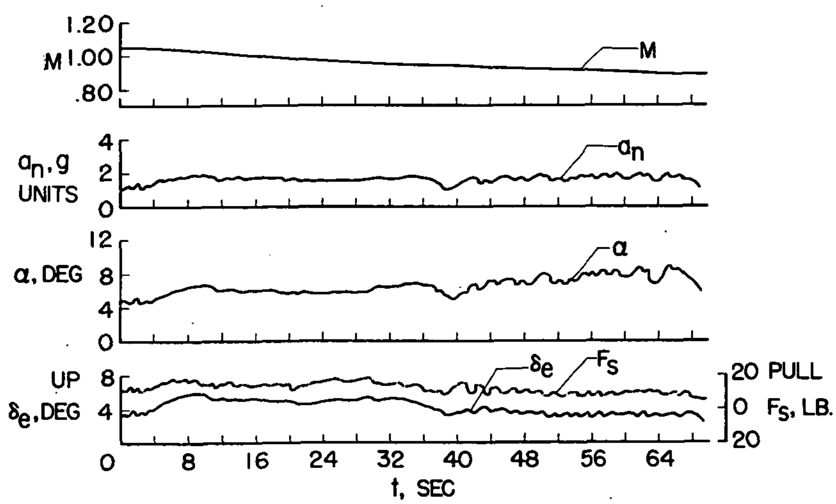

Figure 4

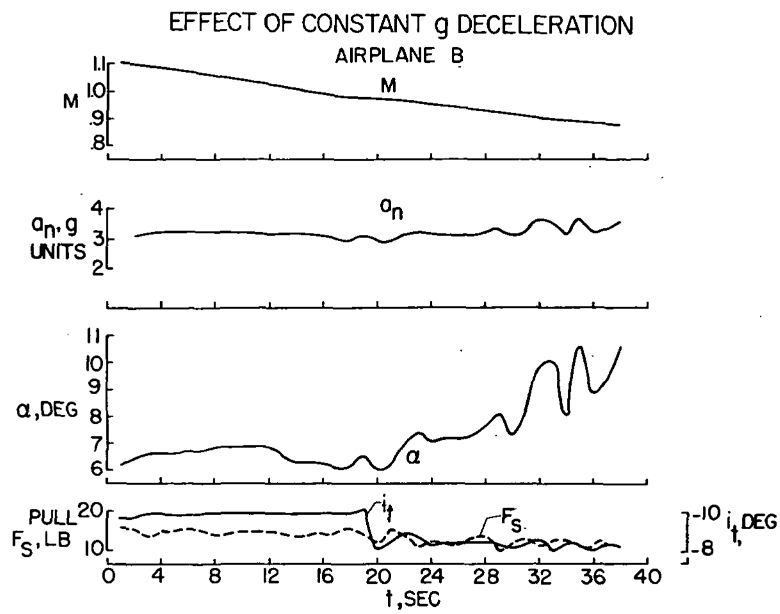

Figure 5

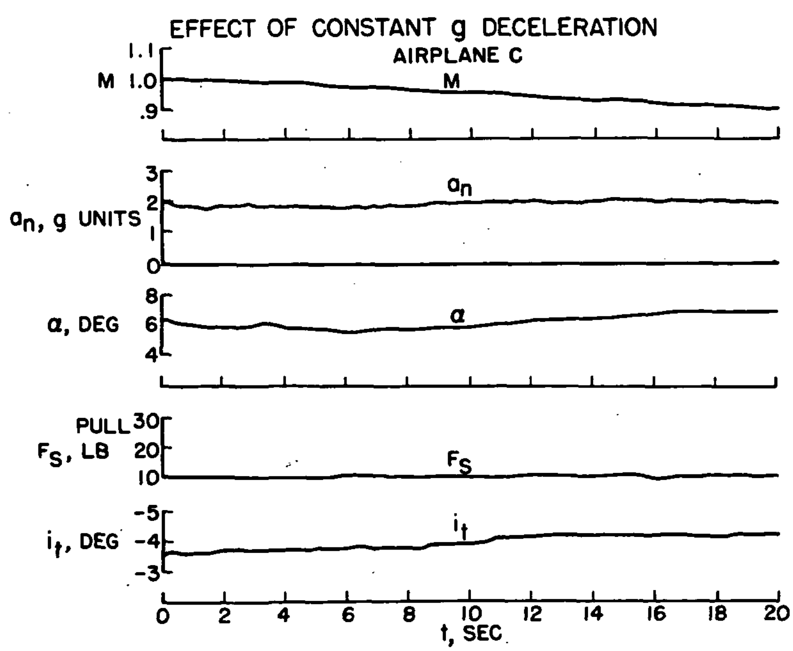

Figure 6

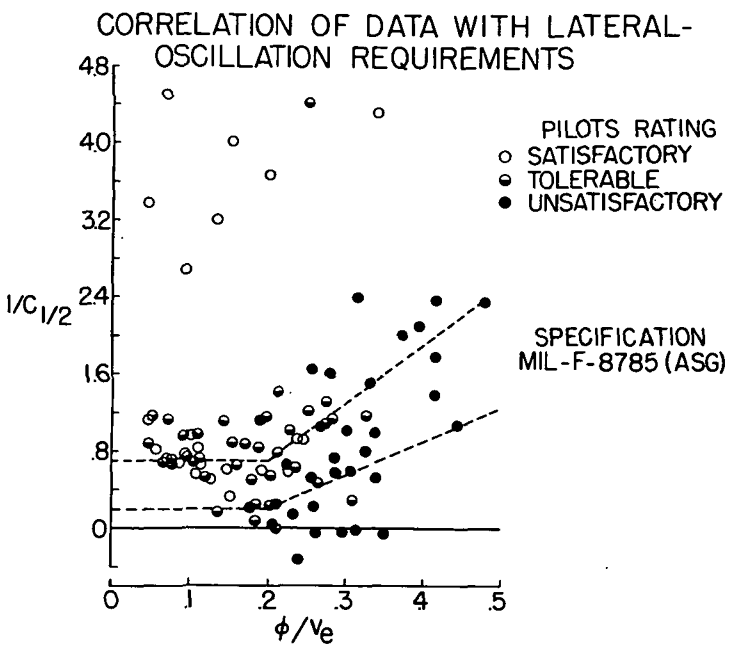

Figure 7

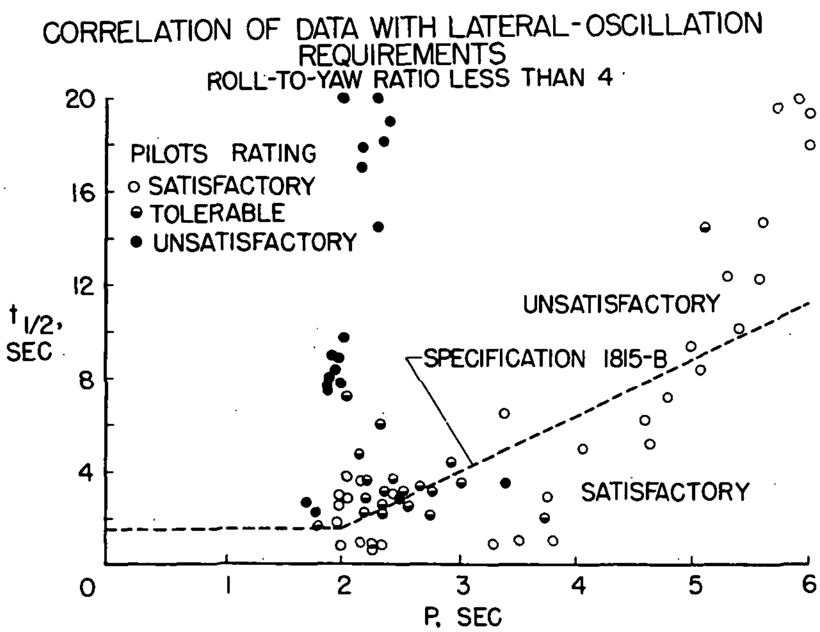

Figure 8

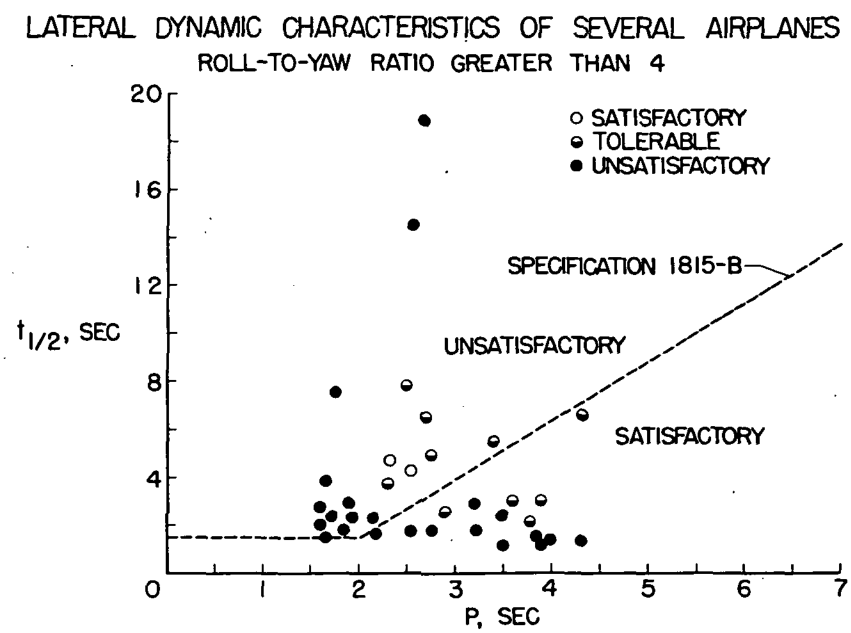

Figure 9

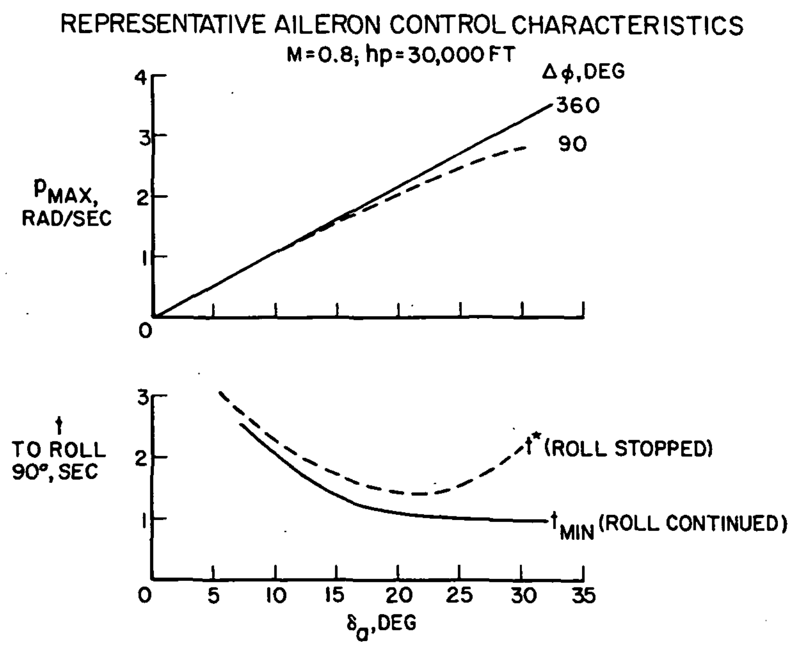

Figure 10

[redacted]

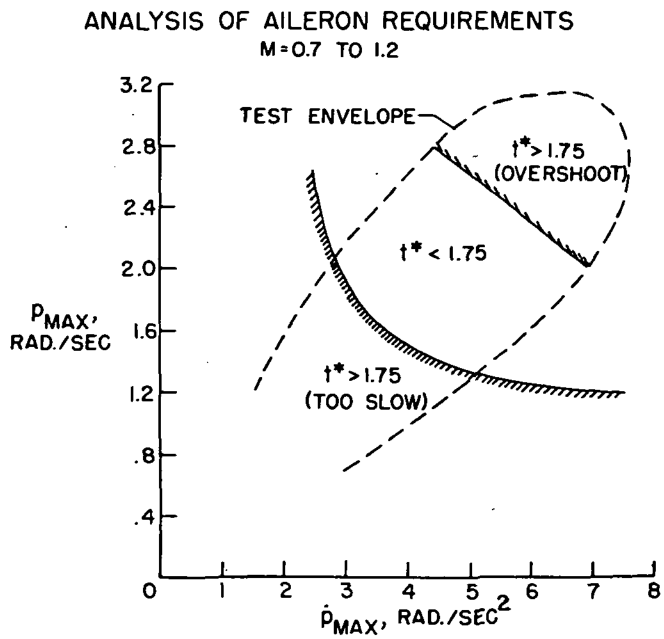

Figure 11

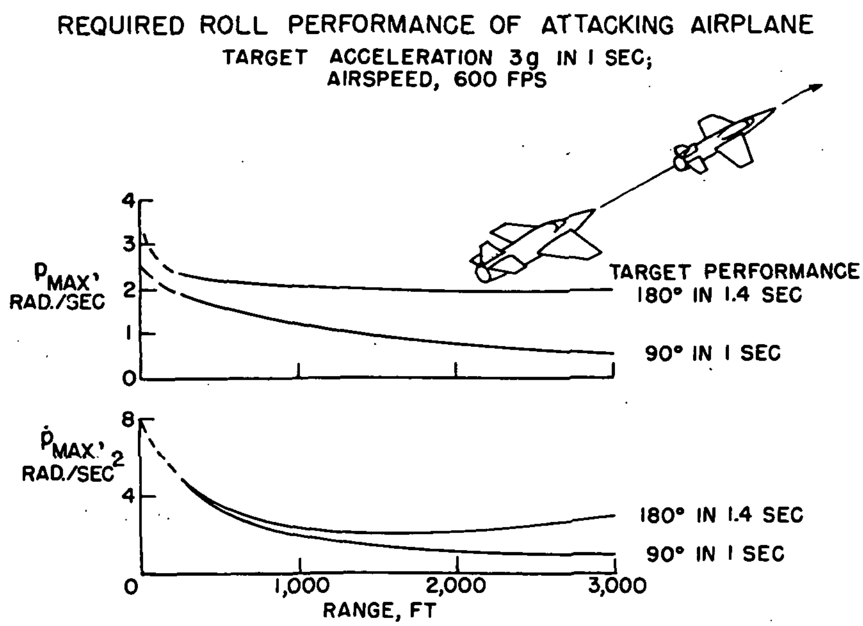

Figure 12

[redacted]

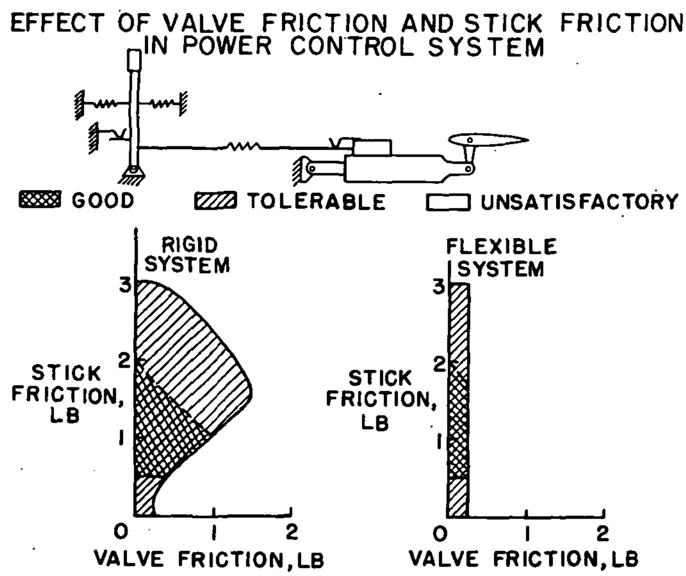
EFFECT OF VALVE FRICTION AND STICK FRICTION
IN POWER CONTROL SYSTEM
GOOD
TOLERABLE
UNSATISFACTORY
RIGID
SYSTEM
STICK
FRICTION,
LB
3
2
1
0
1
2
VALVE FRICTION, LB
FLEXIBLE
SYSTEM
STICK
FRICTION,
LB
3
2
1
0
1
2
VALVE FRICTION, LB

Figure 13

SPINNING AND RELATED PROBLEMS AT HIGH ANGLES OF ATTACK FOR HIGH-SPEED AIRPLANES

By Walter J. Klinar

Langley Aeronautical Laboratory

INTRODUCTION

The mass characteristics of fighter airplanes have changed in recent years from a mass regime wherein the moments of inertia about the pitch and roll axes were nearly equal to a new regime wherein the moments of inertia about the pitch axis are very large with respect to those about the roll axis. This shift in the mass regime is illustrated in figure 1. Variations in the parameter plotted diagonally, $\frac{I_X - I_Y}{mb^2}$, indicate the relative distribution of mass in the wings and the fuselage of an airplane. Positive values of this parameter indicate that the mass is predominantly in the wings and negative values indicate that the mass is primarily in the fuselage. The two designs shown in the lower right of the figure represent the old type of airplanes whereas those in the upper left are examples of present-day fighters which are generally very heavily loaded along the fuselage. The present paper deals with airplanes of this latter type.

Whereas rudder and elevator reversal were recommended for spin recovery with the older type of airplanes, ailerons with the spin are required for recovery (stick right in a right spin) with the present-day fighters unless the airplane has an unusually effective vertical tail. Generally, ailerons designed to provide the required effectiveness in normal flight have been found to be effective in bringing about spin recovery. Combinations of high inertias and possible high angular velocities in spins, however, and also the practice of moving ailerons inboard on the wing or substituting upper-surface spoilers for them may give rise to situations in which the lateral controls may not be sufficiently effective. As a result it may be necessary to resort to other means for spin recovery, and some possible techniques are presented in this paper. The effects in spins of jet-engine installations and pilot confusion in spins are also discussed.

27

[redacted]

RESULTS

In order to review briefly the reasons for the effectiveness of ailerons in spins, it appears desirable to examine the yawing-moment equation because experience has indicated that the yawing moment is the most significant moment affecting spin recovery. The following equation for yawing moment does not include product-of-inertia and engine gyroscopic terms:

$$N_{aerodynamic} + \left(I_X - I_Y\right) pq = I_Z \dot{r} \tag{1}$$

As regards aileron effectiveness in spin recovery, provision of an inertia cross-couple yawing moment to oppose the spin rotation has been found to be very effective. In reference to the inertia cross-couple term of equation (1), it is desirable that the pitching velocity q be positive or nose up to produce a yawing moment opposing the spin for the types of loadings considered. If the inner wing is depressed in a spin, a positive or nose-up pitching velocity will be obtained. Thus, if ailerons displaced with the spin apply a rolling moment sufficient to depress the inner wing below the horizontal in the spin, the pitching velocity will be in the proper sense to provide a yawing moment opposing the spin. The ability of ailerons to apply a rolling moment in the desired direction at spin attitudes is shown in figure 2.

Angle of attack is plotted horizontally and the upper portion of the figure indicates the rolling-moment coefficient provided by the ailerons. Figure 2 indicates that, although the aileron rolling moment drops off as the angle of attack increases, the ailerons are still effective in applying the desired rolling moment even at very flat spinning attitudes for the envelope of rotational rates presented. The lower portion of the figure presents yawing moment against angle of attack and shows that ailerons with the spin also apply an antispin aerodynamic yawing moment

In recent model tests, flat rapidly rotating spins have been obtained on some contemporary fighters having the horizontal tail placed low on the fuselage and on some horizontal tailless designs. In such instances provision of even a large rolling moment with the spin may not be an effective recovery device. Figure 3 gives an indication of the rolling moment required for various airplane angular momenta for airplanes of this type based on a statistical study. The parameter ΩI_Z plotted horizontally is indicative of the angular momentum about the airplane

[redacted]

Z-axis and the parameter $S_a y \delta_a$ plotted vertically is an aileron area moment; increasing values of $S_a y \delta_a$ indicate more effective ailerons. The chart also indicates that for instances where unduly large rotational rates exist extremely large aileron moments may be required unless some other means is employed to slow down the spin rate and thus enable the ailerons to effectively terminate spins.

In the developed spin the rotational rate is directly related to the aerodynamic nose-down pitching moment for a given spin attitude, and large values of nose-down pitching moment lead to rapid rotational rates. Thus, a means of slowing down the spin rotation and rendering the ailerons more effective is by decreasing the aerodynamic nose-down pitching moment. One manner of accomplishing this, which has been found to have some effectiveness, is by deflecting the horizontal tail upward to a large angle.

Another means of slowing down the spin rotation found to be effective in several instances is by extending small canard surfaces that are normally retracted against the sides of the fuselage. (See ref. 1.) Surfaces about 2 to 4 percent of the wing area have been found to be quite effective when they were extended for recovery in conjunction with movement of the regular controls. A typical view of a model with canards installed and extended is shown in figure 4.

In addition to making the canards of sufficient size, it is important that they be placed at a high forward position on the fuselage where there is ample fuselage depth below the canard hinge line. Small aspect ratios also appear desirable. Canards aid in terminating spins because they contribute a nose-up pitching moment which is favorable for reasons previously indicated. The canards also contribute a damping in yaw which has favorable effects.

Another means of providing assistance to lateral controls when they are not sufficiently effective alone in terminating spins of contemporary fighters or when ailerons do not exist on the design is by operating the horizontal tail differentially as ailerons.

In connection with the canard surfaces, results of dynamic model tests of one contemporary fighter design have shown that such surfaces suitably positioned were effective in preventing a directional divergence near the stall. (See ref. 1.) These tests were conducted on the launching apparatus used for incipient spin tests. The model without canard surfaces installed diverged directionally after attaining stalled attitudes because of a loss in directional stability and, in some instances, subsequently entered spins. With suitably placed canard surfaces installed, however, the stalled flights of the model were essentially straight.

The use of jet engines has introduced some important factors in spinning: engine gyroscopic effects, thrust effects, and the possibility of directing the thrust to produce desired moments for spin recovery. Experience in a few instances has shown that applying thrust of about $\frac{1}{2}$ g directed through the center of gravity had no beneficial effect on recovery; in fact, thrust applied in such a manner had a somewhat detrimental effect because of an attendant increase in rotational rate. If the thrust can be applied or directed in such a manner as to give a yawing or rolling moment of sufficient magnitude, however, beneficial effects can be obtained. Experiment has shown that, for one design that spun at moderate attitudes and rates, a yawing or rolling-moment coefficient of 0.02 was sufficient for recovery; whereas for another design that had flat rapidly rotating spins, a yawing-moment coefficient of 0.13 was required.

An important contribution of the jet engine in spins is the gyroscopic moment of the rotating parts of the engine. Although no generalizations can be made on the final effect of the gyroscopic moments, two effects are usually consistent: If engine and airplane rotate in the same sense about their respective axes of rotation (that is, a clockwise rotating engine when viewed from the rear and a right-hand spin), the spin will steepen and the rotational rate will increase; if engine and airplane rotate in opposite senses (as a clockwise rotating engine and a left-hand spin), the converse is true - the spin will flatten and the rotational rate will decrease. The steepening of the spin is not always a beneficial effect, however; nor is the flattening always adverse. Corresponding full-scale engine angular momenta investigated on spin models have been as high as 25,000 slug-ft^2/sec. Results of tests on one model wherein gyroscopic effects of jet-engine rotating parts were simulated are presented in reference 2.

Spins of contemporary fighters are often erratic and oscillatory, and a pilot can become disoriented and place the controls in a manner opposite to that required for recovery. Confusion, however, is more apt to occur in inverted rather than erect spins because, when a pilot is in an inverted spin, the rolling velocity that he experiences is opposite to direction of yawing; thus, a pilot may think he is applying controls to oppose the spin rotation while controls are actually being applied to hold the airplane in the spin. (See ref. 3.) It is suggested that a pilot make use of the turn indicator installed in the airplane to determine the direction of spinning, particularly for inverted spins, to make certain he is applying controls in the proper direction to oppose the spin. It may be pointed out that the Langley Aeronautical Laboratory has a spin-simulator seat mounted on gimbals that is available for aircraft-company test pilots as an aid to orientation in spins.

The foregoing discussion has been based on the results of experimental spin investigations. Theoretical approaches are being undertaken to provide more quantitative information on ~~the~~ factors which affect the spin and recovery.

SUMMARY OF RESULTS

It may be said that to effect satisfactory recoveries from spins obtained on contemporary fighters, aileron deflection with the spin will usually be required and in some instances the lateral controls may require the assistance of other controls such as the horizontal tail or canard surfaces. Canard surfaces may also offer a means of alleviating the directional divergence near the stall and thereby prevent subsequent spin entry for some contemporary fighters. The gyroscopic moments produced by a jet engine can have appreciable effects in spins, and proper direction of engine thrust to provide a rolling or yawing moment offers a means of obtaining satisfactory spin recovery. In order to avoid pilot confusion regarding spin direction, use should be made of the turn indicator.

REFERENCES

1. Klinar, Walter J.: A Study by Means of Dynamic Model Tests of Use of Canard Surfaces as an Aid to Recovery From Spins and as a Means for Preventing Directional Divergence Near the Stall. (Proposed NACA paper.)

2. Bowman, James S., Jr.: Free-Spinning-Tunnel Investigation of Gyroscopic Effects of Jet-Engine Rotating Parts (or of Rotating Propellers) on Spin and Spin Recovery. NACA TN 3480, 1955.

3. Scher, Stanley H.: Pilot's Loss of Orientation in Inverted Spins. NACA TN 3531, 1955.

[redacted]

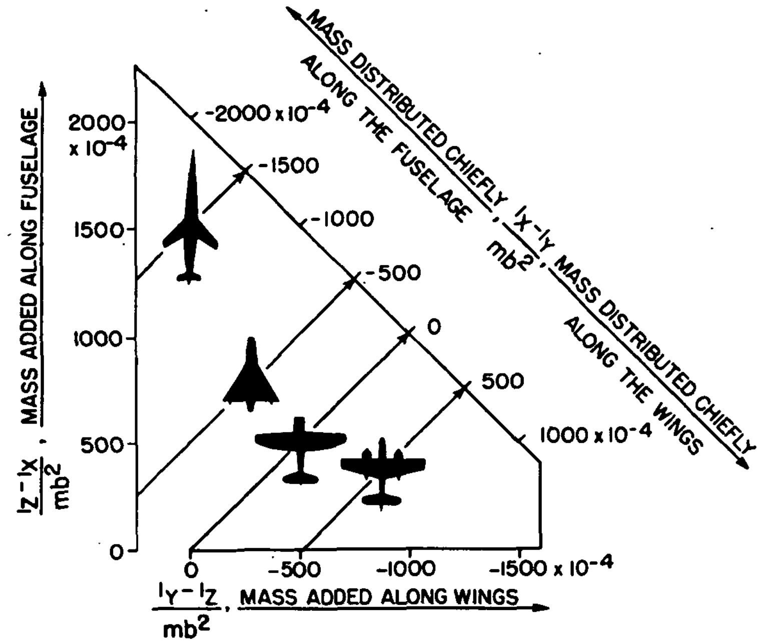

Figure 1

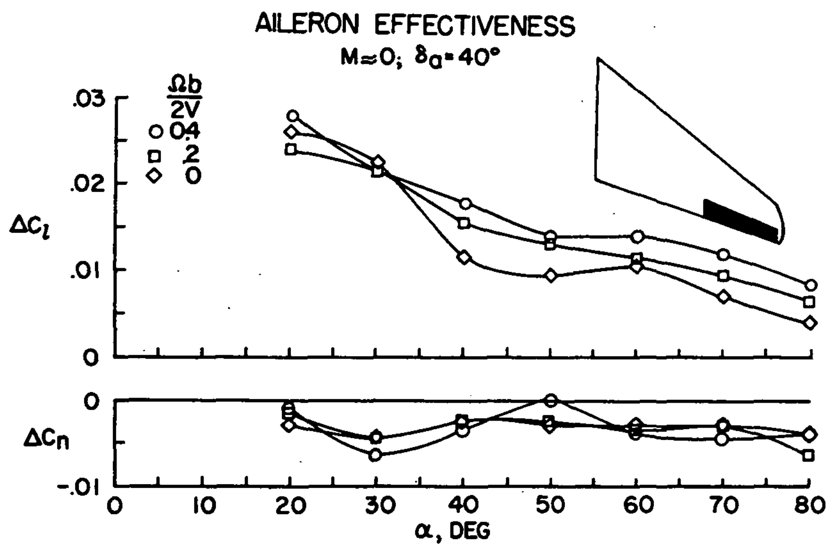

Figure 2

[redacted]

EFFECTIVENESS OF AILERONS IN SPIN RECOVERY

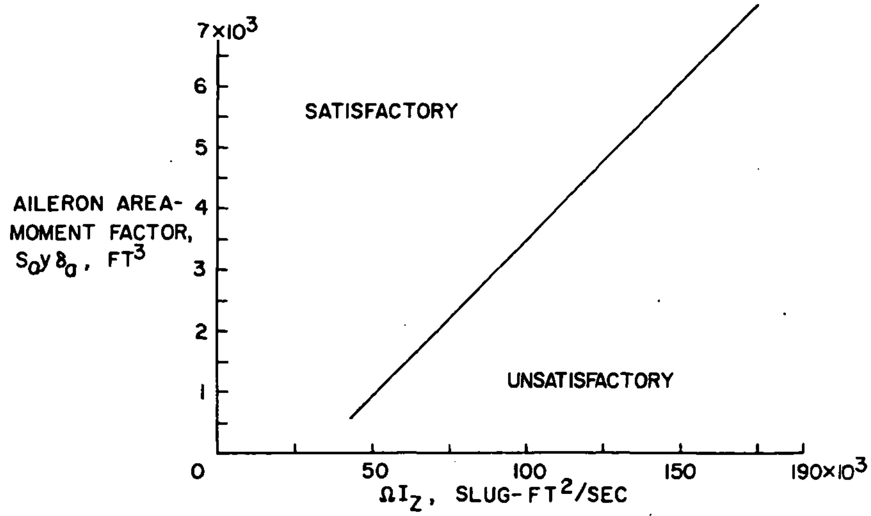

Figure 3

TYPICAL VIEW OF EXTENDED CANARD SURFACE

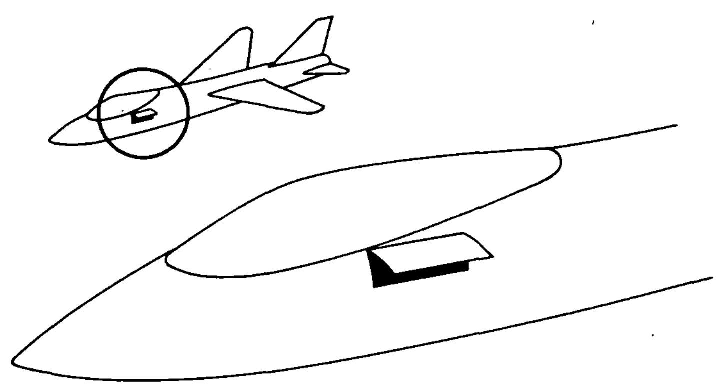

Figure 4

Preceding page blank

RECENT CONTROL STUDIES

By John G. Lowry

Langley Aeronautical Laboratory

SUMMARY

A brief review of the present status of control research is presented and a few of the more recent control studies are discussed. The results indicate that, in addition to flaps and spoilers, air can now be used in the form of jet controls or reaction controls as alternate means of controlling the aircraft.

INTRODUCTION

It is the purpose of this paper to give a brief review of the overall picture regarding control characteristics and then to discuss in some detail a few of the more recent control studies.

Figure 1 shows the types of controls that are considered and the order in which they are discussed. At the top of the figure are the familiar flap and spoiler types. At the bottom of the figure are the jet control and the so-called reaction control. The jet control obtains most of its effectiveness, as does the spoiler, by changing the circulation around the wing, but in addition it may be supplemented by the reaction of the jets blowing out of the wing. In contrast the reaction control obtains all of its effectiveness by deflecting the jet exhaust stream. It should be noted that although the flap, spoiler, and jet controls are pictured here as lateral controls and the reaction control as a longitudinal control, all of the controls can be designed as either lateral, longitudinal, or directional control devices. In order to complete the picture and include the various controls not mentioned here, a bibliography of control work done by the National Advisory Committee for Aeronautics since 1946 is included.

28

COEFFICIENTS AND SYMBOLS

A aspect ratio

A_i cross-sectional area of inlet, sq ft

A_j	cross-sectional area of jets, sq ft
b	wing span, ft
$C_{h_{\delta,\omega}}$	in-phase hinge-moment parameter, $\dfrac{\text{Real part of } M_\delta}{2M'q}$
$C_{h_{\dot{\delta},\omega}}$	out-of-phase hinge-moment parameter, $\dfrac{\text{Imaginary part of } M_\delta}{2M'q}$
C_l	rolling-moment coefficient, $\dfrac{\text{Rolling moment}}{qSb}$
C_N	normal-force coefficient, $\dfrac{\text{Normal force}}{qS}$
C_μ	momentum coefficient, $\dfrac{WV_j}{gqS}$
c	wing chord, ft
c_b	control balance chord ahead of hinge line, ft
c_f	control chord behind hinge line, ft
g	acceleration due to gravity, ft/sec^2
k_a	control-surface reduced frequency, $\dfrac{\omega(c_f + c_b)}{2V}$
M	free-stream Mach number
M'	area moment of control area rearward of hinge line, taken about hinge line, ft^3
M_δ	aerodynamic hinge moment of control per unit deflection, positive trailing edge down, ft-lb/radian
pb/2V	wing-tip helix angle, radians
p	rate of roll, radians/sec
q	free-stream dynamic pressure, lb/sq ft

S	wing area including area within fuselage, sq ft
S_E	exposed wing area, sq ft
V	free-stream velocity, ft/sec
V_j	jet velocity, ft/sec
W	weight rate of flow, lb/sec
α	angle of attack, deg
δ	control deflection, deg
$\Lambda_{c/4}$	sweepback of quarter-chord line, deg
ω	angular frequency of oscillation, radians/sec

DISCUSSION

General

The characteristics of flap-type controls can be estimated in the subsonic speed range by a combination of theoretical and empirical methods. In the transonic speed range empirical correlations and/or specific tests must be relied on almost entirely. At supersonic speeds available theoretical and empirical methods may again be used to predict the characteristics. All of these methods have limitations as to the range of applicability - for example, figure 2 shows the range of angle of attack α and control deflection δ in which the methods apply for flap-type controls at supersonic speeds. Boundaries shown for constant free-stream Mach number represent the values of α and δ below which the available methods will accurately predict the control characteristics. At a Mach number of 3 the range of both α and δ is rather large, but this range decreases as the Mach number is decreased until at $M = 1.25$ the positive range of α and δ has practically disappeared. The scope of this chart is actually expanded by the fact that for symmetrical airfoils the negative angle-of-attack range shown can also be considered as positive angle of attack for negative flap deflections.

The situation is much the same for spoiler-type controls as for flap-type controls except that empirical methods must be used throughout the speed range since separated flow is always associated with spoilers. So little is known about the jet controls and reaction controls at this time that specific tests are generally required when a new configuration is considered.

Flap-Type Controls

Some recent dynamic hinge-moment results obtained at transonic speeds on an unswept wing will be discussed next. Figure 3 shows the variation of the in-phase component of the hinge moment $C_{h_{\delta,\omega}}$ with Mach number M for two controls on an unswept wing at zero angle of attack. The values of $C_{h_{\delta,\omega}}$ are given for a control having a small overhang $\left(\frac{C_b}{C_f} = 0.2\right)$ and a large overhang $\left(\frac{C_b}{C_f} = 1.0\right)$ at a reduced frequency k_a of about 0.10. It can be seen that the variation of the in-phase component of the hinge moment with both M and $\frac{C_b}{C_f}$ is about the same as the variation of the static hinge-moment coefficient. That is, the small overhang is underbalanced throughout the Mach number range, whereas the 100-percent overhang is overbalanced in the Mach number range covered.

Figure 4 presents the damping coefficient or out-of-phase component of hinge moment $C_{h_{\dot{\delta},\omega}}$ plotted against flap deflection for the same controls as shown in figure 3. The parameter $C_{h_{\dot{\delta},\omega}}$ varies with flap deflection at all the Mach numbers shown. Another very significant thing is the pronounced change in damping with overhang. At the lowest subsonic speed $(M = 0.7)$ the 100-percent overhang reduces the damping at all values of δ and, in fact, becomes unstable at large flap deflections. This instability is believed to be associated with the unporting of the balance and the accompanying large changes in flap characteristics. At the higher subsonic Mach number and near the speed of sound a large increase in damping results from the overhang except for very small deflections at $M = 1.01$. This instability may be associated with the effect of the unsteady shock wave on the flap.

Spoiler-Type Controls

Among the advantages cited for the spoiler-type control are good effectiveness throughout the speed range and low wing torsional loads. Figure 5 presents the results of some recent flight tests made by North American Aviation, Inc., with an experimental swept-wing airplane. The variation of rolling effectiveness $pb/2V$ with Mach number M is presented for the airplane equipped with flap-type ailerons and with spoiler-type ailerons (in this case, spoiler-slot-deflectors). Above a Mach number of 0.8 the spoiler-slot-deflector gives a large increase in rolling effectiveness, which demonstrates the advantage of low wing twist associated with spoiler-type controls.

Jet Controls

Another type of control that has characteristics very similar to those of the spoiler type of control is the jet control, which can use either free-stream air or compressed air to obtain control. Figure 6 shows some results for a model of the D-558-II airplane equipped with both flap-type and jet ailerons that were obtained in the Langley high-speed 7- by 10-foot tunnel. The variation of rolling-moment coefficient C_l with angle of attack is shown for both the conventional ailerons and the jet controls at a Mach number of 0.90. The jet control in this case picks up free-stream air in the wing tip inlet, directs it through a duct in the wing, and ejects it normal to the wing trailing edge through a series of holes in the thickened trailing edge. The values of C_l are for the condition in which air is blowing up out of one wing and down out of the other. The jet control at this Mach number was about as effective as the regular ailerons deflected their full amount, $\pm 15^{\circ}$.

The results of some preliminary studies with compressed air are shown in figure 7. In this case compressed air was ejected through the holes located on the 65-percent-chord line. On the left-hand side the rolling-moment coefficient C_l is plotted as a function of the momentum coefficient C_{μ} for the 35° swept wing at an angle of attack of 4° and a Mach number of 0.9. The rolling-moment coefficient varies linearly with momentum coefficient, and a comparison with the computed jet reaction (dashed line) reveals that most of the control power is obtained from changes in the circulation around the wing. On the right-hand side of figure 7, the rolling effectiveness $pb/2V$ is plotted as a function of the weight rate of flow W for an airplane with this plan form and a wing area of 335 square feet, flying at a Mach number of 0.9 and at an altitude of 10,000 feet. These values are based on the air being taken from the tail pipe, and thus on a jet velocity of about 2,000 feet per second. Too little is known about these controls to say how much the amount of air required might be reduced by configuration changes, but a reduction of about 25 percent could be expected if the jets were moved to the trailing edge, the location used in the D-558-II studies of figure 6. If the air for this type of control is taken from the tail pipe, the parameter C_{μ} is essentially the loss in thrust coefficient of the airplane; another way of looking at it is that the value of C_{μ} is the approximate increase in drag coefficient associated with control deflection.

Three different types of jet controls using free-stream air have been studied by the Langley Pilotless Aircraft Research Division by means of rocket models at high subsonic and low supersonic speeds. Figure 8 compares the rolling performance $pb/2V$ over the Mach number range for the three jet controls on an 80° delta-wing configuration. The top configuration picks up air at the wing tip and ejects it normal to the wing surface through holes along the wing trailing edge; and the next one also picks up the air at the tip, but ejects it along the wing surface toward the wing root. These two types have about the same effectiveness at supersonic speeds. The other configuration is the least effective of the three; it picks up the air at the wing root and ejects it along the wing surface toward the wing tip. One current missile requires a value of $pb/2V$ of about 0.02 for roll stabilization throughout the speed range. Thus, any of these configurations would be satisfactory roll-stabilization devices and, due to their nature, could have low operating forces.

Reaction Controls

Any aircraft can have regions of flight (at very low speeds or at very high altitudes) in which the dynamic pressure is so low that conventional control surfaces would have to be very large to provide adequate control. In these regions reaction controls can be used. Figure 9 shows four different reaction controls that have been studied by the NACA. At the top of the figure are two configurations studied at the Lewis Flight Propulsion Laboratory at a Mach number of about 1.6. Hot air was used as the jet exhaust, and the configurations are typical of those that might be used on jet engines. The one on the left obtains its control by deflecting the nozzle to turn the jet exhaust, and the one on the right turns the jet exhaust by deflecting a vane that extends across the jet. At the bottom of the figure are two configurations tested statically with rocket motors by the Langley Pilotless Aircraft Research Division. They represent devices that might be used in a supersonic jet exhaust. The one on the left turns the jet by deflecting a paddle into one side of the jet, and the one on the right turns the jet by deflecting a spoiler into the jet stream. These configurations are only four of the many that have been studied by the NACA and other organizations. They are shown here only to give some idea of the thrust loss that may be associated with this type of control.

Figure 10 shows the thrust loss associated with the lateral force for the four controls of figure 9. In order to generalize the data, both the thrust loss and the lateral force were divided by the basic thrust. Of these configurations, the swiveled nozzle gives the most lateral force for the least thrust. In fact, it is equal to 1 minus the cosine of the deflection angle, the minimum possible loss. All the other devices show more thrust loss for a given lateral force, and the immersed vane has the undesirable feature of causing about a 2 percent loss when in the neutral position. Neither the spoiler nor the paddle appears to be able to furnish the lateral force that can be obtained with either the swiveled nozzle or the immersed vane.

When controls of this type are used on rocket-powered missiles, it is often desirable to maintain control after rocket burnout. One scheme for doing this without adding another control is shown in figure 11, where the trim normal-force coefficient $C_{N_{TRIM}}$ is shown as a function of Mach number for a cruciform delta-wing missile tested by the Langley Pilotless Aircraft Research Division. For control, a paddle-type reaction control was used, but instead of deflecting just one paddle as in figure 9, both the upper and lower paddles were deflected together. The upper vane deflects the jet in the power-on condition and the bottom vane acts as a body flap in the power-off condition. Although the power-off control was not as powerful as the power-on control, trim normal-force coefficients of 1/2 to 2/3 the power-on values could be obtained with power off with this control.

CONCLUDING REMARKS

The results indicate that, in addition to flaps and spoilers, air can now be used in the form of jet controls or reaction controls as alternate means of controlling the aircraft.

BIBLIOGRAPHY

1. Brewer, Jack D.: Description and Bibliography of NACA Research on Wing Controls. January 1946 - February 1955. NACA RM 54K24, 1955.

2. Bond, Aleck C.: Experimental Investigation of a Flat-Plate Paddle Jet Vane Operating on a Rocket Jet. NACA RM L50I20, 1950.

3. Blackaby, James R.: An Investigation of the Effects of Jet-Outlet Cut-Off Angle on Thrust Direction and Body Pitching Moment. NACA TN 2379, 1951.

4. Strass, H. Kurt, and Marley, Edward T.: Recent Experiences With Flutter Failure of Sweptback, Tapered Wings Having Outboard, Partial-Span Spoiler Controls. NACA RM L53H26, 1953.

5. Clevenson, Sherman A., and Tomassoni, John E.: Experimental Investigation of the Oscillating Forces and Moments on a Two-Dimensional Wing Equipped With an Oscillating Circular-Arc Spoiler. NACA RM L53K18, 1954.

6. Englert, Gerald W., and Leissler, L. Abbott.: Preliminary Wind-Tunnel Investigation of Two Types of Jet-Exit Configurations for Control of Aircraft. NACA RM E54E27, 1954.

7. Lord, Douglas R., and Driver, Cornelius: Investigation of the Effect of Balancing Tabs on the Hinge-Moment Characteristics of a Trailing-Edge Flap-Type Control on a Trapezoidal Wing at a Mach Number of 1.61. NACA RM L54F22, 1954.

8. McKay, John B.: Rolling Performance of the Republic YF-84F Airplane As Measured in Flight. NACA RM H54G20a, 1955.

9. Franks, Ralph W.: The Application of a Simplified Lifting-Surface Theory to the Prediction of the Rolling Effectiveness of Plain Spoiler Ailerons at Subsonic Speeds. NACA RM A54H26a, 1954.

10. Monfort, James C., and Wyss, John A.: Effects of Rigid Spoilers on the Two-Dimensional Flutter Derivatives of Airfoils Oscillating in Pitch at High Subsonic Speeds. NACA RM A54I22, 1954.

11. English, Roland D.: Free-Flight Investigation, Including Some Effects of Wing Aeroelasticity, of the Rolling Effectiveness of an All-Movable Horizontal Tail With Differential Incidence at Mach Numbers From 0.6 to 1.5. NACA RM L54K30, 1954.

12. Mellenthin, Jack A.: The Effect of a 4-Percent-High Spoiler on Buffeting Forces on an NACA $65_{(06)}A004$ Two-Dimensional Airfoil at Subsonic Mach Numbers. NACA RM A54L22, 1955.

13. Fischetti, Thomas L., and Loving, Donald L.: Effects of an All-Movable Wing-Tip Control on the Longitudinal Stability of a 60° Sweptback-Wing—Indented-Body Configuration Equipped With Fences at Transonic Speeds. NACA RM L54L30, 1955.

14. Martina, Albert P.: Method for Calculating the Rolling and Yawing Moments Due to Rolling for Unswept Wings With or Without Flaps or Ailerons by Use of Nonlinear Section Lift Data. NACA Rep. 1167, 1954. (Supersedes NACA TN 2937, 1953.)

15. NACA High-Speed Flight Station: Flight Experience With Two High-Speed Airplanes Having Violent Lateral-Longitudinal Coupling in Aileron Rolls. NACA RM H55A13, 1955.

16. Ulmann, Edward F., and Smith, Fred M.: Aerodynamic Characteristics of a 60° Delta Wing Having a Half-Delta Tip Control at a Mach Number of 4.04. NACA RM L55A19, 1955.

17. Morris, Odell A., and Westrick, Gertrude C.: Effects of a Detached Tab on the Hinge-Moment and Effectiveness Characteristics of an Unswept Trailing-Edge Control on a 60° Delta Wing at Mach Numbers From 0.75 to 1.96. NACA RM L55B15, 1955.

18. Lovell, Powell M., Jr.: Flight Tests of a Delta-Wing Vertically Rising Airplane Model Powered by a Ducted Fan. NACA RM L55B17, 1955.

19. Thompson, Robert F., and Taylor, Robert T.: Effect of a Wing Leading-Edge Flap and Chord-Extension on the High Subsonic Control Characteristics of an Aileron Located at Two Spanwise Positions. NACA RM L55B18a, 1955.

20. Dunning, Robert W., and Ulmann, Edward F.: Exploratory Investigation at a Mach Number of 4.06 of an Airplane Configuration Having a Wing of Trapezoidal Plan Form - Longitudinal and Lateral Control Characteristics. NACA RM L55B28, 1955.

21. Fetterman, David E., Jr., Penland, Jim A., and Ridyard, Herbert W.: Static Longitudinal and Lateral Stability and Control Data From an Exploratory Investigation at a Mach Number of 6.86 of an Airplane Configuration Having a Wing of Trapezoidal Plan Form. NACA RM L55C04, 1955.

22. Valerino, Alfred S.: Static Investigation of Several Jet Deflectors for Longitudinal Control of an Aircraft. NACA RM E55D04, 1955.

23. James, Harry A., and Hunton, Lynn W.: Estimation of Incremental Pitching Moments Due to Trailing-Edge Flaps on Swept and Triangular Wings. NACA RM A55D07, 1955.

24. Kaattari, George E., Hill, William A., Jr., and Nielsen, Jack N.: Controls for Supersonic Missiles. NACA RM A55D12, 1955.

25. Henderson, Arthur, Jr., and Goodwin, Julia M.: The Zero-Lift Wave Drag of a Particular Family of Unswept, Tapered Wings With Linearly Varying Thickness Ratio. NACA TN 3418, 1955.

26. Czarnecki, K. R., and Lord, Douglas R.: Simplified Procedures for Estimating Flap-Control Loads at Supersonic Speeds. NACA RM L55E12, 1955.

27. Day, Richard E., and Fischel, Jack: Stability and Control Characteristics Obtained During Demonstration of the Douglas X-3 Research Airplane. NACA RM H55E16, 1955.

28. Hammond, Alexander D.: Loads on Wings Due to Spoilers at Subsonic and Transonic Speeds. NACA RM L55E17a, 1955.

29. Martin, Dennis J., Thompson, Robert F., and Martz, C. William: Exploratory Investigation of the Moments on Oscillating Control Surfaces at Transonic Speeds. NACA RM L55E31b, 1955.

30. Moseley, William C., Jr.: Investigation at Transonic Speeds of the Hinge-Moment Characteristics of a 1/8-Scale Model of the X-IE Aileron. NACA RM L55F06a, 1955.

31. Strass, H. Kurt, Stephens, Emily W., Fields, Edison M., and Schult, Eugene D.: Collection and Summary of Flap-Type-Aileron Rolling-Effectiveness Data at Zero Lift As Determined by Rocket-Powered Model Tests at Mach Numbers Between 0.6 and 1.6. NACA RM L55F14, 1955.

32. Penland, Jim A., Fetterman, David E., Jr., and Ridyard, Herbert W.: Static Longitudinal and Lateral Stability and Control Characteristics of an Airplane Configuration Having a Wing of Trapezoidal Plan Form With Various Tail Airfoil Sections and Tail Arrangements at a Mach Number of 6.86. NACA RM L55F17, 1955.

33. Schult, Eugene D.: A Free-Flight Investigation at High Subsonic and Low Supersonic Speeds of the Rolling Effectiveness and Drag of Three Spoiler Controls Having Potentially Low Actuating-Force Requirements. NACA RM L55G11a, 1955.

34. Turner, Thomas R., and Vogler, Raymond D.: Wind-Tunnel Investigation at Transonic Speeds of a Jet Control on an 80° Delta-Wing Missile. NACA RM L55H22, 1955.

35. Hedgepeth, John M., Waner, Paul G., Jr., and Kell, Robert J.: A Simplified Method for Calculating Aeroelestic Effects on the Roll of Aircraft. NACA TN 3370, 1955.

36. Cahill, Jones F., Underwood, William J., Nuber, Robert J., and Cheesman, Gail A.: Aerodynamic Forces and Loadings on Symmetrical Circular-Arc Airfoils With Plain Leading-Edge and Plain Trailing-Edge Flaps. NACA Rep. 1146, 1953. (Supersedes NACA RM L6K22 by Underwood and Nuber, NACA RM L7H04 by Underwood and Nuber, NACA RM L50H17a by Nuber and Cahill, and NACA RM L9G20 by Nuber and Cheesman.)

37. Lord, Douglas R., and Czarnecki, K. R.: Loads Associated With Spoilers at Supersonic Speeds. NACA RM L55E12a, 1955.

38. Runckel, Jack F., and Gray, W. H.: An Investigation of Loads on Ailerons at Transonic Speeds. NACA RM L55E13, 1955.

39. Critzos, Chris C.: Lateral-Control Investigation at Transonic Speeds of Differentially Deflected Horizontal-Tail Surfaces for a Configuration Having a 6-Percent-Thick 45° Sweptback Wing. NACA RM L55I26, 1955.

40. Klawans, Bernard B., and Johnson, Harold I.: Some Effects of Fuselage Flexibility on Longitudinal Stability and Control. NACA TN 3543, 1955. (Prospective NACA paper.)

41. Canning, Thomas N., and DeRose, Charles E.: Drag and Rolling-Moment Effectiveness of Trailing-Edge Spoilers at Mach Numbers 2.2 and 5.0. NACA RM A55F15, 1955.

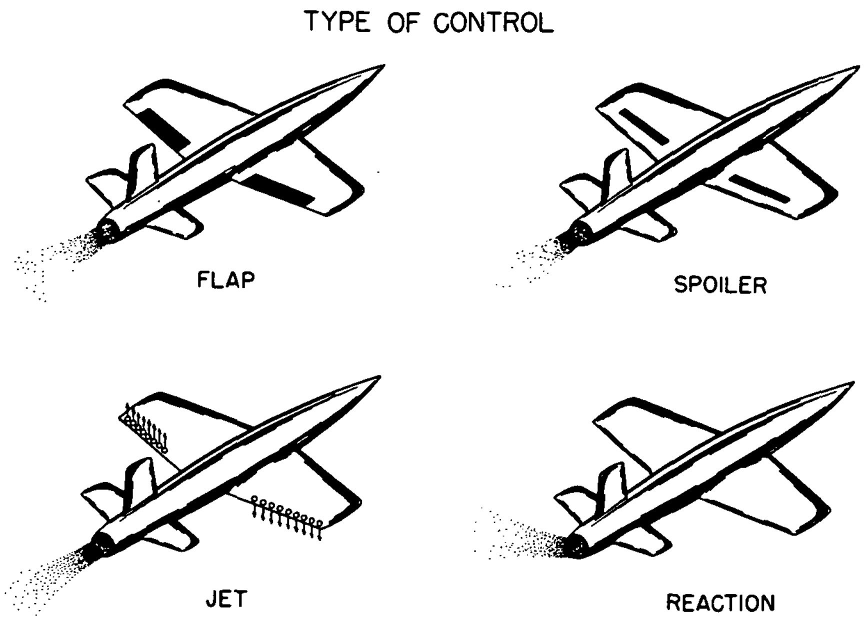

Figure 1

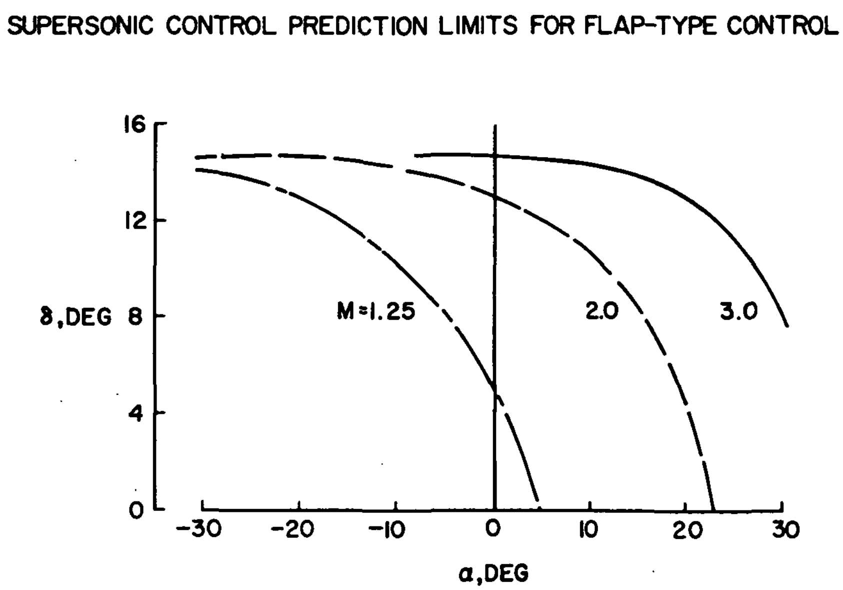

Figure 2

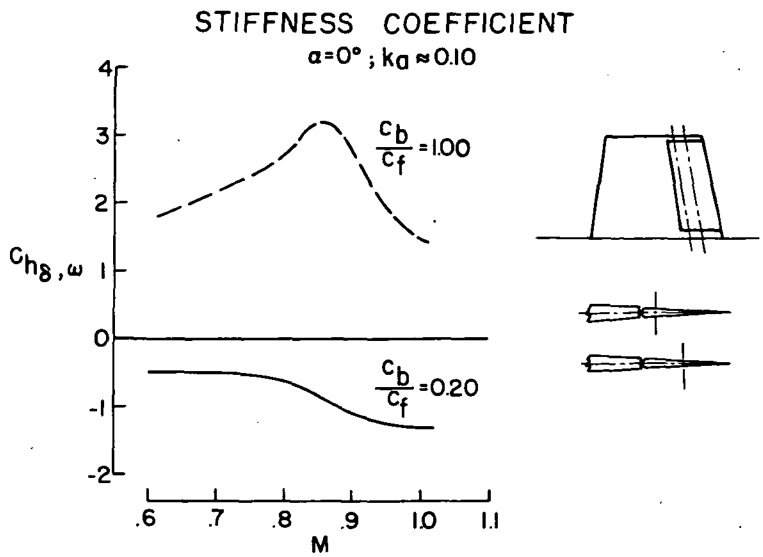

Figure 3

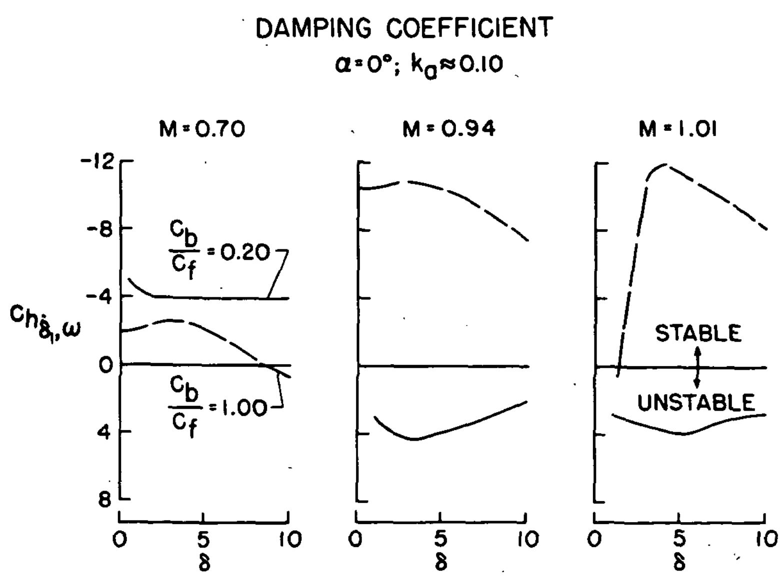

Figure 4

COMPARISON OF FLAP-TYPE AND SPOILER-SLOT-DEFLECTOR AILERONS

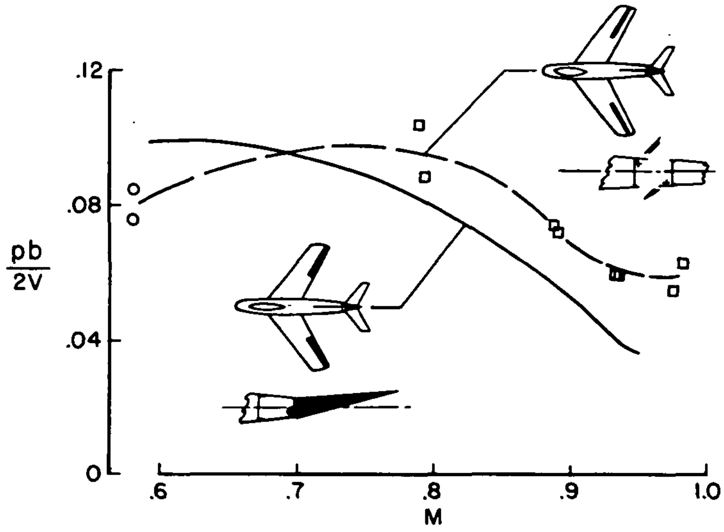

Figure 5

JET CONTROL USING FREE-STREAM AIR
D558-II; M=0.90

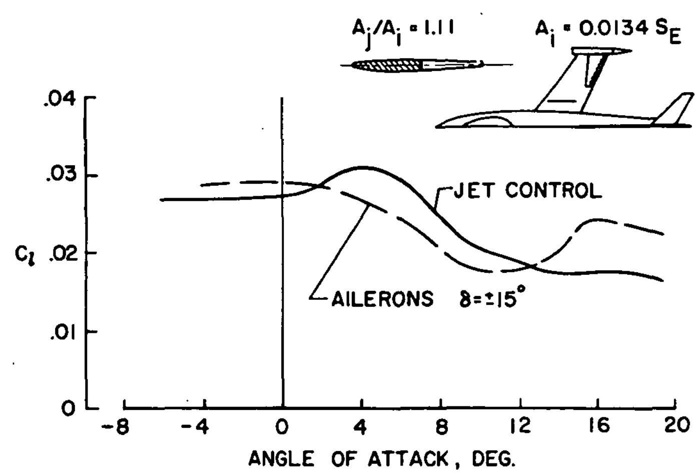

Figure 6

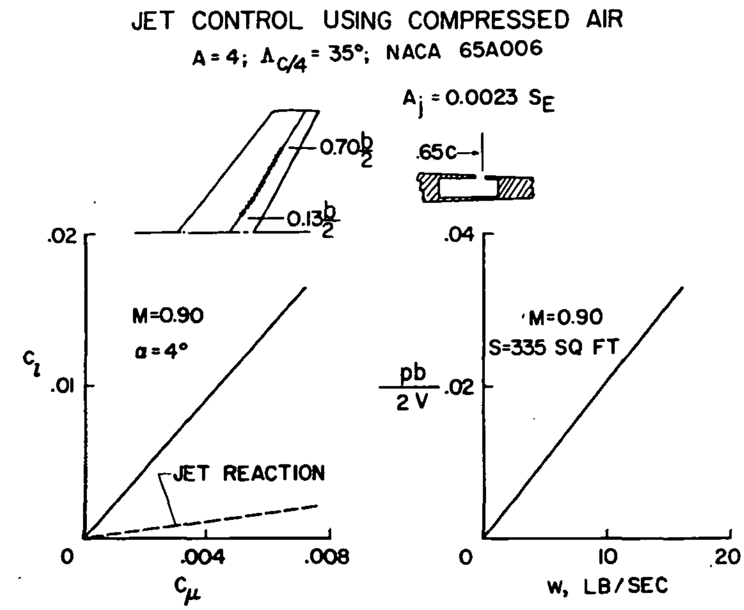

Figure 7

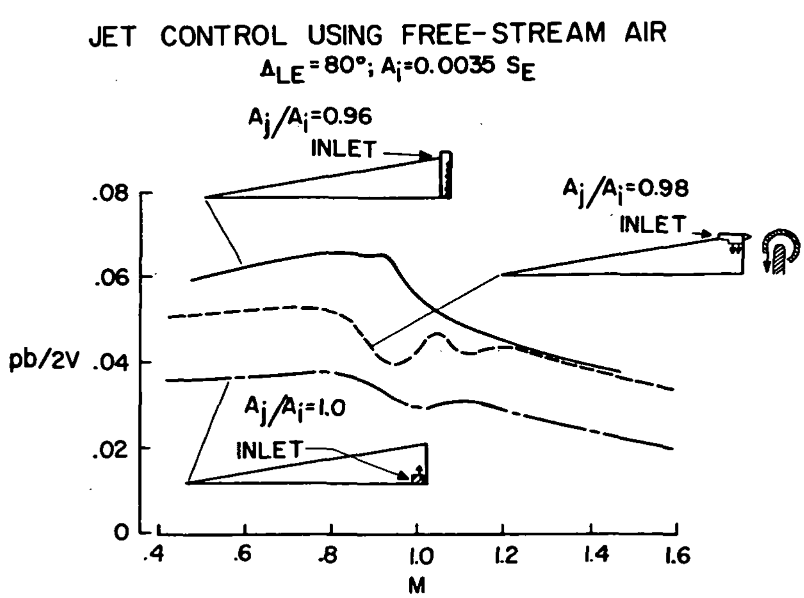

Figure 8

~~CONFIDENTIAL~~

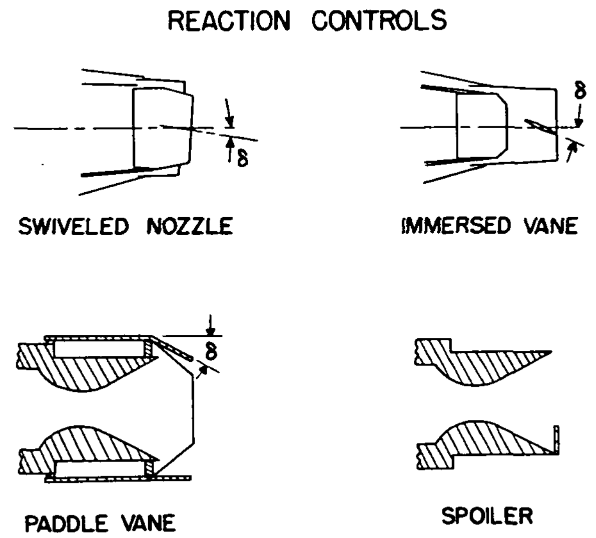

Figure 9

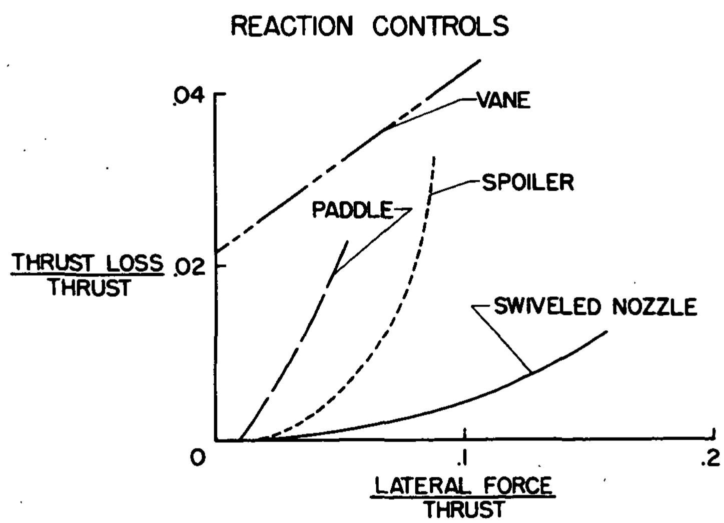

Figure 10

PADDLE VANE-REACTION CONTROL

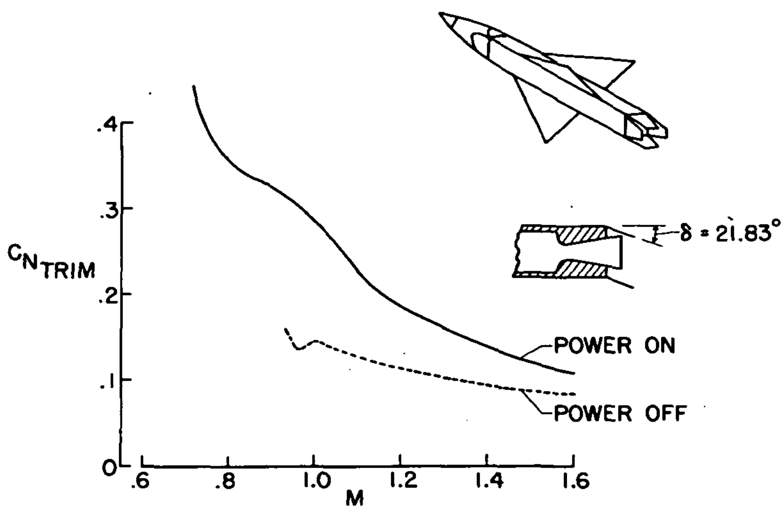

Figure 11

THE USE OF THE HORIZONTAL TAIL FOR ROLL CONTROL

By John P. Campbell

Langley Aeronautical Laboratory

SUMMARY

A summary has been made of the data recently obtained by the National Advisory Committee for Aeronautics on the use of differential horizontal-tail incidence for roll control. In general, the results appear to be fairly promising even though most of the data were obtained with configurations that were not especially designed for the use of such a control. The results indicate that a tail roll control might be satisfactory if the tail is made relatively large to provide adequate effectiveness without excessive deflections, if the airplane is designed so that the longitudinal trim requirements for the tail are minimized so as to avoid interaction of roll and pitch controls, and if the horizontal tail is positioned vertically to avoid excessive favorable or adverse yawing moments.

INTRODUCTION

Because of the serious problems involved in the use of controls on the thin, flexible wings of high-speed airplanes, some designers have considered the possibility of using differential horizontal-tail incidence for roll control. During the last two or three years, the National Advisory Committee for Aeronautics has obtained a limited amount of data on controls of this type. (See refs. 1 to 5.) Since most of these data were obtained by adding a few tests to test programs laid out for other purposes, very few systematic results have been obtained, and the different sets of data are generally unrelated. It is the purpose of this report to summarize and, wherever possible, to correlate these data. Comparisons with conventional aileron control will be given in some cases.

SYMBOLS

b	wing span
$\bar{c}$	mean aerodynamic chord
C_L	lift coefficient

29

C_l rolling-moment coefficient, $\frac{\text{Rolling moment}}{qS}$

$C_{l_\delta} = \frac{dC_l}{d\delta}$

C_m pitching-moment coefficient, $\frac{\text{Pitching moment}}{qS}$

$C_{m_{i_t}} = \frac{dC_m}{di_t}$

C_n yawing-moment coefficient, $\frac{\text{Yawing moment}}{qS}$

$C_{n_\delta} = \frac{dC_n}{d\delta}$

i_t tail incidence

i_w wing incidence

l longitudinal distance from center of gravity to calculated center of pressure of horizontal tail

M Mach number

$\frac{pb}{2V}$ wing-tip helix angle

q dynamic pressure

S wing area

y lateral distance from center of gravity to calculated center of pressure of horizontal tail

α angle of attack

δ total roll-control deflection

RESULTS AND DISCUSSION

Effect of Mach Number

A summary of most of the available data for the clean condition at 0° angle of attack is shown in figure 1 as a plot of the roll-control parameter C_{l_δ} against Mach number. At low subsonic speeds the value of C_{l_δ} varies from about 0.0004 for the two lower configurations with swept and highly tapered tails to a value of about 0.0006 for the model with a high-aspect-ratio unswept tail. These values are only one-third to one-half as large as values of C_{l_δ} for conventional ailerons at low Mach numbers. Two sets of data are shown for the transonic speed range. The lower set of data, which was obtained in the Langley 16-foot transonic tunnel, shows no appreciable variation of C_{l_δ} between Mach numbers of 0.8 and 1.05. The upper set of data, which was obtained with a Pilotless Aircraft Research Division rocket model with a horizontal tail that was relatively large compared with the wing area, shows a slight increase in C_{l_δ} at a Mach number of about 1.2 and then shows a progressive decrease in effectiveness with increasing Mach number because of the decreasing lift-curve slope of the tail. The same general variation of C_{l_δ} with Mach number is shown by the two sets of data for the supersonic Mach numbers from 1.4 to 2.0 obtained in the Langley 4- by 4-foot supersonic pressure tunnel (shown by solid circles connected by lines). In this speed range, ailerons on stiff wings produce about the same value of C_{l_δ} as shown herein for the horizontal tail, but since there will usually be more control deflection available for the ailerons, they will provide the more powerful control - assuming that the wing is fairly stiff.

Effect of Wing Aeroelasticity

Figure 2 shows how the controls might compare if the wing were not stiff. Plots of $\frac{pb/2V}{\delta}$ against Mach number are shown for tail and aileron controls with stiff and flexible wings. The tail data were taken from reference 2 and the aileron data from reference 6. The term $\frac{pb/2V}{\delta}$ expresses the overall rolling effectiveness and is equal to C_{l_δ} divided by the damping-in-roll parameter C_{l_p}. The left plot shows that, for the tail roll control with the stiff wing, there is essentially no variation in rolling effectiveness over the Mach number range covered in the tests, which indicates that the variations of C_{l_δ} and C_{l_p} with Mach number are identical. For the model with the flexible wing, the rolling effectiveness was greater because of the reduced damping in roll provided by the wing.

Now for the aileron control, the situation is reversed. Going from the stiff wing to the flexible wing causes a large reduction in rolling effectiveness which leads to control reversal at some Mach numbers for this particular case. Since the flexible wings used in these tests are generally representative of current design practice, it appears, on the basis of these data, that a tail control might well be superior in some cases to aileron control at supersonic speeds.

Effect of Angle of Attack

Rolling moments.- The results of figures 1 and 2 are only for 0° angle of attack. Figure 3 shows the variation of C_{l_δ} with angle of attack for four Mach numbers for three of the configurations of figure 1. For comparison, there are also shown typical aileron control data for each Mach number. For the subsonic Mach numbers, the variation of C_{l_δ} with angle of attack is not very great for the tail control. For the aileron control, however, the effectiveness drops off rapidly with increasing angle of attack so that at the high angles of attack the values of C_{l_δ} are about the same as those for the tail control. For the case of a Mach number of 1.00, both the controls maintain most of their effectiveness up to the highest angles of attack covered in the tests. For a Mach number of 1.61, the results are quite different from the subsonic cases. The two controls have about the same effectiveness at the lower angles of attack, but at the higher angles of attack the aileron effectiveness increases while the tail-control effectiveness decreases. It should be pointed out that these results were obtained on wind-tunnel models with essentially rigid wings.

Yawing moments.- The yawing-moment data for the same cases are presented in figure 4 in the form of the parameter $\frac{C_{n_\delta}}{C_{l_\delta}}$, the ratio of the yawing moment to the rolling moment produced by control deflection. The aileron data show for all Mach numbers either zero moment or a small positive or favorable yawing moment at 0° angle of attack and an increasingly large negative or adverse yawing moment with increasing angle of attack. For the tail control, at Mach numbers up to 1.00, there are extremely large favorable yawing moments which decrease with increasing angle of attack but remain positive over the angle-of-attack range tested. These large yawing moments, which pilots would probably consider objectionable, are caused by loads on the vertical tail induced by the differentially deflected horizontal-tail surfaces. For the supersonic case, the tail roll control produces smaller, favorable yawing moments at low angles of attack and adverse yawing moments at high angles of attack. The carryover of load from the horizontal tail to the vertical tail is apparently much less in this case than at the subsonic speeds.

All these data were obtained with configurations having low horizontal tails. The next figure shows that the vertical position of the horizontal tail has a pronounced effect on these yawing moments.

Effect of Tail Position on Yawing Moments

The results of figure 5 were obtained at low speed with a model having low, intermediate, and high horizontal-tail positions. For the low position, the large positive values of $\frac{C_{n_\delta}}{C_{l_\delta}}$ are similar to those shown in figure 4 for the subsonic speeds. For the high position, very large negative or adverse yawing moments were obtained; whereas for the intermediate position, the moments were relatively small. The explanation for these results is that the load induced on the vertical tail by the horizontal tail varies both in magnitude and direction with tail position. It appears from these data that the designer might be able to adjust the yawing moments produced by a tail roll control to a satisfactory value by proper positioning of the horizontal tail, assuming, of course, that other considerations, such as the pitch-up problem, permit this to be done. In this connection, it might be pointed out that if a ventral fin is used on the airplane for high-speed stability, the yawing moments for a low tail position would be smaller - more like those shown in figure 5 for the intermediate position. If the yawing moments cannot be adjusted to a satisfactory value by positioning the tail, it might be necessary to adjust them by linking the rudder in with the tail roll control.

Interaction of Roll and Pitch Control

Figure 6 provides some information on one of the problems that usually comes to mind when a tail control is considered, that is, the problem of interaction of roll and pitch control. First, consider the effect of roll control on pitching moments shown in the left plot. The pitching moments are shown for 0° and -15° stabilizer settings (the solid lines); for these same stabilizer settings, $\pm15^\circ$ roll control is superimposed on the pitch control (the dashed lines). The significant result herein is that for the angles of attack at which the model is trimmed longitudinally there is essentially no effect of the roll control on the pitch control. In the right plot the variation of roll control C_{l_δ} with angle of attack is shown for two different settings of the stabilizer, 0 and -15°. At low angles of attack, the effectiveness with -15° incidence is much less than that for 0° because one of the surfaces is stalled; but at high angles of attack, where this negative incidence is required for longitudinal trim, the roll control is better with the -15° incidence, apparently because this incidence tends to keep the tail unstalled at the high angles of attack.

The results shown in figure 6 illustrate the conditions which tend to make the control interaction problem less serious in some cases than might be expected at first glance but they should not lead to the conclusion that there will be no interaction problems in other cases. For other configurations or other flight conditions in which large tail loads are required for longitudinal trim, a serious problem might exist. For example, this same model in the landing condition has a control interaction problem that is shown in the next figure.

Effect of Flaps

The effect of flaps on the tail roll control is shown in figure 7. Values of C_{l_δ} and $\frac{C_{n_\delta}}{C_{l_\delta}}$ are plotted against lift coefficient for two configurations. The data on the left side of the figure, which are for the model shown in figure 6, show that there is less control effectiveness for the landing configuration at all lift coefficients. Apparently, the change in tail angle of attack produced by flap deflection and by the 7° wing incidence used for landing keeps one of the tail surfaces stalled at all times when the stabilizer trim of -15° and the roll-control deflection of $\pm 15^\circ$ are applied simultaneously.

For the configuration on the right side of figure 7 for which the wing incidence was kept at 0° and only -6° stabilizer deflection was required for trim, deflection of the flaps actually led to better control than with flaps retracted at the higher lift coefficients.

For both models, the values of the yawing-moment parameter $\frac{C_{n_\delta}}{C_{l_\delta}}$ for the clean configuration were increased by flap deflection mainly because of the reduction in C_{l_δ}. Results shown in figure 5 indicate that these yawing moments would be quite different for an intermediate or high horizontal-tail position.

Comparison of Measured and Estimated C_{l_δ}

Figure 8 shows a comparison of measured and estimated values of C_{l_δ} for most of the cases shown in figure 1 for the clean condition at 0° angle of attack. In estimating C_{l_δ}, values of $C_{m_{i_t}}$ (the pitching moment due to stabilizer incidence) obtained from force-test data for the particular model were used as shown in the formula at the top of figure 8. The factor of 2 in the formula is required to account for the fact that i_t in $C_{m_{i_t}}$ refers to deflection of both surfaces, whereas δ in C_{l_δ} refers to deflection of one surface. The term $\left(\frac{y}{l}\right)_{tail}$, the ratio of the lateral to the longitudinal distance from the center of gravity to the calculated center of pressure of the tail, and the term $\left(\frac{\bar{c}}{b}\right)_{wing}$ convert the pitching-moment parameter into a rolling-moment parameter.

For the two sets of supersonic test data in figure 8 (solid symbols connected by dashed lines) the agreement is fairly good, but for all the subsonic data the measured values of C_{l_δ} are only about 0.7 to 0.8 times as large as the estimated values. Two factors are apparently responsible for this difference between the measured and estimated values of C_{l_δ} for the subsonic cases. First, the load on the vertical tail which produces a large favorable yawing moment for the low-tail configurations of figures 1 and 4 also produces an adverse rolling moment which is not accounted for in the formula of figure 8. Second, with the differentially deflected horizontal-tail surfaces there is a spreading of the load from one surface to the other across the bottom of the fuselage which causes an inboard shift of the lateral center of pressure (decreased value of y). One reason that the factor of 0.7 or 0.8 does not seem to apply to the supersonic cases is probably that there is much less carry-over of the load from one surface to another at supersonic speeds, as pointed out previously in connection with figure 4.

For a high horizontal-tail position, the load induced on the vertical tail produces an adverse yawing moment (fig. 5) and a favorable rolling moment. The rolling effectiveness at subsonic speeds with a high tail position should therefore be slightly greater than that with a low tail position.

CONCLUDING REMARKS

In summary, the results presented in this report for the tail roll control appear to be fairly promising even though most of the data were obtained with configurations that were not especially designed for the use of such a control. The results indicate that a tail roll control might be satisfactory if (1) the tail is made relatively large to provide adequate effectiveness without excessive deflections, (2) the airplane is designed so that the longitudinal trim requirements for the tail are minimized so as to avoid interaction of roll and pitch controls, and (3) the horizontal tail is positioned vertically to avoid excessive favorable or adverse yawing moments. In many cases it might not prove feasible to use the horizontal tail as the primary roll control, but in these cases the tail control will still warrant consideration as an auxiliary control to supplement the effectiveness of ailerons that are unsatisfactory in some flight conditions.

REFERENCES

1. Koenig, David E.: Tests in the Ames 40- by 80-Foot Wind Tunnel of an Airplane Configuration With an Aspect Ratio 3 Triangular Wing and an All-Movable Horizontal Tail - Longitudinal and Lateral Characteristics. NACA RM A52L15, 1953.

2. English, Roland D.: Free-Flight Investigation, Including Some Effects of Wing Aeroelasticity, of the Rolling Effectiveness of an All-Movable Horizontal Tail With Differential Incidence at Mach Numbers From 0.6 to 1.5. NACA RM L54K30, 1954.

3. Tinling, Bruce E., and Karpen, A. V.: The Effects of Trailing-Edge Flaps on the Subsonic Aerodynamic Characteristics of an Airplane Model Having a Triangular Wing of Aspect Ratio 3. NACA RM A54L07, 1955.

4. Critzos, Chris C.: Lateral-Control Investigation at Transonic Speeds of Differentially Deflected Horizontal-Tail Surfaces for a Configuration Having a 6-Percent-Thick 45° Sweptback Wing. NACA RM L55I26, 1955.

5. Savage, Howard F., and Tinling, Bruce E.: The Static Lateral and Directional Subsonic Aerodynamic Characteristics of an Airplane Model Having a Triangular Wing of Aspect Ratio 3. NACA RM A55B11, 1955.

6. Schult, Eugene D., Strass, H. Kurt, and Fields, E. M.: Free-Flight Measurements of Some Effects of Aileron Span, Chord, and Deflection and of Wing Flexibility on the Rolling Effectiveness of Ailerons on Sweptback Wings at Mach Numbers Between 0.8 and 1.6. NACA RM L51K16, 1952.

HORIZONTAL TAIL FOR ROLL CONTROL

CLEAN CONDITION, $\alpha = 0°$

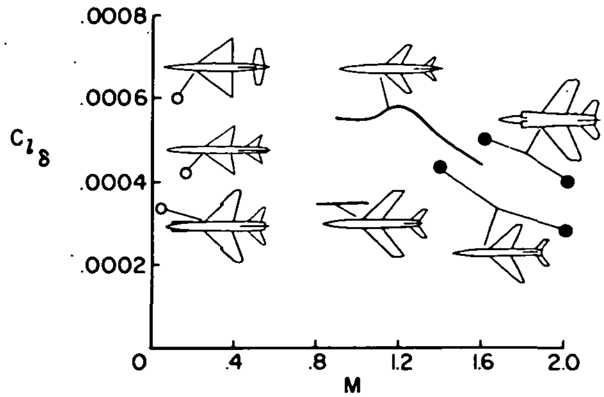

Figure 1

EFFECT OF AEROELASTICITY ON ROLL CONTROL

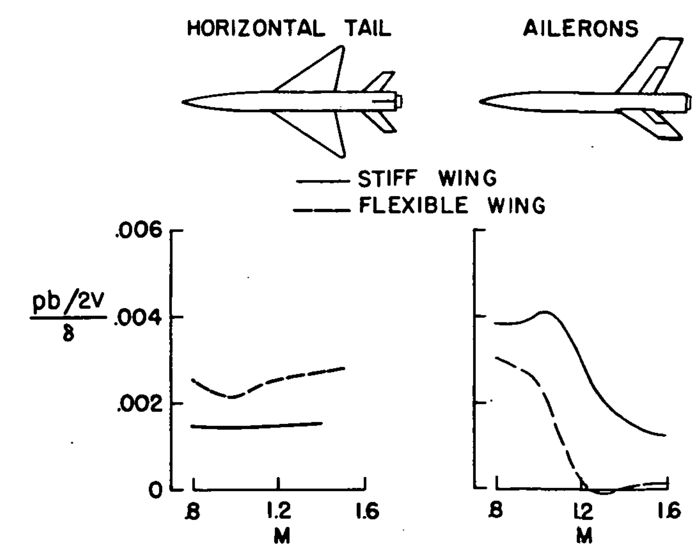

Figure 2

EFFECT OF ANGLE OF ATTACK ON ROLL CONTROL

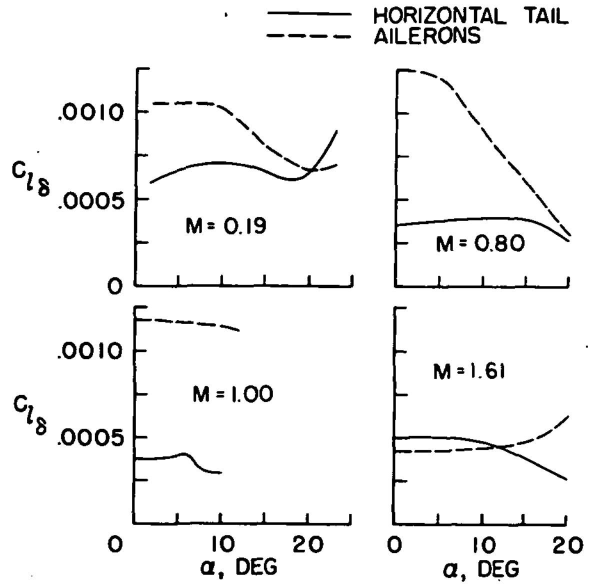

Figure 3

YAWING MOMENTS PRODUCED BY ROLL CONTROL

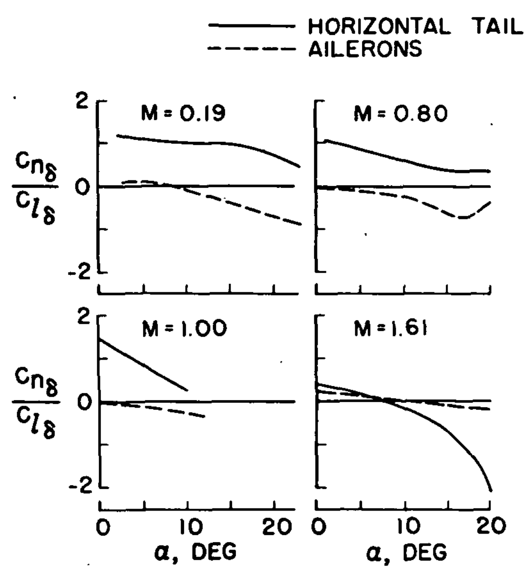

Figure 4

EFFECT OF TAIL POSITION ON YAWING MOMENTS

LOW-SPEED DATA; CLEAN CONDITION; $i_t = 0°$

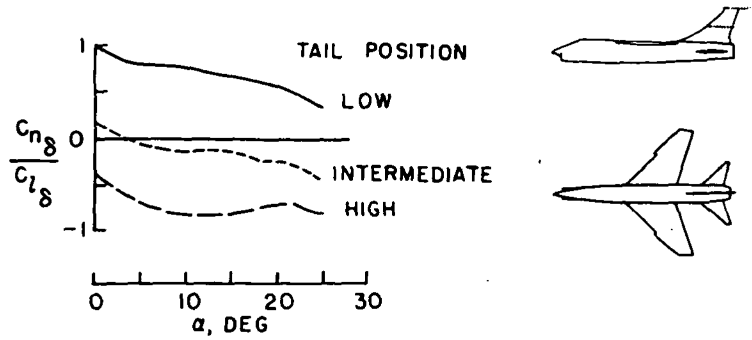

Figure 5

INTERACTION OF ROLL AND PITCH CONTROL

CLEAN CONDITION; LOW-SPEED DATA

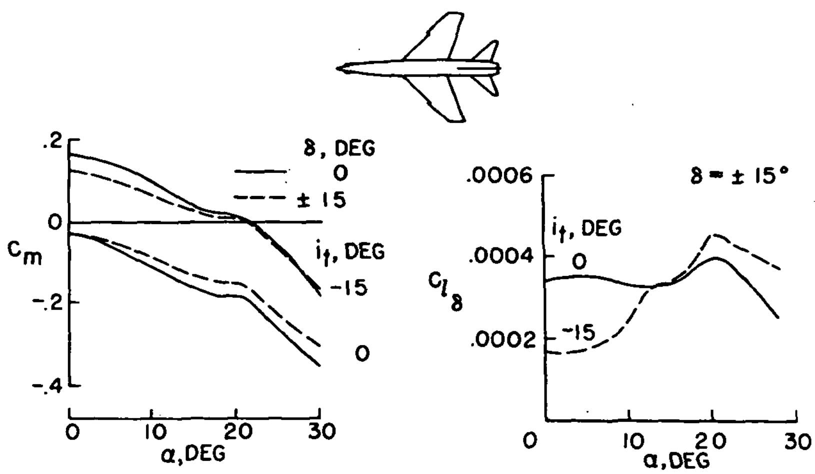

Figure 6

[redacted]

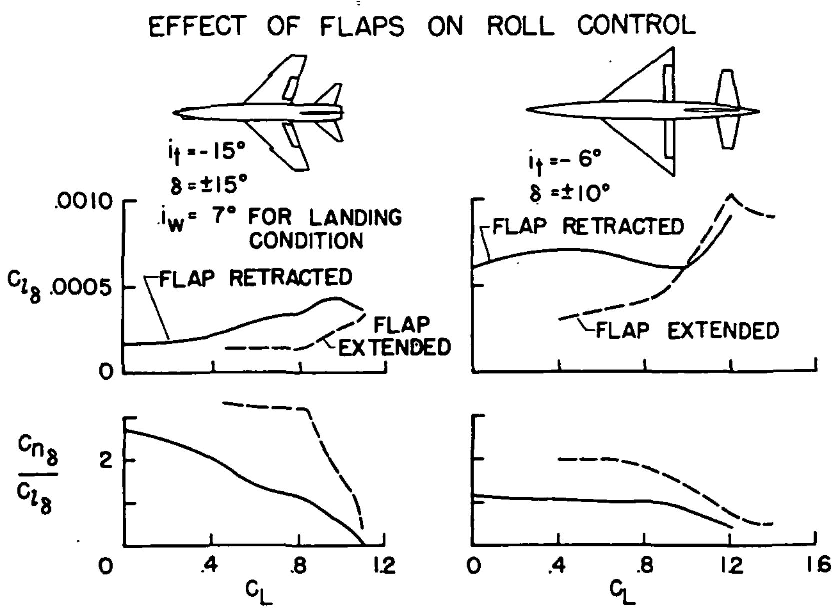

Figure 7

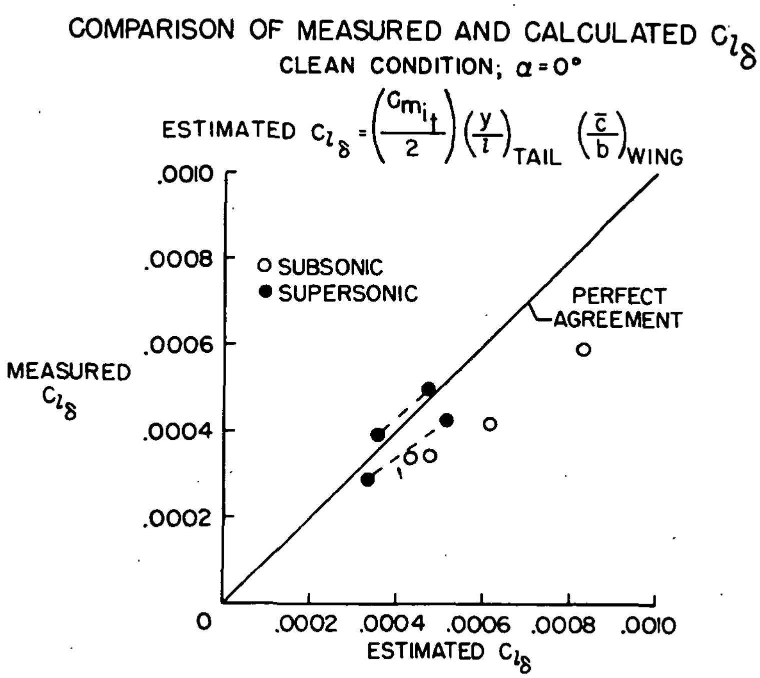

Figure 8

[redacted]

AERODYNAMICS OF BODIES, WINGS, AND WING-BODY COMBINATIONS AT HIGH ANGLES OF ATTACK AND SUPERSONIC SPEEDS

By Jack N. Nielsen, J. Richard Spahr,
and Frank Centolanzi

Ames Aeronautical Laboratory

SUMMARY

Results are presented on the aerodynamic behavior of bodies, wings, and wing-body combinations at high angles of attack and supersonic speeds. Maximum lift coefficients for rectangular and triangular wings are presented, together with some downwash measurements behind a rectangular wing at high angles of attack. A method is given to show how the body vortex strengths and positions presented by Jorgensen and Perkins in NACA RM A55E31 can be used to predict the nonlinear panel normal forces, hinge monents, and rolling moments for cruciform-wing and body combinations at high angles of attack.

INTRODUCTION

Airplanes and missiles sometimes operate in a high range of angle of attack for which most present aerodynamic theory is inapplicable. Therefore, it is important that knowledge of aerodynamics for this range be enlarged. The primary purpose of this paper is to describe progress in the aerodynamics of wings, bodies, and wing-body combinations at high angles of attack.

SYMBOLS

A	aspect ratio of wing or exposed panels joined together
a,r	body radius
C_h	hinge-moment coefficient based on exposed panel area and mean aerodynamic chord
$C_{L_{max}}$	maximum lift coefficient based on wing area

C_l	rolling-moment coefficient based on exposed panel area and combination semispan
C_N	normal-force coefficient based on exposed panel area
d	body diameter
M	free-stream Mach number
Re	Reynolds number based on mean aerodynamic chord of wing panel
s	wing semispan or combination semispan
x	downstream distance from point of body
y	lateral distance measured from wing center line or body center line
z	vertical distance above midchord (hinge line) of rectangular wing
z_v	vertical coordinate of vortex core
α	angle of attack
ϵ	downwash angle
ϕ	bank angle (see fig. 6)

DISCUSSION

Wings Alone

Measurements of forces, moments, pressure distributions, and span loadings have been reported for triangular and rectangular wings at large angles of attack. (See refs. 1, 2, and 3.) Also analytical work on the characteristics of finite-span rectangular and triangular wings for such angles has been reported. (See refs. 4, 5, and 6.) Before the discussion of bodies alone and wing-body combinations, results on the maximum lift coefficient of wings alone and the downwash behind a rectangular wing at high incidence will be considered.

Figure 1 shows information on the variation of maximum lift coefficients of wings alone with Mach number and aspect ratio. The angles of attack for maximum lift was about 40° for all the wings. For the larger aspect ratios and low supersonic speeds, the maximum lift coefficient is about unity. This result was obtained by Gallagher and Mueller (ref. 7) in an earlier investigation of 10 different wings with aspect ratios greater than 1.33. However, for the range of low aspect ratios the triangular wings exhibit a large effect of aspect ratio on $C_{L_{max}}$ and show a significant effect of Mach number for all aspect ratios. For the range of Mach number and aspect ratio shown here, the rectangular wings have maximum lift coefficients between 1.0 and 1.1.

In order to gain some insight into the flow fields behind wings at supersonic speeds and high angles of attack, the downwash, sidewash, total pressure, and Mach number distributions have been measured behind triangular and rectangular wings of aspect ratio 2 for angles of attack up to about 37°. Figure 2 shows the downwash variations for a distance of 1.1 chord lengths behind the midchord of the rectangular wing. The downwash is presented on the left-hand side of the figure for a horizontal line 2.5 percent of the wing semispan above the vortex, and on the right-hand side of the figure, for a horizontal line 10 percent below the vortex. The downwash parameter ϵ/α is plotted against spanwise distance measured from the root chord. The value of y/s of unity corresponds to the wing tip. The downwash angle has been corrected for the downwash that exists behind the wing at an angle of attack of 0° by virtue of wing thickness. For angles of attack up to 30° measurements show that the flow field is dominated by a single tip vortex near the 97-percent-semispan position. The left-hand plot shows the downwash pattern typical of a single vortex for angles of attack of 6° and 20°. The effect of increasing angle of attack is to reduce the magnitude of the maximum and minimum downwash values and to broaden the lateral spacing between them. This behavior would be expected if the vortex core were increasing in diameter as α increased. Such behavior is contrary to that which would be predicted by using horseshoe vortices and the measured span loading (refs. 8 and 9) which becomes more rectangular as α increases.

For the location beneath the vortex comparisons have been made between theory and experiment for 6° and 20°. The theory for $\alpha = 6^{\circ}$, based on the measured span loading and 3 horseshoe vortices, is in good accord with the measurements. The theory for $\alpha = 20^{\circ}$, based on a rectangular span loading and one horseshoe vortex, is in good accord with experiment only outboard of the wing tip. On the basis of these results, it can be said that at high angles of attack the measured span loadings do not account for the downwash patterns as at low angles of attack.

Bodies Alone

Some developments in the study of flows about bodies of revolution are now briefly considered. The viscous crossflow theory of Allen and Perkins (ref. 10) for bodies of revolution shedding vortices on their leeward side is well known. Methods are available for predicting the gross forces and moments on such bodies as well as the distribution of normal force along them (ref. 11). Also Jorgensen and Perkins (ref. 12) have been able to develop a method for predicting the vortex strengths and paths.

Figure 3 shows the downwash angle as predicted and as measured in the crossflow plane about 10 diameters behind the tip of a cylindrical body with an ogival nose of 3 calibers. The measurements are in the plane of the vortices. They are first to be compared with a potential theory neglecting the vortices and then with a potential theory including the effect of the vortices. To make this prediction required a knowledge of the distribution of normal force along the body as well as knowledge of the initial vortex positions. The vortex strengths and paths were then calculated by a step-by-step method. Insofar as is known, the experimental data of Jorgensen and Perkins constitute the only systematic information on vortex strengths and paths for bodies. These data are basic to the account of wing-body interference at high angles of attack which is discussed subsequently.

Wing-Body Combinations

Reliable engineering methods are known for calculating wing-body interference for angles of attack below that for which the body starts shedding vortices (ref. 13). At high angles of attack, vortices generated by the body nose can pass close to the wing panels and modify their aerodynamic characteristics in a nonlinear manner. These nonlinearities were pointed out by Krenkel (refs. 14 and 15) in his cruciform-missile studies. A method for predicting the magnitudes of these effects, which limit the range of linear characteristics of any configuration, would be useful if only as a guide for avoiding the nonlinearities.

With information available on the strengths and positions of the vortices of the body alone, estimates of wing-body interference can be made when important vortex effects occur. In order to obtain data for checking such estimates, measurements were made of normal forces and moments on the panel of the cruciform-wing and body combination (fig. 4) that utilizes the same body and test conditions as the body-alone investigation of Jorgensen and Perkins. The measurements were made for an angle-of-attack range up to 25° for the complete range of bank angles and for all possible combinations of wing panels.

Effect of angle of attack.- Figure 4 shows the effects of angle of attack on the normal force and rolling moment developed by the right wing panel of the cruciform-triangular-wing and body combination. In this case of a bank angle of 0°, the combination could just as well be monowing rather than cruciform. For angles of attack up to 10°, the normal force is in good agreement with low-angle interference theory (ref. 13). For higher angles of attack, the normal force falls even below that for the wing alone; this effect corresponds to a total loss of effective upwash. The normal force for the wing alone is included only for comparative purposes. In order to show that the vortices can account for this loss of normal force, their effect was calculated and added to the low-angle interference theory. The sum is shown in figure 4 by the solid line and is henceforth termed vortex theory. Similar results were calculated for the rolling moment of the panel and are shown on the right-hand side of figure 4. It is seen that the effect of the vortices account for the departures of the measured results from low-angle interference theory.

The calculated results were obtained as follows: First the panel characteristics were calculated by low-angle interference theory (ref. 13) with the use of experimental data for the wing alone. It was then assumed that the strengths and positions of the vortices were the same as those of the body-alone investigation. The downwash at the wing panels was then calculated, and its effect on the aerodynamic coefficients was estimated by strip theory. Admittedly, the method neglects the effect of the panel crossflow field on the vortex strengths and positions which for very low aspect ratios could be important.

The calculative method has also been applied to the combination of the body and rectangular wing shown in figure 5. For this combination the distribution of normal force along the body was close to that measured in the body-alone investigation at $M = 2$. Thus, it was assumed that the vortex strengths for unit free-stream velocity and the vortex paths measured at $M = 2$ applied to this case. Again, it is seen that the vortices account for the departures of the measured results from low-angle theory. In this instance, the measured rolling moment is not closely approximated by that of the wing alone. It is to be noted that plan form, Mach number, and the ratio of body radius to wing semispan in this case differ from those for the preceding case. Anything tending to increase the body vortex strength adjacent to a fixed panel will increase the magnitude of the nonlinearities. Such changes include increases in angle of attack, nose length, or body radius.

<u>Effect of angle of bank</u>.- The effects of the vortices on the panel forces and moments are most pronounced when they pass close to the panel as for some conditions of combined pitch and bank. Figures 6 and 7 show the effects of bank angle on the characteristics of the cruciform combination utilizing triangular wings. Figure 6 shows the normal forces and rolling moments for the panel on the configurations with short and long noses. The sketches show the panel on which the normal force is measured and its bank orientation. For the configuration with the short nose the effects of the vortices are known to be small because the nose length is too short for strong vortices to develop at $\alpha = 20^{\circ}$. The effects of the vortices for the body with the long nose are thus given approximately by the difference between the curves for the bodies with the short and long

noses. It is clear that the effects of the vortices on normal force and rolling moment are similar and that they are a maximum near a bank angle of -70°. For this angle the wing panels would intersect the vortex position for the body alone.

As the banked panel approaches the vortex position, the center of pressure moves outboard and rearward for the configuration with the long nose as opposed to an almost stationary center of pressure for the configuration with the short nose. (See fig. 7.) The large rearward shifts of the center of pressure cause the nonlinear variation of the hinge-moment coefficient shown in the right-hand side of the figure. The hinge line passes through the panel centroid. Data not presented show that panel-panel interference causes effects about half as large as those shown for the body vortices.

A comparison of the measured and calculated panel characteristics as a function of bank angle is presented in figure 8 for the configuration with the long nose at an angle of attack of 20°. The Reynolds number is based on the panel mean aerodynamic chord. Comparison between experiment and theory are shown for normal force, rolling moment, and hinge moment. The interference theory for low angles of attack which neglects the vortices is shown by the dashed lines, and the calculated results including the vortices are shown by the solid lines. It is clear that the nonlinear trends with angle of bank are accounted for by the vortex theory.

In calculating the effects of bank angle, the influence of the vortex on aerodynamic coefficients is computed in the same manner as for a bank angle of 0°. However, under combined pitch and yaw, loading proportional to the product of the angles of pitch and yaw is introduced. The interference theory (ref. 13) used for a bank angle of 0° can be generalized to include the effects of this loading. This generalization is accomplished with the help of a result of Spreiter (ref. 16) for the loading of a slender cruciform missile. This result includes the effects of those square terms in Bernoulli's equation significant in slender-body theory. One of the important effects of bank angle is to change the sweep angle of the leading edge of the panel and thereby to change the lift-curve slope of the panel. This change of sweep angle was interpreted as a change in effective aspect ratio in determining the lift-curve slopes of the wing alone for use in strip theory.

CONCLUDING REMARKS

The calculative method given here is another case - of which there are several - wherein nonlinear aerodynamic behavior can be calculated on the basis of a simple vortex model. It is believed that studies of the present type can be extended to problems of weathercock stability as affected by body vortices and to problems of wing-body configurations employing wings of very low aspect ratio. The present calculative method should be applied to a wider range of missile configuration and to higher angles of attack and Mach numbers to determine its limitations.

REFERENCES

1. Katzen, Elliott D., and Pitts, William C.: Load Distributions on Wings and Wing-Body Combinations at High Angles of Attack and Supersonic Speeds. NACA RM A55E17, 1955.

2. Kaattari, George E.: Pressure Distributions on Triangular and Rectangular Wings to High Angles of Attack - Mach Numbers 1.45 and 1.97. NACA RM A54D19, 1954.

3. Kaattari, George E.: Pressure Distributions on Triangular and Rectangular Wings to High Angles of Attack - Mach Number 2.46 and 3.36. NACA RM A54J12, 1955.

4. Pitts, William C.: Force, Moment, and Pressure Distribution Characteristics of Rectangular Wings at High Angles of Attack and Supersonic Speeds. (Prospective NACA paper.)

5. Vincenti, Walter G., and Fisher, Newman H., Jr.: Calculation of the Supersonic Pressure Distribution on a Single-Curved Tapered Wing in Regions Not Influenced by the Root or Tip. NACA TN 3499, 1955.

6. Fowell, L. R.: An Exact Theory of Supersonic Flow Around a Delta Wing. UTIA Rep. No. 30, Univ. of Toronto, Inst. Aerophysics, Mar. 1955.

7. Gallagher, James J., and Mueller, James N.: Preliminary Tests To Determine the Maximum Lift of Wings at Supersonic Speeds. NACA RM L7J10, 1947.

8. Haefeli, Rudolph C., Mirels, Harold, and Cummings, John L.: Charts for Estimating Downwash Behind Rectangular, Trapezoidal, and Triangular Wings at Supersonic Speeds. NACA TN 2141, 1950.

9. Spreiter, John R., and Sacks, Alvin H.: The Rolling Up of the Trailing Vortex Sheet and Its Effect on the Downwash Behind Wings. Jour. Aero. Sci., vol. 18, no. 1, Jan. 1951, pp. 21-32, 72.

10. Allen, H. Julian, and Perkins, Edward W.: A Study of Effects of Viscosity on Flow Over Slender Inclined Bodies of Revolution. NACA Rep. 1048, 1951. (Supersedes NACA TN 2044.)

11. Perkins, Edward W., and Jorgensen, Leland H.: Comparison of Experimental and Theoretical Normal-Force Distributions (Including Reynolds Number Effects) on an Ogive-Cylinder Body at Mach Number 1.98. NACA RM A54H23, 1954.

12. Jorgensen, Leland H., and Perkins, Edward W.: Investigation of Some Wake Vortex Characteristics of an Inclined Ogive-Cylinder Body at Mach Number 1.98. NACA RM A55E31, 1955.

13. Nielsen, Jack N., Kaattari, George E., and Anastasio, Robert F.: A Method For Calculating the Lift and Center of Pressure of Wing-Body-Tail Combinations at Subsonic, Transonic, and Supersonic Speeds. NACA RM A53G08, 1953.

14. Krenkel, A. R.: Generalized Missile Study First Annual Report. Rep. No. CF-1996, McDonnell Aircraft Corp., May 29, 1953.

15. Krenkel, A. R.: GMS Interim Report on Wing-Body Interference Phenomena, Rep. No. 3524, McDonnell Aircraft Corp., Mar. 1954.

16. Spreiter, John R., and Sacks, Alvin H.: A Theoretical Study of the Aerodynamics of Slender Cruciform-Wing Arrangements and Their Wakes. (Prospective NACA paper.)

MAXIMUM LIFT COEFFICIENTS OF WINGS ALONE

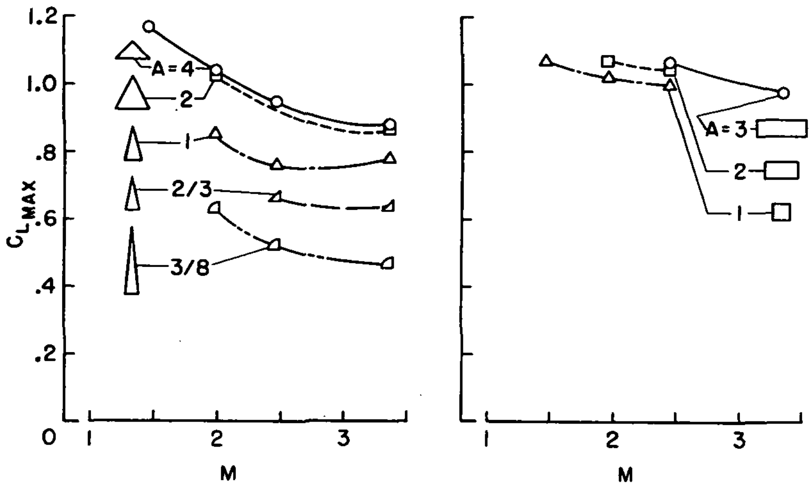

Figure 1

PREDICTED AND MEASURED DOWNWASH
BEHIND RECTANGULAR WING
A = 2
M = 2.46

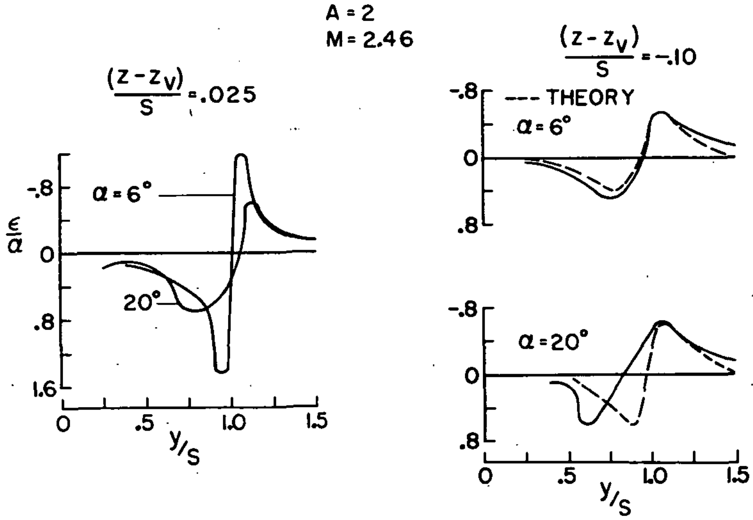

Figure 2

DOWNWASH FIELD THROUGH BODY VORTICES

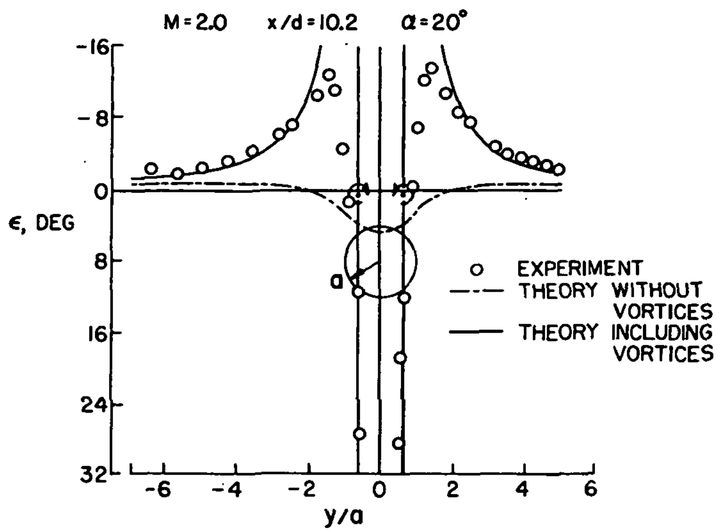

Figure 3

VARIATION OF TRIANGULAR PANEL CHARACTERISTICS WITH ANGLE OF ATTACK

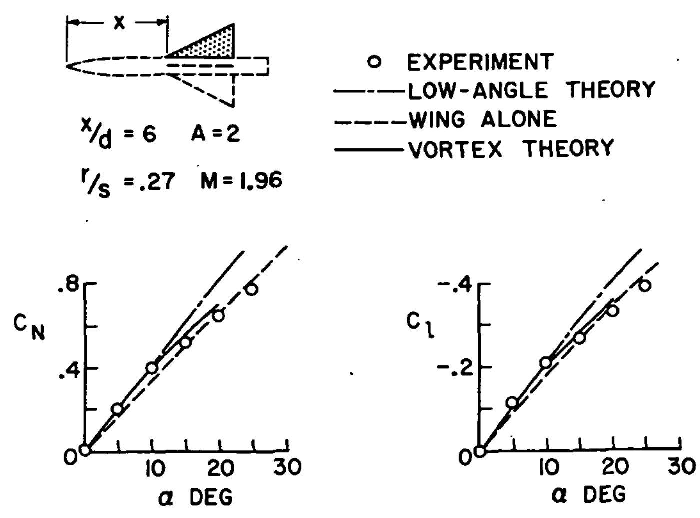

Figure 4

[redacted]

VARIATION OF RECTANGULAR PANEL CHARACTERISTICS
WITH ANGLE OF ATTACK

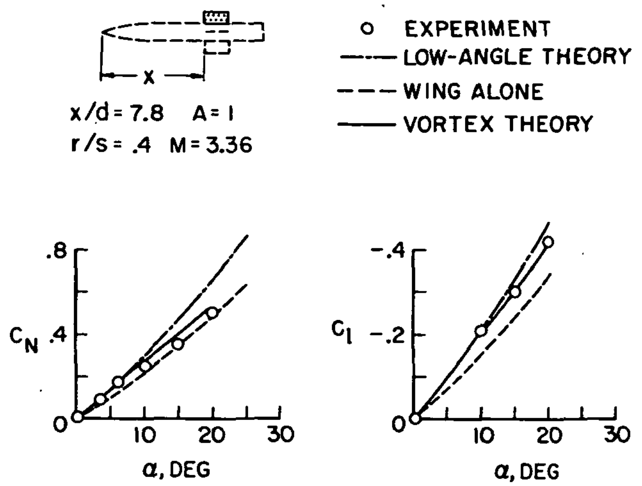

Figure 5

VARIATION OF PANEL NORMAL FORCE
AND ROLLING MOMENT WITH BANK ANGLE

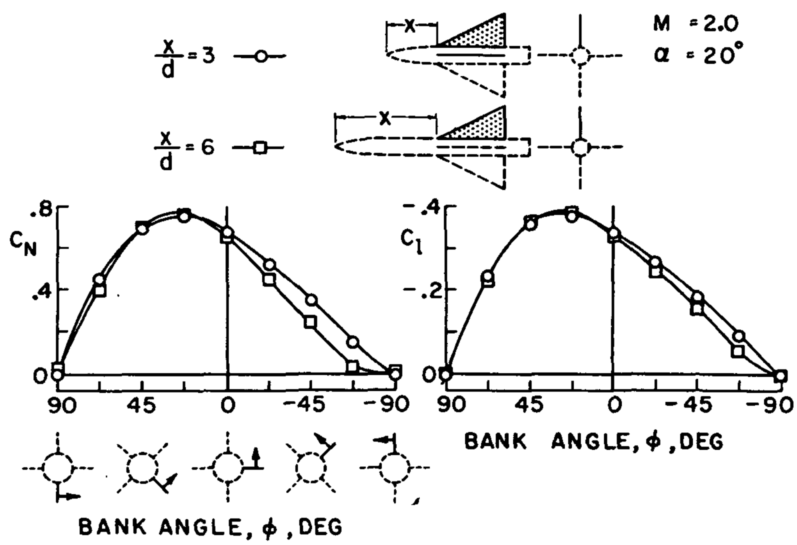

Figure 6

[redacted]

VARIATION OF CENTER OF PRESSURE AND
HINGE MOMENT WITH BANK ANGLE

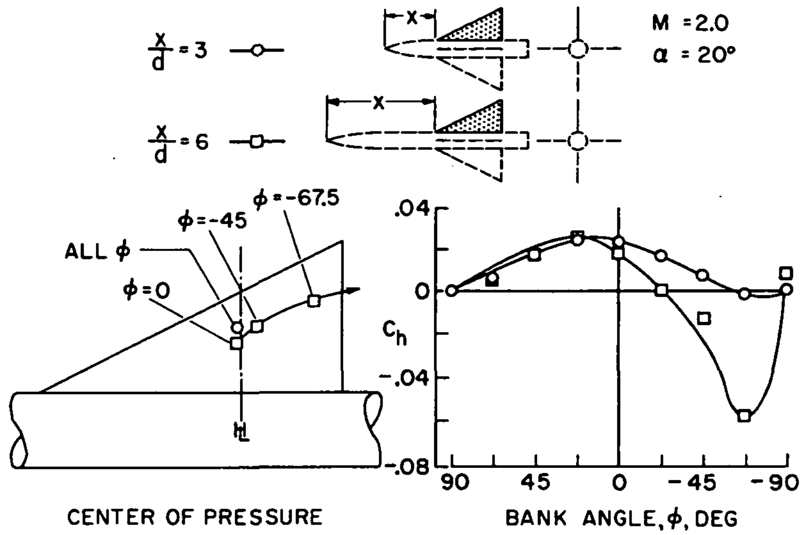

Figure 7

COMPARISON OF CALCULATED AND MEASURED
PANEL CHARACTERISTICS

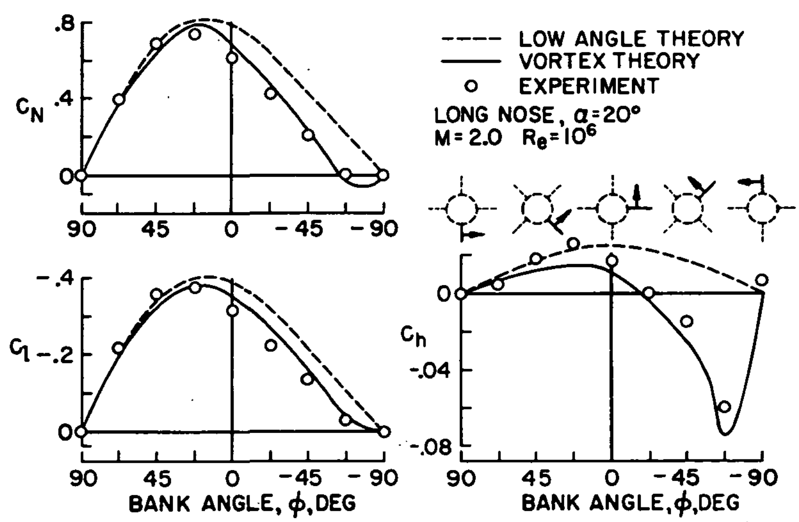

Figure 8

AERODYNAMICS OF MISSILES EMPLOYING WINGS OF VERY LOW ASPECT RATIO

By Elliott D. Katzen and Leland H. Jorgensen

Ames Aeronautical Laboratory

INTRODUCTION

Development tests such as those made by the Douglas and Hughes Aircraft Companies (e.g., refs. 1 to 5) have shown that, for certain applications, missiles employing wings of very low aspect ratio have excellent aerodynamic characteristics. Other studies have focused attention on low aspect ratios by questioning the need for wings of large span or even wings at all. There have been, however, large gaps in our knowledge concerning the aerodynamics of missiles having wings of very low aspect ratio. To help fill some of the gaps, wind-tunnel tests have been performed on a family of missiles. This paper summarizes the results of the investigation; some of the performance and stability and control characteristics of the missiles are discussed.

TESTS

The models studied are shown in figure 1. The basic body had a total fineness ratio of 10, being composed of a fineness-ratio-3 ogival nose and a cylindrical afterbody. In some instances the models were also tested with a Newtonian minimum-drag nose of fineness ratio 5; this resulted in a total fineness ratio of 12.

The aspect ratios of the wings were varied from a little less than 0.1 to 1. This corresponds, for the triangular wings, to semiapex angles from 1.3° to 14°. The wing sections were modified flat plates with leading and trailing edges generally beveled to small radii. In some cases the leading edges were not sharpened but were blunted with relatively large radii.

Various methods of controlling the models were studied. The tail control shown was tested in line and interdigitated 45° with respect to the wings. For comparison with the tail control, the nose of the model was deflected as a control. The planform area of this deflected portion of the nose was equal to that of 2 tail panels.

Data for these models were obtained at Mach numbers of 2.0, 2.9, and 3.3. The angle-of-attack range of the tests was from 0° to 30°; the control-deflection range was $\pm 45^\circ$. The Reynolds number was about 9×10^6 based on the length of the basic body.

RESULTS AND DISCUSSION

Performance Characteristics

The lift of the missiles increases, of course, as planform area is added to the body. However, the question arises of whether the lift effectiveness, or lift per unit area, is also increased by the addition of very small wings. The lift effectiveness of winged and wingless missiles is compared in figure 2. The coefficients are based on total planform area; therefore they represent lift per unit area. At a lift ratio of unity, the lift per unit area is equal to that of the body. Above this value (represented by the dashed line), the lift per unit area is increased to more than that of the body. Even the smallest wing (aspect ratio of 3/32) increases the lift effectiveness appreciably to more than that of the body (fig. 2(a)). At a Mach number of 3.3 and an angle of attack of 10°, for example, the lift per unit area is increased 20 percent by the addition of this small wing. The total lift of this configuration, moreover, is increased an additional 10 percent; this additional increase results in a total increase of 30 percent, because the planform area is increased 10 percent over that of the basic body. As the Mach number or the angle of attack is increased, the lift effectiveness approaches that of the body more closely.

The data presented in figure 2(a) pertain to the family of missiles having wings whose root chords are the same length. As shown in figure 2(b), essentially the same results have been obtained at Mach number 3.3 for other missiles of constant span (ref. 6). It is interesting to note that the geometrically slender models cannot be considered aerodynamically slender at this high a Mach number. By slender-body theory, wing-body combinations of equal span have the same lift. Hence, the lift per unit area should decrease as additional wing area is added to the body. However, the lift of the combinations can be calculated with fair accuracy by the use of standard interference methods (e.g., ref. 7) which use slender-body theory only for the interference ratios. For missiles having very small wings it is especially important in these calculations that the lift of body alone be known accurately either from theory or experiment.

Other wind-tunnel data (ref. 8) for Mach numbers even as high as 6 show that lift effectiveness is much greater for winged than wingless missiles. Depending on specific design considerations, the presence of even a very small wing could improve the lift and maneuverability of a missile over a wide range of Mach number and angle of attack. Of course, the increased weight due to the addition of wings has to be considered.

The increase in fore drag that results from adding wings to the basic body is indicated in figure 3. The drag coefficients are based on the cross-sectional area of the body rather than on total planform area as in figure 2. The drag decreased as the Mach number was increased from 2.0 to 2.9, but there was little difference between the data for Mach numbers 2.9 and 3.3. The horizontal bars in figure 3 indicate the relatively small spread in minimum drag coefficient for the missiles with leading edges curved in planform. These missiles all have the same planform area as the model having wings of aspect ratio 3/8 and straight leading edges. For this same missile, increasing the nose fineness ratio from 3 to 5 reduced the minimum drag coefficient about 30 percent. The effect of changing from a wing section with a relatively sharp leading edge to a section having a blunt leading edge was negligible for this model with aspect ratio 3/8. This indicates that large drag penalties will not be incurred by blunting the leading edges of these highly swept wings to alleviate aerodynamic heating.

In figure 4 the variation with planform area of another performance parameter, the maximum ratio of lift to drag, is illustrated. Increasing planform area (and aspect ratio) increased $(L/D)_{MAX}$, the variation being almost linear. The effect of an increase in Mach number from 2.0 to 3.3 is to cause a decrease in $(L/D)_{MAX}$ for the configurations having the largest wings. Here, wing characteristics are beginning to predominate; the decrease is due principally to the decrease in wing lift-curve slope and, therefore, increased drag due to lift with this increase in Mach number. Since skin-friction is a relatively large part of the drag of these configurations, it must be emphasized that these results were obtained at a Reynolds number of about 9×10^6. Therefore, care should be taken in applying these results to conditions at other Reynolds numbers. The angle of attack for $(L/D)_{MAX}$ decreased from about 11° for the body alone to 6° for the missile having the largest wing. Increasing the nose fineness ratio from 3 to 5 increased $(L/D)_{MAX}$ by about 20 percent. Further increases in $(L/D)_{MAX}$ could be made by taking advantage of some of the favorable interference effects discussed in reference 9.

Stability and Control Characteristics

Performancewise, the advantages of missiles having low-aspect-ratio wings have been discussed. Now the stability and control characteristics of these same models will be presented. In figure 5, the center of pressure, in diameters from the nose, is plotted as a function of angle of attack. The curve for the body alone shows that the center of pressure starts out near the nose at zero angle of attack and moves toward the body centroid of area as the angle of attack is increased. The center-of-pressure position of the body alone can be predicted within less than half a diameter. Adding even a very small wing significantly reduces the center-of-pressure travel with changes in angle of attack and moves the center of pressure rearward, thereby resulting in a more stable configuration. The center of pressure continues to move rearward as the wing aspect ratio is increased and additional wing area is added to the missile. The center-of-pressure travel with angle of attack was negligible for the missiles having wings of aspect ratios 3/8, 2/3, and 1 at this Mach number of 3.3.

The effect of Mach number changes on center of pressure is shown in figure 6. The center-of-pressure movement with changes in Mach number was large for the body alone and decreased as the wing aspect ratios were increased from 0 to 3/8. For the missile having a wing of aspect ratio 3/8, the center-of-pressure travel with changes in Mach number and angle of attack was less than 0.4d. The travel was slightly larger for the configurations with wings of aspect ratios 2/3 and 1. Changes in bank angle of the missiles also caused shifts in center of pressure. The shifts were negligible for the missiles with the smallest wings. For the missile having the largest wing, the effect of changes in bank angle was to approximately double the center-of-pressure travel with changes in angle of attack and Mach number. Results from Douglas Aircraft Co., Inc. (ref. 1) have shown that the already small center-of-pressure shifts associated with configurations like these can be further reduced by the use of small fixed surfaces forward of the wing. These canard surfaces do increase the rolling moments, however, at high angles of attack.

In addition to making the center-of-pressure shifts small, it is desirable to be able to fix the center of pressure at certain positions along the body length. A method of accomplishing this is shown in figure 7. The center of pressure of missiles having wing leading edges curved in planform are shown. The curved leading edges change the centroid of area. For comparison (with the curved-leading-edge data), data for the body alone and for the configuration having a straight-leading-edge wing of aspect ratio 3/8 are repeated from figure 6. The center-of-pressure positions are consistent with the changes in the centroid of planform area. The center of pressure of the model with a convex leading edge was farther forward and the center of pressure of the model with a concave leading edge was farther aft than that for the missile having a wing with a straight leading edge. The configuration having the small wing extending to the tip of the nose was much more stable than the body alone but less stable than the other configurations. The small center-of-pressure shifts associated with these configurations having wings of very low aspect ratio simplify the problem of stabilizing and controlling the missiles.

The effect on missile stability of three types of controls, in-line and interdigitated tail controls and swivel nose, is illustrated in figure 8. The tail controls are composed of single-wedge sections to increase their effectiveness and reduce control center-of-pressure travel with changes in Mach number, thereby reducing hinge moments. The controls are small enough so that their blunt trailing edges do not appreciably increase missile drag. The diamond planform was chosen to reduce control center-of-pressure travel with changes in Mach number. Another reason for this choice is that the diamond planform is structurally adaptable to interdigitation; the control need not be attached to the wing as a short-chord high-aspect-ratio control would. For the examples shown in figure 8, the controls were placed on the missile having a straight-leading-edge wing of aspect ratio 3/8. The pitching-moment coefficients presented are based on body diameter and cross-sectional area. The center-of-gravity location (0.60L, 0.59L, and 0.58L for the interdigitated tail, in-line tail, and swivel-nose models) was chosen so that the three configurations had the same static margin with 0° control deflection at low normal-force coefficients at a Mach number of 2.0. At this Mach number the nose control has the least effectiveness. The effectiveness of the in-line tail control is greater than that of the nose control. The interdigitated control, by virtue of being removed from the wing wake, has greater effectiveness than the in-line control. Control deflections of 15° are adequate for the interdigitated control for obtaining high values of trim normal force.

In figure 9 the effect of control type on stability is again illustrated, but at $M = 3.3$. The center-of-gravity positions have not been changed from those chosen for the data at $M = 2.0$. With the increase in Mach number the effectiveness of the swivel nose has increased so that it now has approximately the same effectiveness as the interdigitated control. The effectiveness of the two tail controls has decreased appreciably.

In figure 10 the effect of planform on missile stability is presented. The same interdigitated tail control was placed on 3 missiles having wings differing in size and aspect ratio. The data were obtained at Mach number 3.3. Here, again, the center of gravity (0.48L, 0.60L, and 0.62L for the models having wings of aspect ratio 3/32, 3/8, and 1) was chosen so that the different missiles have the same static margin for small normal-force coefficients and 0° control deflection. For

15° control deflection the control effectiveness is adequate at low normal-force coefficients for the missile having the smallest wing. However, large trim normal-force coefficients were not obtained because of the relatively large center-of-pressure travel associated with this configuration. The effectiveness is naturally low for the missile having the largest wing because the control is small relative to the wing size. On the other hand, the effectiveness of the control on the missile having a wing of aspect ratio 3/8 is sufficient to trim the missile to large normal-force coefficients.

In figure 11 the effect of various arrangements on rolling moment is illustrated. Rolling-moment coefficient, based on exposed wing area and total span, is plotted as a function of resultant angle of attack. The data are presented for bank angles of 22.5° for cruciform and 45° for monowing models, since maximum rolling moments occur close to these bank angles. The rolling moments are considerably larger for the monowing than for the cruciform arrangement of the same model. The effect of increased forebody length, for the model having this same wing of aspect ratio 3/8, can also be seen to increase the rolling moments. This increase is indicated qualitatively, as discussed in reference 10, by calculations that account for the increased vortex strength associated with the increased forebody length. It is interesting to note that the rolling-moment coefficients fall on the same curve for the cruciform models having the same nose length but wing aspect ratios of 3/8 and 1. The magnitude of the rolling moments for all configurations was less than the amount that was obtained by differential deflection of the interdigitated tail control.

CONCLUDING REMARKS

The results of this investigation indicate that there are distinct aerodynamic advantages to the use of wings of very low aspect ratio for missiles. Some of these advantages performancewise are high lift, compared to wingless missiles, and low drag with shapes that appear to be beneficial for combatting aerodynamic heating. From the standpoint of stability and control, these missiles exhibit small center-of-pressure shifts and small rolling moments for a wide range of supersonic Mach numbers and combined angles of attack and bank so that control problems are simplified.

REFERENCES

1. Buquoi, T. W.: Presentation of Force and Moment Data From a Wind Tunnel Test of an 0.0333 Scale Wing Planform Development Model for the 1810 Missile at Mach Numbers 1.61, 1.97, 2.54, and 2.80 (Phases II and III). Rep. No. SM-18420 (Contract No. DA-30-069-ORD-1082), Douglas Aircraft Co., Inc., Aug. 23, 1954.

2. Buquoi, T. W.: Presentation of Force and Moment Data From Wind Tunnel Tests of an 0.6 Scale Control Development Model for the 1810 Missile at Mach Numbers 1.97, 2.55, and 3.67. Rep. No. SM-14929 (Contract No. DA-30-069-ORD-1082), Douglas Aircraft Co., Inc., Apr. 12, 1954.

3. Edgar, J. M.: Presentation of Force and Moment Data from a Supersonic Wind-Tunnel Test of a 0.06 Scale Hinge Moment Model with Plain-Balanced Elevons for the Model 1810 Missile. Rep. No. SM-18787, Douglas Aircraft Co., Inc., Mar. 2, 1955.

4. Buquoi, T. W.: Presentation of Force and Moment Data From a Wind Tunnel Test of an 0.0333 Scale Wing Planform Development Model for the 1810 Missile at Mach Numbers 1.61, 1.97, 2.54, and 2.80 (Phase I). Rep. No. SM-18410 (Contract No. DA-30-069-ORD-1082), Douglas Aircraft Co., Inc., Aug. 23, 1954.

5. Marriott, Edwin O.: Wind Tunnel Tests of Various Balanced Control Surfaces at Mach Numbers From 1.33 to 4.50. Hughes Aircraft Co. Res. and Dev. Labs. (Culver City, Calif.), Sept. 10, 1952.

6. Hill, William A., and Kaattari, George E.: Force and Pressure Distribution Investigation of All-Movable Triangular and Rectangular Wings in Combination With a Body at $M = 3.36$. (Prospective NACA paper.)

7. Nielsen, Jack N., Kaattari, George E., and Anastasio, Robert F.: A Method for Calculating the Lift and Center of Pressure of Wing-Body-Tail Combinations at Subsonic, Transonic, and Supersonic Speeds. NACA RM A53G08, 1953.

8. Neice, Stanford E., Wong, Thomas J., and Hermach, Charles A.: Lift, Drag, and Static Longitudinal Stability Characteristics of Four Airplane-Like Configurations at Mach Numbers From 3.00 to 6.28. NACA RM A55C24, 1955.

9. Rossow, Vernon J.: A Theoretical Study of the Lifting Efficiency at Supersonic Speeds of Several Airfoil and Fuselage Combinations Which Utilize Indirect Lift. (Prospective NACA paper.)

10. Nielsen, Jack N., Spahr, J. Richard, and Centolanzi, Frank: Aerodynamics of Bodies, Wings, and Wing-Body Combinations at High Angles of Attack and Supersonic Speeds. (Prospective NACA paper.)

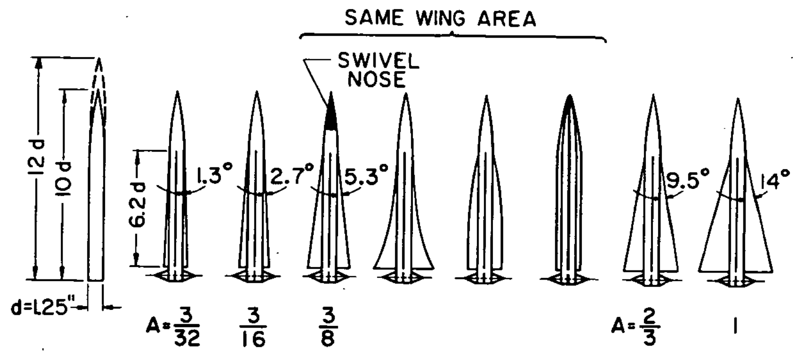

Figure 1

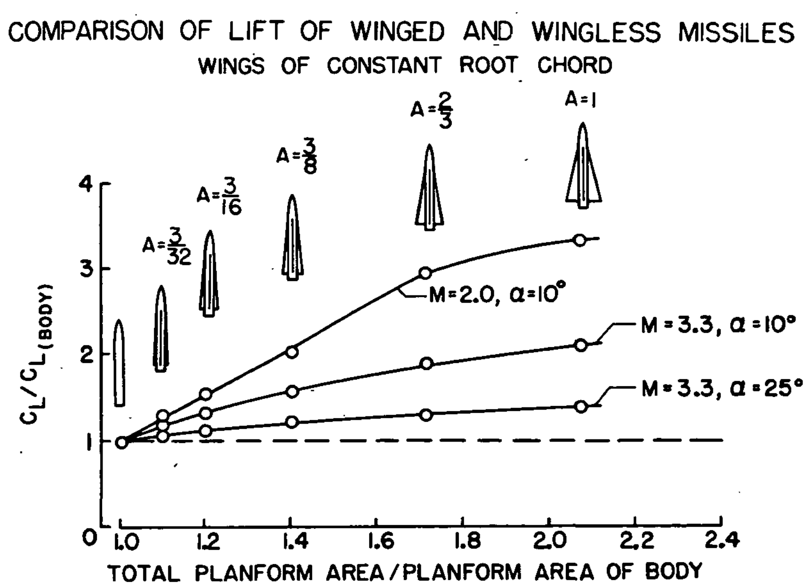

Figure 2(a)

COMPARISON OF LIFT OF WINGED AND WINGLESS MISSILES

WINGS OF CONSTANT SPAN; M = 3.3

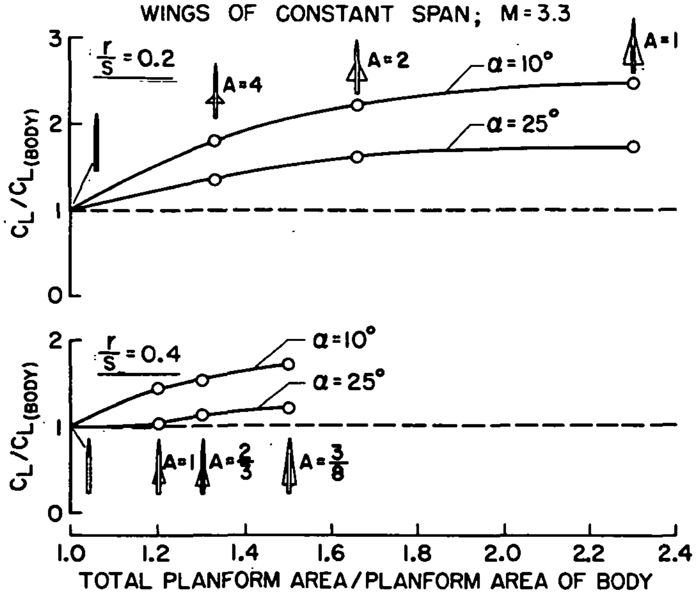

Figure 2(b)

EFFECT OF PLANFORM ON MINIMUM DRAG

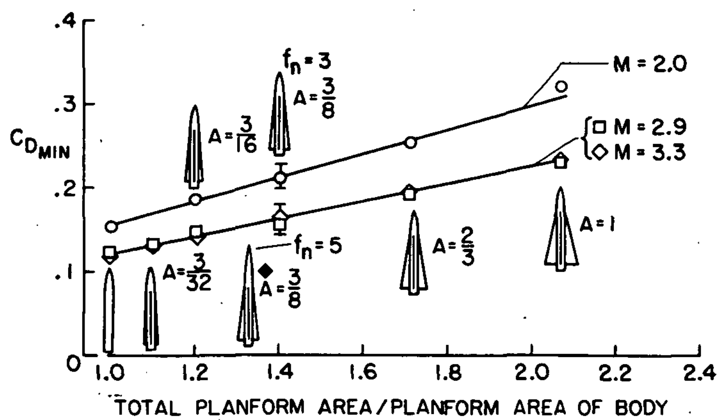

Figure 3

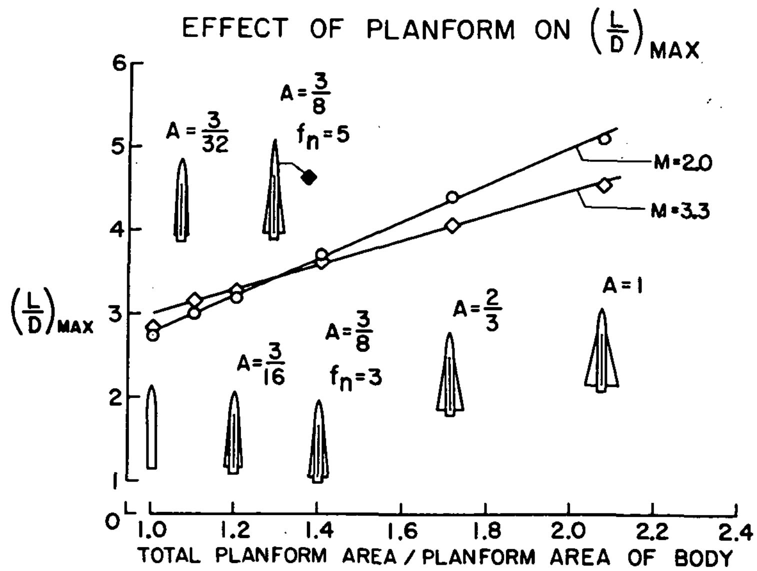

Figure 4

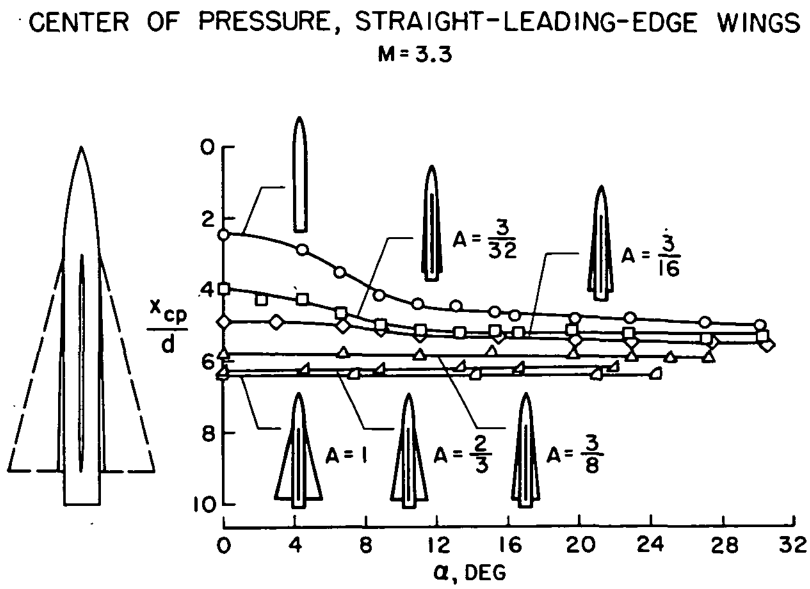

Figure 5

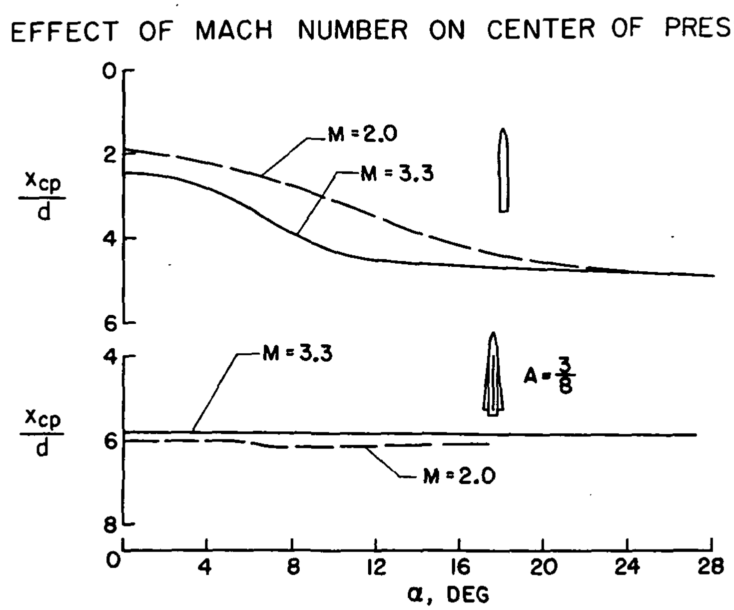

Figure 6

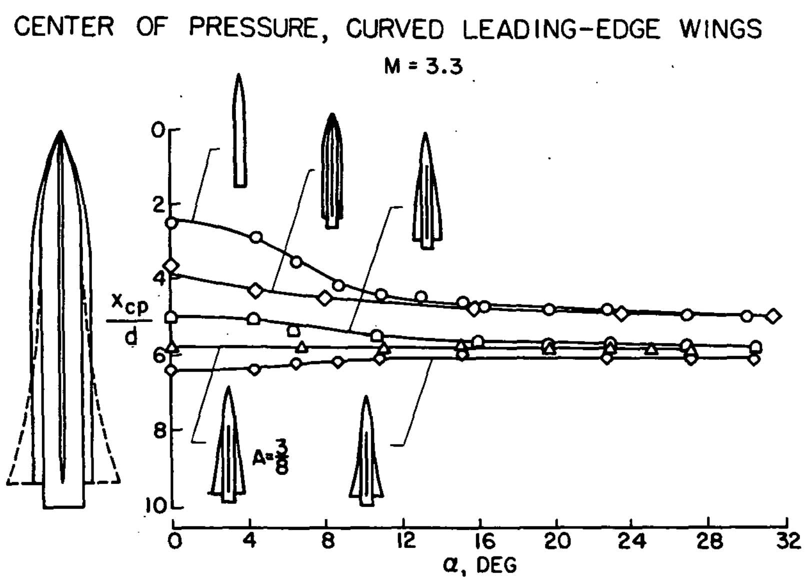

Figure 7

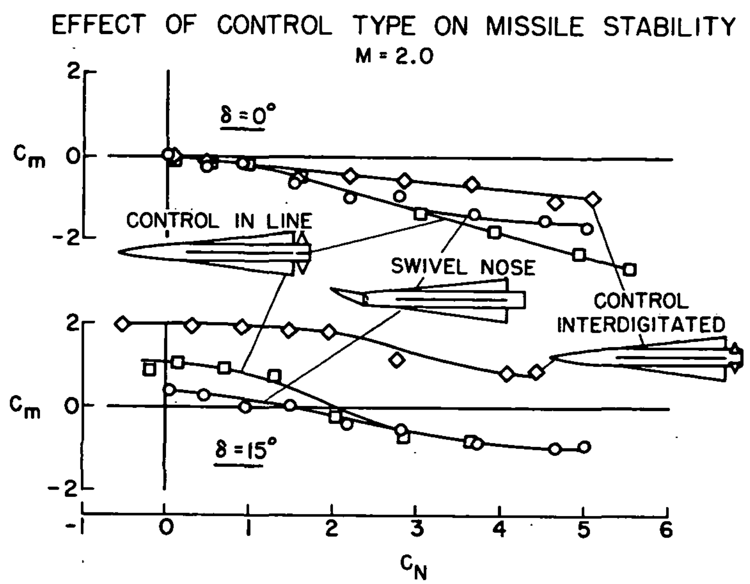

Figure 8

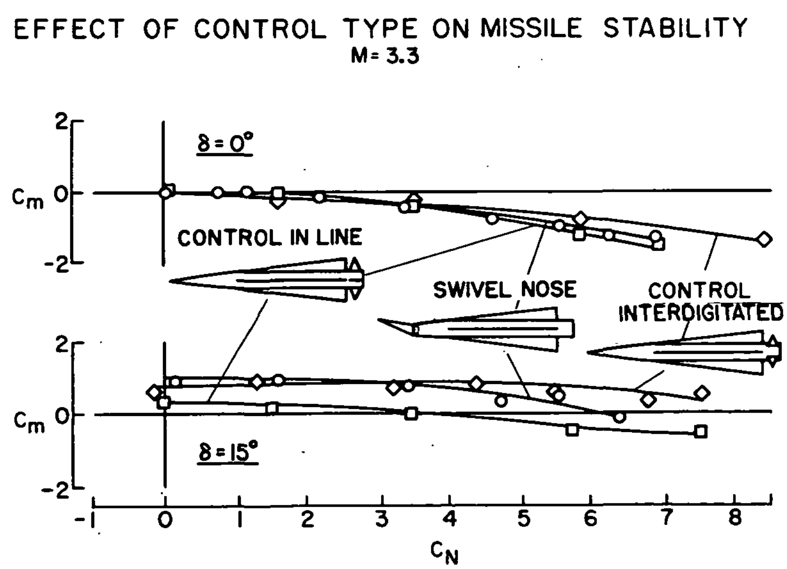

Figure 9

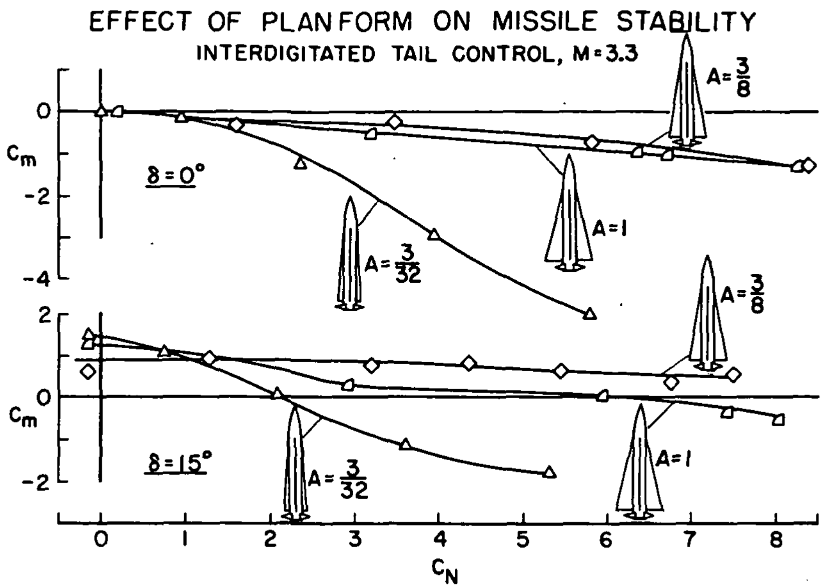

Figure 10

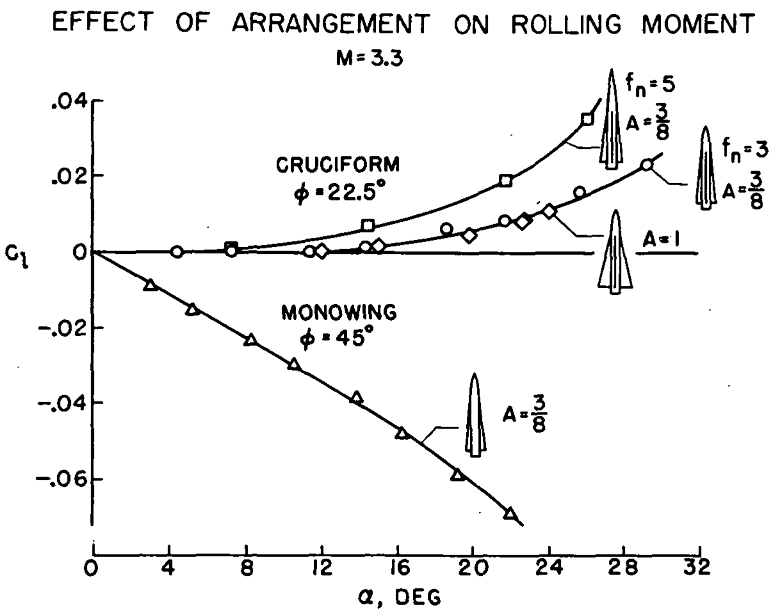

Figure 11

EXPERIMENTAL TECHNIQUES FOR PREDICTING STORE MOTIONS DURING RELEASE OR EJECTION

By Maxime A. Faget and Harry W. Carlson

Langley Aeronautical Laboratory

SUMMARY

A discussion is presented of experimental methods for determining store-release trajectories at supersonic speeds from measured force data on scale models and from dynamic-model tests. The dynamic-similarity laws which are significant when conducting either free-fall or ejected dynamic-model tests are presented and discussed. Results from force tests and dynamic-model tests were used in an effort to evaluate the ability of both techniques to predict full-scale-release trajectories.

INTRODUCTION

With the development of supersonic bombers, the problems of bomb release have become increasingly important. The extremely turbulent and random flow within the open bomb bay, as well as the nonuniform flow field surrounding the airplane, can cause bomb-release motions that endanger the airplane and seriously affect bombing accuracy.

In view of the danger to airplane and crew, it is necessary that the nature of the release be studied before full-scale tests are attempted. This paper presents a discussion of methods for determining store-release trajectories from measured force data on scale models and from dynamic-model tests.

The trajectory of the store following release may be calculated by a step-by-step process, provided that sufficient knowledge of the flow disturbances from the mother ship within the region of possible store trajectories is known. These disturbances have been measured in terms of aerodynamic forces and moments in the Langley 4- by 4-foot supersonic pressure tunnel for a number of store shapes. The results from tests such as these may be used for determining trajectories for any desired set of release conditions, such as angle of attack, altitude, and ejection method.

Store-release trajectories may also be determined from dynamic-model tests. Investigations of this type using ejected stores have been conducted in the preflight jet of the Langley Pilotless Aircraft Research

Station at Wallops Island, Va. Although such tests may be used only for the particular altitude and release conditions simulated, the data, which are given by a Strobolight photograph of the store model's motion, are available for interpretation almost immediately following the tests. Thus, various fixes may be intelligently developed during the test period.

SYMBOLS

$V_{z,0}$ initial vertical ejection velocity, positive downward

z vertical distance traveled

x horizontal distance traveled

t time

l bomb length

θ bomb attitude angle to horizontal

M Mach number

F fineness ratio of bomb

C_m pitching-moment coefficient

$C_{m_\alpha} = \dfrac{\partial C_m}{\partial \alpha_{bomb}}$

α angle of attack of both bomb and airplane

Δt increment of time

$C_{m_q} = \dfrac{\partial C_m}{\partial \frac{ql}{2V}}$ per degree

RESULTS AND DISCUSSION

The setup for the force test is shown in figure 1. Both the wing-body configuration, used as a mother ship, and the store were mounted on six-component balances. During the test period, the wing-body configuration was traversed vertically at several horizontal locations with respect to the store. These traverses were made with the wing-body configuration at angles of attack of 0°, 4°, and 8° and with the store at various attitude angles ranging from -15° to 15° in 5° increments. These force tests were made at $M = 1.6$.

Also shown in figure 1 is a series of store shapes on which data have been obtained. The fineness ratio of these shapes varied from 2.5 to 10. Data on several bluff stores were also obtained.

Typical results obtained from the force tests are shown in figure 2 which is a contour plot of C_m about the 50-percent station for the fineness-ratio-4 store at zero attitude angle. The value assigned to a particular contour line is the moment coefficient experienced when the store midpoint lies on that line. Plots similar to this one are also obtained for C_D and C_L. A complete set of plots for each store attitude angle is required in order that trajectory computations may be carried out. Some idea of the flow angularity in the vicinity of the bomb bay may be obtained from consideration of the fact that $C_{m_\alpha} = -0.02$ for this store. Thus, for the $C_m = 0.12$ contour line, the angularity is equivalent to 6°.

Figure 3 illustrates several factors which might affect the accuracy of trajectories obtained by step-by-step calculations. This is shown by plots of bomb attitude angle against time for the period immediately following release. The first time-history plot shown compares results obtained when a uniform-flow field is used rather than the interference flow existing in the vicinity of the airplane as obtained with the force-measurement technique. From this comparison it is obvious that a knowledge of the interference forces and moments acting on the bomb is necessary in order that accurate predictions of its trajectory may be made. In the second plot, the effect of time increment used in the step-by-step calculation is shown and indicates that small time increments are required for obtaining a suitable accuracy. Experience indicates that angular changes between successive steps should be kept to less than 1°. Only static aerodynamic coefficients are obtained in the force technique. In the third plot, the effect of damping is shown to play a rather minor part in the motion immediately following release. Here, the motion determined by consideration of static forces only is compared with the motion obtained when a damping term is included. The value $C_{m_q} = 0.12$ was obtained analytically by the method outlined in reference 1.

The setup used for making dynamic-model tests is illustrated in figure 4. The photograph shows the wing-fuselage configuration, from which the store was released, mounted in the stream of the blowdown jet. A store is shown mounted in a semisubmerged position from which some of the stores were ejected. Also shown are the camera which took pictures of the model's motion and the bank of Strobolight bulbs which was used for illumination. The test was run as follows: First the tunnel was started and stabilized at operating pressure; then the shutter of the camera was opened. Simultaneously, the store was ejected and the Strobolights were fired in sequence at accurately timed intervals by an electronic timer. Dynamic-model tests were made at $M = 0.8$, 1.4, 1.6, and 2.0.

A typical photograph taken by the camera is shown in figure 5. This figure shows the ejection of a store at $M = 1.4$ with an initial velocity of 30 fps. The images of the store in the photograph are for 2-millisecond time intervals and, as can be seen, the motion of the store is graphically recorded. Data are obtained from the photograph by measuring the vertical and horizontal distances traveled as well as the store attitude angle for each image.

The following discussion lists the requirements to be met for dynamic similarity. First, the model must have the proper center-of-gravity location in order that the aerodynamic forces act about the correct axis and thereby provide correct aerodynamic moment coefficients. In order that the undamped rotary motion of the model be coordinated with the translational motion produced by aerodynamic forces, the model's moment of inertia must be properly related to its mass. This is accomplished by keeping the radius of gyration proportional to the model size. In other words, the mass distribution of the model must be similar to that of the full-scale store. In determining the density of the model, the engineer is faced with conflicting requirements. Proper simulation of damping requires that the ratio of store density to dynamic pressure be kept the same, regardless of scale; whereas, if the gravitational forces are to be kept in proportion to aerodynamic forces, it is required that the ratio of store density to dynamic pressure be inversely proportional to the scale. It should be noted that, for a 1/20-scale test, the model which properly simulates gravity is twenty times as heavy as one in which the damping is properly simulated.

Previous tests, such as those presented in references 2 and 3, have used heavy models which properly simulated the effect of gravity. Since aerodynamic damping was not simulated, the results from tests such as these may be considered conservative. It should be noted, however, that it is not always possible to simulate gravity properly, since the store model may not always be made as heavy as required. This is most apt to be the case when a small scale is used, when the full-scale conditions are at a high altitude, and when a high-density tunnel is used. The heaviest model which can be made is, of course, a solid one. Such a model will invariably have a higher moment of inertia than proper similitude would call for. Tests run with models of this type may be misleading in that the model will be slow to respond to pitching disturbances, and, thereby, not truly represent the severity of these disturbances.

In the dynamic-model tests discussed in this paper, the models were ejected from the bomb bay with a high initial velocity. With this condition, the effect of gravity on the vertical motion of the model is negligible for a short period of time after release. Since it was not considered necessary to simulate gravity, light models were used which properly simulated damping.

The effect of not properly simulating gravity is shown in figure 6. The trajectories shown in this figure were obtained by using the force data to predict the motion of a full-scale store and a 1/20-scale model for three different initial release conditions. The first case is for a free drop with no ejection. It can be seen that the motion of the model falls far short of simulating the motion of the full-scale article. In the next case, a 15-fps ejection velocity is used. It can be seen that the model test agrees fairly well with the actual full-scale case. In the last store position shown, the full-scale store is 17 percent farther down from the release position than would be predicted by the model test. With the initial velocity increased to 30 fps, the dynamic-model tests give a very good picture of the full-scale case. The error in vertical position is about one-half of that shown for the 15-fps ejection.

Figure 7 shows the comparison obtained with dynamic-model tests and calculations for the conditions of this test using force data. The model was ejected at 30 fps at $M = 1.61$ from the wing-body configuration at 4° angle of attack. The calculated time histories of vertical position, horizontal position, and store-attitude angle are shown as solid lines. The data from the dynamic-model tests are shown by circular symbols. The calculations satisfactorily predicted the vertical and horizontal motion of the store, but failed to predict the pitching motion of the store. This is accounted for by the fact that the force balance tests were conducted without the store support which was used to eject the stores in the dynamic-model tests. It is apparent that this support caused an interference large enough to reduce the initial pitching-down moment which was measured in the force tests. Thus, in the dynamic-model tests, the store was not as greatly disturbed as was predicted. These results indicate that details in the bomb bay may have a strong influence on the motion of the stores; and, therefore, as far as is possible, model tests should include all the pertinent details of the full-scale bomb bay.

The experiments conducted with the force tests and the dynamic-model tests include a wide variety of store shapes for many conditions.

However, before closing, it should be pointed out that large changes in bomb motion may result when configuration changes are made. Figures 5 and 8 are photographs taken of two dynamic-model tests using stores that differed in frontal area and fineness ratio. Both stores are closely similar in length, weight, moment of inertia, and stability. Both were ejected at 30 fps at $M = 1.4$. It can be seen that the fineness-ratio-8.5 store made a very good separation; whereas the low-fineness-ratio, less dense store pitched up, reversed its initial vertical direction, and almost hit the rear of the fuselage. Results such as those make it apparent that separation of stores at supersonic speeds should not be attempted without first obtaining conclusive information from which the path of the stores may be predicted. At present, model tests such as those just described are a requirement for such a prediction. Considerable effort is currently being expended, however, to obtain a more general understanding of the problem.

CONCLUDING REMARKS

Various methods of conducting dynamic-model tests as well as a calculation procedure utilizing measured force data have been outlined and discussed. It was shown that the light-model technique (when damping is simulated) is a valid test procedure for reasonably low ejection velocities but not for bombs released without ejection. A comparison of data from an actual model bomb drop with a calculated drop for similar conditions indicated but did not prove the validity of the calculative procedure. The importance of duplicating as far as is possible all details of the bomb and bomb bay was emphasized in the previously mentioned comparison and in a comparison of the dynamic-model release of a fineness-ratio-6 and a fineness-ratio-8.5 bomb.

REFERENCES

1. Martin, John C., Diederick, Margaret S., and Bobbitt, Percy J.: A Theoretical Investigation of the Aerodynamics of Wing-Tail Combinations Performing Time-Dependent Motions at Supersonic Speeds. NACA TN 3072, 1954.

2. O'Hara, J. C.: Wind Tunnel Similitude of Full-Scale Bomb Trajectories. Rep. No. BF-490-D-14, Cornell Aero. Lab., Inc., May 1952.

3. Rainey, Robert W.: A Wind-Tunnel Investigation of Bomb Release at a Mach Number of 1.62. NACA RM L53L29, 1954.

MODELS USED IN FORCE TESTS

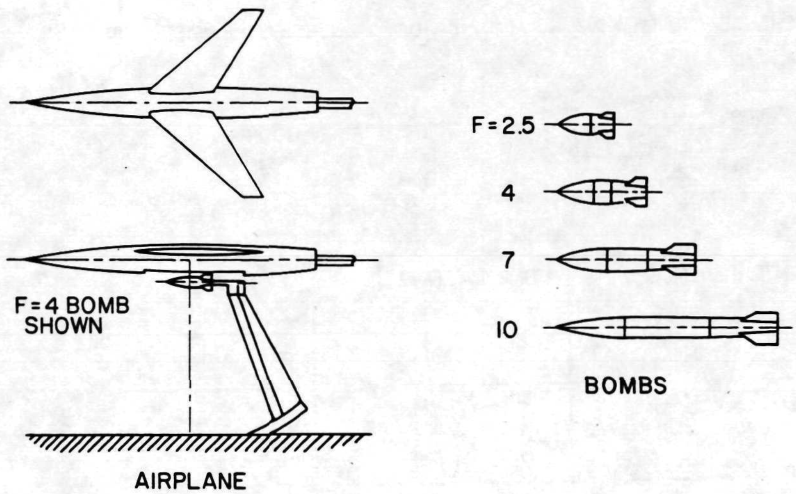

Figure 1

SAMPLE CONTOUR PLOT OF FORCE-TEST DATA

α (AIRPLANE) = 4°; θ (BOMB) = 0°

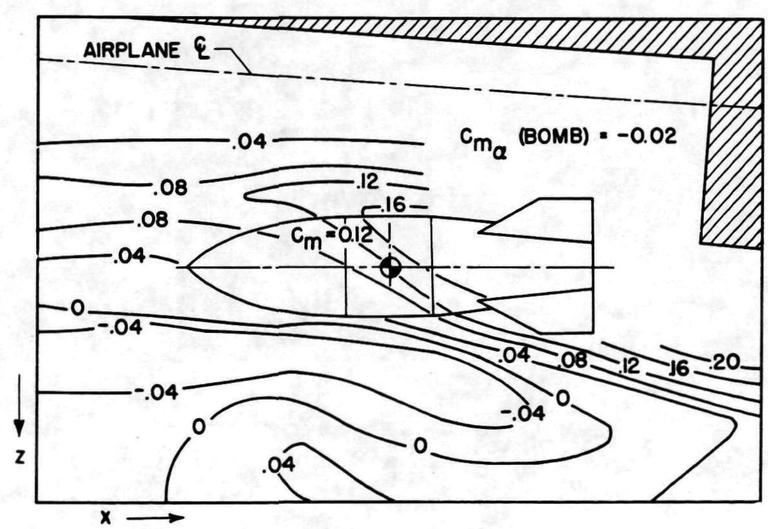

Figure 2

[redacted]

FACTORS INFLUENCING ACCURACY OF CALCULATED RELEASE

INTERFERENCE AND DAMPING INCLUDED; $\Delta t = 0.005$ UNLESS OTHERWISE NOTED

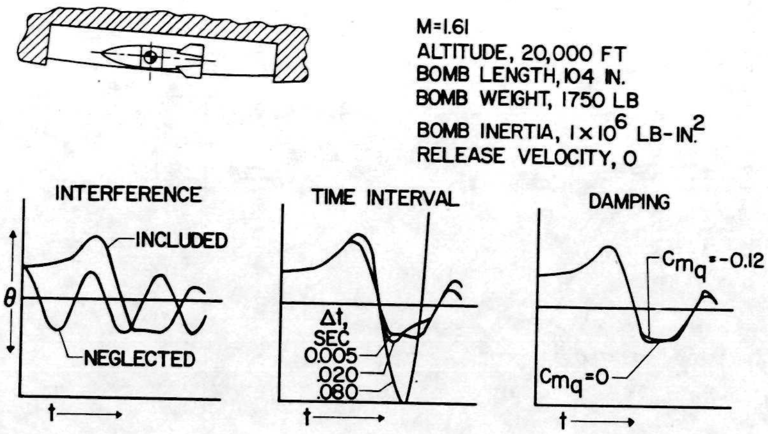

Figure 3

TEST SETUP USED IN DYNAMIC-MODEL TESTS

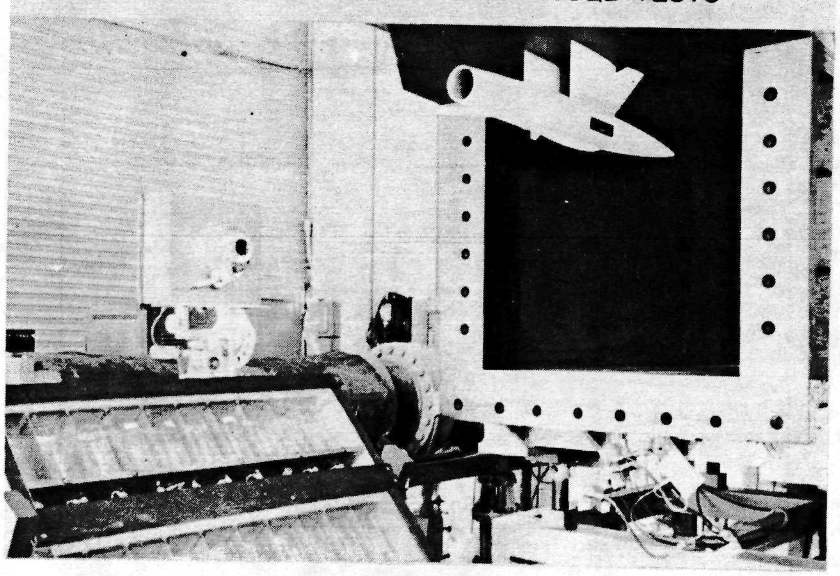

Figure 4

DYNAMIC RELEASE OF STORE OF FINENESS RATIO 8.5

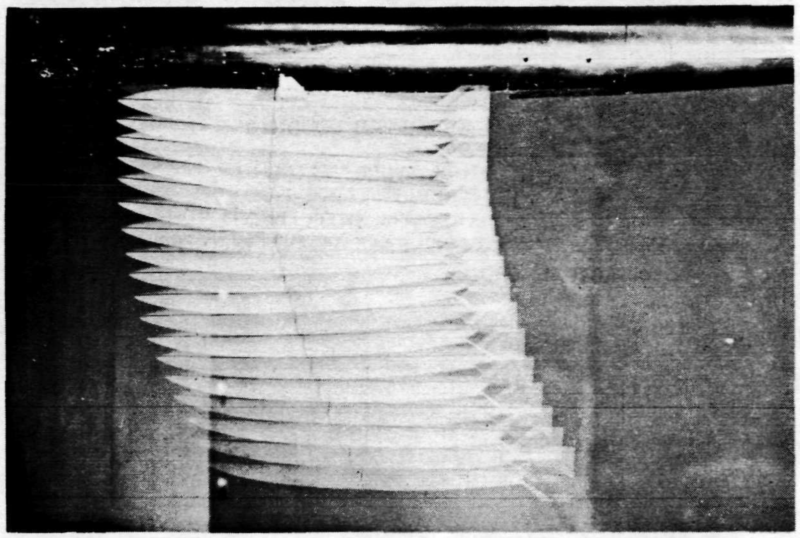

Figure 5

CALCULATED EFFECT OF EJECTION VELOCITY ON SIMULATION

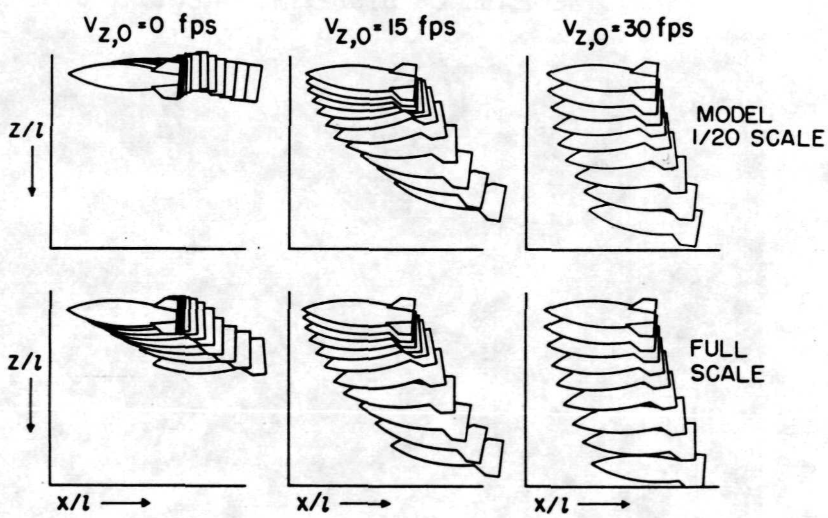

Figure 6

CALCULATED RELEASE COMPARED WITH
ACTUAL MODEL DROP

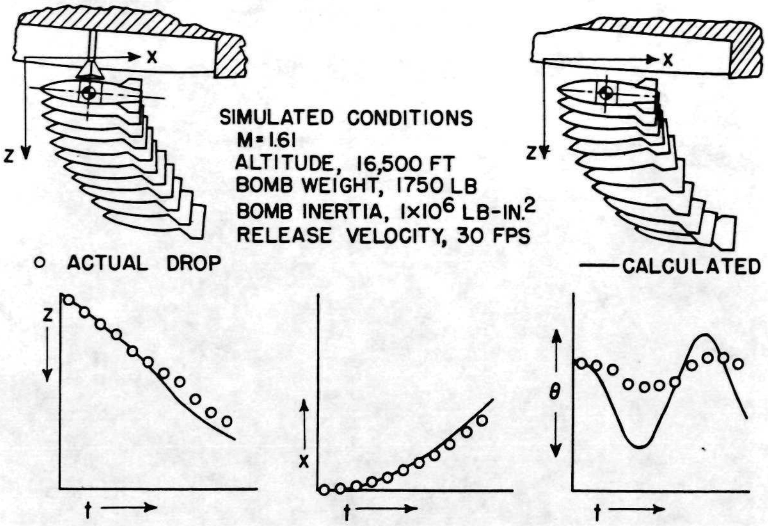

Figure 7

DYNAMIC RELEASE OF STORE OF FINENESS RATIO 6

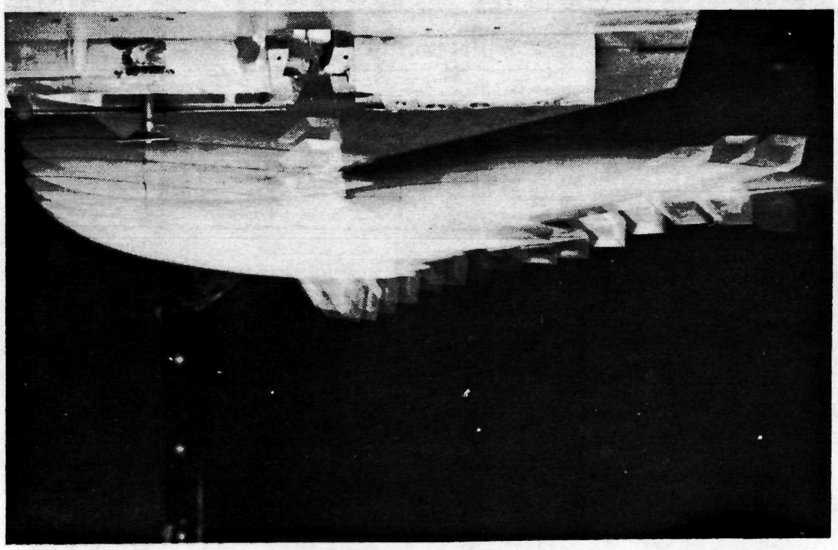

Figure 8

33

AN EXPERIMENTAL STUDY OF AIR LOADS CAUSED BY BLAST-INDUCED GUSTS

By Harold B. Pierce

Langley Aeronautical Laboratory

INTRODUCTION

An airplane exposed to an explosion or blast wave is subjected to complex transient loading. In addition to the direct effect of the blast pressure, the aerodynamic effects of the induced gust and of the shock wave itself are present. Serious questions have arisen concerning the rate of development of lift and the magnitude of the lift, particularly when the gust is very intense. In this case, the gust can change the angle of the relative wind by a large amount and create an angle of attack on the airplane well above its normal stall angle. Since current aerodynamic knowledge is not considered adequate to resolve these problems, the NACA has initiated some experimental studies using free-flying models subjected to gusts from actual explosions. The slow-speed models used thus far are about 6 feet in wing span and are instrumented with high-frequency pressure-measuring equipment which is used to measure load distributions.

This paper presents a brief description of the test method and the results of three phases of the study made to investigate:

(a) The chordwise load distribution on the wing caused by a very intense gust

(b) The loads on the horizontal tail caused by the combined effects of an intense gust and the downwash from the wing

(c) The chordwise load distribution on the wing in a less intense gust where the induced angle of attack is kept below the stall angle

DISCUSSION

Figure 1 illustrates the test conditions and the blast wave relationships. Although a blast gust could strike from any direction, the condition considered of most immediate importance is illustrated by the sketch which shows the airplane in a horizontal position where the shock wave and its accompanying blast gust are shown striking the airplane from below, normal to its flight path. The vector diagram shows how the gust velocity U shifts the relative wind vector V_r and creates an additional angle of attack α on the airplane. It also shows that when the gust velocity is very large the velocity of the relative wind is increased significantly over the original velocity of the airplane V.

As is known, the gust velocity immediately behind the shock is the maximum, with its intensity depending on the shock strength. Then as the shock passes on, the gust velocity acting on the airplane decreases. Thus, for this airplane-blast wave orientation, a plot of angle of attack α versus time t would look much like the curve which is sketched. Defining shock arrival at the airplane as zero time, the maximum angle change occurs instantaneously, followed by a dropoff as the shock wave travels beyond the airplane. In the tests, the model was flown upward instead of horizontally. (See fig. 1.) At the proper time, the explosion was set off on the ground so that the hemispherical blast wave struck normal to the direction in which the model was traveling. Time histories of resultant pressures were measured by ten NACA miniature pressure cells either embedded all in one chord halfway out on the semispan of the wing or divided between this position and the same chord on the horizontal tail. The measurements were transmitted to a ground receiving station by wire telemeter. Further details on the test procedure and the instrumentation are given in reference 1.

The first of the test results to be considered are load distributions on one chord of the wing, obtained in three flights for which the blast-induced gust was very intense. In each case, the initial velocity of the gust produced an angle of attack four times the steady-flow stall angle of the wing. The complete results of this series of tests are given in reference 1. Figure 2 shows representative load distributions. Plotted are load coefficients $\Delta \frac{p_R}{q}$ versus percent chord. The Δ indicates that the resultant pressures p_R were measured from the pressures existing just prior to blast arrival. The three plots are successive in time, with the first being for 3 milliseconds after blast arrival. The angle of attack is 29°, and the model has traveled about one-half a chord while under the influence of the gust. In the second plot, the angle has reduced to 23° and in the third, the angle of attack is about 15°. All of these angles are above the steady-flow stall angle of 9° measured in a wind tunnel. The three flights are identified by the symbols on the curves and it is noted that for two of the flights, ten channels were used, but on one flight, only five channels were used. Considering the high angle of attack and the transient nature of the phenomena, the results are remarkably consistent and it was felt that a good representation would be obtained by averaging the load coefficients at each chordwise station. The distributions obtained are shown in figure 3 as the lines with the points. The other two lines are distributions between which the test data were expected to fall. The solid line was calculated by simple potential-flow theory, ignoring stall and lag in lift effects, while the dashed line is a distribution measured in steady-flow wind-tunnel tests. Obviously, these simple concepts do not apply in this case. The striking difference is the loading peak which travels rearward as time passes. In all cases, the maximum value of the loading peak is above the calculated distribution and it produces high local loadings and contributes heavily to the overall loading on the chord. The resulting section normal-force coefficients were found to be about twice those obtained from the wind-tunnel distributions for the part of the gust shown in figure 3.

A clue as to the source of the loading peak was found in shock-tube studies of the type reported in reference 2, where interferograms show the formation of a strong stationary vortex when a shock wave diffracts around the corner of a bluff body. A similar process is believed possible around the leading edge of the airfoil but the vortex is affected by the sustained flow and passes downstream along the upper surface of the airfoil instead of remaining stationary. The vortex appears to move at about one-third stream velocity because the peak is still present near the trailing edge of the airfoil after it has moved nearly two and one-half chords in the gust. Thus, the results shown on figure 3 indicate that, for intense blast-induced gusts which produce angles of attack well above the stall, a traveling vortex initiated by the diffraction of the shock around the leading edge of the airfoil has a significant effect on the load distribution and makes the possibility of a simple estimate of the loading appear remote.

Considered next are the results of the second phase of the investigation, that of determining the loads on the horizontal tail due to the combined effects of an intense gust and the downwash from the wing. For this, five pressure cells were installed along a chord of the horizontal tail and five were left in their original positions on the wing chord. Three flights were made for the same gust conditions as before and the data for the individual chord stations were again averaged. Since it is fruitless to attempt to define load distributions with only five stations along the chord under the condition found existing in the intense gust, the analysis of the results was made by comparison of the time histories of load coefficient at corresponding stations on the wing and tail. Two of these time-history comparisons, plotted as load coefficient against time in milliseconds, are shown in figure 4. The time histories for the wing are the solid lines and those for the tail, the dashed lines. The comparisons for the 20-percent-chord stations are shown in the upper plot and those for the 40-percent-chord stations, in the lower plot. Three features are to be noted: first, that the load peaks due to the vortex are present on both the wing and the tail; second, that these peaks are of equal intensity. The third feature is that the curves for the wing and the tail are reasonably similar up to about 13 milliseconds, but at that time the tail loading drops abruptly while the loading on the wing shows a more gradual decline. The abrupt decrease in loading on the tail is believed to be the onset of downwash from the wing, since the time interval corresponds closely to what would be predicted by the old rule of Glauert for lag in downwash. These results indicate then, that the wing and tail act as independent lifting surfaces until the tail flies into the downwash from the wing.

Returning to the loading peaks, their travel along the respective chords is shown by the fact that they arrive at the aft stations at a later time. Again the passage over the wing was accomplished in about three chord lengths travel of the wing, but it was found that the passage over the tail was accomplished in three chord lengths travel of the tail. Thus, it appears that the movement of the vortex is a chord-length phenomenon and not a time phenomenon.

In contrast to the complex conditions just described, a test made with the initial angle of attack kept below the stall gave load distributions on the wing chord which were much less complicated. Only one flight has been made in this series and the load distributions for three successive instants in the gust are shown on figure 5. Again load coefficient is plotted against the chordwise station. The angles of attack vary from about 8° in the first plot shown to 6° in the last. The lines with the points are the flight results and the solid line is a potential-flow calculation of the type described previously which predicts the load distribution for a given steady-flow angle of attack. The dashed line is a distribution calculated using the unsteady-lift function given by Wagner for sudden change in angle of attack. The test results and the unsteady-lift calculations agree very well. It is also observed that the loading peak found in the tests at an angle above the stall is not present in this case. It is indicated then that below the stall angle a good estimate of the chordwise loading is obtained from calculations which take unsteady lift into account.

CONCLUDING REMARKS

Obviously, the character of the loading and the ability to predict it depend very much on the existence or nonexistence of the strong moving vortex. Unfortunately, full understanding of the parameters governing the formation of this vortex and its behavior after formation has been hampered by the limited scope of the tests conducted thus far.

In summary, the low-speed tests of the effects of blast gusts which strike normal to the flight path have shown that:

(a) For imposed angles above the stall, a vortex caused by the diffraction of the shock wave around the leading edge of the airfoil significantly alters the load distribution as it travels along the wing chord and no simple method is adequate to predict the loads.

(b) The wing and tail act as independent lifting surfaces until the tail flies into the downwash from the wing.

(c) For angles below the stall angle, calculations using existing unsteady-lift theory appear to predict the chordwise loading.

REFERENCES

1. Pierce, Harold B., and Reisert, Thomas D.: Initial Experimental Investigation of the Aerodynamic Load on the Wing of a Model Caused by a Blast-Induced Gust That Increases the Angle of Attack Into the Stall Region. NACA RM L55H22b, 1955.

2. Bleakney, Walker: Shock Loading of Rectangular Structures. Tech. Rep. II-11 (Contract N6ori-105 Task II), Dept. of Phys., Princeton Univ., Jan. 1952.

RELATIONS FOR BLAST GUST

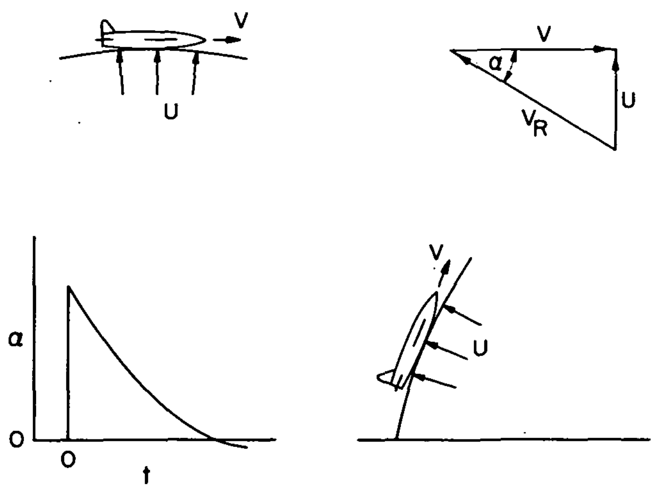

Figure 1

LOAD DISTRIBUTIONS FOR THREE FLIGHTS

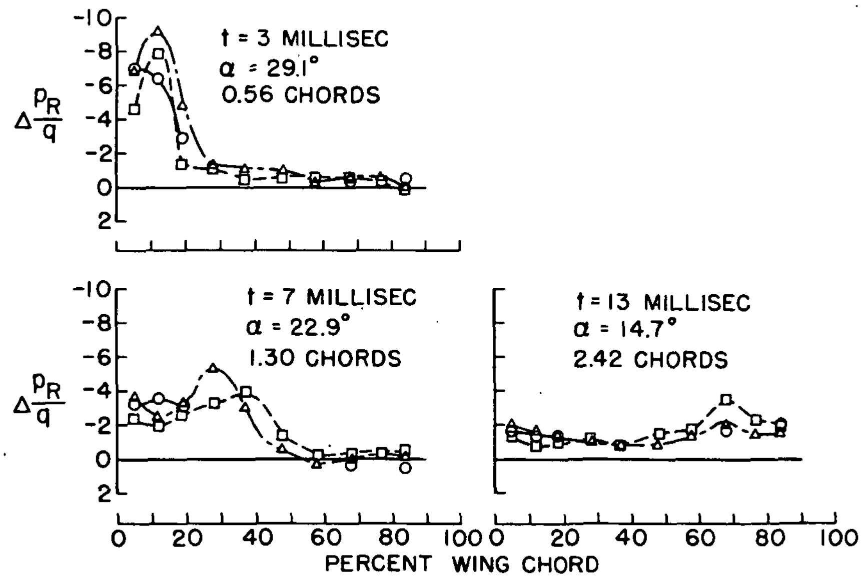

Figure 2

[redacted]

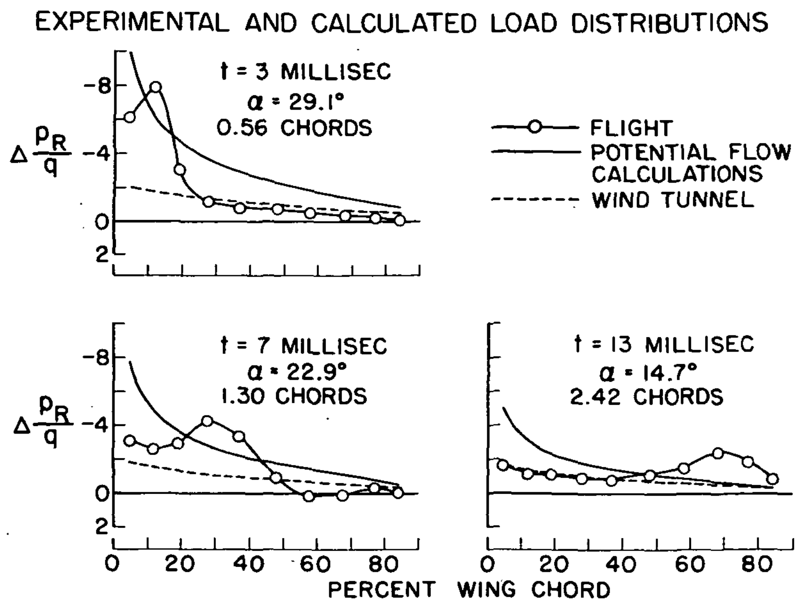

Figure 3

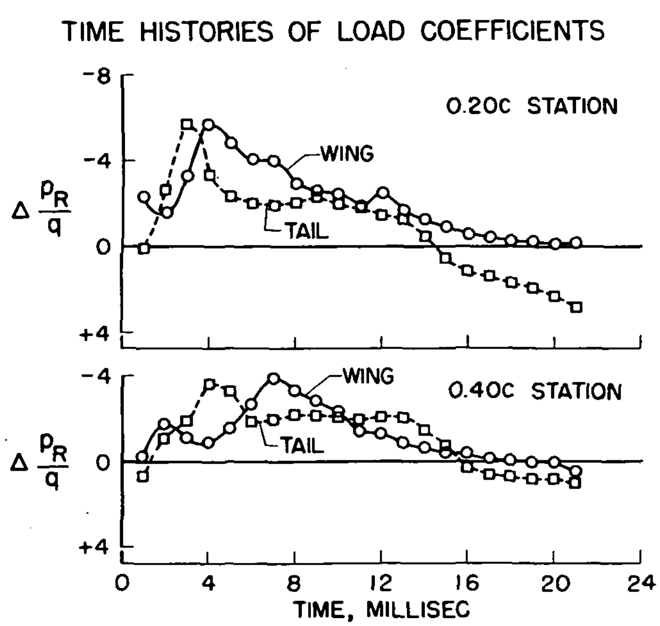

Figure 4

[redacted]

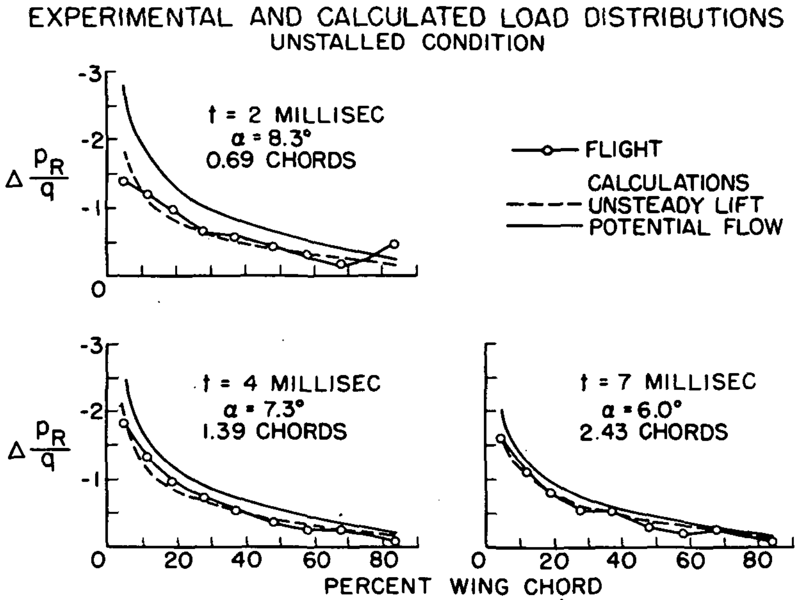
EXPERIMENTAL AND CALCULATED LOAD DISTRIBUTIONS
UNSTALLED CONDITION
t = 2 MILLISEC
α = 8.3°
0.69 CHORDS
FLIGHT
CALCULATIONS
UNSTEADY LIFT
POTENTIAL FLOW
t = 4 MILLISEC
α = 7.3°
1.39 CHORDS
t = 7 MILLISEC
α = 6.0°
2.43 CHORDS
Δ pR/q
-3
-2
-1
0
20
40
60
80
PERCENT WING CHORD

Figure 5

BOUNDARY-LAYER CONTROL AS A MEANS OF INCREASING AIRPLANE LIFT

By Charles W. Harper and Mark W. Kelly

Ames Aeronautical Laboratory

INTRODUCTION

In references 1, 2, and 3 the applications of area suction as a form of boundary-layer control to increase lift at low speeds were considered in detail. The results on which these papers were based came from full-scale wind-tunnel tests of a model with F-86 wing panels.

Since these reports were presented, research has been continued on the use of area-suction boundary-layer control and has been extended to include blowing boundary-layer control. Because it was believed that the wind tunnel could provide only a portion of the required information, the National Advisory Committee for Aeronautics has equipped a number of airplanes with boundary-layer control and evaluated them in flight. It is the purpose of this paper to review this work.

DISCUSSION

Figure 1 shows the general arrangement of the wind-tunnel models to which boundary-layer control has been or is being applied. The primary purpose of this figure is to show the relatively large range of wing plan forms investigated. Details can be found in NACA reports (refs. 1 to 10) on the specific plan forms referenced in table I. An attempt will be made to summarize the more important findings rather than to give a complete exposition of results of the various wind-tunnel investigations.

The most obvious aspects of applying boundary-layer control are the resultant lift gains. The two types of lift gains due to boundary-layer control which are to be considered are: (1) the increase in lift due to increasing flap effectiveness and (2) the increase due to increasing the useful angle-of-attack range.

A useful basis from which to judge the effect of boundary-layer control on flap lift is the lift increment which would be expected if all evidence of flow separation were removed; this is, of course, the increment predicted by theories based on inviscid flow. Figure 2 compares the lift increments predicted by the method of reference 11 with those realized by various flap configurations on the models shown in figure 1 when sufficient boundary-layer control was applied to remove most signs of separation. It is clear that, in most cases, a near-theoretical value of flap lift was realized. In general, it has been found that the agreement between theory and experiment is usually good for flap deflections up to 60°. To illustrate the order of improvement realized, a range of values is also shown for some of the configurations without boundary-layer control. It can be concluded that a fair estimate can be made of the flap lift increment to be expected if boundary-layer control is applied to a flap.

In discussing this figure, it was stated that the values of lift shown were those measured when sufficient boundary-layer control was applied essentially to remove all separation and no distinction was made between area suction and blowing boundary-layer control. A distinction does exist, however, if consideration is given the power required to provide the boundary-layer control and the possible benefits obtainable from the existence of excess power. Figure 3 shows lift increments as a function of horsepower and engine bleed-air requirements obtained from wind-tunnel tests of models having F-86 wing panels. (See refs. 2 and 9.) Compare first the boundary-layer-control requirements in terms of ideal horsepower. This would be of interest where an independent power source and pump would be supplied to provide boundary-layer control. It is clear that there is about 6:1 difference in the horsepower required to reach a value of ΔC_L of about 0.7. For airplanes in which available horsepower is limited, it is apparent that the area suction has a decided advantage. It is also evident that if power requirements were not of concern, then the use of blowing boundary-layer control would enable higher lifts to be reached than area suction. This is of particular interest, since for many of the airplanes now in need of high lift aids, large amounts of horsepower are available in the high-pressure air which may be extracted from a turbojet-engine compressor. For these cases, the important point becomes whether the bleed air available during the landing approach or that which can be tolerated during take-off is sufficient to drive a pump for area suction or directly provide blowing boundary-layer control. Figure 2 shows that, for this airplane, either system can be used without exceeding the bleed-air limits. As a matter of interest, the power requirements corresponding to these maximum bleed-air quantities are about 300 horsepower. The larger bleed-air requirements and larger associated thrust loss of blowing-type boundary-layer control can be offset by a larger lift increase. Calculations, discussed subsequently, show that as far as ultimate take-off and landing performance are concerned, the two systems should give similar benefits. The absolute results shown herein apply, of course, only to this hypothetical airplane. The ultimate choice for other airplanes is likely to depend on details unique to each particular design. It might be noted that these results represent about the minimum boundary-layer-control requirements that the NACA has been able to achieve, and that no evidence of large potential reductions can be found.

Although it has been demonstrated that the application of boundary-layer control to trailing-edge flaps will usually result in large flap lift increments at low angles of attack, it should be noted that highly effective flaps usually tend to reduce the angle of attack for maximum lift. On some aircraft, particularly those employing thin wing sections and plan forms having high sweepback or low taper ratios, this reduction may be sufficient to bring the attitude for maximum lift near the ground angle of the airplane. For these aircraft, it appears that the application of boundary-layer control near the wing leading edge (either directly to the leading edge or to a nose flap) may result in significant gains in performance. This observation is demonstrated in figure 4 which shows the variation of lift coefficient with angle of attack for two wind-tunnel models, one having a thin low-aspect-ratio unswept wing (ref. 8), the other having a high-aspect-ratio wing swept back 45° (ref. 6). For these wings, the application of boundary-layer control to trailing-edge flaps resulted in practically no increase in maximum lift due to the reduction in the angle of attack at which flow separation near the wing leading edge occurred. However, application of area-suction boundary-layer control near the wing leading edge resulted in significant increases in maximum lift for both wings. Exploratory investigations on the application of blowing boundary-layer control to the wing leading edge are under way at the present time.

As noted previously, the most obvious aspect of boundary-layer control is its effect on lift. However, in determining its possible benefits in a particular case, consideration must be given to the resulting drag and moment changes. In particular, the drag changes become important when take-off or wave-off performance is being analyzed.

Where a satisfactory application of boundary-layer control is made to a flap, it would be expected that the flap drag would consist largely of the induced drag due to the change in span loading. Figure 5 shows how the measured drag increment of boundary-layer-control flaps compares with that which would be predicted by a theory (ref. 11) which considered induced drag alone. These increments were computed and measured for zero angle of attack of the wings. Also shown is the band in which the same comparison placed the flaps without boundary-layer control. Where the flap drag is high, the measured drag departs from the theoretical induced drag. It is believed that the deviation is, in part, due to an inadequacy of the theory in attempting to account for the rapid span-loading changes associated with highly effective flaps and, also, a complete neglect of the fuselage effect on span loading. Although the comparison shown herein indicates that good quantitative estimates of the drag change due to the application of boundary-layer control to flaps may not always be obtained, the theory should prove useful in estimating the order of magnitude of this change.

The effect on wing moments of applying boundary-layer control to a flap is small except through the direct effect of the increase in lift. That is to say, the ratio of ΔC_m to ΔC_L is nearly the same for a flap with or without boundary-layer control. If large flap lift increments are obtained by applying boundary-layer control to a flap, large trim requirements will be obtained. These can be estimated by the method of James and Hunton (ref. 12). For any of the models tested, no significant effect of boundary-layer control on tail effectiveness has been found that would not be traced directly to elimination of the stalled wake from the flap without boundary-layer control. Insofar as the tail is concerned, the problem, then, is one of overcoming the moment created by the higher flap lift; no new factors are introduced.

The effect of wing leading-edge boundary-layer control on drag and moments is similar to that of any leading-edge device that successfully prevents leading-edge separation. Where boundary-layer control is provided over the full span, there results a direct extension of the polar and moment curves; where this is done partial-span, the effect is so dependent on the configuration that it is necessary to resort to experiment. Experience in this regard is so limited that generalizations cannot yet be made; a number of investigations are, however, under way.

Up to this point, the discussion has been based on the results of wind-tunnel investigations. In order to gain some insight into pilots' reactions to the use of boundary-layer control, and also of the practical difficulties involved in applying boundary-layer control to actual airplanes rather than to simplified wind-tunnel models, a number of aircraft have been equipped with boundary-layer control and evaluated in flight. Some of the more important results of these investigations will now be discussed.

Perhaps the most direct indication of difficulties associated with a practical boundary-layer-control installation can be had from a consideration of the experience gained at the Ames Aeronautical Laboratory in carrying wind-tunnel studies through to flight installation. This has been accomplished in three separate instances involving application of leading-edge area suction to an F-86F airplane (ref. 13), application of area-suction boundary-layer-control flaps to an F-86A airplane (ref. 14), and application of blowing-type boundary-layer-control flaps to an F-86F airplane (ref. 15).

In general, it can be stated that each airplane finally achieved in flight essentially what had been predicted by the wind-tunnel tests. The use of the word "finally" correctly implies that success was not immediately achieved in all cases. Consideration of the problems encountered sheds some light on probable practical questions. Figure 6 shows for each airplane the variation of C_L with α obtained in the initial flight tests and those from the final flight tests. Wind-tunnel results are also shown for comparison. The improvements for the airplane with leading-edge suction appear as a delay in the angle of stall until higher maximum lifts are reached. The improvements in the cases of the other airplanes appear as increases in the flap lift increment.

The failure of the airplane with the suction leading edge to realize the expected maximum lift when first tested was traced primarily to blockage created by internal supports for the porous material. This blockage occurred at three butt joints between panels of the porous material where the internal supports were especially wide. Leading-edge stall originated at these points and limited maximum lift. It was found that short slots cut through the material and supports eliminated the local stall. Although the local values of flow coefficient increased significantly, the effect on the total flow coefficient was negligible. With this improvement, the flight airplane realized the maximum lift predicted from the wind-tunnel tests.

The successful application of area-suction flaps to the F-86A airplane was realized only after a number of unsatisfactory conditions were eliminated, each having a small effect but the total being significant. These included:

1. Trailing edge of porous opening being too far forward.

2. Rough flow created at inboard end of the flap by improper fairing of external air duct between flap and fuselage.

3. Rough flow on flap created by an undeflected wedge of wing lying between the flap and fuselage.

4. Leakage into the suction duct as a seal opened slightly when the airload came on the flap.

Most of the difficulties encountered herein were associated with the problem of adding a boundary-layer-control flap to an existing airplane without major modifications. It is believed that these difficulties could be readily avoided in an original design if their importance were kept in mind.

In the case of the F-86F airplane with blowing-type boundary-layer control applied to the flap, no difficulties were encountered in realizing in flight the values of lift indicated by the wind-tunnel results. In part, this success was due to the fact that some excess boundary-layer-control power was available - this was not true in the area-suction boundary-layer-control tests. However, it is believed to be largely due to the lesser sensitivity of blowing type boundary-layer control to air-flow disturbances.

No detailed discussion has been made of boundary-layer-control power requirements - that is, flow quantities and pumping pressures in the case of area suction - and engine bleed air and pressure ratios in the case of blowing, since, with the boundary-layer control operating satisfactorily, these requirements were very close to those estimated from wind-tunnel tests.

In concluding the discussion of this point, it might be of interest to point out that no difficulties have been encountered in maintaining operation of any of these boundary-layer-control systems. Boundary-layer-control installation was operated for a period of 19 months on the leading edge of the F-86F wing, the F-86A suction flap for a period of 17 months, and the F-86F blowing flap for a period of 5 months. The airplanes with area suction have shown no evidence of clogging, although no special care has been taken in this regard. Two of the airplanes with area-suction boundary-layer control have been flown in heavy rain with no evidence of deterioration of the boundary-layer-control effectiveness.

Pilots' reactions to the use of boundary-layer control in landing approaches depend, to some degree, on whether carrier-type or sinking-type approaches are used. (See ref. 16.) As a first step in examining these reactions, the Ames Aeronautical Laboratory has made a detailed study of the effect of boundary-layer control on the approach speeds chosen by pilots when making carrier-type landings. It is emphasized that these results were obtained and are being obtained from analysis of a particular type of landing made by research pilots having ample opportunity to acquaint themselves with the airplane and the boundary-layer-control installation. In addition to determining the flight speeds chosen, an effort is also being made to determine what factor fixes this speed and how this factor is related to the airplane characteristics. Figure 7 shows the results of these tests in terms of the location of the average lift coefficient chosen by the pilots on the lift curve for each airplane with boundary-layer control on and off. It is evident that, in each case, an increased C_L was used by the pilot when the boundary-layer control was on. For the airplanes having boundary-layer-control flaps, the pilots used about the same attitude with boundary-layer control on as they did with it off. However, the reasons given for limiting the approach speed indicate that attitude was not a primary factor. The reasons given fall generally into three categories; these are proximity to 1g stalling speed, attitude or visibility, and inadequate altitude control. Inadequate altitude control was stated as being limiting in six of the eight cases shown.

With the F-86F airplane having boundary-layer control applied to the leading edge, most of the pilots reported that they limited the speed either because of proximity to the stalling speed with the boundary-layer control off or because of attitude with boundary-layer control on. The curves shown in figure 7 are consistent with this observation, since boundary-layer control gave an 11° change in stall angle whereas the pilots used only a 6° stall angle.

In the case of the F-86F with blowing flaps, the F9F-4 (ref. 17) with blowing flaps, and the F-86A with area-suction flaps, the reason for choosing the approach speed was given as inadequate altitude control for either the boundary-layer control on or off condition.

The particular characteristics or combination of characteristics of the airplanes which led to the pilots' sensing a "loss of altitude control" or "inability to arrest sink" have not been determined as yet. Among the airplane characteristics which may be expected to influence this speed choice is the variation with airspeed of the thrust required for level flight. Figure 8 shows this variation for the four test airplanes and also the chosen approach speeds. It is evident that in each case the use of boundary-layer control reduced the speed for minimum thrust and also changed the shape of the curve. For the three cases where the approach speed was selected primarily because of loss-of-altitude control, it was found that good correlation was obtained between the speed reduction realized by the pilots and the reduction in speed for minimum thrust. However, in general, it is not felt that the speed for minimum thrust alone will be sufficient to define the speed at which altitude control becomes marginal on all aircraft, since other factors may also be important. Additional research on this problem is in progress.

All of the foregoing comments resulted from evaluation of carrier-type approaches, that is, approaches made at nearly constant altitude and high power settings. Some comments have also resulted from evaluation of sinking-type approaches where considerably less power is used. In these cases the pilots were particularly conscious of any loss in boundary-layer-control effectiveness at the low engine powers used in this type of approach. This emphasizes the necessity of matching the boundary-layer-control bleed-air requirements to the performance of the engine as used in the approach. For the low power settings used in sinking-type approaches, it will usually be required that careful attention be given to the pump efficiency in the case of area-suction flaps and to momentum requirements and nozzle size in the case of blowing flaps.

In connection with the change in boundary-layer control with engine speed, pilots made the observation that the F-86F airplane with blowing flaps provided improved altitude control in the approach through throttle manipulation in a manner similar to that obtained on propeller-type aircraft. However, it has not been possible so far actually to measure or isolate the factors responsible for the pilots' impressions.

Although the carrier-type approach studies are informative in understanding the pilots' reactions to the use of boundary-layer control, they give no quantitative measure of likely reductions in landing or take-off distances. Therefore, calculations have been made to show the effects of boundary-layer control applied to trailing-edge flaps on the take-off and landing performance of three typical airplanes. Figure 9 shows the airplanes chosen for this analysis. It was arbitrarily assumed that the landing and take-off speeds were chosen either from consideration of proximity to the stall or available ground angle. Although the preceding discussion of flight-test results indicates that other factors may be of equal importance, it is believed that these calculations should give a reasonable estimate of the order of magnitude of the changes in landing and take-off distances to be expected. The effects of boundary-layer control on the lift, drag, and pitching moments of these airplanes and the bleed-air requirements were estimated from available data. The thrust loss associated with engine air bleed has also been estimated and included. The ground-angle limitation was arrived at from consideration of the angles available on existing or proposed airplanes. Additional details concerning these analyses are included in tables II and III and appendix A.

The results of the take-off calculations are shown in figure 10 in terms of the percent reduction in ground roll due to boundary-layer control. These results demonstrate two points of particular significance: first, that a well-designed boundary-layer-control system should result in a reduction in take-off distance for airplanes of the type considered; and second, that if each type of boundary-layer control can be made to operate at the highest level of efficiency which has been realized for existing cases, the gains due to each system will be similar. This latter point should be noted since some previous blowing boundary-layer-control results had led to the conclusion that, for most airplanes, this type of boundary-layer control would not give reductions in take-off distance.

Figure 11 shows the results of the landing calculations. It is seen that substantial reductions are indicated for all three airplanes. Also, the results indicate that blowing boundary-layer control should give a larger reduction in landing distance than would be obtained by the use of area suction. These computations were made, as in the take-off analysis, by using momentum coefficients just sufficient to prevent flow separation on the flap. Larger momentum coefficients would give larger flap lift increments. However, these may not result in further reductions in landing distance unless some measure is taken to prevent flow separation from the leading edge of the wings.

CONCLUDING REMARKS

On the basis of the results obtained from the boundary-layer-control studies conducted to date by the National Advisory Committee for Aeronautics, which have been briefly summarized herein, it would appear that some general conclusions can be drawn.

It is believed that sufficient information is available to estimate the change at low speeds in airplane performance brought about by the use boundary-layer control on flaps and to estimate the required cost in power; thus it appears possible to assess the worth of using boundary-layer control in this way. It is concluded that boundary-layer control can be applied to airplane flaps without encountering new or difficult practical problems, and that, if properly applied, the pilots will realize benefits from its use. However, it must be recognized that the application of boundary-layer control, like every other phase of airplane design, can be affected by other details of the aircraft. Careful study and experience will probably be required to realize its full benefits.

On some airplanes it appears that the application of boundary-layer control to trailing-edge flaps will not provide significant increases in maximum lift because of a reduction in angle of attack at which flow separation from the wing leading edge occurs. For these aircraft, it is likely that leading-edge boundary-layer control can provide substantial increases in maximum lift, but additional work is required to provide the detailed information necessary for incorporation of this idea into new or existing designs.

APPENDIX A

SUMMARY OF LANDING AND TAKE-OFF ANALYSES

Airplane and Engine Characteristics

The airplane characteristics of interest in the take-off and landing analyses are given in tables II and III. The aerodynamic characteristics of the subsonic fighter were estimated from data obtained in the wind-tunnel tests reported in references 2 and 9. The aerodynamic characteristics of the bomber and the transonic fighter with area-suction flaps were estimated from the data of references 6 and 7. It was assumed for these airplanes that up to 0.2 increment in maximum lift could be obtained by the use of leading-edge slats or other leading-edge devices. The characteristics of these airplanes with blowing flaps were obtained by assuming that the same relative effectiveness between area suction and blowing boundary-layer control obtained in the investigations of references 2 and 9 would also apply to these 45° sweptback wings.

The flow requirements for all of the area-suction flap configurations were estimated from wind-tunnel data. The momentum requirements for the blowing flaps on the subsonic fighter were obtained from reference 9. The momentum requirements for the transonic figher and the bomber were estimated from those obtained from reference 9 using the following equation (see appendix B for definition of symbols):

$$C_{\mu_2} = C_{\mu_1} \frac{\left(S_f/S\right)_2 \cos^2 \Lambda_{HL_2}}{\left(S_f/S\right)_1 \cos^2 \Lambda_{HL_1}}$$

The engine bleed-air requirements were obtained for the area-suction-flap airplanes from the following equation:

$$W_{BL} = \frac{W_f}{\eta} \frac{T_o}{T_{BL}} \frac{\left[1 - \left(p_d/p_o\right)^{0.286}\right]}{\left[1 - \left(p_o/p_{BL}\right)^{0.286}\right]}$$

where a pump efficiency η of 15 percent is assumed. The bleed-air requirements for the blowing flap installations were estimated from the equation

$$W_j = \frac{C_\mu g q S}{M_j \frac{a_j}{a_d}\sqrt{\gamma R T_d}}$$

where M_j and a_j/a_d are isentropic functions of the bleed-air pressure ratio. For the landing calculations it was assumed that the pressure and temperature of the bleed air corresponded to those obtained from the engine under approach-power conditions, and the nozzle size was selected so that the jet momentum was just sufficient to prevent flow separation. For the take-off calculations it was assumed that a pressure-sensitive valve was used in the bleed-air system to avoid excessive amounts of bleed air and the corresponding high thrust losses.

The thrust losses due to bleed-air extraction for the subsonic fighter were obtained from J-47 engine-performance curves. Those for the supersonic fighter and the bomber were obtained from J-57 engine-performance curves.

Method of Analysis

Take-off ground run.- The take-off ground run was computed from reference 18 (eq. 8:45, p. 8:22). It was assumed that the ground roll was made at constant attitude (given in table II) up to the take-off speed. The take-off speed for the fighters was assumed to be that required for level flight at $0.9C_{L_{max}}$ as long as this lift was obtainable within the maximum ground angle of the airplane. Otherwise, the take-off speed was taken as that required for level flight at the airplane C_L obtained at the maximum ground angle. The same procedure was followed in the bomber take-off calculations except that it was assumed that the ground angle was set at 8° by the use of a bicycle-type landing gear.

Take-off transition.- Although not presented herein, calculations were made of the take-off transition for some of these configurations by numerically integrating the equations of motion of the aircraft. Two results of interest were obtained; these are: (1) at an altitude of 50 feet, the transition to steady climbing flight had not been completed and (2) in all cases there was sufficient thrust available to avoid deceleration before the 50-foot altitude was reached. The steady-state climb angle was usually reduced by the use of boundary-layer control due to the thrust loss and drag increments involved.

Landing flare.- The landing flare was computed by the equations given in reference 19 for the variable-load-factor flare case. It was assumed that the rate of sink of the fighter aircraft was 20 feet per second at a 50-foot altitude, whereas that of the bomber was 10 feet per second at a 50-foot altitude. The approach velocity was computed either from the requirement that the maximum C_L used in the flare would not exceed $0.9C_{L_{max}}$ or that the angle of attack at the conclusion of the flare could not exceed the maximum ground angle of the airplane.

Landing ground roll.- The landing ground roll was computed by use of equation 8:45 of reference 18. The touchdown speed was assumed to be that existing at the end of the landing flare. It was assumed that the roll was made with no engine thrust, with the boundary-layer control off, and with an average braking coefficient of 0.3 applied throughout the roll.

APPENDIX B

SYMBOLS

a	velocity of sound, ft/sec
A	aspect ratio
BLC	boundary-layer control
c	wing chord, ft
C_D	drag coefficient, Drag/qS
C_L	lift coefficient, Lift/qS
C_Q	flow coefficient, $\frac{W_f}{wU_oS}$
C_μ	momentum coefficient, $\frac{W_j/g}{qS}V_j$
g	acceleration of gravity, 32.2 ft/sec/sec
M_j	jet Mach number
p_{BL}	total pressure of bleed air, lb/sq ft
p_d	total pressure in flap duct, lb/sq ft
p_o	free-stream static pressure, lb/sq ft
q	free-stream dynamic pressure, lb/sq ft
R	gas constant for air, 1,715 ft-lb/slug $^{\circ}$R
S	wing area, sq ft
S_f	wing area spanned by flap, sq ft
t	airfoil thickness, ft
T	engine thrust, lb

T_{BL}	total temperature of bleed air, $^{\circ}R$
T_d	total temperature in flap duct, $^{\circ}R$
T_o	free-stream temperature, $^{\circ}R$
U_o	free-stream velocity, ft/sec
V_j	jet velocity, assuming isentropic expansion, $\sqrt{\frac{2\gamma}{\gamma - 1} RT_d \left[1 - \left(\frac{p_o}{p_d}\right)^{\frac{\gamma-1}{\gamma}}\right]}$
W	airplane weight, lb
w	specific weight of air at standard conditions, 0.0765 lb/cu ft
W_{BL}	bleed air flow from engine, lb/sec
W_f	air flow required by suction flap, lb/sec
W_j	air flow required by blowing flap, lb/sec
α	angle of attack, deg
γ	ratio of specific heats, 1.4 for air
δ_f	flap deflection, deg
$\Lambda_{c/4}$	sweep of wing quarter-chord line, deg
Λ_{HL}	sweep of flap hinge line, deg
λ	wing taper ratio

REFERENCES

1. Holzhauser, Curt A., and Martin, Robert K.: The Use of Leading-Edge Area Suction To Increase the Maximum Lift Coefficient of a 35° Swept-Back Wing. NACA RM A52G17, 1952.

2. Cook, Woodrow L., Holzhauser, Curt A., and Kelly, Mark W.: The Use of Area Suction for the Purpose of Improving Trailing-Edge Flap Effectiveness on a 35° Sweptback Wing. NACA RM A53E06, 1953.

3. Holzhauser, Curt A., and Martin, Robert K.: The Use of a Leading-Edge Area-Suction Flap To Delay Separation of Air Flow From the Leading Edge of a 35° Sweptback Wing. NACA RM A53J26, 1953.

4. Kelly, Mark W., and Tolhurst, William H., Jr.: The Use of Area Suction To Increase the Effectiveness of a Trailing-Edge Flap on a Triangular Wing of Aspect Ratio 2. NACA RM A54A25, 1954.

5. Cook, Woodrow L., and Kelly, Mark W.: The Use of Area Suction for the Purpose of Delaying Separation of Air Flow at the Leading Edge of a 63° Swept-Back Wing - Effects of Controlling the Chordwise Distribution of Suction-Air Velocity. NACA RM A51J24, 1952.

6. Griffin, Roy N., Jr., and Hickey, David H.: The Use of Area Suction To Increase Effectiveness of Trailing-Edge Flaps of Various Deflections and Spans on a Wing of 45° Sweepback and Aspect Ratio 6. (Prospective NACA paper.)

7. Holzhauser, Curt A.: Application of Area Suction to the Leading-Edge and Trailing-Edge Flaps of a 44° Sweptback Wing Having an Aspect Ratio of 3.7 and a Taper Ratio of 0.4. (Prospective NACA paper.)

8. Koenig, David G.: The Use of Area Suction for the Purpose of Improving the Longitudinal Characteristics of a Thin Unswept-Wing Model Equipped With Leading- and Trailing-Edge Flaps. (Prospective NACA paper.)

9. Kelly, Mark W., and Tolhurst, William H., Jr.: Full-Scale Wind-Tunnel Tests of a 35° Sweptback Wing Airplane With High-Velocity Blowing Over the Trailing-Edge Flaps. NACA RM A55I09, 1955.

10. Whittle, Edward F., Jr., and McLemore, H. Clyde: Aerodynamic Characteristics and Pressure Distributions of a 6-Percent-Thick 49° Sweptback Wing With Blowing Over Half-Span and Full-Span Flaps. NACA RM L55F02, 1955.

11. DeYoung, John: Theoretical Symmetric Span Loading Due to Flap Deflection for Wings of Arbitrary Plan Form at Subsonic Speeds. NACA Rep. 1071, 1952. (Supersedes NACA TN 2278.)

12. James, Harry A., and Hunton, Lynn W.: Estimation of Incremental Pitching Moments Due to Trailing-Edge Flaps on Swept and Triangular Wings. NACA RM A55D07, 1955.

13. Bray, Richard S., and Innis, Robert C.: Flight Tests of a Leading-Edge Area Suction on a Fighter-Type Airplane With a 35° Sweptback Wing. NACA RM A55C07, 1955.

14. Anderson, Seth B., and Quigley, Hervey C.: Flight Measurements of the Low-Speed Characteristics of a 35° Swept-Wing Airplane With Area-Suction Boundary-Layer Control on the Flaps. (Prospective NACA paper.)

15. Anderson, Seth B., Quigley, Hervey C., and Cooper, George E.: Flight Measurements of the Low-Speed Characteristics of a 35° Swept-Wing Airplane With Blowing-Type Boundary-Layer Control on the Flaps. (Prospective NACA paper.)

16. Cooper, George E., and Innis, Robert C.: Effect of Area-Suction-Type Boundary-Layer Control on the Landing-Approach Characteristics of a 35° Swept-Wing Fighter. (Prospective NACA paper.)

17. Rolls, Stewart L., and Innis, Robert C.: A Flight Evaluation of a Wing-Shroud Blowing Boundary-Layer Control System Applied to the Flaps of the Grumman F9F-4 Airplane. (Prospective NACA paper.)

18. Dommasch, Daniel O., ed.: Advisory Group for Aeronautical Research and Development - Flight Test Manual. Vol. I - Performance.

19. Fusefeld, Robert D.: A Method of Calculating the Landing Flare Path of an Airplane. Aero. Eng. Rev., vol. 10, no. 2, Feb. 1951, pp. 25-30.

TABLE I.- ADDITIONAL INFORMATION FOR MODELS

SHOWN IN FIGURE 1

Configuration	Sweepback of c/4, deg	Aspect ratio, A	Taper ratio, λ	t/c	Type of boundary-layer control	Reference
1	35	4.8	0.51	0.09	Leading-edge suction Trailing-edge flap suction Leading-edge flap suction	1 2 3
2	56	2	0	0.05	Trailing-edge flap suction	4
3	60	3.5	0.25	0.06	Leading-edge suction	5
4	45	6.0	0.30	0.08	Leading-edge suction Trailing-edge flap suction	6
5	44	3.7	0.40	0.08	Leading-edge flap suction	7
6	16	3.0	0.40	0.04	Trailing-edge flap suction Leading-edge flap suction Trailing-edge flap suction	8
7	35	4.8	0.51	0.09	Trailing-edge flap blowing	9
8	45	2.8	0.17	0.05	Trailing-edge flap suction	Unpublished data
9	5	6	0.38	0.13	Leading-edge flap suction Trailing-edge flap suction	Unpublished data
10	36	6.8	0.34	0.09	Trailing-edge flap suction	Unpublished data
11	0	9.7	0.51	0.17	Trailing-edge flaps Trailing-edge flap suction - blowing	Unpublished data
12	45	3.5	0.30	0.06	Trailing-edge flap blowing	10

[redacted]

TABLE II.- SUMMARY OF DATA USED IN TAKE-OFF CALCULATIONS

Airplane	W/S, lb/sq ft	T/W[1]	S, sq ft	Max. ground angle, deg	δ_f, deg	C_Q	C_μ	α used in ground run, deg	C_L used in ground run	C_D used in ground run	α for take-off, deg	C_L for take-off	$C_{L_{max}}$
Subsonic fighter													
No boundary-layer control	51	0.382	288	14	45	-------	------	3	0.57	0.105	14	1.24	1.38
Area-suction flaps	51	.378	288	14	55	0.0005	------	3	.83	.16	12	1.41	1.57
Blowing flaps	51	.375	288	14	45	-------	0.006	3	.82	.15	12	1.39	1.54
Transonic fighter													
No boundary-layer control	65	.654	354	12	50	-------	------	0	.50	.09	12	1.01	1.32
Area-suction flaps	65	.650	354	12	50	.00032	------	0	.61	.10	12	1.13	1.39
Blowing flaps	65	.630	354	12	50	-------	.0073	0	.70	.13	12	1.21	1.44
Bomber													
No boundary-layer control	100	.24	1,667	8	46	-------	------	8	.89	.12	8	.89	1.13
Area-suction flaps	100	.229	1,667	8	55	.0012	------	8	1.09	.15	8	1.09	1.30
Blowing flaps	100	.227	1,667	8	46	-------	.006	8	1.10	.14	8	1.10	1.29

[1]Net thrust including thrust loss due to air bleed.

[redacted]

TABLE III.- SUMMARY OF DATA USED IN LANDING CALCULATIONS

Airplane	W/S, lb/sq ft	S, sq ft	Max. ground angle, deg	δ_f, deg	C_Q	C_μ	$C_{L_{max}}$	$C_{L_{TD}}$	V_{TD}, fps	α used in ground roll, deg	C_L used in ground roll[1]	C_D used in ground roll[1]
Subsonic fighter												
No boundary-layer control	51	288	14	60	------	-----	1.34	1.08	199	0	0.48	0.11
Area-suction flaps	51	288	14	55	0.0005	-----	1.57	1.28	183	0	.48	.11
Blowing flaps	51	288	14	60	------	0.011	1.65	1.36	177	0	.48	.11
Transonic fighter												
No boundary-layer control	65	354	12	50	------	-----	1.32	1.04	231	0	.5	.095
Area-suction flaps	65	354	12	66	.0007	-----	1.42	1.09	224	0	.44	.10
Blowing flaps	65	354	12	66	------	.011	1.50	1.16	217	0	.44	.10
Bomber												
No boundary-layer control	100	1,667	8	55	------	-----	1.20	.95	303	8	.95	.135
Area-suction flaps	100	1,667	8	55	.0012	-----	1.30	1.09	278	8	.95	.135
Blowing flaps	100	1,667	8	55	------	.009	1.41	1.18	267	8	.95	.135

[1]BLC assumed not operating during landing ground roll

[redacted]

RANGE OF WING PLANFORMS USED FOR B.L.C. TESTS

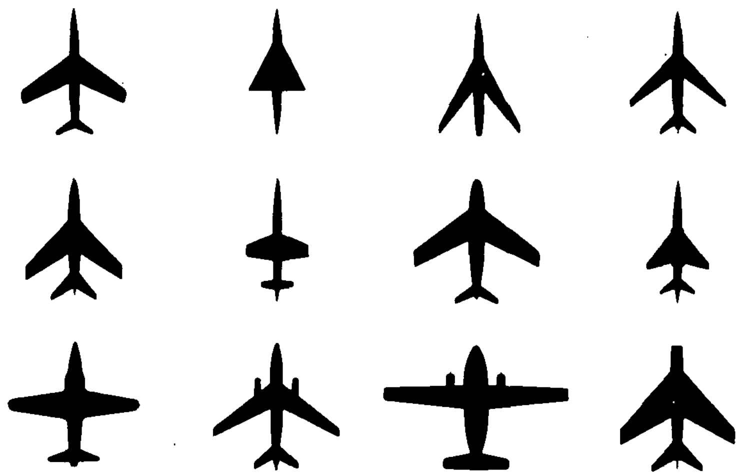

Figure 1

COMPARISON OF THEORETICAL AND REALIZED FLAP LIFT WITH B.L.C.

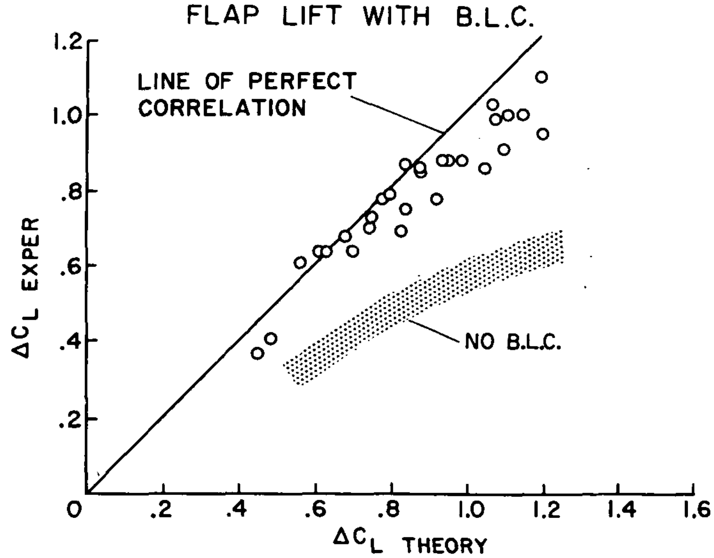

Figure 2

[redacted]

COMPARISON OF POWER AND AIR FLOW FOR TWO TYPES OF B.L.C. APPLIED TO FLAPS

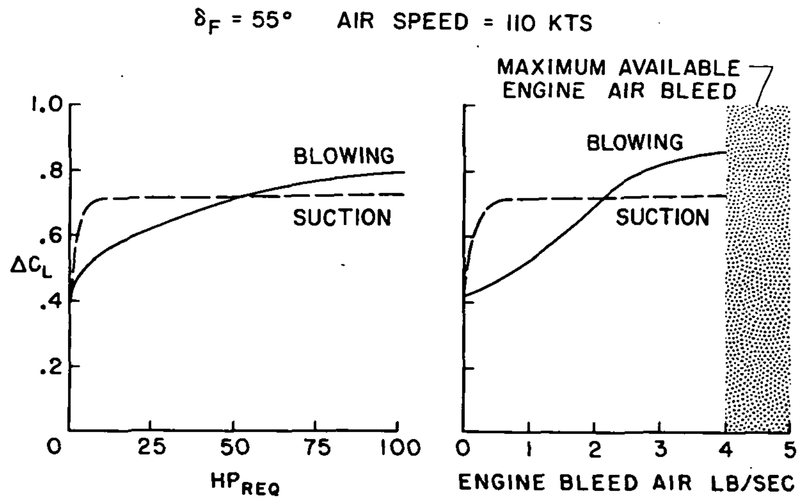

Figure 3

EFFECT ON MAXIMUM LIFT OF DIFFERENT APPLICATIONS OF B.L.C.

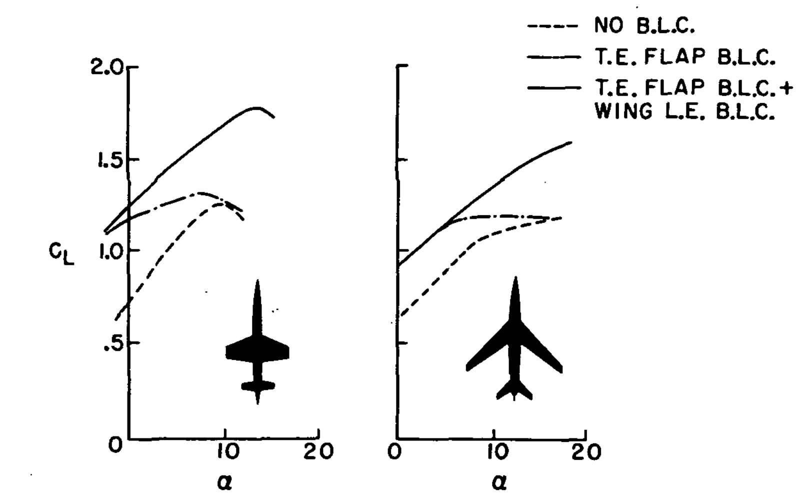

Figure 4

[redacted]

COMPARISON OF THEORETICAL INDUCED DRAG
AND EXPERIMENTAL TOTAL DRAG DUE TO FLAPS

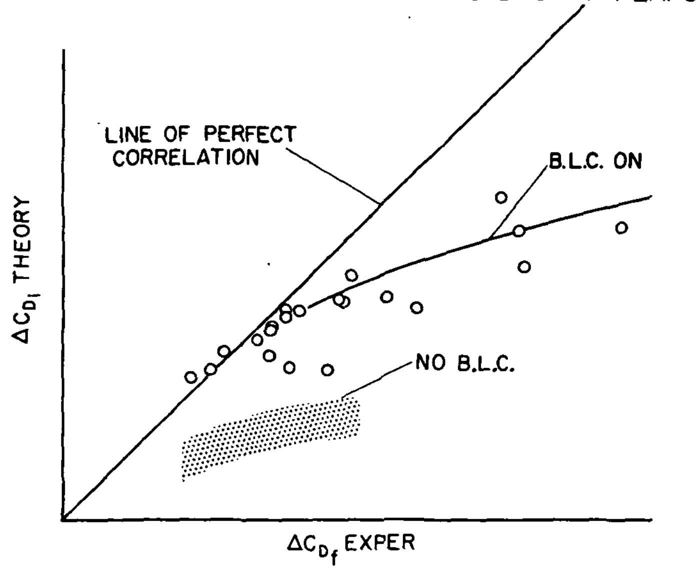

Figure 5

IMPROVEMENTS IN B.L.C. PERFORMANCE OBTAINED
DURING FLIGHT PROGRAM

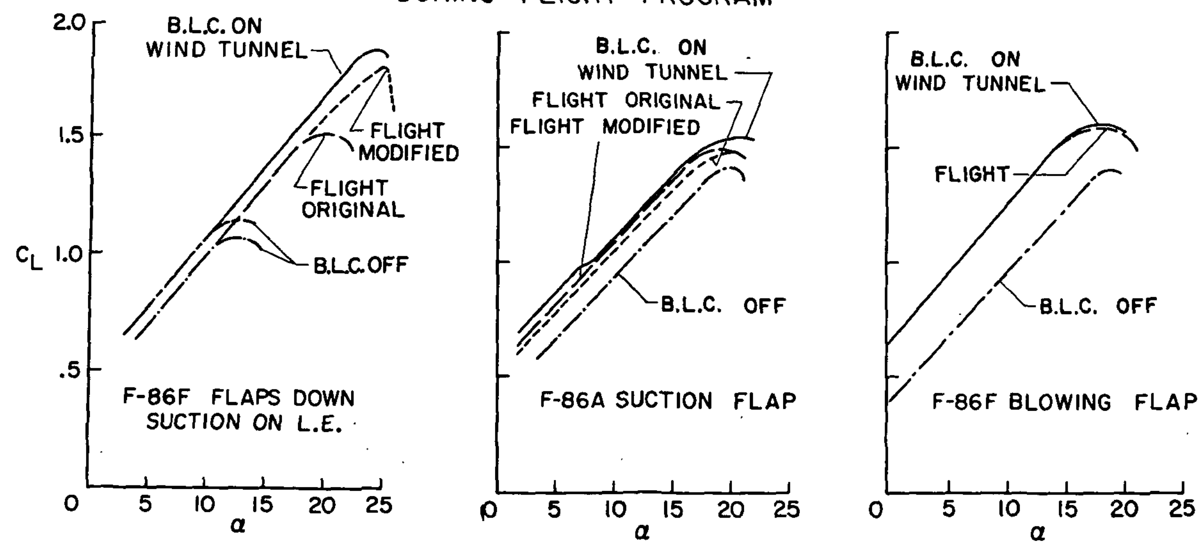

Figure 6

[redacted]

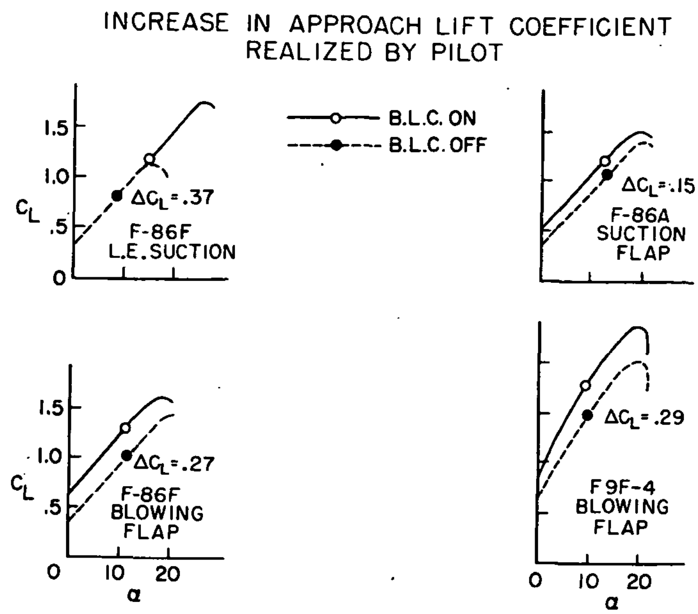

Figure 7

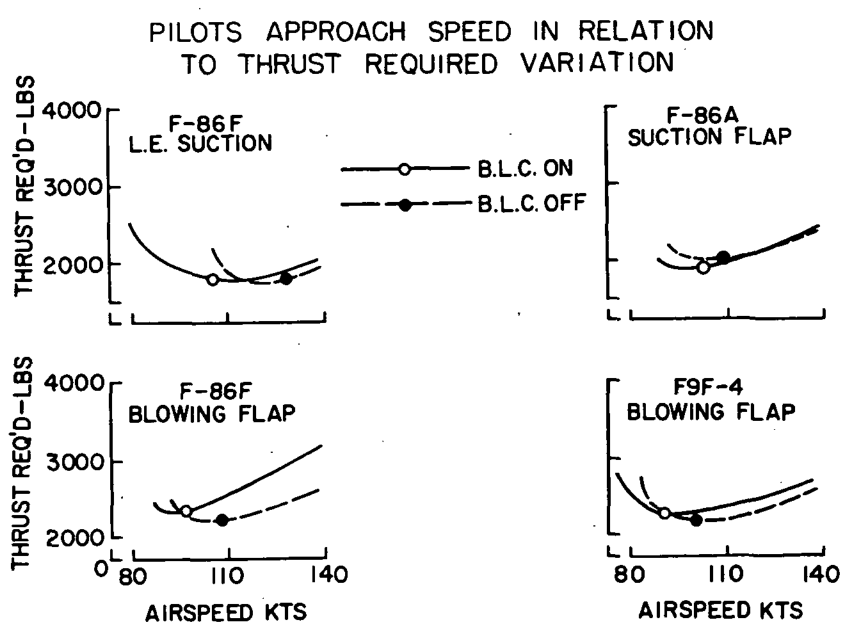

Figure 8

[redacted]

AIRPLANES CHOSEN FOR LANDING AND TAKE-OFF ANALYSES

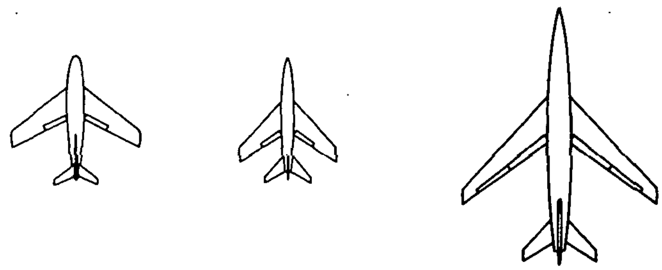

W/S	51	65	100
T/W	.38	.65	.24
	SUBSONIC FIGHTER	TRANSONIC FIGHTER	BOMBER

Figure 9

PERCENT REDUCTION IN TAKE OFF GROUND ROLL DUE TO B.L.C.

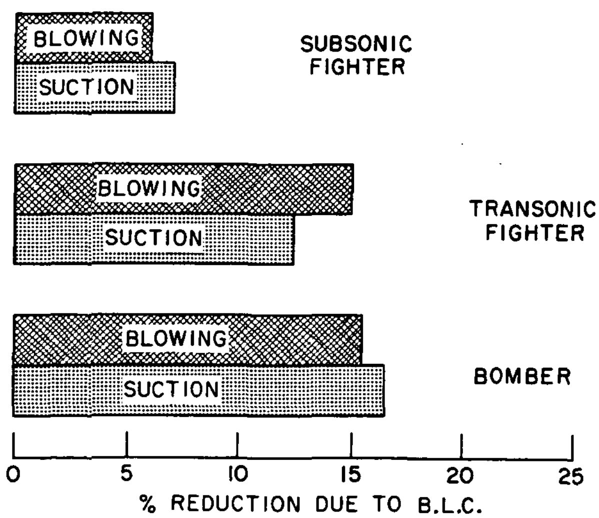

Figure 10

[redacted]

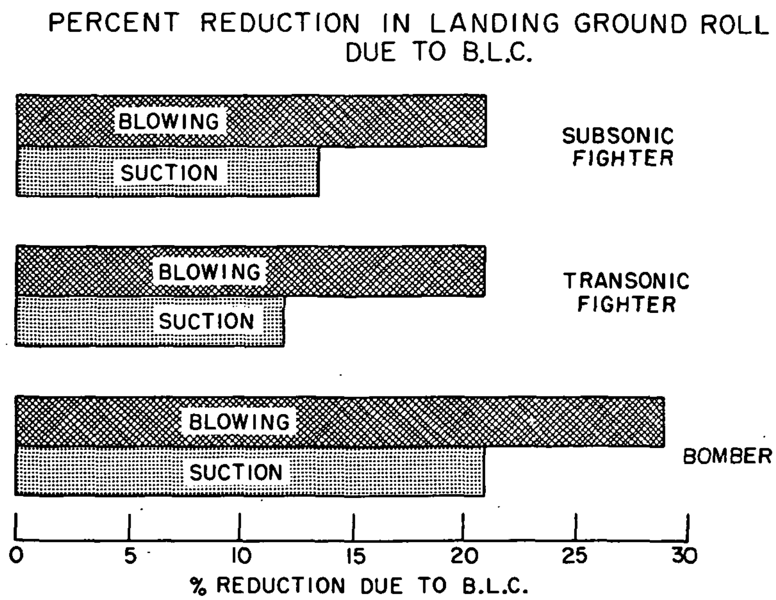
PERCENT REDUCTION IN LANDING GROUND ROLL DUE TO B.L.C.
BLOWING
SUCTION
SUBSONIC FIGHTER
BLOWING
SUCTION
TRANSONIC FIGHTER
BLOWING
SUCTION
BOMBER
0
5
10
15
20
25
30
% REDUCTION DUE TO B.L.C.

Figure 11

Pages 470, 471 and 472 are blank.

Preceding page blank

PROBLEMS OF PERFORMANCE AND HEATING OF HYPERSONIC VEHICLES

By H. Julian Allen and Stanford E. Neice

Ames Aeronautical Laboratory

INTRODUCTION

A particular virtue of high-velocity rockets for military application is the difficulty in effecting countermeasures for defense against them. In consequence, Sänger (ref. 1) devoted considerable effort to the study of several types of rocketcraft and, with Bredt (ref. 2), examined the rocket-powered glider airplane in particular.

There are two principal objections to the rocketcraft when compared to the conventional supersonic airplane powered by air-breathing engines. First, the propulsive efficiency of the chemical rocket is low so that the "all-up" weight at take-off is large in comparison with that at rocket burnout. Second, since the long-range rockets attain very high speeds, they may accordingly be subjected to intense aerodynamic heating when in the atmosphere. Often the heating rates are so great as to preclude the possibility of adequate cooling by radiation alone, in which case they must be protected by providing a sufficient weight of coolant to absorb this heat. At best, the weight of coolant required may be of the order of the payload weight which only serves to amplify the importance of the first objection since, then, a large increase in the initial all-up weight must be provided simply to propel the coolant. In fact, it is possible in certain cases to generate so much heat that no payload can be carried at all since all the available weight at rocket burnout is required for coolant to cool the coolant. Thus, it is seen, as with so many problems in aircraft design, that the cooling problem has a pyramiding nature and is consequently of extreme importance.

35

From what has been said, it is clear that there are two closely connected questions which the designer must ask himself: "Can the rocket vehicle be made reasonably efficient compared with the airplane?" and "What can be done to minimize the aerodynamic heating problem?"

In this paper, three types of hypervelocity vehicles are compared: the ballistic rocket, the skip rocket, and the rocket glider, in a manner somewhat similar to that originally done by Sänger. The trajectories of these rockets are shown in figure 1. The ballistic vehicle considered here is the one which leaves the atmosphere at that angle relative to the earth's surface which requires the least energy input for a given flight range. The skip vehicle travels on a succession of ballistic trajectories, each connected to the next by a "skipping phase" during which the vehicle enters the atmosphere, negotiates a turn, and then is ejected from the atmosphere. The optimum skip vehicle is considered in which the skipping phase of flight is made at the optimum lift-drag ratio and the initial flight angles of the successive ballistic trajectories are those which, for the optimum lift-drag ratio, yield the given flight range for the least energy input. The boost-glide vehicle considered is one which during the powered and the unpowered phase of flight flies in the atmosphere at optimum lift-drag ratio for each point of the trajectory. Thus the flight altitude continuously varies with speed.

These three hypervelocity rockets will be compared efficiency-wise with one another and with assumed supersonic jet airplanes. Next, the hypersonic vehicles will be compared on the basis of aerodynamic heating requirements. Finally, some detailed problems of glide rockets will be discussed.

RANGE EFFICIENCY

In order to compare the efficiency of flight of the various vehicles, it should be apparent at the outset that the efficiency parameter which is truly appropriate depends upon the intended use of the vehicles. Thus, for a missile, the parameter of real interest is the vehicle cost per pound of explosive delivered; whereas, for the usual transport, which is not destroyed on completion of a single mission, the proper parameter would be the total cost of fuel, repairs, and depreciation per pound of payload delivered.

In both cases, these parameters might well be approximated by the ratio of initial weight at take-off to the payload weight. However, the evaluation of this ratio requires a knowledge of the weight of the component parts of the structures which is a matter of detail design beyond the scope of this paper. Accordingly, in this paper the ratio of the initial weight at take-off to the final weight after fuel is expended will be used as the measure of flight efficiency. It is presumed, then, that the reader will temper the results given in the following discussion with the knowledge that the ratio of payload weight to final weight is not the same for the several classes of vehicles considered. In particular, it should be noted that the use of the ratio of initial weight to final weight as the measure of merit is particularly unfair to the ballistic vehicle since its ratio of payload weight to final weight is generally much greater than for the other types.

In order to compare the efficiency of the hypersonic rockets and the airplane, it is desirable to express the range equation in a form of the type first developed by Bréguet, because in this form it is most familiar to the airplane designer. In order to effect such a form for the range equation, the following mathematical development is employed. (See ref. 3.) The effective drag D_e is defined in such a manner that the product of this drag and the range X equals the energy input at burnout as follows:

$$D_e X = \frac{W_f V_f^2}{2g} \tag{1}$$

where V_f is the final speed at rocket burnout, W_f is the corresponding weight, and g is the acceleration due to gravity. Let the effective lift L_e be defined as the weight at rocket burnout; that is,

$$L_e = W_f \tag{2}$$

Combining these two equations then gives the range as

$$X = \left(\frac{L}{D}\right)_e \frac{V_f^2}{2g} \tag{3}$$

The term $(L/D)_e$ will be called the effective lift-drag ratio herein.

Now, the speed at rocket burnout V_f may be related to the ratio of initial weight W_i to final weight W_f in the form

$$V_f = I_e g \ln \frac{W_i}{W_f} \tag{4}$$

where I_e is defined as the effective specific impulse of the rocket propellant which is generally somewhat less than the actual specific impulse because of the requirements of staging and so forth.

If one of the V_f's in equation (3) is replaced by the value from equation (4), the range can be obtained in the form

$$X = \left(\frac{L}{D}\right)_e I_e V_e \ln \frac{W_i}{W_f} \tag{5}$$

wherein the effective speed V_e is just one-half the speed at rocket burnout. For a conventional airplane with air-breathing engine, the Bréguet equation can be written in the form

$$X = \frac{L}{D} I V \ln \frac{W_i}{W_f} \tag{6}$$

where L/D is the aerodynamic lift-drag ratio. It is more usual with airplanes to replace the product IV by the product of the thermal efficiency η and specific-heat value of the fuel h to give

$$X = \frac{L}{D} \eta h \ln \frac{W_i}{W_f} \tag{7}$$

Equation (5) can now be used for comparing the hypervelocity rockets with one another, and these rockets in turn may be compared with the conventional airplane with the use of equation (6) or (7).

Obviously, the most efficient vehicle, based on the definition given, is the one with the largest value of the product $(L/D)(I)(V)$; and this product may be broken down for convenience into the components L/D, which is the measure of aerodynamic efficiency, and IV, which is the measure of propulsive efficiency. In figure 2 is shown a comparison of conventional air-breathing-engine propulsive systems with a typical chemical-rocket system as indicated by the attainable values of IV as a function of speed. Since this product has the dimensions of a length, it has been termed the "propulsive range." This range has been expressed in nautical miles. It is seen that, depending on the speed chosen, the air-breathing-engine system will attain an optimum value of IV which is essentially independent of the speed as has been pointed out by Rutowski (ref. 4) and others. This value is about 700 nautical miles. For rockets, the specific impulse is essentially a constant (assumed herein as 225 seconds) and hence the product has the linear characteristics shown. The high value of 700 nautical miles would not be approached until burnout speed corresponding to the escape speed from the earth is reached. Thus, the rocket has the disadvantage that its propulsive efficiency for normal ranges is low. This is not the whole story, however, since it is the product of propulsive range and the effective lift-drag ratio which is important.

In order to examine the effective lift-drag ratios for the rockets and for the airplane, figure 3 has been prepared. In this figure, values are shown as a function of range in nautical miles. Figure 3(a) is for the case wherein the aerodynamic lift-drag ratio is 2 and figure 3(b) is for the case wherein the ratio is 6. For the airplane, the lift-drag ratio is independent of range, but, for the rockets, it is seen that the effective lift-drag ratio increases with increasing range. This anomalous result occurs because the increased range for the rockets is obtained through increased speed so that an increasingly greater share of the vehicles' weight is borne by centrifugal force on the curved flight around the earth. Thus the aerodynamic lift required decreases and hence also the aerodynamic drag. In fact, when satellite speed is reached, the effective lift-drag ratio becomes infinity. It is of particular interest to note that the ballistic vehicle for which the actual aerodynamic lift-drag ratio is zero behaves practically as though it were a rocket glider having an aerodynamic lift-drag ratio of 2.

If the effective lift-drag ratio is now combined with the propulsive range, the results shown in figure 4 are obtained. The ratio of initial weight to final weight as a function of range for the four types of vehicles is shown in figure 4(a) for an aerodynamic L/D of 2 and in figure 4(b) for an aerodynamic L/D of 6. Here it is noted that all the hypervelocity vehicles look attractive when the flight range is long and the attainable aerodynamic lift-drag ratios are low. Notice also that if the aerodynamic L/D attainable is small, the skip rocket appears to be the best of the hypervelocity vehicles; but, if the aerodynamic L/D is large, then the skip and glide rockets are about equal. It should also be pointed out that, although the ballistic rocket looks poor in figure 4(b), in general, compared to the others, as noted earlier, a larger fraction of its final weight is payload because of the low engine and fuel tankage weight. Hence, if the ratio of initial weight to payload weight had been used as a measure of merit, the ballistic vehicle would appear promising.

AERODYNAMIC HEATING

It was pointed out earlier that all hypervelocity vehicles are subjected to intense aerodynamic heating. If the aerodynamic heat must be absorbed in a coolant and the required coolant weight becomes large, then the all-up weight at take-off can become very great compared with the payload weight. Thus the two questions which must be asked about each of the three types of rockets are: (1) "Is it possible to radiate the incoming aerodynamic heat at a sufficiently high rate to keep the temperature within allowable bounds?" and (2) "If not, can the required quantity of heat which must be absorbed be kept small enough to prevent the necessity of an excessive weight of coolant?"

In order to answer the first question, figure 5 has been prepared to show the maximum value of the average heat transfer rate for each of the three rockets as the speed, and hence the range, is increased. The transfer of kinetic energy to heat occurs in abrupt pulses during the skip phases for the skip rocket. The first-skip heat rate, which is the most severe, is shown here. The ballistic rocket experiences the heat in a single abrupt pulse on atmospheric entry. The glide rocket, on the other hand, gradually converts its kinetic energy to heat over the whole flight trajectory. Thus, the relatively low rate of heat input is not surprising. Also shown in this figure is the rate of heat input for radiation equilibrium at temperatures of 1,000° F, 2,000° F, and 3,000° F. The answer to the first question is clear. The ballistic and skip rockets that are being considered cannot possibly be satisfactorily cooled by thermal radiation alone except for short flight ranges and hence must rely on a coolant. The radiation method of cooling does seem feasible for the glide rocket, although barely so.

The second question is now - "For the ballistic and skip rockets, which appear incapable of being cooled by radiation, can the total heat input be kept sufficiently low so that excessive weight of coolant is not required?" In order to answer this question, first consider the case of the ballistic rocket. In figure 6 is shown the total heat input for a 5,000-pound conical ballistic warhead as a function of cone angle. The chosen base area is 10 square feet and the velocity at atmospheric entry is 20,000 feet per second. It is seen that for turbulent flow there is a pronounced reduction of the heat input with increase in cone angle. The heat input is low for all but the smallest cone angles for the laminar case. The reason for the pronounced reduction of heat input with cone angle for the turbulent flow case is the following (ref. 5): For the warhead weights of usual interest, the kinetic energy near impact is a small fraction of the kinetic energy that the vehicle had on entering the atmosphere. Hence, nearly all this energy must be converted to heat but the fraction of this heat which enters the warhead is proportional to the ratio of the friction drag to the total drag. The remainder of the energy is spent heating the atmosphere. Thus, by making the ratio of friction drag to total drag small - in this case by employing large cone angles - the total heat input is kept small. The question naturally then follows: "Why doesn't a similar large reduction of heat input with cone angle occur in the laminar flow case?" The answer can be gotten from figure 7 wherein the maximum Reynolds number, which is also a measure of the mean Reynolds number, is plotted as a function of cone angle for the cones considered in figure 6. It is seen that there is a large reduction in Reynolds number with cone angle. This change in Reynolds number does not have a very pronounced effect on the turbulent friction coefficient, since this friction coefficient is only a weak function of the Reynolds number. For laminar flow, on the other hand, the friction coefficient varies inversely as the square root of the Reynolds number. Thus the friction coefficient drops rapidly with decrease in cone angle and hence the ratio of friction drag to total drag tends to stay more nearly uniform with cone angle, which explains the behavior of the heat input with cone angle for the laminar case shown in figure 6. Referring again to figure 7, if past experience at lower speeds is typical of the state of affairs at high speeds, it is most unlikely that laminar flow can be maintained at the very high Reynolds numbers associated with the entry of the small angle cones. It is very doubtful that even for the large angle cones continuous laminar flow will occur, but it is probable that during the initial portion of the entry trajectory, when the Reynolds numbers are much less than the maximums shown in figure 7, long runs of laminar flow can be maintained. It is during this initial flight trajectory that the laminar flow is particularly desired since then the flight speed is greatest so that time rates of heat input tend to be most severe. At best, then, the "high drag" solution to the heating problem for the ballistic vehicle would seem to be the most logical course to follow. However, it should be expected that the total heat input will be something between that for all-laminar and all-turbulent flow.

Unfortunately, this "high drag" solution is not open to the skip rocket. This conclusion follows directly from the fact that the skip rocket must develop reasonably high lift-drag ratios to achieve long range. But inasmuch as it is known that high lift-drag ratios are incompatible with high pressure drag, the skip rocket will clearly be relatively slender and consequently will have a relatively high ratio of friction drag to total drag.

Now, the question as to whether the heat input to the ballistic and skip rockets can be kept sufficiently low can be answered. In figure 8 is shown the calculated convective heat input per unit weight for a conical ballistic rocket having a large cone angle (60°) and the convective heat input per unit weight during the first skip for a conical skip rocket having a sufficiently small cone angle to permit a lift-drag ratio of 6. The flow in both cases is assumed laminar. In spite of the fact that the total energy converted to heat in the first skip of the skip rocket is much less than that involved in the entry of the ballistic rocket, the ratio of friction drag to total drag for the skip rocket is so large relative to that for this ballistic rocket that the heat input is seen to be much greater. Thus the ballistic vehicle could be cooled with a not-too-great weight of copper (see dashed curve) as a coolant, but it is doubtful that this skip rocket could be satisfactorily cooled at all, except for very short range flight. Thus when heating is considered, only the glide rocket (which can, in the main, be cooled by radiation) and the ballistic rocket (which is not required to accept an inordinate amount of heat) appear attractive hypersonic types at this time.

What has been said about aerodynamic heating up to this point applies to an average surface element of these vehicles. Of perhaps even greater importance is the heating of particular local surface elements where the heat rates may be many times that for the average surface. Such local elements are commonly the stagnation points of bodies and the leading edges of wings. It should be apparent that pointed noses or sharp leading edges seem impractical as regards aerodynamic heating since not only is the capacity for heat retention small but the heat transfer rate is exceedingly high since it varies nearly inversely as the square root of the radius of curvature. Thus a truly pointed nose or sharp leading edge would ablate, melt, or burn away.

For the ballistic warhead no problem arises in blunting the nose since the important effect of the blunting that may be required is to increase the pressure drag which is a desirable feature as has previously been discussed. (This does not consider possible adverse effects that excessive blunting may have on the transition from laminar to turbulent flow.)

PROBLEMS OF GLIDE ROCKETS

For the glide vehicle, the highest possible lift-drag ratio is urgently desired so that the drag incurred by blunting must be kept to a minimum. For the fuselage nose, slight blunting has been found not to increase the drag, but, for the wing, even a slight blunting is deleterious. However, theoretical and experimental research has shown that the drag increment can be kept low by use of swept leading edges. In fact, it can be shown (see ref. 6) that for a given rate of heat input the drag due to blunting of the leading edge varies approximately as the fourth power of the cosine of the sweep angle. For this and other reasons, one suggested configuration for a man-carrying boost-glide rocket might well look like the configuration shown in figure 9 (ref. 7). In the case of a man-carrying glider, a certain minimum span will be required for landing. The maximum leading-edge sweep will thus be obtained if the leading edge runs from the fuselage nose to the end of the span opposite the fuselage base. For the case shown in figure 9, the leading-edge sweep is 74° and it has been calculated that, at Mach numbers up to the order of 7, the drag due to the required blunting of the leading edge is not large and, for a 50-foot-long vehicle, the lift-drag ratio should be 5 if the boundary-layer flow is turbulent and should be 6 if the boundary-layer flow is laminar. Laminar flow is doubly desirable since it both improves flight efficiency and reduces aerodynamic heating. Now, it should be noted that, for speeds not too near orbital speed, flight at constant lift-drag ratio infers nearly constant dynamic pressure; hence, as shown in figure 10, the Reynolds number decreases with increase in speed. It becomes zero at orbital speed since centrifugal force is all that is needed to support the weight. On the other hand, recent experimental research has shown that the transition Reynolds number generally increases with increasing speed. In fact, in the Ames supersonic free-flight tunnel, continuously laminar flows have been maintained at a Mach number of 7 on bodies of revolution with relatively rough surfaces to Reynolds numbers of the order of 15×10^6 - which is of the order shown here. Thus, it is not surprising that in some recent firings of a model of the three-wing configuration at essentially full-scale Reynolds numbers, the indicated lift-drag ratio was 5.5. Although it is true that this rather high lift-drag ratio can be attained up to Mach numbers of the order of 7, a boost-glide vehicle having this maximum Mach number will have a range of only about 800 nautical miles. In order to increase the range, the Mach number must be increased, but, in so doing, the required leading-edge bluntness must be increased to prevent excessive heating. It can readily be found that the drag incurred by the blunting can then become so large as to reduce the lift-drag ratio seriously. It was shown earlier that the product of $\frac{L}{D} I V$ was a measure of the flight efficiency. Thus, for a given value of L/D, the efficiency improves with increasing speed. On the other hand, if the lift-drag ratio decreases with increasing speed, it is possible for the efficiency to diminish as the range is increased. In this event, rather than to employ the simple boost-glide trajectory for the rocket airplane in which the maximum boost is maintained to give the full speed required for the desired range, it would be preferable to boost to a somewhat lower speed and then sustain this speed with a lower thrust rocket for the distance required to obtain this same range. In this case, the reduced leading-edge radius might well improve the lift-drag ratio enough to more than make up for the reduction in the propulsion efficiency. This situation in which the leading-edge stagnation temperature is restricted to 2,000° F is indicated in figure 11 where range is plotted as a function of the ratio of initial weight to final weight for the three-wing glider shown previously. Each of the individual solid curves corresponds to a particular leading-edge radius. The circled end points correspond to simple boost-glide flight (that is, no sustainer) while the higher values of each curve correspond to increased amounts of sustainer flight for the increased range. The dashed envelope curve, which represents the optimum performance, shows that some sustainer portion of flight is desired when the leading-edge temperature is limited.

If one determines such envelope curves for various leading-edge temperatures, it is possible to express optimum weight ratio as a function of range for various permitted leading-edge temperatures as is shown in figure 12. It is seen that for the larger ranges there is a weight penalty when the radiation equilibrium temperature of the leading edge is limited. Whether some cooling by other means than radiation should be used would depend on how the weight penalty for coolant compares with the penalty shown in figure 12.

In conclusion, it is pertinent to examine what further can be done to improve flight efficiency for glide rockets. First, it is obvious that, since aerodynamic heating appears to preclude the use of the very high speeds required to obtain good efficiency with a simple rocket (see fig. 2), some real effort should be made to develop an engine such as the rocket-ramjet to improve the propulsive range for Mach numbers from 5 to 10. Second, every effort should be made to improve the aerodynamic lift-drag ratio. In this regard, tests have recently been made of configurations of the type shown in figure 13 in which the body bow wave has been used to assist in providing lifting pressures under the wing. The negative dihedral at the tips is not only used to provide directional stability but also to turn the outflow from the body downward to enhance the lift further and so improve the lift-drag ratio. The calculated variation of lift-drag ratio with Reynolds number, with laminar flow assumed, is given in figure 14 for this configuration with the design Mach number of 5. The experimental value of the lift-drag ratio, obtained at a Reynolds number based on body length of 2.5×10^6 in the Ames 10- by 14-inch tunnel, is, as shown, 6.35. This value agrees fairly well with the calculated value of 6.81. At flight Reynolds number, lift-drag ratios of the order of 10 should thus be obtainable. Even with such a high lift-drag ratio, it is important to note that the largest component of the drag is skin friction. It is clear, then, that research should be directed to find ways to reduce the magnitude of the friction drag. Perhaps, for example, the use of transpiration cooling through porous surfaces, which theory indicates (ref. 8) will result in a reduction of the average friction coefficient, should be considered.

REFERENCES

1. Sänger, Eugen: Raketen-Flugtechnik. R. Aldenbourg (Berlin), 1953.

2. Sänger, Eugen, and Bredt, J.: A Rocket Drive for Long Range Bombers. Translation CGD-32, Tech. Information Branch, Bur. Aero., Navy Dept., Aug. 1944.

3. Eggers, Alfred J., Jr., Allen, H. Julian, and Neice, Stanford E.: A Comparative Analysis of the Performance of Long-Range Hypervelocity Vehicles. NACA RM A54L10, 1955.

4. Rutowski, Edward S.: Energy Approach to the General Aircraft Propulsion Problem. Jour. Aero. Sci., vol. 21, no. 3, Mar. 1954, pp. 187-195.

5. Allen, H. Julian, and Eggers, A. J., Jr.: A Study of the Motion and Aerodynamic Heating of Missiles Entering the Earth's Atmosphere at High Supersonic Speeds. NACA RM A53D28, 1953.

6. Eggers, A. J., Jr., Hansen, C. Frederick, and Cunningham, Bernard E.: Theoretical and Experimental Investigation of the Effect of Yaw on Heat Transfer to Circular Cylinders in Hypersonic Flow. NACA RM A55E02, 1955.

7. Seiff, Alvin, and Allen, H. Julian: Some Aspects of the Design of Hypersonic Boost-Glide Aircraft. NACA RM A55E26, 1955.

8. Rubesin, Morris W.: An Analytical Estimation of the Effect of Transpiration Cooling on the Heat-Transfer and Skin-Friction Characteristics of a Compressible, Turbulent Boundary Layer. NACA TN 3341, 1954.

~~CONFIDENTIAL~~

HYPERSONIC VEHICLES

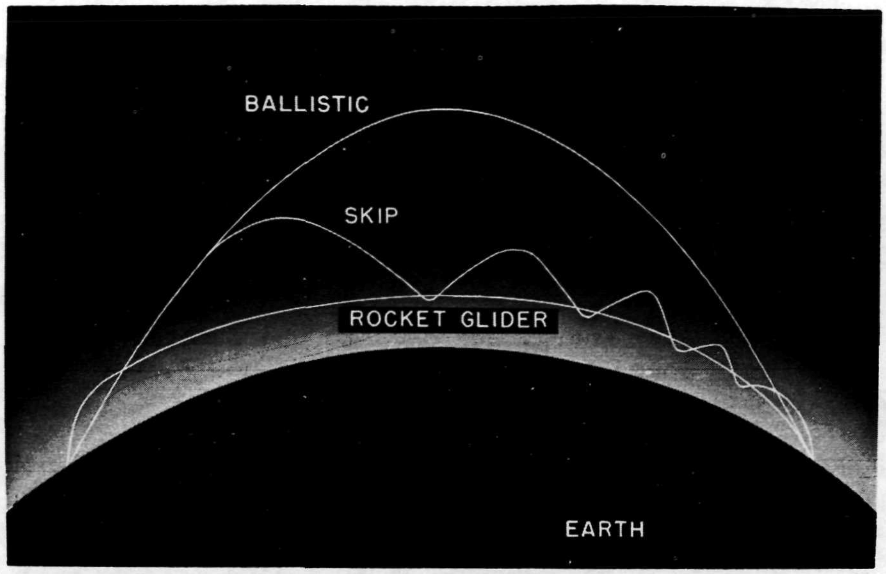

Figure 1

PROPULSIVE RANGE FOR VARIOUS POWER PLANTS

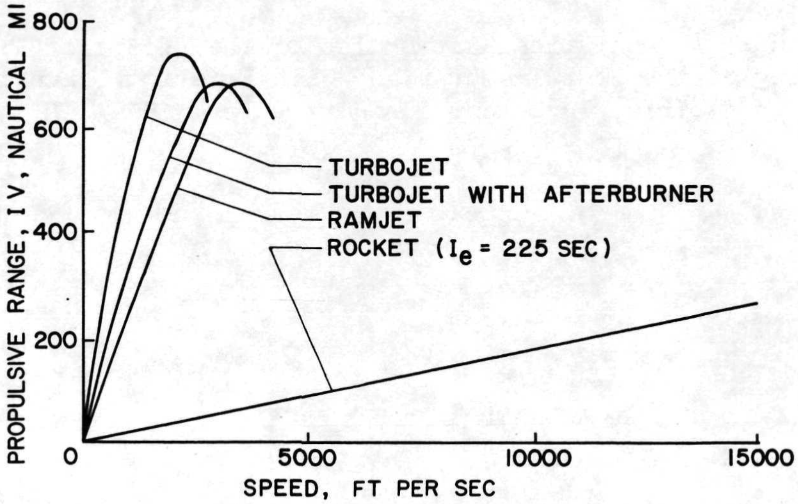

Figure 2

~~CONFIDENTIAL~~

EFFECTIVE LIFT-DRAG RATIO OF HIGH-SPEED VEHICLES: L/D = 2

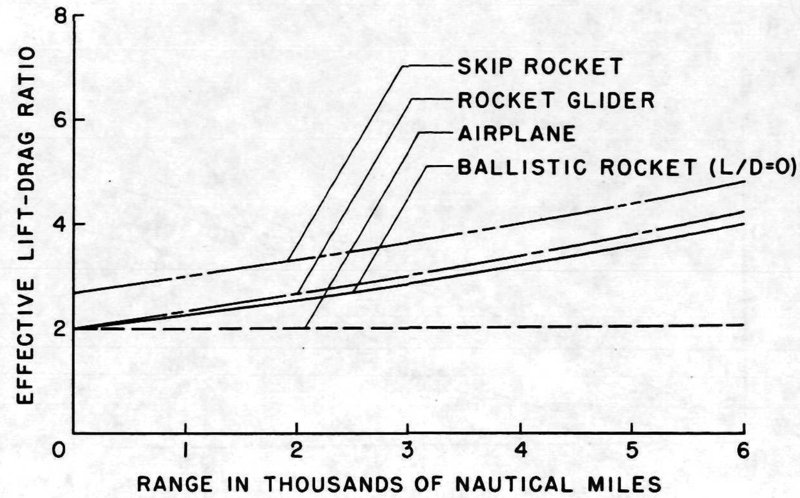

Figure 3(a)

EFFECTIVE LIFT-DRAG RATIOS OF HIGH-SPEED VEHICLES: L/D = 6

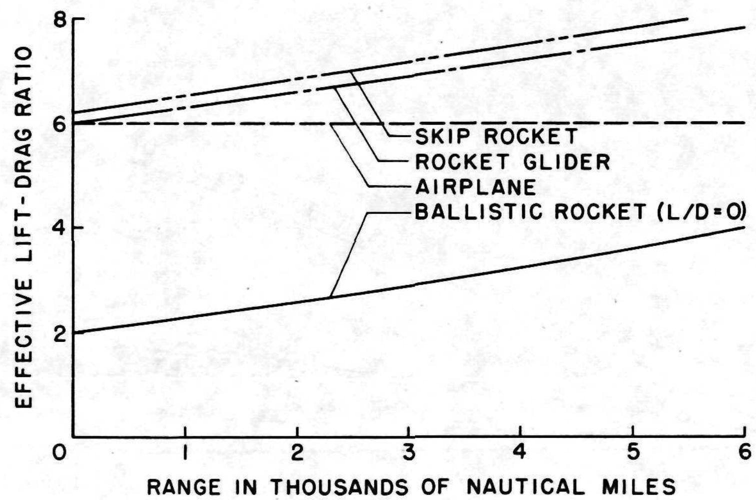

Figure 3(b)

~~CONFIDENTIAL~~

WEIGHT RATIOS FOR HIGH SPEED VEHICLES
L/D = 2

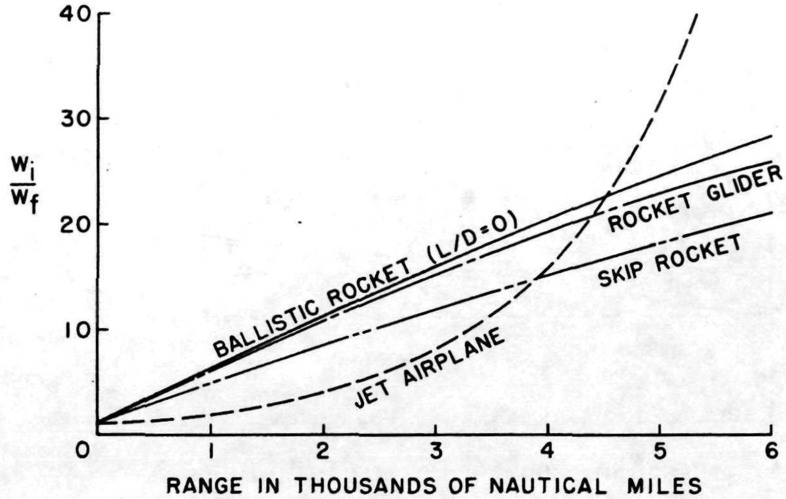

Figure 4(a)

WEIGHT RATIO FOR HIGH SPEED VEHICLES
L/D = 6

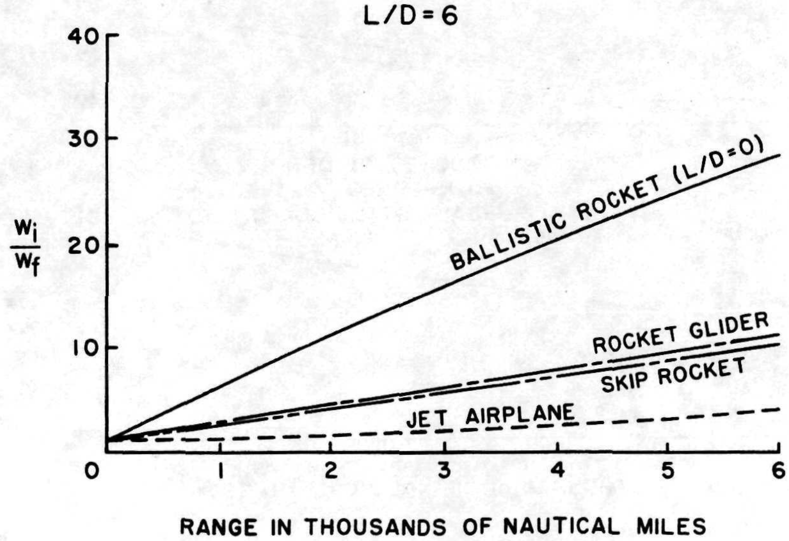

Figure 4(b)

~~CONFIDENTIAL~~

MAXIMUM VALUE OF AVERAGE HEAT RATE

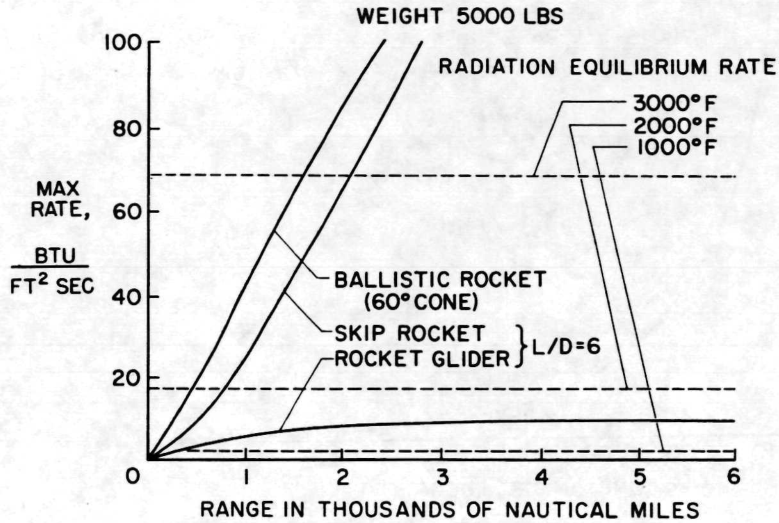

Figure 5

HEAT INPUT TO CONICAL BALLISTIC WARHEAD

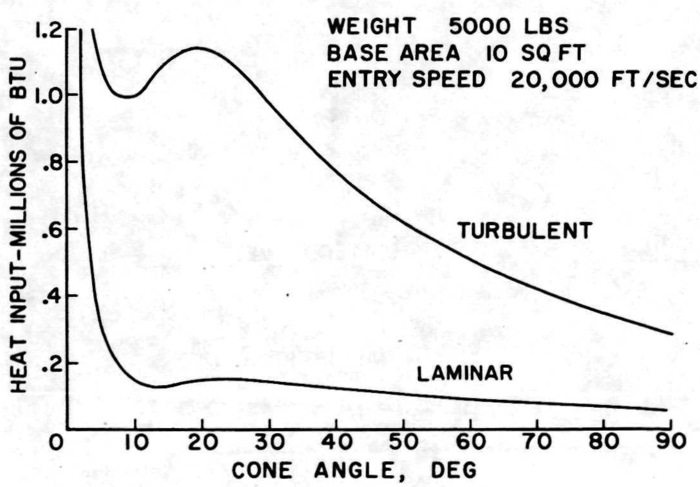

Figure 6

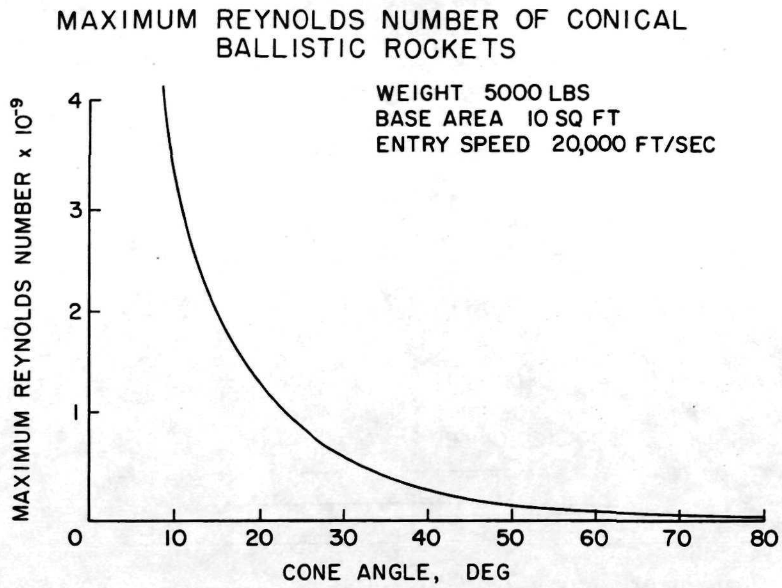

Figure 7

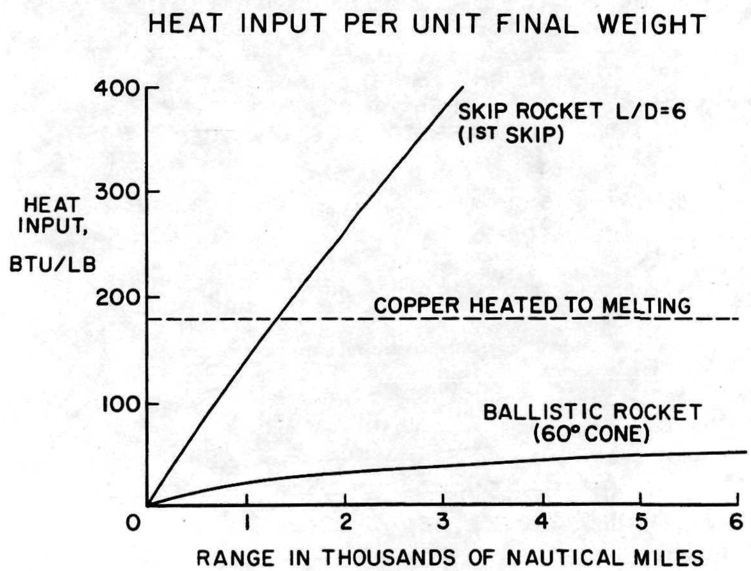

Figure 8

ONE SUGGESTED CONFIGURATION FOR ROCKET GLIDER

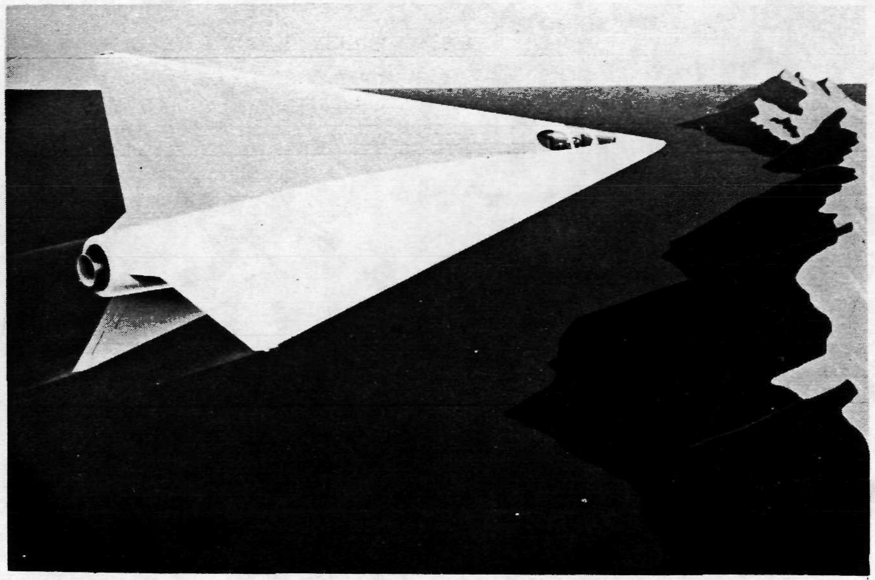

Figure 9

REYNOLDS NUMBER VARIATION WITH SPEED
ROCKET GLIDER (L/D=6, LENGTH=50FT)

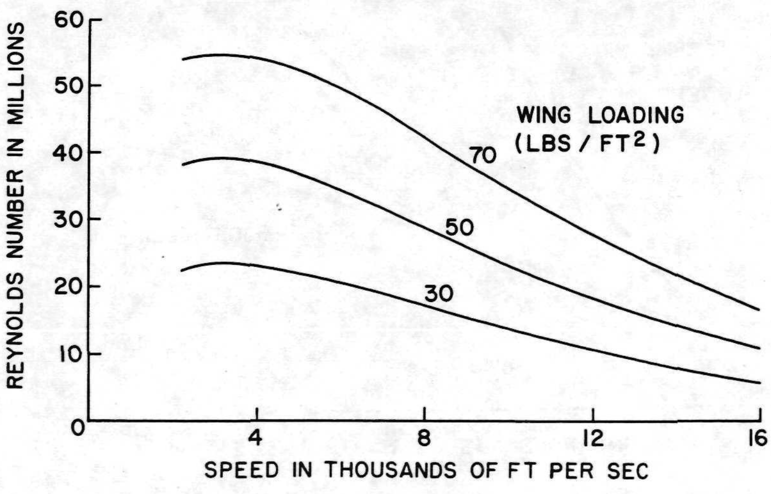

Figure 10

EFFECT OF LEADING-EDGE RADIUS FOR BOOST-SUSTAIN GLIDER

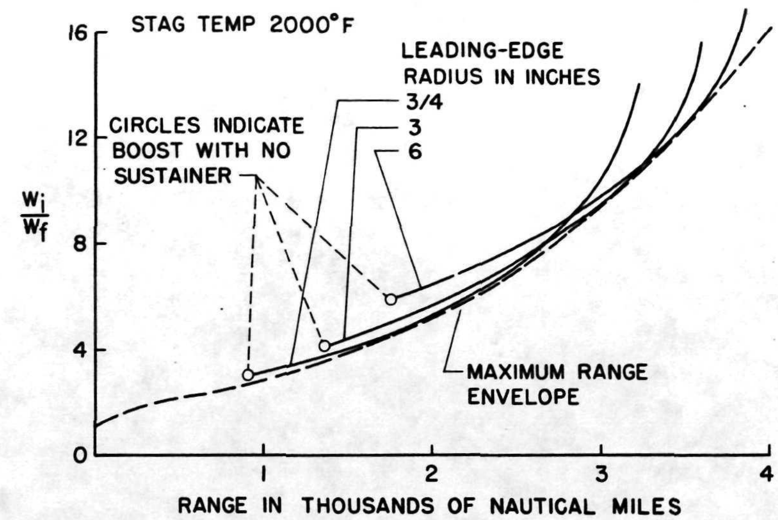

Figure 11

WEIGHT RATIOS FOR RADIATION-COOLED GLIDER

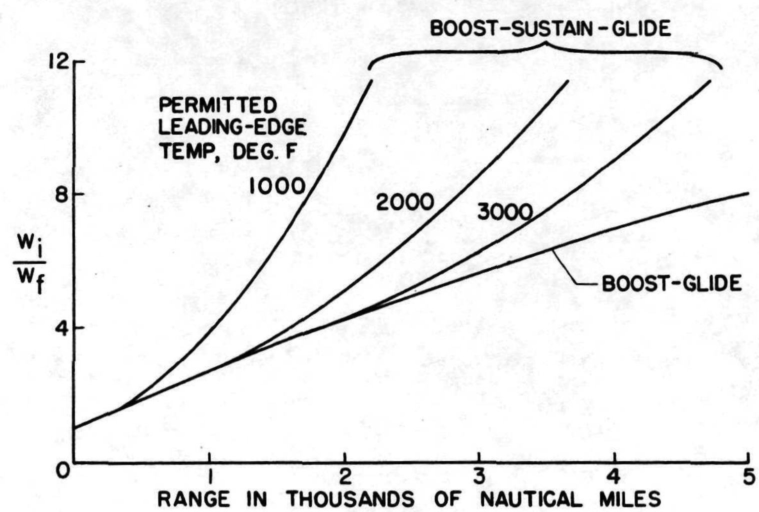

Figure 12

ROCKET GLIDER FOR HIGH LIFT-DRAG RATIO

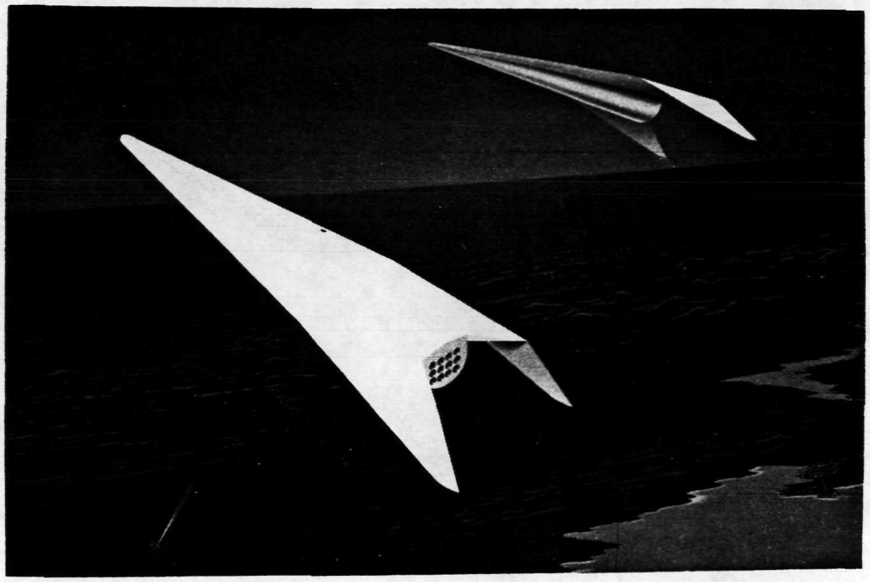

Figure 13

LIFT-DRAG RATIOS FOR A ROCKET GLIDER
AT MACH NUMBER 5

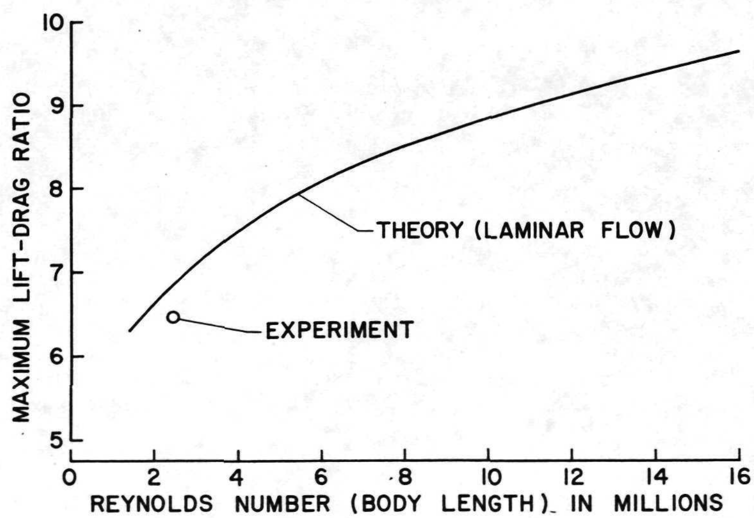

Figure 14

[redacted]

FACTORS AFFECTING THE MAXIMUM LIFT-DRAG RATIO

AT HIGH SUPERSONIC SPEEDS

By Charles H. McLellan and Robert W. Dunning

Langley Aeronautical Laboratory

SUMMARY

A study of the factors affecting the maximum lift-drag ratio $(L/D)_{MAX}$ has been conducted in an effort to determine how to obtain high aerodynamic $(L/D)_{MAX}$ values at high supersonic Mach numbers. Wings, bodies, and wing-body combinations are discussed, and some of the effects of leading-edge heating on wing geometry and $(L/D)_{MAX}$ are included. By utilization of as high a Reynolds number laminar flow as possible, low-aspect-ratio wings, favorable interference effects, and the use of more radical configurations, it appears hopeful that high $(L/D)_{MAX}$ values may be achieved at the high supersonic Mach numbers.

INTRODUCTION

At high supersonic speeds the importance of maintaining high values of maximum lift-drag ratio $(L/D)_{MAX}$ in long-range vehicles is essentially the same as at low speeds (refs. 1, 2, and 3). The range is primarily a function of the lift-drag ratio and the ratio of fuel weight to gross weight. At very high speeds, the centrifugal forces also affect the range; however, in the present paper only the aerodynamic $(L/D)_{MAX}$ will be considered. As at low speeds, $(L/D)_{MAX}$ should not be increased at the expense of excessive structural weight. Compared with the lower speed ranges, the problem of obtaining high lift-drag ratios at very high supersonic speeds is a relatively unexplored field requiring much further investigation. It is the purpose of this paper to examine some of the more important factors affecting $(L/D)_{MAX}$.

SYMBOLS

R	Reynolds number
M	Mach number
L/D	lift-drag ratio
W/S	wing loading, lb/sq ft
S	wing area
T	temperature
t/c	ratio of wing thickness to chord
A	wing aspect ratio
ϵ	emissivity
Λ	leading-edge sweepback, deg
q	heat transfer, Btu/hr

Subscripts:

MAX	maximum
L.E.	leading edge
W	wing

DISCUSSION

The skin friction, and, therefore, Reynolds number, is a major factor and will be discussed first. Figure 1 shows the probable range of Reynolds number per foot for high-speed configurations operating at $(L/D)_{MAX}$. The upper limit is defined by a high wing loading and a high aerodynamic $(L/D)_{MAX}$, whereas the lower limit is defined by a low wing loading and a low $(L/D)_{MAX}$. In figure 1 this upper limit has been chosen arbitrarily as having an $(L/D)_{MAX}$ of 6 and a wing loading of 100 pounds per square foot, and the lower limit as having an $(L/D)_{MAX}$ of 2 and a wing loading of 10 pounds per square foot. With moderate wing loadings,

$(L/D)_{MAX}$ will be reached at altitudes between 100,000 and 200,000 feet for the high supersonic speeds. At these altitudes the Reynolds number will be relatively low (ref. 4) (on the order of 1×10^6 to 10×10^6 on a 10-foot chord) and, on the basis of current research data, it appears hopeful that laminar flow can be maintained over much of the configuration (refs. 5 and 6 and unpublished data obtained in the Langley 11-inch hypersonic tunnel and in the Ames free-flight tunnel).

Therefore, the effect of Reynolds number on $(L/D)_{MAX}$ as the Mach number is increased is presented in figure 2 for the simplest possible case of the two-dimensional flat plate. With a laminar boundary layer at a Reynolds number of 1×10^6, $(L/D)_{MAX}$ decreases with Mach number until it reaches a nearly constant value of about 7 at Mach numbers of 10 and above. For a Reynolds number of 10×10^6, the shape of the curve is the same as at 1×10^6; however, $(L/D)_{MAX}$ is higher, being on the order of 12 at Mach numbers above 10. As expected, the turbulent boundary layer gives values well below those of the laminar boundary layer for the lower Mach numbers; however, at the very high Mach numbers, $(L/D)_{MAX}$ is approaching the laminar values. A 10° cone and an infinite cylinder at a Reynolds number of 1×10^6, which are shown for comparison with the flat plate, have relatively low values of $(L/D)_{MAX}$, and it becomes obvious that the wing should be as big as practical with respect to the body to obtain the highest $(L/D)_{MAX}$. In addition, the Reynolds number should be as high as possible without causing boundary-layer transition.

Of course, a more realistic evaluation of wings requires consideration of the effects of thickness. At high Mach numbers, a flat lower surface and a thin nose angle are desirable (ref. 7), and this can best be obtained in a wedge airfoil. Figure 3 shows the calculated effect of thickness on wedge airfoil sections of infinite-span wings at a Mach number of 7. At the low thicknesses, the upper surface is shielded from the free-stream flow; and as the thickness increased to about 0.07 at $R = 1 \times 10^6$ and 0.04 at $R = 1 \times 10^7$, the upper surface becomes parallel to the free stream at $(L/D)_{MAX}$. Beyond this point, the upper surface is exposed to the stream. It is sometimes supposed that, at high supersonic Mach numbers, thickness can be added to the upper surface in the shielded region without affecting $(L/D)_{MAX}$. It can be seen that even partially filling in the shielded area results in loss in $(L/D)_{MAX}$ at this Mach number. Similar effects can be anticipated for other wing sections.

This is only one of the factors affecting $(L/D)_{MAX}$. As pointed out previously, the Reynolds number should be as great as is consistent with the maintenance of laminar flow. Early in the design of a configuration the wing area and operating conditions will probably be fixed. With a fixed-wing area, the Reynolds number can be increased by decreasing the aspect ratio. Figure 4 shows the variation of $(L/D)_{MAX}$ with aspect ratio for a constant-area rectangular wing with a sharp-leading-edge symmetrical double-wedge section at a Mach number of 7. As the aspect ratio decreases, the wing chord and, consequently, the Reynolds number increase, and the skin friction decreases. Without tip effects, $(L/D)_{MAX}$ would continually increase with decreasing aspect ratio. The tip losses, however, reduce $(L/D)_{MAX}$ more at the low aspect ratios so that, theoretically, a maximum is reached in this particular case at an aspect ratio of about 0.6. The two experimental points appear to agree with this trend even though the section was slightly different for the low-aspect-ratio wing. (A 5-percent-thick symmetrical double-wedge section would be slightly lower.) At higher Mach numbers, the optimum aspect ratios would be smaller. The decrease in aspect ratio will probably reduce the structural thickness requirements and will allow thinner sections to be used, which will increase the values of $(L/D)_{MAX}$ at the lower aspect ratios.

A similar effect would be expected for triangular plan-form wings. In figure 5, $(L/D)_{MAX}$ at $M = 7$ has been plotted against the aspect ratio for the same airfoil section and constant wing area for a family of triangular wings with a laminar boundary layer. The calculated curve is for the region with attached shock where the lift-curve slope and wave drag are constant (ref. 8); the change in estimated $(L/D)_{MAX}$ results from the change in skin friction.

The experimental points seem to verify the theoretical trend. However, in all the experimental work at this Mach number in the Langley 11-inch hypersonic tunnel, the values of $(L/D)_{MAX}$ are lower than the theoretical ones. Because of the so-called shock—boundary-layer interaction, the experimental minimum drag is considerably greater than the predicted drag. At the Mach number and Reynolds number of this investigation, the boundary layer displaces the flow about the wing (ref. 9), resulting in increased pressure which increases the skin friction for the two-dimensional case by about 20 percent. Higher Reynolds numbers will decrease this effect, whereas higher Mach numbers will increase it. As can be seen from figures 4 and 5, there appears to be little difference either theoretically or experimentally between the rectangular wing and the triangular wing of the same aspect ratio, and it would appear that either low-aspect-ratio rectangular wings or very highly swept triangular wings will give the highest values of $(L/D)_{MAX}$. The sweep should not be increased or the aspect ratio decreased to the point where the Reynolds number becomes so high that transition occurs on the wing. Theoretical and experimental results (refs. 10 and 11) indicate that transition occurs earlier with a swept leading edge than with an unswept leading edge. Therefore, higher Reynolds number laminar flow can probably be obtained on rectangular wings than on triangular ones. Furthermore, for the same average Reynolds number, a triangular wing will have a root-chord Reynolds number twice that of the rectangular wing so that transition would be expected at a lower average Reynolds number on the triangular wing. It should also be noted that $(L/D)_{MAX}$ could probably be improved by removing some of the low Reynolds number high-drag tip.

In the high Mach number range, the problem of aerodynamic heating of the leading edge will also enter into the choice of the wing plan form. The highly swept wings have an advantage in that the heat transfer per unit area to a blunt leading edge decreases with leading-edge sweep (refs. 12 and 13) and allows the use of smaller leading-edge diameters. Furthermore, as is well known, the drag of a blunt leading edge decreases with sweep angle (refs. 14 and 15). Therefore, the use of sweep would be expected to decrease not only the required leading-edge diameter but also the loss in $(L/D)_{MAX}$ due to a given leading-edge bluntness. If radiant cooling is used, the diameter required is a function of both Mach number and sweep angle. Figure 6 presents the diameter required for an arbitrary leading-edge equilibrium temperature of 2,500° F with a surface ϵ of 0.8 and at altitudes of interest at the high Mach numbers. Materials are available for use as leading edges which can be operated at this and possibly even greater temperatures. Below $M = 6$, the recovery temperature is below the 2,500° F limit; and a sharp leading edge could be used with this temperature limit and sweep would not be necessary from the standpoint of leading-edge heating. With small leading-edge sweeps, the diameter required increases very rapidly for both the 100,000- and 150,000-foot altitudes as the Mach number is increased above 6. The large sweep angles greatly decrease the required diameter; however, even with large sweep angles, the diameters become very large, on the order of several inches at high Mach numbers, and some other means of cooling may be required.

Since blunted leading edges may be required at the higher Mach numbers, it is of interest to examine their effects on $(L/D)_{MAX}$. As an illustration, figure 7 has been prepared for a 400-square-foot wing at an altitude of 120,000 feet when flying at a Mach number of 11. At lower Mach numbers, the curves are similar to this one. Increasing the sweep increases $(L/D)_{MAX}$ particularly for the large leading-edge diameters. The aspect-ratio-0.3 rectangular wing is about the same as the 60° triangular wing. Except at the very small leading-edge diameters, the 70° swept wing has the highest $(L/D)_{MAX}$.

Since the leading-edge diameter required for radiant cooling decreases rapidly with high sweep angles, the high sweep angles would be preferred for the radiant-cooling case. High sweep, however, may not be necessary or even desirable if some means of forced cooling, such as transpiration cooling, is employed, since the total heat to the leading edge is important. This is illustrated in the following table which presents effects of wing plan form on $(L/D)_{MAX}$ with both forced and radiant cooling for the same conditions as figure 7 for laminar boundary layer and $M = 11$, $S = 400$ square feet, and an altitude of 120,000 feet:

	Forced cooling, $T_{L.E.} = 212^{\circ}$ F[a]			Radiant cooling, $T_{L.E.} = 2{,}500^{\circ}$ F[a], $\epsilon = 0.8$[a]	
	 A = 0.3	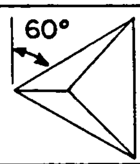	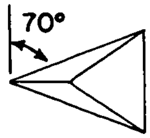	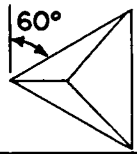	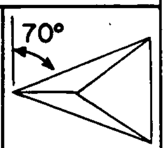
L.E. diam., in.	[a]0.5	[a]0.5	[a]0.5	6.7	3.0
q, Btu $\times 10^6$/hr	.79	2.05	1.61	5.64	2.98
$(L/D)_{MAX}$	6.4	6.3	7.0	2.9	5.4

[a]Assumed value.

The leading-edge diameter should be kept as small as practical with a forced cooling system. For this analysis, a 1/2-inch diameter has been assumed. The rectangular wing with forced cooling would have an $(L/D)_{MAX}$ value of 6.5 and would have a heat transfer to the leading edge of less than 1 million Btu's per hour. This could be absorbed by evaporating less than 1,000 pounds of water per hour. The 60° wing would have about the same $(L/D)_{MAX}$, but because of its greater wing span would have nearly three times the amount of heat to be absorbed. The 70° wing would have a higher $(L/D)_{MAX}$ but would have over twice the amount of heat to be absorbed as the rectangular wing. Furthermore, the cooling system would be spread out over a long leading edge requiring more plumbing. Therefore, for forced cooling, the very low-aspect-ratio rectangular wings appear desirable.

For the radiant-cooled leading edge, $(L/D)_{MAX}$ would be very low on the 60° wing because of the large leading edge required. Even the 70° wing requires a 3-inch leading-edge diameter and has a value of $(L/D)_{MAX}$ of only 5.4. The loss in $(L/D)_{MAX}$ probably would not be quite as great in an actual application since the wings with low $(L/D)_{MAX}$ should be operated at a higher altitude than for those with high $(L/D)_{MAX}$. However, this is a secondary effect which has been neglected. Still larger sweep angles would probably be desirable with radiant cooling.

From the foregoing discussion, both the highly swept triangular wings and the low-aspect-ratio rectangular wings begin to appear like thin bodies, suggesting that the bodies should probably be shaped somewhat like thick wings. Bodies, however, have been discussed extensively in the past (for example, refs. 16 and 17) and will, therefore, be discussed only briefly. Figure 8 shows the general trend of increasing $(L/D)_{MAX}$ as the bodies take on more of a wing-like shape. The bodies in order of the increasing $(L/D)_{MAX}$ are the 20° cone cylinder, the 10° cone cylinder, a drooped-nose flat-bottomed model with the upper surface of the nose approximately filling in the lee side at $(L/D)_{MAX}$, and the upper body in which the aspect ratio has been doubled. These bodies are discussed more extensively in reference 16. The aspect ratios are below the optimum for the flat-bottomed bodies, and a considerable penalty is being paid for filling in the lee side. A thin wing with nearly the same plan form and Reynolds number had an $(L/D)_{MAX}$ of about 5.4 as compared with 4.4 for the best body in this figure.

The final object is to develop complete configurations with high $(L/D)_{MAX}$. At the high supersonic Mach numbers, configurations are still in the early stages of development. In figure 9, the estimated $(L/D)_{MAX}$ for two complete configurations is shown. These configurations, with the same body size, have rounded leading edges for radiant cooling for Mach numbers up to about 7 and provisions for obtaining stability. The calculations have been made for laminar flow at the altitude required for the given wing loadings and the lift coefficients at $(L/D)_{MAX}$.

The more or less conventional configuration with a trapezoidal wing shows the values of $(L/D)_{MAX}$ that can be expected from present-type aircraft. It utilizes wedge-shaped tail surfaces and can be expected to have good stability characteristics throughout the speed range as well as having a landing speed of only 150 knots. The value of $(L/D)_{MAX}$ with all laminar flow varies from 5 to about 4. With this wing loading of 50 pounds per square foot, $(L/D)_{MAX}$ was obtained at a Reynolds number of only 2×10^{6} based on the mean aerodynamic chord, and laminar flow is likely over much of the configuration.

The three-wing configuration proposed in reference 3 to obtain high $(L/D)_{MAX}$ at high Mach numbers is also shown in figure 9. This configuration with laminar flow has an estimated value of $(L/D)_{MAX}$ between 5 and 6.

This relatively high value of $(L/D)_{MAX}$ results largely from the high wing area with respect to the body area, and to the high Reynolds number. The high sweep decreases the leading-edge drag, but the large surface area of the nonlifting upper wing increases the skin-friction drag of the configuration. The negative dihedral is included for the low-speed stability and decreases the value of $(L/D)_{MAX}$ according to unpublished wind-tunnel tests at Mach numbers from 3 to 6 in the Ames 10- by 14-inch tunnel.

In order to obtain higher values of $(L/D)_{MAX}$, more radical configurations should be considered. One possibility is to combine the body and wing features into one. Figure 10 shows two such configurations. No provisions have been made for obtaining stability or cooling of the leading edge on these configurations. The volume normally obtained in a body is obtained by filling in part of the area above the lower surface on these configurations. A rectangular wedge-shaped configuration of aspect ratio 0.4 would have an estimated value of $(L/D)_{MAX}$ of 7 at $M = 3$ and of nearly 10 at $M = 12$. The Reynolds numbers are very high, 30×10^6 at $M = 10$, and transition might occur. The increased skin friction obtained by assuming fully turbulent flow reduced $(L/D)_{MAX}$ to between 6 and 7.

The configuration with a triangular plan form with clipped tips had the same body volume and wing area as the rectangular configuration. The value of $(L/D)_{MAX}$ with laminar flow was about the same for the two configurations. As pointed out previously, transition is more likely on the triangular-plan-form configurations at a given Reynolds number than with the rectangular one.

One factor involved in configuration development which needs to be investigated is that of interference effects between wings and bodies. Ferri, Clark, and Casaccio (ref. 18) have proposed the use of wedges under wings to generate a high-pressure region and thereby increase the lift. If a configuration can be designed so that existing high-pressure regions, such as that emanating from a body nose, are located under the wing, it should be possible to obtain increased values of $(L/D)_{MAX}$ as a result of the interference effects.

Figure 11 shows the results of some unpublished calculations by A. J. Eggers, Jr., and Clarence A. Syvertson of the Ames Aeronautical Laboratory for a highly swept zero-thickness wing in combination with a half-conical body. This curve shows $(L/D)_{MAX}$ for the wing alone, body under the wing, and body above the wing for laminar flow at a Mach number of 7. Putting the cone body on the bottom of the wing entailed much smaller losses than putting the cone body on the top because of the more favorable interference effects of the high pressure from the low body on the wing. Preliminary unpublished experimental results seem to verify this trend. These interference effects are obviously very important and should be investigated further.

CONCLUDING REMARKS

In general, the study of how to obtain high aerodynamic values of maximum lift-drag ratio $(L/D)_{MAX}$ has indicated that configurations should be operated at as high a Reynolds number as possible, providing that the boundary layer remains laminar. Low-aspect-ratio rectangular wings appear to be best when small leading-edge diameters can be used as with transpiration cooling. When radiant cooling of the leading edge is used, a highly swept wing may be desirable. By utilization of favorable interference effects and the use of the more radical configurations, it appears hopeful that high values of $(L/D)_{MAX}$ may be achieved at the high supersonic Mach numbers.

REFERENCES

1. Sänger, Eugen: Raketen-Flugtechnik. R. Aldenbourg (Berlin), 1933.

2. Sänger, E., and Bredt, J.: A Rocket Drive for Long Range Bombers. Translation CGD-32, Tech. Information Branch, Bur. Aero., Navy Dept., Aug. 1944.

3. Seiff, Alvin, and Allen, H. Julian: Some Aspects of the Design of Hypersonic Boost-Glide Aircraft. NACA RM A55E26, 1955.

4. The Rocket Panel: Pressures, Densities, and Temperatures in the Upper Atmosphere. Phys. Rev., vol. 88, no. 5, Dec. 1, 1952, pp. 1027-1032.

5. Korkegi, R. H.: Transition Studies and Skin Friction Measurements on an Insulated Flat Plate at a Hypersonic Mach Number. Memo. No. 17 (Contract No. DA-04-495-Ord-19), GALCIT, July 15, 1954.

6. Jedlicka, James R., Wilkins, Max E., and Seiff, Alvin: Experimental Determination of Boundary-Layer Transition on a Body of Revolution at $M = 3.5$. NACA TN 3342, 1954.

7. Chapman, Dean R.: Reduction of Profile Drag at Supersonic Velocities by the Use of Airfoil Sections Having a Blunt Trailing Edge. NACA RM A9H11, 1949.

8. Bertram, Mitchel H., and McCauley, William D.: An Investigation of the Aerodynamic Characteristics of Thin Delta Wings With a Symmetrical Double-Wedge Section at a Mach Number of 6.9. NACA RM L55B14, 1955.

9. Bertram, Mitchel H.: An Approximate Method for Determining the Displacement Effects and Viscous Drag of Laminar Boundary Layers in Two-Dimensional Hypersonic Flow. NACA TN 2773, 1952.

10. Stuart, J. T.: The Basic Theory of the Stability of Three-Dimensional Boundary Layers. Rep. No. F.M. 1899, British N.P.L. (Rep. No. 15,904, A.R.C.), May 13, 1953.

11. Dunning, Robert W., and Ulmann, Edward F.: Effects of Sweep and Angle of Attack on Boundary-Layer Transition on Wings at Mach Number 4.04. NACA TN 3473, 1955.

12. Feller, William V.: Investigation of Equilibrium Temperatures and Average Laminar Heat-Transfer Coefficients for the Front Half of Swept Circular Cylinders at a Mach Number of 6.9. NACA RM L55F08a, 1955.

13. Eggers, A. J., Jr., Hansen, C. Frederick, and Cunningham, Bernard E.: Theoretical and Experimental Investigation of the Effect of Yaw on Heat Transfer to Circular Cylinders in Hypersonic Flow. NACA RM A55E02, 1955.

14. Penland, Jim A.: Aerodynamic Characteristics of a Circular Cylinder at Mach Number 6.86 and Angles of Attack Up to 90°. NACA RM L54A14, 1954.

15. Jones, Robert T.: Effects of Sweep-Back on Boundary Layer and Separation. NACA Rep. 884, 1947. (Supersedes NACA TN 1402.)

16. Resnikoff, Meyer M.: Optimum Lifting Bodies at High Supersonic Airspeeds. NACA RM A54B15, 1954.

17. Ridyard, Herbert W.: The Aerodynamic Characteristics of Two Series of Lifting Bodies at Mach Number 6.86. NACA RM L54C15, 1954.

18. Ferri, Antonio, Clarke, Joseph H., and Casaccio, Anthony: Drag Reduction in Lifting Systems by Advantageous Use of Interference. PIBAL Rep. No. 272 (Contract AF 18(600)-694), May 1955.

PROBABLE AIRPLANE ENVIRONMENT

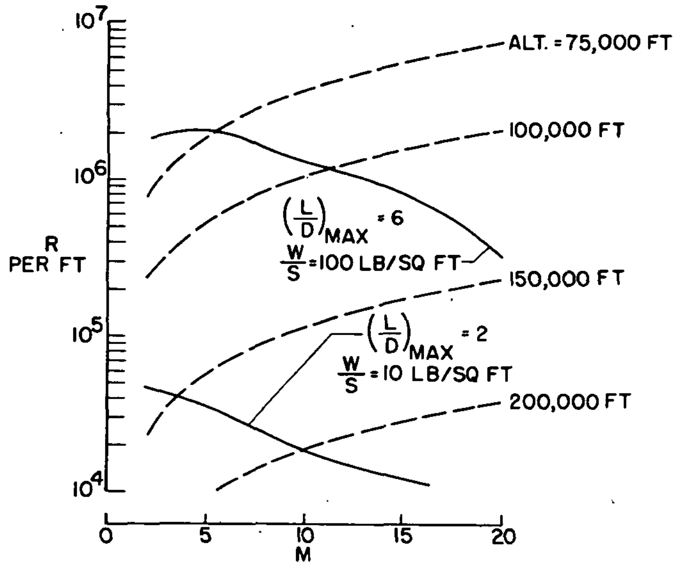

Figure 1

EFFECTS OF REYNOLDS NUMBER AND MACH NUMBER ON $\left(\frac{L}{D}\right)_{MAX}$

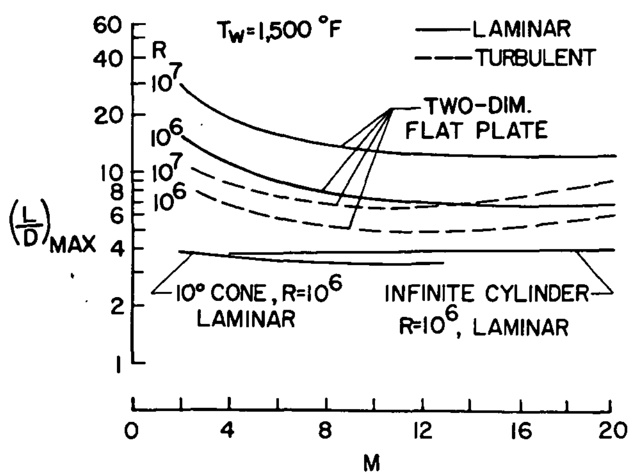

Figure 2

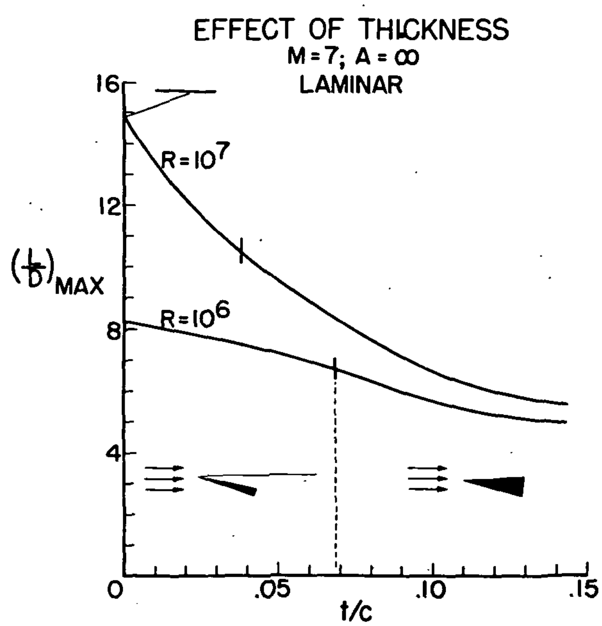

Figure 3

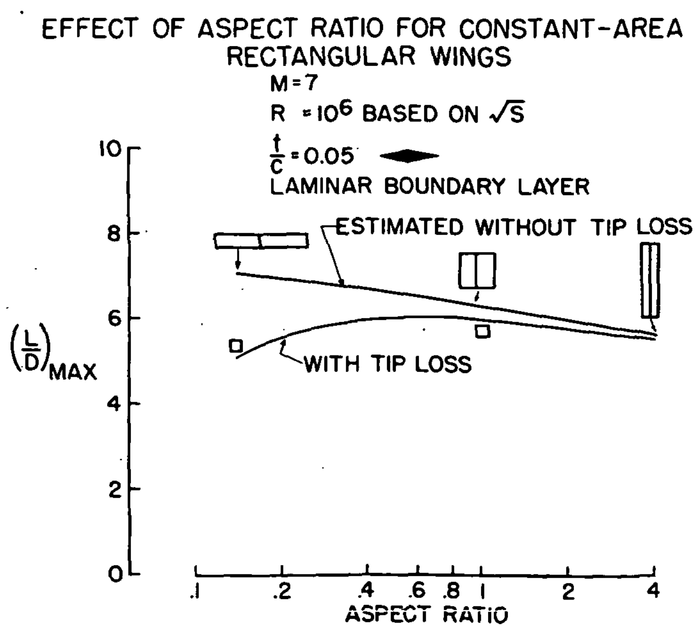

Figure 4

[redacted]

EFFECT OF ASPECT RATIO FOR CONSTANT-AREA TRIANGULAR WINGS

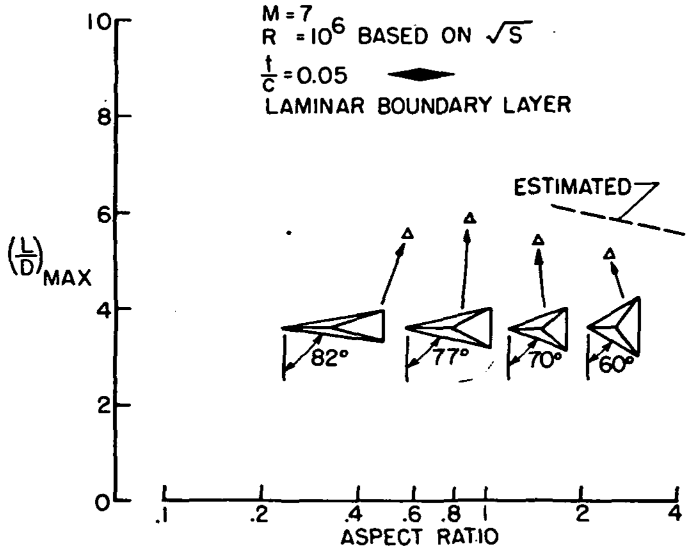

Figure 5

LEADING-EDGE DIAMETER REQUIRED FOR RADIANT COOLING

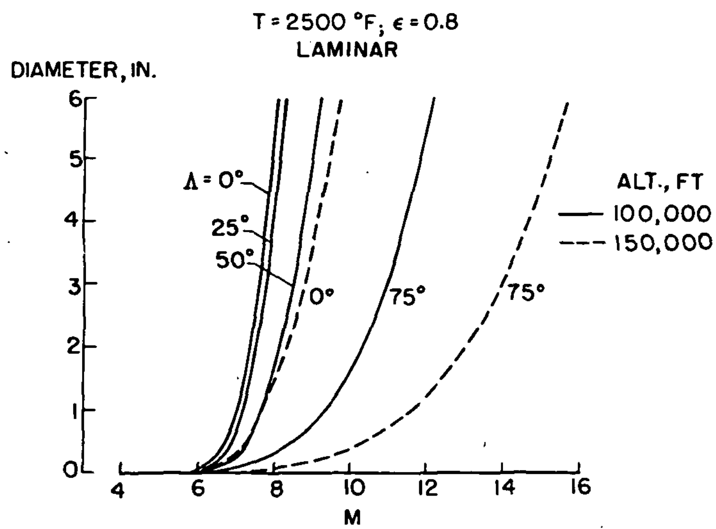

Figure 6

[redacted]

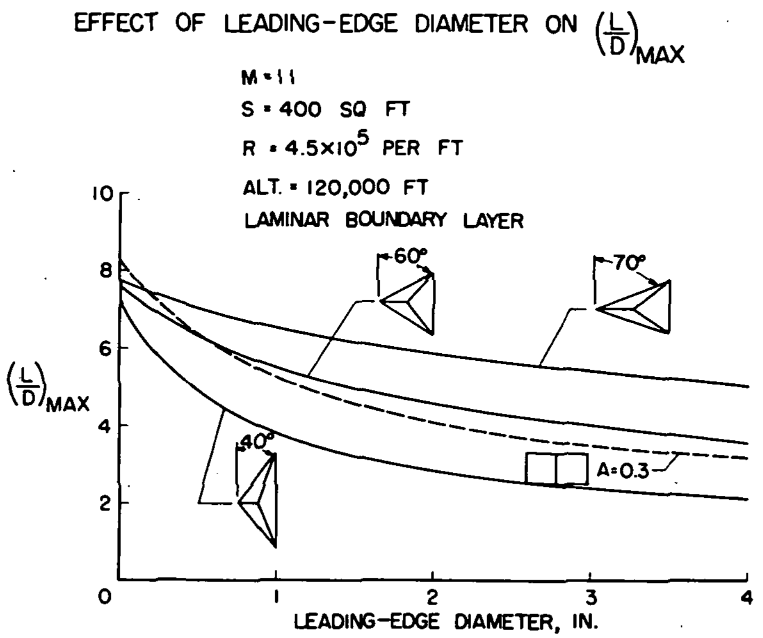

Figure 7

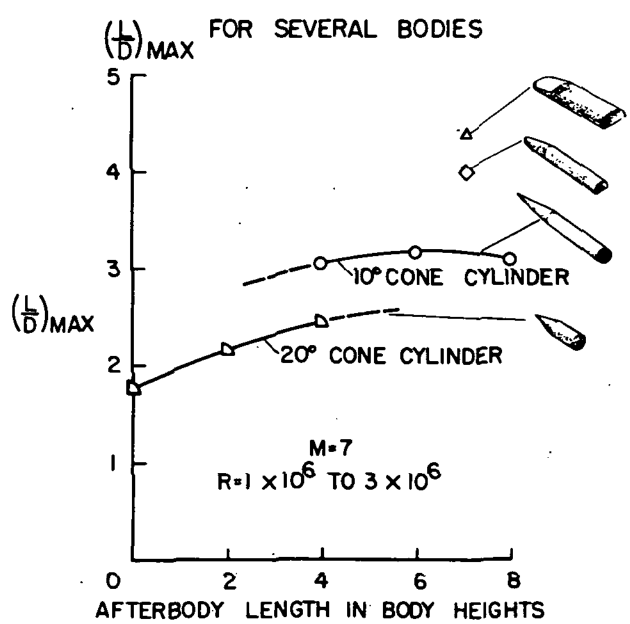

Figure 8

ESTIMATED $\left(\frac{L}{D}\right)_{MAX}$ FOR TWO COMPLETE CONFIGURATIONS

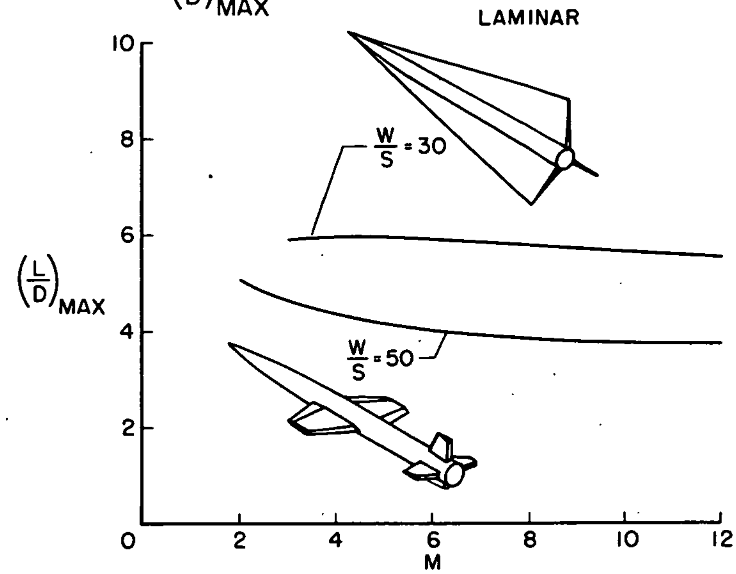

Figure 9

ESTIMATES FOR TWO HIGH $\left(\frac{L}{D}\right)_{MAX}$ CONFIGURATIONS

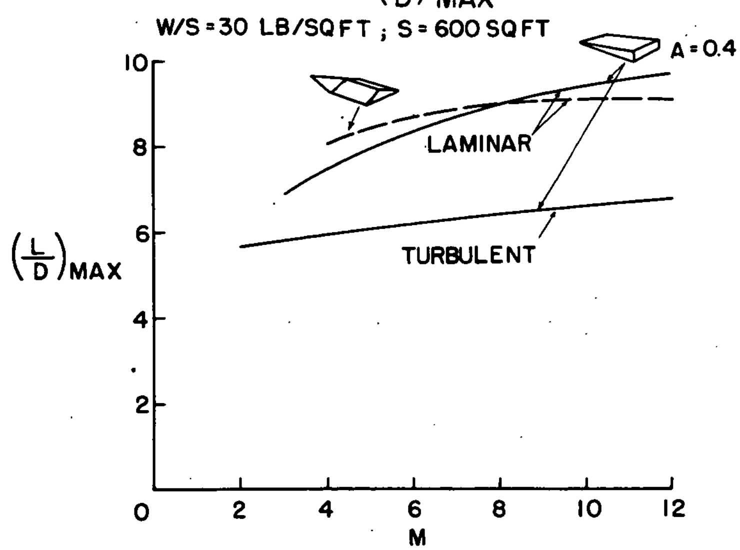

Figure 10

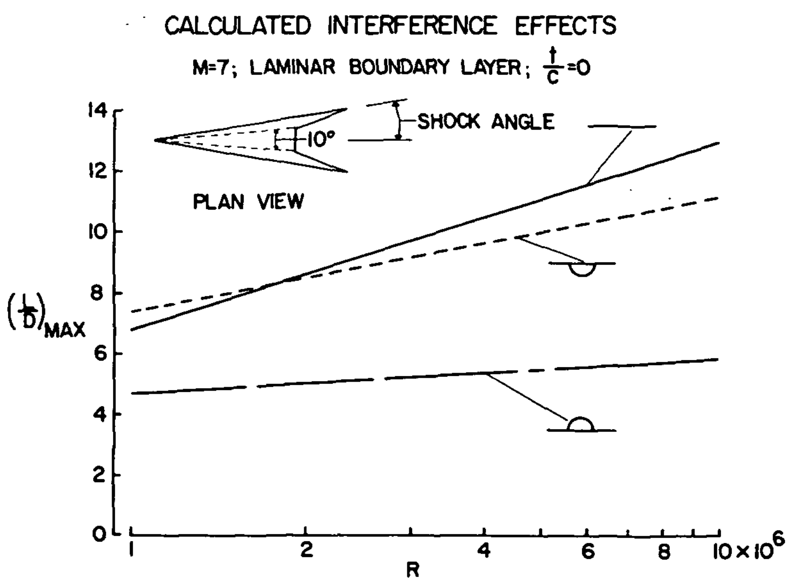
CALCULATED INTERFERENCE EFFECTS
M=7; LAMINAR BOUNDARY LAYER; t/c =0
10°
SHOCK ANGLE
PLAN VIEW
(L/D)MAX
0
2
4
6
8
10
12
14
1
2
4
6
8
10×10^6
R

Figure 11

THE RELATIONSHIP OF AERODYNAMIC HEATING TO AIRFRAME STRUCTURAL PROBLEMS

By Norris F. Dow and Richard R. Heldenfels

Langley Aeronautical Laboratory

The purpose of this paper is to study, from the standpoint of effects induced in the structure and below the 1500° F limit of available airframe materials, how accurately equilibrium temperatures and heat-transfer coefficients need to be known.

Consider first the equilibrium temperature. High equilibrium temperatures reduce structural strength and reduce distortion resistance. Both effects require weight increases. Increases due to loss of strength are indicated in figure 1. In this figure a measure of the weight required for tension (the density divided by the yield stress) is plotted against temperature for the four materials: 2024-T3 aluminum alloy, RC-130A titanium alloy, 17-7PH stainless steel, and Inconel X. For each material, up to some indefinitely defined temperature, the curves show that the weight is not too critically dependent upon the temperature, but the higher temperatures must be accurately known or a substantial weight increase or a higher temperature material must be provided. For example, at 1,000° F, 17-7PH stainless steel might be used, but if the temperature is only 50° to 100° higher, the use of Inconel X may be necessitated to avoid an excessive weight penalty.

These curves indicate that the importance of an accurate knowledge of the temperature increases as the temperature rises. Conversely, below some temperature for each material, the accuracy is relatively unimportant. The latter conclusion, however, may need to be modified if consideration is given to effects other than tension yielding. For example, some materials, particularly the aluminum alloys such as 7075-T6, lose strength with exposure to elevated temperature. Thus, as shown in a plot based on data from references 1 and 2 of weight against temperature for various cumulative lengths of exposure (fig. 2), a small weight penalty is incurred even for only about 3 seconds exposure at 400° F. For an exposure of 1,000 hours, however, twice the weight would be required. Furthermore, the 1,000-hour curve is much steeper and, accordingly, here the temperature needs to be known more accurately. The conclusion is that need for accurate knowledge of temperature increases both with temperature and exposure.

This same conclusion applies for creep in the material. For the airframe which encounters high loads for only a fraction of its lifetime, creep becomes a design criterion only at the higher temperatures, as in the region shown in figure 3 for Inconel X.

Figure 3, based on data from reference 3, gives a measure of the weight to give a 0.2-percent permanent elongation plotted against temperature for various times at temperature and load. As before, the temperature needs to be known more accurately; that is, the curves become steeper as both time and temperature increase.

For transient conditions the problems are somewhat more complex than for the steady-state case. Time is required for the skin to become hot and for the heat to flow into the internal structure, and knowledge of what effect heat-transfer rate has on elevated-temperature structural problems becomes important.

Two cases need to be considered: (1) flights so short that skin temperatures have not even approached equilibrium and maximum thermal-stress conditions are not encountered and (2) flights long enough so that skin temperatures do approach equilibrium.

For the short flights, the values of the heat-transfer coefficient need to be known most accurately in order to determine the maximum temperature attained.

As shown by the curves given in figure 4 for various values of heat-transfer coefficient h at given initial and adiabatic wall temperatures (T_O and T_{AW}, respectively) and at a given heat capacity cwt_S, the change in skin temperature T_S with time τ initially depends directly upon the heat-transfer coefficient. Here, then, as for equilibrium temperatures, the need for accurate heat-transfer coefficients increases as the temperature increases.

When flights are long enough so that the skin approaches its equilibrium temperature and the most severe temperature differentials possible between skin and internal members are encountered, the most severe thermal stresses are induced. For example, consider the case studied in reference 4 of a flight at a 40,000-foot altitude in which the aircraft accelerates at 1g from a Mach number of 0.75 to 3.0, flies at that speed for about 3 minutes, and then decelerates at 1g back to its original speed. (See fig. 5.)

The resulting temperatures induced in typical skin and internal supporting structure are plotted in figure 5 against time. Characteristically, the temperature in the internal member (given by the dashed curve) is less than that in the skin during the heating part of the cycle and higher than that in the skin during the cooling part of the cycle.

The thermal-stress history depends directly upon the time-temperature history. For this case, for example, the peak stresses as calculated for reference 4 and plotted in figure 6 occur at $1\frac{1}{3}$ and 5 minutes after initial acceleration - when the temperature differentials are the greatest.

As has been pointed out by a number of investigators, thermal stresses such as these may produce more or less serious consequences: namely,

(1) If the thermal stresses are great enough, buckling of the skin may be induced during heating, or bucking of the internal members may be induced during cooling, or, as will be discussed later, loss of stiffness of the entire section may be produced.

(2) Due to the cyclic nature of heating, loading, cooling, and unloading, fatigue must be considered. In fact, if the stresses exceed the elastic limit and yielding takes place, residual stresses may be set up which, under certain conditions of heating and cooling, may continue to accumulate from cycle to cycle until fracture occurs.

Clearly, accurate knowledge of such thermal stresses is essential. As is shown in reference 5, the relationship between the accuracy of this knowledge and the accuracy with which the heat-transfer coefficient is known, however, depends upon the parameter plotted as abscissa in figure 7. This parameter incorporates the heat-transfer coefficient h, the length of the internal structural web L, the thermal conductivity k, and the skin thickness t_S; so, for example, large values of the parameter represent large heat-transfer coefficients, deep structural sections of low thermal conductivity, and thin skins. The ordinate for this plot is the ratio of the maximum thermal stress σ_{max} actually produced - that is, the stress when the temperature differential between skin and internal structure is a maximum - to the fictitious extreme thermal stress σ_{ex} which might be produced as in a material of low thermal conductivity at high rates of heat transfer.

This semi-logarithmic plot shows that, for both small and large values of $hL^2/4kt_S$, the maximum thermal stress is insensitive to variations in the heat-transfer coefficient. Even for the intermediate range, the exact value of the heat-transfer coefficient is not too significant; here a change of a factor of 2 in the heat-transfer coefficient, for example, causes only a small change in the thermal stress. In this range, the order of magnitude of the heat-transfer coefficient is needed if the thermal stresses are to be accurately determined, but just the proper order of magnitude is probably good enough. For thick-skinned thin structures, or particularly for thin-skinned deep structures, however, only the maximum temperature attained, not the rate at which is is attained, is important.

The three possibilities - low, intermediate, and high values of the parameter $hL^2/4kt_s$ - are illustrated in figure 8. Three different structural elements are considered: a thick-skin shallow structure of high thermal conductivity, a thin-skin deep structure of low thermal conductivity, and an intermediate case. Plotted against time for each case are the skin temperatures and the temperatures halfway through the structural web. In the first case, as fast as heat is put into the skin, it is conducted down into the web and no appreciable temperature differential results. In the third case, a negligible amount of heat is conducted from the skin to the web by the time the skin has reached its maximum temperature. Here the differential is the equilibrium temperature minus the initial temperature. In the intermediate case, the heat is put into the skin slightly faster than it can be conducted into the web, and so the magnitude of the induced temperature difference may be increased if the heat-transfer coefficient is increased so that the skin is heated more rapidly. In this case, a change in the heat-transfer coefficient may make some difference in the thermal stresses induced in the structure.

For speeds high enough so that thermal radiation reduces the equilibrium temperature below the adiabatic wall temperature, there is essentially a horizontal cutoff to the upper end of the curve in figure 7. The maximum thermal stresses are then primarily a function of the equilibrium temperature rather than the adiabatic wall temperature or the heat-transfer coefficient. Despite the fact that the equilibrium temperature itself depends upon the heat-transfer coefficient even at these higher speeds, approximate values of h are adequate for determining the maximum thermal stresses. As shown in figure 9, the equilibrium temperature depends upon the cube of the adiabatic wall temperature ${T_{AW}}^3$, the emissivity ϵ, the Stephan-Boltzmann constant σ, and inversely on the heat-transfer coefficient h. As shown by the plotted ratio of equilibrium temperature to adiabatic wall temperature T_e/T_{AW}, large changes in heat-transfer coefficient produce only small changes in equilibrium temperatures. Thus, when the maximum thermal stresses depend on the magnitude of the equilibrium temperatures, they are still insensitive to changes in heat-transfer coefficient.

Thermal stresses so far considered represent idealized conditions for simple structural elements. As an example of more complex conditions, consider the problem investigated in reference 6 of the aerodynamic heating of a 3-percent-thick double-wedge section suddenly accelerated to a Mach number of 3 at an altitude of 40,000 feet. A temperature distribution rising to peaks at the leading and trailing edges is produced (see fig. 10), and the most serious condition occurs after 40 seconds because of the induced compression in the leading and trailing edges. These compressive stresses tend to reduce the twisting stiffness of the entire section. The reduction in twisting stiffness with time is plotted in figure 11 as the ratio of GJ for the section to the initial twisting stiffness GJ_0. The magnitude of the reduction depends upon section thickness and Mach number but is essentially independent of heat-transfer coefficient. Changes in heat-transfer coefficient change the time required to achieve the minimum but they do not change the reduction in stiffness appreciably. For a thinner section or a higher Mach number, however, the reduction will be greater than this and may even go to zero - thereby producing buckling of the section.

The relationship between thickness ratio and Mach number which produces torsional buckling is given by the solid line in figure 12, where the ordinate is the thickness ratio and the abscissa is the Mach number. The solid line is essentially correct for either a laminar or turbulent boundary layer (that is, a constant value of h) along the entire chord. Above this line there is no buckling of the section; below the line, the section is buckled.

The dashed line in figure 12 represents the more complicated case caused by an assumed increase of a factor of 10 in heat-transfer coefficient at the midchord of the section because of transition. The dissymmetry of heating actually stiffens up the section so that, for example, a section which would lose all stiffness at a Mach number of 4 with laminar or turbulent flow over the whole chord would not buckle below a Mach number of 5 for this unsymmetrical heating.

Structural effects produced by unequal heating, such as that considered in this example, are many and varied. The magnitude of the structural difficulties, however, is related to the equilibrium temperatures and heat-transfer coefficients in somewhat the same fashion as for the examples cited; hence, from these examples, the general deductions may be made that:

(1) Accurate knowledge of the heat-transfer coefficient is not critical in determining maximum thermal stress and buckling conditions, but the order of magnitude of the heat-transfer coefficient may need to be known.

(2) Complex structural effects may be produced by local changes in the heat-transfer coefficient. These effects are not necessarily harmful, but they may require detailed evaluation.

(3) Accurate knowledge of heat-transfer coefficients is most important for determining temperatures for short, transient heating conditions.

(4) The need for accurate knowledge of temperatures increases as the temperature and the time at temperature increase.

REFERENCES

1. Heimerl, George J., and Inge, John E.: Tensile Properties of 7075-T6 and 2024-T3 Aluminum-Alloy Sheet Heated at Uniform Temperature Rates Under Constant Load. NACA TN 3462, 1955.

2. Anon.: Strength of Metal Aircraft Elements. ANC-5, Munitions Board Aircraft Committee, Dept. of Defense. Revised ed., June 1951.

3. Anon.: Inconel "X" - A High Strength, High Temperature Alloy, Data and Information. The International Nickel Co., Inc., Dev. and Res. Div., Jan. 1949.

4. Heldenfels, Richard R.: Some Elevated Temperature Structural Problems of High-Speed Aircraft. Preprint No. 559, SAE Golden Anniversary Aero. Meeting, Oct. 11-14, 1955.

5. Heldenfels, Richard R.: Some Design Implications of the Effects of Aerodynamic Heating. NACA RM L55F22, 1955.

6. Budiansky, Bernard, and Mayers, J.: Influence of Aerodynamic Heating on the Effective Torsional Stiffness of Thin Wings. (Prospective NACA paper.)

WEIGHT FOR TENSION YIELDING

FIXED EXPOSURE TIME

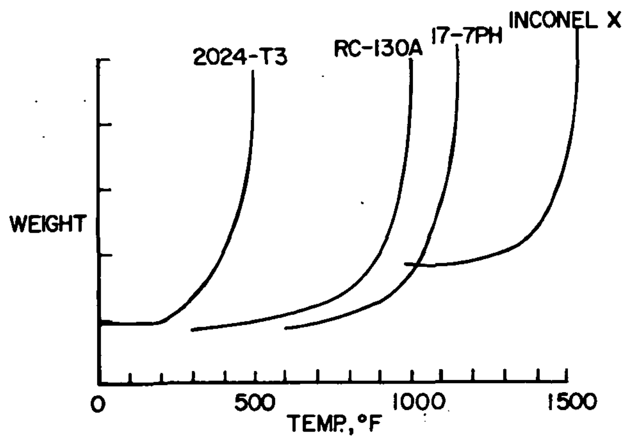

Figure 1

EFFECT OF TEMPERATURE AND TIME ON WEIGHT FOR YIELDING

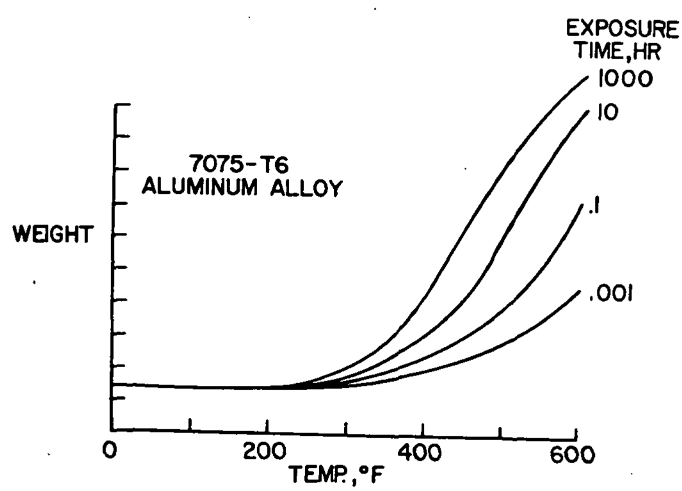

Figure 2

EFFECT OF TEMPERATURE AND TIME ON WEIGHT FOR CREEP
0.2% ELONGATION

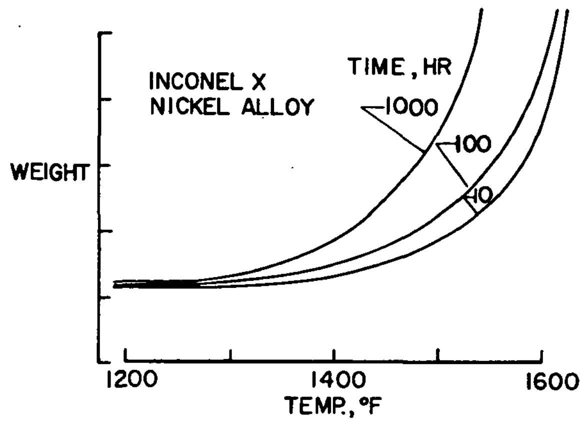

Figure 3

RELATION OF SKIN TEMPERATURE TO HEAT-TRANSFER
COEFFICIENT DURING TRANSIENT HEATING

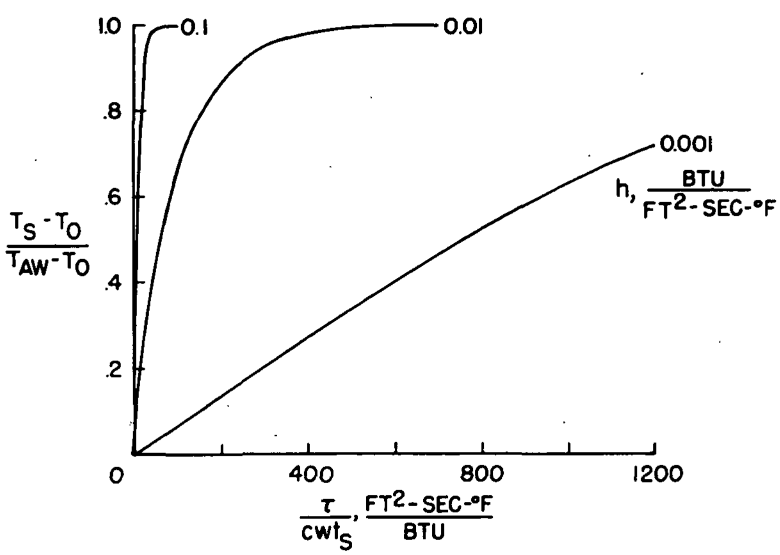

Figure 4

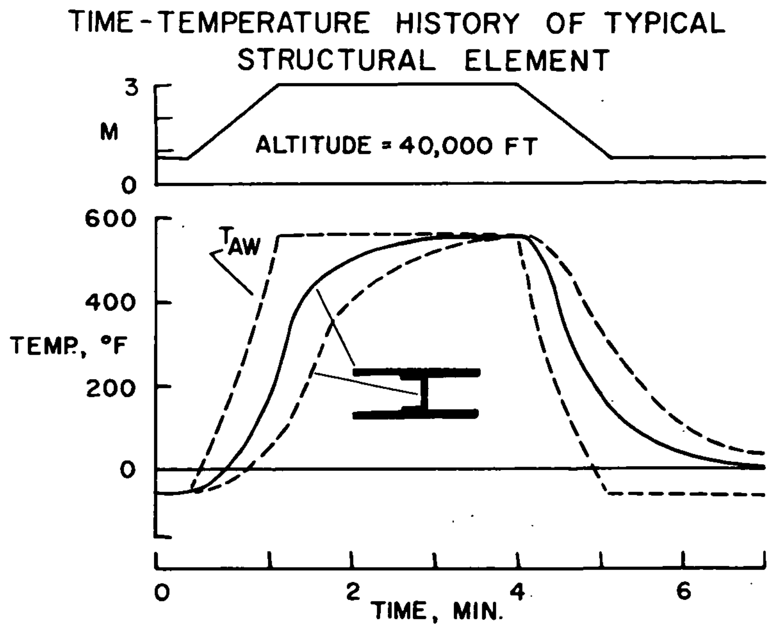

Figure 5

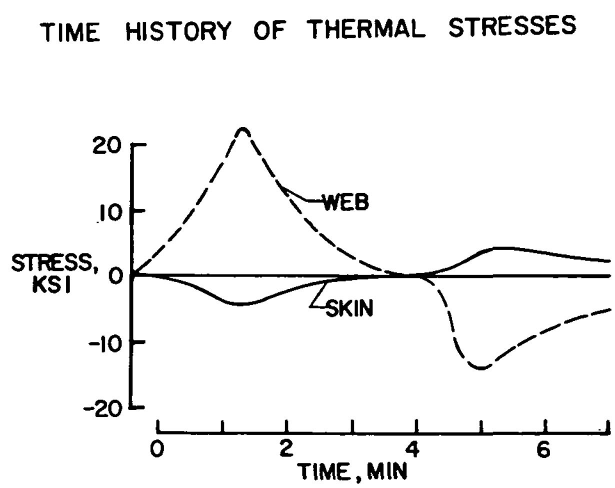

Figure 6

EFFECT OF HEAT-TRANSFER COEFFICIENT
ON THERMAL STRESS

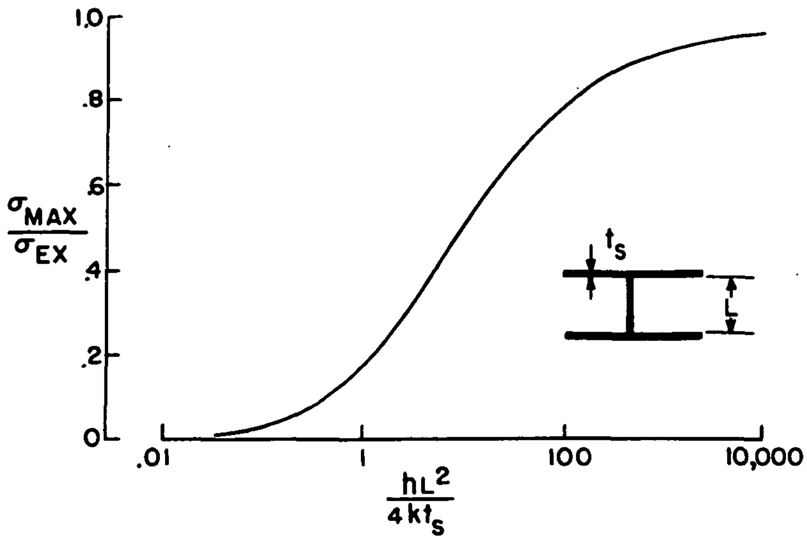

Figure 7

TIME-TEMPERATURE CHARACTERISTICS
OF VARIOUS STRUCTURES

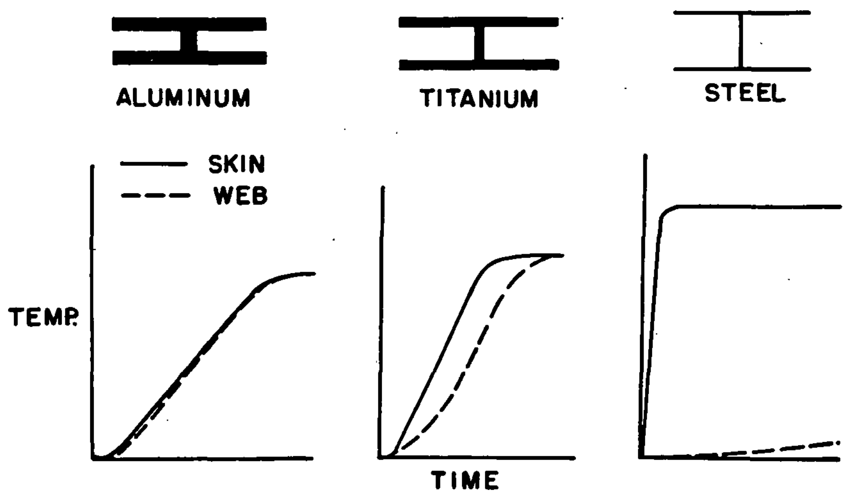

Figure 8

EFFECT OF HEAT-TRANSFER COEFFICIENT
ON EQUILIBRIUM TEMPERATURE

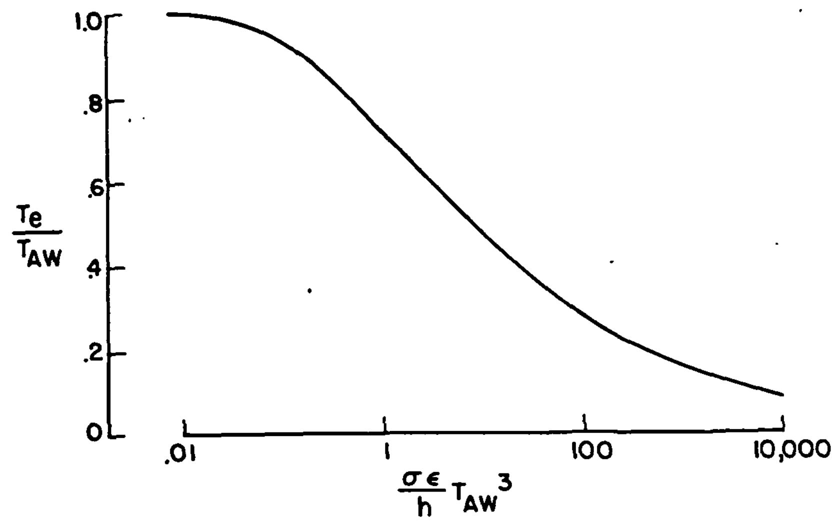

Figure 9

THERMAL STRESSES IN SOLID-STEEL DOUBLE-WEDGE SECTION
M=3; TIME=40 SEC

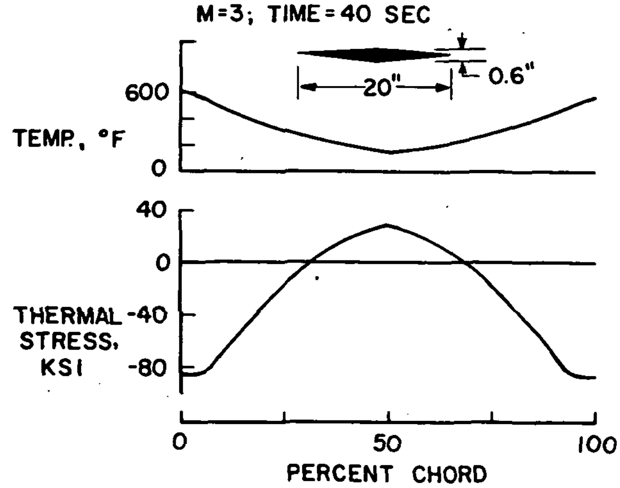

Figure 10

TWISTING STIFFNESS OF DOUBLE-WEDGE SECTION

M = 3

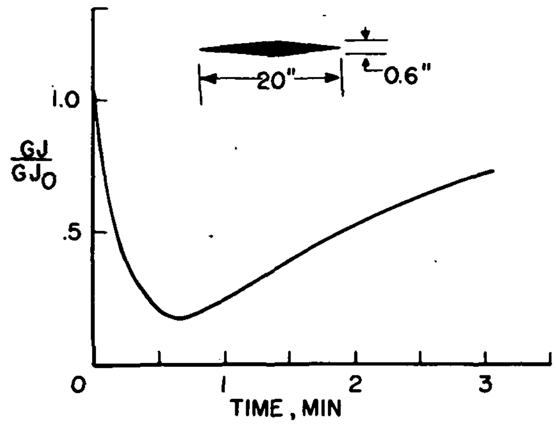

Figure 11

THICKNESS RATIO FOR
THERMAL TORSIONAL BUCKLING

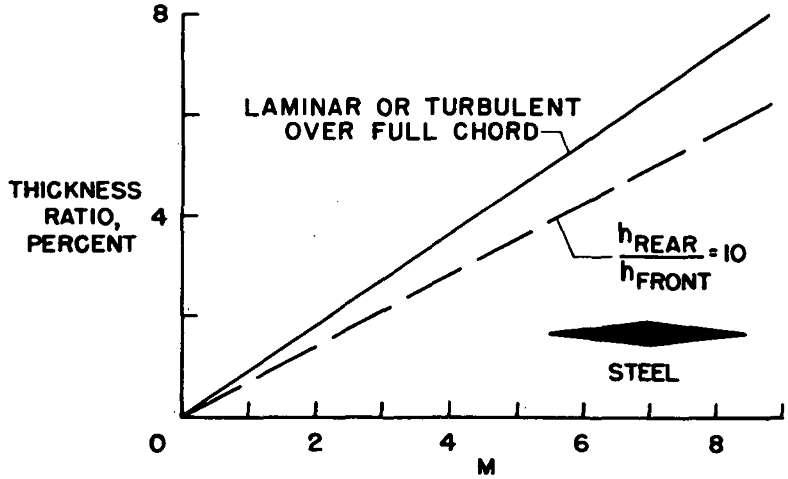

Figure 12

HEAT-TRANSFER CHARACTERISTICS OF BLUNT TWO- AND THREE-DIMENSIONAL BODIES AT SUPERSONIC SPEEDS

By Glen Goodwin

Ames Aeronautical Laboratory

SUMMARY

Measured local- and average heat-transfer coefficients on the front side of swept cylinders are presented for Mach numbers from 3.9 to 9.8, sweep angles from 0° to 70°, Reynolds numbers from 2,000 to 180,000, and ratios of wall temperature to stream stagnation temperature from 0.24 to 1.0. An analysis is presented which predicts the average heat-transfer coefficient on swept cylinders over this range of variables to an accuracy sufficient for most engineering purposes.

Local-heat-transfer coefficients are presented on hemispherically tipped cones and on a hemispherical cylinder. The theory of Stine and Wanlass is shown to correlate well the data over a Mach number range from 3.9 to 6.9 and over a local Reynolds number range from 100 to 400,000 for these blunt bodies.

INTRODUCTION

High-speed flight of aircraft now contemplated has brought with it the problem of aerodynamic heating of the skin and structure of the aircraft. Two of the areas on the aircraft structure where the heating is most severe are on the leading edge of wings and on the nose of bodies.

In general, pointed shapes and sharp leading edges of the wings are advantageous in that they tend to reduce the drag of the configuration; however, pointed shapes and sharp leading edges of the wings aggravate the heating problem because of two factors. The sharp pointed shapes accept heat from the hot boundary layer at a very high rate; it can be shown, for example, that the heat-transfer coefficient tends toward infinity at the point of a sharp object. Also, these sharp objects have little material with which to absorb and dissipate the incoming heat. One way out of this dilemma is to blunt the leading edge of wings and the nose of bodies. By this method, two advantages are achieved and one disadvantage is incurred.

38

Blunting a leading edge reduces the local rate of heat transfer to it and provides material to absorb this incoming heat. Also, blunting provides space for a leading-edge cooling system. In addition, it provides some added strength at a point where thermal stresses tend to be high. Sweeping the blunt leading edge of a wing further reduces the local rate of heat transferred to it.

The main disadvantage of blunting is that it increases the pressure drag of the wing or body over that of a sharp-edged configuration. For wings, the leading-edge drag may be drastically reduced by sweeping the wing. It can be shown from experimental measurements and from theoretical considerations that the drag of the front side of a cylinder of unit length is reduced by a factor equal to the cube of the cosine of the sweep angle. For example, a cylinder of unit length swept 60° has only $12\frac{1}{2}$ percent of the drag of an unswept cylinder.

For bodies required to carry a given volume, it is shown in reference 1 that an optimum shape for minimum drag requires some blunting of the nose; and for certain applications, for example, a body which is required to enter the atmosphere at high speeds, a blunt shape may have great advantages over a pointed shape. This advantage is primarily due to the fact that a high-drag body slows down at high altitudes where the heat-transfer rate is relatively low and also to the fact that the heat-transfer coefficients on the nose of a blunt body are smaller than those on a sharp pointed body.

This paper considers the heat-transfer characteristics of both two- and three-dimensional bodies. The body chosen for analysis and for testing was a hemispherical cylinder. This body was chosen because it represents a simple shape for a leading edge of a wing. Most of the experimental work available has been done at Reynolds numbers of 1.8×10^5 or lower and indicates the presence of a laminar boundary layer on the front side of cylinders. Therefore, the method used to calculate the heat-transfer coefficients will be to solve the laminar-boundary-layer equations.

Many solutions of these equations are available for the case where the cylinder is normal to the stream, and some work has been done for the case where the cylinder is swept with respect to the stream.

A summary of these theoretical investigations is shown in the following table:

Investigator	Fluid properties	Sweep angle	Remarks
Squire	Constant	0°	$u_1 = cx$
Eckert and Drewitz	Constant	0°	$u_1 = cx^m$
Brown and Donoughe	Variable	0°	Small heat transfer
Cohen and Reshotko	Variable	0°	$U_1 = cx^m$; $\frac{T_w}{T_\infty}$ variable
Crabtree	Variable	10° maximum	$u_1 = cx^m$
Beckwith	Variable	Variable	Integral method
Eggers, Hansen, and Cunningham	Variable	Variable	$x = 0$; $T_w \ll T_0$
Goodwin, Creager, and Winkler	Constant	Variable	Properties evaluated locally in application

Squire (see ref. 2) assumed constant fluid properties, neglected the pressure terms and the dissipation function, and obtained a solution to the laminar-boundary-layer equations over an unyawed cylinder where the velocity at the outer edge of the boundary layer is proportional to the distance from the stagnation point. This solution is, therefore, limited to low-speed flow and small temperature differences.

Eckert and Drewitz (ref. 3) assumed constant fluid properties and that the velocity at the edge of the boundary layer was proportional to some power of the distance from the stagnation point. (This is the so-called wedge-type flow solution.)

Brown and Donoughe (ref. 4) assumed essentially the same velocity distribution over the cylinder as that in reference 3, but allowed fluid properties to vary. Their solution is limited to zero sweep and small rates of heat transfer to the cylinder.

Cohen and Reshotko (ref. 5) allowed fluid properties to vary and assumed that the velocity at the outer edge of the boundary layer could be expressed as $U_1 = cx^m$. Their investigation was limited to zero sweep. They also investigated the effect of allowing the ratio of the wall temperature to the stream stagnation temperature to vary.

Crabtree (ref. 6) allowed fluid properties to vary and treated the case of a swept cylinder. His solution was valid only for small angles of sweep where the free-stream Mach number was high.

Beckwith (ref. 7) treated both variable fluid properties and variable sweep by using integral methods. These methods, however, lack generality. Eggers, Hansen, and Cunningham (ref. 8) allowed both properties and sweep angle to vary, but limited their analysis to the stagnation point on the cylinder and to the case where the cylinder temperature was negligible with respect to the stagnation temperature of the stream.

None of these investigations yielded an analytic expression for the heat transfer to the entire front side of a swept cylinder which would point out the effects of single variables or allow the correlation of all of the available experimental information. In an effort to find a solution which would do this, the subsequent analysis was performed.

SYMBOLS

a speed of sound, ft/sec

D cylinder diameter or diameter of hemispherical cone tip, ft

h local-heat-transfer coefficient, $\dfrac{\text{Btu}}{(\text{hr})(\text{sq ft})(^\circ\text{F})}$

k thermal conductivity of air, $\dfrac{\text{Btu}}{(\text{hr})(\text{sq ft})(^\circ\text{F/ft})}$

M Mach number

Nu_{av} average Nusselt number, $\dfrac{h_{av}D}{k_t}$

Nu_L local Nusselt number, $\dfrac{hD}{k_t}$

Nu_x	local Nusselt number, $\frac{hx}{k_1}$
p	pressure, lb/sq ft
Pr	Prandtl number
R_x	local Reynolds number, $\frac{\rho_1 u_1 x}{\mu_1}$
R_2	Reynolds number evaluated behind normal shock wave, $\frac{\rho_\infty u_\infty D}{\mu_t}$
u	fluid velocity, ft/sec
U	transformed velocity at edge of boundary layer (see ref. 5)
x	surface coordinate on cylinder or cone
Λ	sweep angle, deg
ϕ	azimuth angle on cylinder, deg
ρ	density of air, slugs/cu ft
γ	ratio of specific heats
μ	viscosity of air, lb-sec/sq ft

Subscripts:

av	average conditions
t	reservoir or total conditions
1	conditions at outer edge of boundary layer at x
∞	conditions in free stream

ANALYSIS

The continuity, momentum, and total-energy equations for the laminar boundary layer over a swept cylinder were derived by using the order-of-magnitude arguments pointed out by Sears (ref. 9) for the continuity and momentum equations and by Crabtree (ref. 6) for the total-energy equation. This set of equations was solved under the following assumptions: The Prandtl number was unity, the velocity at the outer edge of the boundary layer was a linear function of the distance from the forward stagnation point, and the flow in the boundary layer was incompressible.

The solution to this set of equations was, then, identical with the solution obtained by Squire for the heat-transfer rate over a cylinder in subsonic flow.

This solution gave no hint as to where in the boundary layer the fluid properties should be evaluated. Some further assumptions were, therefore, made: The pressure was evaluated locally, and the viscosity and thermal conductivity of the air were linear functions of the temperature. It was also assumed that, for variable Prandtl number, the correction obtained by Cohen and Reshotko for the unswept cylinder would apply to the swept case.

The main results of the analysis which is given in detail in reference 10 are as follows:

The local Nusselt number for $Pr = 0.7$ is given by

$$Nu_L = \frac{h_L D}{k_t} = 0.73\sqrt{R_2 F(\Lambda,M) G(M) \Phi(\phi)} \qquad (1)$$

where

$$F(\Lambda,M) = \frac{p_{x=0}}{p_{t_2}} \frac{a_{x=0}}{a_t}$$

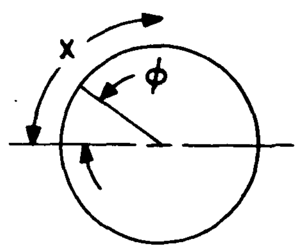

$$G(M) = \frac{p_{t_2}}{p_\infty} \frac{a_\infty}{a_t} \frac{1}{M}$$

$$\Phi(\phi) = \frac{p_x}{p_{x=0}} = \left[1 + \frac{\gamma - 1}{2}\left(2.13\,\frac{x}{D}\right)^2\right]^{\gamma/(\gamma-1)}$$

$$\frac{p_{x=0}}{p_{t_2}} = \cos^2\Lambda + \left[\frac{\left(\frac{2\gamma M^2}{\gamma + 1} - \frac{\gamma - 1}{\gamma + 1}\right)^{1/(\gamma-1)}}{\left(\frac{\gamma + 1}{2}\,M^2\right)^{\gamma/(\gamma-1)}}\right]\sin^2\Lambda$$

$$\frac{a_{x=0}}{a_t} = \left[1 - \frac{\frac{\gamma - 1}{2}\,M^2\sin^2\Lambda}{1 + \frac{\gamma - 1}{2}\,M^2}\right]^{1/2}$$

The average Nusselt number over the front side of the swept cylinder is obtained by integrating equation (1) over the front side of the cylinder; therefore,

$$Nu_{av} = 0.52\sqrt{R_2 F(\Lambda,M)G(M)} \qquad (2)$$

RESULTS AND DISCUSSION

Heat-Transfer Characteristics of Two-Dimensional Bodies

Before comparing these results with experimentally measured heat-transfer coefficients on swept cylinders, the pressure-ratio distribution over swept and unswept cylinders at high Mach numbers will be shown in order to assess the validity of the assumption that the velocity at the outer edge of the boundary layer varies linearly with the distance from the leading edge of the cylinder.

Figure 1 shows the ratio of the pressure on the surface of the cylinder to the pressure at the stagnation point plotted against azimuth angle for a cylinder normal to the stream. The experimental points are shown for a range of free-stream Mach numbers from 2.5 to 7 and over a range of Reynolds numbers from 6,700 to 180,000. The solid-line curve was calculated by assuming that the velocity at the outer edge of the boundary layer varied linearly with the distance along the surface from the stagnation point. It can be seen that the pressure-ratio distribution is unaffected by both free-stream Mach number changes from 2.5 to 7 and by Reynolds number variations from 6,700 to 180,000. Also, it can be seen from the agreement between the points and the solid-line curve that the assumption that the velocity varies linearly with surface distance is valid.

Figure 2 has the same quantities plotted as were shown in figure 1. In figure 2, however, the points were obtained at two Mach numbers, 3.9 and 6.9, but with angle of sweep varying from 0° to 60°. The solid-line curve is the same as that shown previously, and it can be seen that sweeping the cylinder did not change the pressure-ratio distribution over it. Thus, it can be concluded that at high Mach numbers the pressure-ratio distribution is a unique function of the azimuth angle only.

The actual pressure at the leading edge of a swept cylinder can be calculated with good accuracy by using Rayleigh's equation based upon the component of Mach number normal to the cylinder axis.

This fact and the fact that the pressure-ratio distribution can be calculated allow the effect of sweep on the pressure drag to be determined. The result for a unit-length cylinder is that the pressure-drag coefficient varies directly as the cube of the cosine of the sweep angle.

Since the assumption has been shown that the flow velocity at the outer edge of the boundary layer varies linearly with the surface distance for Mach numbers above 2.5, results of the analysis will now be compared with experimentally measured local-heat-transfer coefficients.

Figure 3 shows the ratio of the local-heat-transfer coefficient at any azimuth angle to that at the stagnation point as a function of azimuth angle. The points shown are measured values obtained at 0° sweep, 30° sweep, and 44° sweep. The experimental values were obtained in the Ames low-density wind tunnel at a Mach number of 3.9 and at Reynolds numbers from 2,100 to 6,700. The experimental method was to measure the heat transferred from a small plug which was thermally insulated from the test cylinder. The test plug was kept at the same temperature as the test body in order to avoid the complication of having to evaluate the effect of a variable surface temperature on the heat-transfer coefficient. A complete description of the test method is given in reference 10 and, for that reason, it will not be discussed further herein.

The experimental data exhibit some experimental scatter; but within the accuracy of the measurements, no definite trend of this ratio with sweep angle could be determined.

The result of the analysis of reference 10 is shown by the solid-line curve, and it can be seen that this curve agrees reasonably well with the experimental points. Also, the analysis indicated no variation of this ratio with sweep angle.

For comparison, the theory of Cohen and Reshotko for a compressible boundary layer on an unswept cylinder is shown as the dashed-line curve. It can be seen that there is little difference between the two theories. The small difference is attributed to the fact that the local Mach number is relatively low over the cylinder; the local Mach number is always less than 2.0.

Sweeping the cylinder did not affect the ratio of the local-heat-transfer coefficient to that at the stagnation point of the cylinder, but it did affect the level of the data and this effect is shown in figure 4. In this figure the ratio of the average Nusselt number over the front half of the cylinder divided by the average Nusselt number at zero sweep is plotted against the sweep angle. The circular symbols shown at 30° sweep and 44° sweep were obtained in the Ames low-density wind tunnel at a Mach number of 3.9, and the square symbols were obtained at the Langley 11-inch hypersonic tunnel at a Mach number of 6.9. (The latter tests were reported in ref. 11.) It can be seen that sweeping the cylinder reduced the heat transfer to it; at 60° sweep the Nusselt number is reduced to one-half of its no-sweep value. The solid-line curve is the result of the analysis evaluated at a Mach number of 3.9, and the dashed-line curve is the result of the analysis evaluated at a Mach number of 6.9. It can be seen that, up to sweep angles of about 45°, the analysis predicts the experimental data well. However, for sweep angles above 45°, the analysis predicts more of a decrease of the Nusselt number with sweep than is actually measured experimentally. The departure of the data from the theory at sweep angles above 45° is also corroborated by the tests reported in reference 8.

The temperature-recovery factors were also reduced by sweep; however, the reduction is small compared with the reduction in Nusselt number. Measured recovery factors on the front half of swept cylinders were 1.0, 0.924, 0.900, and 0.888 for sweep angles of 0°, 20°, 40°, and 60°, respectively. These values were measured at a Mach number of 6.9.

One of the results of this analysis is that it yields a correlation parameter whereby the average Nusselt number over the front half of the cylinder can be correlated over a wide range of free-stream Mach numbers, Reynolds numbers, and sweep angles. Figure 5 shows this correlation. In this figure the average Nusselt number evaluated at stagnation temperatures for the front half of swept cylinders is plotted against the correlation parameter given by the analysis. This correlation parameter is defined in equation (1). The circular symbols shown at the upper right-hand corner of figure 5 were obtained in the Langley 11-inch hypersonic tunnel at a Mach number of 6.9, a ratio of wall temperature to stagnation temperature from 0.5 to 1.0, and a range of sweep angles from 0° to 60°. The square symbols shown in about the center of the chart were obtained in the Ames low-density wind tunnel at a Mach number of 3.9 and a wall temperature equal to stagnation temperature for three sweep angles - 0°, 30°, and 44°. The diamond symbols shown toward the lower left-hand side of figure 5 were obtained in the Ames gun tunnel at a Mach number of 9.8, a ratio of wall temperature to stagnation temperature of 0.24, and a range of sweep angles from 0° to 70°. The data shown in this figure represent a Reynolds number range from 315 for some of the points taken in the gun tunnel to 180,000, which corresponds to the Reynolds number obtained in the Langley 11-inch hypersonic tunnel. The solid-line curve shown in figure 5 is the result of the analysis of reference 10. It can be seen that the analysis represents the data well.

The data shown in figure 5 were obtained over a range of stream stagnation temperatures from room temperature to $2{,}200^{\circ}$ R and over a range of ratios of body temperature to stream stagnation temperature from 0.24 to 1.0. These data, then, represent flight temperature conditions up to flight Mach numbers of about 5.0. Although boundary-layer theory for unswept cylinders indicated that the analysis shown is conservative at higher flight Mach numbers, this indication has not been checked by experiment.

The data shown in figure 5 represent the case where the boundary layer on the cylinder was laminar. Some very recent (unpublished) measurements by Beckwith indicate that, if the free-stream Reynolds number is sufficiently high, sweeping the cylinder will cause transition to turbulent flow in the boundary layer and will cause the heat-transfer coefficients to be increased by sweep. The flight Reynolds number at which transition can be triggered by sweep is as yet undetermined.

Heat-Transfer Characteristics of Three-Dimensional Bodies

Local-heat-transfer coefficients have been measured on hemispherically tipped cones and on a hemispherical cylinder. Figure 6 shows these data. In this figure the ratio of the local-heat-transfer coefficient to that at the stagnation point is plotted along the ordinate. The distance along the surface of the cone from the stagnation point, divided by the diameter of the hemispherical tip, is shown along the abscissa.

The cones were tested in the Ames low-density wind tunnel at a Mach number of 3.9, and the hemispherical cylinder was tested in the Langley 11-inch hypersonic tunnel at a Mach number of 6.9. It can be seen that the heat-transfer-coefficient ratios reach a value of 1.0 on the noses of these bodies but fall rapidly as the distance from the nose increases.

The heat-transfer-coefficient ratio measured on the nose of the hemispherical cylinder agrees well with that measured on the hemispherical nose of the $22\frac{1}{2}^{\circ}$ half-angle cone. This trend was not followed on the bluntest cone. On the bluntest cone, the heat-transfer-coefficient ratio on the nose was lower than that for the other bodies except very near the stagnation point. The nose-cone juncture of the bodies is shown by the vertical lines in figure 6, for example, at $x/D = 0.785$ for the hemispherical cylinder.

The same general method will be used to calculate the heat-transfer coefficients over the blunt bodies as was used to calculate the heat-transfer coefficients over unswept cylinders. The main difference is that now the flow in the boundary layer is three-dimensional. However, three-dimensional axisymmetric boundary-layer equations can be transformed by use of Mangler's transformation to an equivalent set of two-dimensional equations. This has been done by Stine and Wanlass (ref. 12) and by Cohen and Reshotko (ref. 5). The main simplifying assumption used in these analyses is that the velocity at the outer edge of the boundary layer can be expressed as some power of the distance from the forward stagnation point. However, in an actual case, the velocity at the outer edge of a boundary layer does not vary in this fashion except very near the forward stagnation point. In the application of these analyses to real problems, the exponent is evaluated locally from measured pressure-distribution data.

Data obtained on these blunt bodies of revolution are shown in figure 7 in nondimensional form. In this figure, the local Nusselt number is plotted along the ordinate. The product of the local Reynolds number and a function of body shape and pressure distribution is plotted along the abscissa. The solid-line curve is the result given by the Stine and Wanlass analysis (ref. 12). The circular symbols were obtained on the bluntest cone and the square symbols were obtained on the less blunt cone. The diamond symbols were obtained on the hemispherical cylinder.

It can be seen that the data are well correlated by this method over a range of local Reynolds numbers from 100 to 400,000 and at two Mach numbers of 3.9 and 6.9. Also, a wide range of blunt body shapes is covered.

The correlation parameter plotted along the abscissa of figure 7 is taken from the analysis of Stine and Wanlass and is equal to

$$f\left(\frac{x}{D}, \frac{p}{p_{x=0}}\right) = \frac{Nu_x}{\sqrt{R_x}} \tag{3}$$

which is given by equations (2) to (7) in reference 12.

Heat-transfer coefficients were also determined for the 55° half-angle hemispherically tipped cone at angle of attack. The results of these tests are shown in figure 8. In this figure are plotted along the ordinate the ratio of the local-heat-transfer coefficients divided by the value at the stagnation point on the body for the case when the body was at zero angle of attack. The distance along the surface of the cone divided by the tip diameter, denoted by x/D, is plotted along the abscissa of figure 8. Positive values of x/D shown on the right-hand side of this figure represent the windward side of the body, and negative values of x/D shown at the left-hand side of the figure represent the other side of the body. It can be seen that the heat-transfer coefficients over the hemispherical nose were not markedly altered by angles of attack of 12° and 24°. However, the heat-transfer coefficients on the conical section were increased by angle of attack on the windward side of the body and were considerably decreased on the other side of the body. It was found, however, that, on an average basis, angle-of-attack variations up to 24° did not appreciably change the total amount of heat transfer to the body.

CONCLUDING REMARKS

It can be concluded from the data presented herein that the theoretical methods appear adequate to predict the heat-transfer coefficients on the noses of blunt bodies and on the front side of swept cylinders over a wide range of Mach numbers and Reynolds numbers up to flight temperature conditions corresponding to flight at Mach numbers of approximately 5, provided the boundary-layer flow is laminar.

REFERENCES

1. Eggers, A. J., Jr., Dennis, David H., and Resnikoff, Meyer M.: Bodies of Revolution for Minimum Drag at High Supersonic Airspeeds. NACA RM A51K27, 1952.

2. Squire, H. B.: High Speed Flow. Heat Transfer. Vol. II of Modern Developments in Fluid Dynamics, ch. XIV, L. Howarth, ed., The Clarendon Press (Oxford), 1953, pp. 757-853.

3. Eckert, E., and Drewitz, O.: Calculation of the Temperature Field in the Laminar Boundary Layer of an Unheated Body in a High Speed Flow. R.T.P. Translation No. 1594, British Ministry of Aircraft Production. (From Luftfahrtforschung, vol. 19, no. 6, June 20, 1942, pp. 189-196.)

4. Brown, W. Bryon, and Donoughe, Patrick L.: Tables of Exact Laminar-Boundary-Layer Solutions When the Wall Is Porous and Fluid Properties Are Variable. NACA TN 2479, 1951.

5. Cohen, Clarence B., and Reshotko, Eli: Similar Solutions for the Compressible Laminar Boundary Layer With Heat Transfer and Pressure Gradient. NACA TN 3325, 1955.

6. Crabtree, L. F.: The Compressible Laminar Boundary Layer on a Yawed Infinite Wing. Aero. Quarterly, vol. V, July 1954, pp. 85-100.

7. Beckwith, Ivan E.: Theoretical Investigation of Laminar Heat Transfer on Yawed Infinite Cylinders in Supersonic Flow and a Comparison With Experimental Data. NACA RM L55F09, 1955.

8. Eggers, A. J., Jr., Hansen, C. Frederick, and Cunningham, Bernard E.: Theoretical and Experimental Investigation of the Effect of Yaw on Heat Transfer to Circular Cylinders in Hypersonic Flow. NACA RM A55E02, 1955.

9. Sears, W. R.: The Boundary Layer of Yawed Cylinders. Jour. Aero. Sci., vol. 15, no. 1, Jan. 1948, pp. 49-52.

10. Goodwin, Glen, Creager, Marcus O., and Winkler, Ernest L.: Investigation of Local Heat-Transfer and Pressure-Drag Characteristics of a Yawed Circular Cylinder at Supersonic Speeds. (Prospective NACA paper.)

11. Feller, William V.: Investigation of Equilibrium Temperature and Average Laminar Heat-Transfer Coefficients for the Front Half of Swept Circular Cylinders at Mach Number of 6.9. NACA RM L55F08a, 1955.

12. Stine, Howard A., and Wanlass, Kent: Theoretical and Experimental Investigation of Aerodynamic-Heating and Isothermal Heat-Transfer Parameters on a Hemispherical Nose With Laminar Boundary Layer at Supersonic Mach Numbers. NACA TN 3344, 1954.

CYLINDER PRESSURE RATIO;
ZERO SWEEP

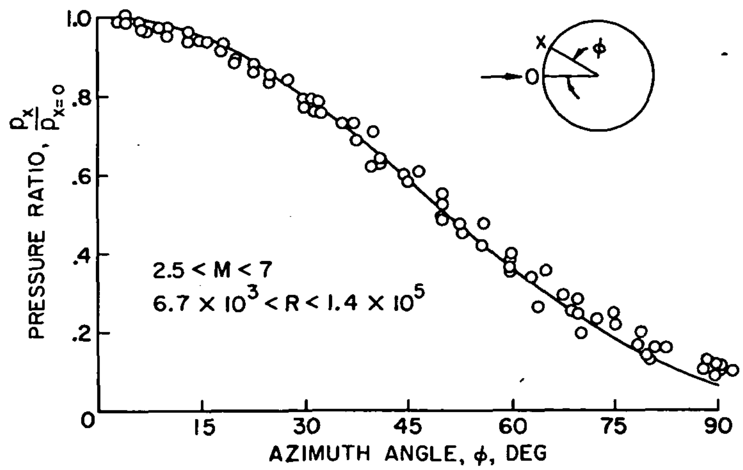

Figure 1

CYLINDER PRESSURE RATIO
WITH SWEEP

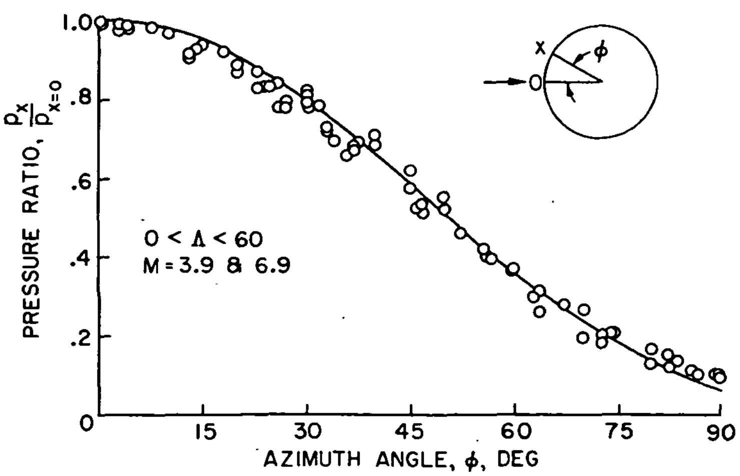

Figure 2

[redacted]

DISTRIBUTION OF HEAT-TRANSFER-
COEFFICIENT RATIO

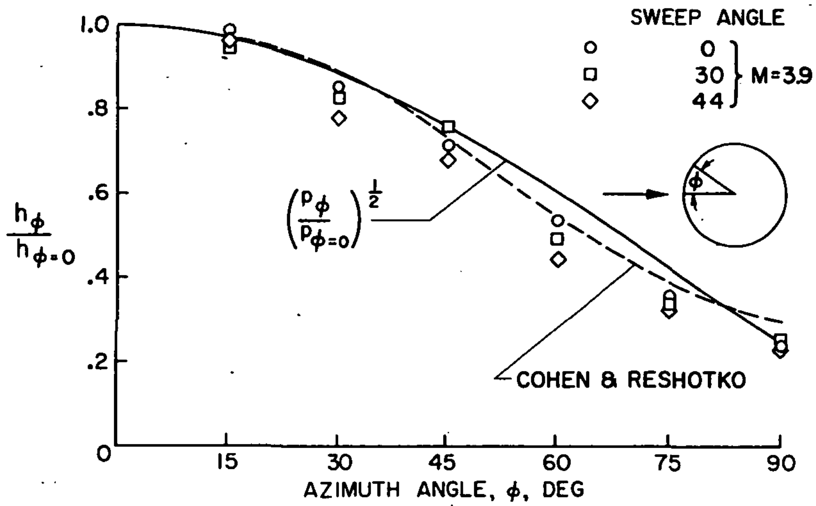

Figure 3

VARIATION OF AVERAGE HEAT TRANSFER WITH SWEEP ANGLE

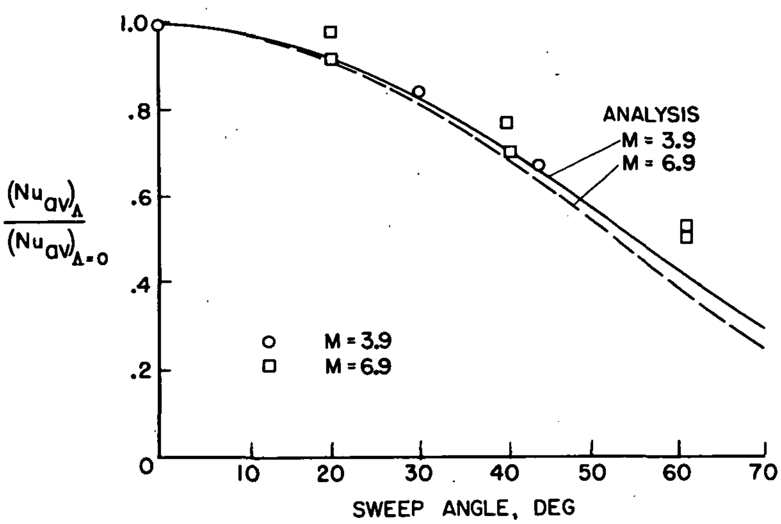

Figure 4

[redacted]

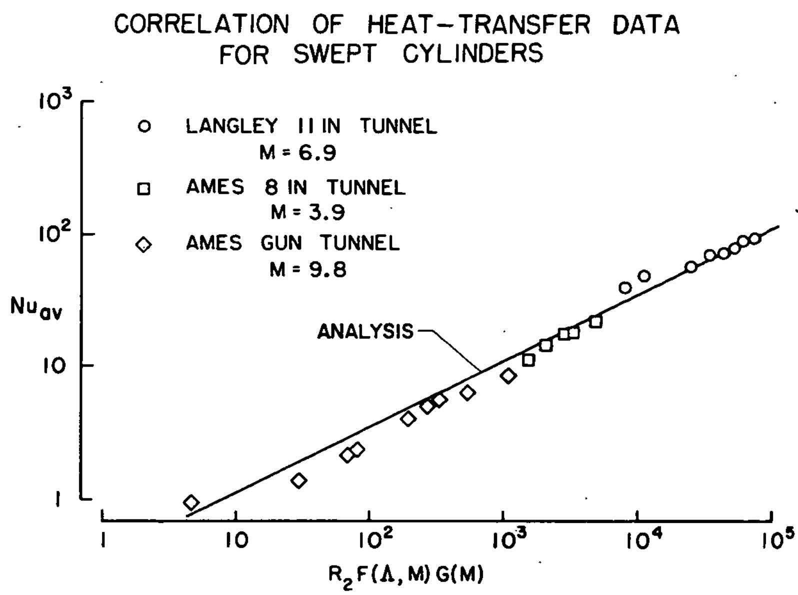

Figure 5

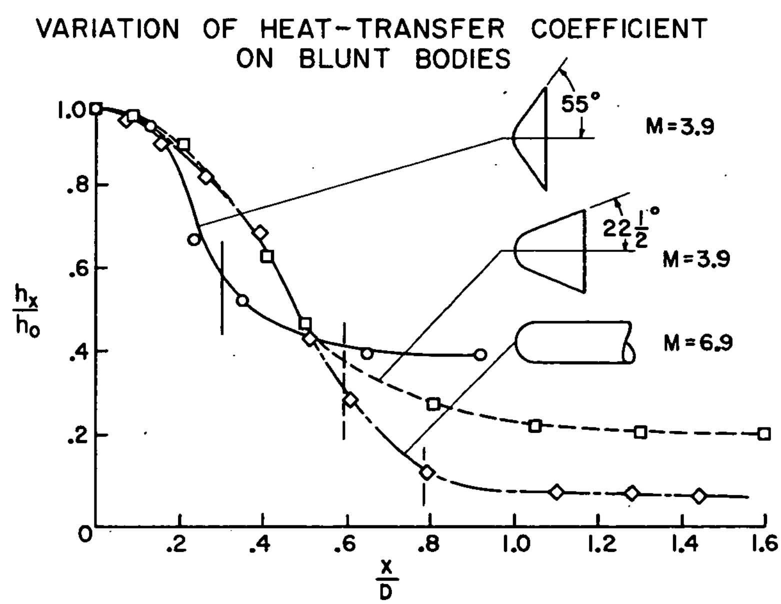

Figure 6

[redacted]

LOCAL HEAT TRANSFER ON BLUNT BODIES

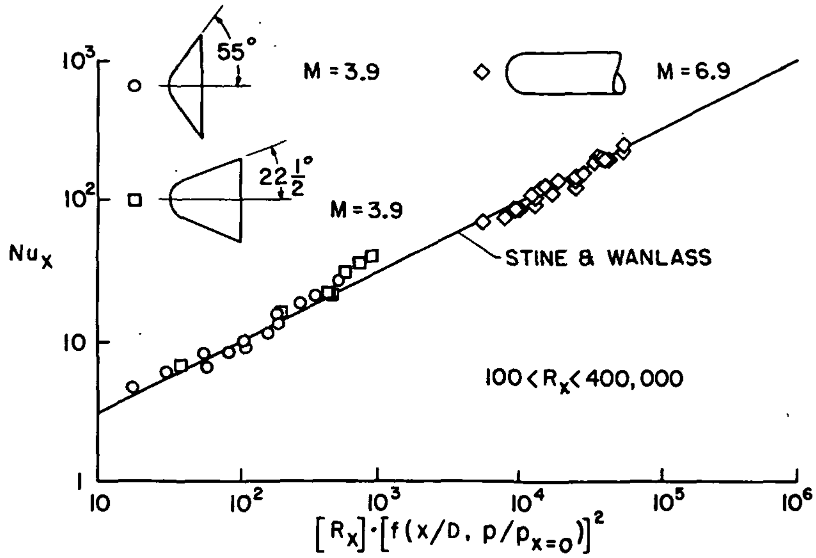

Figure 7

VARIATION OF HEAT-TRANSFER COEFFICIENT
ON BLUNT CONE

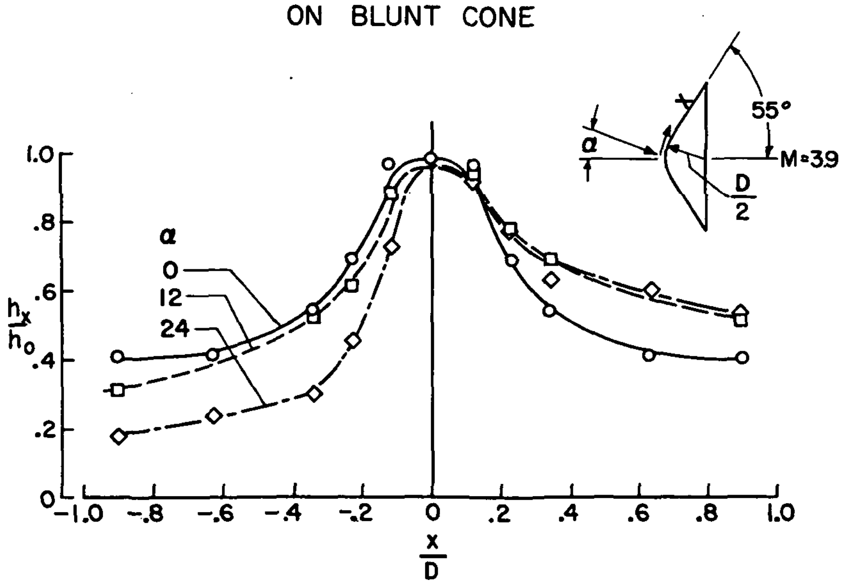

Figure 8

[redacted]

PRELIMINARY HEAT-TRANSFER MEASUREMENTS AT HIGH STAGNATION TEMPERATURES IN A SHOCK TUBE

By Morton Cooper and Jim J. Jones

Langley Aeronautical Laboratory

At the present time, a considerable effort (for example, refs. 1 to 7) is being expended to develop high-stagnation-temperature research facilities in order better to simulate hypersonic flight conditions. Of the many schemes now being investigated, the shock tube (ref. 7) appears to be one of the most promising, particularly for the study of aerodynamic heating. The purpose of this paper is to present a progress report of some preliminary heat-transfer measurements very recently obtained in a new shock tube at the Langley Aeronautical Laboratory of the National Advisory Committee for Aeronautics.

The basic elements of shock-tube flow are presented in figure 1. In figure 1(a), a hydrogen-air shock tube is shown schematically; an instantaneous pressure distribution along the tube at a representative time t_1 is shown in figure 1(b); and a characteristic diagram is shown in figure 1(c). Flow in the shock tube is initiated by rupturing the diaphragm separating the high-pressure hydrogen and the low-pressure air, thereby sending a strong shock wave down the tube. The air behind the shock wave is set in uniform motion to the right at a Mach number whose maximum value is 1.89 based on the assumption of a perfect gas. The static temperature is very high. In order to obtain a supersonic flow field for testing at Mach numbers in excess of 1.89, the flow must be further expanded through a nozzle, as discussed in references 2 and 7. For the present tests, no supersonic nozzle was used; the model was mounted directly in the low-pressure tube.

One of the inherent limitations of the shock tube is its short running time, of the order of 0.001 second. In order to obtain heat-transfer measurements in so short a time interval, new types of model instrumentation must be used. Figure 2 shows an illustrative sketch of a thermocouple heat-transfer model developed for these tests. It consists of a sting-supported glass sphere approximately $1\frac{1}{8}$ inches in diameter on which two bands of metal, one nickel and the other silver, have been evaporated. The bands overlap only at the stagnation point to form a thermocouple. The thermocouple is so thin, being only a small fraction of a micron, that its heat capacity can be neglected. Its output is then simply the temperature rise of the glass surface. By use of this temperature rise as the boundary condition on the one-dimensional unsteady-heat-flow equation, the heat flux into the model at any time during the run can be computed.

The stream conditions for the present tests are summarized in figure 3(a). The Mach number in region (2) is 1.75 (perfect gas). Of all the conditions specified, the pressure and temperature in region (1), together with the shock velocity, were the only ones experimentally determined. The remaining conditions have been computed on the basis of perfect-gas assumptions with constant specific heat and constant γ. For these extreme temperatures, such assumptions break down as is shown by a comparison at the stagnation point with real-gas properties (ref. 8) computed by assuming equilibrium conditions throughout. The temperature drops from 7,820° R to 5,670° R as the energy goes into modes other than molecular translation and rotation. In figure 3(b), an oscilloscope record obtained during one test is reproduced. The base line to the left of the origin represents the unheated state of the model before the shock passage. The rapid rise from the origin corresponds to heating after the shock passage. From records such as this, the heat flux is computed.

Figure 4 summarizes the heat-transfer data obtained during these preliminary tests. Figure 4(a) shows a typical temperature-time variation. The surface temperature rises about 100° F in 0.4 millisecond. Since this temperature rise is so small as compared with the temperature potential, a constant heat flux, independent of time, would be expected. For such a case, the one-dimensional unsteady-heat-flow equation indicates a square-root variation of temperature rise with time. This is verified in figure 4(b) where ΔT is plotted against the square root of time. The slope of this curve is directly proportional to the heat flux. In figure 4(c), heat-transfer data obtained from six different tests on three different models are summarized. The constancy of the heat flux with time is again verified within the band of the data. The horizontal band of data represents a $\pm$10-percent deviation from a mean. Because the data were so recently obtained, no theoretical computations which consider dissociation have been made for the heat-transfer rate. Included, however, is a perfect-gas estimate made on the basis of Beckwith's integral analysis (ref. 9). On the basis of existing comparisons of equilibrium dissociation and perfect-gas heat-transfer calculations (ref. 9, for example), not too significant a change in the perfect-gas estimate because of equilibrium dissociation would be expected for these conditions. The mean of the experimental data is approximately 20 percent below the perfect-gas estimate. It is somewhat reassuring that such a simple estimate gives a reasonable prediction of the heat-flow rate for these conditions.

Although the results of these tests have been obtained at an extremely high temperature for the test Mach number, there is a reasonable flight counterpart as shown in figure 5. In this figure, a comparison of the shock-tube conditions is made with those occurring in flight at an altitude of 109,000 feet. The free-stream Mach number in the tube is 1.75; the flight Mach number is 9.0. The perfect-gas temperature and pressure behind the detached shock wave at station (3) are the same in both cases. There is, of course, a difference in Mach number. In order to compare heat-transfer results for these two conditions (assuming nonequilibrium effects to be negligible), the heat-transfer rate must be corrected for the difference in stagnation-point velocity gradient with Mach number.

REFERENCES

1. Resler, E. L., Lin, Shao-Chi, and Kantrowitz, Arthur: The Production of High Temperature Cases in Shock Tubes. Jour. Appl. Phys., vol 23, no. 12, Dec. 1952, pp. 1390-1399.

2. Hertzberg, Abraham: A Shock Tube Method of Generating Hypersonic Flows. Jour. Aero. Sci., vol. 18, no. 12, Dec. 1951, pp. 803-804, 841.

3. Ferri, Antonio, Libby, Paul A., and Zakkay, Victor: A Theoretical Analysis of a New Type of Heater For An Intermittent Hypersonic Wind Tunnel. PIBAL Rep. No. 201 (Contract No. AF 33(616)-17), July 1952.

4. Dodge, John A.: Ultra-High Temperature Aerodynamic Testing Facilities. AEDC-TN-54-61 (Contract No. AF 18(600)-1233), Arnold Eng. Dev. Center, Apr. 1955.

5. Eggers, A. J., Jr., Hansen, C. Frederick, and Cunningham, Bernard E.: Theoretical and Experimental Investigation of the Effect of Yaw on Heat Transfer to Circular Cylinders in Hypersonic Flow. NACA RM A55E02, 1955.

6. Charters, A. C., Denardo, B. Pat, and Rossow, Vernon J.: Development of a High-Velocity Free-Flight Launcher: The Ames Light Gas Gun. (Prospective NACA paper.)

7. Hertzberg, A., Smith, W. E., Glick, H. S., and Squire, W.: Modifications of the Shock Tube for the Generation of Hypersonic Flow. AEDC-TN-55-15 (AD-789-A-2) (Contract No. AF 40(600)-6), Arnold Eng. Dev. Center, Mar. 1955.

8. Anon.: Handbook of Supersonic Aerodynamics. NAVORD Rep. 1488 (vol. 5), Bur. Ordnance, Aug. 1953.

9. Beckwith, Ivan E.: Heat Transfer and Skin Friction by an Integral Method in the Compressible Laminar Boundary Layer With a Streamwise Pressure Gradient. NACA TN 3005, 1953.

[redacted]

SHOCK-TUBE FLOW DIAGRAM

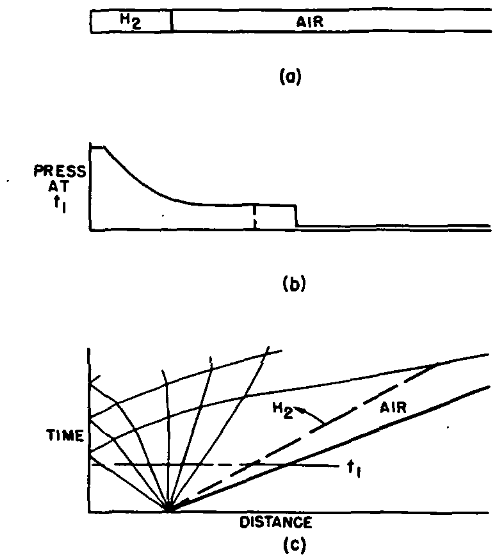

Figure 1

HEAT TRANSFER MODEL

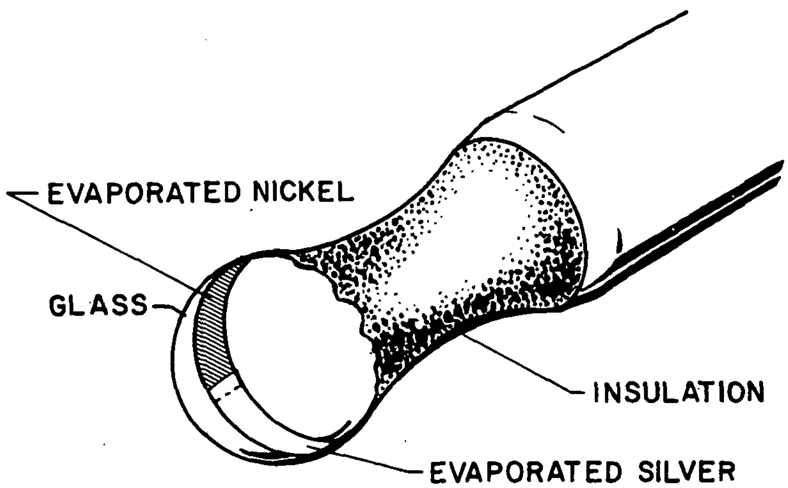

Figure 2

[redacted]

[redacted]

ILLUSTRATIVE TEST

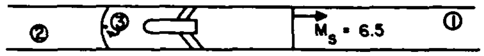

	①	②	③	STAGNATION IDEAL	STAGNATION REAL
P, ATM	0.004	0.21	0.72	0.93	1.2
T, °R	530	4850	7250	7820	5670

(a)

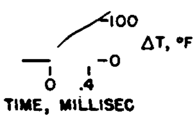

(b)

Figure 3

STAGNATION-POINT HEAT TRANSFER

M = 1.75; T_{STAG} = 7820°R; P_{STAG} = 0.93 ATMOS

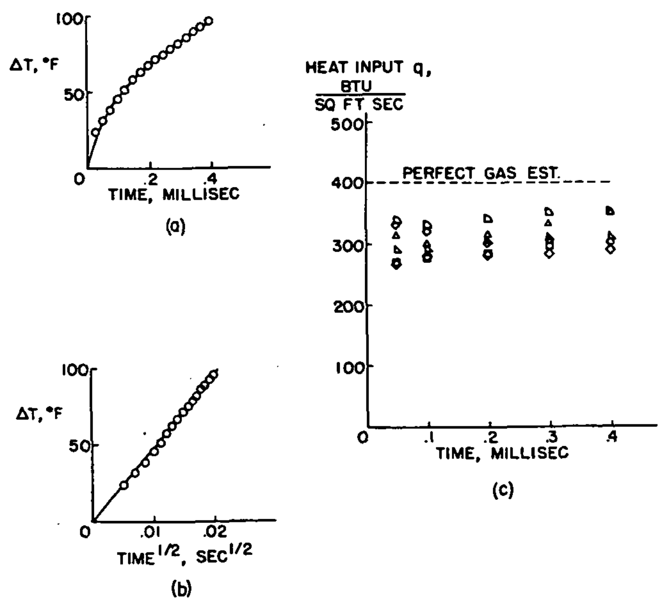

Figure 4

[redacted]

FLIGHT COMPARISON

	2	3		
	M	M	P, ATM	T,°R
TUBE	1.75	0.63	0.72	7250
ALTITUDE 109,000'	9.0	.39	.72	7250

Figure 5

[redacted]

HIGH-TEMPERATURE OXIDATION AND IGNITION OF METALS

By Paul R. Hill, David Adamson, Douglas H. Foland,
and Walter E. Bressette

Langley Aeronautical Laboratory

SUMMARY

A study of the high-temperature oxidation of several aircraft construction materials was undertaken to assess the possibility of ignition under high-temperature flight conditions. Tests were made in free jets and in a pressurized vessel containing an atmosphere of oxygen, using various artificial devices to heat the specimens. When heated in an atmosphere of oxygen or when heated and plunged into a supersonic airstream, titanium, iron, carbon steel, and common alloys such as 4130 were found to have spontaneous-ignition temperatures in the solid phase (below melting) and they melted rapidly while burning. Inconel, copper, 18-8 stainless steel, Monel, and aluminum could not be made to ignite spontaneously at temperatures up to melting with the equipment available. Magnesium ignited spontaneously in either type of test at temperatures just above the melting temperature.

A theory for the spontaneous ignition of metals, based on the first law of thermodynamics, is presented. Good correlation was obtained between calculated spontaneous-ignition temperatures and values measured in supersonic jet tests.

There appears at the present time to be no need for concern regarding the spontaneous ignition of Inconel, the stainless steels, copper, aluminum, or magnesium for ordinary supersonic airplane or missile applications where the material temperature is kept within ordinary structural limits or at least below melting. For hypersonic applications where the material is to be melted away to absorb the heat of convection, the results of the present tests do not apply sufficiently to allow a conclusion.

INTRODUCTION

In the engineering of missiles or other aircraft to fly at extremely high speeds it has been customary to choose materials that retain strength at design temperature. More recently, designers who have been concerned with aircraft under transient thermal conditions have planned to use the skin as a heat sink and, in some extreme cases, to use the heat of fusion, or melting, as a possible means of absorbing the aerodynamic heating.

However, since most materials of construction are combustible if heated sufficiently, the possible rapid oxidation at high temperatures makes it necessary to consider the problem from a chemical as well as from the thermodynamic viewpoint.

One of the main factors that tends to inhibit the oxidation of metals is the formation of an oxide film which separates the air from the base metal. The oxides of some metals are very effective inhibitors. Aluminum and chromium are perhaps the two best known examples of metals that form an effective protective oxide coating. On the other hand, molybdenum and tungsten are examples noted for their porous, powdery oxide that gives practically no protection.

Some experience with the combustion of metals has been obtained in connection with oxygen cutting torches in standard shop practice. Here, experience has shown that most nonstainless steels cut readily, whether plain carbon steels or common alloys. However, for chrome-bearing steels, the speed of cutting decreases, and the cutting temperature necessary increases as the chrome content is increased.

Also, there has been considerable research on the oxidation of metals, but most of it has consisted of measurement of corrosion rates or the rate of scaling of various metals in air or other mediums at high temperature over prolonged periods. In the present paper, however, oxidation is considered from the viewpoint of possible ignition and combustion due to the heat release from accelerated oxidation. It is proposed that if the oxidation occurs with sufficient rapidity, the heat of oxidation will overbalance the heat dissipated in various ways, and ignition and combustion will follow.

EQUIPMENT AND TESTS

It is difficult to design equipment to investigate high-temperature oxidation because oxidation destroys the equipment. Since, at this time, no adequate ground-test facilities are available to determine ignition temperatures and oxidation rates under very realistic conditions, various phases of the problem have been investigated in the facilities available by resorting to subterfuges to bring the material tested up to temperature. In one of these, metal rods attached to a radius-arm support were preheated in a coke furnace and then swung quickly into a supersonic blowdown jet having a stagnation temperature of 600° F.

The rod samples had hemispherical noses of 3/8-inch diameter which were instrumented with chromel-alumel thermocouples. When preheated to 2,400° F, rods of cold-rolled steel, 4130 steel, and Graphmo tool steel rose almost instantly to their melting temperatures of approximately 2,600° F and burned. Combustion appeared to take place over the entire nose and over the first inch of the cylinder, which usually necked down. From this point back, molten metal in a very fluid state streamed over the surface and terminated 4 to 5 inches back of the nose. Apparently this stream of metal evaporated and joined the conflagration. The entire rod was bathed in a luminous and ever-growing sheath of flame. Steels with substantial chrome content, such as 18-8 stainless steel, did not undergo spontaneous ignition, although these materials were heated close to their melting temperatures.

A solid magnesium 20° total-angle cone was tested in a 1.5- by 4-inch nozzle at the Langley 11-inch hypersonic tunnel at a Mach number of 5.2 and an air stagnation temperature of 630° F. A graphite electric radiator with a radiating capacity of 100 kw/sq ft raised the magnesium temperature to 1,150° F. Structural disintegration of the cone occurred before an ignition temperature was reached.

An identical cone sample was placed in a $1\frac{1}{2}$-inch-diameter air jet issuing from an electrically heated stainless-steel pipe at a velocity of 300 ft/sec and a temperature of 1,600° F. Ignition of the cone followed a heating period during which about 1/4 inch of the nose melted off. The cone then burned steadily at the blunted nose until the entire cone was consumed.

In order to study some of the details of the mechanism of ignition under conditions of a controlled heat balance, wires of various materials about 1/16 inch in diameter and 2 inches long were heated by passing a high-amperage alternating current through the wire which, at the same time, was immersed in a static atmosphere of air, oxygen, or nitrogen. The wire was mounted normal to the axis of a 5-inch-diameter cylinder in which it was enclosed. The cylinder was able to withstand pressures up to 800 lb/sq in. and had a quartz window in one end to allow observation of ignition and burning. The wires were instrumented with chromel-alumel thermocouples 0.005 inch in diameter, capable of giving temperature measurements to 2,400° F.

DEFINITIONS

Before proceeding further with a discussion of oxidation and ignition, it seems in order to give some definitions and to examine the basic principles of spontaneous ignition. The symbols used herein are defined in the appendix. Consider a metallic surface oxidizing at high temperature. Figure 1 is a schematic representation of two quantities: The steeper curve represents the rate of heat released by oxidation, and the other curve represents the losses, which may be composed of convection, conduction, and radiation. The point where the rate of oxidation is equal to the losses is a critical point. If the slope of the oxidation-rate curve is greater than the slope of the losses curve, as in this figure, the temperature is in unstable equilibrium at this point. The temperature at this critical point will be referred to as the spontaneous-ignition temperature. If the temperature exceeds the spontaneous-ignition temperature it will continue to increase and, because of the exponential nature of the oxidation process with temperature, to increase rapidly. If the temperature is less than the critical value it will tend to decrease. Of course, the surface would never reach the spontaneous-ignition temperature if it were not heated by some forcing function, which is usually convection. In this case, convection reinforces oxidation and cannot be regarded as a loss. The spontaneous-ignition temperature is obviously a function of the particular environmental conditions as well as the material and, as is shown later, also depends on the history of temperature and environment. It may or may not exist below the melting temperature of the material.

RESULTS AND ANALYSIS

Figure 2 gives the results of heating a 1/16-inch-diameter wire in an atmosphere of air at 500 lb/sq in. abs. The wire, although nominally referred to as 1010 steel, is believed to contain somewhat less than 1 percent carbon. Figure 2(a) gives a time history of the wire temperature when heated with a 94-ampere current. For comparison, a time history of the temperature in an atmosphere of nitrogen at approximately the same pressure is shown. Although there is not much spread between the two curves, the difference in slopes is significant. To obtain figure 2(b) the wire is considered as a calorimeter. The slopes of the curves in figure 2(a) are plotted against temperature, but expressed as an apparent heating rate by using weight and specific heat as conversion factors. If the radiation and convection are assumed to be essentially the same in air and nitrogen at the same pressure and temperature, the difference in the apparent heating rate is due to oxidation. The difference, or oxidation rate, is plotted against temperature in figure 2(c) as the curve labeled 94 amp. The other curve, labeled 63 amp, is seen to have a considerably lower oxidation rate. The reason for this is shown in figure 2(d). The rate of oxidation, Btu/sec, is proportional to the rate of growth of oxide thickness. If the oxidation rate is converted to units of oxide thickness per second, if the oxide is assumed to be Fe_2O_3 with a heat of formation of 2,155 Btu/lb and a density of 327 lb/ft^3, and if the rate of thickness formation is integrated with time, the oxide thickness shown in figure 2(d) is obtained for the two heating rates. The wire with the slower heating rate has more time to oxidize and forms a greater thickness of oxide. The greater film thickness inhibits oxidation and gives the lower oxidation rate, as shown in figure 2(c).

If the electric power was cut off at any time during the 63-ampere test, the temperature immediately fell off, showing that the losses were greater than the oxidation heat rate.

The leveling off, or negative slope, of the oxidation-rate curve above 2,200° F for the 94-ampere case is believed to be due to a nitrogen enrichment in the immediate vicinity of the wire, resulting from the high rate of oxygen usage and the small flow of air by natural convection. This belief is strengthened by the observed behavior of the temperature when the electric power was cut off at about 2,200° F. The temperature rose, showing that the losses were exceeded, but after rising a few hundred degrees the upswing stopped and the temperature fell back. This could hardly be due to anything other than exhaustion of the local supply of oxygen. With a replenishment of air the temperature started up again. This process was repeated as many as three times in a few seconds, after which the wire cooled off. It was therefore thought that wire tests in an atmosphere of oxygen would give more information pertinent to high-speed flight conditions in which oxygen supply is sufficient for spontaneous ignition.

Theoretically, the gas pressure does not affect the oxidation rate. A series of tests were made on steel wires in an atmosphere of oxygen to determine whether the pressure had a noticeable effect on the rate of oxidation. The pressure was varied from 1/2 atmosphere to 53 atmospheres. Any effect of pressure on oxidation rate was too small to be determined. A pressure of 33 atmospheres or 500 lb/sq in. abs was chosen for further work, and the results are shown in figure 3.

Figure 3(a) shows the rate of oxidation for three heating rates, and the curve labeled losses intersects the other curves at spontaneous-ignition temperatures. If the electric power was cut off at higher temperatures, the temperature rose rapidly, after which the wire burned until it was consumed. The integrated oxide thicknesses for the same heating rates are shown in figure 3(b).

Constant-temperature cross plots of figures 3(a) and 3(b) yield oxidation rate as a function of oxide thickness, as shown in figure 3(c). The points are experimental values obtained from the cross plots and were used to establish the coefficients of the engineering formula for oxidation rate,

$$Q_o = \frac{134500}{\delta} e^{-\frac{42170}{T}} \tag{1}$$

which is represented by the solid lines in figure 3(c). The numerator of this expression is the well-known Arrhenius function which gives the reaction rate of many chemical reactions and, in particular, of many oxidation processes. The denominator contains simply the oxide thickness δ. The dependence of the oxidation rate on the reciprocal of the oxide thickness is in conformity with the ion diffusion theory developed by Wagner. It agrees with the present data for fast rates of oxidation and also agrees with much of the oxidation data in the literature obtained on steels at lower oxidation rates. The form of equation (1) was obtained by making the observation that the diffusion function $\text{Constant}/\delta$ and the Arrhenius temperature function $Ae^{-B/T}$ are independent of each other, so that a combined equation can be obtained simply as the product of the two functions. This equation can be expressed as a rate of weight gain instead of rate of heat release, and integrated with respect to time at constant temperature. In that form it is known as the parabolic law of oxidation because the weight gain is proportional to the square root of the time (ref. 1). The parabolic law agrees with much of the constant-temperature test data in the literature for the oxidation of both ferrous and nonferrous metals which have nonporous or nonpowdery oxides, such as certain steels, chrome, copper, and aluminum. It follows that the form of the diffusion formula herein presented should apply for these metals over any range of conditions for which their oxidation characteristics have been shown to fit the parabolic law of oxidation. The constants must be adjusted for the particular metal according to test results.

However, the application of this formula has certain limitations. It obviously cannot apply at oxide thicknesses approaching zero. However, this formula apparently applies for a coating as thin as 0.0001 or 0.0002 inch. Strictly, the constants in the equation are adjusted for oxygen, but the equation may be used with air provided the surface is fully supplied with oxygen so that it remains saturated in spite of the rapid usage of oxygen. This point is illustrated in a subsequent paragraph. For aerodynamic ignition, saturation of the surface with oxygen seems to imply only that there must be a substantial mass flow of air or a substantial stagnation pressure. These conditions are usually present with high rates of heat transfer.

In order to determine whether the spontaneous-ignition temperature can be calculated for steel in a supersonic airstream, computations were made for the conditions of the round-nose rods tested in the preflight jet of the Langley Pilotless Aircraft Research Station at Wallops Island, Va. The test conditions are stated at the top of figure 4. The spontaneous-ignition temperature equation, which is a form of the first law of thermodynamics, is

$$Q_O \quad = \quad Q_{CONV} \quad + \quad Q_{RAD}$$

$$\frac{134500}{\delta} e^{-\frac{42170}{T}} = 1.32 \frac{k}{d} R^{.5} N_{PR}^{\ .4}\left(T_{AW} - T\right) + 0.000048\epsilon\left(\frac{T}{100}\right)^4 \qquad (2)$$

Conduction is omitted because the rods were quite uniformly heated. The first term represents oxidation and is taken from equation (1). The second term is Sibulkin's theory for the heat transfer on a hemispherical nose, which, in this case, had a diameter of 3/8 inch. The last term is the usual expression for radiation. The value of emissivity was taken as 0.88. The unknown quantity T, the surface temperature for equilibrium conditions, appears in each term. The solutions of this equation for oxide thicknesses of 0.0001 and 0.001 are plotted in figure 4. The theory shows a slight drop in spontaneous-ignition temperature with airspeed because the convection represents a loss. The measured spontaneous-ignition temperatures also show a slight drop with speed at the higher speed range. At 150 ft/sec, no ignition was obtained although the specimens were heated to near melting. Insufficient oxygen, together with nitrogen enrichment of the boundary layer, seems to be the most probable cause of the failure to ignite at low airspeed, although reduced erosion may possibly affect the result.

Some nonferrous materials such as Inconel and copper were tested to temperatures approaching melting in a supersonic blowdown jet with a stagnation temperature of 600° F, without obtaining ignition. The same results were obtained from the simple heated-wire tests in an atmosphere of oxygen. Figure 5 shows temperature-time histories for wires of several materials tested in oxygen at 500 lb/sq in. abs. Although the Inconel and copper were heated until they melted, no ignition was obtained. The rate of oxidation of these materials was too small to be measured by the techniques used. The break in the titanium curve is not associated with oxidation but is believed to be due to a change in the specific heat. When the electric power was cut off at 2,100° F the titanium spontaneously ignited and burned vigorously. Titanium was also found to burn vigorously in an atmosphere of pure nitrogen as well as in an atmosphere of air. The spontaneous ignition temperature in air at a pressure of 1 atmosphere was 2,900° F. Magnesium was observed to ignite when it melted, possibly because some of the protective oxide coating was floated off.

CONCLUSIONS

Tests of low-carbon steel and several other materials heated artificially in wind tunnels, in air jets, and under static conditions in atmospheres of air, oxygen, and nitrogen indicate the following:

1. When rapidly heated in an atmosphere of oxygen or when heated and plunged into a supersonic jet at Mach 1.4 or 2.0,

(a) Iron or carbon steel and common alloys such as 4130 were found to have spontaneous ignition temperatures in the solid phase (below melting) and melted very rapidly while burning.

(b) Inconel, copper, 18-8 stainless steel, Monel, and aluminum did not have a spontaneous ignition temperature in the solid phase, nor could they be made to ignite at, or close to, melting with the equipment available.

(c) Titanium burned in atmospheres of air, oxygen, or nitrogen.

2. A good correlation of experimental and theoretical spontaneous-ignition temperatures was obtained for steel in supersonic airstreams. Comparable spontaneous-ignition temperatures were obtained by simulation in an atmosphere of oxygen.

3. The fact that the oxidation rate of some materials varies inversely with the oxide thickness suggests that, for some materials, catastrophic release of heat by oxidation may be prevented either by heating gradually or by prior oxidation.

4. There appears at the present time to be no need for concern regarding the ignition of Inconel, the stainless steels, copper, or magnesium for any ordinary supersonic airplane or missile applications where the material temperature is kept within ordinary structural limits or at least below melting. For hypersonic applications where the material is to be melted away to absorb the heat of convection, the results of the present tests do not apply sufficiently to allow a conclusion.

APPENDIX

SYMBOLS

N_{Pr}	Prandlt number
Q_O	rate of heat generated by oxidation, Btu/sec-ft^2
Q_L	rate of heat loss, Btu/sec-ft^2
Q_{CONV}	rate of convective heat loss, Btu/sec-ft^2
Q_{RAD}	rate of radiation loss, Btu/sec-ft^2
R	Reynolds number (based on nose diameter)
T	temperature, $^{\circ}$F abs
T_{AW}	adiabatic wall temperature, $^{\circ}$F abs
d	nose diameter of specimen, ft
k	conductivity of air, Btu/(sec-ft^2)($^{\circ}$F/ft)
δ	oxide thickness, in.
ϵ	emissivity, Btu/(sec-ft^2)($^{\circ}$F)

REFERENCE

1. Miley, H. A.: Fundamentals of Oxidation and Tarnish. The Corrosion Handbook, Herbert H. Uhlig, ed., John Wiley & Sons, Inc., 1948, pp. 11-20.

DEFINITIONS

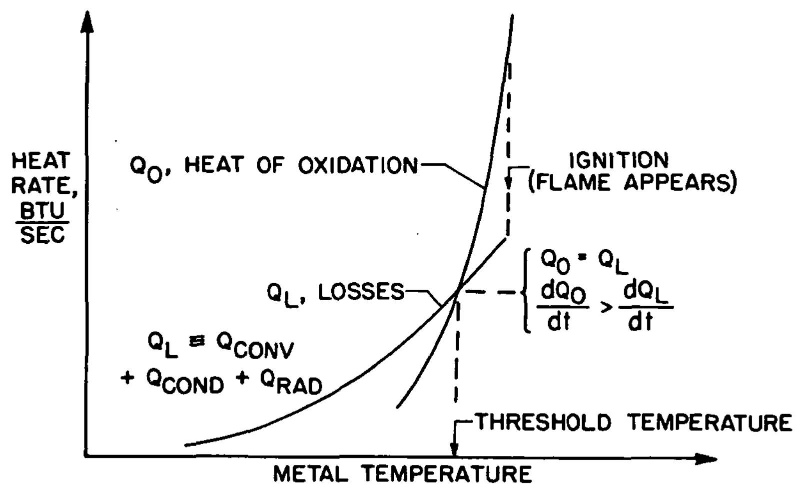

Figure 1

BOMB TEST TECHNIQUE

AIR; p=500 LB/SQ IN., ABS; 1010 STEEL

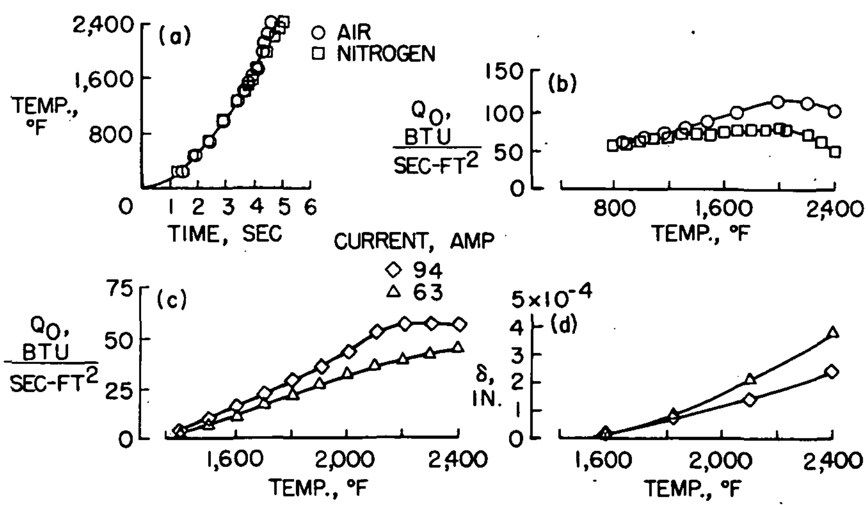

Figure 2

~~CONFIDENTIAL~~

EFFECT OF OXIDE THICKNESS ON OXIDATION
1010 STEEL; p = 500 LB/SQ IN., ABS; OXYGEN

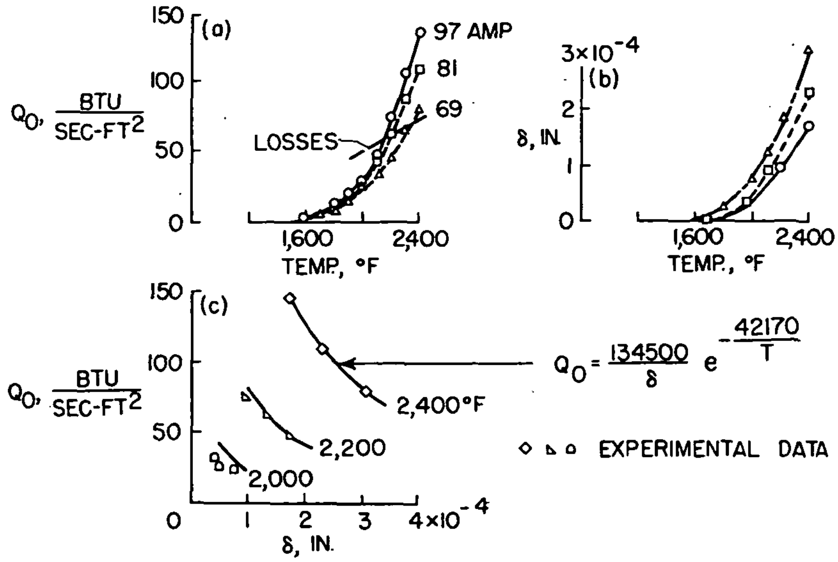

Figure 3

SPONTANEOUS-IGNITION TEMPERATURE COMPUTATION
1020 STEEL; STAGNATION TEMP., 600° F; ATM. PRESSURE

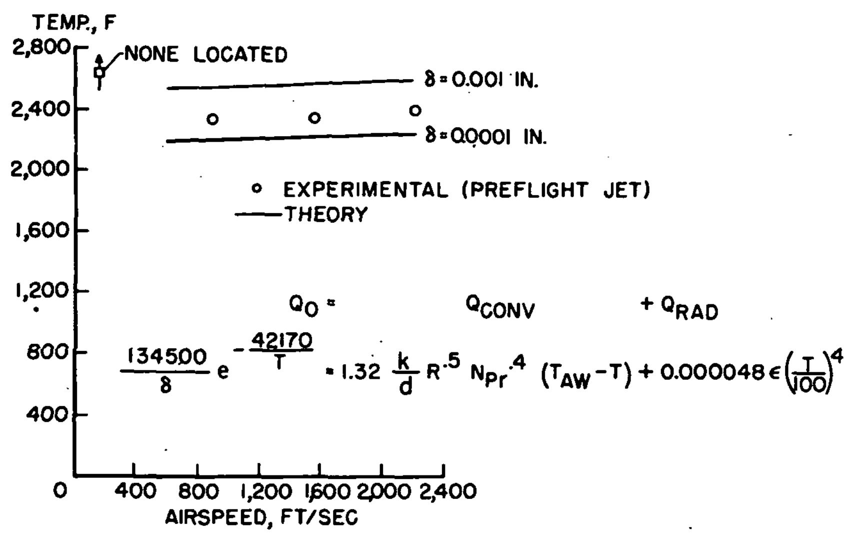

Figure 4

~~CONFIDENTIAL~~

[redacted]

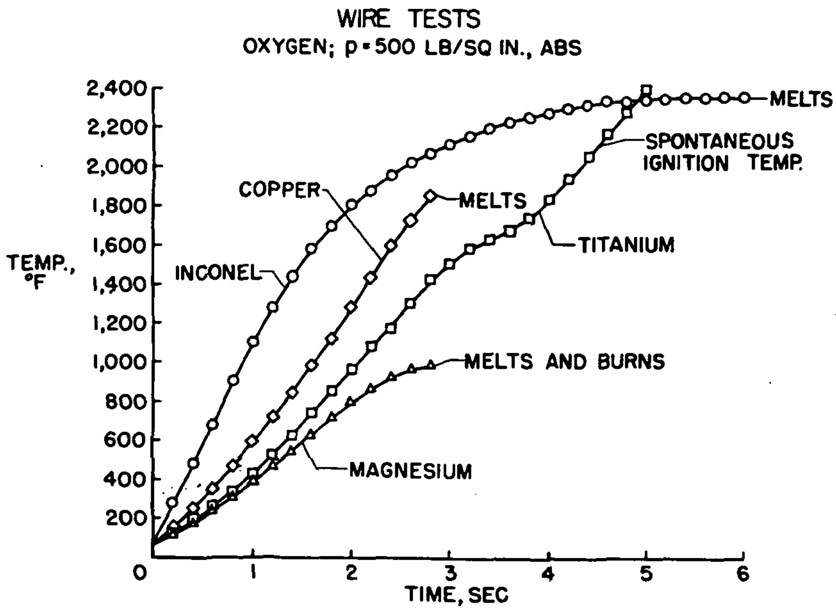

Figure 5

[redacted]

AERODYNAMIC HEATING OF AIRCRAFT COMPONENTS

By Leo T. Chauvin

Langley Aeronautical Laboratory

SUMMARY

Aerodynamic heat-transfer data obtained at supersonic speeds are presented for various airplane components such as a conical nose, a blunt conical nose, a cone-cylinder body, a flat-faced canopy, a delta wing at angle of attack, and a deflected flap. The data are correlated on the basis of Stanton number for various supersonic Mach numbers and Reynolds numbers.

For all cases investigated, measurements were in reasonable agreement with theoretical predictions, except for the sheltered surface of the delta wing at angle of attack.

In addition to the heat transfer measured on the 50° blunt cone, transition was found to occur at a transition Reynolds number of 0.5×10^{6} based on local conditions at a free-stream Mach number of 4.84.

INTRODUCTION

The designer of the supersonic airplane is confronted with the analysis of various airplane components for aerodynamic heating. Inasmuch as most heating data have been for very simple shapes, the importance of detail design may easily be missed. Recently, large-scale heat transfer data have been obtained from free-flight and free-jet tests of such airplane components as blunt noses, canopies, wings at angle of attack, and deflected control flaps. The purpose of this paper is to review new and significant data which will be of interest to designers in determining the heating of these components. A comparison with existing theory to indicate its adequacy in each case is also presented.

SYMBOLS

M Mach number

R Reynolds number

N_{St} Stanton number, $h/c_p \rho V$

h local aerodynamic heat-transfer coefficient, $\frac{\text{Btu}}{(\text{sec})(\text{sq ft})(^{\circ}\text{F})}$

c_p specific heat of air at constant pressure, $\frac{\text{Btu/slug}}{^{\circ}\text{F}}$

ρ density of air, slugs/cu ft

V velocity, ft/sec

x distance along model surface, ft or in. as indicated

α angle of attack, deg

δ control deflection, deg

T temperature, $^{\circ}$F or $^{\circ}$F abs

Subscripts:

l outside the boundary layer

T transition

W conditions pertaining to the skin of model

∞ free stream

AIRPLANE COMPONENTS

A breakdown of the various components of the airplane for which heat-transfer data are available is presented in the following table:

Nose: cone, circular arc, parabola, hemisphere, Von Kármán
Body: cylinder, cone cylinder, hemispherical-nose cylinder, parabola
Canopy: flat-faced canopy
Wing: plan form: unswept, delta
Control: sealed flap

As can be seen, data are available for a wide range of nose shapes and bodies; whereas information is limited to only one canopy shape, two wing plan forms, and one flap arrangement. Information for some of the listed components can be found in references 1 to 12.

Nose and Body

In order to investigate heat transfer on a simple nose shape at high Reynolds number, flight tests were made on a large 10° cone. This test model, shown in figure 1, had an 18-inch base and was 7.5 feet long. The model was rocket launched at low altitude, which for $M_l = 3$ gave a Reynolds number per foot of 18×10^6, or 135×10^6 based on the full cone length. In order to keep a low skin temperature favorable for laminar flow, the skin was made of 0.08-inch copper and the model was accelerated rapidly.

The thermocouple locations are indicated on the sketch shown in figure 1. The skin temperature and Stanton number are shown plotted against body length. Note that the maximum temperature was obtained about 2 feet back from the nose tip and this result indicates that transition to turbulent flow had taken place. The condition of the boundary layer is shown more clearly by the heat-transfer data in the lower part of the figure plotted as local Stanton number. The data show laminar heat transfer for the forward part of the nose, with transition occurring at 1.85 feet from the nose tip at a Reynolds number of 33×10^6. The measured heat-transfer coefficients for the laminar region agree well with the theory of reference 13. For the turbulent region, the theory of reference 14 is in good agreement when the characteristic length for the theory is the length behind the transition point. This agreement is quite significant in view of the rather large longitudinal temperature gradient that existed when the measurements were made and the fact that the theory assumes constant wall temperature.

A large amount of large-scale data are available for parabolic noses and complete bodies such as the NACA RM-10 missile. For a cone-cylinder body, however, only recently have large-scale data been obtained at high Mach numbers. A part of these new data are shown in figure 2. A 15° conical nose on an 8.5-inch-diameter cylinder was flown to a Mach number of approximately 5. The heat-transfer data are presented as a function of body length for two flight conditions. For $M_l = 4.5$ and R_l per foot of 5.5×10^6, the data on the nose are laminar and agree with theory (ref. 13); transition occurs shortly after the cone-cylinder juncture and is spread over a wide region. The data rearward of the transition region are in agreement with turbulent theory (ref. 14). For $M_l = 3.0$ and R_l per foot of 16.4×10^6, turbulent heat transfer existed at all measurement stations and is in good agreement with theory except for the cylindrical section where the data are lower than the theoretical results. The theory for this case overestimates the value for the heat transfer.

In view of the interest in blunt noses for radomes and, in particular, to avoid the high heating rate on the extreme point, a large blunted cone has been flight tested to a Mach number of 5. This nose as shown in figure 3 had a 50° total angle with a base diameter of approximately 18 inches and a nose diameter one-half this value. Both temperatures and pressures were measured at the station shown. Figure 3 gives the measured wall temperature plotted against length from the stagnation point in inches for $M_{\infty} = 4.84$ as the model accelerated to $M_{\infty} = 5$. The Reynolds number based on free-stream conditions was 22.4×10^{6} per foot. The temperature data indicate that transition started at approximately 2 inches from the stagnation point or at approximately 30° corresponding to $R_{\infty} = 3 \times 10^{6}$. Converting this transition Reynolds number to local conditions yields a value of only 0.5×10^{6}, even though the local temperature ratio was only 0.48. Measured heat-transfer coefficients are shown plotted as a function of distance from the stagnation point. At the stagnation point, the theory of Sibulkin (ref. 15) is in good agreement with the experiment, whereas for the rearmost station on the cone the data are approximately 10 percent lower than the theory for turbulent cones when the theory is based on the distance from the transition point. It is evident from these data that this nose shape poses a severe heating problem because of the unexpected early transition.

Canopy

A very important component of the airplane for which the design requires large-scale heat-transfer data is the canopy. Heat transfer on a typical flat-faced canopy has been recently measured from a flight test and is shown in figure 4. The canopy was located 4 feet back of the nose of a parabolic body 12.5 feet long. The flat windshield was sweptback 63°. The heat transfer measured at $M_{\infty} = 3.0$, $R_{\infty} = 13 \times 10^{6}$ per foot is presented as a function of canopy length; also shown as a dashed curve is heat transfer on the basic body. It can be seen that the heat transfer on the face of the canopy is more than twice that on the basic parabolic body. The heat transfer on the rear of the canopy is considerably less than the corresponding heat transfer on the basic body. Two-dimensional shock theory was used for the local conditions on the windshield, and the theory (ref. 14) based on these local conditions is in fair agreement with the heat-transfer measurements. Theoretical heat-transfer coefficients calculated for the rear of the canopy by use of Prandtl-Meyer expansions for the local conditions are somewhat higher than the measurements.

Wing and Controls

Consideration is next given to the possibilities of computing the heat transfer on typical wings and controls. Figure 5 shows typical aerodynamic heat-transfer coefficients obtained on a 60° delta wing of NACA 65A005 section. The tests were made in a free jet at $M_\infty = 2.0$ and Reynolds number of 14×10^6 per foot. In order to minimize the thermal stresses normally encountered in this type of test, the wing skin was constructed from 0.032-inch Invar, which has a low coefficient of thermal expansion. The Stanton number is shown plotted against distance in percent chord for angles of attack of 0°, 3°, and 6°. Turbulent flow is indicated by the heat-transfer data at all stations. The Reynolds number at the forward station was 5×10^6. The data show that, for the lower surface, increasing α to 6° caused approximately a 15-percent increase in the heat-transfer coefficient, whereas for the upper surface the heat-transfer coefficient is approximately 15 percent lower for $\alpha = 3^\circ$ and approximately 30 percent lower for $\alpha = 6^\circ$.

In order to indicate the possibility of predicting the heat transfer from theory, the heat-transfer coefficients on the wing from figure 5 are replotted in figure 6, together with data at $\alpha = 9^\circ$. These data are correlated as the ratio of experimental Stanton number to theoretical Stanton number (ref. 14), where the parameters are based on local conditions in which the length factor is the distance from the leading edge to the measurement stations. The data are plotted against distance in percent chord. Perfect agreement with theory is a ratio of 1.0. The chart shows good correlation at all angles of attack on the lower surface, whereas on the upper surface good correlation is obtained only at $\alpha = 3^\circ$. At $\alpha = 6^\circ$, the experimental data give a heating rate only 78 percent of that predicted by theory and at $\alpha = 9^\circ$ the experimental values are 65 percent of the theoretical values. This difference is believed to be due to separation at the higher angles of attack.

Heat transfer to a deflected control surface is presented in figure 7. The data are for a flap control of the sealed type extending across the trailing edge of a delta wing. Data were obtained from flight tests as the model accelerated to $M_\infty = 2.7$. The model had four wings in a cruciform arrangement with controls deflected like ailerons. Two opposing flaps were deflected 10° and the other two were deflected 20° in a direction to oppose the roll of the first two. As a result, a small rate of roll remained, which induced an angle of attack at the measuring station of less than 1°. The Stanton number based on free-stream conditions is plotted against flight Mach number for a midspan station near the trailing edge. The Reynolds number was approximately 9×10^6 per foot. The filled-in symbols are for the lower surface and the open symbols for the upper surface of the flap. The data for the lower surface with the 20° deflection are approximately 4 times those of the upper surface for all Mach numbers, and 2.5 times those of the upper surface for the 10° deflection.

A comparison with theory at $M_\infty = 2.64$ and a flap deflection of 10° is presented in figure 8. Stanton number is plotted against chord length for two measurement stations on the flap and one station on the wing ahead of the flap. The data are in good agreement with theory (ref. 14) for a deflected plate based on the length from the leading edge of the wing.

CONCLUDING REMARKS

The heat transfer obtained in supersonic flight tests for a conical nose, a blunt conical nose, a cone-cylinder body, a flat-faced canopy, and a deflected flap has been experimentally measured. For a delta wing, data were obtained in a blowdown-type jet at a Mach number of 2.0 for various angles of attack.

Early transition was obtained from the flight test of the 50° blunt cone at a Mach number of 4.84 and a Reynolds number (per foot) of 22.4×10^{6} based on free-stream conditions. Transition from laminar to turbulent boundary layer occurred at 1.5 inches from the stagnation point corresponding to a Reynolds number of 0.5×10^{6} based on local conditions. The theory of Sibulkin for the stagnation-point heat transfer was in good agreement with the measurements.

The heat-transfer data for the various components investigated were in good agreement with the predicted heat transfer except for the sheltered surface of the delta wing at angle of attack.

REFERENCES

1. Rumsey, Charles B., Piland, Robert O., and Hopko, Russel N.: Aerodynamic-Heating Data Obtained From Free-Flight Tests Between Mach Numbers of 1 and 5. NACA RM L55A14a, 1955.

2. Rumsey, Charles B.: Free-Flight Measurements of Aerodynamic Heat Transfer to Mach Number of 3.9 and of Drag to Mach Number 6.9 of a Fin-Stabilized Cone-Cylinder Configuration. NACA RM L55G28a, 1955.

3. Rabb, Leonard, and Simpkinson, Scott H.: Free-Flight Heat-Transfer Measurements on Two 20° Cone-Cylinders at Mach Numbers From 1.3 to 4.9. NACA RM E55F27, 1955.

4. Messing, Wesley E., Rabb, Leonard, and Disher, John H.: Preliminary Drag and Heat-Transfer Data Obtained From Air-Launched Cone-Cylinder Test Vehicle Over Mach Number Range From 1.5 to 5.18. NACA RM E53I04, 1953.

5. Scherrer, Richard: Comparison of Theoretical and Experimental Heat Transfer Characteristics of Bodies of Revolution at Supersonic Speeds. NACA Rep. 1055, 1951. (Supersedes NACA RM A8L28 by Scherrer, Wimbrow, and Gowen; NACA TN 1975 by Wimbrow; NACA TN 2087 by Scherrer and Gowen; NACA TN 2131 by Scherrer; and NACA TN 2148 by Wimbrow and Scherrer.)

6. Chauvin, Leo T., and Maloney, Joseph P.: Turbulent Convective Heat-Transfer Coefficients Measured From Flight Tests of Four Research Models (NACA RM-10) at Mach Numbers From 1.0 to 3.6. NACA RM L54L15, 1955.

7. Piland, Robert O., and Collie, Katherine A.: Aerodynamic Heating of Rocket-Powered Research Vehicles at Hypersonic Speeds. NACA RM L55E10c, 1955.

8. Sommer, Simon C., and Short, Barbara J.: Free-Flight Measurements of Turbulent-Boundary-Layer Skin Friction in the Presence of Severe Aerodynamic Heating at Mach Numbers from 2.8 to 7.0. NACA TN 3391, 1955.

9. Chauvin, Leo T., and Maloney, Joseph P.: Experimental Convective Heat Transfer to a 4-Inch and 6-Inch Hemisphere at Mach Numbers From 1.62 to 3.04. NACA RM L53L08a, 1954.

10. Stine, Howard A., and Wanlass, Kent: Theoretical and Experimental Investigation of Aerodynamic-Heating and Isothermal Heat-Transfer Parameters on a Hemispherical Nose With Laminar Boundary Layer at Supersonic Mach Numbers. NACA TN 3344, 1954.

11. Korobkin, Irving: Laminar Heat Transfer Characteristics of a Hemisphere for the Mach Number Range 1.9 to 4.9. NAVORD Rep. 3841 (Aeroballistic Res. Rep. 257), U. S. Naval Ord. Lab. (White Oak, Md.), Oct. 10, 1954.

12. Jones, Ira P., Jr.: Measurements of Aerodynamic Heating Obtained During Demonstration Flight Tests of the Douglas D-558-II Airplane. NACA RM L52I26a, 1952.

13. Van Driest, E. R.: Investigation of Laminar Boundary Layer in Compressible Fluids Using the Crocco Method. NACA TN 2597, 1952.

14. Van Driest, E. R.: Turbulent Boundary Layer in Compressible Fluids. Jour. Aero. Sci., vol. 18, no. 3, Mar. 1951, pp. 145-160, 216.

15. Sibulkin, M.: Heat Transfers Near the Forward Stagnation Point of a Body of Revolution. Jour. Aero. Sci. (Readers' Forum), vol 19, no. 8, Aug. 1952, pp. 570-571.

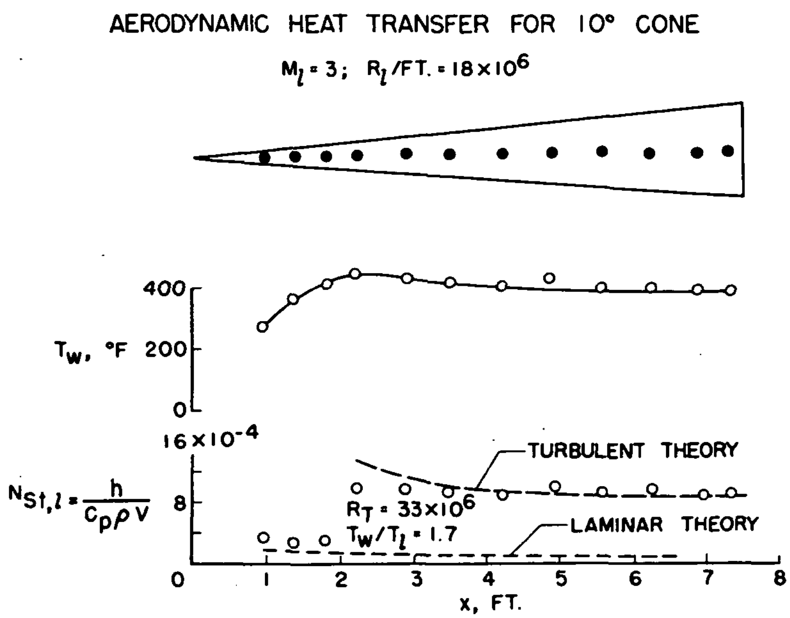

Figure 1

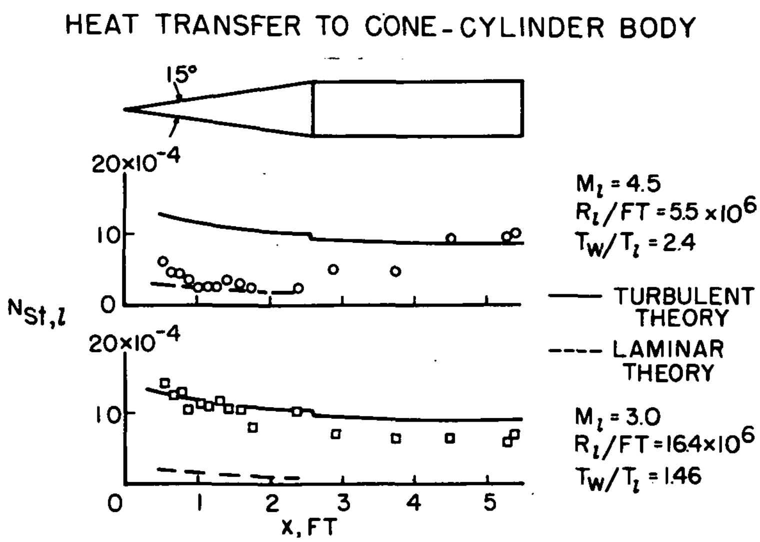

Figure 2

[redacted]

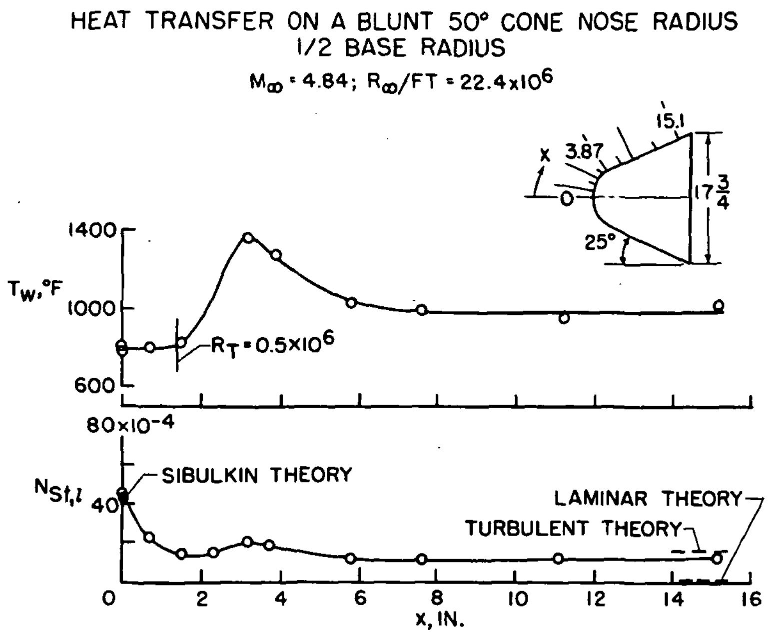

Figure 3

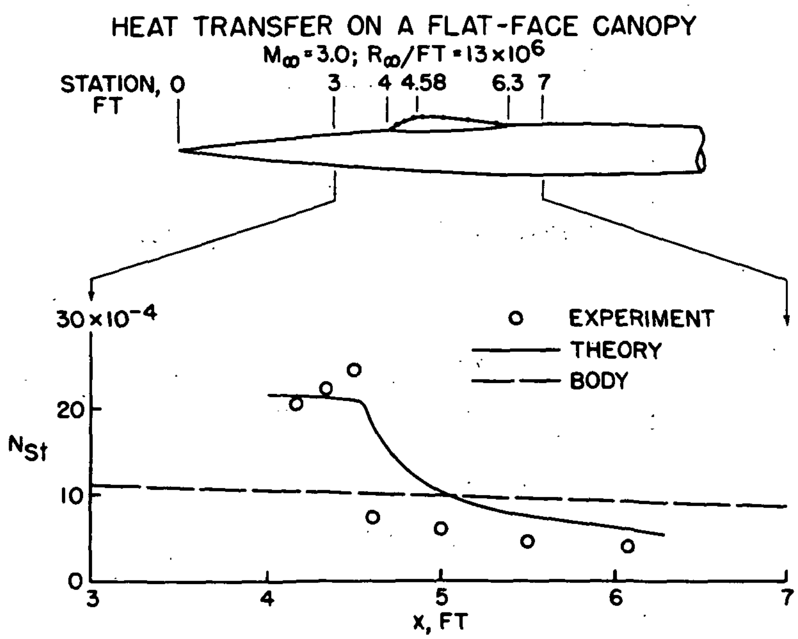

Figure 4

[redacted]

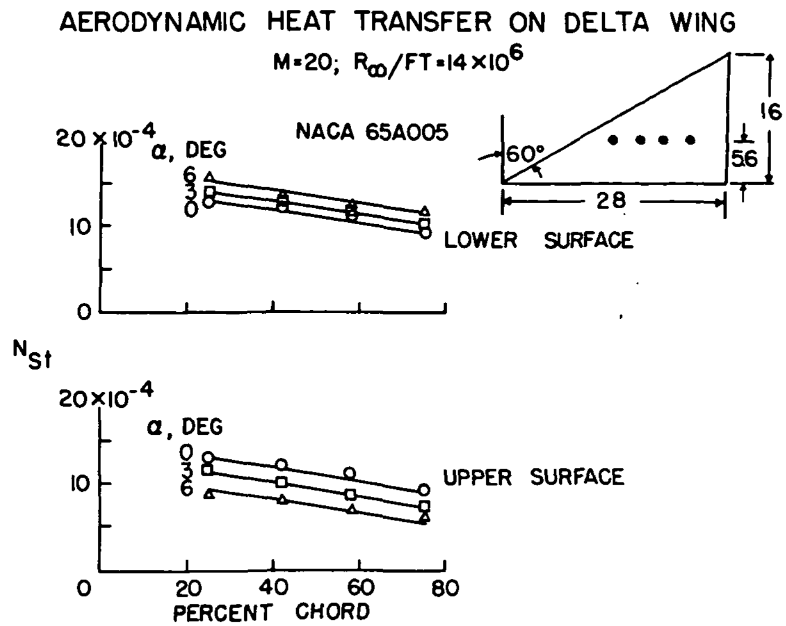

Figure 5

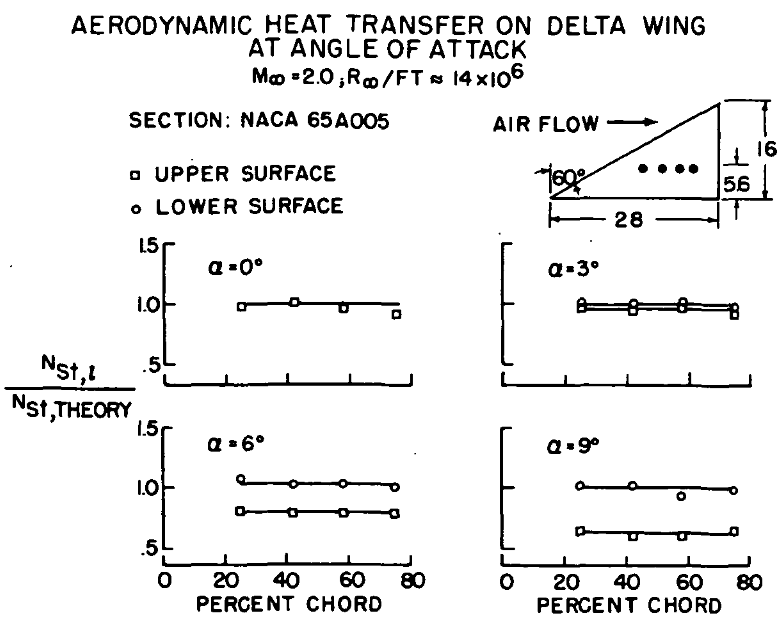

Figure 6

[redacted]

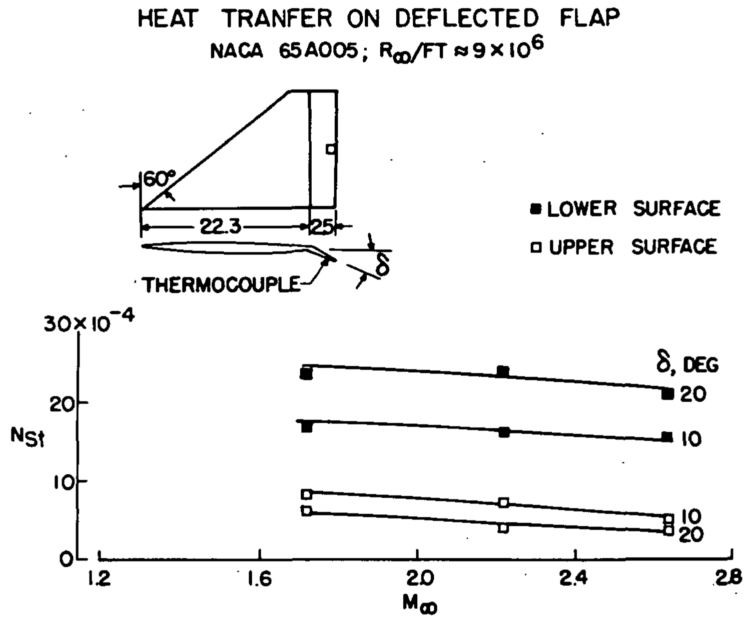

Figure 7

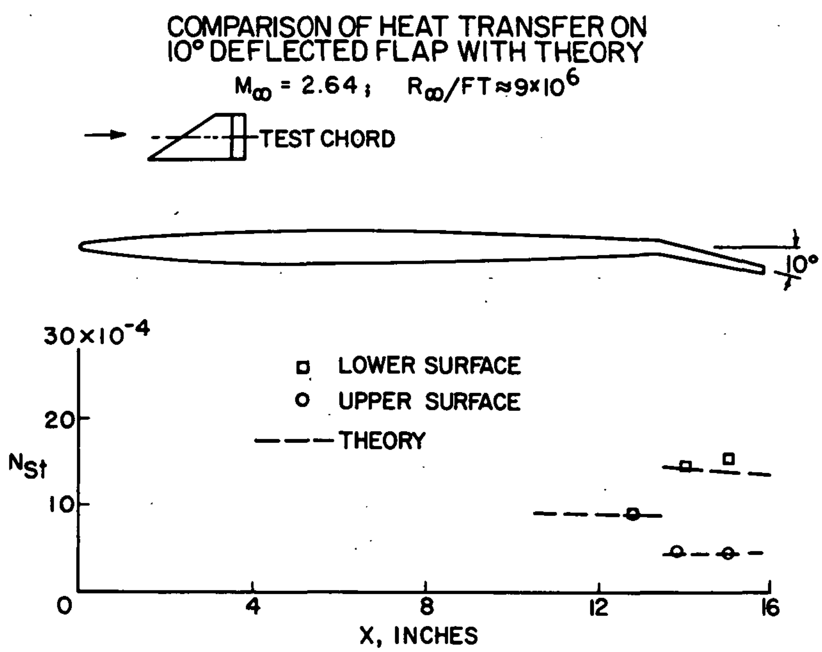

Figure 8

[redacted]

THE INFLUENCE OF SURFACE INJECTION ON HEAT TRANSFER AND SKIN FRICTION ASSOCIATED WITH THE HIGH-SPEED TURBULENT BOUNDARY LAYER

By Morris W. Rubesin

Ames Aeronautical Laboratory

SUMMARY

Existing analyses of the effect of surface injection on the heat transfer and skin friction associated with the turbulent boundary layer at high speeds are correlated to eliminate, largely, the effects of Mach number and Reynolds number. It is shown that surface injection reduces greatly both skin friction and heat transfer. Data for heat transfer and skin friction at Mach numbers of 0, 2.0, and 2.7 are compared with the analyses and the agreement is rather good.

From an example employing evaporative cooling with water, it is concluded that at high Mach numbers transpiration cooling is much more effective than a conventional cooling system.

INTRODUCTION

One cooling system for high-speed aircraft experiencing aerodynamic heating that shows promise is a transpiration cooling system. The schematic diagram in figure 1 helps to indicate what is meant by a transpiration cooling system for an aircraft. In such a system the coolant passes from the interior of the aircraft through a porous outer skin and into the hot boundary layer. The system shows promise for two reasons. First, in passing through the skin, the coolant reaches the temperature of the skin because of the large amount of surface area for heat transfer existing within the pores. Thus, the coolant reaches the maximum temperature of the system and is used most effectively. In terms of a heat exchanger, this is called 100 percent effectiveness. The second contributing reason is that as the coolant passes into the hot boundary layer it cools the inner portion of the boundary layer and forms a buffer between the hot gases of the boundary layer and the skin that is being cooled. Thus, the amount of heat entering the surface is reduced by the injection of a coolant.

There are also disadvantages in a transpiration cooling system. The porous material is difficult to manufacture, and the inherent weakness of the material requires more difficult and complex structural design. Also, the roughness of the porous materials and the effect of fluid injection are such that the normally laminar boundary layers may be tripped into turbulent boundary layers and in that way increase the amount of heat entering the body. A transpiration cooling system, therefore, would probably be considered only for cases where turbulent flow exists normally or where extremely favorable pressure gradients exist so as to insure laminar flow. In view of these disadvantages, it is believed that only a complete systems analysis will show whether or not a sound engineering solution will require transpiration cooling. In order to perform these systems analyses the designer will require knowledge of how surface injection affects the heat transfer and skin friction associated with boundary layers.

This paper presents available information on the effect of injection on the turbulent boundary layer. Theory and experiment are compared to determine whether or not the theoretical results can be used to extrapolate the limited amount of available data. After this comparison is made, an example of some advantages of transpiration cooling over conventional cooling systems is shown.

SYMBOLS

C_f	local skin-friction coefficient
F	injection parameter, $\rho_w v_w / \rho_1 u_1$
M	Mach number
Pr	Prandtl number
R_x	Reynolds number based on length along surface
St	Stanton number
t	temperature
T	absolute temperature
u	velocity parallel to surface
v	velocity normal to surface
w	weight flow rate of coolant

x distance along surface from leading edge

ϵ surface emissivity

η_v temperature recovery factor

ρ density

Subscripts:

0 zero surface injection

1 condition at outer edge of boundary layer

∞ free-stream condition

w surface condition

ANALYTICAL RESULTS

Two analyses exist at present which are concerned with the effect of the injection of air into air in a compressible turbulent boundary layer. Both are based on mixing-length theory and differ mainly in the manner in which arbitrary constants introduced in each analysis are handled. The analysis of Dorrance and Dore (ref. 1) considers the Prandtl number to be 1 and the turbulent boundary layer to extend down to the surface. The author's analysis (ref. 2) considers the Prandtl number to be 0.72, includes the existence of a laminar sublayer, and requires knowledge of its thickness. In both analyses plausible assumptions based on empirical knowledge are made to identify the arbitrary constants introduced.

Skin Friction

A comparison of the effects of injection on skin friction, as determined by the two analyses, is made in figure 2. The ordinate is the local skin-friction coefficient divided by the local skin-friction coefficient for zero injection and the abscissa is the dimensionless injection parameter F divided by half the local skin-friction coefficient for zero injection. The injection parameter F is the coolant mass-flow rate per unit area normal to the surface divided by the mass flow per unit area of the main airstream. The shaded areas on this figure represent the numerical results obtained over a large range of the parameters: Mach number, Reynolds number, and the ratio of wall to free-stream temperature. For instance, for the analysis of the Dorrance and Dore calculations were made in which the Mach number ranged from 0 to 20, the ratio of wall temperature to free-stream temperature ranged from 1 to 3, the Reynolds number ranged from 10^7 to 10^9, although higher Reynolds numbers also fall within this shaded region. In the author's analysis, the Mach number ranged from 0 to 8, the ratio of wall to free-stream temperature ranged from 1 to 3, and the Reynolds number ranged from 10^6 to 10^8. The effect of these parameters is largely eliminated by this type of coordinate system. Note that calculations with both F constant along the body and F proportional to the local skin-friction coefficient have been plotted on this figure. Both analyses, although yielding different results, show that the effect of injection on skin friction can be very large; reductions down to 1/5 of the zero-injection skin-friction coefficient are shown.

Heat Transfer

The calculated effect of injection on heat transfer is shown in figure 3. In this figure the ordinate is the ratio of the local Stanton number to the local Stanton number for zero injection and the abscissa is the blowing parameter F divided by the local Stanton number for zero injection. The results of the analysis of Dorrance and Dore are not plotted here as they would result in a curve identical to that shown in figure 2. The reason for this is that the Prandtl number of 1 used in their analysis results in an exact Reynolds analogy between skin friction and heat transfer.

The region shown, representing the author's analysis, is quite similar to the region in figure 2 for the skin-friction relationship, even though the Prandtl number is 0.72 and no exact Reynolds analogy exists. Apparently the effect of Prandtl number is largely absorbed in the choice of coordinates for figure 3. In effect, the results of heat transfer can be considered essentially identical to those of skin friction for both analyses when plotted as in this figure. Thus, the analyses predict that heat transfer is also reduced considerably by surface injection.

The relatively small difference between the two analytical results should not be considered as an indication of the certainty of these results. Other analyses, based on equally plausible flow models, could yield results that differ greatly from these results. Ultimately, the worth of these analyses can be assessed only through a comparison with experimental data. Agreement between analysis and data, however, should not imply a verification of the physical assumptions of the theory, but should be considered simply as providing a systematic means of extending the range of applicability of the limited amount of data now available.

COMPARISON OF ANALYSIS WITH EXPERIMENT

Low-Speed Data

Mickley, Ross, Squyers, and Stewart (ref. 3) obtained skin-friction and heat-transfer data while injecting air into the boundary layer on a flat plate. The free-stream air flows were at speeds below 60 feet per second. Data were obtained for constant values of the blowing parameter F along the plate and for values of F varied proportionately to the skin-friction coefficient.

Skin friction.- The skin friction was measured by surveying the boundary layer with impact-pressure probes and then calculating the momentum thickness of the boundary layer at several stations along the plate. The local skin-friction coefficient was determined from the difference between the local momentum-thickness gradient and the local injection parameter. Because this difference was often small compared with the individual terms, errors in the momentum thickness or local injection rate produced larger errors in the skin-friction coefficient. The data, therefore, scatter considerably. Another factor requiring mention is that the plate under zero injection was not aerodynamically smooth, the skin-friction coefficient being in general about 15 percent higher than on a smooth plate.

A comparison of these data with the analyses is shown in figure 4. The ordinate is again the ratio of the local skin-friction coefficient to its value for zero injection, and the abscissa is the injection parameter divided by half the local skin-friction coefficient for zero injection. The skin-friction data decrease considerably with increased injection, the reduction being as high as 90 percent of its initial value at the highest injection rate. The roughness of the plate is not expected to alter these results significantly. It can be concluded, therefore, that within the scatter of the data, there is general agreement between the analyses and the data for skin friction.

Heat transfer.- Heat-transfer measurements were made in the investigation of reference 3 by employing heaters placed locally within the porous plate. The local heat-transfer coefficients were calculated from a heat balance on the individual elements of the plate containing heaters. Thus, these data were obtained in a somewhat more direct fashion than the skin friction. Because heat-transfer data is not affected greatly by surface roughness (ref. 4), these heat-transfer data are considered to be reliable. These data are compared with the analyses in figure 5. The ordinate is the ratio of local Stanton number to its value for zero injection and the abscissa is the injection parameter divided by the Stanton number for zero injection. Data are shown for both constant and varying injection parameter along the plate.

Although the data show considerable scatter, a marked decrease in Stanton number with increased injection rate can be discerned. The agreement between data and analyses is again good, the data in general lying between the analytical results.

High-Speed Data

Several tests have been performed recently to determine the effect of surface injection on the turbulent boundary layer at supersonic speeds. (See, for example, refs. 5 and 6.) All these tests are of a preliminary nature, where thoroughness has been sacrificed to expedite obtaining the results. Tests of limited accuracy, however, still supply significant results when there are expectations of large changes in the quantity measured, and when no data exist on the subject.

Skin friction.- Two sets of skin-friction data were obtained at the Ames Aeronautical Laboratory at a free-stream Mach number of 2.7, with air injection. One set was obtained on a porous frustum of a cone (made of sintered woven stainless steel) preceded by a solid ogive. The other set was obtained on a porous flat plate made of sintered powdered stainless steel.

The cone frustum data were obtained by direct force measurements. The average skin-friction drag over the cone frustum was determined from the measurements of total drag, base drag, and fore pressure drag, with estimations made for the influence of the skin friction on the solid nosepiece and of the boundary-layer trip ahead of the porous portion. The injection rate along the cone was nearly uniform. The skin-friction coefficient for zero injection was about 25 percent higher and showed less Reynolds number dependence than is expected on a smooth body. These results were not surprising, since the cone appeared to be aerodynamically rough. This measured skin-friction coefficient, nevertheless, is used as the reference value in the correlations that follow.

The flat-plate data were obtained by boundary-layer surveys with an impact probe. The local skin-friction coefficient was determined from the derivative of the momentum thickness with respect to distance along the plate minus the local injection parameter F. At the higher injection rates this difference becomes small compared with the magnitude of the individual quantities, and errors in the momentum thickness or the local injection rate produce larger errors in the skin-friction coefficient. For the zero injection case, however, it was found that the data agreed with data obtained on a solid smooth surface.

The data from the two tests are plotted in figure 6. The ordinate is the ratio of the skin-friction coefficient to its value for zero injection and the abscissa is the injection parameter F divided by half the skin-friction coefficient for zero injection. Although average skin-friction coefficients are used for the cone data and local skin-friction coefficients are used for the flat-plate data, it can be shown analytically that essentially the same curves should result when the data are plotted on this coordinate system. On examining the data, it is found that the two sets of data obtained in different ways agree very well with each other, even though the cone was initially rough. Both sets of data show a considerable reduction in skin-friction coefficient with increasing injection rate and are in good agreement with the analytical results, especially the analysis of reference 2. The reduction in skin friction shown here at $M = 2.7$ is quite similar to that determined at $M = 0$.

Heat transfer.- Two sets of data are available showing the effect of surface injection on heat transfer in the turbulent boundary layer at supersonic speeds. One set (ref. 5) was obtained on a porous frustum of a cone made of sintered powdered stainless steel preceded by a solid steel nosepiece. These data were obtained at $M = 2.02$ with nitrogen, helium, and water as coolants. The water data will not be reported here because the amount of evaporation taking place during the tests was not known; thus correlation of these data with the gas data is impossible. The other set of data (ref. 6) was obtained on a porous flat plate at $M = 2.7$. Air was used as a coolant in these tests.

In both sets of tests, the amount of heat transferred to the model was determined by measuring the temperature rise of the coolant as it passed from the inside of the model to the outer surface of the porous skin. Average heat transfer was determined on the cone, whereas local values were determined on the flat plate. In the flat-plate tests pains were taken to separate the individual effects of injection on the Stanton number and on the temperature-recovery factor. Because of this the flat-plate data will be discussed first in terms of Stanton number and of recovery factor, and then comparison will be made of the overall cooling effects of both sets of tests.

A comparison of the flat-plate data and the analyses is made in figure 7. The ratio of Stanton number to its value for zero injection is plotted against the injection parameter divided by the Stanton number for zero injection. The data points represent the reduction experienced by the local Stanton numbers, averaged over all the tests. The data show a marked decrease in local Stanton number with increased injection. The reduction in Stanton number, however, is not as large as the analyses indicate or as was shown by the $M = 0$ data. This point should not be emphasized because a saving feature appears. This is shown in the next figure.

The effect of surface injection on the temperature-recovery factor is shown in figure 8. Here the ratio of recovery factor to its value

[redacted]

for zero injection is plotted against the injection rate divided by the local Stanton number for zero injection. The data correlate quite well on this type of plot and show a reduction with increased injection, the reduction being as much as 20 percent. Neither analysis, even the one for $Pr = 0.72$, predicts this reduction.

The heat transfer to a surface, now, depends on both the reduction in Stanton number and the reduction in recovery factor. This combined effect is shown in figures 9(a) and (b). In these figures the ordinate is a dimensionless grouping composed of the wall temperature, the coolant's initial temperature, and the recovery temperature under zero injection conditions. This is a parameter known to the designer and one which he must design for. The abscissa is the injection parameter divided by the Stanton number for zero injection, an average value for the cone data and local value for the flat-plate data. The data for the cone and the flat plate with nitrogen or air as the coolant (fig. 9(a)) agree well with each other and with the analytical results. The data, however, are a little lower in general at the lower values of injection parameter. At higher values of injection there is excellent agreement. It is noted that the surface temperatures in this case are much lower than would be produced by a conventional heat exchanger of 100 percent effectiveness.

The data shown in figure 9(b) give some indication of how analyses based on air-to-air injection predict the behavior transpiration cooling systems employing helium. The data were obtained on the cone. It is seen that the data, like the data for air at these injection rates, lie a little below the analytical values. The analytical values were determined by using the assumption that helium injection affects the boundary layer in the same manner as air injection, but that helium acts as a more effective coolant because of its high specific heat. Although it appears that the analyses for air agree with data for helium as the coolant almost as well as they do for air, it must be cautioned that the data shown in figure 9(b) were not obtained at sufficiently high rates of coolant flow. This is seen from the curve representing the conventional heat exchanger of 100 percent effectiveness, which does not differ greatly from the curves predicted by the analyses.

CONCLUDING REMARKS AND PRACTICAL APPLICATION

From the figures shown we can conclude that there is a general agreement between existing experiment and analysis for both skin friction and heat transfer under conditions of surface injection with air. The effect of other gases as coolants is at present somewhat inconclusive. All the experimental data are too limited in their range of variables and accuracy to allow formulation of empirical laws at this stage. At

[redacted]

present, therefore, it is necessary to rely on the analyses in extrapolating the available experimental data to conditions which the designer must face. From what has been shown, the analysis of either reference 1 or 2 can be used with some degree of confidence.

An example of the results obtained by using analytical extrapolation is shown in figure 10. Here the ordinate represents the ratio of coolant flow rate required for a transpiration cooling system to that required in a conventional system employing a heat exchanger of 100 percent effectiveness. The abscissa is the Mach number of flight. A surface temperature of 1,200° F and 300° F is maintained by each cooling system. Other conditions in the heat balance are that the altitude is 120,000 feet, the surface emissivity is unity, the position is 1 foot from a leading edge, the temperatures are at steady state, and the coolant is water that is evaporated. It is assumed that the effect of steam injection on the boundary layer is the same as that of air injection. No dissociation is assumed in the boundary layer. It is observed that the transpiration cooling system always requires less coolant than does the conventional system, the ordinate being always less than unity. The reduction, however, becomes significant only at the higher Mach numbers. The case with the cooler surface shows a little more advantage of a transpiration cooling system. It can be concluded, therefore, that at extremely high Mach numbers transpiration cooling may be the most effective means of attacking the aerodynamic-heating problem. In addition, the reduction in skin friction accompanying the transpiration cooling process may further increase the advantage of this type of cooling system.

REFERENCES

1. Dorrance, William H., and Dore, Frank J.: The Effect of Mass Transfer on the Compressible Turbulent Boundary-Layer Skin Friction and Heat Transfer. Jour. Aero. Sci., vol. 21, no. 6, June 1954, pp. 404-410.

2. Rubesin, Morris W.: An Analytical Estimation of the Effect of Transpiration Cooling on the Heat-Transfer and Skin-Friction Characteristics of a Compressible, Turbulent Boundary Layer. NACA TN 3341, 1954.

3. Mickley, H. S., Ross, R. C., Squyers, A. L., and Stewart, W. E.: Heat, Mass, and Momentum Transfer for Flow Over a Flat Plate With Blowing or Suction. NACA TN 3208, 1954.

4. McAdams, William H.: Heat Transmission. Second ed., McGraw-Hill Book Co., Inc., 1942, p. 175.

5. Chauvin, Leo T., and Carter, Howard S.: Exploratory Tests of Transpiration Cooling on a Porous 8° Cone at $M = 2.05$ Using Nitrogen Gas, Helium Gas, and Water as the Coolants. NACA RM L55C29, 1955.

6. Rubesin, Morris W., Pappas, Constantine C., and Okuno, Arthur F.: The Effect of Fluid Injection on the Compressible Turbulent Boundary Layer - Preliminary Tests on Transpiration Cooling of a Flat Plate at $M = 2.7$ With Air as the Injected Gas. NACA RM A55I19, 1955.

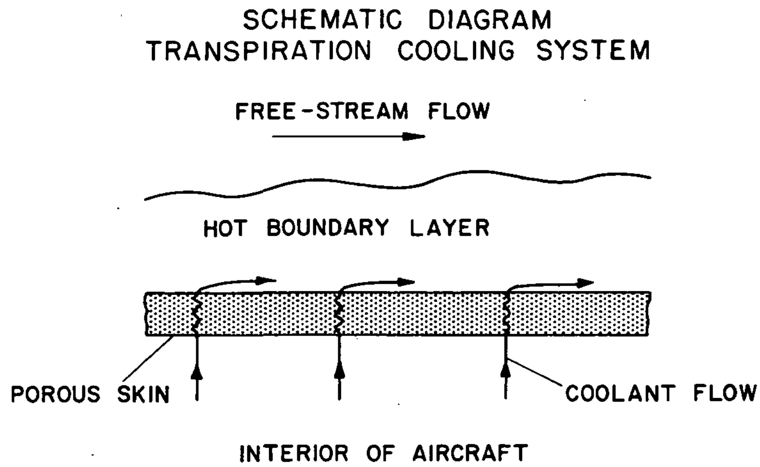

Figure 1

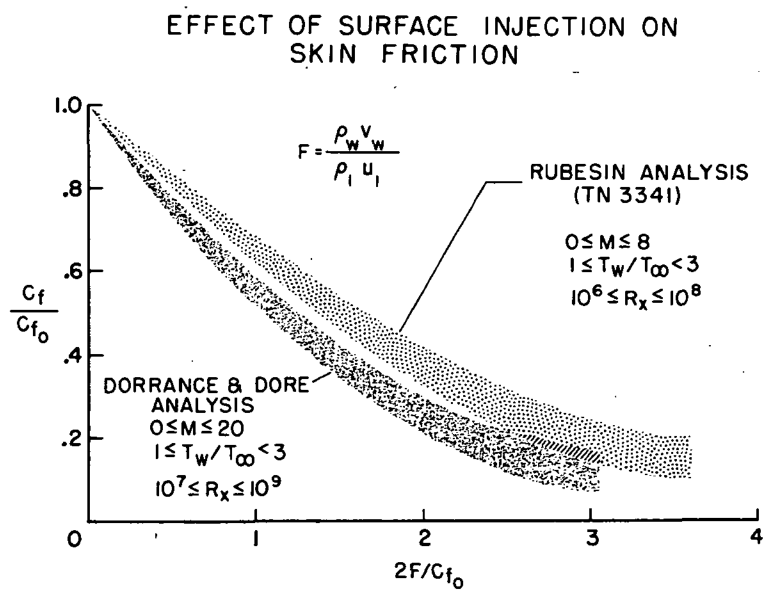

Figure 2

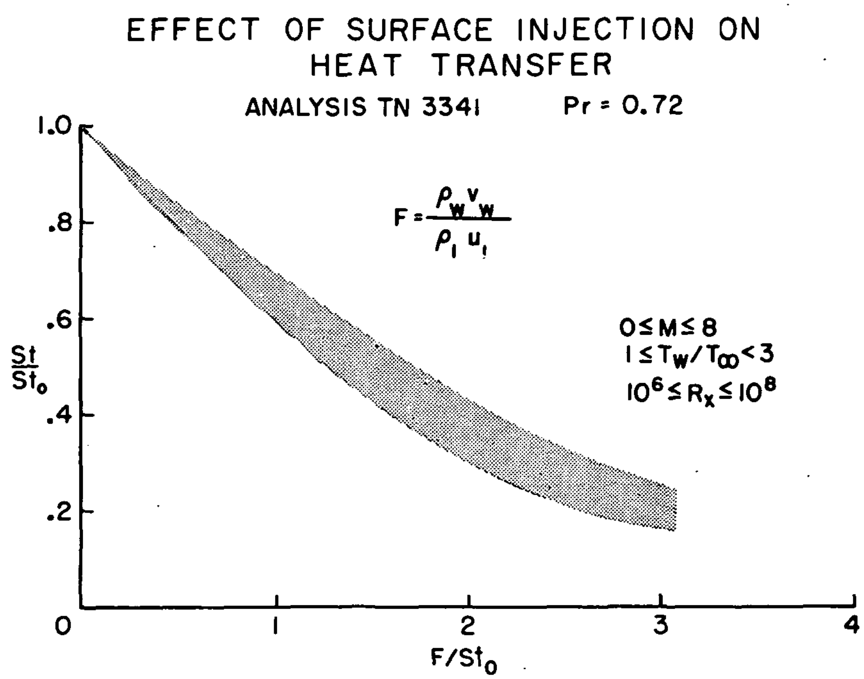

Figure 3

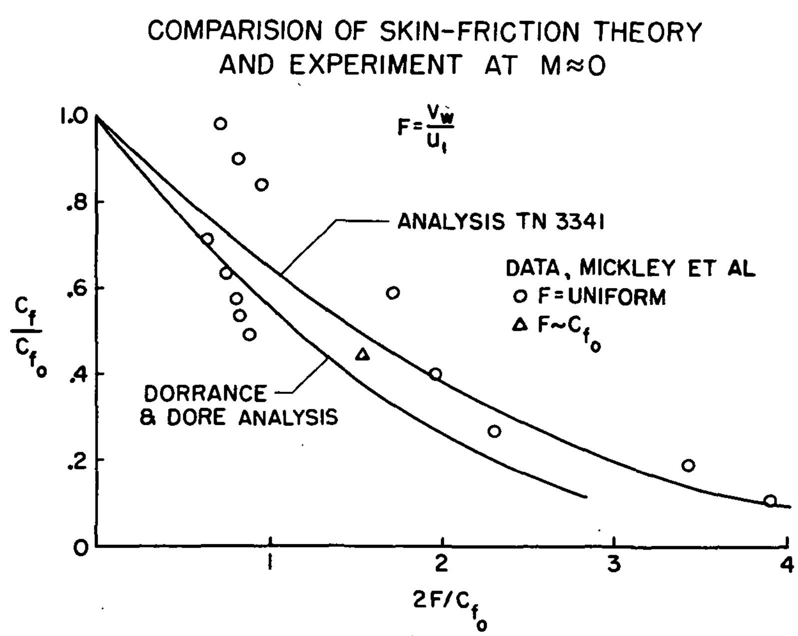

Figure 4

COMPARISON OF HEAT-TRANSFER THEORY AND EXPERIMENT AT M≈0

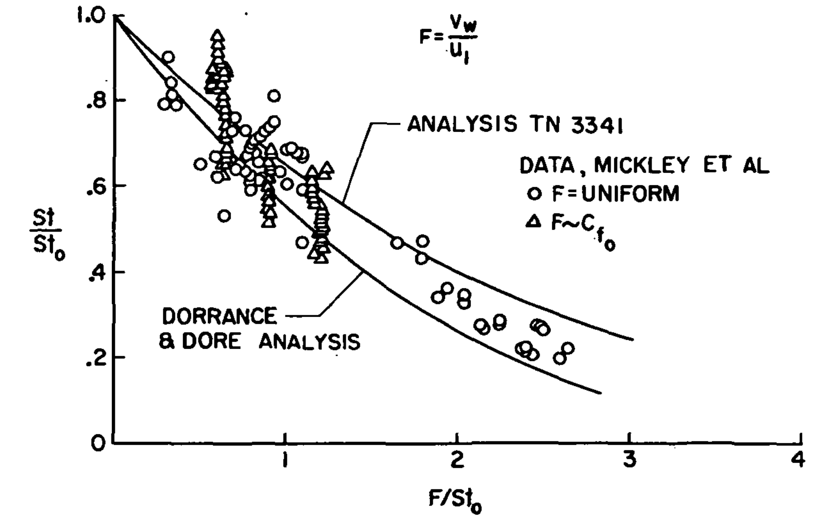

Figure 5

COMPARISON OF SKIN-FRICTION THEORY AND EXPERIMENT AT M=2.7

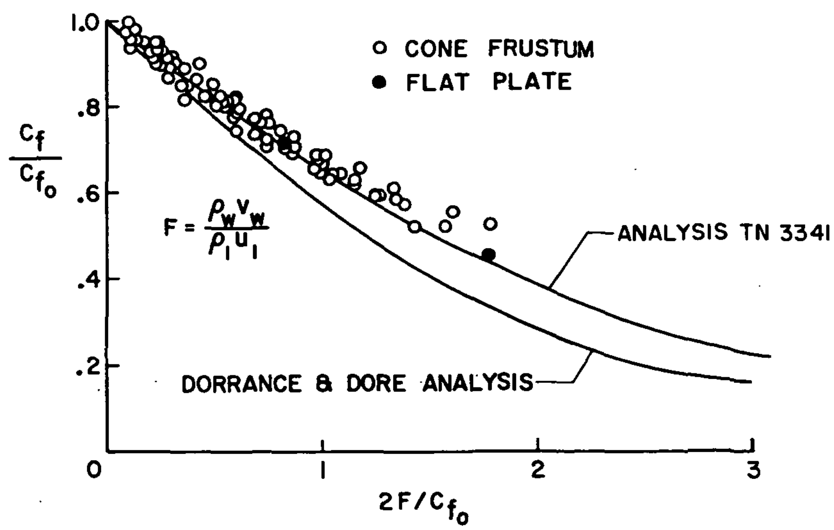

Figure 6

COMPARISON OF HEAT-TRANSFER THEORY AND EXPERIMENT AT M=2.7

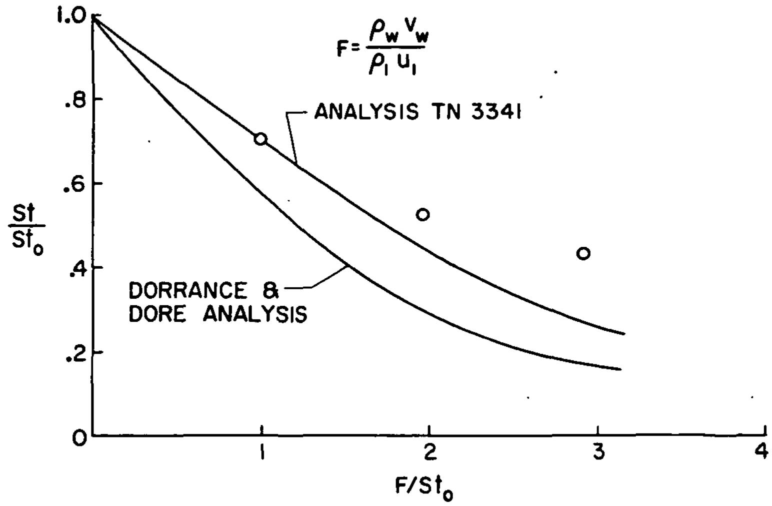

Figure 7

EFFECT OF SURFACE INJECTION ON TEMPERATURE RECOVERY FACTOR AT M=2.7

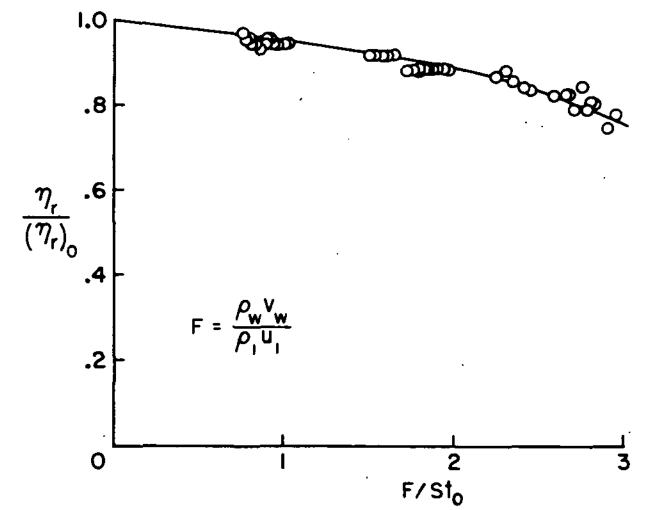

Figure 8

EFFECT OF TRANSPIRATION COOLING ON SURFACE TEMPERATURE

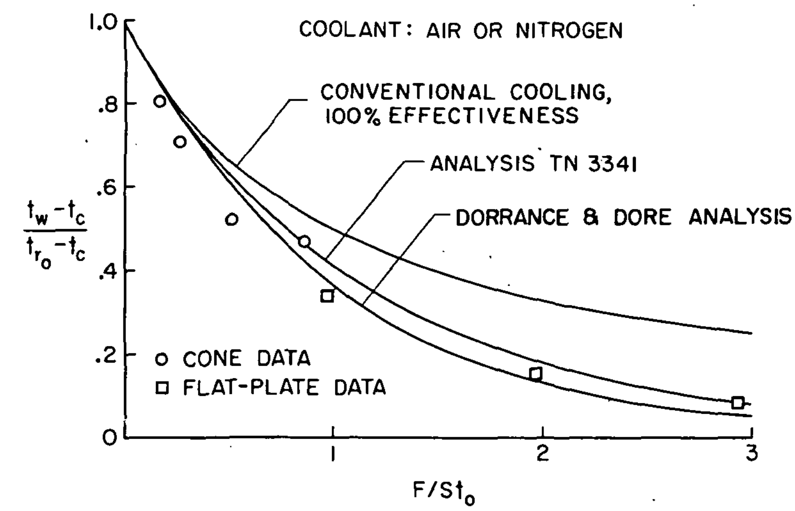

Figure 9(a)

EFFECT OF TRANSPIRATION COOLING ON SURFACE TEMPERATURE

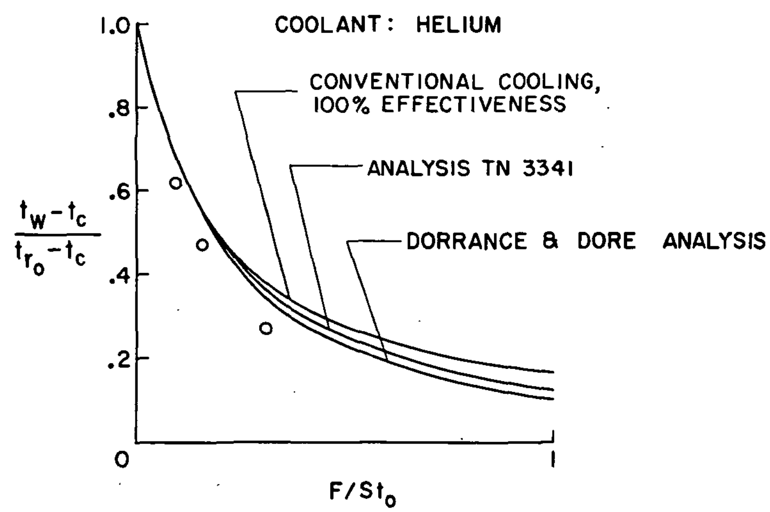

Figure 9(b)

COMPARISON OF COOLANT RATES REQUIRED FOR TRANSPIRATION & CONVENTIONAL COOLING SYSTEM

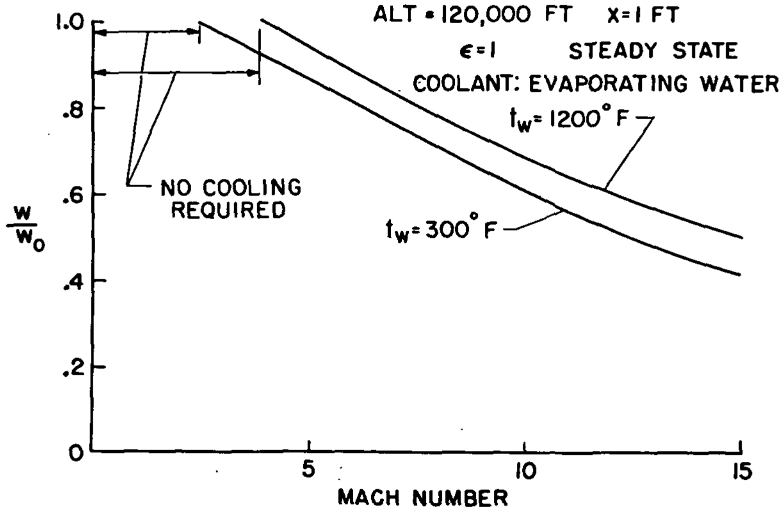

Figure 10

A REVIEW OF RECENT INFORMATION ON BOUNDARY-LAYER TRANSITION AT SUPERSONIC SPEEDS

By Alvin Seiff

Ames Aeronautical Laboratory

SUMMARY

Several experimentally observed characteristics of boundary-layer transition at supersonic and hypersonic speeds are discussed. These include favorable effects of low wall temperature and increasing Mach number. It appears that moderately long laminar runs will be obtained even on relatively rough threaded surfaces at cold-wall conditions and high supersonic speed, provided that pressure-rise coefficients are kept below the critical values. Still higher transition Reynolds numbers can occur on polished models at low wall temperature. The effect of leading-edge thickness on slender bodies appears to be favorable at moderate supersonic speeds. The low-fineness-ratio configurations which have been proposed for ballistic missiles are the least favorable of those studied to date; this indicates that further work is required to find ballistic missile shapes conducive to laminar flow.

INTRODUCTION

Numerous authors (see, for example, refs. 1 and 2) have discussed the desirability of maintaining laminar boundary layers to the maximum possible extent on supersonic airplanes and ballistic missiles. The benefits to be derived thereby are two: significantly reduced aerodynamic heating and improved aerodynamic efficiency. There has therefore been considerable research recently devoted to the study of factors affecting boundary-layer transition at supersonic speeds. This research is aimed, in general, at defining the relationships between the extent of laminar flow and such variables as surface smoothness, wall temperature, pressure gradient, and Mach number. The purpose of this paper is to review briefly the results that have been obtained from this research.

SYMBOLS

h roughness height, in.

M Mach number

$\frac{\Delta p}{p_o}$ pressure-rise coefficient

R_T transition Reynolds number based on free-stream conditions

R_x Reynolds number based on free-stream properties and axial distance from the leading edge

R_l length Reynolds number based on free-stream properties

$(R_1)_B$ local Reynolds number outside the boundary layer of a blunted body

$(R_1)_S$ local Reynolds number outside the boundary layer of a pointed body

T_r laminar recovery temperature, $^\circ R$

T_w body-surface temperature, $^\circ R$

T_1 boundary-layer-edge temperature, $^\circ R$

δ laminar boundary-layer thickness, in.

θ_c cone half-angle, deg

Subscripts:

o free stream

1 boundary-layer edge

c cone

p flat plate

DISCUSSION

Effect of Wall Temperature Ratio

Over the past several years, a number of investigators have studied the effect of body surface temperature on transition, both theoretically and experimentally. Theoretically, according to Lees and Lin (ref. 3), lowering the body surface temperature improves the stability of the laminar boundary layer to two-dimensional disturbances as is evidenced by an increase in the minimum Reynolds number at which the disturbances are amplified. Experimentally, variation of the wall temperature at constant Mach number has given the results shown in figure 1. Wind-tunnel investigations, of which two are represented on the figure (refs. 4 and 5), have shown that lowering the wall temperature increases the extent of laminar flow. Recent flight data (ref. 6 and unpublished data from the Langley Pilotless Aircraft Research Division) tend to support this finding for moderate reductions in wall temperature ratio. Some of the flight data indicate, however, that a leveling off in this generally favorable effect of lowering the wall temperature can occur under certain conditions (lower curve of PARD data) and one set of data showing an unfavorable effect of lowering the wall temperature has also been recorded. However, it is very difficult in these flight tests to hold all variables constant except one; in this particular case, length Reynolds number varied simultaneously with wall temperature. The effects of the two variables may then be mixed in producing the result shown.

The theory of Lees and Lin (ref. 3), in addition to predicting the favorable effect of lowering the wall temperature, further predicts that reducing the wall temperature below certain critical values which are a function of Mach number will produce complete laminar stability, such that small two-dimensional disturbances of all frequencies are damped at all Reynolds numbers. The wall-temperature limits of the completely stable region of this type calculated by Van Driest (ref. 7) from the theory of Lees and Lin are shown in figure 2 and compared with the temperature conditions of recent tests which entered the theoretically stable region. This region had sometimes been hopefully regarded as a region in which transition would not occur, but it has been conclusively shown by the tests at the conditions indicated in figure 2 (and the earlier data of ref. 8) that transition will occur in the region of complete stability in response to surface roughness and other causes. In this connection, it should be noted that Dunn and Lin (ref. 9) have analyzed the case of three-dimensional disturbances and found that the laminar "boundary layer can never be completely stabilized with respect to all three-dimensional disturbances." According to this theory, then, for three-dimensional disturbances, no counterpart to the fully stable region of figure 2 exists. This does not detract, however, from the observed advantages (fig. 1) of low wall temperature for purposes of maintaining laminar boundary layer.

Effect of Mach Number

In order to investigate the effect of Mach number on transition at constant low values of the wall temperature ratio, tests have recently been made in the Ames supersonic free-flight wind tunnel. The Mach numbers and wall temperature ratios covered are indicated in figure 2 by the diamond symbols. The models employed are shown in figure 3. Previous experience had indicated that on very smooth surfaces transition would be far back on the models at all Mach numbers so that no observations of the effects of Mach number could be made. It was necessary, therefore, to use rough surfaces to bring transition forward, and for reasons of reproducibility, fine-threaded surfaces of the type shown in the microphotograph were selected. The location of transition was measured from shadowgraphs as described in reference 8. The results of tests with the ogive-cylinder models (ref. 10) are shown in figure 4. Increasing the Mach number had a pronounced favorable effect on the extent of laminar flow over a given surface, particularly when certain critical combinations of Mach number and thread height were reached. After the increase, the transition Reynolds number appeared to level off at stations near the base of the model, but this was not conclusively shown since some cases of fully laminar flow up to the fins were recorded in this region. These are indicated by the points with arrows as being beyond the range of observation. In figure 5, two of the shadowgraph pictures obtained are reproduced to show directly the change in the boundary layer associated with raising the Mach number from 1.87 to 3.40 on a 0.0004-inch threaded surface.

In order to investigate the effect of the type of roughness on this result, a series of smooth models were sandblasted with fine grit to produce the roughness described at the right side of figure 4. The trend observed with these models is shown by the inverted filled triangles to be similar to that found with the threaded surfaces. It is interesting that the sandblasted surface, with roughness height generally less than 1/3 that of the roughest thread, nevertheless had lower transition Reynolds numbers at all observed test Mach numbers which suggests that a threaded (two-dimensionally) roughened surface is superior to a bumpy (three-dimensionally) roughened surface.

The flight data of figure 2 can be examined for the effect of Mach number at constant wall temperature ratio on relatively smooth bodies. Results obtained are shown in figure 6 and compared with the data of figure 4. At Mach numbers above 2, the highly polished flight models seem to show trends similar to those from the tests with the roughened small-scale models. However, the data of Rabb and Disher (ref. 6), when laminar, were actually fully laminar with transition beyond the range of the measurements. Thus, no definite information on effect of Mach number is contained in the two points shown. The flight data of the Langley Pilotless Aircraft Research Division are similar to the small-scale test data at Mach numbers above 2. At lower Mach numbers, an opposite trend is shown. Whether this can be explained in terms of the length Reynolds number variations present in the flight tests, or whether there is really a reversal in this region, is not yet established.

Cross plots of the data shown in figure 4 together with data from tests with the contoured tubes can be made to define the effect of roughness height on transition Reynolds number at several fixed Mach numbers. For generality, it was desired to relate the roughness height h to the laminar boundary-layer thickness δ. For surfaces of constant roughness height at all stations, however, the ratio of roughness height to boundary-layer thickness varies with axial position on the model. Therefore, a parameter to represent the relationship of roughness height to boundary-layer thickness over the entire surface was sought. Examination of the equations for h/δ as a function of the Reynolds number based on axial distance from the leading edge R_x showed that a dimensionless group $\frac{h}{\delta}\sqrt{R_x}$ was constant over the surface of a flat plate with constant roughness height and a given Reynolds number per foot, and would therefore specify the relation of roughness to boundary-layer thickness for all points on the surface. Accordingly, this was the roughness parameter used. In figure 7, comparison of the ogive-cylinder data and the contoured-tube data on the basis of this parameter is shown for a Mach number of 4.9 and a wall temperature ratio of 1.8. The two models differed in boundary-layer growth rates because of shape and because of Reynolds number differences, 27 million per foot for the ogive-cylinder and 36 million per foot for the contoured tube. The pressure and Mach number distributions on the nose sections were, however, nearly identical by design. The correlation shown in the figure was realized only when the boundary-layer-growth equations for the nose sections of the bodies were used rather than those for the cylindrical sections. This implies that the observed roughness effects are predominantly controlled by the flow on the body nose.

The effect of the roughness parameter on transition at other Mach numbers is shown in figure 8 and is compared with the curve for a Mach number of 4.9. The wall temperature ratios for the free-flight wind-tunnel curves are 1.8 at the two higher Mach numbers and 1.0 at $M = 3.5$. Examination of the upper two curves indicates that increasing the Mach number at constant wall temperature ratio increased the maximum extent of laminar flow over threaded surfaces and also increased the permissible roughness. The curve for $M = 7$ is characterized by insensitivity to roughness height up to a critical roughness height, followed by an abrupt forward movement of transition.

These curves are incomplete in that they are undefined between roughness parameters of 0 and 60. Data in this region have been obtained from other wind-tunnel and flight tests and are indicated by the three points shown. It is evident that at low values of the roughness parameter, of the order of 10 and less, and at low wall temperature ratios, very substantial laminar runs are realized. This was first demonstrated by Sternberg (ref. 11) who achieved a transition Reynolds number greater than 57 million in flight testing a polished cone (roughness parameter of 17) at a wall temperature ratio of 1.2.

Effect of Angle of Attack

The above considerations have been limited to the case of zero angle of attack. Experiments have shown that when slender bodies of revolution are smooth enough so that roughness does not cause transition, transition due to angle of attack can occur on the sheltered side at angles of attack above certain critical values. It has been suggested (ref. 8) that this results from the pressure rise encountered by streamlines flowing over the sheltered side, due partly to the axial pressure distribution and partly to the cross-flow pressure distribution. This reasoning leads to the expectation that the critical angle of attack will depend, among other things, on the pressure distribution at zero angle of attack. If the axial-pressure-rise coefficient is too great, pressure-rise transition would be expected to occur at zero angle of attack. Mach number also should influence sheltered-side transition through its effect on the pressure distributions, and through its effect on the critical pressure-rise coefficient. An effect of Mach number on sheltered-side transition was observed in the tests of reference 10. The critical angle of attack appeared to decrease with increasing Mach number. When analyzed to determine the pressure-rise coefficient at the transition point, these observations led to the data of figure 9, where critical pressure-rise coefficient is plotted as a function of Mach number. The critical pressure-rise coefficients in the form $\Delta p/p_o$ (where p_o is the static pressure in the free stream) are relatively independent of Mach number. Additional cases in which transition was apparently caused by pressure rise at zero angle of attack, on cone-cylinders and other models, have been collected by Carros (ref. 10) and are included in the figure, and they tend to support the tentative conclusion that at supersonic speeds, the critical pressure-rise coefficient is independent of Mach number and wall temperature ratio. It will be desirable to test this finding by comparison with additional experiments. In all probability, further work will show at least a small dependence of critical pressure-rise coefficient on Reynolds number and on pressure distribution. The implication of figure 9 for bodies of low fineness ratio, and in particular, bodies with continually favorable pressure gradient, is that such bodies should be free of sheltered-side transition in the low angle-of-attack range. However, it has not been demonstrated that the pressure-rise effect is the only effect which can influence sheltered-side transition, and additional experiments are required to investigate the case of low-fineness-ratio bodies.

The preceding discussion has been mostly devoted to sharp slender bodies. Since, at hypersonic speeds, thick leading edges are indicated and, for ballistic missiles, bodies of low fineness ratio offer advantage (ref. 1), it is important to determine the effects of leading-edge bluntness and low fineness ratio on transition.

Effects of Low Fineness Ratio and Tip Bluntness

Recently, Brinich (ref. 12) has made tests to determine the effect of leading-edge thickness on transition on hollow tubes at a free-stream Mach number of 3.1. His data are shown in figure 10(a). As leading-edge thickness was increased, transition Reynolds number increased to the maximum values shown for the 0.008-inch leading edge. Further increases in leading-edge thickness had no discernible effect. These data prompted Moeckel (ref. 13) to examine the effect of blunting on surface Reynolds number, since with a blunt leading edge, the air at the surface of the cylinder will have passed through a normal shock wave and will be altered in density, velocity, and temperature from the corresponding values with a sharp leading edge. This effect of the normal shock wave on the surface Reynolds number at a station far downstream of the bluntness is shown in figure 11, as a function of free-stream Mach number, for a relatively slender cone and a low-fineness-ratio cone. In both cases, the surface Reynolds number of the cones when blunt is a small fraction of the surface Reynolds number when sharp, particularly for the more slender cone. It should be noted, however, that, except for the bluntest cones at very high Mach number, the surface Reynolds number when sharp will fall well above the free-stream Reynolds number, so that the surface Reynolds number for blunt, low-fineness-ratio cones will not be reduced too far below free-stream values. Moeckel was able to explain the data of Brinich (ref. 12) on the basis of these Reynolds number changes.

As an independent check on the data of Brinich, tests have very recently been conducted in the Ames supersonic free-flight wind tunnel by C. S. James, again using a tubular model with zero pressure gradient. The results are shown in figure 10(b). When the blunt leading edge was square cornered and normal to the airstream, the effect of increasing bluntness was adverse. Rounding the leading edge, however, produced the very favorable effect shown. Thus, it appears that leading-edge shape is significant as well as leading-edge thickness.

In addition to the favorable effect of blunting, pointed out by Moeckel, on the local surface Reynolds numbers, there are some additional effects, in this case, unfavorable, associated with low fineness ratio; these are shown in figure 12. On the left the local surface Mach numbers are plotted as a function of cone angle for free-stream Mach numbers of 4, 8, and 20. The local Mach numbers on the cones of 30° half angle and greater are reduced to low supersonic values, almost independent of the free-stream Mach number. Blunting the cones further reduces the local Mach numbers to values indicated by the dashed curves. In view of the results for effect of Mach number on transition, it is conceivable that the compression to low local Mach numbers will have a destabilizing effect on the laminar boundary layers.

In the right half of the figure, the effects on boundary-layer thickness of cone angle and tip blunting are shown. Boundary-layer thickness on the cone is compared with that on a flat plate of equal length at identical free-stream conditions. The boundary-layer thickness on the cone differs from that on the flat plate as a result of several effects: the well known lateral spreading effect on the cones which reduces it by $\sqrt{3}$; the effect of the changed Mach number and air temperature at the boundary-layer edge; and the effect of the change in local surface Reynolds number. All these effects are included in the figure, which shows that the low-fineness-ratio cones have thin boundary layers relative to the corresponding flat plates. Increasing the Mach number reduces the relative thickness. Thin boundary layers would be expected to increase the tendency for roughness to cause transition. Slight blunting of the cones is therefore favorable in this sense, since the normal shock wave acts to make the boundary layer thicker than on corresponding sharp cones.

In figure 13, some preliminary data obtained by S. C. Sommer in the supersonic free-flight wind tunnel and by L. T. Chauvin at the Langley Pilotless Aircraft Research Division (filled circles) on transition on low-fineness-ratio bodies are shown. The bodies tested have included a 60° cone, 50° and 60° cones with spherical tips, a hemisphere, and a pointed ogive with steadily favorable pressure gradient. The observed locations and lengths of the observed transition regions are indicated by the vertical lines through the data points. The agreement between the data from the two facilities is remarkably good, and this may be only fortuitous in view of differences in the test Reynolds numbers. It has been apparent in these tests that the ease of obtaining laminar runs at Reynolds numbers of 10 million and greater which was experienced with the slender test models was not now present. A beneficial effect of increasing the Mach number is, however, shown as in the case of the slender models. The free-flight wind-tunnel models have been polished, in general, to a smoother condition than the corresponding slender models. They have, however, had some residual polishing scratches, mainly circumferential. It should be noted that transition data from the shadowgraphs are not nearly as precise or definite as with slender bodies, but it can usually be decided definitely whether the boundary layer coming off the model base is laminar or turbulent. It was, for example, almost invariably turbulent off the base of the blunted cone. The pointed 60° cone at $M = 8.25$ has given the longest laminar run to date, remaining laminar to a diameter behind the model base.

The difficulty in avoiding transition on these models is believed due to the thinning of the boundary layers and to the low surface Mach numbers. Additional work will be required to investigate these causes and to find the most favorable low-fineness-ratio shapes. It should be noted that ballistic missiles sometimes operate at Reynolds numbers per foot comparable to those in the tests (18 to 36 million per foot). The absolute smoothness requirements for the missiles, then, will be comparable to those of the tests.

CONCLUDING REMARKS

From the preceding discussion, it would appear that on slender bodies with low surface temperature in flight at supersonic and hypersonic Mach numbers up to 7, it should be possible to maintain laminar boundary layers to Reynolds numbers of the order of 20 million. To do so, however, it will be necessary, even in the region of complete stability to two-dimensional disturbances given by theory, to avoid tripping the boundary layer by use of unduly rough surfaces or such other trips as angle-of-attack vanes on the body nose. One encouraging observation is that perfect smoothness is not required to maintain moderately long laminar runs if the roughness is of the two-dimensional threaded type described herein. With such surfaces, the permissible roughness increases with increasing Mach number. A favorable effect of increasing Mach number also seems to occur in tests with smooth surfaces, but further work will be required before this can be stated with assurance. The blunt leading edges required from the viewpoint of heating of the leading edge appear to be favorable in their effect on the extent of laminar flow on slender bodies.

Transition due to pressure rise along streamlines may prove to be more difficult to avoid than transition due to roughness. Pressure rise can occur as a result of angle of attack as well as configuration. Further investigation will be required to define the types of configuration which are most favorable in these respects.

When bodies of low fineness ratio are considered, several new effects are encountered. These include boundary layers considerably thinner than on slender bodies, strong favorable pressure gradients in some cases, and low Mach numbers at the boundary-layer edge. Experiments available to date show that the net effect of these factors is unfavorable - the transition Reynolds numbers observed have been generally below 10 million. Further study of this problem is necessary.

REFERENCES

1. Allen, H. Julian, and Eggers, A. J., Jr.: A Study of the Motion and Aerodynamic Heating of Missiles Entering the Earth's Atmosphere at High Supersonic Speeds. NACA RM A53D28, 1953.

2. Seiff, Alvin, and Allen, H. Julian: Some Aspects of the Design of Hypersonic Boost-Glide Aircraft. NACA RM A55E26, 1955.

3. Lees, Lester, and Lin, Chia Chiao: Investigation of the Stability of the Laminar Boundary Layer in a Compressible Fluid. NACA TN 1115, 1946.

4. Jack, John R., and Diaconis, N. S.: Variation of Boundary-Layer Transition With Heat Transfer on Two Bodies of Revolution at a Mach Number of 3.12. NACA TN 3562, 1955.

5. Czarnecki, K. R., and Sinclair, Archibald R.: An Extension of the Investigation of the Effects of Heat Transfer on Boundary-Layer Transition on a Parabolic Body of Revolution (NACA RM-10) at a Mach Number of 1.61. NACA TN 3166, 1954. (Supersedes NACA RM L53B25.)

6. Rabb, Leonard, and Disher, J. W.: Boundary-Layer Transition at High Reynolds Numbers As Obtained in Flight of a 20° Cone-Cylinder With Wall to Local Stream Temperature Ratios Near 1.0. NACA RM E55I15, 1955.

7. Van Driest, E. R.: Calculation of the Stability of the Laminar Boundary Layer in a Compressible Fluid on a Flat Plate With Heat Transfer. Jour. Aero. Sci., vol. 19, no. 12, Dec. 1952, pp. 801-812.

8. Jedlicka, James R., Wilkins, Max E., and Seiff, Alvin: Experimental Determination of Boundary-Layer Transition on a Body of Revolution at M = 3.5. NACA TN 3342, 1954.

9. Dunn, D. W., and Lin, C. C.: On the Stability of the Laminar Boundary Layer in a Compressible Fluid. Jour. Aero. Sci., vol. 22, no. 7, July 1955, pp. 455-477.

10. Carros, Robert J.: Variation of Boundary-Layer Transition With Mach Number Including Some Effects of Pressure Rise and Surface Roughness on an Ogive-Cylinder Body With Cold Wall Conditions. (Prospective NACA paper.)

11. Sternberg, Joseph: A Free-Flight Investigation of the Possibility of High Reynolds Number Supersonic Laminar Boundary Layers. Jour. Aero. Sci., vol. 19, no. 11, Nov. 1952, pp. 721-733.

12. Brinich, Paul F.: Effect of Leading Edge Geometry on Transition at Mach 3.1. (Prospective NACA paper.)

13. Moeckel, W. R.: Some Effects of Bluntness on Transition and Heat Transfer at High Supersonic Speeds. (Prospective NACA paper.)

[redacted]

EFFECT OF BODY SURFACE TEMPERATURE ON TRANSITION

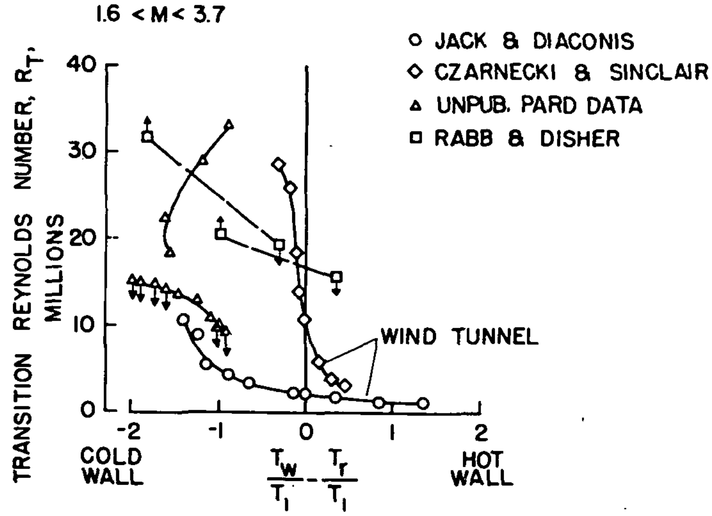

Figure 1

RECENT DATA WHICH ENTER THEORETICAL REGION OF LAMINAR STABILITY TO 2-DIMENSIONAL DISTURBANCES

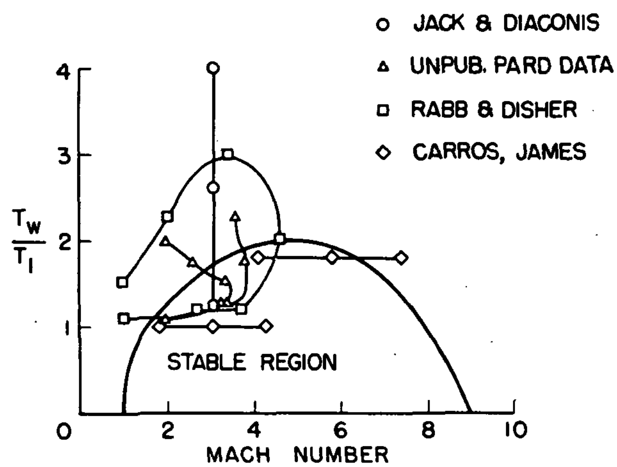

Figure 2

[redacted]

MODELS AND SURFACE FINISH USED
IN FREE-FLIGHT TRANSITION EXPERIMENTS

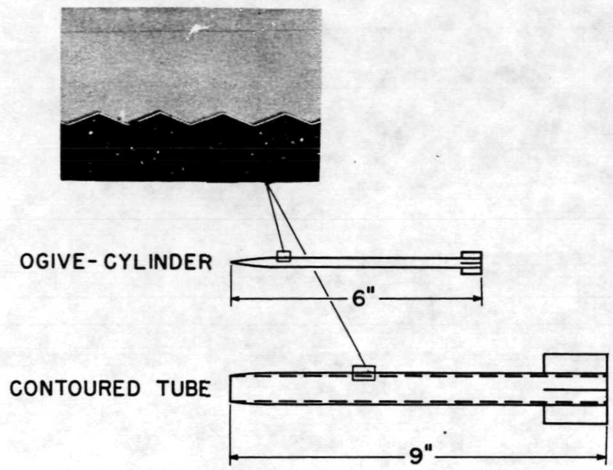

Figure 3

EFFECT OF MACH NUMBER ON TRANSITION
ON A COLD ROUGH WALL

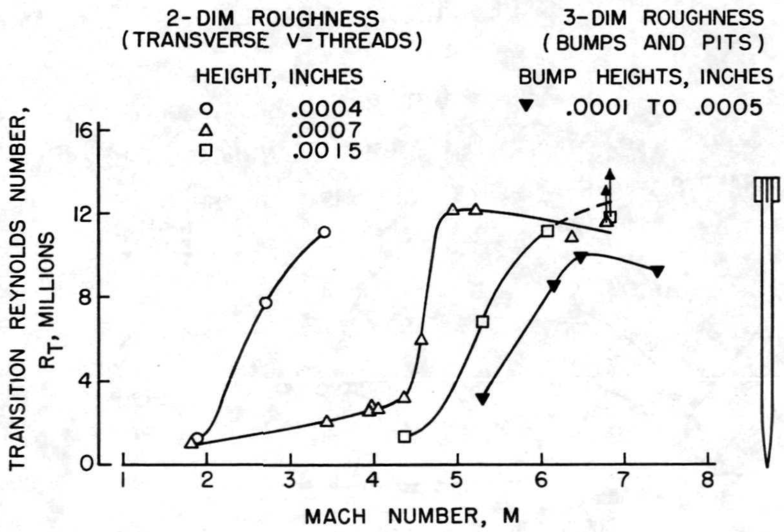

Figure 4

SHADOWGRAPHS OF TRANSITION ON A .0004-INCH THREADED SURFACE

M=1.87, R_1 =12.5 x 10^6

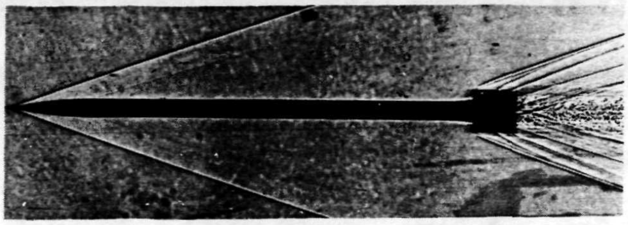

M=3.40, R_1 =13.1 x 10^6

Figure 5

MACH NUMBER EFFECT IN ROCKET-POWERED LARGE-SCALE FLIGHT TESTS

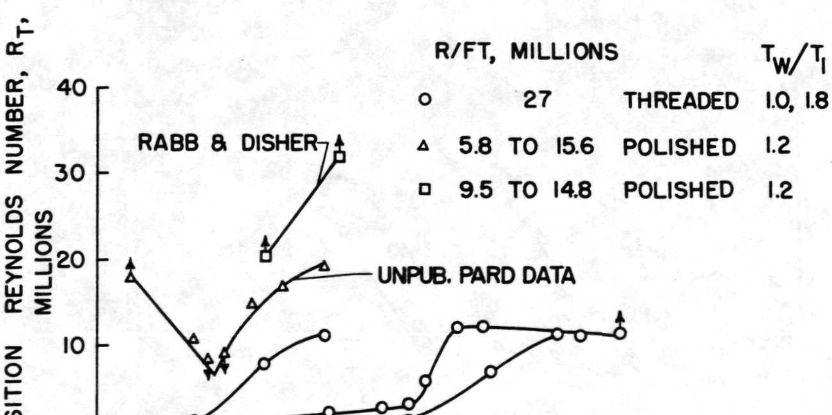

Figure 6

CORRELATION OF DATA ON BASIS OF ROUGHNESS PARAMETER

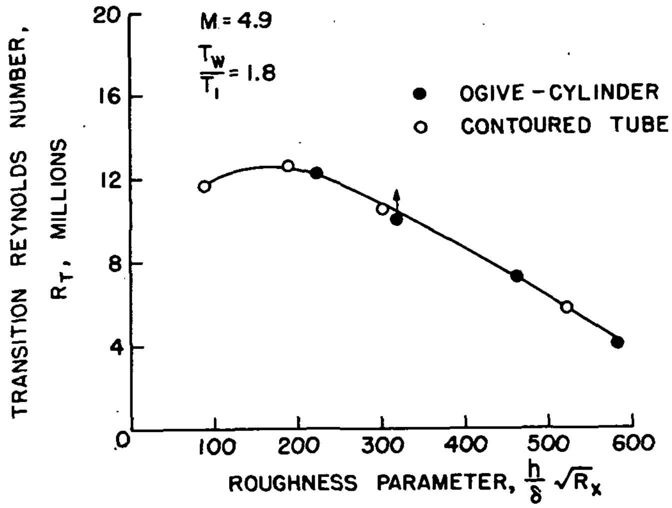

Figure 7

EFFECT OF ROUGHNESS PARAMETER ON TRANSITION

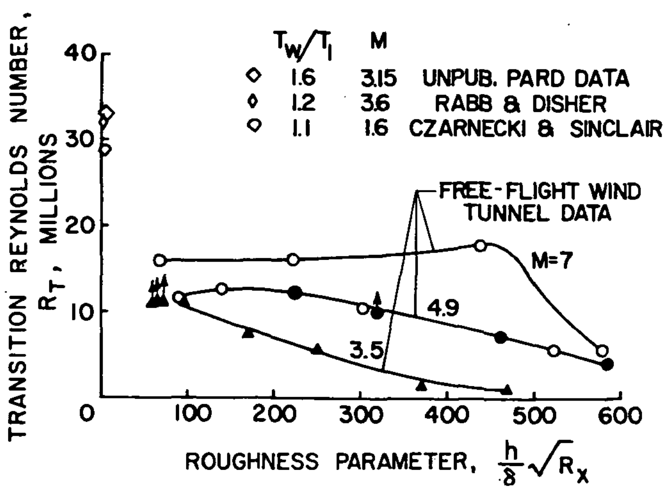

Figure 8

COLLECTED DATA ON CRITICAL PRESSURE-RISE COEFFICIENT

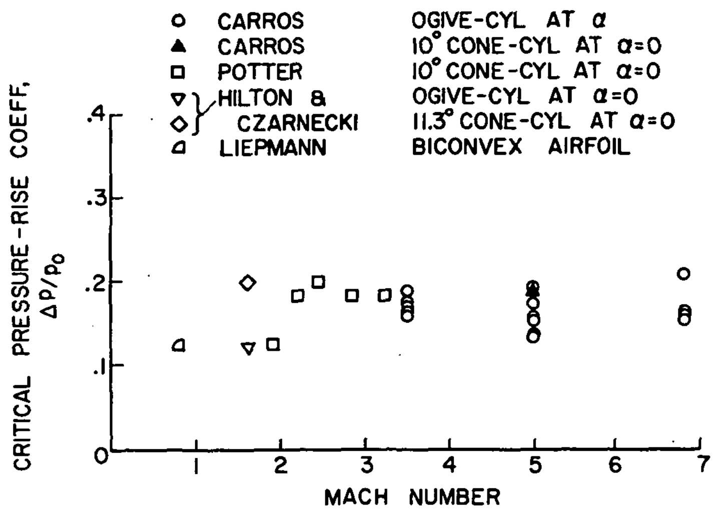

Figure 9

EFFECT OF LEADING-EDGE THICKNESS ON TRANSITION

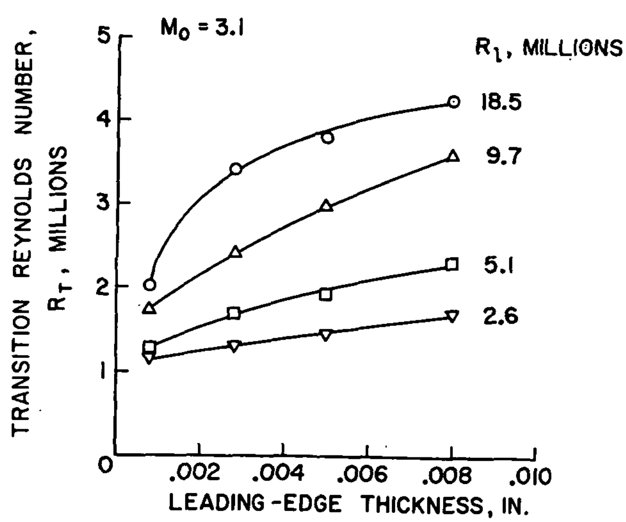

Figure 10(a)

ADDITIONAL DATA ON LEADING-EDGE THICKNESS EFFECT

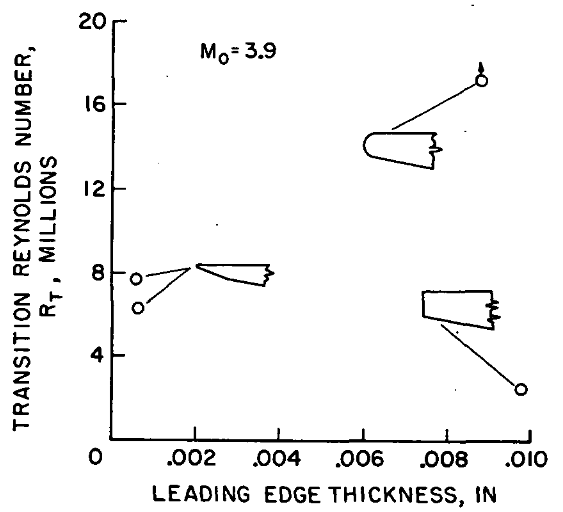

Figure 10(b)

EFFECT OF BLUNT NOSE ON LOCAL SURFACE REYNOLDS NUMBER

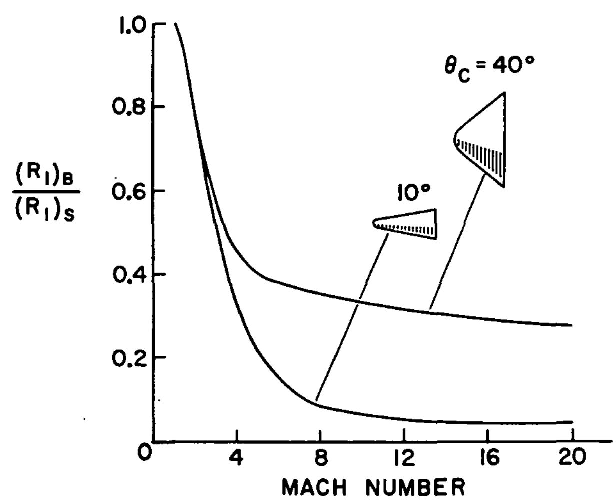

Figure 11

EFFECTS OF CONE ANGLE AND TIP BLUNTING ON LOCAL MACH NUMBER AND BOUNDARY-LAYER THICKNESS

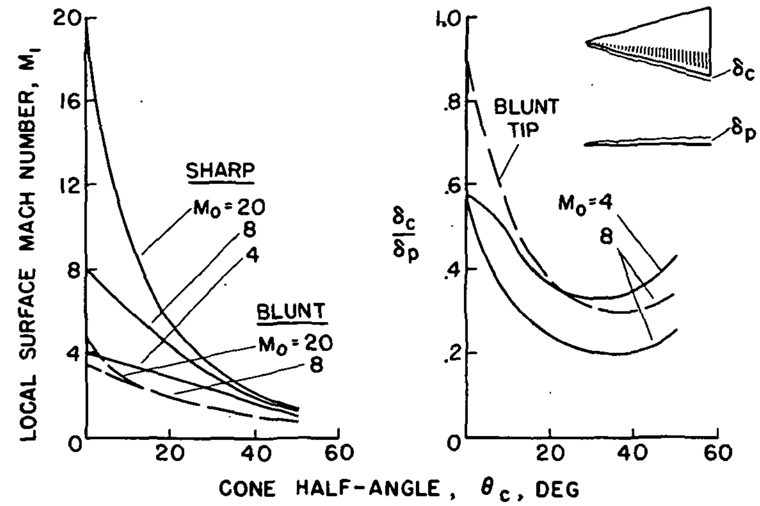

Figure 12

PRELIMINARY TRANSITION DATA FOR LOW FINENESS RATIO CONFIGURATIONS

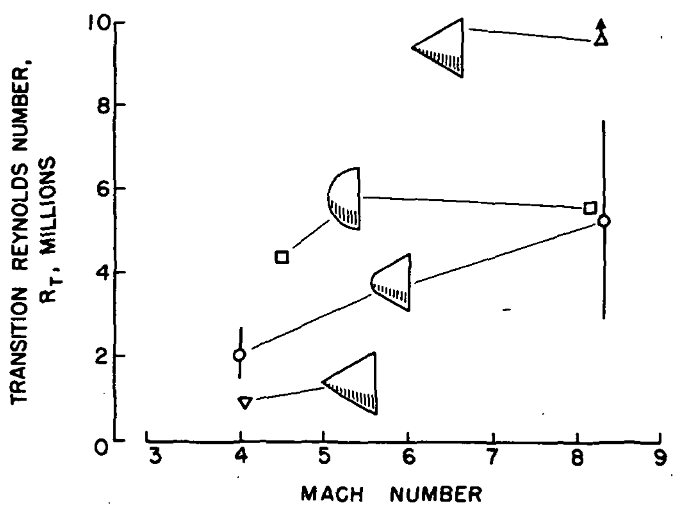

Figure 13

SEPARATED SUPERSONIC AND SUBSONIC FLOWS

By Dean R. Chapman, Donald M. Kuehn,
and Howard K. Larson

Ames Aeronautical Laboratory

This paper summarizes a considerable body of unpublished experimental and theoretical research conducted on the general problem of flow separation. The purpose of the research was to obtain fundamental information which would lead to better understanding of flow separation phenomena, and which, it was hoped, would lead to some results of broad applicability. The research is partly theoretical, though mostly experimental; it comprises measurements at subsonic as well as supersonic speeds and includes various two-dimensional model shapes, each involving separation. These comprise forward-facing steps (which would simulate, for example, the flow upstream of a spoiler control), rearward-facing steps (which would simulate the flow behind a base or a spoiler), compression corners (which would simulate the flow over a duct ramp or a deflected flap), curved concave surfaces (which would simulate the flow over one side of a compressor blade), models producing leading-edge separation, and configurations producing separation by reflecting a shock wave from a boundary layer.

44

The most general result arising from the research is that a single variable appeared dominant throughout in controlling pressure distribution - irrespective of the particular Mach number, Reynolds number, or model shape investigated. This signal variable is the location of transition relative to the reattachment and separation positions. Because transition is so important, classification of the separated flows is made at the outset, as illustrated in figure 1, into three essentially different types depending on the relative location of transition: a "pure laminar" type for which transition is downstream of reattachment, a "transitional" type for which transition is between separation and reattachment, and a "turbulent" type for which transition is upstream of separation. The pressure distributions represent wall static pressures. As is indicated, the particular configuration for figure 1 is a step model tested at a Mach number of 2.3. The characteristics exhibited, however, actually are quite general. The separation point S, determined by oil-film observations, is associated with a relatively small pressure rise in laminar flow and is seen to be about one-half the overall rise to the plateau pressure which represents the dead-air pressure of the separated region. High-speed motion pictures taken of this pure laminar separation at several thousand frames per second show the flow field to be remarkably steady. Such characteristics are in contrast to those of the transitional type of separation shown in the center part of figure 1. The pressure rise to separation, and the plateau pressure rise remain small, but an abrupt pressure rise associated with transition, and occurring at about the same streamwise location as transition, now makes itself evident and alters the flow field. High-speed motion pictures showed this transitional type of separation to be unsteady. Random movements of the shock waves were observed as were random changes in the angle of flow separation. Perhaps this should be expected since the transition phenomenon itself, which is of dominant importance to these flows, is known not to be steady. Some of these characteristics of transitional separation are in contrast to those of turbulent separation represented by the example on the right-hand side of figure 1. The pressure rise to the turbulent separation point is about 5 times greater than that to a laminar separation point. There is no plateau pressure, although there is a peak pressure in the separated region. Downstream of this region, the pressure rises to a terminal value higher than the peak pressure. Plateaus in pressure are associated with laminar separations, and may be thought of as approximating the idealized dead-air region; but in turbulent separations an eddying motion keeps the air very much alive so that the term "dead air" is only a figurative one. It was somewhat surprising to observe in high-speed motion pictures that this turbulent type of separation is relatively steady - not rock-like steady as the pure laminar separations, but nevertheless quite steady compared with the transitional separations.

It is not necessary to exemplify further the three types of flow separation, although each type has been found and studied for the various other models investigated. They exhibit the same qualitative phenomena - they show transition to be dominant in controlling pressure distribution throughout the investigation.

An explanation can be given as to why transition location is so important to a separated flow. This explanation is based on a theoretical mechanism postulated as fundamental to all separated flows. Very briefly, the mechanism requires that a balance exist between the mass flow scavenged out of the dead-air region by the separated mixing layer and the mass flow reversed back into this region by the pressure rise through the reattachment zone. Inasmuch as the mechanism explains other results to be presented later, a momentary digression is undertaken to present some results of special experiments designed to quantitatively test this mechanism.

There are certain special conditions for which both the mass flow scavenged from a separated region and the mass flow reversed back into the region can be calculated without empirical information. These conditions are for pure laminar separations with zero boundary-layer thickness at separation. All calculation details will be bypassed. The end results are illustrated in figure 2. The theory provides an equation in closed form for the dead-air pressure as a function of the Mach number M' and the pressure p' which exist just downstream of the reattachment zone. The equation, which is not very complicated, is as follows:

$$\left\{\left[\frac{2+(\gamma-1)M'^2}{2+\dfrac{(\gamma-1)M'^2}{0.65}}\right]^{\frac{\gamma}{\gamma-1}}-1\right\}\frac{2}{\gamma M'^2}$$

As shown, the equation contains the ratio of specific heats γ, the Mach number, and a number 0.655* which arises from the solution of a nonlinear differential equation with definite boundary conditions. This number involves no empirical information; it cannot be adjusted to take up any slack between experiment and theory. The data points represent both supersonic separations from the present experiments and low-speed subsonic separations from some experiments of Roshko at the California Institute of Technology. Three different models are represented in figure 2: a model producing leading-edge separation, a flat plate normal to the stream, and a circular cylinder. It is evident that the strictly theoretical calculation, which indicates the dead-air pressure to be independent of both Reynolds number and model shape, agrees well with the experiments.

Recently, H. H. Korst et al. at the University of Illinois independently have analyzed the analogous problem of calculating dead-air pressure for turbulent separation with zero boundary-layer thickness at separation. Their method is essentially the same in principle (although not in details) as the method described previously for pure laminar separation. They obtained good agreement with experimental data on turbulent separations behind bases, and it appears that the two researches yield complimentary results.

With a knowledge that the mechanism postulated has satisfactorily been put to quantitative test, a brief explanation of why the location of transition relative to reattachment is so important to a separated flow can be made. Compared to pure laminar separation, the introduction of transition just upstream of reattachment has a pronounced effect of reducing the reversed mass flow, but a negligible effect on the scavenged mass flow. Consequently, balance of the two mass flows occurs at a much different pressure when transition moves upstream of reattachment.

Several experimental trends observed to be general in the present research can be illustrated from a plot of the dead-air pressure in various separated regions as a function of Reynolds number. Figure 3 is such a plot in which pure laminar separations, transitional separations, and turbulent separations are presented. The Reynolds number is based on body length. Individual data curves in this figure are not identified, as this is unnecessary for the general purpose at hand. Suffice it to say that these curves represent various combinations of Mach

*The number 0.655 represents the quantity $1 - \bar{u}^2/u_e^2$, where u_e is the velocity at the outer edge of the mixing layer and $\bar{u}$ is the velocity along the "dividing" streamline which passes through the separation point. The ratio $\bar{u}/u_e$ is independent of Mach number and heat transfer (according to the mixing-layer analysis which assumes viscosity to be proportional to temperature).

number and model shape. The ordinate is the pressure rise $|p' - p|$ across the reattachment region divided by the pressure p' just downstream of reattachment; p is measured at an arbitrary fixed point in the separated region. It is noted that some of the pure laminar separations (see left-hand side of fig. 3) are affected to a negligible extent by variation in Reynolds number. This is consistent with the theory which indicates no effect of Reynolds number on those pure laminar separations for which the boundary-layer thickness at separation is zero. Some of these curves show a Reynolds number effect which amounts at the most to only about a one-fourth power variation. In these cases the boundary-layer thickness at separation is not negligible. Generally speaking, though, pure laminar separations are affected only to a small extent by Reynolds number. From the transitional-separation plots shown in the center portion of figure 3, it can be seen, in contradistinction, that these flows can be affected markedly by variation in Reynolds number. Such effects are particularly pronounced when transition is near reattachment, as is the case for the left portion of each curve. Moreover, the effect is in the same direction as required by the theoretical mechanism; namely, a movement of transition upstream of reattachment (brought about by an increase in Reynolds number) increases the pressure rise through the reattachment region. Turning now to the turbulent separations on the right portion of the figure, it is seen that for this type of separation no significant effect of Reynolds number can be discerned from the data.

Although distinction need not be made between subsonic and supersonic separations when considering qualitatively the importance of transition, it is necessary to make such distinction when considering most other aspects of flow separation. There is a basic difference between subsonic and supersonic separation which should be recognized before discussing such questions as what pressure rise will separate a given boundary layer. Figure 4 shows the pressure distribution upstream of a compression corner in subsonic flow at various Reynolds numbers. The dashed line represents the calculated distribution that would exist in inviscid flow. Variation in Reynolds number is seen to bring about only small departures from this distribution. Moreover, the separation point indicated by the filled symbols and the pressure rise to separation are essentially independent of Reynolds number. These results indicate only a minor interaction of boundary layer and external subsonic flow. The situation is quite different in supersonic flow, as first anticipated by Oswatitsch and Wieghardt, and as illustrated in figure 5. These data are for the same model as in figure 4, tested in the same wind tunnel, and investigated over the same Reynolds number range - only at a supersonic Mach number of 2. In this case the dashed line representing pressure distribution in inviscid flow bears little resemblance to the experimental distributions. Moreover, both the location of separation and the pressure rise to supersonic separation depend considerably on the Reynolds number. Such results indicate a dominant interaction of boundary layer and external supersonic flow. It will be seen that local interaction of this type near supersonic separation can dominate the picture to the exclusion, for example, of effects of downstream object shape. Such supersonic separations can be termed "free interactions."

Free interactions are subject only to the boundary-layer equations and the external-flow equations; it turns out that they are amenable to a simple dimensional analysis, the details of which will not be presented. The end result of such analysis, for both laminar and turbulent separation, is that the pressure rise in a free-interaction flow is proportional to the square root of the local skin-friction coefficient existing at the beginning of interaction. Comparison of this theoretical result with experiment is made in figures 6 and 7 for laminar and turbulent separation, respectively. In figure 6, two different pressure rises - the plateau pressure rise and the pressure rise to the laminar separation point - are plotted as a function of Reynolds number for various model shapes. Both are seen to be independent of object geometry inasmuch as four different shapes are represented - a compression corner, a step, a shock reflection, and a curved surface. Such independence would be required of a free interaction. Also the variation in both cases follows closely the theoretical variation as the square root of skin friction, which for laminar flow is a variation as $(Re)^{-1/4}$. Mention is made that for the special case of pressure rise to a laminar separation point, the variation of $(Re)^{-1/4}$ was first calculated by Lees in 1949, although various subsequent analyses - most of which neglect the interaction phenomenon - have obtained different variations. The present experiments cover a wide enough range in Reynolds number (a factor of 50 to 1) under sufficiently controlled conditions to settle finally this question of Reynolds number dependence in two-dimensional, supersonic, laminar separation.

Turning now to free interactions in turbulent flow, it is clear that the square root of turbulent skin-friction coefficient will vary little with Reynolds number, so the pressure rise to turbulent separation also should vary little with Reynolds number. Experimental data confirm this, as shown in figure 7, which includes some data of Gadd obtained at the National Physical Laboratory in England. The trend of data is consistent with the dashed line representing a variation as the square root of turbulent skin-friction coefficient.

In order to simulate in a wind tunnel any flow separation phenomenon of flight, it is necessary that the location of transition relative to reattachment be duplicated. This requirement is especially pertinent to hypersonic-wind-tunnel investigations as a consequence of two results: (1) If a separated laminar mixing layer is relatively stable, transition will occur near reattachment under which condition Reynolds number effects are most pronounced and (2) the stability of a separated mixing layer increases markedly with increasing Mach number. The first of these results has been illustrated previously in figure 3; the second result is illustrated in figure 8. Plotted against Mach number are data points representing the maximum Reynolds number up to which pure laminar type of separations were found under the wind-tunnel conditions of zero heat transfer. The reference length for this Reynolds number is the distance Δx along the separated layer between the reattachment point and the separation point. Consequently, such a Reynolds number measures the stability of a separated laminar mixing layer. It is evident that an increase in Mach number has a pronounced stabilizing effect on the mixing layer. In subsonic flow the separated laminar layer was stable only to about a Reynolds number of 30,000, whereas at Mach numbers near 5 it is stable to a Reynolds number of several million. The shaded area toward the lower right represents the domain of pure laminar separations as found to date in wind tunnels.

For purposes of comparison in figure 8, an analogous boundary is shown which represents the maximum Reynolds numbers of transition reported to date from wind tunnels under comparable conditions of essentially constant pressure and zero heat transfer. The area under this boundary represents the domain of laminar boundary-layer flow under the wind-tunnel conditions. Flight conditions, of course, differ from these; also, it might be expected that experiments in other wind tunnels would yield different curves for the domain of pure laminar separations. Consequently, the detailed position or shapes of these two boundaries should not be weighed too heavily. Instead, the important qualitative trend to note from this figure is that under comparable conditions the stability of a separated laminar mixing layer is encroaching on that of the laminar boundary layer as the hypersonic regime is entered.

Because of this trend, pure laminar separations - which have been primarily laboratory curiosities in the past - might become common practical phenomena in the future. There are several reasons why this trend looks significant and warrants much research effort. One reason, already mentioned, is that it means the Reynolds numbers of hypersonic wind tunnels must match those of flight more closely than has been customary in the past. Another reason is that separated laminar regions have some uncommon characteristics which are intriguing from the viewpoint of opening new possibilities; for example, the skin friction in such regions obviously is a small thrust due to the reversed flow and this is quite nice from the viewpoint of drag. Also, the heat-transfer characteristics would be different from those of a boundary layer. In fact, a recent theoretical calculation, as yet unpublished and untested by experiment, indicates the heat transfer in a laminar mixing layer to be about 0.6 of that in a comparable boundary layer. Such considerations outline what appears to be a profitable and interesting task for future research.

As a final topic for discussion, distinction is made between various types of pressure rise associated with separated flow, and an opinion is given as to their significance for design purposes. Only turbulent separations are considered. Schematically illustrated in figure 9 are three types of pressure rise. Here two flow conditions are depicted for a simple compression corner which can be thought of as a deflected flap. One flow condition, represented by the dashed line, corresponds to pressure distribution when the flow is separated. The other flow condition, represented by the solid line, corresponds to a somewhat smaller flap deflection for which there is no appreciable separated region, but for which the flow is just on the verge of separating. Distinction is made between (1) the pressure rise to the separation point, (2) the peak pressure rise, and (3) the overall configuration pressure rise for incipient separation. The pressure rise to separation is not likely to be of interest to a designer, but would be to a research worker concerned with the mechanism of turbulent separation. The peak pressure rise, on the other hand, would be of interest to a designer concerned with loads, hinge moments, or flap effectiveness. The pressure rise for incipient separation would be of interest to a designer who does not want a flow to separate, yet wants to achieve the maximum pressure rise possible, such as is the case for inlet design. All three types of pressure rise are compared in figure 10. The smallest pressure rise is the pressure rise to the separation point. This is indicated by a single dashed line inasmuch as it is independent of the mode of inducing separation. The peak pressure rise always is greater than the rise to the separation point and depends on the geometry inducing separation (as indicated by the shaded region). The overall pressure rise for incipient separation of a configuration - represented by the curves through data points - also depends on the particular configuration. In fact, this dependence is a strong one. The three sets of data represent shock reflections (taken from Bogdonoff's work), compression corners, and a curved surface. It is realized that these available data on overall pressure rise for incipient turbulent separation are rather meager since geometry is such an important parameter to incipient separation. Consequently, more information along these lines currently is being obtained.

THREE REGIMES FOR A STEP (M = 2.3)

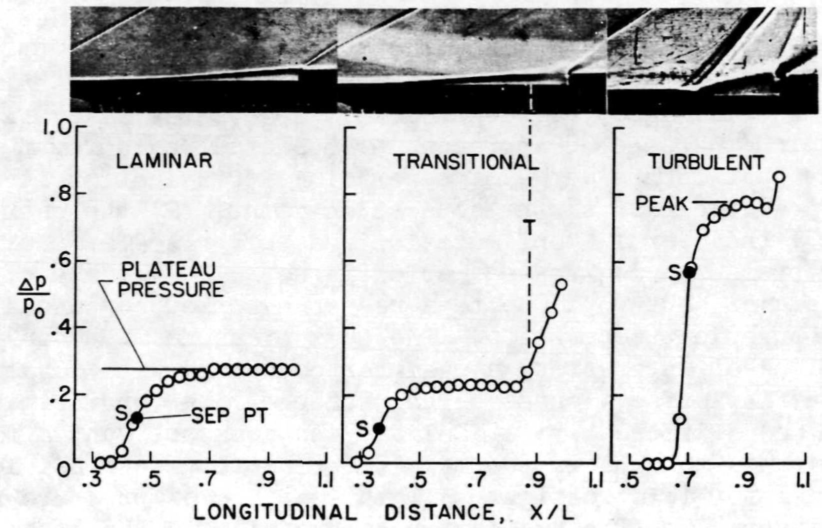

Figure 1

TEST OF THEORY FOR PURE LAMINAR FLOW

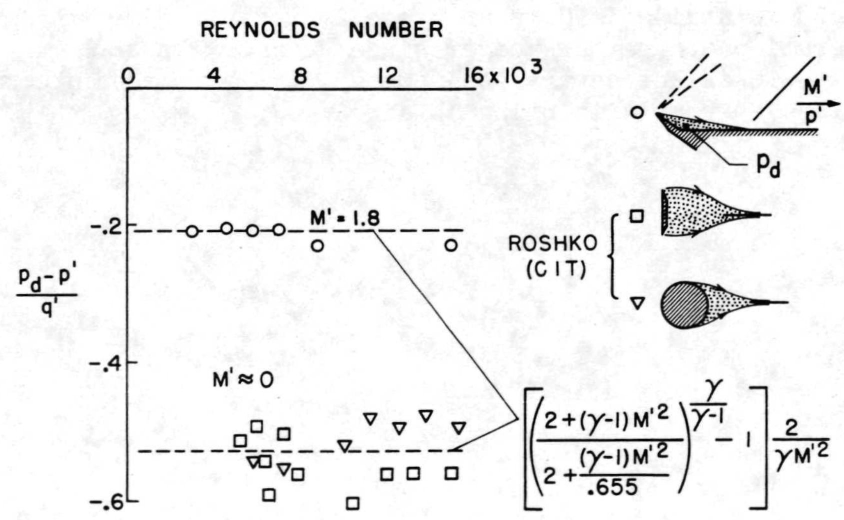

Figure 2

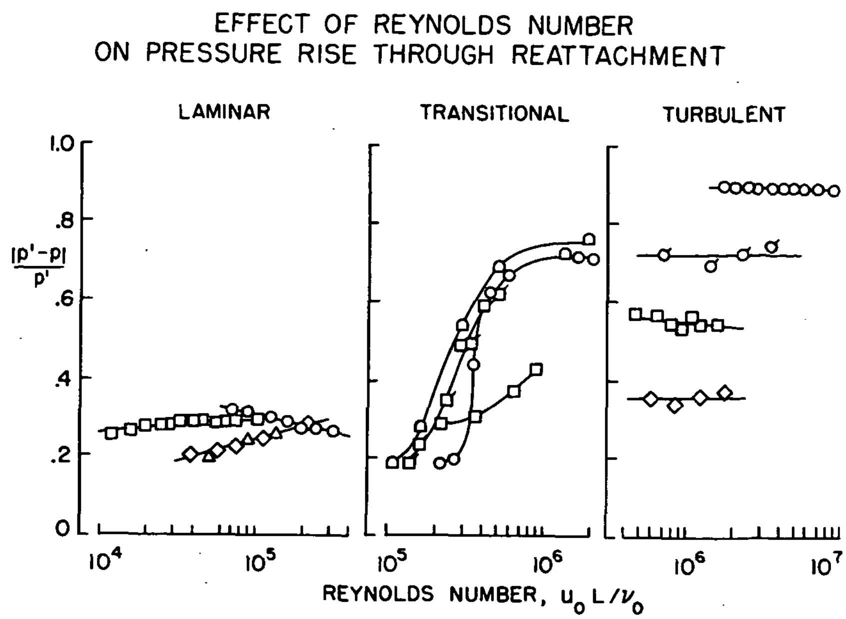

Figure 3

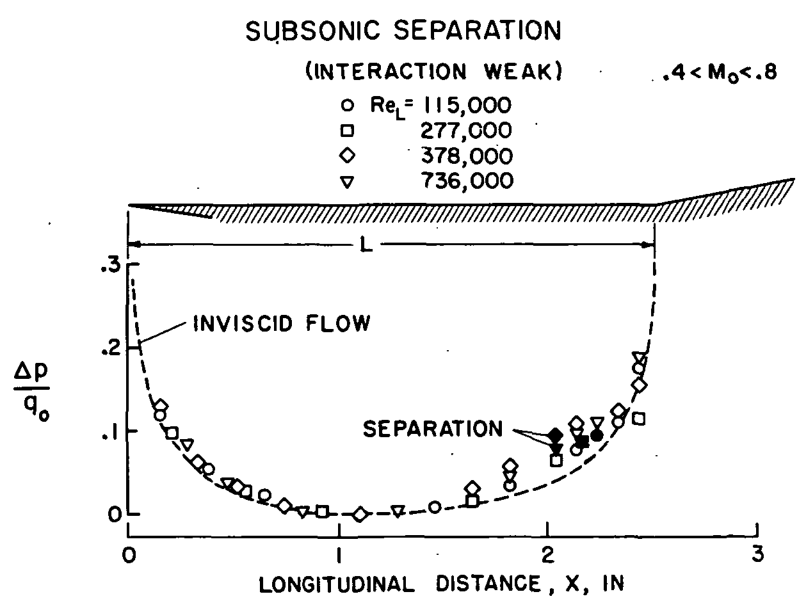

Figure 4

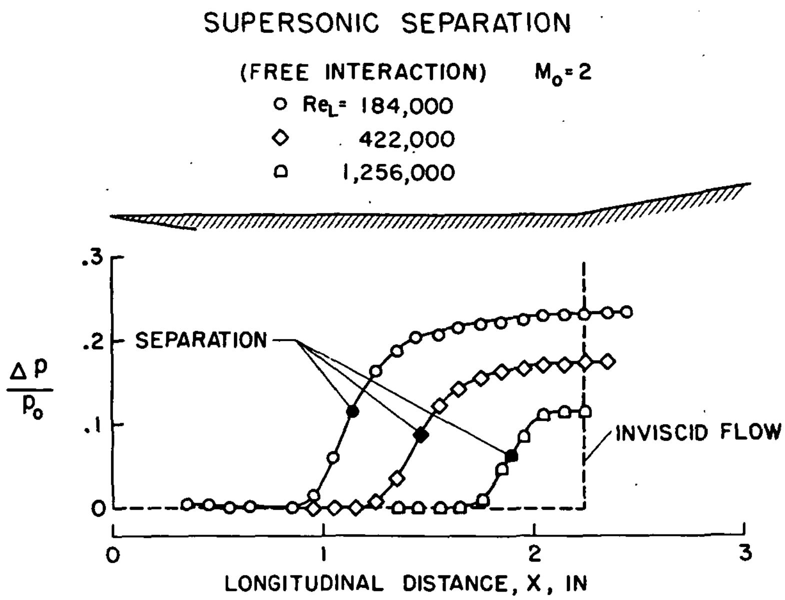

Figure 5

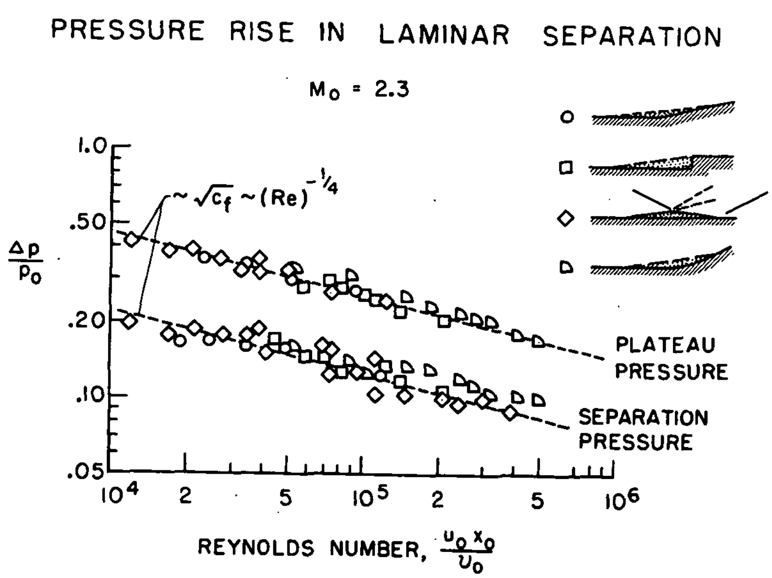

Figure 6

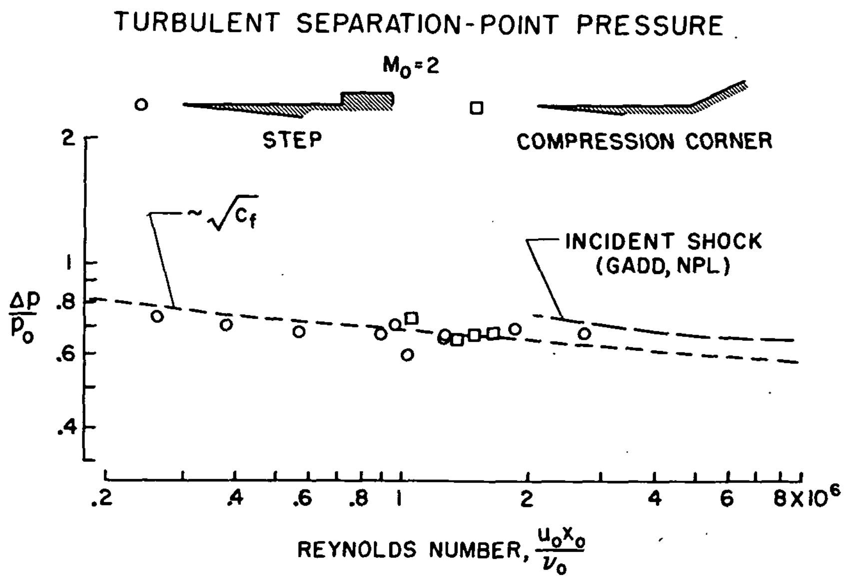

Figure 7

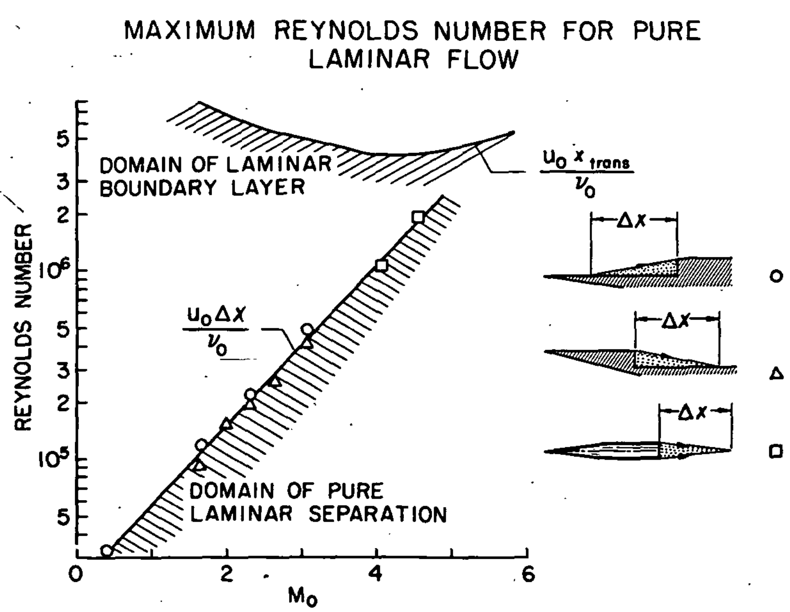

Figure 8

PRESSURE RATIOS ASSOCIATED WITH TURBULENT SEPARATION

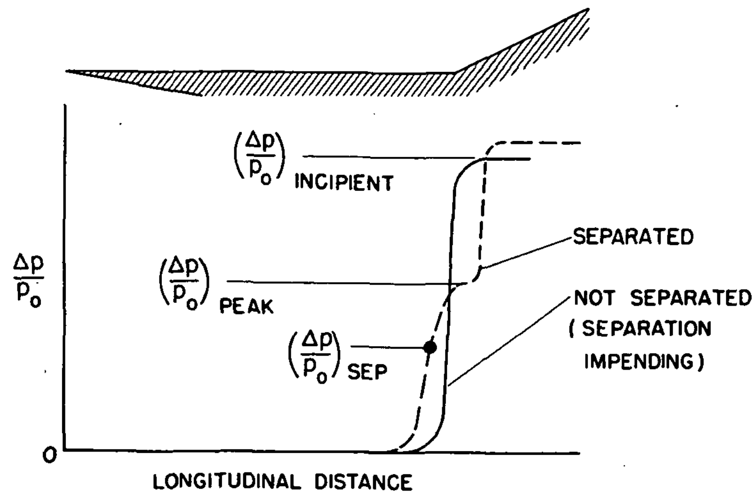

Figure 9

PRESSURE RATIOS FOR TURBULENT SEPARATION

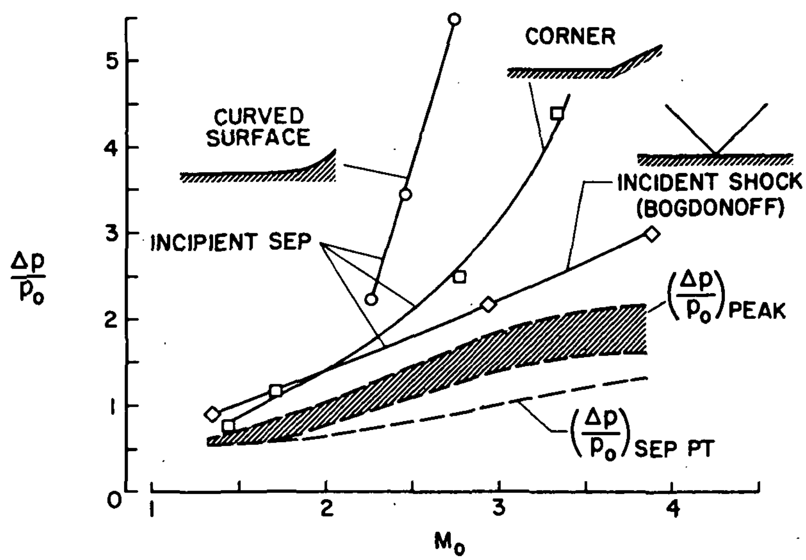

Figure 10

NACA - Langley Field, Va.